

Yassine Slimani  
Essia Hannachi *Editors*

# Superconducting Materials

Fundamentals, Synthesis and  
Applications

 Springer

# Superconducting Materials

Yassine Slimani · Essia Hannachi  
Editors

# Superconducting Materials

## Fundamentals, Synthesis and Applications

 Springer

*Editors*

Yassine Slimani  
Department of Biophysics  
Institute for Research and Medical  
Consultations (IRMC)  
Imam Abdulrahman Bin Faisal University  
Dammam, Saudi Arabia

Essia Hannachi  
Department of Nuclear Medicine Research  
Institute for Research and Medical  
Consultations (IRMC)  
Imam Abdulrahman Bin Faisal University  
Dammam, Saudi Arabia

ISBN 978-981-19-1210-8

ISBN 978-981-19-1211-5 (eBook)

<https://doi.org/10.1007/978-981-19-1211-5>

© The Editor(s) (if applicable) and The Author(s), under exclusive license to Springer Nature Singapore Pte Ltd. 2022

This work is subject to copyright. All rights are solely and exclusively licensed by the Publisher, whether the whole or part of the material is concerned, specifically the rights of translation, reprinting, reuse of illustrations, recitation, broadcasting, reproduction on microfilms or in any other physical way, and transmission or information storage and retrieval, electronic adaptation, computer software, or by similar or dissimilar methodology now known or hereafter developed.

The use of general descriptive names, registered names, trademarks, service marks, etc. in this publication does not imply, even in the absence of a specific statement, that such names are exempt from the relevant protective laws and regulations and therefore free for general use.

The publisher, the authors and the editors are safe to assume that the advice and information in this book are believed to be true and accurate at the date of publication. Neither the publisher nor the authors or the editors give a warranty, expressed or implied, with respect to the material contained herein or for any errors or omissions that may have been made. The publisher remains neutral with regard to jurisdictional claims in published maps and institutional affiliations.

This Springer imprint is published by the registered company Springer Nature Singapore Pte Ltd. The registered company address is: 152 Beach Road, #21-01/04 Gateway East, Singapore 189721, Singapore

# Preface

The research activities in the field of superconductivity have been full of theoretical challenges and practical developments during the last century. It has fascinated scientists during the last period and is continuing to do so. New compositions of superconducting materials with elevated critical transition temperatures are always being discovered, and this is an ongoing matter. Due to the rapid technological developments, superconducting materials, that provide zero resistance to electrical currents and repel the flux lines of magnetic fields, found vast promising applications during recent years. As the research activities in the field of superconductivity are increasing rapidly during recent years, we thought that it is time to evaluate, review, and summarize the fundamental properties, recent progress in superconducting materials, and their potential applications in an exclusive book.

The current book *Superconducting Materials: Fundamentals, Synthesis and Applications* consists of thirteen chapters. It delivers an all-inclusive overview of the sciences of superconducting materials. It covers the superconductivity field from the point of view of fundamentals and theories. Subjects of special interest involving mechanisms of high-temperature superconductors, tunneling, transport properties, magnetic properties, critical states, vortex dynamics, etc., are reported. Furthermore, this book assists as a fundamental resource on the developed methodologies and techniques involved in the synthesis, processing, and characterization of superconducting materials. The book covers numerous classes of superconducting materials including fullerenes, borides, pnictides, or iron-based chalcogen superconductors, alloys, and cuprate oxides. Their crystal structures and properties are described. Thereafter, the book focuses on the progress of the applications of superconducting materials into superconducting magnets, fusion reactors, accelerators, and other superconducting magnets. The applications cover also recent progress in superconducting wires, power generators, powerful energy storage devices, sensitive magnetometers, RF and microwave filters, fast fault current limiters, fast digital circuits, transport vehicles, and medical applications.

We, as Editors, tried to harness our experiences in investigating superconducting materials and their potential applications to prepare this book and we hope that it will contribute significantly to the service of the scientific community. We take

this opportunity to thank all authors for their valuable contributions. We greatly appreciate their commitment. We are also thankful to the Institute for Research and Medical Consultations (IRMC) at Imam Abdulrahman Bin Faisal University (Dammam—Saudi Arabia) for its endless supports.

Dammam, Saudi Arabia

Yassine Slimani  
Essia Hannachi

# Contents

<b>Superconductivity Phenomenon: Fundamentals and Theories</b> .....	1
Zayneb Trabelsi, Essia Hannachi, Sarah A. Alotaibi, Yassine Slimani, Munirah A. Almessiere, and Abdulhadi Baykal	
<b>Transport Properties of Superconducting Materials</b> .....	29
Ahmet Ekicibil, Faruk Karadağ, Selda Kılıç Çetin, Ali Osman Ayaş, Gönül Akça, Mustafa Akyol, and Doğan Kaya	
<b>Magnetic Properties of Superconducting Materials</b> .....	61
Michael R. Koblishka and Anjela Koblishka-Veneva	
<b>Mechanical Properties of Superconducting Materials</b> .....	89
Essia Hannachi and Yassine Slimani	
<b>Type I and Type II Superconductivity</b> .....	123
Siti Fatimah Saipuddin, Azhan Hashim, and Nurbaisyatul Ermiza Suhaimi	
<b>Classical Superconductors Materials, Structures and Properties</b> .....	147
Michael R. Koblishka and Anjela Koblishka-Veneva	
<b>High-<math>T_c</math> Cuprate Superconductors: Materials, Structures and Properties</b> .....	181
Anjela Koblishka-Veneva and Michael R. Koblishka	
<b>Noncuprate Superconductors: Materials, Structures and Properties</b> .....	211
Soubhik Bhattacharyya and P. M. Sarun	
<b>Design of Cuprate HTS Superconductors</b> .....	239
Devendra K. Namburi and David A. Cardwell	
<b>Fabrication Technologies of Superconducting Cables and Wires</b> .....	271
Yassine Slimani and Essia Hannachi	

**Progress in Superconducting Materials for Powerful Energy Storage Systems** ..... 301  
Essia Hannachi, Zayneb Trabelsi, and Yassine Slimani

**Rotating Machines Based on Superconducting Materials** ..... 339  
Abdurrahman Erciyas, Şükrü Yıldız, and Fedai Inanir

**RF and Microwave Applications of High Temperature Superconductors** ..... 373  
Essia Hannachi and Yassine Slimani



# Editors and Contributors

## About the Editors

**Yassine Slimani** is a Senior Researcher at the Institute for Research and Medical Consultations (IRMC) at Imam Abdulrahman Bin Faisal University (Saudi Arabia). He has completed his Ph.D. degree in Materials Physics and Applications from the Faculty of Sciences of Bizerte, University of Carthage (Tunisia) in 2015. His main current research activities cover Superconductors, Advanced nanomaterials, Magnetism, Ceramics, Magnetolectric composites, Multiferroic materials, Dielectric materials, Semiconductors, Energy storage systems (Supercapacitors, Batteries, Fuel cells), Green Production, etc. He is interested in energy, technological, biological, and environmental applications of these materials. Until today, Dr. Yassine Slimani published more than 260 papers in peer-reviewed international journals, over than 20 books and book chapters, and several US patents of his innovations. He participated in numerous international and national scientific conferences by making different presentations and sharing many sessions. Dr. Yassine has been also involved in many international and national research projects, as principal investigator and co-investigator. Dr. Yassine has been selected as one of the “Top 2% world’s ranking scientists” starting from the year of 2019. He received several other awards such as “Top 10 Highly Published Faculty in IAU - 2020” and “Top 10 Highly Cited Faculty in IAU - 2020” in the University President’s List of Distinguished Researchers released in 2021 by Imam Abdulrahman Bin Faisal University (Saudi Arabia), “The Best Achievement in Publication” in 2018 from the Institute for Research and Medical Consultations (IRMC, Saudi Arabia), “Young Scientist in Nanotechnology” in 2018 from 4th Venus International Research Awards - VIRA 2018 (India). Dr. Yassine serves as an editor and reviewer for many well-known reputed journals (in Elsevier, Springer, Wiley, RSC, MDPI, Bentham, ACS, IEEE, World Scientific Publishing, etc.). He won the “Top Peer Review 2019” award as the top 1% of reviewers in Physics on Publons global reviewer databases during the year 2018-2019 powered by Publons and Web of Science Groups.

**Essia Hannachi** is a doctor in Physics from the Faculty of Sciences of Bizerte, University of Carthage (Tunisia). She is working as Visiting Scientist at Imam Abdulrahman Bin Faisal University (Saudi Arabia) and as a Researcher at University of Carthage (Tunisia). Her research focuses on various advanced nanomaterials and their potential and real-life applications. The primary task of her scientific publications is studying the physical properties (as electrical, magnetic, dielectric, and mechanical) of diverse types of ceramics including, superconductor materials, ferroelectric, multiferroic materials, and magnetoelectric composites. Dr. Essia Hannachi has to her credit numerous articles in international refereed journals. She has contributed as an author to several book chapters. She was also a reviewer for several prestigious journals in the field of material science and technology. She participated in several arbitration committees for a number of international institutions and organizations.

## Contributors

**Gönül Akça** Department of Physics, Faculty of Science and Art, University of Çukurova, Adana, Turkey

**Mustafa Akyol** Department of Materials Science and Engineering, Faculty of Engineering, Adana Alparslan Türkeş Science and Technology University, Adana, Turkey

**Munirah A. Almessiere** Department of Biophysics, Institute for Research & Medical Consultations (IRMC), Imam Abdulrahman Bin Faisal University, Dammam, Saudi Arabia;  
Department of Physics, College of Science, Imam Abdulrahman Bin Faisal University, Dammam, Saudi Arabia

**Sarah A. Alotaibi** Department of Biophysics, Institute for Research & Medical Consultations (IRMC), Imam Abdulrahman Bin Faisal University, Dammam, Saudi Arabia

**Ali Osman Ayaş** Department of Physics, Faculty of Science and Art, University of Adiyaman, Adiyaman, Turkey

**Abdulhadi Baykal** Department of Nanomedicine Research, Institute for Research & Medical Consultations (IRMC), Imam Abdulrahman Bin Faisal University, Dammam, Saudi Arabia

**Soubhik Bhattacharyya** Department of Physics, Indian Institute of Technology (Indian School of Mines), Dhanbad, Jharkhand, India

**David A. Cardwell** Department of Engineering, University of Cambridge, Cambridge, UK

**Selda Kılıç Çetin** Department of Physics, Faculty of Science and Art, University of Çukurova, Adana, Turkey

**Ahmet Ekicibil** Department of Physics, Faculty of Science and Art, University of Çukurova, Adana, Turkey

**Abdurrahman Erciyas** Department of Physics, Science and Faculty, Yildiz Technical University, Istanbul, Turkey

**Essia Hannachi** Department of Nuclear Medicine Research, Institute for Research & Medical Consultations (IRMC), Imam Abdulrahman Bin Faisal University, Dammam, Saudi Arabia

**Azhan Hashim** Faculty of Applied Sciences, Universiti Teknologi MARA (UiTM) Jengka Campus, Bandar Tun Abdul Razak, Pahang, Malaysia

**Fedai Inanir** Department of Physics, Science and Faculty, Yildiz Technical University, Istanbul, Turkey

**Faruk Karadağ** Department of Physics, Faculty of Science and Art, University of Çukurova, Adana, Turkey

**Doğan Kaya** Department of Electronics and Automation, Vocational School of Adana, University of Çukurova, Adana, Turkey

**Anjela Koblichka-Veneva** Experimental Physics, Saarland University, Saarbrücken, Germany

**Michael R. Koblichka** Experimental Physics, Saarland University, Saarbrücken, Germany

**Devendra K. Namburi** Department of Engineering, University of Cambridge, Cambridge, UK;  
Electronic and Nanoscience Engineering, University of Glasgow, Glasgow, UK

**Siti Fatimah Saipuddin** Faculty of Applied Sciences, Universiti Teknologi MARA (UiTM) Jengka Campus, Bandar Tun Abdul Razak, Pahang, Malaysia;  
Faculty of Applied Sciences, Universiti Teknologi MARA (UiTM), Shah Alam, Selangor, Malaysia

**P. M. Sarun** Department of Physics, Indian Institute of Technology (Indian School of Mines), Dhanbad, Jharkhand, India

**Yassine Slimani** Department of Biophysics, Institute for Research & Medical Consultations (IRMC), Imam Abdulrahman Bin Faisal University, Dammam, Saudi Arabia

**Nurbaisyatul Ermiza Suhaimi** Faculty of Applied Sciences, Universiti Teknologi MARA (UiTM), Shah Alam, Selangor, Malaysia

**Zayneb Trabelsi** Department of Physics, Faculty of Sciences Bizerte, University of Carthage, Bizerte, Tunisia

**Şükrü Yıldız** Department of Metallurgical and Materials Engineering, Faculty of Engineering and Architecture, Ahi Evran University, Kırşehir, Turkey

# Superconductivity Phenomenon: Fundamentals and Theories



Zayneb Trabelsi, Essia Hannachi, Sarah A. Alotaibi, Yassine Slimani,  
Munirah A. Almessiere, and Abdulhadi Baykal

**Abstract** Since their discovery, superconductor materials have been the subject of extensive studies thanks to their original properties. Such materials are endowed by zero resistance at a low temperature making it possible to conduct the electric current without loss of energy. In addition, magnetic fields are deeply affected in superconductors, they can be canceled completely in the material, or they can be pinned in a so-called mixed zone where both superconducting and normal states co-exist. Thus, thorough knowledge of the phenomena which occur within these materials is very necessary to enlarge their fields of integration. According to BCS theory, the superconductivity phenomenon in low-temperature Superconductors (LTS) originates from the pairing of electrons through phonons. Thus, researchers try to explain superconductivity in HTS materials which helps to improve the performance of applications that use superconductors. Although the LTS materials are exploited intensively in many areas, the problem of cryogenics still faces their industrial emergence. The manipulation of superconductors cooled with liquid nitrogen (77 K) instead of

---

Z. Trabelsi

Department of Physics, Faculty of Sciences of Bizerte, University of Carthage, 7021 Bizerte, Tunisia

E. Hannachi (✉)

Department of Nuclear Medicine Research, Institute for Research & Medical Consultations (IRMC), Imam Abdulrahman Bin Faisal University, P.O. Box 1982, Dammam 31441, Saudi Arabia

e-mail: [hannechi.essia@gmail.com](mailto:hannechi.essia@gmail.com)

S. A. Alotaibi · Y. Slimani (✉) · M. A. Almessiere

Department of Biophysics, Institute for Research & Medical Consultations (IRMC), Imam Abdulrahman Bin Faisal University, P.O. Box 1982, Dammam 31441, Saudi Arabia

e-mail: [slimaniyassine18@gmail.com](mailto:slimaniyassine18@gmail.com); [yaslimani@iau.edu.sa](mailto:yaslimani@iau.edu.sa)

M. A. Almessiere

Department of Physics, College of Science, Imam Abdulrahman Bin Faisal University, P.O. Box 1982, Dammam 31441, Saudi Arabia

A. Baykal

Department of Nanomedicine Research, Institute for Research & Medical Consultations (IRMC), Imam Abdulrahman Bin Faisal University, P.O. Box 1982, Dammam 31441, Saudi Arabia

liquid helium (4.2 K) opens up market opportunities for high-temperature superconductivity technology. Works devoted to improving the critical temperature in view of reaching room temperature superconductivity are in permanent progression.

**Keywords** Superconductors · Perfect diamagnetic · Cooper pairs · Transition temperature · Order parameter

## 1 Introduction

Electrical conduction is a very precious natural phenomenon that caught the attention of researchers who have worked hard on this subject to provide clear explanations of the mechanisms that occur within materials. They found that this property is intimately related, according to quantum physics, to how electrons or electric currents move through the sample. The materials are then classified into three categories ranging from perfect conductors of electrical current to insulators that do not conduct electricity at all; the intermediate case is preserved for semiconductors. However, after having liquefied the helium, research has been directed towards a new axis that aims primarily to investigate the behavior of electrical resistivity in materials at very low temperatures. This research led to the discovery of the unexpected phenomenon of superconductivity. Vanishing of electrical resistivity and expulsion of the magnetic field from a material are the principal characteristics of superconductors. They also feature a hugely high current carrying density, very low resistance at power frequencies, and high sensitivity to the magnetic field. All these specifications make superconductivity the origin of new commercial devices that are altering our economy and everyday life. Superconductor materials make it possible to propagate considerable electrical currents without energy dissipation. In these materials, it is also possible to store electricity without loss in a long term and exploit the intense magnetic fields surrounding them to allow the levitation of strong metallic charges and to move them without mechanical friction.

This chapter aims to provide the essential bases for understanding the phenomena which take place within superconductor materials. We first give a simple description of the development of these materials since their discovery, recalling their strange properties and the theories which explain them. We then underline the particularity of type II superconductors compared to those of type I. Finally, special attention is devoted to following the latest advancements in the world of superconductivity which aim to improve the performance of these materials.

## 2 Discovery and Chronological Development

### 2.1 Zero Electrical Resistance (1911)

Cooled below a certain temperature, often referred to as transition temperature or critical temperature (denoted  $T_c$ ), various materials get in a superconducting state and exhibit zero resistance to the crossing of electrical current. This phenomenon was discovered in 1911 by the Dutch physicist Onnes [1]. His discovery was a consequence of previous studies investigating the effect of temperature on electrical conduction mechanisms in metals. Indeed, after the success in the liquefaction of helium, the variation of electrical resistance with temperature in metals constituted a research problem to resolve. It was demonstrated that around room temperature, resistivity varies linearly with temperature. However, this behavior can look different at low temperatures. So there, some predictions have been proposed whose schematic illustration is provided in Fig. 1. According to J. Dewar, the electrical resistance proceeds to linearly decrease with temperature heading toward zero. While L. Kelvin predicted that it could reach a minimum and rise again at low temperature. On another side, Matthiessen believed that resistivity can stabilize at a limit value.

This difference in opinions pushed Onnes to better understand the behavior of the resistivity at absolute zero. For his investigation, he used mercury (Hg) as a sample, because of its low melting and boiling temperatures and its very low impurity levels. In 1911, when he was studying the behavior of electrical resistance of pure Hg with respect to temperature, he found that Hg's resistance drops abruptly to zero below 4.2 K ( $-269^\circ\text{C}$ ) [1] which is the temperature of liquid helium. Then, he appreciates that below 4.2 K the Hg passed to a new state of matter named superconductivity. The historic plot of the first superconducting state observation published by K. Onnes is depicted in Fig. 2 [2]. This unexpected finding ignored all the last predictions.

K. Onnes has then realized the possibilities offered by the zero-resistance property. For example, it is possible to circulate a permanent electric current in a superconducting ring by looping the sample around itself. After this discovery, K. Onnes

**Fig. 1** The resistivity-temperature behavior at very low temperature as predicted by Dewar, Kelvin, and Matthiessen

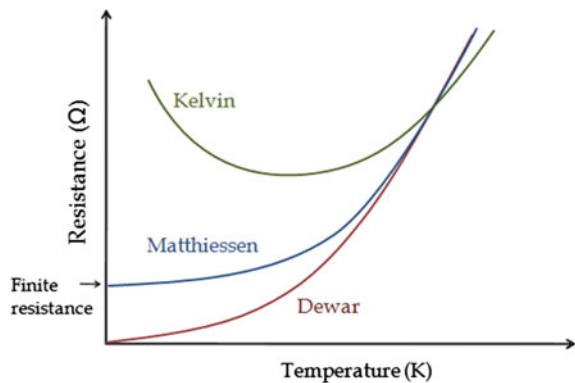
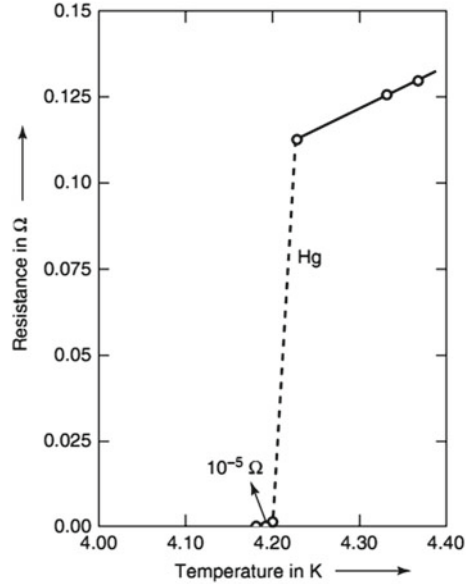


**Fig. 2** Historic plot of the dependence of mercury's resistance ( $\Omega$ ) on temperature (K) shows the superconducting transition at 4.2 K (October 1911)



continued his research by large amounts of experimental studies. Soon he extended the list of superconductors by Sn ( $T_c = 3.7\text{K}$ ) and Pb ( $T_c = 7.2\text{K}$ ). In addition, he demonstrates that adding impurity did not destroy superconductivity and such phenomenon is an intrinsic property of materials. Since then, the history of superconductivity began and the most of chemical elements are marked superconducting at a fairly low temperature.

## 2.2 Meissner Effect, Perfect Diamagnetism (1933)

In contrast to what was believed for many years, superconductivity is more than just the disappearance of resistance. This has been proven in 1933 by the discovery of an interesting phenomenon called the Meissner effect [3] showing that a superconductor is extremely diamagnetic, i.e., it highly expels all magnetic fields that would normally flow through. We give here a simple explanation of this phenomenon. At temperatures above  $T_c$ , a superconductor under an external magnetic field behaves exactly like a normal metal, meaning that a finite magnetic field resides within the material. By decreasing the temperature and keeping the applied magnetic field, the sample expels the magnetic field from its interior at the superconducting transition. This observation is unexpected because it is known that a perfect conductor maintains its interior magnetic field without expelling it. The electric voltage is zero ( $E = 0$ ), for an ideal conductor. Thus, in accordance with Maxwell equation:



$$\vec{\nabla} \times \vec{E} = -\frac{\partial \vec{B}}{\partial t} \tag{1}$$

Since  $E = 0 \rightarrow \frac{\partial B}{\partial t} = 0 \rightarrow B = \text{constant}$ .

Thus, the magnetic flux within the superconductor must be constant. However, Meissner and Ochsenfeld have shown the opposite. They observed that the magnetic flux is completely ejected from the interior of the superconducting material when it is cooled below  $T_c$ . The drawing in Fig. 3 illustrates the Meissner effect. In this way, the superconductor behaves both as an ideal conductor and a perfect diamagnetic for  $T < T_c$ .

Such magnetic field expulsion comes from the fact that the screening currents running along the superconductor surface induce an opposing magnetic field that cancels any exterior ones. Consequently, a superconductor material repels all magnetic objects with an opposing and balanced magnetic field. These objects are then levitating. Such a prominent phenomenon is called magnetic levitation that can be described as a magnet placed above a superconductor pellet cooled by liquid nitrogen floats because the superconductor creates a magnetic field opposite to that of the magnet.

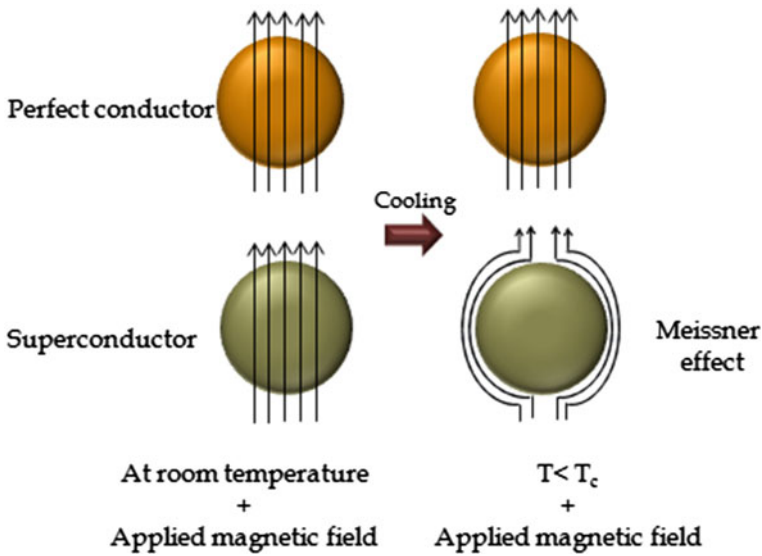


**Fig. 3** Description of the Meissner effect. A superconductor sample in a constant applied magnetic field excludes the magnetic flux when it is cooled below its critical temperature  $T_c$

### 2.3 Critical Parameters

While trying to generate high magnetic fields without losing energy, K. Onnes found that the Meissner effect is suppressed when the superconductor material is subjected to a low magnetic field. He realized that each material has its critical magnetic field  $B_c$ , above which the superconductivity is destroyed. As shown in Fig. 4a, the dependence of  $B_c$  on temperature depicts a parabolic behavior expressed as follows [4]:

$$B_c(T) = B_0 \left[ 1 - \left( \frac{T}{T_c} \right)^2 \right] \quad (2)$$

It is clear that  $B_c$  is maximum ( $B_c = B_0$ ) at  $T = 0$ , then it drops to 0 at  $T = T_c$ . It is then possible to convert a metal from the superconducting state to the normal state by increasing either the temperature or the magnetic field.

In addition to these two parameters ( $B_c$  and  $T_c$ ), Silsbee [5] demonstrated that the electric current that can be carried by a superconductor without resistance has a limit. Beyond a critical current density denoted  $J_c$ , the material ceases to be a superconductor and begins to dissipate energy. These three parameters are interdependent. They delimit a critical surface, shown in Fig. 4b, outside which the superconductor returns to its normal state, i.e., if one of these parameters is exceeded, the superconductivity will be destroyed.

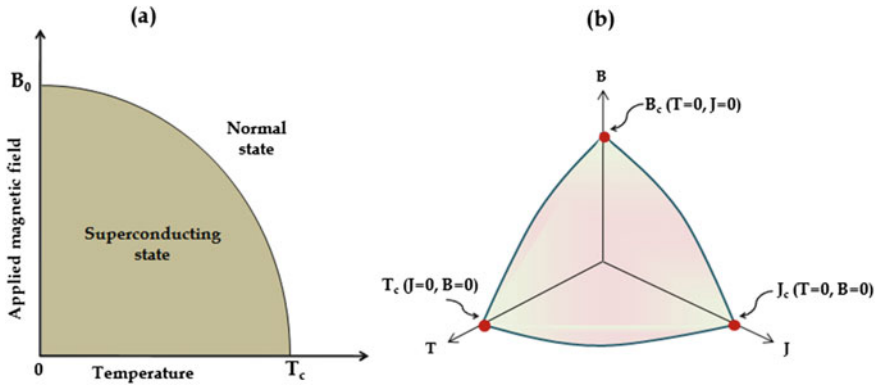


**Fig. 4** **a** The dependence of applied magnetic field on temperature shows a parabolic curve separating between the normal state and the superconducting state. **b**  $B$ - $T$ - $J$  characteristic showing the superconducting area

## 2.4 London Theory and Penetration Length (1935)

In 1935, London brothers (Fritz and Heinz London) [6] succeeded to give the first phenomenological equations for superconducting metals that explain the Meissner effect and predicted the existence of an electromagnetic penetration length (denoted  $\lambda_L$ , informing how deep a magnetic field could be across a superconductor). After few years, in 1939, their prediction was confirmed experimentally. London brothers came up with other phenomenological equations when they realized that Maxwell equations are insufficient to explain the phenomenon of superconductivity. They assumed that the superconducting current is carried by free charges. Thus, their first equation applies the fundamental law of dynamics to free charges in the presence of a constant electric field such as [4, 7]:

$$\frac{d\vec{j}}{dt} = \frac{n_e e^2}{m_e} \vec{E} \quad (3)$$

where  $n_e$  is the electron density,  $e$  denote the electron charge and  $m_e$  is the electron mass. Using the local Maxwell equation in a conductive medium  $\vec{rot} \vec{E} = -\frac{d\vec{B}}{dt}$  and applying the rotational operator to Eq. 3, one finds [4, 7]:

$$\vec{rot} \left( \frac{d\vec{j}}{dt} \right) = -\frac{n_e e^2}{m_e} \left( \frac{d\vec{B}}{dt} \right) \quad (4)$$

Applying the rotational operator again to Eq. 3, one gets [4, 7]:

$$\vec{rot} \vec{rot} \left( \frac{d\vec{j}}{dt} \right) = -\frac{n_e e^2}{m_e} \frac{d}{dt} \vec{rot} \vec{B} \quad (5)$$

By relying on vector operators and the fourth Maxwell equation in stationary regime, one finds [4, 7]:

$$\Delta \left( \frac{d\vec{j}}{dt} \right) = \frac{\mu_0 n_e e^2}{m_e} \left( \frac{d\vec{j}}{dt} \right) = \frac{1}{\lambda_L^2} \left( \frac{d\vec{j}}{dt} \right) \quad (6)$$

where  $\mu_0$  is the permeability. Thus, a homogeneous term at a length appears denoted by  $\lambda_L$  and given as follow [4, 7]:

$$\lambda_L = \sqrt{\frac{m_e}{\mu_0 n_e e^2}} \quad (7)$$

$\lambda_L$ , called London penetration depth, is a specific length of superconductors defining the thickness over which the magnetic field penetrates the material. The

equations governing the spatial evolution of the temporal derivatives of  $\vec{B}$  and  $\vec{j}$  are given by [7]:

$$\Delta \left( \frac{d\vec{B}}{dt} \right) = \frac{1}{\lambda_L^2} \left( \frac{d\vec{B}}{dt} \right) \quad (8)$$

$$\Delta \left( \frac{d\vec{j}}{dt} \right) = \frac{1}{\lambda_L^2} \left( \frac{d\vec{j}}{dt} \right) \quad (9)$$

To establish their second equation, the London brothers proposed to replace the temporal variation  $\left( \frac{d\vec{B}}{dt} \right)$  and  $\left( \frac{d\vec{j}}{dt} \right)$  by  $\vec{B}$  and  $\vec{j}$  respectively, which results in the following equations [7]:

$$\Delta \vec{B} = \frac{1}{\lambda_L^2} \vec{B} \quad (10)$$

$$\Delta \vec{j} = \frac{1}{\lambda_L^2} \vec{j} \quad (11)$$

Equations (Eqs. 10) and (11) make it possible to obtain the second London equation given by [4, 7]:

$$\mu_0 \text{rot} \vec{j} = -\frac{1}{\lambda_L^2} \vec{B} \quad (12)$$

Considering a superconductor material occupying the half-space ( $x > 0$ ) of an infinitely large superconducting surface located at  $x = 0$ . The solution to Eq. 10 which reproduces the Meissner effect is given by [4, 7]:

$$B(x) = B_0 \exp\left(-\frac{x}{\lambda_L}\right) \quad (13)$$

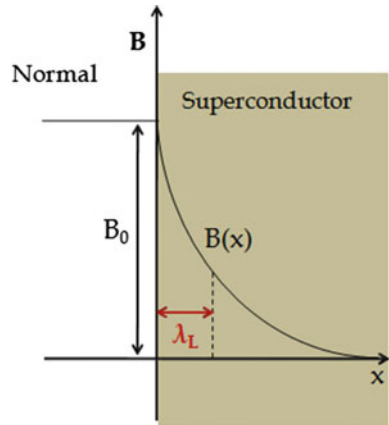
As displayed in Fig. 5, the density of the magnetic flux  $B$  decreases exponentially over a depth  $\lambda_L$ , then vanishes deep inside the superconductor.

## 2.5 Ginzburg-Landau Theory and Coherence Length (1950)

### 2.5.1 Concept of Coherence Length

The estimated London penetration depth  $\lambda_L$  has always been found to be less than that experimentally measured. To explain this difference between theory and experience, Pippard [8] postulated another characteristic length called coherence length

**Fig. 5** Exponential decrease of the magnetic flux  $B$  with distance  $x$  into a superconductor



$\xi$ . Indeed, London’s theory assumed that the superconductor electrons density  $n_s$  suddenly passes from 0 to its value inside the superconductor. However, Pippard estimated that the superconducting-normal transition of  $n_s$  must progress slowly over a finite distance called the coherence length such that its maximum value  $\xi_0$  is reached at 0 K for a pure metal.  $\xi_0$  represents a veritable intrinsic property of superconducting materials. When increasing the temperature,  $\xi$  decreases as and drops to 0 for  $T = T_c$ . Note that  $\xi$  depends on the purity of the metal due to its proportionality to the mean free path  $\uparrow_e$  [4]:

$$\xi = (\xi_0 \ell_e)^{1/2} \tag{14}$$

Thus, for non-pure metals,  $\xi$  is shorter and it is of the order of  $\uparrow_e$  at the high level of impurity. The value of  $\xi_0$  can be estimated according to the following relation [4]:

$$\xi_0 = 0.18 \frac{\hbar v_F}{k_B T_c} \tag{15}$$

$\hbar = h/2\pi$  where  $h$  is the Planck constant,  $v_F$  is the Fermi velocity and  $k_B$  is the Boltzmann constant.

### 2.5.2 Ginsburg-Landau Theory

A generalization of the London theory was established by V. Ginsburg and L. Landau in 1950, known as the Ginsberg-Landau theory [9]. This new phenomenological theory, valid only near  $T_c$ , appears as an extension of Landau’s model of second-order phase transitions. Indeed, the reversibility of the Meissner effect makes it possible to consider superconductivity as a phase transition. In their approach, Ginsburg and Landau described the superconducting state by a complex wave function or order

parameter  $\Psi(r) = |\Psi(r)|e^{i\varphi(r)}$  whose square of the norm  $|\Psi(r)|^2$  is related to the density of the superconductor charge carriers,  $n_s$ .  $\varphi$  is the phase. The model must take into account, on the one hand, the dynamics of the superconductor. The order parameter can vary according to the regions of the material and therefore a kinetic term must be inserted in the formula of the free energy. On the other hand, the order parameter depends on the surrounding magnetic field which can destroy the superconducting phase. The order parameter must be coupled to the magnetic field via the electromagnetic potential  $A$ . It is then possible to write the free energy, near  $T_c$ , in power series expansion of  $\Psi(r)$  as follows [4].

$$F(\Psi(r)) = \int a|\Psi(r)|^2 + \frac{b}{2}|\Psi(r)|^4 + d\xi^2|\nabla\Psi(r) - (ie^*/\hbar)A\Psi(r)|^2 + \frac{1}{2}\mu_0 \int |B(r)|^2 dr \quad (16)$$

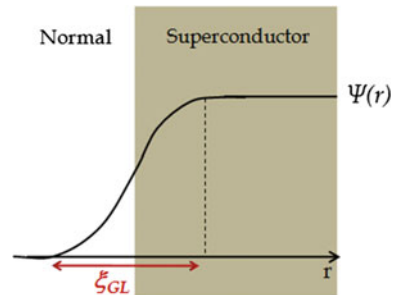
where  $e^*$  was estimated to be equal to  $2e$  according to the microscopic theory (formation of Cooper pairs  $e^* = 2e$  (see Sect. 2.6)). The coefficients  $a$ ,  $b$  and  $d$  represent the energy density terms.  $a$  is assumed to be temperature-dependent satisfying the following relation [4]:

$$a = a_0[(T - T_c)/T_c] \quad (17)$$

while  $b$  and  $d$  are assumed to be temperature independent. The quantity  $\xi$  has the dimension of length determining the distance over which  $\Psi(r)$  varies. The last term represents the contribution of the magnetic field to the free energy density. As a consequence, a second characteristic length of superconductivity results from this theory which is the coherence length often referred to as Ginsburg-Landau coherence length  $\xi_{GL}$ . It is interpreted as the minimum distance necessary for the variation of the superconductor electrons density (see Fig. 6). It is given by [4]:

$$\xi_{GL} = \frac{\hbar}{|2m^*a(T)|^{1/2}} \quad (18)$$

**Fig. 6** Spatial extent of the order parameter  $\Psi(r)$  over a consistent length  $\xi_{GL}$



For a pure superconductor close to 0 K,  $\xi_{GL} = \xi_0$  (Pippard coherence length). When  $T \rightarrow T_c$ ,  $\xi_{GL}$  approach infinity. Following the addition of impurities to the superconductor, the mean free path decreases resulting in a reduction of the coherence length.

Furthermore, Ginzburg and Landau have also introduced in their theory a parameter called the Ginzburg-Landau parameter

$$\kappa = \frac{\lambda_L}{\xi_{GL}} \quad (19)$$

It characterizes superconductors and allows to classify them into two kinds: type I and type II superconductors. We come back in detail on these two types of superconductors in Sect. 3.2.

Although the Ginzburg–Landau theory attempted to explain superconductivity and provided derivation for the London equations, it was not accepted by the scientific community, and it was not until the BCS theory that it was fully recognized.

## 2.6 BCS Theory (1957)

The superconductivity phenomenon was still quite mysterious as to its microscopic origin until 1957. In that year, the trio John Bardeen, Leon N. Cooper and John Robert Schrieffer of the United States developed the first fully quantum theory, BCS theory, which successfully explains the microscopic behavior of superconductivity in metals and alloys [10] and won them a Nobel prize in 1972. This theory reposes primarily on an earlier discovery by L. Cooper who proclaimed that the attractive electron–electron interaction through an interchange of virtual phonons (lattice vibration) gives birth to Cooper pair. They have bound states formed by two electrons of opposite spins and momenta. Such attractive interaction takes place when the energy separating the electronic states is smaller than the phonon energy  $\hbar\omega$  around the Fermi level  $E_F$ . The process of forming Cooper pairs is shown and explained in Fig. 7. The spatial extent of a Cooper pair is given by the coherence length  $\xi$ , much greater than the interatomic distance of the lattice. In a superconductor, electrons mate in Cooper pairs moving correlatively and without friction within the solid thus forming a coherent macroscopic ground state defined by a collective wave of phase  $\varphi$  as postulated by Ginzburg-Landau. This means that it is impossible to modify one pair without modifying the state of all the others. The quantum nature of the resulted wave allows to understand all the properties of superconductors and to predict the behavior of their characteristic quantities.

The electron–electron attractive interaction mediated by phonon gives rise to a gap energy  $\Delta$  between the BCS ground state and the excited states. This gap is at the origin of exceptional properties, whether optical or electromagnetic, in these materials. The gap energy for a classic superconductor, displayed in Fig. 8, is given by [10]:

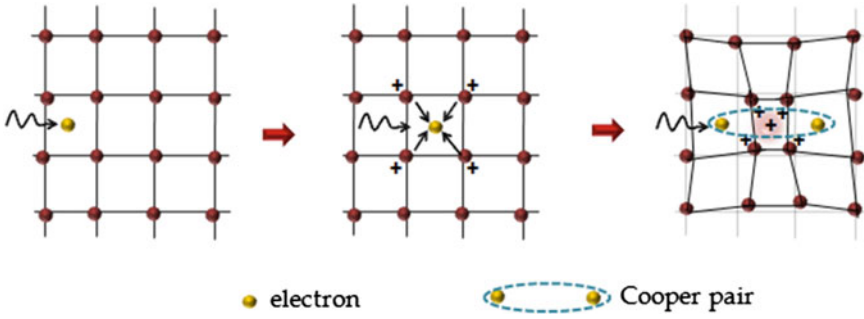


**Fig. 7** Cooper pair formation. When an electron crosses a crystal lattice, the ions will be attracted by its negative charge allowing them to move slightly and cause a lattice deformation. This leads to the emission of phonons generating a positively charged zone which will attract another electron. Thus, two electrons, which would normally repel each other, are indirectly attracted and linked forming a Cooper pair

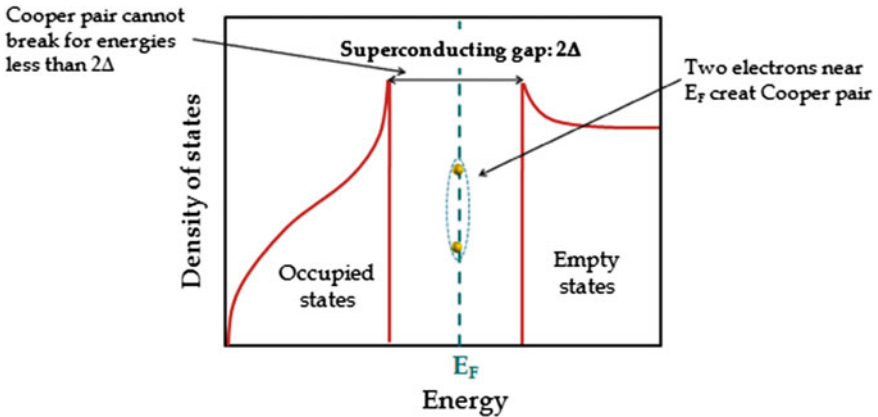


**Fig. 8** Energy diagram of a superconductor showing the superconducting gap

$$E_g = 2\Delta \sim 3.5k_B T_c \quad (20)$$

For energies below  $2\Delta$ , the Cooper pairs remain in their ground state without causing the slightest dissipation of energy. Thus to dissociate a pair, it is required to supply energy higher than or equal to  $E_g$ , hence the need to reach a critical temperature of the order of  $\Delta/k_B$  to break the superconducting phase. For a weak coupling ( $k_B T_c \ll \hbar\omega$ ), the expression of the transition temperature  $T_c$  is given by [10]

$$k_B T_c = 1.14\hbar\omega \exp\left[\frac{-1}{N(0)V}\right] \quad (21)$$



where  $N(0)$  is the density of states of at the Fermi energy and  $V$  represent the electron–phonon interaction potential.

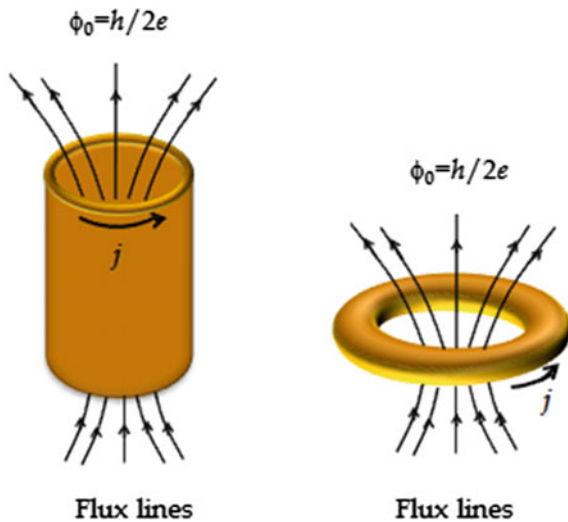
Scientists believed that superconductivity was fully understood and that critical temperatures could not increase beyond about 30 K, a theoretical limit determined by the weak attractive interaction between electrons of the BCS theory. This interaction is very sensitive to thermal agitation, low temperatures are then necessary for superconductivity. This theory made it possible to predict with great precision all the thermodynamic, electromagnetic, and spectroscopic properties of the superconductors known at that time, often called BCS superconductors, or conventional superconductors. However, subsequent studies have shown that the BCS theory does not appear to be applied in HTS [11–13] where superconductivity can be generated by processes other than the electron–phonon interaction.

## 2.7 Flux Quantization and Josephson Effect (1961)

### 2.7.1 Flux Quantization

F. London predicted that a magnetic flux  $\phi$  within a superconductor ring is quantized [14]. This prediction was nicely confirmed in 1961 through precision experiments done by Doll and Nábauer’s group [15] with Deaver and Fairbank’s group [16]. They found that the magnetic flux going across a cylinder can only be a multiple of the flux quantum  $\phi_0$  as shown in Fig. 9. This quantification comes essentially from the uniqueness of the phase  $\varphi(r)$  of the wave function whose variation on a contour  $C$  within a superconductor material is equal to a multiple of  $2\pi$  such that [4]:

**Fig. 9** Flux quantization in a superconducting ring and cylinder



$$\oint_C \vec{\nabla} \varphi(r) \cdot d\vec{l} = 2n\pi \quad (22)$$

where  $n$  is a relative integer. Given that this contour is located inside the superconductor very far from its surface, in other words at a much greater distance than  $\lambda_L$ , the supercurrent  $j$  is always zero. The circulation of the vector density of the current is therefore zero [4]:

$$\oint_C \vec{j} \cdot d\vec{l} = \frac{e^* n_s}{m^*} \oint_C \left( \hbar \vec{\nabla} \varphi(r) - e^* \vec{A} \right) d\vec{l} = 0 \quad (23)$$

Let us consider a surface  $S$  resting on this contour, the circulation of the vector potential of this contour is equal to the flux of the magnetic field  $\phi$  through this surface such that [7]

$$\oint_C \vec{A} \cdot d\vec{l} = \iint_S \text{rot} \vec{A} \cdot d\vec{s} = \iint_S \vec{B} \cdot d\vec{s} = \phi \quad (24)$$

The relationship (Eq. 23) becomes [4, 7]:

$$\frac{e^* n_s}{m^*} (\hbar 2\pi n - e^* \phi) = 0 \quad (25)$$

$$\Rightarrow \phi = \frac{\hbar 2\pi n}{e^*} = \frac{nh}{2e} \quad (26)$$

This result shows directly that the ground state is a superposition of two-particle states, with a charge  $2e$ . The flux  $\phi$  of the magnetic field through a surface based on a closed contour  $C$  is, therefore, an integer multiple of a fundamental quantity called the flux quantum or fluxon  $\phi_0$ :

$$\phi = n\phi_0 \text{ with } \phi_0 = \frac{nh}{2e} = 2.07 \times 10^{-15} \text{T.m}^2 \quad (27)$$

### 2.7.2 Josephson Tunneling Effect

When two superconductors are separated by a thin insulating barrier (of the order of a few nanometers), a continuous electric current suddenly appears; this phenomenon is the Josephson effect. In 1962, B. D. Josephson [17] noticed that the Cooper pairs (previously seen in Sect. 2.6) of a superconductor can pass through the insulator by tunnel effect creating a continuous electric current (see Fig. 10). By applying a constant electric voltage, an alternating current this time appears. The Josephson current offers some unusual properties, greatly related to the phase of the collective wave function describing the superconducting state. As we have seen previously,

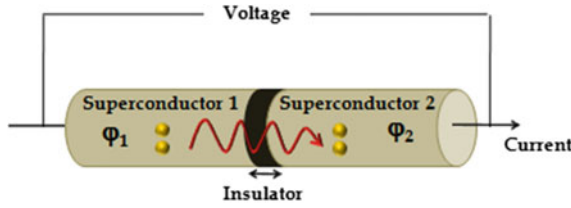


**Fig. 10** A Josephson junction is formed by two superconductors 1 and 2 separated by an insulator. Each superconductor is characterized by its phase. The passage of Cooper pairs from one superconductor to another is done by tunneling

a superconducting material is characterized by an order parameter  $\Psi(r)$  having a constant phase  $\varphi$ . A phase variation causes the current to flow. In the case where two superconductors are weakly coupled and having two different phases  $\varphi_1$  and  $\varphi_2$ , an arisen current will flow through the thin insulating layer. This current, depending on the phase shift  $\Delta\varphi = \varphi_1 - \varphi_2$ , is given by the first equation of Josephson [4]:

$$I = I_C \sin \Delta\varphi \tag{28}$$

where  $I_C$  denotes the critical current of the junction, it is controlled by the temperature and the junction parameter. When  $\Delta\varphi = 0$ , no current is flowing. For currents lower than  $I_C$ ,  $\Delta\varphi$  stabilizes allowing Cooper pairs to cross the junction and a supercurrent  $j$  is observed up to a maximum current density  $J_C$ . We then speak about the DC Josephson effect. When a potential difference  $V$  is applied to the junction as shown in Fig. 10,  $\Delta\varphi$  decreases as a function of time. The current of the Cooper pairs oscillates and an electromagnetic wave emission of frequency  $\nu$  is manifested.

This frequency is given by the second equation of Josephson that translates the AC Josephson effect [4]:

$$\nu = \frac{2eV}{h} = \frac{V}{\phi_0} \tag{29}$$

This frequency turns out to be  $483.6\text{GHz/mV}$ . The oscillation frequency can be adjusted employing the applied voltage which makes the Josephson effect very promising for many applications especially the SQUID (Superconducting Quantum Interference Device). Such devices, primarily based on Josephson junctions, provide an accurate measurement of exceedingly weak electromagnetic signals, in particular those submitted by the human brain.

## 2.8 Towards Room-Temperature Superconductivity

The record of  $T_c$  for LTS, also known as conventional superconductors, was 23.2 K for  $\text{Nb}_3\text{Ge}$ . The physical properties of this family are explained within the framework of the BCS theory. Since 1986, the year of the discovery of high-temperature superconducting materials, the BCS theory is no longer valid. The first HTS was an oxide-based ceramic, La-Ba-Cu-O system, discovered by J. G. Bednorz and K. A. Müller. It was found to superconduct as high as 35 K [18], a temperature that exceeds and challenges the limit of BCS theory. These superconductors are then classified as unconventional. This finding opened the door for researchers to develop new generations of compounds that could be superconducting at temperatures exceeding that of liquid nitrogen (77 K) like Y-Ba-Cu-O ( $T_c \sim 92$  K), Bi-Sr-Ca-Cu-O ( $T_c \sim 110$  K) and Ti-Sr-Ca-Cu-O ( $T_c \sim 125$  K). In 1994, the record for  $T_c$  was 164 K, reported for mercury cuprates  $\text{HgBa}_2\text{Ca}_2\text{Cu}_3\text{O}_{8+x}$ , under 30GPa of pressure [19]. All these compounds have in common the existence of a copper oxide plane  $\text{CuO}_2$  carrying superconductivity, hence their generic name of cuprates. This new generation of materials exhibits a superconductivity which goes beyond the framework of the BCS theory. Scientists have succeeded in synthesizing new families of HTS, depicted in Fig. 11, namely organic superconductors (carbon based), doped fullerenes ( $T_c \sim 40$  K, 1991), the  $\text{MgB}_2$  compound ( $T_c \sim 39$  K, 2001), the family of pnictides (iron-based compounds) ( $T_c \sim 55$  K, 2008).

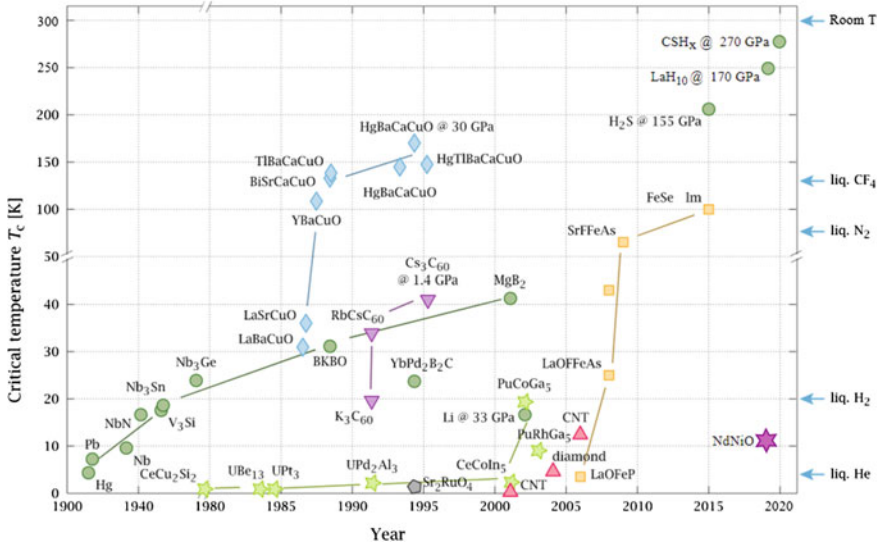


**Fig. 11** Chronology of superconductors. Cuprates are displayed as blue diamonds, BCS superconductors are marked by green circles, and iron-based superconductors by yellow squares. The advent of HTS modified the dynamics of refrigeration by admitting smaller, less expensive, and more efficient system cooling for certain applications [20]

Extensive efforts are now in an attempt to improve  $T_c$  and reach superconductivity at room temperature. Very recently, in 2015, superconductivity was demonstrated in the  $H_3S$  compound which exhibited a  $T_c$  of 200 K under a pressure above 200 GPa [21]. Likely, the story will not stay there...! Further advancements in the field of superconductor materials will be briefly discussed in Sect. 4.

### 3 Magnetic and Electromagnetic Properties

An increase in the applied magnetic field destroys the superconductivity by suppressing the Meissner effect. This occurs when the intensity of the applied field exceeds a certain limit often known as a critical magnetic field  $B_c$  already seen in Sect. 2.3. Depending on the nature of the material, two behaviors of the magnetic field are possible above  $B_c$ :

- It penetrates suddenly in the material and destroys the superconductivity in its whole. In this case, only one critical magnetic field exists. These materials, which are endowed by perfect diamagnetism, are identified as type I superconductors (Fig. 12a). They couldn't maintain their superconducting state at higher temperatures, and they fall under the BCS theory. All pure metals except niobium are type I superconductors having extremely low critical fields for use in magnets.
- It penetrates locally within the material allowing it to maintain the superconductivity in the presence of intense magnetic fields, so they are not perfectly diamagnetics. Such materials are called type-II superconductors. A mixed state

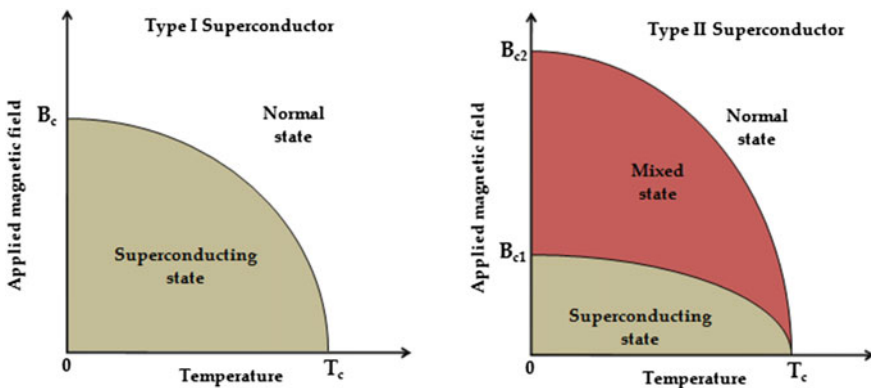


**Fig. 12** Phase diagrams of type I and type II superconductors (magnetic field versus temperature). For type II superconductor, the material is superconducting below  $B_{c1}$ , just like type I. Between  $B_{c1}$  and  $B_{c2}$ , the material is in a mixed state where the field partially penetrates in the form of small tubes of magnetic flux called vortices. Beyond  $B_{c2}$ , the material returns to its normal state

limited by two critical magnetic fields,  $B_{c1}$  and  $B_{c2}$ , then exists in which the material can present both superconducting and normal areas (Fig. 12b). The first type II superconductors discovered were alloys, such as Pb-In. The critical fields  $B_{c1}$  and  $B_{c2}$  depend very appreciably on the intrinsic properties and the purity of the material. Type II superconductors, featuring a strong critical field  $B_{c2}$ , have made it possible to produce magnets for particle accelerators due to their high resistivity to intense magnetic fields.

The phase diagrams of the two superconductor types are shown in Fig. 12.

### 3.1 Magnetization in Type I and Type II Superconductors

The induced magnetic field in a type I superconductor tends to push back the applied field until to the critical value  $B_c$  at which the material suddenly returns to its normal state describing the first-order transition as shown in Fig. 13 (green curve). In the superconducting phase, the material behaves like a perfect diamagnetic within which the magnetization is given by:

$$M = \chi \frac{B}{\mu_0} = -\frac{B}{\mu_0} \quad (30)$$

$\chi = -1$  is the magnetic susceptibility for a perfect diamagnetic.

During an increase in the magnetic field applied to a type II superconductor, the penetration of the flux into the material begins at a lower field  $B_{c1}$  ( $< B_c$ ) and increases continuously until a higher field  $B_{c2}$  ( $> B_c$ ) from which the material

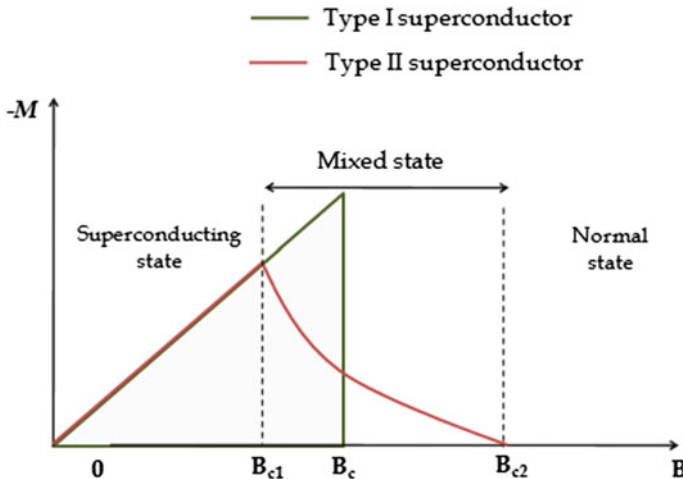


Fig. 13 Comparison between typical magnetization curves of type I and type II superconductor

becomes normal. The magnetic behavior of this type of superconductor is described in Fig. 13 (red curve). For  $B < B_{c1}$ , the material behaves exactly like a type I superconductor. Magnetization decreases with increasing applied field up to  $B_{c1}$  and begins increasing continuously until it becomes zero at  $B_{c2}$ . The superconductor-normal transition, in this case, is of second order. Between  $B_{c1}$  and  $B_{c2}$ , the material is in the mixed state where it admits lines of quantized magnetic flux surrounded by eddies of non-dissipative current. These flux lines are often referred to as vortices (more details will be provided in Sect. 3.3).

### 3.2 Classification in Terms of Surface Energy

Another classification of superconductor material can be envisaged based on the surface energy concept which separates the normal phase from the superconducting one and that depends mainly on the London penetration depth  $\lambda_L$  and the Ginsburg-Landau coherence length  $\xi_{GL}$ . In this context, Abrikosov [22] developed his approach of type II superconductors founded on the Ginsburg-Landau phenomenological theory [9]. To have a stable normal-superconductor interface, the free energies per unit volume in both regions must be equal ( $f_n = f_s$ ). In the superconducting state, two contributions to free energy exist; the first one is due to the presence of super-electrons ordered over a distance  $\xi_{GL}$  lowering the density of free energy by a quantity  $f_n - f_s = \frac{B_c^2}{2}$ . While the second contribution comes from the acquired magnetization to repel the flux which brings magnetic energy equal to  $\frac{B_c^2}{2}$  over a distance  $\lambda_L$ . Thus, each contribution cancels the other inside the superconductor. But since for most metal superconductors  $\xi_{GL} \gg \lambda_L$ , very close to the normal-superconducting interface, there is small positive energy, called the surface energy, approximately equal to  $\frac{B_c^2}{2} \frac{1}{(\xi_{GL} - \lambda_L)}$ . In this case, it is energetically unfavorable to form an interface: the material will tend to separate the normal and the superconducting areas by minimizing the contact surface between them. Abrikosov called these materials type I superconductors to distinguish them from others. For Type II superconductors, mainly compounds and alloys,  $\xi_{GL}$  is very low because the mean free path is very short. These materials are then endowed by a coherence length significantly shorter than the penetration depth,  $\xi_{GL} \ll \lambda_L$ , leading to negative surface energy. It is so energetically favorable to form an interface, and the material will tend to create as many interfaces as possible by mixing normal and superconducting areas inside the material. Difference between type I and type II superconductor in regard to the spatial extent of the electron density  $n_s$  and the magnetic field  $B$  is depicted in Fig. 14

The Ginsburg-Landau parameter  $\kappa = \frac{\lambda_L}{\xi_{GL}}$  is then introduced to estimate the value of the surface energy and therefore the category to which the superconductor belongs. Abrikosov showed that there is a limit value for this ratio separating the two classes of superconductors. For metallic or type I superconductors  $\kappa < 1/\sqrt{2}$ , a positive surface energy exists. While for type II superconductors  $\kappa > 1/\sqrt{2}$ , the surface energy is negative; in this case, when the first critical field  $B_{c1}$  is reached, the magnetic flux

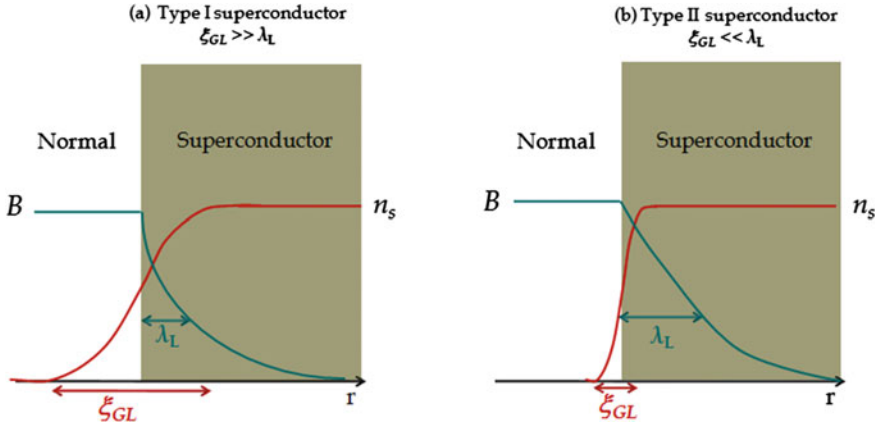


**Fig. 14** Spatial extent of the electron density  $n_s$  and the magnetic field  $B$  for type I and type II superconductors

is partially admitted in the form of cylindrical zones, or flux lines, centered on non-superconducting cores of diameter  $2\xi_{GL}$ .

For more information, we give below the quantitative relations allowing us to estimate the values of the lower critical field  $B_{c1}$ , the upper one  $B_{c2}$  and even the thermodynamic field  $B_c$  which was not directly measurable. These relations derive from the phenomenological theory of Ginsburg-Landau-Abrikosov-Gorkov (GLAG theory) [23–25]:

$$B_{c1} = \frac{\phi_0}{2\pi\lambda_L^2} \frac{\ln\kappa}{2} \quad (31)$$

$$B_{c2} = \frac{\phi_0}{2\pi\xi_{GL}^2} \quad (32)$$

$$B_c = \frac{\phi_0}{2\pi\lambda_L\xi_{GL}} \frac{1}{\sqrt{2}} \quad (33)$$

It is very clear that  $B_{c1}$  is related to  $\lambda_L$ :  $B_{c1}$  is reached when a flux quantum  $\phi_0$  crosses a London region of area  $\sim \lambda_L^2$ . While  $B_{c2}$  is related to  $\xi_{GL}$ :  $B_{c2}$  is reached when a flux quantum  $\phi_0$  passes through a vortex core of the area  $\sim \xi_{GL}^2$ .

The relation between the different critical fields is given by:

$$B_c = \frac{\lambda_L}{\xi_{GL}} B_{c1} \frac{1}{\sqrt{2}\ln\kappa} = \frac{\xi_{GL}}{\lambda_L} B_{c2} \frac{1}{\sqrt{2}} \quad (34)$$

The GLAG theory also gives the energy added to the system by the presence of vortices, it is written as follows:



$$E_{vortex} = \frac{\phi_0}{2\pi\lambda_L^2\mu_0} \frac{\ln\kappa}{2} \tag{35}$$

### 3.3 Quantized Flux Lines: Vortices

#### 3.3.1 Abrikosov Lattice

The existence of a negative surface favors the partial penetration of the flux lines inside the sample in the form of vortices. A vortex, as described in Fig. 15a, is a magnetic flux line of magnitude  $\phi_0 = h/2e$  that cross the length of the sample in parallel to the applied field. This magnetic flux is carried by the vortex core of diameter  $2\xi_{GL}$ , where the superconductivity is destroyed. The core is surrounded by a supercurrent which is responsible for (i) generating the magnetic flux in the normal core and (ii) screening it in the surrounding material. Thus, a type II superconductor can be in a mixed state because it includes normal zones, which are the vortices cores, surrounded by a superconducting matrix. Because of the mutual repulsion between vortices arising from superconducting currents which circulate in the same direction around normal cores, these vortices are arranged into a regular triangular lattice in an ideal superconductor referred to as Abrikosov lattice. They form then a fine structure with a periodicity of less than  $10^{-6}cm$  making the mixed state an intrinsic property of type II superconductors (see Fig. 15b). It should be noted that due to the anisotropy of some materials, the vortices lattice can take a square shape. The presence of vortices in the mixed state of alloy superconductors, allowing the

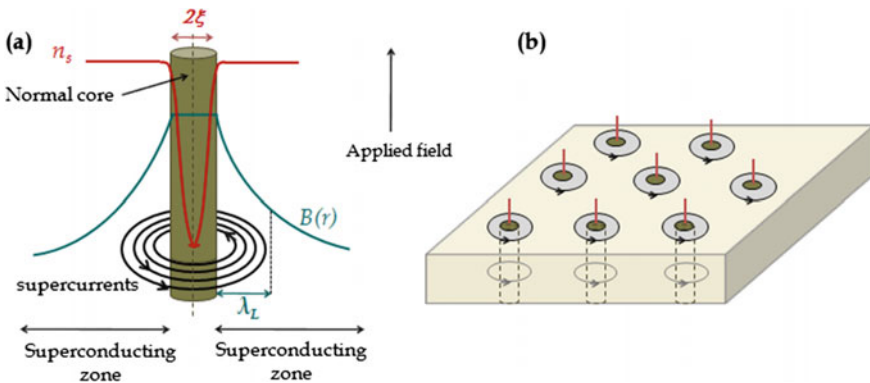


**Fig. 15** **a** Vortex description. The vortex includes a  $2\xi$  diameter non-superconducting core surrounded by a vortex of non-dissipating current. This current generates a flux density (magnetic induction)  $B(r)$ , with an integrated value equal to  $\phi_0 = h/2e$ . The density  $n_s$  of Cooper pairs continuously decreases until it disappears in the center of the core. **b** Mixed state of type II superconductors with vortices arranged in a triangular Abrikosov lattice

magnetic flux to penetrate through them, clearly explained the cause of the imperfect Meissner effect in this area. This mixed state is then stable up to a large critical field.

### 3.3.2 Dissipation and Vortices Pinning in Type-II Superconductors

If no current is applied to the superconductor material, no dissipation exists. However, when a supercurrent of density  $\vec{J}$  flows in a type II superconductor, it exerts a Lorentz force  $\vec{F}_L$  on all the flux lines:

$$\vec{F}_L = \vec{J} \wedge \vec{B} \quad (36)$$

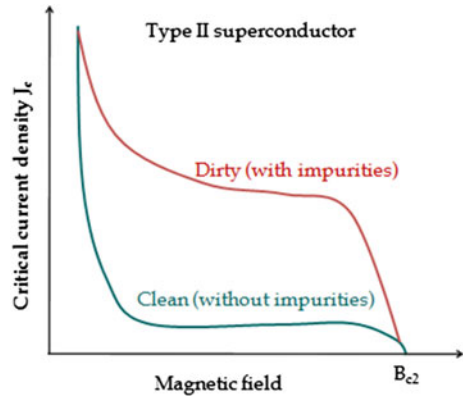
This force tends to move the vortices in a direction perpendicular to both electric and magnetic fields. If the material does not contain impurities or defects (ideal superconductor), the vortices freely move to lead to energy dissipation within the material and a finite resistance. This is called the flux flow regime making the superconductor material useless for technical applications. The vortices must then be trapped or pinned to ensure their stability and therefore the conduction of current without loss. A real material naturally contains defects (dislocations, twins, microcavities, grain boundaries, etc.) which will interact with the vortices. Energetically, these vortices will tend to position themselves on defects zones that act as pinning centers. The pinned vortex is then subjected to two forces: the pinning force  $\vec{F}_p$  which tends to maintain it in its initial position and the Lorentz force  $\vec{F}_L$  which tends to move it. The vortices do not move until the Lorentz force does not exceed the pinning force. A critical state is then defined as being a critical current density  $J_c$  is reached. Once  $J_c$  is exceeded, the vortices start to move, and the material recovers its normal state. The behavior of the critical current density  $J_c$  against the applied magnetic field for a defect-free type II superconductor (clean superconductor) is different from that containing defect (dirty superconductor).

As shown in Fig. 16,  $J_c$  suddenly drops to a low value for a clean superconductor. While a dirty superconductor can carry a large current over a broad range of high magnetic fields. Thus, impurities and defects play an important role in the pinning mechanisms making type II superconductors interesting for powerful applications such as the magnet devices for particle accelerators which require intense magnetic fields. It is to note that the artificial adding of impurities (by irradiation for example) greatly enhances the vortices pinning and thus improves the performance of the material.

## 4 Some Latest Advancements

Nowadays, it is difficult or even impossible to imagine our life without motors, generators, or magnetic resonance imaging, etc. This fact well appreciates the importance

**Fig. 16** Dependence of the critical current density  $J_c$  as function of the magnetic field  $B$  for free-defects (clean) and with defects (dirty) type II superconductors



of superconductivity in our daily life, which is considered to be an inspiring technology for high-performance electronics. Thanks to their unique properties, superconductors have paved the way for several innovative technology applications in different areas like medicine, communication, transportation, industry, etc. Even though radical developments have started in the superconductivity field since its finding, searching for novel superconductors continues to be a major scientific target. For that, scientific researchers have not ceased to deeply understand and enrich their knowledge of the fundamentals and basic principles of superconductivity to ensure its best implications [26–39]. Recently, lots of significant improvements in the properties of superconducting materials have occurred. Here, we collect briefly the latest advancements experienced in the world of superconductivity:

- (i) The advancement of high-temperature superconductors (HTS) always remains intended because of their powerful applications that enhance the performance of many devices. Their introduction extends almost all areas like magnetic resonance imaging (MRI) for medical applications, superconducting quantum interference (SQUID), microwave ovens, magnetic energy stores, Maglev train, waves, and resonators for high energy physics experiments [40]. The challenge was to fabricate high-quality HTS nanostructures beneficial for the design of novel devices. Recently, HTS  $\text{YBa}_2\text{Cu}_3\text{O}_{7-x}$  (YBCO) films, with a reduced size down to  $\sim 50$  nm, were successfully created [41, 42]. A similar study has focused on the understanding of reversible discontinuous voltage jumps caused by instabilities of the vortex dynamics (flux-flow) in HTS nanowires. The main goal is to hold repeated brusque voltage jumps with narrow switching current distributions by controlling magnetic field, temperature, and nanowire width. To achieve this objective,  $\text{YBa}_2\text{Cu}_3\text{O}_{7-x}$  (YBCO) nanowires are fabricated using high-resolution focused ion beam lithography and counting on optimization of patterning conditions to have high-quality superconducting nanowires of various widths. As a result, sharp voltage switching very close to the critical current density is acquired in nanowires with 50 nm widths, being especially attractive for practical applications [43].

- (ii) Developments also included the  $\text{MgB}_2$  materials to exploit their potential in new applications. Since their discovery in 2001 [44], raising the critical transition temperature ( $T_c$ ) of  $\text{MgB}_2$  superconductors was the main goal of several researchers. They tend to transcend the McMillan limit temperature predicted to be 40 K for conventional BCS superconductors [45]. In this context, doping and chemical substitution are used to improve the superconductivity of  $\text{MgB}_2$  but the majority of efforts are failed and confirm that these methods reduce the  $T_c$  of  $\text{MgB}_2$ . A new approach consists of the structural design of metamaterials is exploited for improving the superconductivity [46, 47]. In this method, a smart meta-superconductor (SMSC) is formed by directly doping electroluminescence (EL) materials into a superconductor. Contrary to traditional doping, the  $T_c$  of SMSC materials can be tuned and enhanced by the stimulus of external field. In the last few years, studies show that this new method of doping has well succeeded to increase the  $T_c$  of  $\text{MgB}_2$  but the obtained  $\Delta T_c$  ( $\Delta T_c = T_c - T_{c,pure}$ ) values are generally small which greatly affect the further improvement of the  $T_c$ . Very recently (in 2021), Li et al. [48] pay special attention to enhancing  $\Delta T_c$  in  $\text{MgB}_2$  SMSCs. Thus, they doped two types of inhomogeneous phases,  $\text{Y}_2\text{O}_3:\text{Eu}_3^+$  and  $\text{Y}_2\text{O}_3:\text{Eu}_3^+/\text{Ag}$ , into three  $\text{MgB}_2$  raw samples having various particle sizes in order to investigate the effect of doping concentration on the  $\Delta T_c$ . Findings reveal that the optimal doping concentration of inhomogeneous phases increases from 0.5 to 1.2% when reducing the  $\text{MgB}_2$  particle size favoring a rise in  $\Delta T_c$  from 0.4 K to 1.2 K respectively. These values are encouraging compared to those found in previous works (varies between 0.2 and 0.4 K) [49–51]. This result shows that the SMSC method affords new manners of improving the  $T_c$  of superconductors. We report that the same approach is applied to  $\text{Bi(Pb)SrCaCuO}$  (BSCCO) where the zero-resistance temperature  $T_{c0}$  and onset transition temperature  $T_{c,on}$  of  $\text{Y}_2\text{O}_3:\text{Eu}_3^+ + \text{Ag}$  doped sample are found to be 4 and 6.3 K higher than those of pure B(P)SCCO, respectively [52].

## 5 Conclusion

Throughout this chapter, we have underlined the particularity of superconductor materials due to the unusual phenomena and effects which occur within which namely the zero resistance, the Meissner effect, the electron–phonon interaction, and the Josephson effect. With the fundamental phenomenological theory of Ginzburg-Landau which reveals the notion of the order parameter, then that of Bardeen-Cooper-Schrieffer (BCS theory) based on the total wave function of superconducting electrons and finally the discovery of the Josephson effect, superconductivity now seems to be successfully described, in particular for low-temperature superconductors. However, some details remain unclear for high-temperature superconductors. The particular attention to this field confirms the importance of superconductor materials compared to others which are proven by their integration in high-performance

applications. Superconductivity is very useful in many fields, both in basic research and in everyday life. The number of superconductor materials today is incredibly varied with critical temperatures that can exceed 200 K in some cases. Likely, we are not at the end of the road in this fascinating field, and new surprises are well expected.

## References

1. H.K. Onnes, Commun. Phys. Lab. Univ. Leiden. Suppl. **29** (1911)
2. H. Kamerlingh-Onnes, Commun. Phys. Lab. Univ. Leiden **120b** (1911), reprinted in Proc. K. Ned. Akad. Wet. **13**, 1274 (1911)
3. W. Meissner, R. Ochsenfeld, Einneuer Effekt bei Eintritt der Supraleitfähigkeit. Naturwissenschaften **21**(44), 787–788 (1933)
4. R.G. Sharma. *Superconductivity* (Springer Science and Business Media LLC, 2021)
5. F.B. Silsbee, J. Wash. Acad. Sci. **6**, 597 (1916)
6. F. London, H. London, The electromagnetic equations of the supraconductor. Proc. R. Soc. Lond. **A149**, 71 (1935)
7. S. Hurand, Supraconductivité: Cours de Master 2—Université de Poitiers. Master. Supraconductivité, Poitiers—Futuroscope, France. fhal-03135765 (2021)
8. A.B. Pippard, Proc. R. Soc. London, Ser. A **216**, 547 (1953); A.B. Pippard, Proc. Cambridge Philos. Soc. **47**, 617 (1951)
9. V.L. Ginzburg, L.D. Landau, Zh. Eksperim i Teor. Fiz. **20**, 1064 (1950)
10. J. Bardeen, L.N. Cooper, J.R. Schrieffer, Theory of superconductivity. Phys. Rev. **108**, 1175–1204 (1957)
11. L.J. De Jongh, A comparative study of (bi) polaronic (super) conductivity in high- and low  $T_c$  superconducting oxides. Physica C **152**, 171–216 (1988)
12. D. Emin, Large bipolarons and superconductivity. Phys C Supercond, 185–189, Part 3, 1593–1594 (1991)
13. J.E. Hirsch, Bose condensation versus pair unbinding in short-coherence-length superconductors. Physica C **179**, 317–332 (1991)
14. F. London, *Superfluids*, vol. 1 (Wiley, New York, 1950)
15. R. Doll, M. Näbauer, Phys. Rev. Lett. **7**, 51 (1961)
16. B.S. Deaver Jr., W.M. Fairbank, Phys. Rev. Lett. **7**, 43 (1961)
17. B.D. Josephson, Phys. Lett. **1**, 251 (1962)
18. J.D. Bednorz, K.A. Mueller, Possible high  $T_c$  superconductivity in the Ba–La–Cu–O system. Z. Phys B Condensed Matter **64**, 189 (1986)
19. A. Schilling, M. Cantoni, J.D. Guo, H.R. Ott, Superconductivity above 130 K in the Hg–Ba–Ca–Cu–O system. Nature **363**, 56–58 (1993)
20. P. Jensen Ray, Figure 2.4 in master’s thesis, structural investigation of  $\text{La}_{2-x}\text{Sr}_x\text{CuO}_{4+y}$  - following staging as a function of temperature. Niels Bohr Institute, Faculty of Science, University of Copenhagen (Copenhagen, Denmark, 2015). <https://doi.org/10.6084/m9.figshare.2075680.v2>
21. A.P. Drozdov, M.I. Erements, I.A. Troyan, V. Ksenofontov, S.I. Shylin, Conventional superconductivity at 203 kelvin at high pressures in the sulfur hydride system. Nature **525**, 73 (2015)
22. A.A. Abrikosov, On the magnetic properties of superconductors of the second group. Zh. Eksperim. Teor. Fiz. **32**, 1442 (1957), Soviet Phys. JETP **5**, 1174 (1957)
23. M. Tinkham, *Introduction to superconductivity* (Dover Publications, New York, 1996)
24. P.G. de Gennes, *Superconductivity of Metals and Alloys* (Westview Press, 1999)

25. W. Buckel, R. Kleiner, *Superconductivity: Fundamentals and Applications* (Wiley-VCH Verlag GmbH, Weinheim, 2004)
26. M.K. Ben Salem, E. Hannachi, Y. Slimani, A. Hamrita, M. Zouaoui, L. Bessais, M. Ben Salem, F. Ben Azzouz, SiO<sub>2</sub> nanoparticles addition effect on microstructure and pinning properties in YBa<sub>2</sub>Cu<sub>3</sub>O<sub>y</sub>. *Ceram. Int.* **40**, 4953–4962 (2014)
27. Y. Slimani, M.A. Almessiere, E. Hannachi, M. Mumtaz, A. Manikandan, A. Baykal, F. Ben Azzouz, Improvement of flux pinning ability by tungsten oxide nanoparticles added in YBa<sub>2</sub>Cu<sub>3</sub>O<sub>y</sub> superconductor. *Ceram. Int.* **45**, 6828–6835 (2019)
28. Y. Slimani, M.A. Almessiere, E. Hannachi, F.O. Al-qwairi, A. Manikandan, A. Baykal, F. Ben Azzouz, AC susceptibility, DC magnetization and superconducting properties of tungsten oxide nanowires added YBa<sub>2</sub>Cu<sub>3</sub>O<sub>y</sub>. *Ceram. Int.* **45**(17), 21864–21869 (2019)
29. Y. Slimani, E. Hannachi, A. Ekicibil, M. A. Almessiere, F. Ben Azzouz, Investigation of the impact of nano-sized wires and particles TiO<sub>2</sub> on Y-123 superconductor performance. *J. Alloy. Compd.* **43**, 664–673 (2019)
30. E. Hannachi, M.A. Almessiere, Y. Slimani, A. Baykal, F. Ben Azzouz, AC susceptibility investigation of YBCO superconductor added by carbon nanotubes. *J. Alloy. Compd.* **812**, 152150 (2020)
31. Y. Slimani, E. Hannachi, F. Ben Azzouz, M. Ben Salem, Impact of planetary ball milling parameters on the microstructure and pinning properties of polycrystalline superconductor Y<sub>3</sub>Ba<sub>2</sub>Cu<sub>8</sub>O<sub>y</sub>. *Cryogenics* **92**, 5–12 (2018)
32. R.A. Al-Mohsin, A.L. Al-Otaibi, M.A. Almessiere, H. Al-badairy, Y. Slimani, F. Ben Azzouz, Comparison of the microstructure and flux pinning properties of polycrystalline YBa<sub>2</sub>Cu<sub>3</sub>O<sub>7-d</sub> containing Zn<sub>0.95</sub>Mn<sub>0.05</sub>O or Al<sub>2</sub>O<sub>3</sub> nanoparticles. *J. Low Temp. Phys.* **192**, 100–116 (2018)
33. M.A. Almessiere, Y. Slimani, E. Hannachi, R. Algarni, F. Ben Azzouz, Impact of Dy<sub>2</sub>O<sub>3</sub> nanoparticles additions on the properties of porous YBCO ceramics. *J. Mater. Sci. Mater. Electron.* **30**(19), 17572–17582 (2019)
34. R. Algarni, M.A. Almessiere, Y. Slimani, E. Hannachi, F. Ben Azzouz, Enhanced critical current density and flux pinning traits with Dy<sub>2</sub>O<sub>3</sub> nanoparticles added to YBa<sub>2</sub>Cu<sub>3</sub>O<sub>7-d</sub> superconductor. *J. Alloy. Compd.* **852**, 157019 (2021)
35. Michael Rudolf Koblichka, Anjela Koblichka-Veneva, XianLin Zeng, Essia Hannachi, Yassine Slimani, Microstructure and Fluctuation-Induced Conductivity Analysis of Bi<sub>2</sub>Sr<sub>2</sub>CaCu<sub>2</sub>O<sub>8+δ</sub> (Bi-2212) Nanowire Fabrics. *Curr. Comput. Aid. Drug Des.* **10**(11), 986 (2020)
36. A. Hamrita, Y. Slimani, M.K. Ben Salem, E. Hannachi, F. Ben Azzouz, L. Bessais, M. Ben Salem, Superconducting properties of polycrystalline YBa<sub>2</sub>Cu<sub>3</sub>O<sub>7-d</sub> prepared by sintering of ball-milled precursor powder. *Ceram. Int.* **40**, 1461–1470 (2014)
37. Q. Nouailhetas, A. Koblichka-Veneva, M.R. Koblichka, S.P.K. Naik, F. Schäfer, H. Ogino, C. Motz, K. Berger, B. Douine, Y. Slimani, E. Hannachi, Magnetic phases in superconducting, polycrystalline bulk FeSe samples. *AIP Adv.* **11**, 015230 (2021)
38. M.R. Koblichka, Y. Slimani, A. Koblichka-Veneva, T. Karwoth, X. Zeng, E. Hannachi, M. Murakami, Excess conductivity analysis of polycrystalline FeSe samples with the addition of Ag. *Materials* **13**(21), 5018 (2020)
39. M.I. Sayyed, E. Hannachi, K.A. Mahmoud, Y. Slimani, Synthesis of different (RE)BaCuO ceramics, study their structural properties, and tracking their radiation protection efficiency using Monte Carlo simulation. *Mater. Chem. Phys.* **276**, 125412 (2022)
40. G. Burns, *High-Temperature Superconductivity* (IBM Thomas J Watson Research Center Yorktown Heights, New York, 2004)
41. R. Arpaia, D. Golubev, R. Baghdadi, R. Ciancio, G. Dražić, P. Orgiani, D. Montemurro, T. Bauch, F. Lombardi, Transport properties of ultrathin YBa<sub>2</sub>Cu<sub>3</sub>O<sub>7-x</sub> nanowires: a route to single photon detection. *Phys. Rev. B.* **96**, 64525 (2017)
42. G. Papari, F. Carillo, D. Stornaiuolo, D. Massarotti, L. Longobardi, F. Beltram, F. Tafuri, Dynamics of vortex matter in YBCO sub-micron bridges. *Phys. C Supercond. Appl.* **506**, 188–194 (2014)

43. V. Rouco, D. Massarotti, D. Stornaiuolo, G.P. Papari, X. Obradors, T. Puig, F. Tafuri, A. Palau, Vortex lattice instabilities in  $\text{YBa}_2\text{Cu}_3\text{O}_{7-x}$  Nanowires. *Materials* **11**, 211 (2018)
44. J. Nagamatsu, N. Nakagawa, T. Muranaka, Y. Zenitani, J. Akimitsu, Superconductivity at 39 K in magnesium diboride. *Nature* **410**, 63–64 (2001)
45. W.L. McMillan, Transition temperature of strong-coupled superconductors. *Phys. Rev.* **167**, 331–344 (1968)
46. W.T. Jiang, Z.L. Xu, Z. Chen, X.P. Zhao, Introduce uniformly distributed ZnO nano-defects into BSCCO superconductors by nano-composite method. *J. Funct. Mater.* **38**, 157–160 (2007)
47. S.H. Xu, Y.W. Zhou, X.P. Zhao, Research and development of inorganic powder EL materials. *Mater. Rep.* **21**, 162–166 (2007)
48. Y. Li, G. Han, H. Zou, L. Tang, H. Chen, X. Zhao, *Materials* **14**, 3066 (2021)
49. H.G. Chen, Y.B. Li, G.W. Chen, L.X. Xu, X.P. Zhao, The effect of inhomogeneous phase on the critical temperature of smart meta-superconductor  $\text{MgB}_2$ . *J. Supercond. Nov. Magn.* **31**, 3175–3182 (2018)
50. Y.B. Li, H.G. Chen, W.C. Qi, G.W. Chen, X.P. Zhao, Inhomogeneous phase effect of smart meta-superconducting  $\text{MgB}_2$ . *J. Low. Temp. Phys.* **191**, 217–227 (2018)
51. S. Tao, Y.B. Li, G.W. Chen, X.P. Zhao, Critical temperature of smart meta-superconducting  $\text{MgB}_2$ . *J. Supercond. Nov. Magn.* **30**, 1405–1411 (2017)
52. H. Chen, M. Wang, Y. Qi, Y. Li, X. Zhao, *Nanomaterials* **11**, 1061 (2021)

# Transport Properties of Superconducting Materials



Ahmet Ekicibil, Faruk Karadağ, Selda Kılıç Çetin, Ali Osman Ayaş, Gönül Akça, Mustafa Akyol, and Doğan Kaya

**Abstract** In superconducting materials, a phase transformation occurs at critical transition temperature,  $T_c$ , and they show zero resistivity below  $T_c$ . The relation between zero resistivity and superconducting properties is an interesting and important issue to understand the mechanism of superconductivity especially for high- $T_c$  superconductors (HTSCs). To determine the behavior of superconducting materials under an applied magnetic field, many remarkable studies that have been conducted due to their great technological and industrial importance. The magnetic field causes a change in the transition temperature, the width of resistance transition and activation energy of superconducting materials. Energy dissipation is one of the important obstacles to obtain superconducting material with desired properties for practical industrial applications. Thus, some important models that make an explanation about the dissipation mechanism have been explained and interpreted. The

---

A. Ekicibil (✉) · F. Karadağ · S. K. Çetin · G. Akça  
Department of Physics, Faculty of Science and Art, University of Çukurova, Adana, Turkey  
e-mail: [ahmetcan@cu.edu.tr](mailto:ahmetcan@cu.edu.tr)

F. Karadağ  
e-mail: [fkaradag@cu.edu.tr](mailto:fkaradag@cu.edu.tr)

S. K. Çetin  
e-mail: [kilics@cu.edu.tr](mailto:kilics@cu.edu.tr)

G. Akça  
e-mail: [gdayan@cu.edu.tr](mailto:gdayan@cu.edu.tr)

A. O. Ayaş  
Department of Physics, Faculty of Science and Art, University of Adıyaman, Adıyaman, Turkey  
e-mail: [aayas@adiyaman.edu.tr](mailto:aayas@adiyaman.edu.tr)

M. Akyol  
Department of Materials Science and Engineering, Faculty of Engineering, Adana Alparslan Türkeş Science and Technology University, Adana, Turkey  
e-mail: [makyol@atu.edu.tr](mailto:makyol@atu.edu.tr)

D. Kaya  
Department of Electronics and Automation, Vocational School of Adana, University of Çukurova, Adana, Turkey  
e-mail: [dogankaya@cu.edu.tr](mailto:dogankaya@cu.edu.tr)



critical current density has been discussed with early and recent models, experimental methods, and recent studies on HTSCs. In addition, a transverse voltage difference (the Hall voltage) can be observed in superconductor materials, especially in HTSCs, under perpendicular magnetic fields. But, the sign of Hall voltage becomes opposite to the ordinary Hall effect.

**Keywords** Superconductivity · Zero resistivity · Magnetoresistivity · Energy dissipation · Critical current density · Hall effect

## 1 Introduction

It was understood soon after the discovery of the electron that the high thermal and electrical conductivity of metals depend on the movement of electrons in the metal. Classical theories of metallic conductivity explained these electrons as an independent gas of particles colliding with lattice defects in the metal. Following, many experimental results showed that the electrical and thermal conductivity can be explained using classical kinetic theory methods. However, the wave property of electrons and the exclusion principle were considered only in conjunction with quantum mechanism. There are many unsolved issues in these theories that need to be studied to explain superconductivity. For example, the Fermi distribution for free electrons in superconductor material needs to consider understanding the electronic contribution to the specific heats of solids. Other applications of wave ideas yield to the quantization of energy levels and the band theory of solids, which largely explained the reason for the electrical and thermal conductivities observed in normal solids. The free-electron model approach found an average of the changes in the interactions of electrons with each other and with the ions in the lattice. This model explains the reason of resistance to electron flow under normal conditions. However, this independent particle model fails to explain superconductivity. In order to understand this phenomenon, it is necessary to explain the reason for the common behavior of electron and lattice ions in solids. It is also important to take into account the so-called many-body effects.

In 1911, Heike Kammerling Onnes found that when solid mercury is cooled below a certain temperature, called the critical temperature,  $T_c$ , its electrical resistance drops to an immeasurably small value [1]. This experimental result showed that when the temperature drops below 4.2 K for mercury, a phase transition occurs from a normal conductive to a superconducting state. Since then, many other elements have been found as superconductors as high as 23 K.

The phase transition in material from the normal to the superconducting state indicates a clear conducting phase change without losing its physical shape and appearance. This phase transition occurs at  $T_c$  which is specific temperature for different materials. The normal states of a metal or alloy exist at a temperature above  $T_c$  while the superconducting state takes a place below  $T_c$ . This critical temperature value emphasizes that matter is in equilibrium and every temperature has equilibrium

energy. During cooling, there are only two different states with the same equilibrium energies at  $T_c$  and there is a jump from one to the other. This jump is called a phase transition in superconductors.

As can be predicted, many factors contribute to the electrical resistivity of a solid. Electrons are scattered because the structural defect or impurity changes present in a crystal, compared to a perfect lattice. Also, lattice ions in normal modes have lattice vibrations, called phonons, which produce an event similar to sound waves moving through a solid. As the temperature increases, more phonons are formed in the lattice, resulting in an electron–phonon interaction that scatters conduction electrons and causes more resistance. Therefore, under normal conditions, the electrical resistance of the solid should decrease as the temperature decreases. However, a residual resistance is expected even around absolute zero due to crystal defects. Therefore, it seems extraordinary that the electrical resistivity of some solids disappears completely at sufficiently low temperatures. In general, one of the most interesting properties of some metals and alloys is that their electrical resistivity completely disappears below a certain temperature value. This zero resistivity or infinite conductivity is one of the important properties of superconductivity.

The resistivity of a conductor can be measured via passing a current through the conductor under a voltage difference. Another method is the energy loss method that the direct consequence of passing current creates heat in the conductor. Although similar processes can be applied to superconductor materials, they can carry electrons without any resistance or energy loss. The behavior of electrons in a superconductor is quite different while impurities and knitting defects also exist in the structure. However, the superconducting electrons in the conductor move in the mixed lattice without being exposed to any obstacles. So that no collision and friction occur in the structure and current and energy are transmitted without any loss. The maximum resistance occurs applying a high voltage which results in an energy loss in the conductor. But in some conductors, when the material is cooled below  $T_c$ , the electrons lose their ability to convert their energy into heat, and the resistance drops to zero. In this case, it is possible to create a current without applying any voltage. In an ideal metallic structure, the phonon effect disappears and the electrons move freely in the structure without interacting with the lattice below  $T_c$ . In this case, the resistance of the structure suddenly drops to zero which is called superconducting material. However, the reason for this phase transition in the material is the result of only a small part of the electrons passing with a different quantum state, no difference is observed in the other properties of the material. Existing theoretical studies on superconductivity are extremely difficult to understand and are full of unexplained information.

The resistance of a conductor can be calculated by the formula  $V = I.R$ . If the voltage is zero, the resistance is also zero. Differently, superconductors can accommodate electric current without applying voltage, this property is provided by superconducting electromagnets (Ex: Magnetic Resonance Imaging devices). Experiments have shown that an electric current can continue unabated in a superconducting coil for an estimated time of about 100,000 years. Theoretical evidence, on the other hand, suggests that the universe may last longer than its lifetime, or even forever.

In a normal conductor, the electric current can be considered as a mass of electrons moving in an ionic lattice. These electrons are in constant collision with the ions, and each collision results in vibrational kinetic energy in the lattice. So that, the energy, which is created by the electric current, is absorbed by the lattice and converted into heat. As a result, the energy that is carried by the current is constantly dissipated. This distribution creates electrical resistance and Joule heating. This situation is different for superconductors for which the clump of electrons cannot disperse into individual electrons. Instead, they are found in pairs called Cooper pairs. The reason for this pairing is the force of attraction between the electrons as a result of the exchange of phonons. According to quantum mechanics, there is an energy gap in the energy spectrum of Cooper pairs in the material, and a minimum energy change is required to excite the electrons to surpass the gap. If this energy change is greater than the thermal energy of the lattice, the electron stack will not be fragmented by the lattice, based on the formula  $kT$  ( $k$ , Boltzmann constant;  $T$ , temperature). The stack of Cooper pairs is, therefore, superfluid and can move without the loss of electrons.

Superconductivity can also be affected by an external applied magnetic field. Superconductivity disappears in an externally applied magnetic field which is stronger than the critical magnetic field,  $H_c$  of superconductor material at a constant temperature below  $T_c$ . This is because the Gibbs free energy of the superconducting state increases second order with the magnetic field, while the free energy of the normal state is independent of the magnetic field. If a substance exhibits superconductivity without a magnetic field, the free energy of the superconducting state is less than the free energy of the normal state. At a finite value for the magnetic field (this value should be proportional to the square root of the difference of the free energies in the zero magnetic field), the two free energies are equal to each other and a transition to the normal state is observed. In general, a higher temperature and a stronger magnetic field result in fewer superconducting electrons and a greater London penetration depth of external magnetic field. The depth of penetration becomes absolute at a state change.

The type of transition to superconductivity between states was a long-standing debate. Experiments showed that the process is of the second type (non-latent heat). However, there is latent heat in the presence of a magnetic field because the superconducting state has lower entropy than the normal state below the critical temperature.

Superconductors can be classified as Type I and Type II according to their behavior under the applied magnetic field. Type I superconductors fully comply with the Meissner effect which occurs below  $H_c$ . When the applied magnetic field exceeds the  $H_c$  value, the superconducting state disappears and is called as normal state. However, type II superconductors can be divided into two regions. In the first region, the superconducting sample completely excludes the magnetic field. In the second region, the magnetic field remains partially inside. At this point, type II superconductors show little resistance. This is due to the movement of quantized magnetic fluxes called as vortices in the electronic superfluid. These vortices reduce some of the energy of the electric current. If the electric current is very low, the vortices become established and the resistance disappears. The resistance created by this effect is

much less than that of non-superconducting materials. However, if the temperature drops well below the transition temperature, the magnetic vortices can be fixed in an irregular but established position, in which case the resistance of the material is completely disappeared.

Characteristic features of superconducting materials begin to appear when the temperature of the material decreases below the  $T_c$ . The value of  $T_c$  varies from substance to substance. For example, while the critical temperature of solid mercury is 4.2 K, cuprate superconductors have much higher critical temperatures, such as 92 K for  $\text{YBa}_2\text{Cu}_3\text{O}_7$ . In 1986, it was discovered that some cuprate (compounds bearing anion-copper complexes) and perovskite (any compound with the same crystal structure as a calcium titanium oxide compound) ceramics have a critical temperature above 90 K. Theoretically, they were called HTSCs because such a high exchange temperature was impossible for known superconductors. Liquid nitrogen, an easily available refrigerant, boils at 77 K, so superconductivity experiments below this temperature facilitates is impractical. The critical temperature of mercury-based cuprate materials can also exceed 130 K. There is no enough explanation yet for these high critical temperatures mechanism. However, superconductivity can be explained by electron pairing, which occurs with phonon exchange in superconductors, but this mechanism cannot explain newly discovered superconductivity with a high critical temperature.

In this section, detailed explanations about the transport mechanism in superconducting materials are discussed. For this, the physical mechanism about the transition from the normal state to the superconducting state occurs at  $T_c$ , resistivity changes under the magnetic field, the activation energy state in superconductors, the critical current density, and the Hall effect are discussed with experimental and theoretical aspects. In the first part of the chapter, a brief introduction is reported on the conduction mechanism in superconducting materials. The second part of the chapter deals with the subject of electrical resistivity which is considered for the normal state and superconducting state. In the same section, how the resistivity changes in superconducting materials under magnetic field is also discussed. Immediately after, the issue of activation energy in superconducting materials was explained. Following, the critical current density is discussed in terms of theoretical models, current-voltage measurements, and pinning mechanism in superconductors. In the last part of the chapter, the Hall effect is explained in detail.

## 2 Electrical Resistivity

The inverse of electrical conductivity is electrical resistivity,  $\rho$ . The electrical resistivity of a conductor, which is a characteristic property of each material, is proportional to the surface area and length of the conductor. It arises from the scattering of conduction electrons by the lattice phonons and the defects in the lattice. It is known that the electrical resistivity of a conductor varies with the temperature. As explained above that when a superconductor material cooled below a characteristic

temperature,  $T_c$ , its resistance to the flow of current disappears, and it transforms to a superconducting state. The normal state resistivity of a conductor affects its resistivity in the superconductivity state. Therefore, in this section, the normal state resistivity, its temperature, and anisotropy dependency will be discussed. In addition to normal state resistivity, applied magnetic field dependence of resistivity is another important parameter for superconductor materials. When a magnetic field is applied to the material, a magnetic force acts on the charge carriers. In this case, the resistance of the material and the number of collisions between the charge carriers increase. The change in the electrical resistance of the material under the influence of the applied magnetic field is called magnetoresistance. When a magnetic field is applied to a superconductor, it exhibits different effects in the region above and below  $T_c$ . The magnetic field causes a change in the transition temperature of superconducting materials, the width of the resistance transition, and the activation energy.

In order to increase the ability of usage superconductors in technological applications, it is needed to understand the physical background and improve controlling the energy dissipation mechanism. Therefore, many models that include the normal state resistivity and magneto-resistivity behavior have been introduced in the literature to explain the energy dissipation. In this part of the chapter, after giving brief information about these models, the energy dissipation behavior will be introduced and interpreted in detail with three important successful models.

## 2.1 Normal-State Resistivity

Electric current occurs when negative and positive (ions and holes) charges move in the material. The electric current is defined as the number of electrons passing through any point of the wire per unit of time. The electrons can move freely through metals in a crystal structure which has perfectly ordered atoms [2]. But, in some cases, the electrons moving in metal materials can be scattered by phonons, lattice defects, impurity atoms, and other defects. These scatterings produce resistance against the electric current [3]. So that the resistivity is a characteristic feature of materials and it is briefly known as the inverse of conductivity. Total resistivity of a pure metal defined by Matthiessen's rule is given as following equation [4, 5];

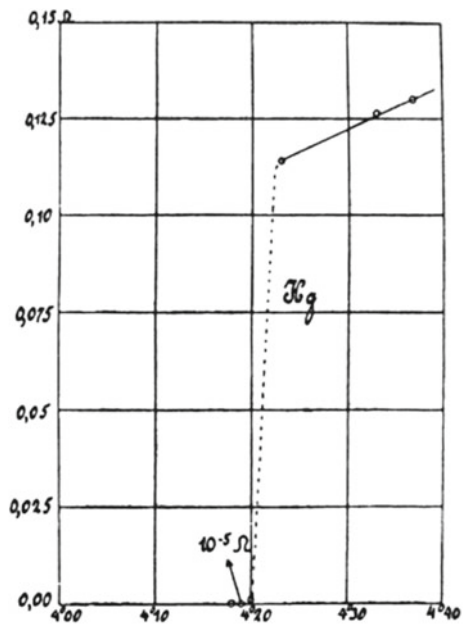
$$\rho = \rho_T + \rho_R \quad (1)$$

where  $\rho_T$  is the resistivity arisen from the scattering of electrons by phonons that occurs with the temperature effect and changes linearly with temperature at high-temperature region [6]. Total residual resistivity,  $\rho_R$ , describes the contribution arising from conduction electrons scattering by defects in the lattice. For a pure metal,  $\rho_R$  value is important and it is nearly constant at low temperatures. It also shows quite a weak temperature dependency [7]. According to Matthiessen rule, the resistivity should be different than zero.

Lord Kelvin (Wiliam Thomson) argues that the resistivity would increase at low temperatures as a result of the freezing of electrons of the atoms in the material [8]. According to Drude, the resistivity should be zero by lowering the temperature to very low temperatures since the scattering of electrons by lattice vibrations is being ineffective [9]. To test the validity of Drudes' theory on the resistivity of metals at low temperatures, Kamerlingh Onnes and one of his collaborator's Gilles Holst measured the resistivity of mercury as a function of temperature. They observed that the resistivity suddenly drops to zero at 4.2 K as shown in Fig. 1. At this temperature, the mercury transforms from a normal metallic state to a new state called superconductivity. The zero resistance is an important property that characterizes superconductivity. The temperature where the resistivity becomes zero is defined as critical temperature,  $T_c$ . It is a characteristic property of the materials. The midpoint of the temperature dependence of the resistivity,  $\rho(T)$ , curve is generally accepted the  $T_c$  value, although some researchers have used the point where the first derivative of the  $\rho(T)$  curve to determine the  $T_c$  value [10–12].

To explain the superconducting properties, Gorter and Casimir developed a two-fluid model in which electrons are separated into two groups as super and normal electrons [14]. Above  $T_c$ , the resistivity increases linearly with increasing temperature. In this state, the conductivity is provided by normal electrons that are equal to those of the electron system in a normal metal. This state is known as normal state in which the material shows electrical resistivity. In the superconductivity state, super electrons are responsible for conductivity. A transition from normal to the superconducting state occurs when the normal metal was cooled below its  $T_c$ . At

**Fig. 1** The temperature dependence of the resistivity for the mercury (Onnes, 1913). Reproduced with permission from [13]



this temperature, a sharp or gradual transition which depends on the material, may arise. Whether the transition is gradual or sudden, it is important for the purity and goodness of the material [3].

The normal state resistivity of some group superconductors [11, 15–18] has attracted attention by researchers. The reason for this interest is the linear variation of the normal state resistance especially for high- $T_c$  superconductors over a large temperature range [19]. The relationship between the normal state resistivity with  $T_c$  also has been an interesting topic for researchers. Various theories have been propounded to determine this relation [20, 21]. According to many researchers, the linear temperature dependency of  $\rho$  arises from resistivity saturation [22]. It is important for understanding the mechanism of the transition from normal state to superconductivity state to investigate the relation between superconductivity and normal state resistivity. To study the correlation between the normal state resistivity and superconductivity properties, Xiao et al. [23] have been investigated the  $\rho(T)$  of  $\text{La}_{1.85}\text{Sr}_{0.15}(\text{Cu}_{1-x}\text{Zn}_x)\text{O}_4$  system. They have reported that all samples show metallic behavior at room temperature and the resistivity values of the samples are constant. The samples have been shown superconducting properties below their  $T_c$  temperatures. To investigate the relationship between the linearity of the temperature dependence of normal state resistivity, they used given the following relation described the resistivity of the high- $T_c$  oxides in the normal state [23];

$$\rho = \rho_0 + \rho(x) + a(x)T \quad (2)$$

where  $\rho_0$ , which is known as residual resistivity, arises from grain boundary, dislocation, and point defects.  $\rho(x)$  is the residual resistivity induced from impurity. The sum of these residual resistivities gives the total  $\rho_R$  of the systems.  $a(x) T$  describes the  $\rho(T)$  and  $a(x)$  is the slope of the curve of  $\rho(T)$ . According to obtained results, the temperature dependence of the normal state resistivity is linear; this result is related to the scattering mechanism [23]. It means that there is a strong correlation between  $T_c$  value and the slope of the normal state resistivity.

Anisotropy dependence of the electrical properties of cuprate superconductors has been reported by Ito et al. [24]. The resistivity may be parallel or perpendicular to the Cu–O planes. In view of this information, Jin et al. [17] have studied the anisotropic behavior of normal state resistivity for  $\text{Bi}_{1.95}\text{Sr}_{1.65}\text{La}_{0.4}\text{CuO}_{6+\delta}$  single crystals. They have obtained some important results that described the characteristic properties of certain superconductors, especially HTSCs. The  $ab$ -plane resistivity,  $\rho_{ab}$ , value is quite small and changes linearly with temperature in the parallel direction. However,  $c$ -axis resistivity,  $\rho_c$ , is large and increases with decreasing temperature in the perpendicular direction. In the normal state,  $\rho_{ab}$  behaves like a metallic with changing temperature. But, in the  $c$ -axis,  $\rho_c$  is dependent on the sample's crystal structure and carrier [17]. The normal state resistivity has significant effects on the transport properties of the superconductors. Therefore, the anisotropy and the temperature dependence of the normal state resistivity should be examined with attention. To measure electrical resistance, different methods and models have been improved and used for

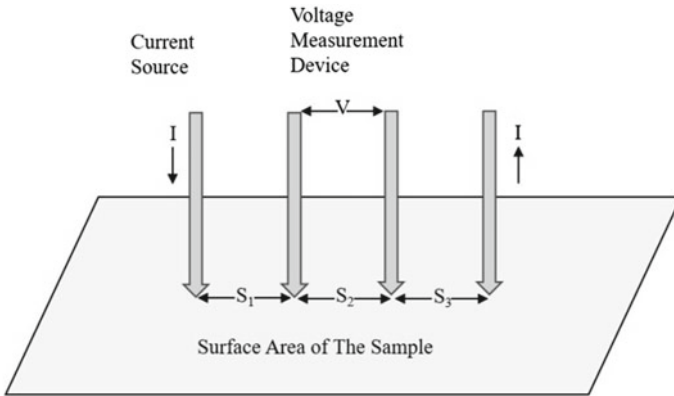


**Fig. 2** Electrical resistivity measurement by four-point probe method

years [25]. Among them, the four-point probe method is the most commonly preferred method because of its ability to measure the resistivity of small-sized samples [25]. In order to minimize measurement errors and to obtain more clear results, attention should be paid to equal distances between the probes and the dimensions of the sample. Moreover, probes should not be too close to the edges of the sample. The details of this method were reported by Valdes et al. [26]. The schematic illustration of this method is given in Fig. 2. In the application of the method, four probes are placed on the surface area of the sample. The current follows the outer probes while the produced potential is measured across the inner probes. The distance,  $S$ , between the probes should be equal to obtain consistent results.

## 2.2 Magnetoresistivity

When a current is applied to the material, collisions may occur between the charge carriers and atoms or defects in the crystal structure. This situation adversely affects the excellent transmission of charge carriers in the material and creates electrical resistivity. Increasing the temperature of the material increases the electrical resistance due to inducing the vibrations of the atoms. Similarly, applied magnetic field also creates a change in the resistance of the material. When a magnetic field is applied to the material, the resistance increases due to the magnetic force on the charge carriers and increased the number of collision events between the carriers. The change in electrical resistance of a material as a result of exposure to a magnetic field is called *magnetoresistivity*. It is proportional to the differences of resistance between two magnetic field measuring points and define as the percent change in the resistance value in a magnetic field and expressed as,



$$\%MR = \frac{\Delta\rho}{\rho_0} \times 100 \quad (3)$$

where  $\Delta\rho = \rho_H - \rho_0$ ;  $\rho_H$  and  $\rho_0$  are the resistance values under a certain magnetic field and zero magnetic field, respectively.

Magnetoresistance (MR), which is revealed by an applied magnetic field on the material, occurs in all metals. The resistance may increase (positive MR) or decrease (negative MR) with an increasing magnetic field. The MR effect depends not only on the magnitude of the applied magnetic field but also the direction of the magnetic field relative to the current. Thomson, who discovered the magnetoresistive effect in ferromagnetic materials for the first time in 1857 [27], defined anisotropic magnetoresistance (AMR) behavior which resistance changes depending on the direction of the applied field (transverse or longitudinal). Thomson made this discovery in his work on a piece of iron, by obtaining a change in the resistance value of 2% with the application of the magnetic field [27]. Thomson, in his experiment on the piece of iron, discovered that the resistance increases when the magnetic force is in the same direction with current and decreases when it makes an angle of  $90^\circ$  [27]. The fact that the MR could be adjusted according to the strength and direction of the magnetic field made it possible for engineers to create sensors that could read data stored as magnetic bits on the hard drives of old computers [28].

By 1988, Baibich discovered a giant magnetoresistance (GMR) in Fe/Cr superlattices and explained it as a function of an applied field and spin-dependent transitions between Fe layers [29]. Here, the effect is associated with the transition between the ferromagnetic and antiferromagnetic states between magnetic layers. The magnetoresistance values were found up to 50% at low temperatures. In the same year, Fert and Grünberg independently observed a very high resistance change in layered magnetic structures with antiferromagnetic interlayers and they were awarded the Nobel Prize in 2007 [29–31]. In 1994, Jin et al. investigated the magnetoresistance properties on the La-Ca-Mn-O thin film samples produced by applying different heat treatments [32]. As a result of temperature optimizations, they observed the magnetoresistance in excess of  $\sim 100,000\%$  near 77 K [32]. It is called as colossal magnetoresistance (CMR) which is quite different from the mechanism of GMR caused by spin-dependent scattering in multilayer or heterogeneous metal films [32]. While the GMR effect arises from extrinsic properties affecting the material, the CMR effect arises from intrinsic properties of the material and exists around the metal–insulator transition temperature.

Magnetoresistors are used in many technological fields such as magnetic sensors, detecting weak magnetic fields, transmitting signals at an excellent signal-to-noise ratio, magnetic data recording system (MRAM), bio-sensors, etc. [33, 34]. The behavior of superconducting materials, which have great technological and industrial importance with their zero resistance, exhibits remarkable results with an applied magnetic field. When examining the behavior of superconducting materials in an applied magnetic field, it is also useful to examine dependency of temperatures below the  $T_c$  (superconducting region) and above the  $T_c$  (normal region), separately.

In the resistance transition curves under the applied magnetic field, two separate parts are occurred that one is not affected by the field and the other one expands towards low temperatures in the form of a tail as the field value increases. With the application of the field in the superconducting region, the resistance transition and critical temperature shift towards lower temperatures and the width of the resistance transition increases [35].

**Fig. 3** Magnetoresistivity measurements,  $\rho(T,H)$ , of pure YBCO, Y-Ti NPs and Y-Ti NWs samples under an applied magnetic field change from 0 to 7 T. Reproduced with permission from Ref. [36]

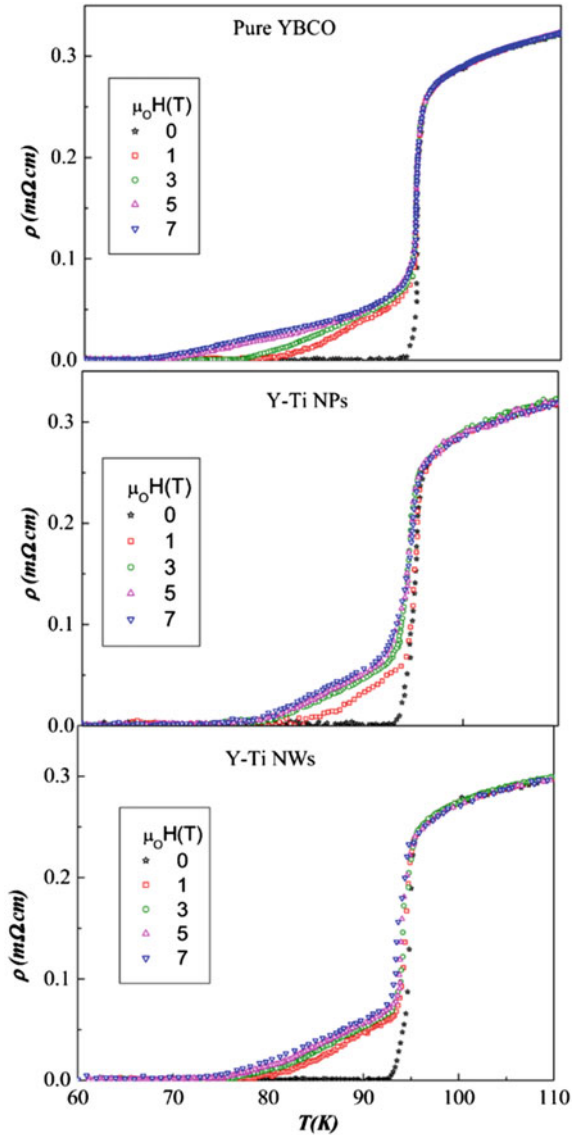


Figure 3 shows the electrical resistivity measurements of pure YBCO ceramics, TiO<sub>2</sub> added YBCO nanoparticles (Y–Ti NPs), and nanowires (Y–Ti NWs) under an applied magnetic field change from 0 to 7 T [36]. As can be clearly seen from the figure, the measurements recorded under zero magnetic field show a sharp transition to zero resistance at the critical temperature. With the application of the magnetic field, it is useful to examine the change of resistance as a function of temperature in two separate regions, the superconducting region below the critical temperature and above the critical temperature. It is seen that there is no change in the region above the critical temperature. In the region below  $T_c$ , it is seen that the resistive transition changes in the form of a tail towards lower temperatures with the increase of the applied field. It is known that the tail behavior is associated with the high thermal energies of the vortices and the irregularities in the percolation path between the grains due to different directions in polycrystalline compounds [37].

This situation negatively affects the flux pinning strength and causes greater resistance. In addition, the shift of the resistivity curve towards low temperatures with an applied magnetic field also increases the change of  $\Delta T_c$  ( $T_c^{onset} - T_c^{offset}$ ) value. The reason for this increase in  $\Delta T_c$  is generally due to a decrease in the  $T_c^{offset}$  value.  $T_c^{onset}$  value is related to the transition of isolated grains to superconductivity, while the  $T_c^{offset}$  value is related to the intergranular bonding of the cuprate superconductor [38]. Since the applied magnetic field mostly affects the intergranular bonding of cuprate superconductors,  $T_c^{onset}$  is not affected by the field, while  $T_c^{offset}$  decreases due to the movement of fluxons under applied magnetic field [39].

The energy consumed in the tail-shaped expansion of the resistance transition, which makes it difficult to determine  $T_c$  precisely, is expressed by the Arrhenius equation given below [40];

$$\rho(T, H) = \rho_0 \exp(-U(H, T)/k_B T). \quad (4)$$

where  $U$  is the activation energy depends on the magnetic field and temperature,  $k_B$  is the Boltzmann constant and  $\rho_0$  is the field-independent pre-exponential factor.  $U$  is important in that it acts as a potential energy barrier to keep the magnetic flux in the pinning center [39].  $U$  is determined from the slope of the  $\ln(\rho/\rho_0)$  versus  $1/T$  plots which is called as Arrhenius plot. Figure 4 shows  $\ln \rho$  versus  $1/T$  plots of film samples of different sizes obtained by deposition of YBa<sub>2</sub>Cu<sub>3</sub>O<sub>7- $\delta$</sub>  on a SrTiO<sub>3</sub> substrate by pulsed laser deposition [41]. Activation energy values can be determined by taking the slope of each curve in the low resistivity region. When Fig. 4 is examined, it is clearly seen that while the superconductor transition curve is sharp under zero field, it widens with the application of the magnetic field. Since the slope of the curves will decrease due to the expansion observed in the superconducting transition curve with the increase of the applied magnetic field, the activation energy decreases with the increase of the field. The decrease in the activation energy with the application of the field results from the increase in the motion of the vortices, and the thermal activation of the magnetic flux as a result of the decrease in the pinning barrier height [41, 42].

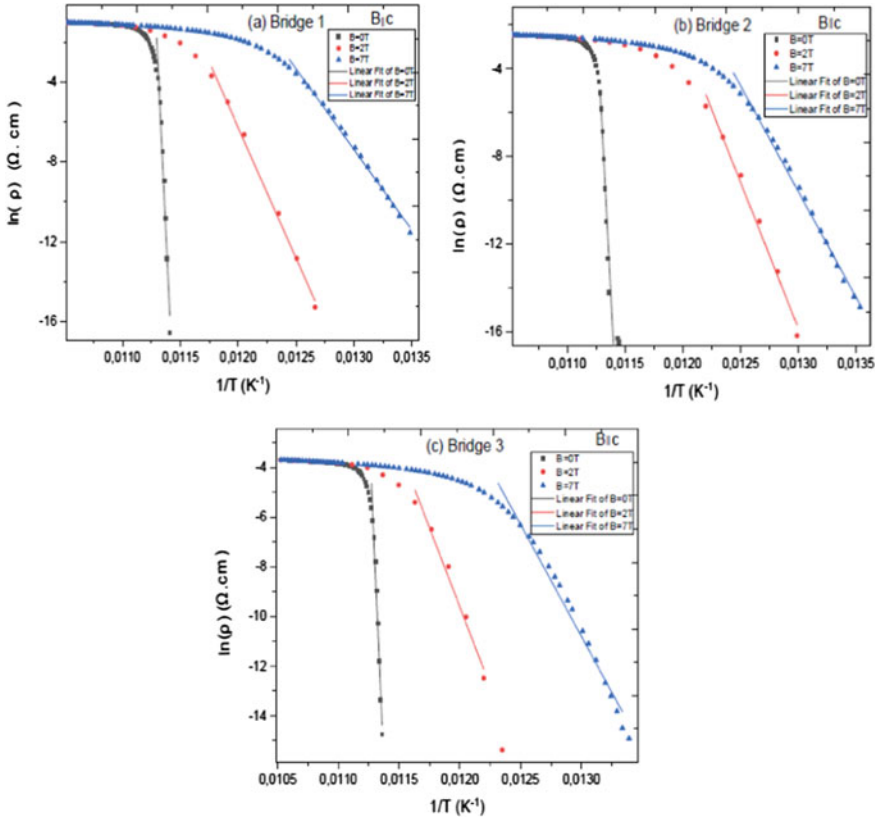


**Fig. 4** Arrhenius plots of the micro-bridges (films of  $\text{YBa}_2\text{Cu}_3\text{O}_{7-\delta}$  deposited on a  $\text{SrTiO}_3$  substrate by pulsed laser deposition) of  $\text{YBa}_2\text{Cu}_3\text{O}_{7-\delta}$  (a)  $10 \mu\text{m} \times 575 \mu\text{m}$ , (b)  $50 \mu\text{m} \times 575 \mu\text{m}$ , (c)  $100 \mu\text{m} \times 300 \mu\text{m}$  at different applied magnetic fields. Reproduced from Ref. [41]

### 2.3 Dissipation Mechanisms and Activation Energy

Attractive features of the superconducting materials that increase the research interest of the researchers also include some challenges to solve in particularly energy dissipation [43]. This problem limits superconductor materials’ technological applications, such as sustainable energy generators, storage and transport, magnetic levitation, novel electronic devices, and fault current limiters [44]. A roadmap document (2015–2030) developed by International Energy Agency for the superconductivity based electric power sector indicates that the sector members including cryogenics, wires, transformers, generators, electric grid systems, superconductor based energy storage systems, and fault current limiters have big potential to increase efficiency and it is expected to occur a big change driven by superconductivity in near future [44]. From the view of this aspect, understanding both the mechanism of the dissipation and behaviour with some parameters becomes important.

Electrical energy sector members mainly focus on the zero-resistance property of the superconducting materials. However, an important problem with this property occurs in HTSCs. HTSCs exhibit a mixed state under a magnetic field of  $H$  which has higher value than lower critical field value  $H_{c1}$ . As explained above, when a HTSC material is in the mixed state, the sample starts to include vortices. Just above  $H_{c1}$ , the vortices are strong in the center while they become weak by increasing distance from this center point. The vortices can move when an applied magnetic field is increased. This movement occurs when the energies of vortices exceed their activation energies. This movement yields to overlap and becomes stronger at every point in the HTSC material. When the applied magnetic field reaches the upper critical magnetic field of  $H_{c2}$ , the superconductivity disappears. These properties of the vortices like motion and magnitude changes lead to resistance and energy dissipation in the HTSC material. This situation makes HTSCs as unattractive materials from the view of the energy applications. Due to the reasons explained above, understanding the energy dissipation mechanism and the vortex behaviours with parameters like applied magnetic field become important for practical applications.

### 2.3.1 Vortices Properties

In this part of the section, vortices properties have been explained briefly to explain the dissipation mechanism and activation energy. It is known that vortices properties are more complicated, but these properties are explained briefly in this part because the vortices properties are not the subject of this chapter. It is known that the applied magnetic field,  $H_{app}$ , penetrates into the HTSC materials as tube-like vortices under  $H_{c1} < H_{app} < H_{c2}$  conditions [45]. When the applied magnetic field is at the minimum level ( $H_{c1}$ ), the penetrated vortices are near the surface and are isolated. These penetrated vortices are strong at the center point of the vortices called core and become weak by distance. By increasing the applied magnetic field, more vortices start to occur in the HTSC material. Interaction of these vortices is repulsive and hence they behave to keep each other away. Due to this fact, the vortices in HTSC material form two-dimensional hexagonal arrangement for high Ginzburg–Landau parameter ( $\kappa = \frac{\lambda}{\xi}$ ,  $\lambda > \xi$ , where  $\lambda$  is penetration depth,  $\xi$  is coherence length) condition. When the magnetic field is even increased, vortices start to move and overlap. Finally, the magnetic field in the vortices becomes strong at every point of HTSC material. By reaching  $H_{c2}$ , the materials phase changes from HTSC to normal state. The explained properties of the vortices above may yield flux motion and energy dissipation.

### 2.3.2 Energy Dissipation

From the view of the technological applications, the explanation for the vortices-driven energy dissipation is important, and many researchers work on this parameter by using some approximations. Some important examples of these approximations

are Ambegaokar-Halperin, fluctuation, flux-flow, glass model, Kosterlitz–Thouless, thermally activated flux flow, and flux creep. In this part of the chapter, these models will be explained. In some examples, it is not possible to distinguish from each other from the view of explaining energy dissipation on specific experimental results. It is known that Ambegaokar-Halperin, thermally activated flux flow, and Kosterlitz–Thouless models are commonly used models due to the advantages of explaining energy dissipation mechanism over other models in the literature. For this reason, in this section, detailed information about these three models will be explained after giving brief information about other proposed models.

According to the spin fluctuation model, anisotropic superconductivities observed in HTSC cuprates and organic superconductors with 2D structure come from the spin fluctuation mechanism [45]. This model shows good agreement between experimental resistivity values and theoretical value obtained from the model for  $\text{Ln}_2\text{CuO}_4$  (Ln = lanthanides) structure (especially for  $(\text{La}_{1-x}\text{Sr}_x)_2\text{CuO}_4$  ( $x = 0.068$ ) sample) [46] but includes a serious unsolved problem about pseudo-gap phenomena for some cuprates and organic superconductors with  $\mu\text{-(ET)}_2\text{X}$  (ET = bis(ethylenedithio)tetrathiafulvalene, X = inorganic anions) salts structure [45, 46]. In the flux flow approximation, creep motion becomes viscous like flow that is named flux flow by Lorentz forces' exceeding pinning force [47]. This flux-flow movement creates a flux-flow resistance which can be defined as  $\rho_f = \rho_n(\frac{H}{H_{c2}})$  formula. It should be noted that this flux-flow system of the vortex yields to non-linear  $I$ - $V$  characteristic in HTSC films. When the random pin potential is high enough, defects in the vortex system occur that destroy the vortex lattice [48]. This fact yields to a non-linear  $I$ - $V$  characteristic. This model is more suitable for high fields superconductors and this situation also limits its validation range [47]. The superconducting glass model suggests the existence of Josephson junctions between granular areas [49–52]. Additionally, magnetic irreversibility is attributed to the superconducting glass model under small magnetic field change due to the weakly coupled superconducting grains and is more conventional when the applied field exceeds 10 kOe [52]. One another approximation about the energy dissipation is flux creep model. This model is commonly known under the  $J \approx J_c$  condition and has well explanation about flux dynamics for homogeneous HTSC materials like perfect single crystals. As explained above, the mentioned models have both success and restrictions.

Ambegaokar-Halperin ( $A$ - $H$ ) model is mainly used to analyse the energy dissipation in granular HTSC, such as YBCO family [53]. According to  $A$ - $H$  model, HTSC samples always display thermally activated phase slim process-driven finite resistance even the current is less than  $I_c$  [53]. The thermal and noise current superimposed on the Josephson junction and the time-averaged voltage value is given by:

$$V = IR_0 \left[ I_0 \left( \frac{Y}{2} \right) \right]^{-2} \quad (5)$$

$$\frac{R}{R_0} = \left[ I_0 \left( \frac{Y}{2} \right) \right]^{-2} \quad (6)$$

here, the  $R_0$  and  $I_0$  are the normal state resistance and the zero-order modified Bessel function, respectively.  $\gamma$  is the ratio of Josephson coupling energy to the thermal energy given by  $\gamma = hI_c/2\pi ek_B T$ . To determine the energy dissipation for HTSC materials, Tinkham offered [54]  $\gamma$  as,

$$\gamma = A'(1-t)^{\frac{3}{2}} \quad (7)$$

In Eq. (7),  $A' = A/B$ ,  $A$  is an experimental constant and  $B$  is the flux density related with the sample,  $t = T/T_c$  is the reduced temperature. Equation (8) can be written when Eq. (7) is added to Eq. (6) [53].

$$\frac{R}{R_0} = \left[ I_0 \left( A'(1-t)^{\frac{3}{2}} \right) \right]^{-2} \quad (8)$$

In order to calculate the energy dissipation, some attempts have been made and normalized resistances ( $R/R_0$ ) at different temperatures are computed in these works [53]. In some cases, theoretical values are in accordance with experimental values at low-temperature range [42, 53] and it is not convenient with some others [54–57]. In order to solve this problem, Eq. (8) is modified as:

$$\frac{R}{R_0} = \left[ I_0 \left( A'(1-t)^m \right) \right]^{-2} \quad (9)$$

Equation (9) is defined by replacing the 3/2 value with the  $m$  value in Eq. (8) to consider size, the orientation of Josephson junctions, structural irregularities, and changing the degree of anisotropy parameters of the HTSC materials [53]. It is needed to plot  $\ln(\gamma)$  vs.  $\ln(1-t)$  plot by using  $I_0(\frac{\gamma}{2})$  value obtained from the Eq. (6) and evaluating  $R = R_0$  at different temperatures. Then upgraded zero-order Bessel functions' standard plot can be used to obtain  $\gamma$  [53]. The  $m$  value is determined from the slope of  $\ln(\gamma)$  vs  $\ln(1-t)$  graph [53]. Different  $m_x$  and  $A_x$  ( $x = 1, 2, 3$ ) data sets are possible to obtain from the slope of  $\ln(\gamma)$  vs  $\ln(1-t)$  graph in accordance with the applied magnetic field. It is also possible to plot  $R$ - $T$  curves by using the non-linear least square method. These theoretical  $R$ - $T$  graphs that based on each  $m_i$  and  $A_i$  data sets may show a good fit with the whole side or some part of the experimental  $R$ - $T$  graph like the lower or upper-temperature side. In some cases, each theoretical curve based on the data set value may fit a different part of the experimental  $R$ - $T$  graph for the same HTSC samples. For example, one curve for one dataset like  $m_1$  and  $A_1$  shows a good fit for the low temperature side of the experimental  $R$ - $T$  curve while another curve obtained from another data set like  $m_2$  and  $A_2$  may show a good fit for the high-temperature side of the experimental  $R$ - $T$  curve. Additionally, these two curves may show crossover at any temperature means dissipation crossover temperature,  $T_{BP}$ . Observing  $T_{BP}$  without a magnetic field indicates the existing thermally produced vortices in HTSC samples [53, 58, 59]. The existence of  $T_{BP}$  value in any HTSC material means two different types of dissipation mechanisms are possible for this material. The first dissipation mechanism is valid for a higher temperature than  $T_{BP}$

region of the superconducting part of  $R$ - $T$  curve. At this region, the dissipation mechanism is governed by the order parameter-driven phase slip process [53]. The latter dissipation mechanism is active in the lower temperature than  $T_{BP}$  range of the  $R$ - $T$  curve. In this region, energy dissipation occurs due to the motion of the vortices. This situation comes from two parameters called the vortex dynamics and the order parameter fluctuations [53]. Although it is possible to determine conceivable reasons for energy dissipations at the lower and upper sides of the  $T_{BP}$ , in some cases, it can be possible an overlap of the lower and upper sides of the  $T_{BP}$  and different parameters may occur at the same temperature [53]. According to the  $A$ - $H$  model, it needs to determine the energy dissipation parameters of both the upper and lower sides of the  $T_{BP}$ . It is helpful to control this energy dissipation mechanism of the HTSC materials for technological applications by this model. On the other hand, the  $A$ - $H$  model cannot explain adequately the tail part of the  $R$ - $T$  graph [53, 60, 61].

One another model that is frequently used to perform the energy dissipation is the Thermally Activated Flux Flow, TAFF, model. According to this model, the dissipation behaviour can be divided into three situations in the transition region between  $T_c^{\text{onset}}$  and  $T_c^{\text{offset}}$  [62–65]. The first is flux flow if the  $J > J_c$ , the second is TAFF if  $J < J_c$ , and the last is the flux creep if the  $J \approx J_c$ . According to Palstra et al. [62], the phase transition regime is called “flux creep”, if the pinning force is dominant. Otherwise, it is called “flux flow” under the Lorentz force domination [62]. In the TAFF model, a universal formula for TAFF resistivity is given as follows:

$$\rho = \left( \frac{2\nu_0 LH}{J} \right) \exp\left( -\frac{J_{c0} HVL}{T} \right) \sinh\left( \frac{JHVL}{T} \right) \quad (10)$$

here  $\nu_0$  is the attempt frequency for hopping a flux group,  $L$  is hopping distance,  $H$  is magnetic induction,  $J$  is applied current density,  $J_{c0}$  is critical current density under flux creep condition,  $V$  is bundle volume, and  $T$  is temperature. If the applied current density is small enough and  $JHVL/T \ll 1$ , and Eq. (10) becomes,

$$\rho = \left( \frac{2\rho_c U}{T} \right) \exp\left( -\frac{U}{T} \right) = \rho_{0f} \exp\left( -\frac{U}{T} \right) \quad (11)$$

here,  $U$  is Thermal Activation Energy, TAE, and given as  $J_{c0}HVL$ , and  $\rho_c = \frac{\nu_0 LH}{J_{c0}}$ . For HTSC cuprates the  $2\rho_c U/T$  is generally accepted as a constant  $\rho_{0f}$  [66]. For activation energy, in addition to Eq. 4, given three assumptions are also accepted:

$$U(T, H) = U_0(H) \left( 1 - \frac{T}{T_c} \right) \quad (12)$$

$$\ln \rho(T, H) = \ln \rho_0(H) - \left( \frac{U_0(H)}{T} \right) \quad (13)$$



$$\ln \rho_0(H) = \ln \rho_{0f} + \left( \frac{U_0(H)}{T_c} \right) \quad (14)$$

Then  $\ln \rho$  vs  $1/T$  becomes Arrhenius relation. Moreover:

$$\frac{\partial \ln}{\partial \left( \frac{1}{T} \right)} = U_0(H) \quad (15)$$

The plot of the  $\ln \rho$  vs  $1/T$  should be linear in the TAFF region [66] and the slope of this graph gives the  $U_0$ . The behaviour of the activation energy may be parabolic or different power-law exponent of the magnetic field rely on the flux pinning and the type of HTSC materials [63, 67]. Palstra et al. offered a relation about power law dependence as  $U_0 \sim H^{-\alpha}$ . Some other relations depending on the materials are possible like Kucera's offers as  $U_0 \sim H^{-\frac{1}{2}} \left( 1 - \frac{T}{T_c} \right)$  [68]. To increase the success of the TAFF model, some researchers offer a consideration including the relation between  $U(T, H)$  vs  $T$ , and temperature-dependent prefactor [64, 69]. By using  $U(T, H) = U_0(H) \left( 1 - \frac{T}{T_c} \right)^q$  relation and Eq. (11), it can be defined as:

$$\ln \rho = \ln(2\rho_c U_0) + q \ln(1 - T/T_c) - \ln T - U_0(1 - T/T_c)^q/T, \quad (16)$$

$$\frac{\partial \ln}{\partial \left( \frac{1}{T} \right)} = \left[ U_0 \left( 1 - \frac{T}{T_c} \right)^q - T \right] \left[ 1 + \frac{q \left( \frac{T}{T_c} \right)}{\left( 1 - \frac{T}{T_c} \right)} \right] \quad (17)$$

In these Eqs. (16) and (17),  $\rho_c$  and  $U_0$  values are not relying on temperature, and  $T_c$  is observed from Arrhenius relation [64]. Determining the correct  $q$  value and 3D or 2D behaviour of the HTSC materials are important to apply the modified TAFF model. In some HTSC materials in the literature, the modified TAFF model shows a good agreement with experimental data [64, 66]. It should be noted that the success of the TAFF model is valid in a restricted area in the transition temperature range [61].

Some HTSCs including cuprates exhibit strongly 2D behaviour. Especially in cuprates, some properties like anisotropic behaviour of the normal state resistivity, critical current, and upper critical field indicate weakly paired superconductor  $\text{CuO}_2$  planes. In this kind of HTSCs, understanding 2D fluctuation is important to explain the main superconducting properties. The energy dissipation of these materials is mainly related to the thermally excited pairs of the vortices with inverse direction when the thermal fluctuations behave parallel with  $\text{CuO}_2$  planes by keeping 2D structure. If the vortex pairs keeping coupled structure below  $T_c$  then Kosterlitz-Thouless,  $KT$ , the model may explain the phase transition and the energy dissipation [70–72]. In this kind of materials, the explained properties occur above a temperature called Kosterlitz-Thouless temperature,  $T_{KT}$ , and  $KT$  model still valid just below (a few degrees below) the Ginzburg–Landau transition temperature,  $T_{G-L}$  [61]. It is

known that  $T_{G-L}$  is determined as the peak point of the  $d\rho/dT$  vs  $T$  graph [61, 73]. All vortices below the  $T_{KT}$  are coupled in frozen vortex and anti-vortex structures. This situation means no free vortices are available at and below this temperature [61]. However, by increasing temperature, some vortices become free from the vortex and anti-vortex structure that introduces the energy dissipation to the HTSC material [53]. In the light of the given information, Halperin and Nelson [73] offered a zero-temperature coherence length,  $\xi_0$ , and mean free path,  $l$ , dependent resistivity formula given below:

$$\frac{\rho}{\rho_N} = A \frac{l}{\xi_0} \exp \left[ -\beta \left( \frac{T_{G-L} - T}{T - T_{KT}} \right)^{0.5} \right] \quad (18)$$

here,  $\rho_N$  is normal state resistivity,  $\beta$  and  $A$  define non-universal constants related to the order of unity [73]. By considering the results obtained from the literature, it can be argued that  $KT$  model successfully describes the energy dissipation mechanism in 2D cuprates HTSC materials, such as BSSCO and YBCO families within the  $T_{KT} < T < T_{G-L}$  temperature range [43, 53, 61]. It is possible to observe a small amount of deviation between the experimental value and the value observed from the  $KT$  model at temperatures close to the  $T_{KT}$  and  $T_{G-L}$ . This possible deviation may be related to the level of the fluctuations in the order parameter.

In conclusion, to explain the energy dissipation that is based on the vortex mechanism, many models have been offered in the literature. In this part of the chapter, energy-dissipation related to superconducting properties like normal state resistivity and magnetoresistivity have been expressed and then these models have been explained and interpreted. These explanations are useful to understand the physical mechanism of the energy dissipation in HTSC materials and are also useful to control it.

### 3 Critical Current Density

After the discovery of superconductivity in mercury at 4.2 K in 1911 by Kamerlingh Onnes at  $H_c$  of around 0.1 T, a threshold value of  $J_c$  is observed around 1000 A/cm<sup>2</sup>. Simply  $J_c$  can be calculated by critical current,  $I_c$ , divided by the cross-sectional area  $S$  of the superconducting region:

$$J_c = I_c/S \quad (19)$$

Experimental results showed that  $J_c$  exhibits temperature dependence behavior expressed as following equation:

$$J_c(T) = J_c(0)(T_c - T)T_c \quad (20)$$

Below  $T_c$ , superconductors exhibit zero electrical resistivity which means the superconductor can carry current without resistance and produce a high magnetic field. Following the discovery of superconductivity in mercury, Onnes in 1913 observed superconducting behavior in a solenoid that is made of tin and lead [74]. After a year, Onnes's studies showed that superconducting transition in lead can be controlled by an applied magnetic field. This study confirmed that applied magnetic field induces heat and above  $H_c$ , superconductivity disappears [74]. The relation between critical current and critical magnetic field was explained by Silsbee in 1927. He described the critical current in the conductor proportional to the critical magnetic field due to the current flow in the conductor reduces down the middle of the conductor and given with following formula:

$$I_c = 2\pi a H_c \text{ and } J_c = 2H_c/a \quad (21)$$

here,  $a$  is the radius of the conductor.  $I_c$  increases with increasing  $a$ . Following, it was understood that the critical current density also depends on  $a$ , so that it is not an intrinsic property of superconductors. Independently, the Leiden laboratory also confirmed the critical current properties of the tin film similar to Silsbee's findings. Moreover, the experimental studies on tin revealed the critical field as a function of temperature in the Leiden laboratory with the formula [74]:

$$H_c(T) = H_c(0) \left[ 1 - \left( \frac{T}{T_c} \right)^2 \right] \quad (22)$$

Following Meissner in the Leiden laboratory continued to work on superconducting transition metals, in particular their alloy forms of Ta-Nb and Pb-Bi in which a critical field of 20 kg was obtained at 4.2 K. Meissner and Ochsenfeld performed an experimental study by measuring the magnetic field between two parallel superconducting cylinders. They observed an enhanced magnetic field below  $T_c$  that flux was being expelled from the body of the superconductors [74]. They were also found that Silsbee's hypothesis was not valid for alloy forms of superconductors.

### 3.1 Measurement Method for $J_c$

To determine  $J_c$ , there are various methods, such as current vs applied voltage ( $I$ - $V$  curve), magnetization vs DC and AC applied field ( $M$ - $H$  curve), Lorentz force, or collective pinning force methods. For possible applications of superconductors, a high-level accuracy in measurements is required for any material. Overall, in this section,  $J_c$ , which is one of the most important parameters of a superconducting material, will be considered in terms of measurement methods. Figure 5 shows the  $M$ - $H$  curves for the Type I and II superconductors [75]. In Type I superconductors, the normal state above  $H_c$  and Meissner state below  $H_c$ , occur in which perfect

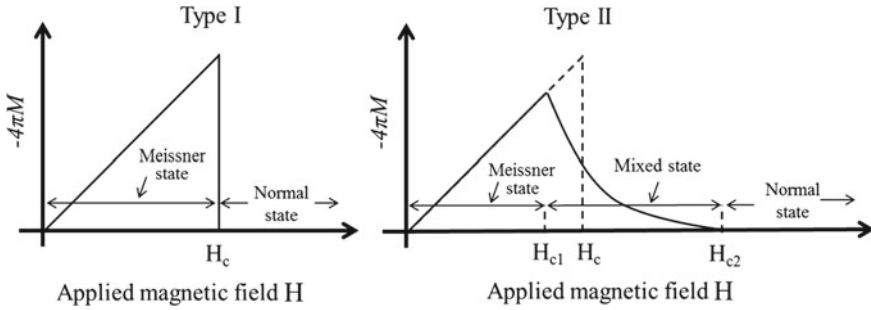


**Fig. 5** *M-H* curve of Type I and II superconductors. **a** Showing Normal and Meissner states in which perfect diamagnetism occurs. **b** normal, mixed state (the field partially penetrates), and Meissner state of superconductor materials. Reproduced with permission from Ref. [75]

diamagnetism occurs (see the left image in Fig. 5). In Type II superconductors, the normal, mixed state (the field partially penetrates), and Meissner states occur. In contrast to Type I SCs, there are two critical fields,  $H_{c1}$ , and  $H_{c2}$  in Type II SCs (see the right image in Fig. 5).

The most preferred method is the direct measurement of  $J_c$  with measuring current,  $I$ , as a function of applied voltage,  $V$ , which is called  $I-V$  curve. In this curve, the voltage level can be lowered to  $\mu V$  level, and the current density usually reaches a range of  $10^5 \text{ Acm}^{-2}$ . When the current density is equal to the critical current density, the resistivity of the superconductor becomes  $10^{-12} \Omega\cdot\text{cm}$ . To determine  $J_c$ , there are three criteria usually used for superconductors as seen in Fig. 6a [76]. The first criterion is the off-set method (A) at which takes a tangent of the straight part of the curve.

The point where it intercepts the  $x$ -axis shows the  $J_c$ . The second criterion is considering electric field ( $B$ ) reaches an optimum value between  $10 \mu\text{Vm}^{-1}$  and  $100$

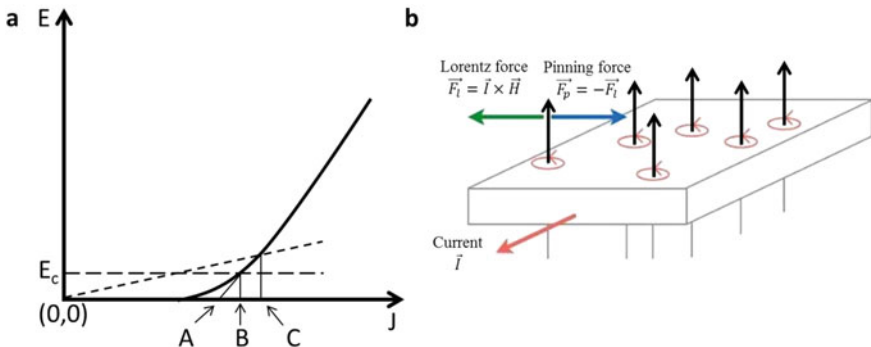


**Fig. 6** **a** Determining  $J_c$  from the  $E-J$  curve via A: Off-set method, B: Electric field creation, C: Resistivity creation. **b** Applied current in an external magnetic field which creates Lorentz force acting on the flux lines in a superconductor. For more details see Ref. [77].

$\mu\text{Vm}^{-1}$ . Drawing a line at  $E = E_c$  across the curve, the intersection point attributes to  $J_c$  on the  $x$ -axis. The last criterion is taking into account the resistivity of the superconductor (C), when the resistivity of the superconductor reaches a value in between  $10^{-13} \Omega\cdot\text{m}$  and  $10^{-14} \Omega\cdot\text{m}$  ( $\rho = \rho_c$ ).

$J_c$  can also be determined by measuring magnetization as a function of applied magnetic field ( $M$ - $H$ ) which is modified persistent current in the superconductor (see Fig. 7a). The theoretical model for  $J_c$  was revealed by Bean who used a model to extract  $J_c$  from the hysteresis loop [78]. This measurement can be performed on small quantities of materials, so it has become popular in recent studies. The average critical current density can be estimated via magnetic moment differences (DC magnetization) and the slap thickness in superconductor by  $J_c = \Delta M/d$ .  $\Delta M$ , so that  $J_c$ , inverse proportion to the external magnetic field,  $H_e$ , which is applied along with the long slap. It can be estimated that an increase in  $H_e$  results in a decrease in  $J_c$  in superconducting material. It is clear from the formula that  $J_c$  also decreases with increasing  $d$ . The critical current density of various materials such as YBCO:  $H\parallel$ tape plane, YBCO:  $H\perp$ tape plane, Nb-Ti LHC at 1.9 K, 2212: 100 bar, 2223:  $H\perp$ tape surface, 2212: 1 bar, and Nb<sub>3</sub>Sn as a function of the applied field are presented in Fig. 7a. It can be seen from the figure,  $J_c$  decreases with increasing applied field up to 44 T. YBCO:  $H\parallel$ tape plane sample exhibits the largest  $J_c$  over  $10^5 \text{ Amm}^{-2}$  (or  $\text{A}\cdot\text{cm}^{-2} \times 10^2$ ) value.

On the other hand, AC magnetic field ( $H_e = h_0\cos\omega t$ ) can be used to determine  $J_c$  by measuring the penetrating flux. With this method, the pinning force and the displacement of the flux density can also be estimated. The magnetic flux distribution in the inner region of superconductor wire increases linearly with critical current density and the high external magnetic field forces to flow the current in the surface region. AC measurement requires much more data and analyses comparing to the

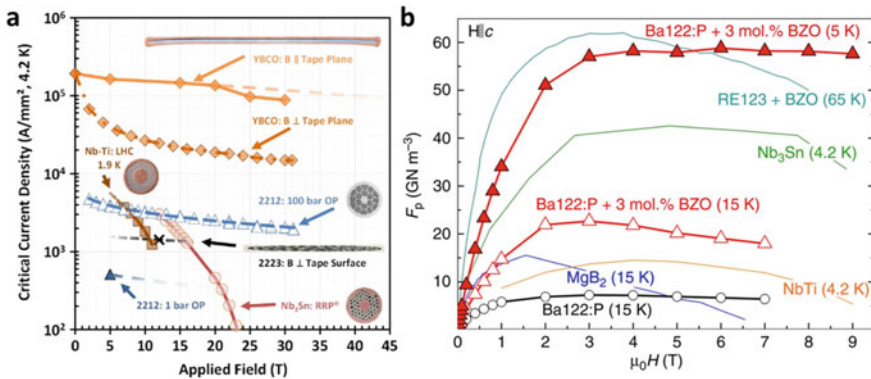


**Fig. 7** **a** Critical current density recorded for YBCO:  $H\parallel$  tape plane, YBCO:  $H\perp$  tape plane, Nb-Ti at 1.9 K, 2212: 100 bar, 2223:  $H\perp$  tape surface, 2212: 1 bar, and Nb<sub>3</sub>Sn as a function of the applied field. Reproduced from Ref. [79]. **b** The summary of the flux pinning force values as a function of applied magnetic field for the thin film superconductor tapes. Reproduced with permission from Ref. [80]

four terminal and the DC magnetization methods. However, inhomogeneous current flow throughout the surface and close to the surface, the AC magnetization method provides clear results for  $J_c$ .

The flux lines and defects in superconductors create flux pinning interactions which result in the maximum superconducting current density. The pinning force,  $F_p$ , depends on the microstructure and local defects of superconducting.

Figure 6b shows a schematic diagram in which the vortices experience the Lorentz force under current flow and magnetic field [77, 81]. If  $F_p$  is larger than the Lorentz force, the vortices do not occur, and no voltage will be detected due to the applied current density. Once the applied current increased to a certain value, at which the Lorentz force exceeds the pinning force, the vortices will start to move in superconductor and a voltage will be measured. At this condition of  $F_L = F_p$ , the critical current density will be equal to:

$$J_c = F_p/H_e. \quad (23)$$

The flux pinning force values for the thin film superconductor tapes are presented as a function of an applied magnetic field in Fig. 7b [80]. The critical current density of the thin film superconductor tape can be enhanced by a factor of 7 to 10 with an applied field of 1 T without any other atomic dopant. As seen in Fig. 7b, the pinning force increases fast with increasing applied field up to 3 T. Beyond 3 T,  $F_p$  becomes stable with the applied magnetic field. The experimental results of Ba122:P film with doping BaZrO<sub>3</sub> (BZO) nanoparticles at 5 K exhibited three times larger pinning force than the Ba122 film at 15 K [80]. Comparing these results with the data for NbTi at 4.2 K, MgB<sub>2</sub> (Hllab) at 15 K, Nb<sub>3</sub>Sn at 4.2 K, and RE123 + BZO-coated conductor at 65 K show that Ba122 + BZO film provides enhanced  $F_p$  values [80]. On the other hand, BaZrO<sub>3</sub> superconductor with doping 15% to 25% of Zr was provided enhances critical current densities due to pinned magnetic flux lines in the film structure. Here, the defects, which are created by Zr doping, play a key role in the pinning flux force. In another study, the highest  $J_c$  was recorded above  $20 \times 10^6$  Acm<sup>-2</sup> at 30 K, 3 T for Gd and Y doped Ba<sub>2</sub>Cu<sub>3</sub>O<sub>x</sub> superconductor and record-high pinning force levels above  $1.7 \times 10^{12}$  Nm<sup>-3</sup> at 4.2 K, 30 T [82]. It can be noted that the pinning force strongly depends on the applied magnetic field and temperature. So that the fast increase in  $F_p$  induces an increase in  $J_c$  at low applied field, but the stabilization of  $F_p$  at high field results in a decrease of  $J_c$  values.

### 3.2 Recent Findings

From early 1900 to 2020, single elements, alloys, and compounds have been studied at various compositions, applied magnetic field, thickness, pressure, and shape to increase the critical temperature,  $T_c$ , for practical applications.  $J_c$  is one of the important criteria to consider the material as a superconductor if only  $J_c$  reaches  $10^5$  Acm<sup>-2</sup> level along with high  $T_c$ . Today's technology-relevant applications of

superconductors are based on NbTi alloys and Nb<sub>3</sub>Sn compounds. Alloying Nb with  $\alpha$ -Ti creates the pinning centers which results in high  $J_c$ . On the other hand, the new type of superconductors based on YBCO exhibits high  $T_c$  which creates potential applications if only  $J_c$  reaches  $10^5 \text{ Acm}^{-2}$  level. With this purpose, MgB<sub>2</sub> and YBa<sub>2</sub>Cu<sub>3</sub>O<sub>7</sub> type compounds exhibit superconducting effects at 20 K and 77 K, respectively. Besides these superconductors, Nd-123 exhibited superconductivity at 77 K with a field-dependent  $J_c$  maximum  $2 \times 10^4 \text{ Acm}^{-2}$  under 0 T and this value is reduced to  $1 \times 10^4 \text{ Acm}^{-2}$  under 4 T. Discovery of superconductivity in MgB<sub>2</sub> thin film at 39 K achieved large  $J_c$  values  $10^6 \text{ Acm}^{-2}$  under 1 T and  $10^5 \text{ Acm}^{-2}$  under 10 T [83]. For Nb<sub>3</sub>Sn case with a thickness of 3.9 nm provides enhanced critical values:  $J_c \approx 1.1 \times 10^{12} \text{ Am}^{-2}$  and  $J_{c1} \approx 8.0 \times 10^{10} \text{ Am}^{-2}$  were obtained at 4.2 K when the critical field reaches to  $\mu_0 H_c \approx 0.5 \text{ T}$  and  $\mu_0 H_{c1} \approx 20 \text{ mT}$ , respectively [84]. The small thickness of superconductor wires is rather difficult to fabricate, hence  $J_{c1}$  is not suitable for practical applications.

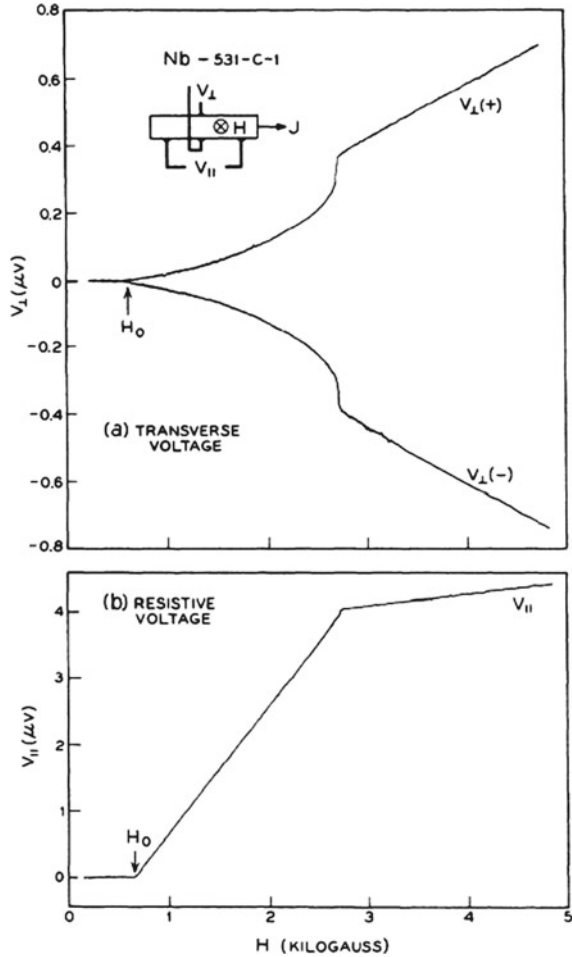
## 4 Hall Effect

A voltage difference (the Hall voltage) across to an electric current direction applied to a semiconductor or conductor materials can be measured when they are placed under a perpendicular magnetic field. This kind of voltage difference is known as Hall effect discovered by Edwin Hall in 1879 [85]. In semiconductor or conductor, the Hall coefficient ( $R_H$ ) can be formulized as:

$$R_H = \rho_{xy}/H = 1/nec\sqrt{b^2 - 4ac} \quad (24)$$

where  $\rho_{xy}$  is the Hall resistivity,  $H$  is the applied magnetic field,  $n$  is the charge carrier density,  $e$  is the electron's charge, and  $c$  is the speed of light. The sign of  $R_H$ , the polarity of the voltage difference between  $xy$ -plane in a Hall bar device, determines the type of semiconductors that the orientation of the applied magnetic field and electric current. On the other hand, the Hall effect in a rod of Nb superconductor material was first experimentally observed in 1965 by Reed et al. [86]. The Hall effect measurement was performed at 4.2 K with a current density of  $460 \text{ Acm}^{-2}$ . Figure 8 shows the experimental data for the transverse ( $V_{\perp}$ ) and longitudinal ( $V_{\parallel}$ ) voltages for the Nb sample at 4.2 K. The transverse voltage was measured under positively and negatively directed magnetic fields labeled as  $V_{\perp}(+)$  and  $V_{\perp}(-)$ , respectively. The longitudinal voltage, related to the resistance, is zero up to  $H_0$  field (see Fig. 8b). Above the  $H_0$  field, the resistance in mixed state linearly changes with the applied field up to upper critical field  $H_{c2}$ . Here, the Hall voltage is almost proportional to  $(H - H_0)^2$  which means the voltage rapidly increases up to the upper critical magnetic field value. After this point, the resistance becomes normal state behavior that it changes more slowly with an increasing magnetic field.

**Fig. 8** The experimental data for the (a) transverse ( $V_{\perp}$ ) and (b) longitudinal ( $V_{\parallel}$ ) voltages for the Nb sample at 4.2 K. The transverse voltage curves labeled as  $V_{\perp}(+)$  and  $V_{\perp}(-)$  were measured under positive and negative magnetic fields, respectively. The difference between these curves is equal to twice the Hall voltage. Reproduced with permission from Ref. [86]



When a superconductor, especially HTSCs, because of their London penetration lengths in HTSCs that are larger in magnitude than others, is used as a material in Hall bar device, the sign of Hall voltage becomes reverse relative to the normal state that it means the negative (positive) terminal becomes positive (negative) as the temperature decreases through the fluctuation region of superconducting material. This abnormal behavior of Hall resistance in HTSCs has not been fully understood for decades because of avoiding a definitive explanation and leftovers unsolved questions behind its physical mechanism. The reason for this sign change was first assumed due to skew scattering in the fluctuation region and the influence of the non-isothermal effects [87–89]. But, these effects cannot explain the whole mechanism of the sign reversal in the Hall resistance. Many theories have been put forward to explain the abnormal behavior of Hall resistance, including many effects such as vortex pinning,



hydrodynamic effects, superconducting fluctuations, Berry phase, and charges in the vortex core [90–98].

In 1995, Feigel'man et al. wrote a theory on the sign change in Hall voltage in HTSCs by considering both topological and normal excitation scattering effects. They referred that the sign change is the result of the density of normal excitations in the vortex core rather than what is far from the vortex when a superconductor is placed in a magnetic field. In this theory, the Hall conductivity  $\sigma_{xy}$  was expressed as the following relation:

$$\sigma_{xy} = \sigma_{xy}^s - \frac{\partial \Omega_{SC}}{\partial \mu} \frac{ec}{B} \quad (25)$$

where  $\sigma_{xy}^s$  is normal state excitation,  $\partial \Omega_{SC}(r)$  is the superconducting part of the thermodynamic potential density, which depends on the distance  $r$  from the vortex core, and  $\mu$  is chemical potential. The second part of the right of Eq. (25) is related to the topological contribution  $\sigma_{xy}^t$  that contributes to a double sign change in Hall effect. We should first describe the formation of the Hall effect in HTSC material. The voltage difference in the transverse can be formed by the force experienced by a vortex moving with a velocity under applied electric current. At least there are two contributions to the transverse force which are non-dissipative momentum transfer from the moving vortex to infinity and momentum transfer from the vortex to the normal excitations in the vortex core. Since the chemical potential is different between the normal phase and the superconducting phase, the vortex core can become charged that is opposite to the sign of dominant charge carriers. Although *Feigel'man's* theory can be used to define the experimental data as applied to various works [99–101], the carrier density in the vortex core must be assumed to be larger than outside of the vortex. This contradictory situation in the sign of the vortex core charge was modeled by *Khomskii* and *Freimuth* in 1995 [98]. However, the additional transverse force comes from the *Khomskii's* model due to the opposite sign creates the Magnus force in the Galilean invariant case.

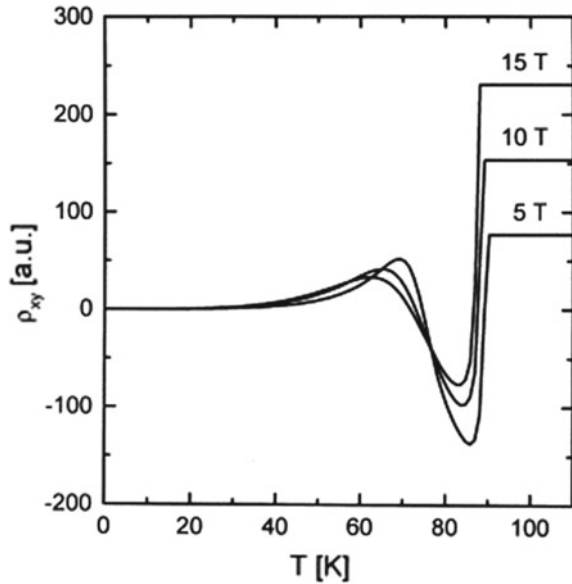
In a recent model, the Magnus force was assumed that it comes from the interaction between vortices and superconducting fluid, whereas the Lorentz force is responsible for the interaction between vortices and the normal state fluid [93]. These correlatively interacting subsystems, such as vortices, superconducting, and normal state fluids, contemporaneously solve the equations of motion. Hence, the solution in this model explains the Hall voltage sign reversal and simple numerical calculations merge with the experimental data.

The longitudinal ( $\rho_{xx}$ ) and Hall resistivities ( $\rho_{xy}$ ) can be expressed as following relations based on the model created by *Kolacek* and *Vasek* [93]:

$$\rho_{xx} = \left[ \tau_n \omega_c f_n (1 + \tau_v^2 \Omega^2) + \tau_v \Omega (f_s^2 + \tau_n^2 \omega_c^2) \right] \frac{\omega_c}{0 \omega_p^2 D} \quad (26)$$

$$\rho_{xy} = \left[ (f_s - f_n) (f_s f_n \tau_v^2 \Omega^2 - \tau_n^2 \omega_c^2) - f_s (1 + 4 f_n \tau_n \omega_c \tau_v \Omega) \right] \frac{\omega_c}{0 \omega_p^2 D} \quad (27)$$

**Fig. 9** Temperature dependence of the Hall resistivity under different magnetic fields. Parameters of the model are  $\Omega_0\tau_v = 50$ ,  $\alpha = 0$ ,  $1/\tau_n = 35 \text{ cm}^{-1}$ . Reproduced with permission from Ref. [93]



where the subscripts of  $n$ ,  $s$ , and  $v$  mean the normal state, superconducting state, and vortex, respectively.  $\Omega$  is the angular frequency which is  $nh/2m_v$ .  $\omega_c$  is the cyclotron frequency of superconducting charge carriers.  $\tau_v$  ( $\tau_n$ ) is the vortex (normal state) relaxation time.  $f_n$  ( $f_s$ ) is the normal (superconducting) state fraction on the magnetic field. Equation (27) can be applied to HTSCs. Since the London penetration depth in HTSCs is larger than others, the magnetic field becomes almost homogenous in superconductors. Figure 9 shows the model's curves of the temperature dependence of the Hall resistivity under different magnetic fields. The resistivity of the HTSC becomes negative when its temperature reaches its mixed state region, and it becomes positive again even the temperature is reduced below its critical temperature.

In addition to the ordinary Hall effect, spin Hall effect (SHE) and quantum Hall effect (QHE) can also be observed in a special structure that consists of superconductor-ferromagnetic and semiconductor-superconductor, respectively. Spin-dependent transport in a heterostructure creates nonequilibrium spin accumulation and spin current that will be an application in spintronics. SHE can be generally seen in ferromagnet and nonmagnetic material systems, f.e. heavy metal and semiconductors. Recent progress on the SHE in superconductor system shows that the generation and controlling of spin-polarized triplet Cooper pairs in superconductor-ferromagnetic interface. In addition to SHE, QHE was also observed in a heterostructure consists of semiconductor-superconductor system such as ZnO/MoGe [102] and GaN/NbN [103]. A precise voltage across the opposite surface of a thin conductor or semiconductor sheet can be observed when an electric current is passed along the longitudinal of this sheet under a strong magnetic field is applied perpendicular to the sheet. This kind of voltage drop is quantized that it means the voltage can only

change in discrete steps which are called as quantum Hall effect. The strong magnetic fields usually destroy the superconducting properties because of their upper critical fields. Thus, the juxtaposition of the two terms of superconductivity and the quantum Hall effect constitutes an oddity. The electronic states of the surface of the sheet are topologically protected because the electrons in the edge states can only move in one direction. An edge electron having a certain momentum cannot scatter into a state with opposite momentum (or spin). Therefore, topologically protected states might be used in quantum-computing applications.

Figure 10a shows the longitudinal ( $R_{xx}$ , black curve) and transverse resistance ( $R_{xy}$ , red curve) as a function of the gate voltage applied to a Hall bar device under 45 T magnetic field at 390 mK in GaN/NbN heterostructure [103]. Here, NbN is a superconductor film with a thickness of 50 nm and GaN is semiconductor. The plateaus  $R_{xy}$  data clearly shows the QHE in such a heterostructure (see Fig. 10a). In each peak position of  $R_{xx}$  value, the plateaus of the QHE state transits to the other state that it occurs when the Fermi level is located inside a Landau level. The upper critical magnetic field that is applied perpendicular to the heterostructure, as a function of temperature is shown in Fig. 10b. The gray region shows the superconductor property of NbN film in GaN/NbN heterostructure. Although the superconductivity is seen in a wide temperature range up to 16.5 K which is the critical temperature of NbN, the integer QHE can be observed at extremely low temperature and strong magnetic field region (see the upper gray region in Fig. 10b). When the same experiment is performed under moderately low perpendicular magnetic field (15 T), the QHE plateaus cannot be seen for low  $n$  values (see Fig. 10c). In a summary, direct injection of Cooper pairs from superconductor NbN layer into the IQHE edge states can be observed in such heterostructure.

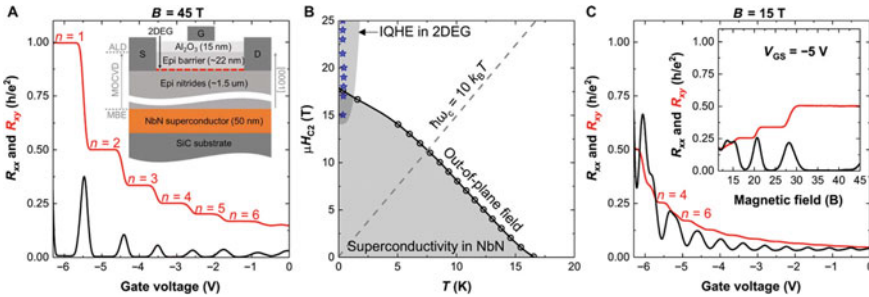


**Fig. 10** a Longitudinal ( $R_{xx}$ ) and transverse resistance ( $R_{xy}$ ) as a function of the gate voltage applied to a Hall bar device under 45 T magnetic field at 390 mK. b out-of-plane magnetic field versus temperature and c  $R_{xx}$  and  $R_{xy}$  versus gate voltage under 15 T magnetic field. Inset:  $R_{xx}$  and  $R_{xy}$  versus out-of-plane magnetic field at constant 5 V gate voltage. Reproduced from [103]

## 5 Conclusion

Superconductivity is a phenomenon that occurs when materials called superconductors are cooled to below the  $T_c$  where the electrical resistance of the material is zero. A metal conductor, whose temperature is lowered, begins to lose its electrical resistance in proportion to the temperature drop. In ordinary conductors such as copper and silver, this property is limited by impurities and other defects, they show some resistance even when close to absolute zero. In superconductors, on the other hand, when the temperature of the material drops below its critical temperature, its resistance becomes zero.

Since electrons have also a wave structure, the electron moving in the metal is represented by a plane wave moving in the same direction. Thus, electrons can freely move through the crystal without losing momentum. If there are impurity atoms or structural defects in the crystal lattice, it breaks the perfect periodicity. Resistance in metals is formed by the scattering of electrons from phonons, impurities, and crystal defects. In perfectly pure metals, the resistance is only due to the scattering of electrons by the phonons formed by the effect of temperature. Therefore, as the temperature drops to 0 K in pure metals and the resistance will decrease to zero value. However, since any metal always has impurities, the electrons will also scatter regardless of the temperature and thus show resistance even at 0 K. On the other hand, the resistance of superconducting material (in normal state) decreases continuously with the decreasing temperature, but the resistance suddenly goes to zero below  $T_c$ . In the superconducting case, the electrical resistance for direct current is zero, so in the superconducting case, there is no loss in current. Therefore, the current can flow without a loss for a very long time in a superconducting ring. The relation between normal state resistivity and superconducting properties is an interesting and important issue to understand the mechanism of superconductivity, especially for HTSCs. By applying a magnetic field to a superconducting material, the resistance transition and critical temperature shift to lower temperatures and the width of the resistance transition increases. While the magnetic field also causes these changes in the superconducting region, it does not create a change in the region above the critical temperature. Applied magnetic field also induces energy dissipation by introducing vortices into the HTS materials. This energy dissipation of the HTSC materials due to the vortices' mechanism is one of the important parameters that blocks usages of these materials in technological applications. For this reason, it is needed a deeper understanding of the background of the mechanism of these dissipation mechanisms. To do this, the most important models that explain the energy dissipation mechanism in HTSC materials are explained and discussed. The critical current density,  $J_c$ , is another important characteristic of the superconductor's materials from the view of the transport properties.  $J_c$  is explained with the Meissner effect, Bean's model, Silsbee's hypothesis,  $I$ - $V$  curve flux pinning, and the critical state. Determining  $J_c$  around  $10^5 \text{ Acm}^{-2}$  level is one of the important criteria for realistic superconductor applications. The Magnus force can be assumed that it comes from the interaction between vortices and superconducting fluid, whereas the

Lorentz force is responsible for the interaction between vortices and the normal state fluid. These correlatively interacting subsystems, such as vortices, superconducting, and normal state fluids, contemporaneously solve the equations of motion. Hence, the solution explains the Hall voltage sign reversal and simple numerical calculations merge with the experimental data.

## References

1. H.K. Onnes, Commun. Phys. Lab. Univ. Leiden, **12**(120) (1911)
2. C. Kittel, *Introduction to Solid State Physics*, 7th edn. (Wiley, Unites States of America, 1996)
3. C.P. Poole, H.A. Farach, R.J. Creswick, R. Prozorov, *Superconductivity* Elsevier (2007)
4. P. Klemens, G. Lowenthal, Aust. J. Phys. **14**(3) (1961)
5. A. Matthiessen, C. Vogt, Philos. Trans. R. Soc. Lond. **154**(1864)
6. J.V. Yakhmi, Introduction to Superconductivity, Superconducting Materials and Their Usefulness, in *Superconducting Materials and Their Applications* (2021)
7. D.K.C. MacDonald, Prog. Met. Phys. **3**(1952)
8. L. Kelvin, London, Edinb. Dublin Philos. Mag. J. Sci. **3**(15) (1902)
9. K.I. Wysokinski, Acta Phys. Pol. A **121**(4) (2012)
10. J. Azoulay, Phys. Rev. B **44** (13) (1991)
11. V.A. Gasparov, H.S. Jeevan, P. Gegenwart, JETP Lett. **89**(6) (2009)
12. R.K. Nkum, W.R. Datars, Phys. C: Superconduct. **192**(1) (1992)
13. H.K. Onnes, Nobel Lect. **4** (1913)
14. A. Mourachkine, *Room- Temperature superconductivity*. Cambridge International Science Publishing (2004)
15. R. Caton, R. Viswanathan, Phys. Rev. B **25**(1) (1982)
16. S. Ramakrishnan, G. Chandra, Phys. Lett. A **100**(8) (1984)
17. R. Jin, H.R. Ott, D.P. Grindatto, Phys. C: Superconduct. **250**(3) (1995)
18. B.S. Shastry, P. Mai, Phys. Rev. B **101**(11) (2020)
19. S. Martin, et al., Phys. Rev. B **39**(13) (1989)
20. D.W. Woodard, G.D. Cody, Phys. Rev. **136**(1A) (1964)
21. M. Milewits, S.J. Williamson, H. Taub, Phys. Rev. B **13**(12) (1976)
22. G.M. Carneiro, J. Phys.: Condens. Matter **3**(20) (1991)
23. G. Xiao, et al., Phys. Rev. B **39**(1) (1989)
24. T. Ito, et al., Nature **350**(6319) (1991)
25. Y. Singh, Int. J. Mod. Phys.: Conf. Ser. **22**(2013)
26. L.B. Valdes, Proc. IRE, **42**(2) (1954)
27. W. Thomson, Proc. Royal Soc. London (8) (1857)
28. S. Ornes, Proc. Natl. Acad. Sci. **110**(10) (2013)
29. M.N. Baibich, et al., Phys. Rev. Lett. **61**(21) (1988)
30. G. Binasch, et al., Phys. Rev. B **39**(7) (1989)
31. P.A. Grünberg, Rev. Mod. Phys. **80**(4) (2008)
32. S. Jin, et al., Science **264**(5157) (1994)
33. R. Weiss, R. Mattheis, G. Reiss, Meas. Sci. Technol. **24**(8) (2013)
34. *State of the Art Magneto-resistance Based Magnetic Field Measurement Technologies*, in *Magnetic Field Measurement with Applications to Modern Power Grids*. p. 25–51 (2019)
35. W. Woch, et al., J. Superconduct. Novel Magn. **30**(3) (2017)
36. E. Hannachi, et al., J. Mater. Sci.: Mater. Electron. **30**(9) (2019)
37. M.R. Mohammadzadeh, M. Akhavan, Supercond. Sci. Technol. **16**(4) (2003)
38. D. Yazici, M. Erdem, B. Ozcelik, J. Superconduct. Novel Magn. **25**(4) (2012)
39. G. Yildirim, et al., J. Superconduct. Novel Magn. **25**(4) (2012)

40. M. Nikolo, et al., *J. Superconduct. Novel Magn.* **27**(10) (2014)
41. A. Abou El Hassan, et al. *Irreversibility line and thermally activated flux flow in Micro-bridges of high-temperature superconductor. in E3S Web of Conferences.* 2021. EDP Sciences
42. T.T.M. Palstra, et al., *Phys. Rev. B* **41**(10) (1990)
43. G.L. Bhalla, et al., *Phys. C: Superconduct.* **391**(1) (2003)
44. B. Marchionini, et al., *IEEE Trans. Appl. Superconduct.* **27** (2017)
45. A.A. Abrikosov, *J. Phys. Chem. Solids* **2**(3) (1957)
46. K. Kadowaki, et al., *Phys. Rev. B* **50**(10) (1994)
47. Y.B. Kim, C.F. Hempstead, A.R. Strnad, *Phys. Rev.* **139** (4A) (1965)
48. H.J. Jensen, et al., *Phys. Rev. B* **38**(13) (1988)
49. K.A. Müller, M. Takashige, J.G. Bednorz, *Phys. Rev. Lett.* **58**(11) (1987)
50. G. Deutscher, K.A. Müller, *Phys. Rev. Lett.* **59**(15) (1987)
51. I. Morgenstern, K.A. Müller, J.G. Bednorz, *Phys. B: Condensed. Matt.* **152**(1) (1988)
52. V.N. Vieira, P. Pureur, J. Schaf, *Phys. C: Superconduct.* **353**(3) (2001)
53. G.L. Bhalla, Pratima, *Phys. C: Superconduct.* **406**(3) (2004)
54. M. Tinkham, *Phys. Rev. Lett.* **61**(14) (1988)
55. R. Griessen, R.J. Wijngaarden, B. Dam. *Magnetization Relaxation and Resistive Behaviour of High-Tc Superconductors BT—Advances in Superconductivity II.* Tokyo: Springer Japan (1990)
56. M.A. Dubson, et al., *Phys. Rev. Lett.* **60** (11) (1988)
57. B. Oh, et al., *Phys. Rev. B* **37**(13) (1988)
58. L. Miu, et al., *Phys. Rev. B* **57**(5) (1998)
59. C. Paracchini, et al., *Phys. C: Superconduct.* **223**(1) (1994)
60. E. Hannachi, et al., *Phys. B: Condens. Matter* **430**(2013)
61. Y. Slimani, et al., *J. Superconduct. Nov. Magn.* **28**(2) (2015)
62. T.T.M. Palstra, et al., *Phys. Rev. Lett.* **61**(14) (1988)
63. D. Sharma, R. Kumar, V.P.S. Awana, *Solid State Commun.* **152**(11) (2012)
64. Y.Z. Zhang, H.H. Wen, Z. Wang, *Phys. Rev. B* **74**(14) (2006)
65. M. Akyol, et al., *Bull. Mater. Sci.* **38**(5) (2015)
66. Y. Jang Song, et al., *EPL (Europhys. Lett.)* **97**(4) (2012)
67. S.D. Kaushik, V. Braccini, S. Patnaik, *Pramana*, **71**(6) (2008)
68. J.T. Kucera, et al., *Phys. Rev. B* **46**(17) (1992)
69. Y.Z. Zhang, Z.A. Ren, Z.X. Zhao, *Supercond. Sci. Technol.* **22**(6) (2009)
70. S. Martin, et al., *Phys. Rev. Lett.* **62**(6) (1989)
71. P.C.E. Stamp, L. Forro, C. Ayache, *Phys. Rev. B* **38**(4) (1988)
72. N.C. Yeh, C.C. Tsuei, *Phys. Rev. B* **39**(13) (1989)
73. B.I. Halperin, D.R. Nelson, *J. Low Temp. Phys.* **36**(5) (1979)
74. D. Dew-Hughes, *Low Temp. Phys.* **27**(9) (2001)
75. V. Selvaanicam, *App. Phys. Lett.* **106**(3) (2015)
76. T. Matsushita, Measurement methods for critical current density, in *Flux Pinning in Superconductors.* (Springer, Berlin, Heidelberg, 2014), pp. 189–209
77. T. Shibata, S.-I. Sakai, *J. Phys.: Conf. Ser.* **744** (2016)
78. C.P. Bean, *Phys. Rev. Lett.* **8**(6) (1962)
79. D. Larbalestier, et al., *ArXiv* (2013)
80. M. Miura, et al., *Nat. Commun.* **4**(2013)
81. T. Matsushita, *Flux Pinning in Superconductors.* Springer (2007)
82. P. Chaddah, Sadhana, **28**(1) (2003)
83. C.B. Eom, et al., *Nature* **411**(6837) (2001)
84. X. Xu, *Supercond. Sci. Technol.* **30**(9) (2017)
85. E.H. Hall, *Am. J. Math.* **2**(3) (1879)
86. W.A. Reed, E. Fawcett, Y.B. Kim, *Phys. Rev. Lett.* **14** (19) (1965)
87. A.G. Aronov, A.B. Rapoport, *Mod. Phys. Lett. B* **06**(16n17) (1992)
88. A. Freimuth, C. Hohn, M. Galfy, *Phys. Rev. B* **44**(18) (1991)
89. A.G. Aronov, S. Hikami, *Phys. Rev. B* **41**(13) (1990)

90. N.B. Kopnin, Phys. Rev. B **54**(13) (1996)
91. Z.D. Wang, J. Dong, C.S. Ting, Phys. Rev. Lett. **72**(24) (1994)
92. Y. Kato, J. Phys. Soc. Jpn. **68**(12) (1999)
93. J. Kolářček, P. Vašek, Phys. C: Supercond. **336**(3) (2000)
94. S. Ullah, A.T. Dorsey, Phys. Rev. B **44**(1) (1991)
95. T. Nishio, H. Ebisawa, Phys. C: Supercond. **290**(1) (1997)
96. K. Michaeli, K.S. Tikhonov, A.M. Finkel'stein, Phys. Rev. B **86**(1) (2012)
97. P. Ao, D.J. Thouless, Phys. Rev. Lett. **70**(14) (1993)
98. D.I. Khomskii, A. Freimuth, Phys. Rev. Lett. **75**(7) (1995)
99. S.Y.F. Zhao, et al., Phys. Rev. Lett. **122**(24) (2019)
100. K. Nakao, et al., Phys. Rev. B **57**(14) (1998)
101. J.I. Martín, et al., Phys. Rev. B **55**(9) (1997)
102. K. Kobayashi, JPSJ News Comments **16** (2019)
103. P. Dang, et al., Sci. Adv. **7** (8) (2021)

# Magnetic Properties of Superconducting Materials



Michael R. Koblichka and Anjela Koblichka-Veneva

**Abstract** This chapter deals with the magnetic properties of superconductors, especially such which are not part of the textbook superconductivity chapters. The response of superconductors to the magnetic field led to the classification into type-1 and type-2 superconductors, and to the definition of flux quanta, vortices, and the various critical fields. The Meissner-Ochsenfeld effect, i.e., the expulsion of magnetic flux from a sample leading to a diamagnetic response, is one of the hallmarks of superconductivity, however, there is now also a so-called paramagnetic Meissner effect, which was observed in high- $T_c$  as well as in conventional superconducting samples. To sustain high transport currents—which is essential for the applications—the vortices must be fixed at flux pinning sites to avoid dissipation effects, which sets the main goal for material research on superconducting materials. With the upcoming of the high-temperature superconductors and their much higher operation temperatures, effects of thermal activation and flux creep came into the picture. With the use of modern imaging technologies, flux structures in superconductors revealed instability effects in the vortex lattice. Thus, there are numerous phenomena related to superconductors exposed in magnetic fields, in both conventional and high- $T_c$  superconducting materials. On the other hand, the ongoing research has shown that superconductivity may coexist with magnetism as superconductors with internal magnetic contributions exist, leading to a variety of magnetization curves, where para- or ferromagnetic moments are measured together with the superconducting diamagnetic contributions. The recent findings in this field are discussed in detail.

**Keywords** Superconductors · Magnetic properties · Meissner effect · PME · Vortex lattice · flux creep · Instabilities · Magnetic moments

---

M. R. Koblichka (✉) · A. Koblichka-Veneva  
Experimental Physics, Saarland University, P.O.Box 151150, 66041 Saarbrücken, Germany  
e-mail: [m.koblichka@ieee.org](mailto:m.koblichka@ieee.org); [m.koblichka@gmail.com](mailto:m.koblichka@gmail.com)

A. Koblichka-Veneva  
e-mail: [a.koblichka@gmail.com](mailto:a.koblichka@gmail.com)



## 1 Introduction

There are two hallmarks of superconductivity, the loss of electric resistance—with which superconductivity was originally discovered in 1911 [1, 2]—and the Meissner effect, discovered in 1933 [3] describing the expulsion of magnetic flux from the superconducting sample when cooling it in an applied magnetic field below the superconducting transition temperature,  $T_c$  (field cooling, FC). These two hallmarks of superconductivity are depicted schematically in Fig. 1. The Meissner effect pinpoints the magnetic characteristic of the superconducting state—superconductors show a diamagnetic response below the superconducting transition temperature,  $T_c$ . The implications of the Meissner-Ochsenfeld effect led directly to the development of the basic theories of superconductivity (London, Ginzburg-Landau and BCS).

Thus, the detection of the Meissner effect is the key that a new material can be accepted as a true superconductor. On the other hand, superconductivity can be destroyed by applying too high magnetic fields or by too high currents,  $j$ , passing through (see the phase diagram in Fig. 2), thus the answer of superconductors to magnetic fields and currents is very important for all kinds of possible applications of superconductors. Consequently, the basic magnetic properties of superconductors are a main topic in all teaching books of superconductivity, see e.g. Refs. [4–10], so we will here not repeat these standard treatments, but will point out new results achieved and new insights which came up due to the intense research on superconducting materials in the years after the discovery of high- $T_c$  superconductivity in 1988 [11]. This includes both conventional, low- $T_c$  (sometimes called also “classic”) superconductors like several metallic alloys,  $\text{MgB}_2$  (the metallic superconductor with the highest  $T_c$  known to date [12]) as well as the new high- $T_c$  superconducting families (cuprate HTSc materials, where superconductivity takes place in the Cu–O-planes [13], and the iron-based superconductors (IBS) [14]). Examples for these new findings are type-1.5 superconductors [15], the paramagnetic Meissner effect

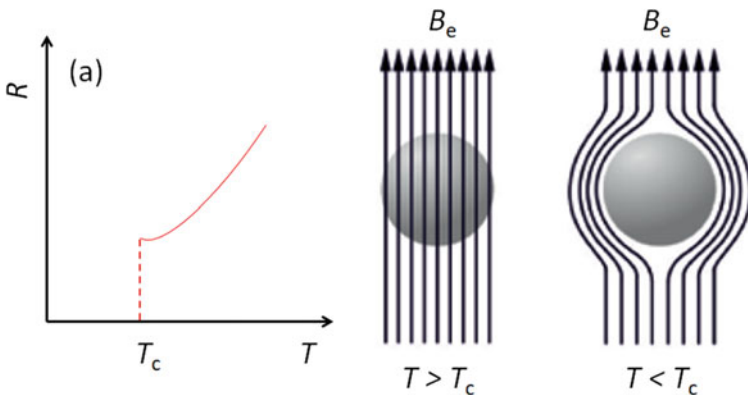
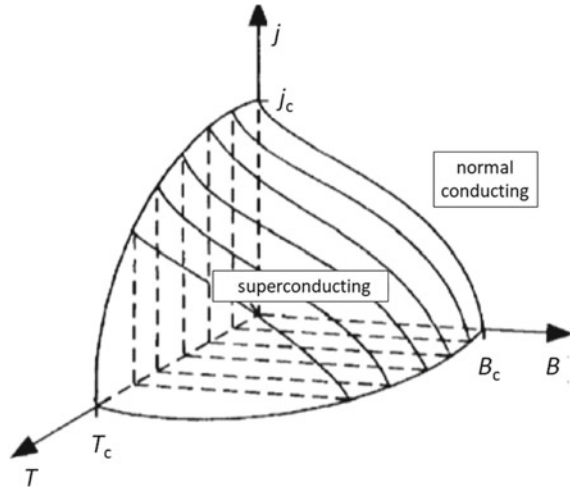


**Fig. 1** Resistance versus temperature and flux expulsion (Meissner-Ochsenfeld effect) when cooling a superconducting sample in a magnetic field below  $T_c$

**Fig. 2** Phase diagrams of superconductors. Superconductivity can be destroyed by temperatures  $> T_c$ , magnetic fields  $> H_{c2}$  and currents  $> j_c$



(PME) [16, 17], multiband-superconductors [18], the iron-based superconductors (IBS), 2D-superconducting materials [19], topological superconductors [20], nanostructured superconducting materials including nanoparticles and nanowires [21, 22], and the recently found room-temperature superconductors under high pressure [23, 24]. Consequently, there are many new observations concerning the magnetic properties of superconducting materials in the literature, which cannot be found in present day textbooks.

In this chapter, we will thus discuss experimental results concerning the paramagnetic Meissner effect (PME), type-1.5 superconductivity, effects of thermal activation on the vortex lattice and on the magnetization loops, the influence of the crystal structure of HTSc cuprates on the vortices (“pancake vortices”), instabilities in the vortex lattice (“flux turbulence” and dendritic flux penetration) and the coexistence of magnetism and superconductivity in specific types of samples.

## 2 Type-1 and Type-2 Superconductors

Firstly, we give a definition of type-1 and type-2 superconductors. These are defined via

$$\kappa < \frac{1}{\sqrt{2}} \text{ (type - 1) and } \kappa > \frac{1}{\sqrt{2}} \text{ (type - 1)} \tag{1}$$

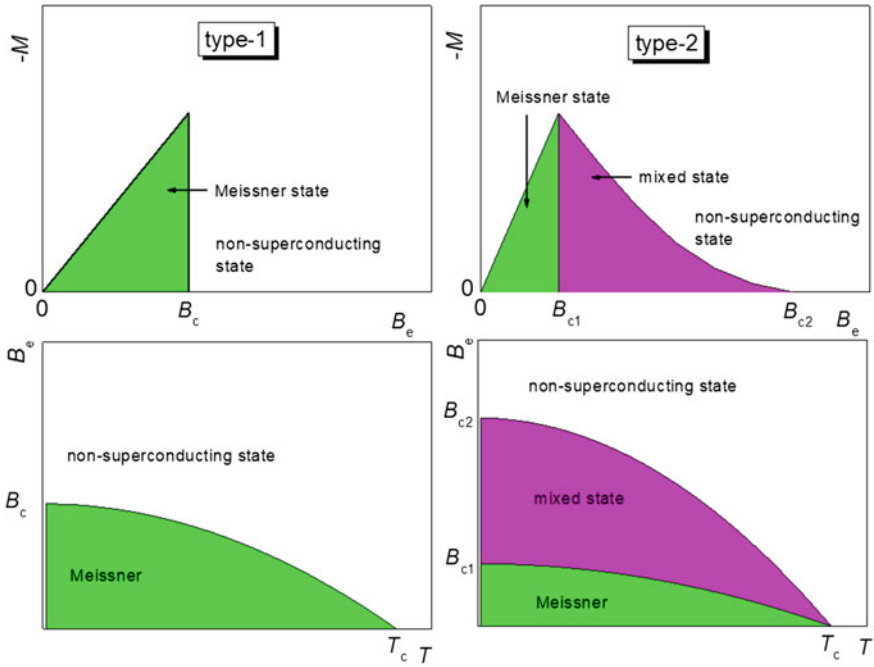


**Fig. 3** Schematic  $M(B)$  and  $B(T)$ -diagrams of type-1 and type-2 superconductors. A mixed state or Shubnikov phase is formed in a type-2 superconductor above the lower critical field,  $B_{c1}$ , which persists until the upper critical field,  $B_{c2}$ , is reached. Note here that  $B_{c2}$  can be much larger as the critical field  $B_c$ ; in case of the HTSc materials, even fields larger than 200 T are possible

where  $\kappa = \lambda_L/\xi$  denotes the Ginzburg–Landau parameter with  $\lambda_L$  denoting the London penetration depth and  $\xi$  the coherence length. This is known from the textbooks. Figure 3 presents schematic magnetization versus field and magnetization vs. temperature-curves of type-1 and type-2 superconductors.

Type-1 superconductors are in the Meissner state up to the critical field,  $B_c$ , and then turn normal (non-superconducting) if the applied magnetic field is increased further. Type-1 superconductors are to be searched among the elemental superconducting materials, with the exception of Nb, which is type-2. Figure 4 gives a schematic illustration of (a) the field distribution inside a superconductor in the Meissner state. Here it is important to note that in a surface layer with the depth defined by  $\lambda_L$ , the so-called Meissner currents shielding the sample interior are flowing. For normal situations, this surface layer is commonly neglected, but may have an important effect in specific situations as we will see later on. In (b), the behavior of the Cooper pair density,  $n_s$ , and the local magnetic fields  $B_i/B_e$  between a superconductor and a normal metal is depicted. Depending if the sample is type-1 or type-2, the decay of the Cooper pair density,  $n_s$ , and the local field  $B$  may look completely different. Here, we have to note that type-1 superconductors are not useful for current-carrying applications, as only small currents can be sent through

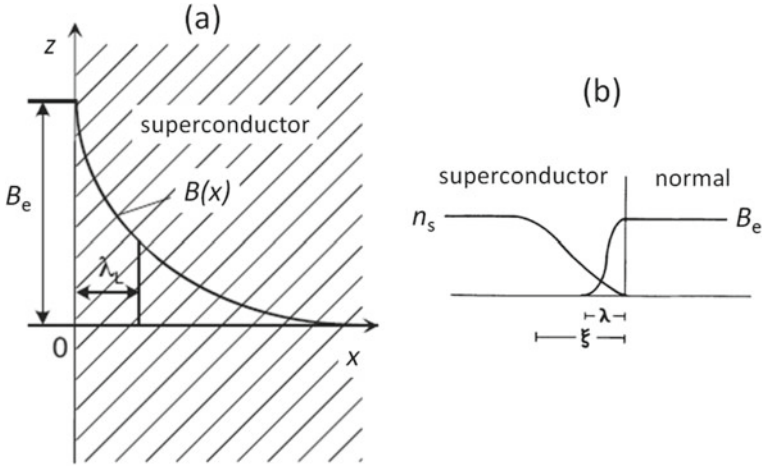


**Fig. 4** **a** Sketch of the magnetic field inside a superconductor in the Meissner state. **b** the density of superconducting electrons,  $n_s$ , and the local magnetic field  $B_i/B_e$  inside and outside of a superconductor

such samples, and the critical fields are quite low (typically much less than 1 T) [25]. However, when physically treating a type-1 superconductor sample by mechanical deformation, e.g., rolling, pressing, etc., a large number of defects will be introduced, rendering the material type-2. Magneto-optic imaging of flux structures in superconductors is thus an ideal tool to investigate this situation [26–28], as the typical domain patterns of type-1 superconductors can be observed as well as the vortices of type-2 superconductors. To understand the specific nature of the type-2 superconductors, we have to regard a solution of the Ginzburg-Landau equations presented by Abrikosov [29] (Nobel prize 2007). He showed that vortices, carrying one flux quantum each, are stable in a type-2 superconductor and form a vortex lattice. The field distribution around an Abrikosov vortex is depicted in Fig. 5a below.

The peak in the MHL of a type-2 superconductor at the lower critical field,  $H_{c1}$ , is due to the entry of exactly one vortex into the superconducting sample. To the contrary, the upper critical field,  $H_{c2}$ , is reached when the cores of the vortices begin to overlap each other, that is, the material is rendered fully normal. Figure 5b presents a schematic drawing of the flux-line lattice (FLL). The arrangement of the vortices is ideally hexagonal, but of course, flux density gradients and defects lead to rearrangements. Thus, a properly arranged hexagonal vortex lattice can be only observed in a field-cooled state. Depending on the interaction forces between the vortices, also other arrangements may be realized as described in [26]. Figures 5c, d and e give examples of vortices observed with various imaging techniques, (c) decoration or Bitter technique ( $T = 1.2$  K, field cooling in 2 mT [30]), (d) scanning SQUID (field cooling in 6.93  $\mu$ T to 4 K, [31]) and (e) magneto-optics ( $T = 4.3$  K, field cooling in 0.3 mT [32]). The respective samples are Pb with 6.3% In, a 200 nm thick YBCO film, and a NbSe<sub>2</sub> single crystal. All other superconducting materials, including the

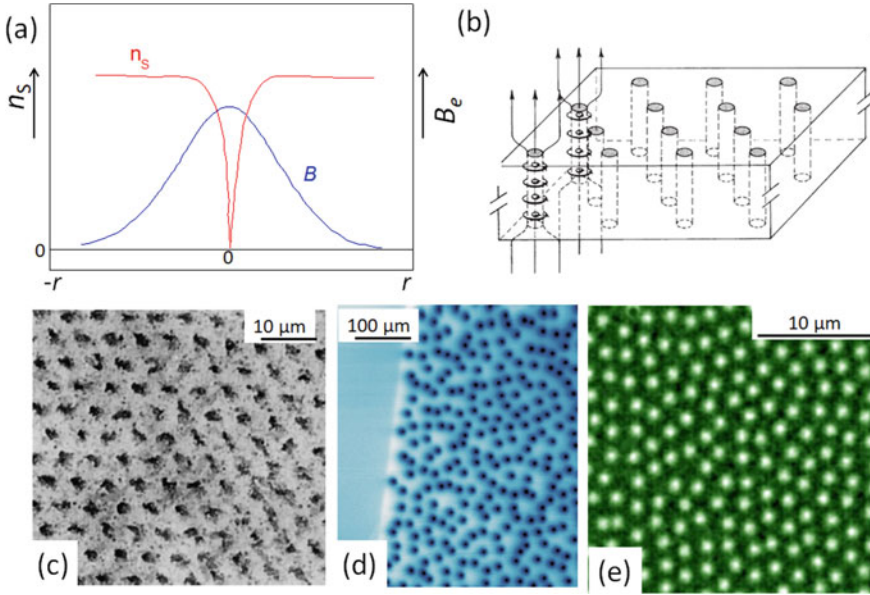


**Fig. 5** **a** Field distribution around a vortex and **b** a schematic view of the vortex lattice. **c** FLL with decoration technique, courtesy U. Ebmann [30], **d** FLL by scanning SQUID [31] and **e** FLL by magneto-optics [32]. All images were taken after field-cooling. [31] Image 5 d was reproduced with permission Image 5e was reproduced with permission [32]

high- $T_c$  superconducting families, are type-2 superconductors, distinguished by their values of  $\kappa$ .

The research on various new superconducting materials brought up a new version—the type-1.5 superconductivity [15]. The existence of type-1.5 superconductors was discussed since the discovery of multi-band superconductors [33], an example of which is  $\text{MgB}_2$ , the metallic superconductor with the highest  $T_c$  known to date (38.5 K) [12]. Moshchalkov et al. [15] studied the vortex distribution in an ultra-clean  $\text{MgB}_2$  single crystal, where a unique combination of both type-1 and type-2 superconductor conditions is realized for the two components of the order parameter. Their observations using the Bitter decoration technique on  $\text{MgB}_2$  single crystals as shown in Fig. 5a revealed vortex arrangements, where an attractive vortex-vortex interaction at long distances and a repulsive one at short distances is realized, the combination of which can stabilize such unconventional stripe- and gossamer-like vortex patterns in the sample as proven by the simulations given in Fig. 6b. The colors in both images represent the vortex-vortex interactions, which are clearly different from a homogeneous, hexagonal vortex lattice. Figure 6c presents another interesting observation on a Pb thin film: It was shown already in [26] that thin Pb films do exhibit the penetration of vortices, if the thickness is about  $xx \mu\text{m}$ . These vortices are, however, different from the vortices of type-2 superconductors: The vortices carry more than one flux quantum, depending on the thickness of the

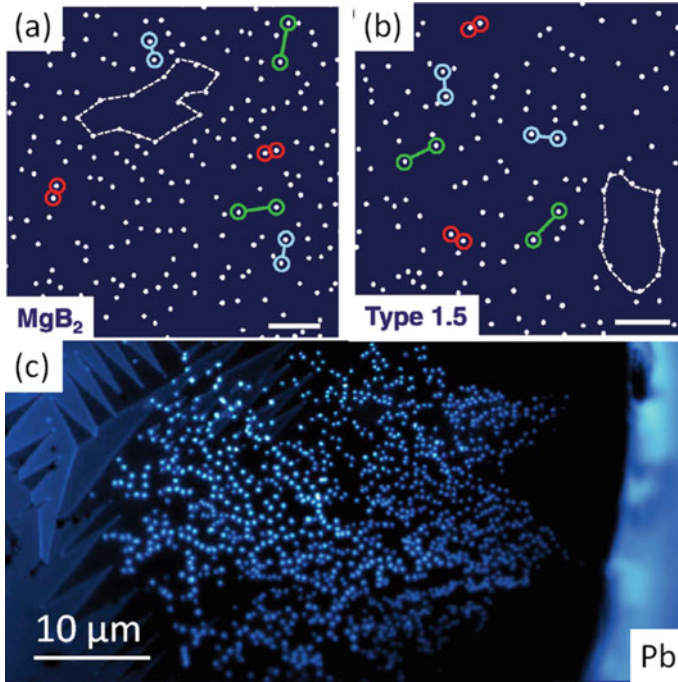


**Fig. 6** **a** Decoration experiment on  $\text{MgB}_2$  single crystal, **b** simulated patterns revealing type-1.5 superconductivity with colors indicating the vortex interactions. The scale bars are  $10\ \mu\text{m}$ . Reproduced with permission from Ref. [15] **(c)** MO-image of a lead thin film. showing the penetration of macrovortices. Image provided by C. Brisbois and A. Silhanek (U Liège)

sample. Increasing temperature makes the sample then behave like a real type-1 superconductor again.

Using the MO technique, these so-called macrovortices can be studied in detail, and as shown in Refs. [34, 35] even be employed to simulate a vortex memory, which is nowadays again a very interesting topic for quantum computing using superconducting elements, e.g., flux qubits [36].

### 3 Paramagnetic Meissner Effect

As mentioned before, the response of a superconductor, when being cooled in the presence of a magnetic field, should be diamagnetic. But this is not always the case. It is important to note here that the ideal Meissner effect requires always a surface layer of the thickness of  $\lambda_L$ , where the Meissner currents can flow to shield the remainder of the sample against the external magnetic field. As said already

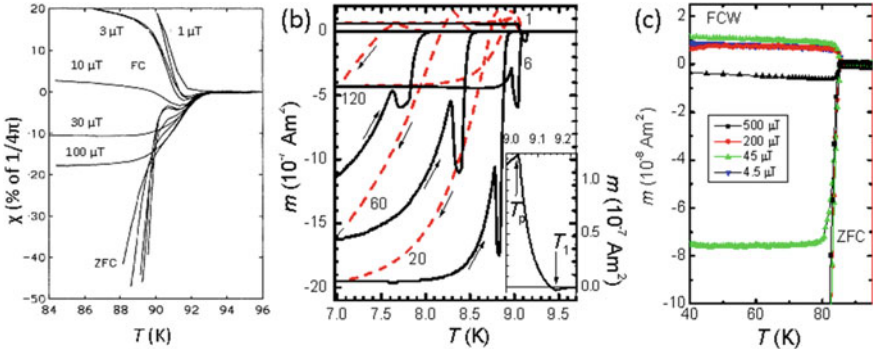


**Fig. 7** **a** The first measurements of the PME on polycrystalline Bi-2212 HTSc, recorded in field-cooling (FC) conditions [38]. Note here that the susceptibility,  $\chi$ , is going first negative just below  $T_c$ , and then turns up to positive, paramagnetic values. Also, the applied magnetic fields are uncommonly small. **b** PME measurements on a Nb disk [45, 46]. There are remarkable sparks on cooling and warming curves, and the effect persists up to relatively high fields. **c** shows the PME on a patterned YBCO thin film [47], but here the negative turn close to  $T_c$  is completely missing

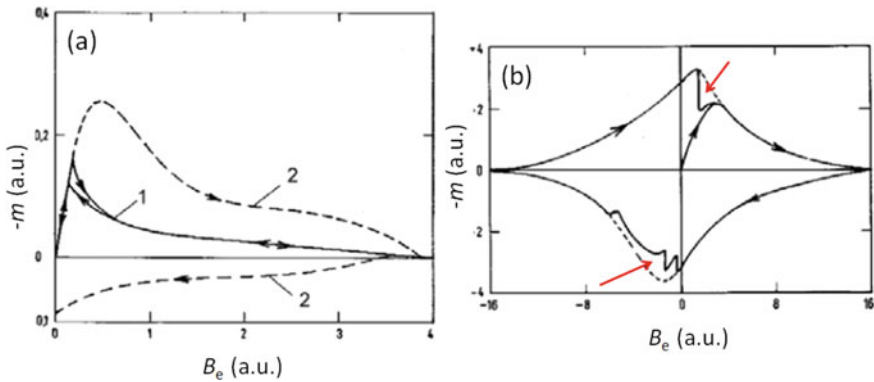
before, the presence of this surface layer is commonly neglected. The first experimental observations of superconducting transitions of Bi-based, high- $T_c$  superconductors (HTSc) to a paramagnetic state instead of a diamagnetic one were more treated as experimental mishaps and went mostly unnoticed by the community [37]. The situation changed with more detailed measurements on granular, HTSc of the  $\text{Bi}_2\text{Sr}_2\text{CaCu}_2\text{O}_{8+\delta}$  (Bi-2212) family by Braunisch et al. [38, 39]. The first explanations for this effect were linking the observation of a superconducting transition towards the paramagnetic state with unique features of the HTSc, i.e., the so-called  $d$ -wave superconductivity [40] and effects of granularity ( $\pi$ -junctions between the superconducting grains). Possible theoretical explanations for the PME were reviewed by Li [41]. These first experiments, shown in Fig. 7a, were soon followed by other researchers, applying also different measurement techniques including AC susceptibility to exclude experimental artifacts [42–44].

Following these works, several theoretical approaches concerning this effect were published in the literature, now commonly named paramagnetic Meissner effect (PME) or Wohlleben effect [40, 48]. Thus, it came as a big surprise as Thompson et al. presented an observation of PME on bulk, niobium disks, a classical  $s$ -wave superconductor [45, 49]. Typical results of the PME on Nb are presented in Fig. 7b. The inset to Fig. 7b gives the definitions of two temperatures,  $T_1$  and  $T_p$ , characterising the turnpoints of the magnetization. Such turnpoints are visible on both FC warming and cooling curves. Finally, Fig. 7c presents a PME measurement on an artificially granular, patterned YBCO thin film [47, 50]. Here, this effect can only be seen again in small applied magnetic fields, but here even the slight negative (diamagnetic) turn of the magnetization is missing [47]. The PME was further observed in mesoscopic small superconducting samples (micrometer-sized disks of Al and Nb)

by Geim et al. [51]. As result, the explanation for the PME in conventional superconductors favors the giant vortex state (which is formed due to field trapping) [52, 53]. The compressed flux in the giant vortex is  $L \cdot \Phi_0$ , with  $L$  denoting the quantum number corresponding to the number of nodes of  $\Psi$  along the sample circumference [51]. This giant vortex state explains the PME for conventional superconductors, while for the HTSc samples like the granular Bi-2212, the influence of  $d$ -wave superconductivity cannot be ruled out. For the artificially granular YBCO thin film (and recently a very similar PME was observed in YBCO nanowire fabrics), the field trapping in the open spaces between the superconducting material is the reason for the PME [47, 52].

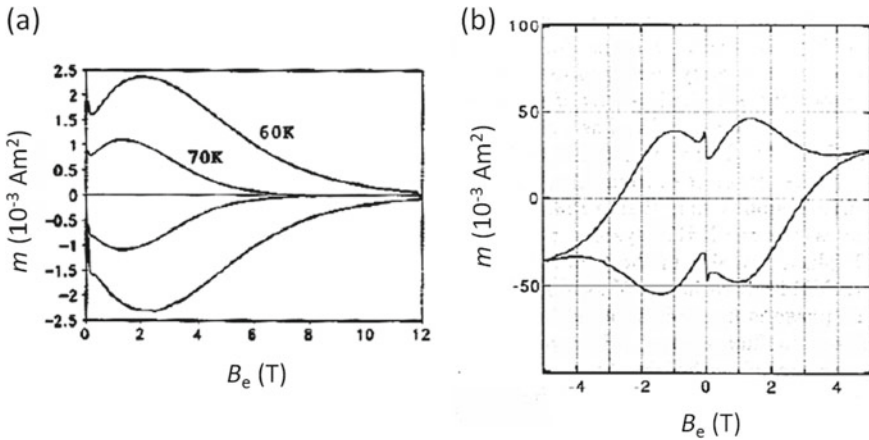
## 4 Real Magnetization Loops

Figure 3 presented a textbook-like magnetization loop (MHL) and a magnetic phase diagram for a classical type-2 superconductor. Here, it must be noted that it requires an extremely clean crystal to observe such a completely reversible magnetization loop. When defects are present in the sample, there will be no clear peak at the entry of the first flux quantum, and of course, the magnetization loop will not be reversible. As a result, the MHLs will look more like as shown in Figs. 8a and b below [54]. The  $\text{Nb}_{55}\text{Ta}_{45}$  alloy measured in (a) is still close to the “clean” situation, and thermal annealing brings the MHL again close to the textbook-like appearance. In contrast to this, Fig. 8b shows a MHL of a Pb-Bi alloy with well-developed flux pinning properties, and close to zero field, so-called flux jumps [55] appear, which are due to thermal instabilities within the sample. Such flux jumps are problematic for several



**Fig. 8** “Real” magnetization loops (MHLs) of type-2 superconductors with flux pinning [54]. **a** MHLs of a  $\text{Nb}_{55}\text{Ta}_{45}$  alloy before (2) and after (1) thermal annealing. **b** presents a full MHL (all 4 quadrants) of a Pb-Bi alloy with well-developed flux pinning. Close to zero field, flux jumps appear as marked by red arrows. The black arrows indicate the field sweep direction





**Fig. 9** MHLs of high- $T_c$  superconductors demonstrating the so-called fishtail (or “secondary peak”) effect [54]. In **a**, two MHLs were measured on a YBCO single crystal at 60 and 70 K, showing a broad, secondary peak and the irreversibility line. The MHL on a  $\text{NdBa}_2\text{Cu}_3\text{O}_x$  sample presented in **b** exhibits the peak effect and an additional paramagnetic moment superimposed on the normal MHL

applications of superconductors, especially for the metallic superconductors  $\text{Nb}_3\text{Sn}$  and  $\text{MgB}_2$  [56, 57].

Figure 9 presents MHLs common for the cuprate HTSc,  $\text{YBa}_2\text{Cu}_3\text{O}_{7-\delta}$  (YBCO). These MHLs show a secondary peak at elevated fields, which is responsible for the nickname of these curves: “fishtail effect” [58]. In the case of YBCO (a), the effect is still weak, but in the case of a melt-textured NdBCO sample, the fishtail effect is quite strong, and the MHL shows further a superimposed paramagnetic signal. This signal stems from the strong paramagnetism of Nd [59].

The origin of the fishtail effect was widely discussed in the literature [58, 60–62]. The final explanation of this effect requires, however, a detailed analysis of the microstructure. In the case of YBCO, the oxygen stoichiometry plays the key role—a fully oxygen-loaded sample does not exhibit the fishtail effect, and when removing oxygen, the fishtail effect appears [62].

In the case of NdBCO, there is the possibility of replacing Ba-ions by Nd-ions, which have approximately the same size. The Ba-rich compound has a lower critical temperature,  $T_c$ , as compared to the remaining superconducting matrix [63]. Furthermore, the formation of the Ba-rich compound is stable and cannot be reversed by intense oxygenation treatments. If these zones of reduced  $T_c$  are large enough, then these zones can act as effective, additional flux pinning sites (field-induced flux pinning, as a high applied magnetic field may render these zones normal). Thus, the secondary peak effect of NdBCO samples is very strong and also irreversible in contrast to YBCO [64].

## 5 Thermal Activation and Flux Creep

In Fig. 10, a typical situation found in the current-voltage  $I/V$  (or electric field-current density  $E/j$ )-curves of high- $T_c$  superconductors is depicted. The signal below the critical current density,  $J_c$ , is not zero, but finite. This regime is called thermal activated flux flow. Here, vortices are depinned from their pinning sites by thermal activation. This also implies that the effect is less pronounced at low temperatures, and increases strongly with increasing temperature. Thus, TAFF is a problem when aiming at applications at high temperatures close to  $T_c$ , e.g., 77 K (the temperature of liquid N<sub>2</sub>). When reaching  $J_c$ , the depinning gets stronger and the regime of flux creep is reached, and when approaching the Ohmic line, the entire flux-line lattice is moving (“flux flow” regime).

The effects of TAFF and flux creep are visible also in the magnetization data. As example, we show in Fig. 11 torque ( $t = m \times B$ ) magnetization loops, measured in applied magnetic fields between 0 and 7 T at various field sweep rates between 2.5 and 40 mT/s. The loops measured at the high sweep rate are wider as the ones measured at the lowest sweep rate. The distance between the loops can be evaluated to yield the dynamic sweep rate,  $Q$ , which was shown to be equal to the sweep rate measured as function of time after stopping a field sweep,  $S$  [65]. Of course, also conventional metallic superconductors do show these effects, but the measurements done at 4.2 K are not significantly affected.

This influence of thermal activation was already observed in the very first publications after the discovery of YBCO as it leads directly to a new contribution in the phase diagram, the so-called irreversibility line,  $B_{irr}(T)$ . All the consequences of the thermal activation were summarized in Ref. [66]. The resulting phase diagram for HTSc is depicted in Fig. 12 below.

$B_{irr}(T)$  is always lower than  $B_{c2}(T)$ , and thus describes the limit of strong flux pinning in a sample. Thus, this line is most important for applications of HTSc.  $B_{irr}(T)$  is not intrinsic to the material as it can be influenced by the pinning landscape, so e.g.,  $B_{irr}(T)$  can be moved towards  $B_{c2}(T)$  by introducing strong flux pinning sites like by heavy-ion irradiation [67]. Regarding the situation from a vortex lattice (FLL), at low  $T$  and small  $B$ , a true regular FLL is formed. This FLL gets distorted, forming a so-called vortex glass, by increasing temperature and/or magnetic field. When

**Fig. 10** Schematic  $E/j$  ( $U/I$ )-curve showing the definitions of thermally activated flux flow (TAFF), flux creep and flux flow

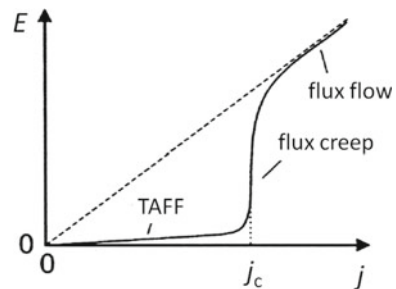


**Fig. 11** Torque ( $\tau = m \times B$ ) hysteresis loops measured on an YBCO thin film in magnetic fields up to 7 T. The upper plot (A) was measured at a low temperature of 1.6 K, the lower plot (B) shows the same situation at  $T = 10$  K. The sweep rate of the external magnetic field is ranging between 2.5 and 40 mT/s

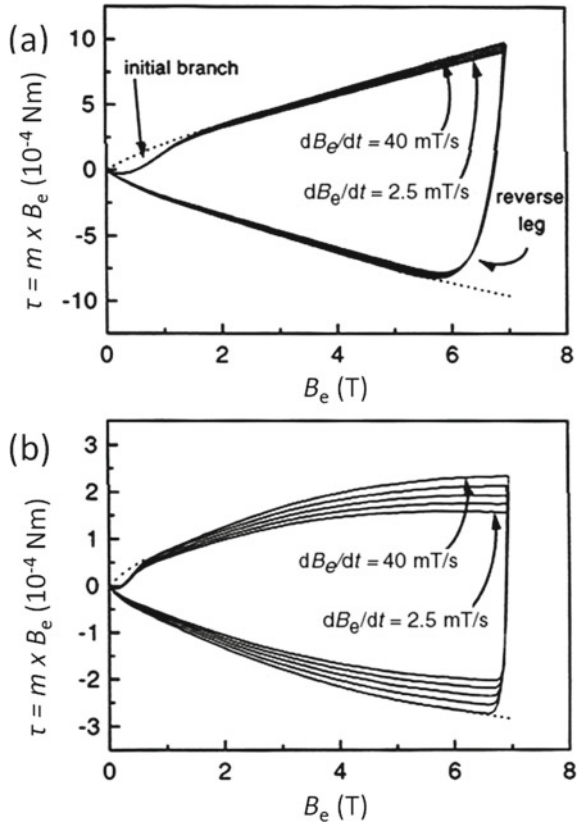
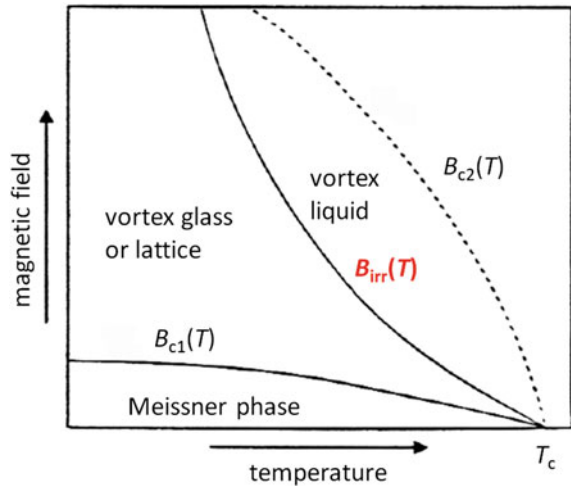


**Fig. 12** Magnetic phase diagram for HTSc, showing the irreversibility line,  $B_{irr}(T)$ , which is always below  $B_{c2}(T)$ , thus limiting the application range of the HTSc



reaching  $B_{irr}(T)$ , all vortices are depinned from their pinning sites, and a vortex liquid is created which can easily be moved by field changes [68]. Finally, this liquid densifies when increasing the magnetic field further, and superconductivity in the sample is destroyed at  $B_{c2}(T)$ .

## 6 Thermal Activation and Flux Creep

The 2D character of the crystal structure of the HTSc is responsible for another specific feature of the vortices. The superconductivity is concentrated in the Cu-O-planes, and so a vortex can only exist within this plane (so-called “pancake” vortex [69]), and is not a continuous, cylindrical object like in a conventional superconductor. The individual pancakes are coupled together by Josephson currents, but this coupling is only weak, and increasing temperature or the angle  $\beta$  to the applied magnetic field may lead to a complete decoupling. One important consequence is depicted in Fig. 13a: A rigid cylindrical vortex can be effectively pinned by one single pinning center (black dot) somewhere along its length, whereas each vortex pancake may require a pinning site in each of the Cu-O-planes to provide effective flux pinning. Figure 13b shows the situation when the external magnetic field is applied at an angle  $\beta$  to the sample surface. If the angle  $\beta$  is large enough, a decoupling

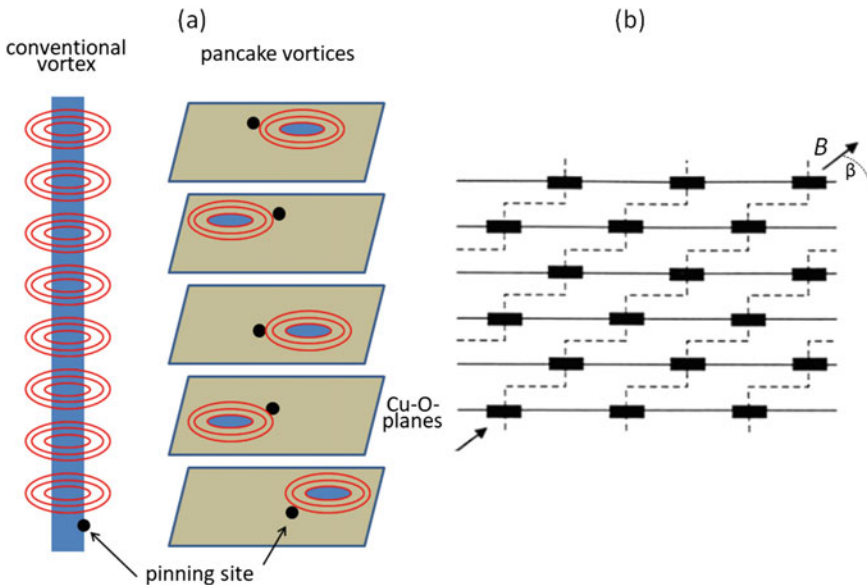


**Fig. 13** **a** Vortices and pancake vortices in HTSc. The black dots indicate flux pinning sites. **b** Pancake vortices when the external magnetic field is inclined with an angle  $\beta$  with respect to the Cu-O planes

of the pancake strings takes place. In case that the pancakes are fully decoupled, they may move easily in the sample, and flux pinning goes towards zero. This situation poses a problem for applications, especially for the highly anisotropic HTSc as their irreversibility lines only allow high currents at temperatures below 50 K. The most pronounced example for this is the Bi-2212 HTSc [70] with its very high anisotropy.

## 7 Effects of Granularity

Figure 14 presents the flux penetration in a granular HTSc sample, here a polycrystalline YBCO sample. The magnetization follows a straight line when starting from zero magnetic field, which corresponds to a full Meissner effect. The signal deviates from this straight line at the lower critical field,  $B_{c1}^J$ , where so-called Josephson vortices enter the sample via the grain boundaries (GBs). These Josephson vortices are similar to the Abrikosov vortices, but do not have a normal core. Increasing the applied magnetic field further, again a linear Meissner-like behavior is observed, but this time describing the Meissner effect of the superconducting grains. Finally, at a field  $B_{c1}^G$ , Abrikosov vortices can enter into the grains which are oriented to the field with the lowest critical field. All these situations are depicted schematically on the right side of Fig. 14.

The granularity can also be nicely visualized using magneto-optic imaging [71–74]. Figure 15 presents the flux distributions of an YBCO thin film patterned into a rectangular shape, a YBCO single crystal and a monofilamentary Bi-2223 tape. The thin film sample (upper row) shows the typical Landau-pattern (or discontinuity “d”-lines [75]) of a homogeneous superconductor. The currents flow always parallel

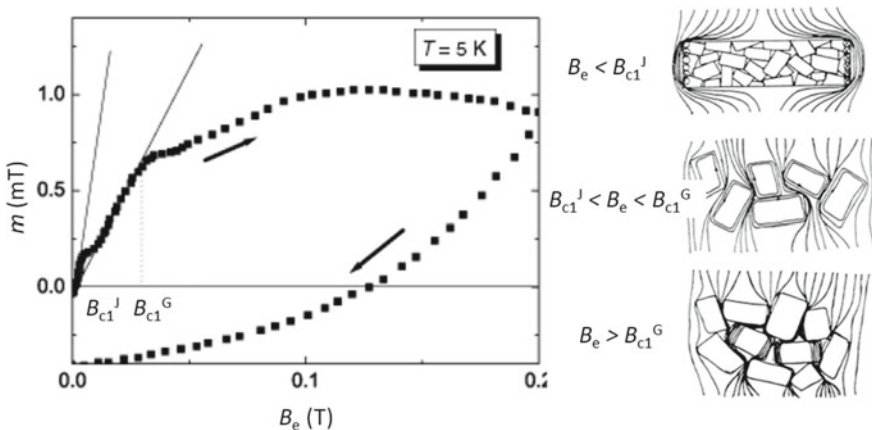
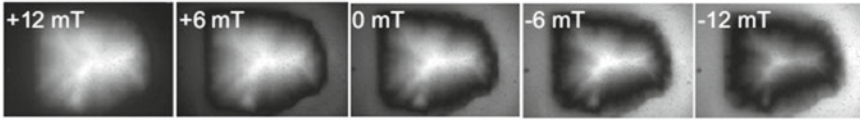


**Fig. 14** MHLs of a granular, polycrystalline YBCO sample measured at 5 K in low applied magnetic fields, showing the lower critical fields  $B_{c1}^J$  and  $B_{c1}^G$ . The schematic sketches on the right side give the corresponding flux penetration steps

## YBCO thin film



## YBCO single crystal



## Bi-2223 monofilamentary tape

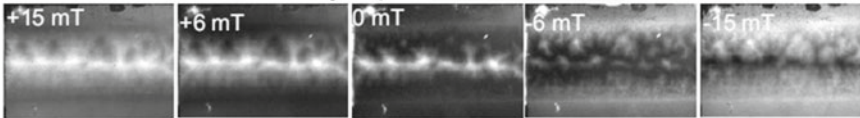


**Fig. 15** Flux distributions in different types of HTSc samples observed by MO imaging. Upper row: YBCO thin film, patterned as a rectangle, middle row: a nearly cubic YBCO single crystal, and lower row: a section of an Ag-sheathed Bi-2223 monofilamentary tape. The values of the applied magnetic field are indicated at each image, the observation temperature is 18 K. *Reproduced with permission from Ref. [76]*

to the sample edges, and at the d-lines, the current turn direction. No current flow takes place in the sample center.

The thin homogeneous sample also reveals another feature at zero applied field: Along the sample edges, there is a rim of flux in the sample. In dedicated experiments, one could show that this flux is of negative sign, which means that vortices of opposite polarity enter the sample. The high demagnetization factor of a thin film enables this penetration of negative vortices already in small positive fields. On increasing negative field, this small rim of negative vortices grows, and annihilation of vortices of opposite polarity takes place. The much thicker YBCO single crystal shows only some traces of the d-lines. This is due to the presence of twin boundaries, where flux can easily rush along the weaker zones as indicated by the stripe pattern. Also, the lower demagnetization factor allows the appearance of negative flux only when also a larger external negative field is applied. The monofilamentary Bi-2223 tape is a polycrystalline material, with many Bi-2223 grains semi-aligned by the mechanical treatment. The covering Ag-sheath was removed from the sample prior to imaging. The sample thickness of a filament is larger than that of a thin film, but still comparable.

As result, the overall behavior of the flux patterns is similar, but there is no strong shielding of the sample due to the easy flux penetration along the GBs. Very remarkable is the appearance of negative vortices already at still positive fields (+6 mT), which leads to a central peak in a MHL shifted to positive fields as described in [77–79]. Otherwise, the flux patterns obtained are typical for all types of granular HTSc.

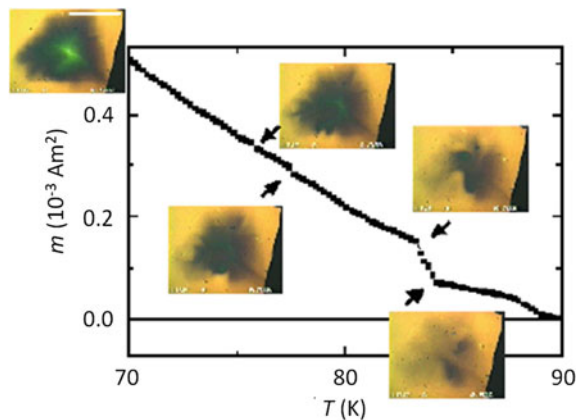
## 8 Instability of the Vortex Lattice

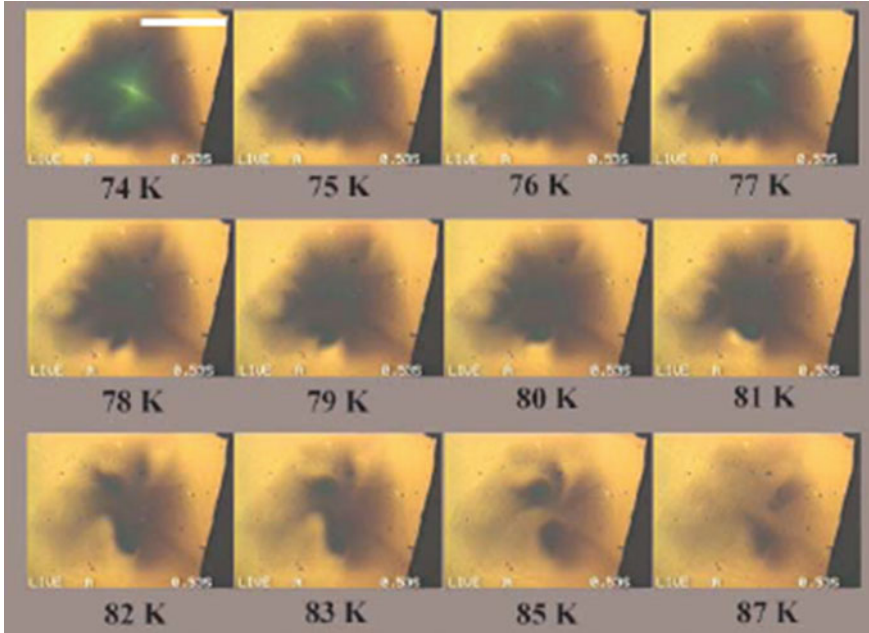
Figure 16 presents a magnetization measurement together with the corresponding magneto-optic images of a NdBCO single crystal. The initial state is prepared at 70 K with an applied external magnetic field of 500 mT, then the field is removed and a field in the opposite direction of  $-60$  mT is applied. As consequence, the crystal carries a rim of negative flux along the sample edges, and an annihilation zone separates the positive and negative flux. The sample is warmed up with a sweep rate of 1 K/min, and MO images were recorded continuously on video tape. On increasing the temperature, the flux front develops an irregular shape, and at about 82 K, the negative flux starts to move in a spiral-like fashion, annihilating all the remaining trapped flux in the sample.

Figure 17 presents the same experiment in more detail. Important is here to note that the detailed shape of the flux patterns never reproduces exactly in subsequent experimental runs. Thus, the formation of the turbulent flux patterns is not a fingerprint of a non-uniform distribution of crystal defects or of the available flux pinning sites. This is in direct contrast to the initial flux penetration into the same sample, which is always fully reproducible, even in samples exhibiting the flux turbulence [80].

Figure 18 presents  $m(T)$ -measurements by SQUID magnetometry on an NdBCO single crystal showing turbulence (solid lines, indicating various applied negative fields between 0 (i.e., remanent state and  $-800$  mT applied field). The arrows point to the events of the turbulent behavior, when the right conditions are met. The circles indicate a measurement on a melt-textured NdBCO sample under the same conditions. The upper inset demonstrates the non-reproducibility of the turbulent events in subsequent runs, and the lower inset compares the onset temperature of the turbulent behavior with the irreversibility line. Here it is important to point out that these SQUID measurements are done in continuous, controlled temperature sweep mode, which is essential to observe such effects [81].

**Fig. 16** Flux distributions and magnetization measurement on a NdBCO single crystal. See the main text for the preparation of the initial magnetic state. The marker is 1 mm. *Reproduced with permission from Ref. [81]*





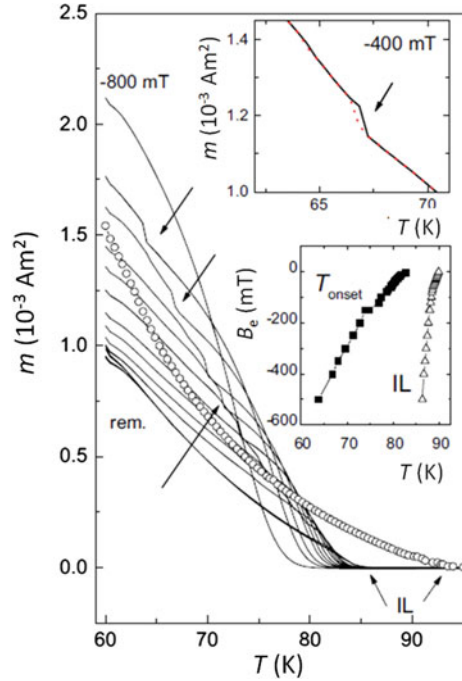
**Fig. 17** Flux distributions of the same NdBCO crystal during the warm-up experiment (controlled temperature sweep rate 1 K/min) showing the turbulent flux move. The yellow color indicates negative flux, green trapped positive flux. The temperature is indicated on each image. The marker is 1 mm. The turbulent flux movement sets in at 82 K, and then, flux is moving in a spiral-like fashion towards the sample center. *Reproduced with permission from Ref. [79]*

A first theoretical explanation of the flux turbulence phenomena was presented by Bass et al. [82] regarding the heat release during the flux annihilation process, which is, however, limited to the interface between the positive and negative flux in the sample. Furthermore, the heat release due to the annihilation is quite small, so that it is unlikely that the entire flux pattern of the sample can be affected. Another approach by Fisher et al. [83] used the tangential discontinuity in classical hydrodynamics as a base, requiring an anisotropy of the electromagnetic properties of the superconducting material. This is provided in (RE)-BCO superconductors by the twin pattern. Both models predict a temperature window where the instability may occur which corresponds to the experimental observations.

The instability phenomenon leads furthermore to another very interesting type of flux penetration observed in  $\text{MgB}_2$  samples, here an  $\text{MgB}_2$  thin film sample with a thickness of 400 nm [84]. The resulting magnetic behavior is found to differ totally from the usual critical-state type of smooth flux penetration patterns. The images for increasing field (a)–(d) indicate that the flux instead penetrates in dendritic structures which, one after the other, invade the entire film area. The dendrites nucleate at seemingly random places along the film edges, and then grow to their final size in less than 1 ms (which corresponds to the time resolution of the CCD system used



**Fig. 18** Flux turbulence on a NdBCO single crystal observed by SQUID magnetometry. The various steps in the  $m(T)$ -behavior are marked by arrows, IL denotes the location of the respective irreversibility field,  $B_{irr}$ . The circles show  $m(T)$  of a melt-textured NdBCO sample measured under the same conditions. The upper inset demonstrates the non-reproducibility of the  $m(T)$ -curves, and the lower inset gives a comparison of  $B_{irr}$  with the appearance of the turbulence in the NdBCO single crystal. *Reproduced with permission from Ref. [81]*



in this experiment). Moreover, it is found that once a dendrite is formed, its size remains constant although the applied magnetic field continues to increase. When the magnetic field is subsequently reduced again as shown in images (e, f), the flux redistributes in the same abrupt manner leading to a remanent state with an overlapping mixture of two types of dendrites—one of them containing the trapped flux of initial polarity and one containing the negative due to penetration of the reverse return field of the trapped vortices. Further dedicated experiments have shown that such dendritic flux structures appear only as the field exceeds a certain temperature-dependent threshold value. The morphology of the dendrites is also changing with temperature. Thus, a thermo-magnetic origin of the dendritic instability is the most likely explanation for this phenomenon, and is further supported by simulations based on the Maxwell and heat diffusion equations [85] (Fig. 19).

## 9 Magnetism and Superconductivity, Magnetic Superconductors

Magnetism and superconductivity are commonly treated as order phenomena, which exclude each other categorically. Many experiments have shown that this picture is not correct. The HTSc materials (see the generic phase diagram of cuprate HTSc

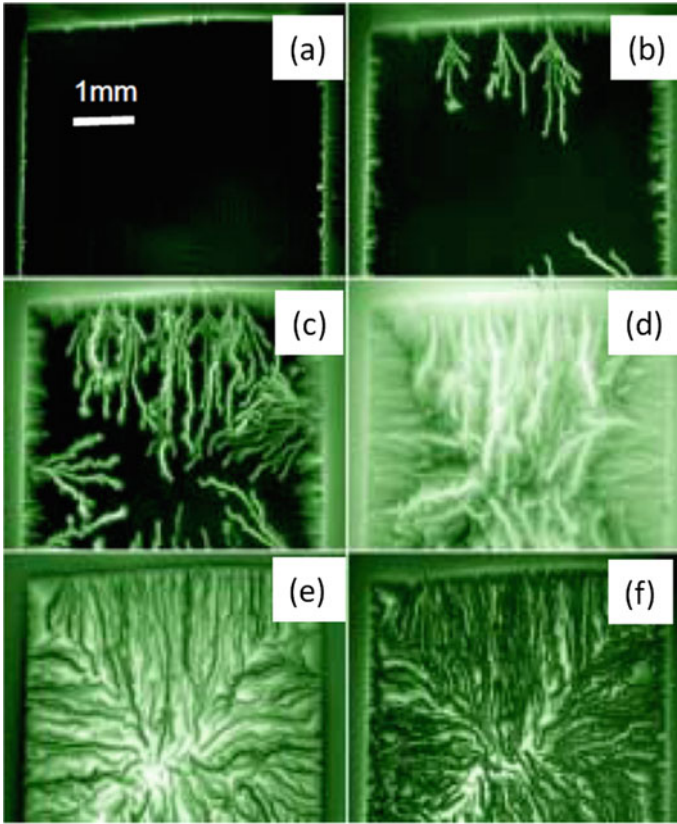


**Fig. 19** MO images of flux penetration into the virgin state of an  $\text{MgB}_2$  thin film at  $T = 5$  K (image brightness represents the flux density). **a, b, c** and **d** Images taken at applied fields (perpendicular to the film) of 3.4, 8.5, 17, 60 mT, respectively. **e, f** Images taken at 21 and 0 mT during the subsequent field reduction. Except for an initial stage, the flux penetration is strongly dominated by the abrupt appearance of dendritic structures nucleating at seemingly random places at the sample edge. The behavior is essentially independent of the field sweep rate [84]. Image reproduced from the arXiv version of Ref. [84]

presented in Fig. 20a [86]) are coexisting with aniferromagnetism, depending on the charge carrier concentration,  $p$ . The charge carriers in most cuprate HTSc are holes, not electrons. It is even speculated that the presence of the magnetic ordering is giving a boost to the formation of Cooper pairs in the HTSc compounds [87]. Figures 20b, c and d present temperature-pressure diagrams of several low- $T_c$ , but unconventional, superconductors revealing the coexistence of superconductivity with paramagnetism, antiferromagnetism and even ferromagnetism as a function of applied pressure. Figure 20b shows the pressure dependence of the cubic, heavy-fermion metal  $\text{CeIn}_3$  which shows superconductivity under pressure with a  $T_c$  of about 230 mK [88, 89], (c) gives the pressure dependence of  $\text{UGe}_2$  [90] which is a magnetically

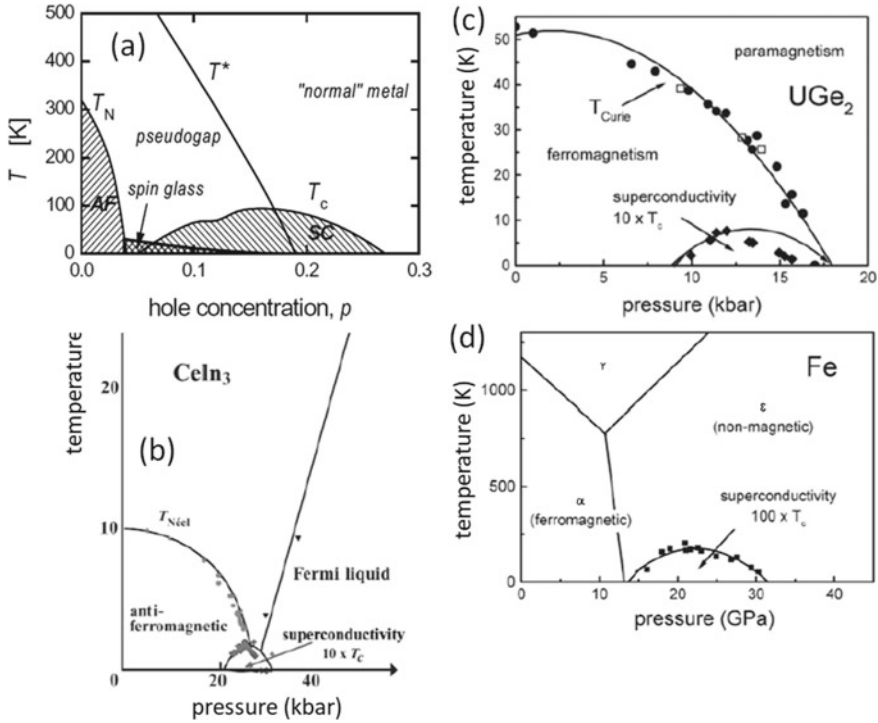


**Fig. 20** a Generic phase diagram of cuprate HTSc superconductors showing the coexistence of superconductivity and antiferromagnetism as function of the charge carrier concentration (holes) (Reproduced with permission from Ref. [86]). b Temperature versus pressure-diagram of  $CeIn_3$ , c Temperature versus pressure-diagram of  $UGe_2$  and d the temperature versus pressure-diagram for Fe (Reproduced with permission from Ref. [7])

active material with a  $T_c \sim 0.8$  K at above 1 GPa, belonging to the heavy-fermion compounds. Figure 20d gives the pressure dependence of metallic Fe, which surprisingly can be a superconductor under pressure. The crystal structure of Fe changes at  $\sim 13$  GPa from fcc to hcp ( $\epsilon$ -Fe) [91], which implies the loss of the ferromagnetic ordering. Superconductivity is then obtained in the hcp-structure.

All these observations provide new space for detailed investigations on the mechanism of Cooper pair formation, not only in the HTSc compounds, but also in conventional uncommon superconductors.

Figure 21 presents  $m(T)$  measurements (field-cooling) in a variety of applied magnetic fields. Above about 0.1 T, the magnetization is no more negative (diamagnetic), but fully paramagnetic. This paramagnetic signal stems from the paramagnetic moment of the  $Nd^{3+}$ -ion. In the case of GdBCO, this effect is even much stronger due to the high paramagnetic moment, which can be driven to a ferromagnetic state by high fields and low temperatures [93].

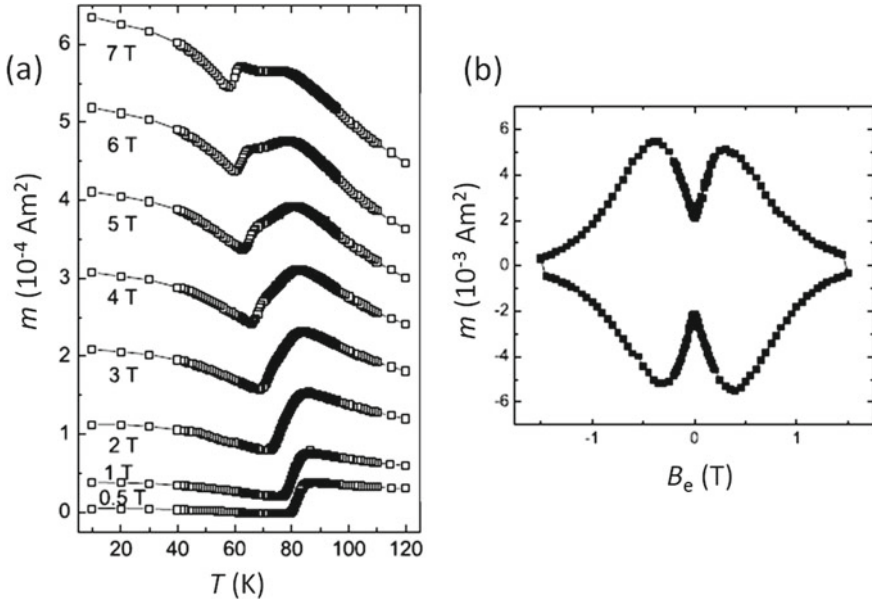


**Fig. 21** **a** Measurements of  $m(T)$  at various applied magnetic fields (field-cooling) ranging between 0.5 and 7 T and **b** the corresponding MHL  $m(B_e)$  of NdBCO measured at 77 K, exhibiting a strong fishtail effect [64, 92]. Note the appearance of a secondary transition in fields above 3 T

Note here that above an applied magnetic field of 3 T, a secondary superconducting transition appears, which belongs to the Nd-rich phase having a lower  $T_c$  of about 65 K as compared to NbBCO. This secondary phase is then responsible for the strong, irreversible peak effect in the RE-BCO compounds. These measurements further demonstrate that superconductivity can coexist with a large paramagnetic moment being present within the same unit cell.

In the case of the most primitive iron-based (IBS) superconductor, FeSe, with a  $T_c$  of  $\sim 8$  K, the preparation of polycrystalline, bulk samples proves to be very complicated due to the phase diagram [95, 96], which does not allow to get the superconducting  $\beta$ -FeSe phase directly. Using the classic solid-state ceramic processing route, the fabrication of phase-pure, large bulk FeSe samples is quasi impossible as there will be always contributions of other phases, which are para- or even ferromagnetic, embedded in the bulk sample. In Ref. [94], these magnetic phases were analyzed in detail using magnetic measurements as well as electron microscopy. Figure 22a demonstrates the ferromagnetic MHLs recorded at 4.2 and 20 K. The only contribution of superconductivity to the MHL is the central peak at zero field. To obtain only the superconducting contribution, the MHL measured at 20 K (only ferromagnetic) must be subtracted from the one measured at 4.2 K, and the final result is shown in Fig. 22b. The resulting MHL is asymmetric, revealing the effects of granularity as expected from a polycrystalline sample.

**Fig. 22** **a** Magnetization loops of polycrystalline, bulk FeSe at  $T = 4$  K (black) and 20 K (red). The contribution of superconductivity is only visible at the zero-field peak, otherwise the measured curve is dominated by ferromagnetism. **b** presents the subtracted MHL, i.e.,  $m(4.2\text{ K}) - m(20\text{ K})$ , which reveals the superconducting behavior. *Reproduced from Ref. [94]*

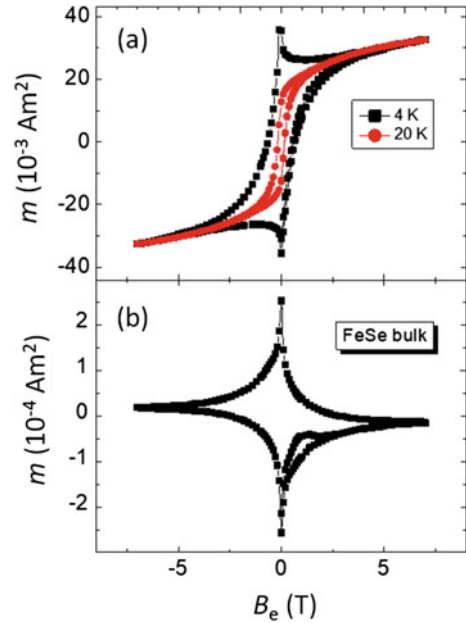
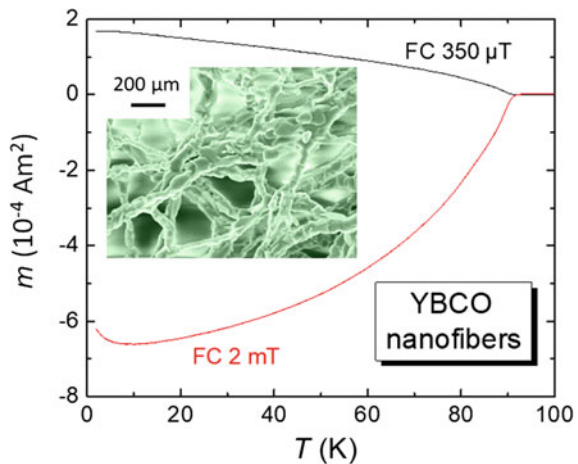


Figure 23 shows a field-cooling (FC) experiment on an YBCO nanofiber mat sample, produced by solution blow-spinning [98]. This superconducting nanofiber mat consists of a large number of nanofibers with typical dimensions of 300–500 nm in diameter and up to 100  $\mu\text{m}$  in length, and with numerous, superconducting interconnections between the nanofibers. These nanofiber mats are thus a new class of superconducting, porous material with unique properties as described in the reviews of Refs. [99, 100]. The magnetization data were recorded in two applied magnetic

**Fig. 23** Field-cooling experiments on a YBCO nanowire fiber mat, revealing the paramagnetic Meissner effect. The FCC curve at 2 mT reveals a paramagnetic upturn at low  $T$ . The inset gives an SEM image of the nanofibers, revealing the numerous interconnects [97]



fields, 350  $\mu\text{T}$  and 2 mT [97]. While the  $m(T)$ -curve at 350  $\mu\text{T}$  exhibits a PME as discussed already in Sect. 3, the  $m(T)$ -curve taken at 2 mT is archetypically negative (diamagnetic), but at very low temperatures, a paramagnetic upturn of the  $m(T)$ -behavior can be seen. A possible explanation for this upturn of the magnetization may be the presence of Cu-O-chain fragments as discussed in Refs. [101, 102]. These Cu-O-fragments are caused by oxygen loss, which can easily happen to the sample, even if the oxygenation process of a nanofiber mat is simple due to the open structure. The diamagnetic superconducting  $m(T)$ -signal of the nanofiber mat is relatively small, so this paramagnetic contribution may get visible.

Figure 23 demonstrates that new types of sample shapes may create fully new and different magnetic behaviors, which are worth to be investigated in detail. Here, it should be mentioned that even applications of these nanofiber mats are already envisaged, as the materials are extremely light, and thus are interesting wherever the weight counts [99, 100].

## 10 Conclusion

To conclude this chapter, we can state that the magnetic properties of superconductors are a wide and rich field, for both conventional and HTSc superconductors. The effects of thermal activation, flux creep, granularity, anisotropy and the fishtail shape of the magnetization loops were intensively discussed in the literature, also often from different viewpoints, e.g., seen from the vortex lattice or from the microstructure of the respective samples. The more recent observations of magnetic superconductors, the coexistence of superconductivity with magnetic ordering, the paramagnetic Meissner effect and the flux instabilities in HTSc as well as in conventional superconductors provided new insights and new theoretical treatments. The appearance of new sample shapes of known superconducting materials like the nanofiber mats and fully new superconducting materials will further contribute to the development of this field.

## References

1. H.K. Onnes, The superconductivity of mercury. *Commun. Phys. Lab. Univ. Leiden* **120b**(122b), 124c (1911)
2. D. van Delft, P.H. Kes, The discovery of superconductivity. *Phys. Today* **63**, 38–43 (2010)
3. W. Meissner, R. Ochsenfeld, Ein neuer Effekt bei Eintritt der Supraleitfähigkeit. *Naturwissenschaften* **21**, 787–788 (1933)
4. M. Tinkham, *Introduction to Superconductivity*, 2nd edn. (Dover Publications Inc., New York, 1996)
5. E.M. Savitskii, V.V. Baron, Yu.V. Efimov, M.I. Bychkova, L.F. Myzenkova, *Superconducting Materials*, 1st edn. (Plenum Press, New York, London, 1973)
6. W. Buckel, R. Kleiner, *Supraleitung Grundlagen und Anwendungen*, 7th edn. (Wiley-VCH, Weinheim, 2013)

7. K.H. Bennemann, J.B. Ketterson (eds.), *Superconductivity* (Springer-Verlag, Berlin, Heidelberg, Germany, 2008)
8. P. Mangin, R. Kahn, *Superconductivity* (Springer-Verlag, Cham, Switzerland, 2017)
9. C.P. Poole (ed.), *Handbook of Superconductivity*, 1st edn. (Elsevier, Amsterdam, The Netherlands, 1995)
10. A.V. Narlikar, *Superconductors* (Oxford University Press, Oxford, U.K., 2014)
11. K.A. Müller, J.G. Bednorz, Possible high  $T_c$  superconductivity in the Ba-La-Cu-O system. *Z. Phys. B* **64**, 189-193 (1986)
12. C. Buzea, T. Yamashita, Review of the superconducting properties of  $MgB_2$ . *Supercond. Sci. Technol.* **14**, R115–R146 (2001)
13. D.A. Cardwell, D.S. Ginley (eds.), *Handbook of Superconducting Materials* (CRC Press, London, U.K., 2002)
14. H. Hosono, K. Kuroki, Iron-based superconductors: current status of materials and pairing mechanism. *Phys. C* **514**, 399–422 (2015)
15. V. Moshchalkov, M. Menghini, T. Nishio, Q.H. Chen, A.V. Silhanek, V.H. Dao, L.F. Chibotaru, N.D. Zhigadlo, J. Karpinski, type-1.5 Superconductivity. *Phys. Rev. Lett.* **102**, 117001 (2009)
16. M.S. Li, Paramagnetic Meissner effect and related dynamical phenomena. *Phys. Rep.* **376**, 133–223 (2003)
17. M.R. Koblischka, L. Püst, A. Koblischka-Veneva, C.S. Chang, The paramagnetic Meissner effect (PME) in metallic superconductors. *Metals*, submitted for publication
18. W.-M. Huang, H.-H. Lin, Pairing mechanism in multiband superconductors. *Sci. Rep.* **10**, 7439 (2020)
19. D. Qiu, C. Gong, S. Wang, M. Zhang, C. Yang, X. Wang, J. Xiong, Recent advances in 2D superconductors. *Adv. Mater.* **33**, 2006124 (2021)
20. M. Sato, J. Ando, Topological superconductors: a review. *Rep. Prog. Phys.* **80**, 076501 (2017)
21. G. Xie, G. Cheng, D. Zhu, J. Yan, J. Ma, T. Lv, J. Zhang, W. Han, Y.Z. Long, Progress of superconducting nanofibers via electrospinning. *J. Phys. Condensed Mat.*, **34**, 043002 (2022).
22. M.R. Koblischka, A. Koblischka-Veneva, Fabrication of superconducting nanowires using the template method. *Nanomaterials* **11**, 1970 (2021)
23. A.P. Drozdov, M.I. Eremets, I.A. Troyan, V. Ksenofontov, S.I. Shylin, Conventional superconductivity at 203 kelvin at high pressures in the sulfur hydride system. *Nature* **525**, 73–76 (2015)
24. A.P. Drozdov, P.P. Kong, V.S. Minkov, S.P. Besedin, M.A. Kuzovnikov, S. Mozaffari, L. Balicas, F.F. Balakirev, D.E. Graf, V.B. Prakapenka, E. Greenberg, D.A. Knyazev, M. Tkacz, M.I. Eremets, Superconductivity at 250 K in lanthanum hydride under high pressures. *Nature* **569**, 528–533 (2019)
25. B. Seeber (ed.), *Handbook of Applied Superconductivity* (IOP Publishing, Bristol, UK, 1999)
26. R.P. Huebener, *Magnetic Flux Structures in Superconductors*, 2nd edn. (Springer, Heidelberg, Germany, 2001)
27. M.R. Koblischka, R.J. Wijngaarden, Magneto-optical investigations of superconductors. *Supercond. Sci. Technol.* **8**, 199–213 (1995)
28. C. Jooss, J. Albrecht, H. Kuhn, S. Leonhardt, H. Kronmüller, Magneto-optical studies of current distributions in high- $T_c$  superconductors. *Rep. Prog. Phys.* **65**, 651–788 (2002)
29. A.A. Abrikosov, The magnetic properties of superconducting alloys. *J. Phys. Chem. Solid.* **2**, 199–208 (1957)
30. H. Träuble, U. Essmann, Die Beobachtung magnetischer Strukturen von Supraleitern zweiter Art. *Phys. stat. sol.* (b) **20**, 95–111 (1967)
31. F.S. Wells, A.V. Pan, X. Renshaw Wang, S.A. Fedoseev, H. Hilgenkamp, Analysis of low-field isotropic vortex glass containing vortex groups in  $YBa_2Cu_3O_{7-x}$  thin films visualized by scanning SQUID microscopy. *Sci. Rep.* **5**, 8677 (2015)
32. T.H. Johansen, P.E. Goa, D.V. Shantsev, E.I. Il'yashenko, Y.M. Galperin, Å.A.F. Olsen, M. Baziljevich, Magneto-optical imaging of superconducting vortices, in: *Magneto-Optical Imaging*, ed. by T.H. Johansen, D.V. Shantsev (NATO Science Series II: Mathematics, Physics and Chemistry 142. Kluwer Academic Publishers, Dordrecht, The Netherlands, 2004)

33. E. Babaev, M. Speight, Semi-Meissner state and neither type-I nor type-II superconductivity in multicomponent superconductors. *Phys. Rev. B* **72**, 180502(R) (2007)
34. J. Parisi, R.P. Huebener, A superconducting vortex-memory system. *IEEE Trans. Electron. Dev.* **31**, 310–314 (1984)
35. J. Parisi, R.P. Huebener, B. Mühlemeier, Experimental study of a superconducting vortex-memory device. *Appl. Phys. Lett.* **40**, 907–909 (1982)
36. M.H. Devoret, R.J. Schoelkopf, Superconducting circuits for quantum information: An outlook. *Science* **339**, 1169–1174 (2013)
37. P. Svedlindh, K. Niskanen, P. Norling, P. Nordblad, L. Lundgren, B. Lönnberg, T. Lundström, Anti-Meissner effect in the BiSrCaCuO system. *Phys. C* **162–164**, 1365–1366 (1989)
38. W. Braunisch, N. Knauf, V. Kataev, S. Neuhausen, A. Grütz, A. Kock, B. Roden, D. Khomskii, D. Wohlleben, Paramagnetic Meissner effect in Bi high-temperature superconductors. *Phys. Rev. Lett.* **68**, 1908–1911 (1992)
39. W. Braunisch, N. Knauf, G. Bauer, A. Kock, A. Becker, B. Freitag, A. Grütz, V. Kataev, S. Neuhausen, B. Roden, D. Khomskii, D. Wohlleben, Paramagnetic Meissner effect in high- $T_c$  superconductors. *Phys. Rev. B* **48**, 4030–4042 (1993)
40. M. Sigrist, T.M. Rice, Unusual paramagnetic phenomena in granular high-temperature superconductors—A consequence of d-wave pairing? *Rev. Mod. Phys.* **67**, 503–513 (1995)
41. U. Atzmony, L.H. Bennett, L.J. Swartzendruber, Is there a paramagnetic Meissner effect? *IEEE Trans. Magn.* **31**, 4118–4120 (1995)
42. J. Kötzler, M. Baumann, N. Knauf, Complete inversion of the Meissner effect in  $\text{Bi}_2\text{Sr}_2\text{CaCu}_2\text{O}_{8+\delta}$  ceramics. *Phys. Rev. B* **52**, 1215–1218 (1995)
43. C. Heinzel, T. Theilig, P. Ziemann, Paramagnetic Meissner effect analyzed by second harmonics of the magnetic susceptibility: consistency with a ground state carrying spontaneous currents. *Phys. Rev. B* **48**, 3445–3454 (1993)
44. R. Lucht, H.V. Löhneysen, H. Claus, M. Kläser, G. Müller-Vogt, Surface-sensitive paramagnetic Meissner effect in  $\text{YBa}_2\text{Cu}_3\text{O}_x$  single crystals. *Phys. Rev. B* **52**, 9724–9726 (1995)
45. D.J. Thompson, M.S.M. Minhaj, L.E. Wenger, J.T. Chen, Observation of paramagnetic Meissner effect in niobium disks. *Phys. Rev. Lett.* **75**, 529–532 (1995)
46. P. Kostic, B. Veal, P. Paulikas, U. Welp, V.K. Todt, C. Gu, U. Geiser, J.M. Williams, K.D. Carlson, R.A. Klemm, Paramagnetic Meissner effect in Nb. *Phys. Rev. B* **53**, 791–801 (1996)
47. A.L. Pessoa, A. Koblishka-Veneva, C.L. Carvalho, R. Zadorosny, M.R. Koblishka, Microstructure and paramagnetic Meissner effect of YBCO nanowire networks. *J. Nanopart. Res.* **22**, 360 (2020)
48. D. Khomskii, Wohlleben effect (Paramagnetic Meissner effect) in high-temperature superconductors. *J. Low Temp. Phys.* **95**, 205–223 (1994)
49. M.S.M. Minhaj, D.J. Thompson, L.E. Wenger, J.T. Chen, Paramagnetic Meissner effect in a niobium disk. *Phys. C* **235–240**, 2519–2520 (1995)
50. M.R. Koblishka, L. Püst, A. Galkin, P. Nálezka, M. Jirsa, T.H. Johansen, H. Bratsberg, B. Nilsson, T. Claeson, Flux penetration into an artificially granular high- $T_c$  superconductor. *Phys. Rev. B* **59**, 12114–12120 (1999)
51. A.K. Geim, S.V. Dubonos, J.G.S. Lok, M. Henini, J.C. Maan, Paramagnetic Meissner effect in small superconductors. *Nature* **396**, 144–146 (1998)
52. A.E. Koshelev, A.I. Larkin, Paramagnetic moment in field-cooled superconducting plates: Paramagnetic Meissner effect. *Phys. Rev. B* **52**, 13559–13562 (1995)
53. V.V. Moshchalkov, X.G. Qiu, V. Bruyndoncx, The paramagnetic Meissner effect resulting from the persistence of the giant vortex state. *J. Low Temp. Phys.* **105**, 515–520 (1996)
54. M.R. Koblishka, *Magnetic properties of high-temperature superconductors* (Alpha Science International Ltd., Oxford, U.K., 2009)
55. R.G. Mints, A.L. Rakhmanov, Critical state stability in type-II superconductors and superconducting-normal-metal composites. *Rev. Mod. Phys.* **53**, 551–592 (1981)
56. J. Coello de Portugal, R. Tomás, L. Fiscarelli, D. Gamba, and M. Martino, Impact of flux jumps in future colliders. *Phys. Rev. Accel. Beams* **23**, 011001 (2020)



57. H. Fujishiro, H. Mochizuki, T. Naito, M.D. Ainslie, G. Giunchi, Flux jumps in high- $J_c$  MgB<sub>2</sub> bulks during pulsed field magnetization. *Supercond. Sci. Technol.* **29**, 034006 (2016)
58. M. Däumling, J.M. Seuntjens, D.C. Larbalestier, Oxygen-defect flux pinning, anomalous magnetization and intra-grain granularity in YBa<sub>2</sub>Cu<sub>3</sub>O<sub>7- $\delta$</sub> . *Nature* **346**, 332–335 (1990)
59. S.I. Yoo, R.W. Mc Callum, Phase diagram in the Nd-Ba-Cu-O system. *Phys. C* **210**, 147–156 (1993).
60. A.A. Zhukov, H. Küpfer, G. Perkins, L.F. Cohen, A.D. Caplin, S.A. Klestov, H. Claus, V.I. Voronkova, T. Wolf, H. Wühl, Influence of oxygen stoichiometry on the irreversible magnetization and flux creep in RBa<sub>2</sub>Cu<sub>3</sub>O<sub>7- $\delta$</sub>  ( $R = Y, Tm$ ) single crystals. *Phys. Rev. B* **51**, 12704–12714 (1995)
61. M. Jirsa, L. Püst, D. Dlouhy, M.R. Koblischka, Fishtail shape in the magnetic hysteresis loop for superconductor: Interplay between different pinning mechanisms. *Phys. Rev. B* **55**, 3276–3284 (1997)
62. A. Erb, J.-Y. Genoud, F. Marti, M. Däumling, E. Walker, R. Flükiger, Reversible suppression of the so-called fishtail effect in ultra pure single crystals of YBa<sub>2</sub>Cu<sub>3</sub>O<sub>7- $\delta$</sub>  achieved by proper oxygenation. *J. Low Temp. Phys.* **105**, 1023–1028 (1996)
63. M.J. Kramer, A. Karion, K.W. Dennis, M. Park, R.W. Mc Callum, Enhanced superconductivity in Nd<sub>1-x</sub>Ba<sub>2-x</sub>Cu<sub>3</sub>O<sub>7- $\delta$</sub>  by low oxygen partial pressure annealing. *J. Electron. Mater.* **23**, 1117–1120 (1994)
64. M.R. Koblischka, M. Murakami, Pinning mechanisms in bulk high- $T_c$  superconductors. *Supercond. Sci. Technol.* **13**, 738–744 (2000)
65. A.J.J. van Dalen, M.R. Koblischka, R. Griessen, Equivalence of dynamic and conventional magnetic relaxation in high- $T_c$  superconductors. *Phys. C* **259**, 157–167 (1996)
66. Y. Yeshurun, A.P. Malozemoff, A. Shaulov, Magnetic relaxation in high-temperature superconductors. *Rev. Mod. Phys.* **68**, 911–949 (1996)
67. G. Blatter, M.V. Feigel'man, V.B. Geshkenbein, A.I. Larkin, V.M. Vinokur, Vortices in high-temperature superconductors. *Rev. Mod. Phys.* **66**, 1125 (1994)
68. W.K. Kwok, S. Fleshler, U. Welp, V.M. Vinokur, J. Downey, G.W. Crabtree, M.M. Miller, Vortex lattice melting in untwinned and twinned single crystals of YBa<sub>2-x</sub>Cu<sub>3</sub>O<sub>7- $\delta$</sub> . *Phys. Rev. Lett.* **69**, 3370–3373 (1992)
69. J.R. Clem, Pancake vortices. *J. Supercond.* **17**, 613–629 (2004)
70. M.R. Koblischka, J. Sosnowski, Temperature-dependent scaling of pinning force data in Bi-based high- $T_c$  superconductors. *Eur. J. Phys. B* **44**, 277–280 (2005)
71. M.R. Koblischka, N. Moser, B. Gegenheimer, H. Kronmüller, Determination of flux density gradients in YBa<sub>2-x</sub>Cu<sub>3</sub>O<sub>7- $\delta$</sub>  superconductors using the high-resolution Faraday effect. *Phys. C* **166**, 36–48 (1990)
72. M.R. Koblischka, T. Schuster, H. Kronmüller, Influence of additions and radiation damage on the superconducting properties of sintered YBa<sub>2-x</sub>Cu<sub>3</sub>O<sub>7- $\delta$</sub> . *Phys. C* **211**, 263–278 (1993)
73. M.R. Koblischka, T. Schuster, H. Kronmüller, Flux penetration in granular YBa<sub>2-x</sub>Cu<sub>3</sub>O<sub>7- $\delta$</sub>  samples: a magneto-optical study. *Phys. C* **219**, 205–212 (1994)
74. M.R. Koblischka, T.H. Johansen, H. Bratsberg, P. Vase, Flux patterns of monofilamentary Bi<sub>2</sub>Sr<sub>2</sub>Ca<sub>2</sub>Cu<sub>3</sub>O<sub>10+ $\delta$</sub>  tapes at various temperatures. *Supercond. Sci. Technol.* **12**, 113–119 (1999)
75. T., Schuster, M.V. Indenbom, M.R. Koblischka, H. Kuhn, H. Kronmüller, Observation of current-discontinuity lines in type-II superconductors. *Phys. Rev. B* **49**, 3443–3452 (1994)
76. M.R. Koblischka, L. Püst, M. Jirsa, T.H. Johansen, Formation of the low-field peak in magnetization loops of high- $T_c$  superconductors. *Phys. C* **320**, 101–114 (1999)
77. M.R. Koblischka, L. Püst, A. Galkin, P. Nálevka, Anomalous position of the maximum in magnetic hysteresis loops measured on (Bi, Pb)<sub>2</sub>Sr<sub>2</sub>Ca<sub>2</sub>Cu<sub>3</sub>O<sub>10</sub>/Ag tapes. *Appl. Phys. Lett.* **70**, 514–516 (1997)
78. D.V. Shantsev, M.R. Koblischka, Y.M. Galperin, T.H. Johansen, L. Püst, M. Jirsa, Central peak position in magnetization loops of high- $T_c$  superconductors. *Phys. Rev. Lett.* **82**, 2947–2950 (1999)

79. M.R. Koblishka, M. Murakami, T.H. Johansen, M. Baziljevich, T. Frello, T., Wolf, Instability of the critical state in  $\text{NdBa}_2\text{Cu}_3\text{O}_{7-\delta}$  single crystals. *Phys. Stat. Sol. (b)* **215**, R11–R12 (1999)
80. M.R. Koblishka, T.H. Johansen, M. Baziljevich, H. Hauglin, H. Bratsberg, B.Y. Shapiro, Turbulent relaxation in the vortex lattice. *Europhys. Lett.* **41**, 419–424 (1998)
81. M.R. Koblishka, T.H. Johansen, M. Baziljevich, M. Murakami, SQUID and magneto-optic investigations of flux turbulence in the critical state. *J. Supercond.* **15**, 153–157 (2002)
82. F. Bass, B.Y. Shapiro, I. Shapiro, M. Shvartser, Flux-antiflux interface in type-II superconductors. *Phys. Rev. B* **58**, 2878–2885 (1998)
83. L.M. Fisher, P.E. Goa, M. Baziljevich, T.H. Johansen, A.L. Rakhmanov, V.A. Yampolskii, Hydrodynamic instability of the flux-antiflux interface in Type-II superconductors. *Phys. Rev. Lett.* **87**, 247005 (2001)
84. T.H. Johansen, M. Baziljevich, D.V. Shantsev, P.E. Goa, Y.M. Galperin, W.N. Kang, H.J. Kim, E.M. Choi, M.S. Kim, S.I. Lee, Dendritic magnetic instability in superconducting  $\text{MgB}_2$  films. in: *Magneto-Optical Imaging*, ed. by T.H. Johansen, D.V. Shantsev (NATO Science Series II: Mathematics, Physics and Chemistry 142. Kluwer Academic Publishers, Dordrecht, The Netherlands, 2004)
85. T. Qureishy, J.I. Vestgarden, A.J. Qviller, A.S. Fjellvag, J.M. Meckbach, A. Torgovkin, T.H. Johansen, K. Ilin, M. Siegel, I. Maasilta, P. Mikheenko, Energy of dendritic avalanches in thin-film superconductors, *AIP Adv.* **8**, 085128 (2018)
86. J.L. Tallon, Oxygen in high- $T_c$  cuprate superconductors, in *Frontiers in Superconducting Materials*, ed. by A.V. Narlikar (Springer-Verlag, Berlin, Heidelberg, Germany, 2005)
87. A. de Visser, Magnetic field-boosted superconductivity. *Phys. Today* **73**, 44–50 (2020)
88. S. Kawasaki, M. Yashima, Y. Kitaoka, K. Takeda, K. Shimizu, Y. Oishi, M. Takata, T. C. Kobayashi, H. Harima, S. Araki, H. Shishido, R. Settai, Y. Onuki, Pressure-induced unconventional superconductivity in the heavy-fermion antiferromagnet  $\text{CeIn}_3$ : an  $^{115}\text{In}$ -NQR study under pressure. *Phys. Rev. B* **77**, 064508 (2008)
89. P.J.W. Moll, T. Helm, S.S. Zhang, C.D. Batista, N. Harrison, R.D. McDonald, L.E. Winter, B.J. Ramshaw, M.K. Chan, F.F. Balakirev, B. Batlogg, E.D. Bauer, F. Ronning, Emergent magnetic anisotropy in the cubic heavy-fermion metal  $\text{CeIn}_3$ . *npj Quantum Mater.* **2**, 46 (2017)
90. D. Aoki, K. Ishida, J. Flouquet, Review of U-based ferromagnetic superconductors: comparison between  $\text{UGe}_2$ ,  $\text{URhGe}$ , and  $\text{UCoGe}$ . *J. Phys. Soc. Jpn.* **88**, 022001 (2019)
91. K. Shimizu, T. Kimura, S. Furomoto, K. Takeda, K. Kontani, Y. Onuki, K. Amaya, Superconductivity in the nonmagnetic state of iron under pressure. *Nature* **412**, 316–318 (2001)
92. M.R. Koblishka, Nanoengineering of flux pinning sites in high- $T_c$  superconductors. *Tsinghua Sci. Technol.* **8**, 280–291 (2003)
93. M.R. Koblishka, M. Murakami, Magnetic properties of superconducting and nonsuperconducting  $(\text{Nd}_{0.33}\text{Eu}_{0.33}\text{Gd}_{0.33})\text{Ba}_2\text{Cu}_3\text{O}_y$ . *J. Supercond.* **14**, 415–419 (2001)
94. Q. Nouailhetas, A. Koblishka-Veneva, M. R. Koblishka, S. Pavan Kumar Naik, F. Schäfer, H. Ogino, C. Motz, K. Berger, B. Douine, Y. Slimani, E. Hannachi, Magnetic phases in superconducting, polycrystalline bulk  $\text{FeSe}$  samples. *AIP Adv.* **11**, 015230 (2021)
95. H. Okamoto, The Fe–Se (iron-selenium) system. *J. Phase Equilibria* **12**, 383–389 (1991)
96. E. Pomjakushina, K. Conder, V. Pomjakushin, M. Bendele, R. Khasanov, Synthesis, crystal structure, and chemical stability of the superconductor  $\text{FeSe}_{1-x}$ . *Phys. Rev. B* **80**, 024517 (2009)
97. A.L. Pessoa, A. Koblishka-Veneva, C.L. Carvalho, R. Zadorosny, M.R. Koblishka, Paramagnetic Meissner effect and current flow in YBCO nanofiber mats. *IEEE Trans. Appl. Supercond.* **31**, 7200105 (2021)
98. J.L. Daristotle, A.M. Behrens, A.D. Sandler, P. Kofinas, A review of the fundamental principles and applications of solution blow spinning. *ACS Appl. Mater. Interf.* **8**, 34951–34963 (2016)
99. M.R. Koblishka, A. Koblishka-Veneva, Porous high- $T_c$  superconductors and their applications. *AIMS Mater. Sci.* **5**, 1199–1213 (2018)
100. D.M. Gokhfeld, M.R. Koblishka, A. Koblishka-Veneva, High-porous superconductors: synthesis, investigations and perspectives. *Phys. Met. Metall.* **121**, 1026–1038 (2020). ((in Russian))

101. G. Uimin, Order and disorder in the ensemble of Cu-O chain fragments in oxygen-deficient planes of  $\text{YBa}_2\text{Cu}_3\text{O}_{6+x}$ . *Phys. Rev. B* **50**, 9531–9547 (1994)
102. G. Mamsurova, N.G. Trusevich, K.S. Pigalskiy, A.A. Vishnev, I.V. Mamsurov, Paramagnetism of copper-oxygen chains in high-temperature  $\text{YBa}_2\text{Cu}_3\text{O}_{6+\delta}$  superconductors. *Bull. Russ. Acad. Sci. Phys.* **80**, 504–507 (2016)

# Mechanical Properties of Superconducting Materials



Essia Hannachi and Yassine Slimani

**Abstract** Superconducting materials are currently the key research target in the field of basic and applied superconductivity. The intrinsic brittleness and the poor mechanical properties of several superconductors such A15 alloys, high  $T_c$  superconductors (HTSc) and non-cuprates superconductors, halt in the pathway of a broad extent of actual applications. In order to be better commercialized, some factors have to be controlled and optimized among which is the development of exceptional processing methods for fabrication of usable superconductors. This book chapter examines the up-to-date of mechanical characteristics of superconducting materials. We start by giving an overview of the different testers used for measuring the mechanical behavior. One of the most significant mechanical properties to be enhanced is the microhardness. Therefore, we focused in the next section to microhardness and various models adopted to analyze it. Also, the mechanical nature of different types discovered superconductors from alloys, cuprates, to non-cuprates has been deeply reviewed and discussed. For each case, challenges and recent results for getting commercialized superconductors material with good mechanical properties were presented.

**Keywords** Superconductor · Mechanical · Microhardness · Stress–strain · Commercialization

## 1 Introduction

Superconducting materials have huge potential to bring about drastic revolutions in electric power and giant-field magnet technology and, allowing high-capability

---

E. Hannachi (✉)

Department of Nuclear Medicine Research, Institute for Research & Medical Consultations (IRMC), Imam Abdulrahman Bin Faisal University, P.O. Box 1982, Dammam 31441, Saudi Arabia

Y. Slimani

Department of Biophysics, Institute for Research & Medical Consultations (IRMC), Imam Abdulrahman Bin Faisal University, P.O. Box 1982, Dammam 31441, Saudi Arabia  
e-mail: [yaslimani@iau.edu.sa](mailto:yaslimani@iau.edu.sa)

dissipation-lower transmission of electric power, high-productivity electric power generation, ultra-high magnetic field production for magnetic resonance imaging (MRI) systems with good resolution, tiny lightweight electrical apparatus, high-speed maglev transportation, nuclear fusion reactors, nuclear magnetic resonance (NMR), and imminent progressive extreme energy particle accelerators, etc. The economy, functioning, and operational parameters (magnetic fields and temperatures) of these applications intensely dependent on the mechanical and electromagnetic characteristics, as well as the production and price of materials. The mechanical performance of superconducting materials has been of relevance and concern to researchers in this field. The brittleness inherent in several high-field superconductors needs the development of unique processing techniques for manufacture of usable conductors. Fundamental investigations of the influences of mechanical stress on superconducting characteristics offer a deep insight into the nature of superconductors. In last years, attention in the mechanical comportment of commercialized superconductors has increased due to the great mechanical forces anticipated in projected superconducting devices like energy storage, rotating machines, magnets for plasma confinement and, and electrical transmission lines [1–3]. In many laboratories located around the world, equipment for examining the mechanical properties of superconducting materials has been developed. Results from these measurements have become more accessible over the past years; Thus, it is exciting to examine the mechanical behavior and impacts of stress in superconducting materials. The assessment of mechanical properties led to distinguish and enhance the permanence of traditional devices. This chapter will review the mechanical properties of superconducting alloys and compounds at ambient and low temperatures, the stress effects on superconducting characteristics, and their implications for superconducting applications.

## 2 Mechanical Properties Measurements

The Mechanical features of superconducting materials are fully linked to other including electrical, structural, and physical characteristics to establish the devices execution. The mechanical characteristics of the material are usually measured by hardness test, compression tests and tensile tests, bending test.

### 2.1 Hardness Test (HT)

HT is the most general test that is employed to assess mechanical characteristics. Hardness is defined as the capacity of one material to scratch another material or the resistance to indentation. The indentation hardness is the most usually employed form of hardness. Conical, pyramidal, or spherical indenters have been employed for the indentation hardness tests. There are three main standard test methods for

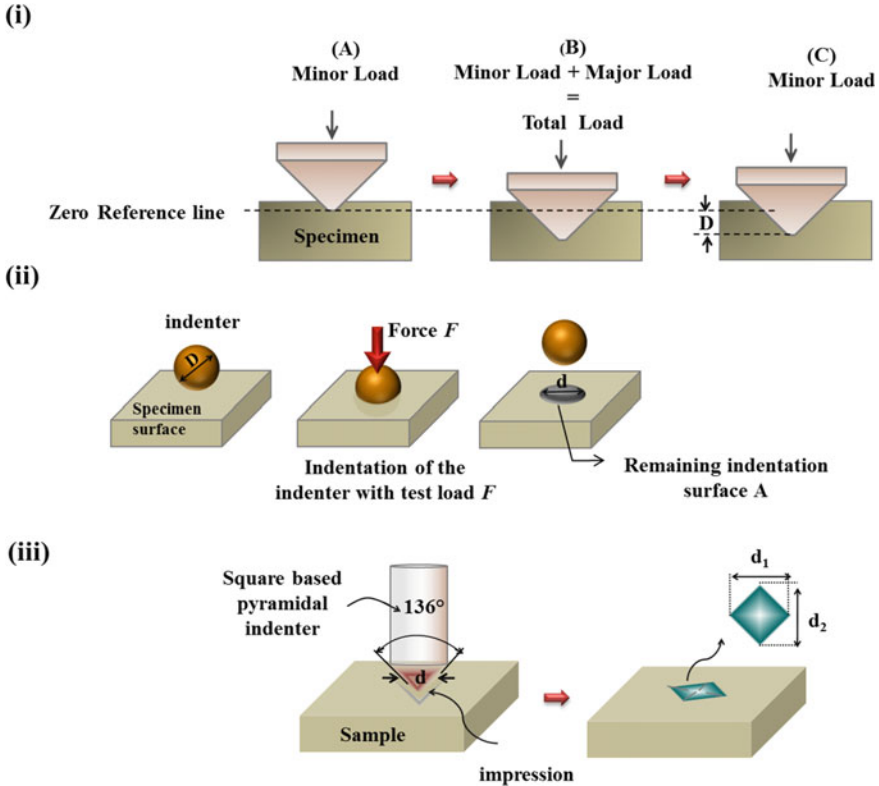


Fig. 1 (i) Rockwell hardness testing, (ii) Brinell hardness testing, and (iii) Vickers hardness testing

manifesting the correlation between hardness and impression size: Brinell, Vickers, and Rockwell (Fig. 1).

The HT have certain benefits and disadvantages. For instance, no scale, in the simplest and most widely employed indentation hardness, Rockwell hardness, extends sufficiently to the full range of materials used to make sheet metal. Also, each thickness gauge has the minimum required to avoid the effect of the anvil, i.e. the effect of the outrigger or support on the observed hardness. The benefits of indentation hardness techniques are that they are less destructive, fast, and can be applied to small material samples and localized materials in fashion.

## 2.2 Compression Test (CT) and Tensile Test (TT)

Compression test (CT) includes a specimen of the material having dimensions defined by the proper standard by carrying two pressure plates together to press the sample. Special procedures require material cylinder pressure but the particular material

shape can change depending on the normal protocol. The exerted force and cross shift data are amassed in real time and the test goes on till the specimen flops or the tester selects to terminate the test. The CT can give the yield strength, ultimate compressive strength, modulus of elasticity and hardness of the sample. The TT is the most extensively employed test in controlling the mechanical characteristics of the materials. In TT, a particularly fabricated sample is exposed to steadily rising uniaxial tension force. The material elongation is measured instantaneously. The measurement via TT yields to curves of the engineering strain and stress. The engineering strain and stress are given by the following expressions, respectively [4]:

$$S = P/A_0 \quad (1)$$

$$e = \Delta l/l_0 \quad (2)$$

where  $A_0$  is the initial cross-section sample area,  $\Delta l$  is the variation in length, and  $l_0$  is the original length of the sample. At the start of the test, the material stretches flexibly, and if the load is released, the specimen returns to its original length. The material is said to have exceeded elastic limit 3 when the load is enough to begin a plastic or non-recoverable deformation. On additional loading, the stress due to continuous plastic deformation increases with increasing plastic stress, i.e., the hardening of the metallic strain. Compression is reached at maximum tensile strength. At this point the embedding initiates and the engineering stress declines with more pressure until the material breaks down.

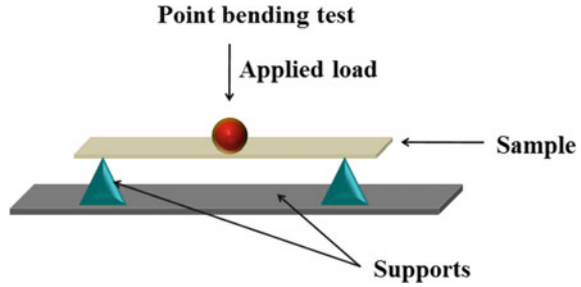
The engineering strain–stress curves does not provide a correct clue of the deformation properties of a material since it is based on the primary sample dimensions. Yet, the dimensions of the sample vary uninterruptedly during the test. If the stress is measured from the instant cross-sectional area related to a special load rather than the original stress, then it is named the true stress  $\sigma$ . The true stress is termed as the ratio of the load of the specimen  $A_i$  to the instant least cross-sectional area reinforcing that load  $w$ .

The true strain  $\varepsilon$  is given by [4]:

$$\varepsilon = \ln\left(\frac{l_i}{l_0}\right) \quad (3)$$

Here  $l_0$  is the original length and  $l_i$  the instant length. The tensile tests have some limitations. They are usually time expending, destructive and necessitate particularly prepared samples.

**Fig. 2** 3-Point bending test method. three-point bending delivers three points of contact; dual supports and one center point where the loading is applied



### 2.3 Three-Point Bending Tests

Bending tests (BT) are usually performed to control the mechanical characteristics of the material like ductility, bend strength, fracture strength of the material to fracture. BT distort the test material at its midpoint allowing it to form a concave or bend surface without fracture with a particular radius of curvature (Fig. 2). There are four known kinds of BT. In a guided BT, the specimen is positioned horizontally via two supports and after that a force exerted to the top of the midpoint distorting the specimen into a “U” form. In a semi-guided BT, the midpoint of the specimen is bent at a certain angle or internal radius. In a free BT, the extremities of the specimen are pushed together, without any application of the force to the bend itself. Finally, ASTM E399; the common fracture toughness tester which consists of a specimen with a pre-cracked initial crack on the underside of the midpoint that is loaded into a three-point bending point such that midpoint force is applied to the opposite face of the fracture. 3-point bending tests provide information about the flexural stress, flexural strain of bending, and elastic modulus a material. Hard materials like high temperature superconductors can be analyzed by means of BT as a gauge of the material in both compression (the top of the material as it is tested) and tension (the bottom side of the specimen as it is tested).

### 2.4 Instrumented Indentation

Indentation testing is a useful technique that is based principally on the contact between the material of concern, whose mechanical characteristics like hardness, elastic modulus are unidentified, with another material, whose characteristics are identified [5]. The technology’s origins date back to the 1822 Mohs hardness scale, in which material capable of leaving a lasting abrasion in another material were classified as harder, with diamonds designated a value of 10 on the scale as a maximum. The creation of Vickers, Brinell, Rockwell and Knoop testing comes from an improvement in the indentation test method, in which the penetration length scale is measured in nanometer scale instead of millimeters or microns, the latter being frequent in traditional HT. Aside from the displacement scale included, the hallmark of the majority



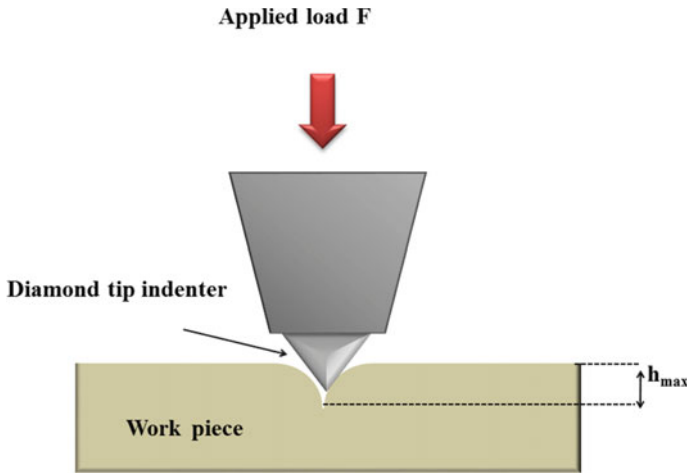


**Fig. 3** Schematic illustration of nano indentation test

nanoscale indentation tests is the indirect measurement of the contact area. In traditional HT, the contact area is determined from direct measurements of the extents of the impression remaining in the sample's surface when the load is removed. In nanoscale indentation tests, the residual impression size is on the order of microns and too miniature to be opportunely measured directly. Consequently, it is common to determine the contact area by computing the depth of the indentation mark in the sample of concern. Figure 3 illustrates schematic depiction of nano indentation test. This, along with the known indenter geometry, offers an indirect measurement of the contact area at filled load. For this purpose, nano indentation can be deemed as a particular case of instrumented indentation test or depth sensing indentation. Nano indentation has been extensively employed for describing the mechanical properties of nano materials [6], and thin film [7], due to its exalted sensitivity and the outstanding resolution for getting the nano hardness, elastic modulus and the plastic/elastic deformation behaviors in a quite simpler mode. Over a nano indentation test, a diamond tip is compressed into the sample till a specified extreme load or depth is attained and then the load is detached. Instantaneously, the displacement of, as well as the load on, the indenter is registered. The results of instrumented indentation deliver evidence about the mechanical characteristics of the material, involving hardness, plastic deformation and elastic moduli. One main parameter of indentation test is that the tip requires to be monitored by displacement or force that could be measured instantaneously in the indentation cycle [8]. Some of the usually measured mechanical characteristics include the hardness, the ultimate tensile strength, the Young's modulus yield strength, and work hardening coefficients. The mechanical characteristics offer evidence on the strength and for the specification of materials.

### 3 Microhardness and Models

Microhardness is the hardness of a material as defined by forcing an indenter such as a Vickers or Knoop onto the material's surface under a load from 15 to 1000 gf; frequently, the indents are so tiny that they need to be measured with a microscope. The frequently checked static process HT entails applying a static load to an indenter of diamond and measuring, by means of microscope, the transverse indentation size on the sample surface after unloading. The most commonly employed form of indenter geometry, the angle of a diamond pyramid with a square base between the opposite facades of the pyramid is  $136^\circ$  as the indent, which is the Vickers indenter [9]. On account of the shape the indenter is termed the diamond pyramid hardness (DPH) test [10]. Recently, Vickers microhardness testing has been utilized in numerous kinds of materials including ceramic, alloys superconductors, polymers, semiconductors, and thin films [11–15]. The microhardness of a material is dependent on the applied load [16, 17]. This fact is recognized as indentation size effect (*ISE*) behavior, elucidating the reduction in the hardness with the increase of the applied load. This comportment can result from diverse aspects such as plastic and elastic deformations, temperature, size of indentation, degree of voids/cracks and friction of the indenter [18]. The reverse of this phenomenon is known as reverse *ISE* (*RISE*) behavior, which explains the increase of microhardness as the applied load increases. As described above, the hardness is the most common test to examine the mechanical characteristics of a material since it is simple to operate, less destructive to the surface of the specimen. Other benefit of the hardness measurement allows to attain the supplementary parameters including brightness index, yield strength, fracture toughness, and elastic modulus.

The Vickers microhardness values ( $H_V$ ) can be computed using to the conventional definition [19]:

$$H_V = 1854.4 \left( \frac{F}{d^2} \right) (\text{GPa}) \quad (4)$$

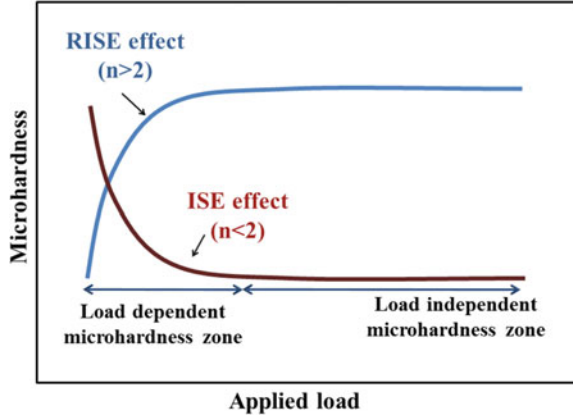
$F$  is the applied load and  $d$  is the indentation diagonal length. Many approaches have been used to analyze Vickers microhardness data.

#### 3.1 Meyer's Theory

The Meyer's concept is frequently employed measure of indentation hardness. Meyer proposed a power law empirical relation that correlates the load,  $F$ , and  $d$  corresponding to the following Meyer's theory:

$$d^n = F/A \quad (5)$$

**Fig. 4** The variation of  $H_v$  a function of applied load.  $H_v$  decreases with increasing the applied load (ISE), whereas  $H_v$  increases with increasing the applied load (RISE). For normal ISE,  $n$  value  $<2$ , whereas for RISE,  $n$  is  $>2$



Here  $A$  is a constant, representing the load needed to begin unit indentation.  $n$  is the Meyer’s index, which defines the ISE. For normal ISE,  $n$  value  $<2$ , whereas for RISE,  $n$  is  $>2$ . If  $n = 2$ ,  $H_v$  is not dependent on the applied load (Fig. 4). Hence, ISE or RISE can be distinguished based on the obtained  $n$  values. So, Knowledge on the increment or decrement of microhardness with applied load can be identified.

### 3.2 Hays/Kendall Model

In 1973, the model of energy losses has been predicted by Hays and Kendall [20]. This concept anticipated that there is a least test load  $w$ , named the specimen resistance pressure, which is compulsory to start plastic deformation, and further down it is merely elastic deformation happens. In another meaning, the indenter can enter the material beyond a particular value of load called the critical value of the applied load. Therefore, the size of the indentation begins to rise after the critical applied load value, and is proportionate to the effective load as  $F_{eff} = F_{max} - W_{HK}$  rather than the applied load:

$$F_{max} - W_{HK} = A_{HK}d^2 \tag{6}$$

$A_{HK}$  represents the hardness constant and it is applied load independent. From the plots of  $F_{max}$  versus  $d^2$ ,  $W_{HK}$  and  $A_{HK}$  are obtained. In addition, the subtraction  $W_{HK}$  from the applied load, the true microhardness can be estimated as:

$$H_{HK} = 1854.4 \frac{F_{max} - W_{HK}}{d^2} \text{ (GPa)} \tag{7}$$

Therefore, the slope of the  $F_{max}$  versus  $d^2$  gives  $A_{HK}$  and  $W_{HK}$  values. The positive value of  $W_{HK}$  signifies that the material exhibits the ISE behavior while the

negative value of  $W_{HK}$  indicates RISE feature for the sample. The positive value is enough to create the elastic and the plastic deformations in the material. The negative value signifies that the plastic deformation is dominant in the system [21].

### 3.3 Proportional Specimen Resistance (PSR) Model

PSR model was suggested by Li and Bradth [22] and is able to investigate the ISE behavior. This model contains the elastic resistance of the test specimen and the frictional effects at the indenter facet/specimen interface during micro indentation. According to PSR concept, the microhardness test load,  $F$ , and the resultant indentation size,  $d$ , showed to survey the following relation:

$$F = ad + bd^2 = ad + \left(\frac{F_c}{d_0^2}\right)d^2 \quad (8)$$

where the values of  $a$  and  $b$  are computed from the  $F/d$  versus  $d$  plots. The parameter  $a$  typifies the load reliance of hardness. The value of the real microhardness is proportionate to  $b$ . Based on Li and Bradth analysis,  $a$  and  $b$  parameters can be correlated to the elastic and the plastic characteristics of the tested material, respectively. The ISE is a result of the relative resistance of the indentation size of the test specimen as defined by  $a$ . Whereas,  $b$  was found to be related to the load indentation that is non-reliant to hardness. It contains the critical indentation load,  $F_c$ , and the characteristic indentation size,  $d_0$ . Particularly,  $b$  is proposed to be a gauge of what is termed “true hardness;  $H_{PSR}$ ”. For the micro indentation testing through a Vickers indenter,  $H_{PSR}$  can be estimated directly from  $b$  as [14]:

$$H_{PSR} = \frac{F - ad_0}{26.43d_0^2} = \frac{b}{26.43} \quad (9)$$

To confirm the validation of the PSR model in investigating the ISE, two series of the values of  $H_{PSR}$  were used as:  $H_{PSR}' = \frac{b}{26.43}$ , and  $H_{PSR}'' = \frac{F - ad_0}{26.43d_0^2}$ .

### 3.4 Modified PSR (MPSR) Model

MPSR model has been suggested by Gong and co-workers. [16] to study the ISE effect in different materials. The MPSR model was mainly introduced that the sample surface is generally subjected to a similar variety of stress triggered by automated processing and sample polishing [16]. This stress alters the resistance coefficient of the samples to  $W = \alpha_0 + \alpha_1 d_0$ , where  $\alpha_0$  is related to the residual surface stress with negative low value and  $\alpha_1$  with positive value so long as the lasting deformation is

formed. Bearing in mind these effects, Gong and co-workers proposed that the PSR approach could be revised as:

$$F = a + bd_0 + cd_0^2 \quad (10)$$

where  $a$ ,  $b$  and  $c$  are experimental constants.  $a$  is a gauge of the minimum load that we would require to reach an indentation,  $b$  is linked to the loosed energy to create a novel surface per unit area, and  $c$  is the power necessitated to create a lasting deformation of unit volume which can also be considered as hardness value that non-reliant to a load. Analogously to the PSR model, the determination of true hardness [23] is obtained with two ways for the MPSR model as  $H_{PSR}' = \frac{b}{26.43}$ , and  $H_{PSR}'' = \frac{F-a-bd_0}{26.43d_0^2}$ .

### 3.5 Elastic/Plastic Deformation (EPD) Model

Traditional indentation HT includes the measured size of a plastic impression remaining in the sample as a function of the indenter load. In microhardness tests, the indentation size is computed after eliminating the sharp indentation from the top of the sample that was an impression of residual surface. This impression includes some slowing of the unloading, which means that the unloading process arises flexibly. Owing to this impression, the indentation size would be somewhat reduced [24]. In this characteristic, the measured indentation size can be changed by a refined expression to compute true hardness [25].

$$H_{EP} = A \frac{F}{(d_0 + d_c)^2} \quad (11)$$

where  $A$  is a constant that is depends on the indenter shape,  $d_0$  is the variation in the indentation size, and  $d_c$  credited to the elastic recovery. To study the numbers of nano indentation, the previous equation can be rewritten as

$$F^{1/2} = \beta^{1/2}d_0 + \beta^{1/2}d_c \quad (12)$$

where  $\beta = H_{EP}/A$  is constant correlated to the true hardness. The plots of  $F^{1/2}$  versus  $d_c$  yields to  $d_0$  and  $\beta$  values.

### 3.6 Indentation-Induced Cracking (IIC) Model

In an endeavor to elucidate the inverse ISE, Li and Bradth [26] have believed that the applied indenter test load is balanced by the total resistance of the four-component sample at the point of maximum penetration throughout a loading half-cycle owing to: (i) frictional effect at the interface of sample/indenter, (ii) elastic deformation, (iii) plastic deformation, and (iv) sample fracturing. Conferring to Li and Bradth [26], indentation cracking participates to RISE, whereas elastic and frictional effects conduce to normal ISE. The PSR model proposed by Lee and Bradth [22, 27] took into consideration the elastic and frictional effects. In indentation cracking case, the evident hardness is measured as [26]:

$$H_v = \varepsilon_1 K1 \left( \frac{F}{d^2} \right) + K2 \left( \frac{F^{1.66}}{d^3} \right) \quad (13)$$

Here,  $d$  is the indentation mark diameter.  $K1$  is associated to the geometry of indenter,  $K2$  is dependent on the applied load. For a perfectly plastic material,  $H_v = \varepsilon_1 K1 \left( \frac{F}{d^2} \right)$ ,  $\varepsilon_1 = 1$ , and for a perfect brittle solid  $K2 \left( \frac{F^{1.66}}{d^3} \right) = 0$  while  $\varepsilon_1 = 0$  [27].  $H_v = \varepsilon_1 K1 \left( \frac{F}{d^2} \right) + K2 \left( \frac{F^{1.66}}{d^3} \right)$  is applicable if there are no elastic recoveries occur after the elimination of load. For an ideal brittle material like superconductor materials, true hardness can be written as:

$$H_v = K (F^{1.66}/d^3)^m \quad (14)$$

Here  $K$  and  $m$  are constants that are non-reliant to both the load and the material adopted during the measurements. For  $m$  higher than 0.6, the ISE behavior is occurred whereas for the value of  $m$  less than 0.6 the RISE behavior is dominant.

From microhardness measurement, other important parameters can be extracted like fracture toughness ( $K_{IC}$ ), elastic modulus ( $E$ ), yield strength ( $Y$ ) and by using the following expressions:

$$K_{IC} = \sqrt{2Ex} \quad (x, \text{ surface Energy})(\text{Pa} \cdot \text{m}^{1/2}) \quad (15)$$

$$E = 81.8635 H_v \quad (\text{GPa}) \quad (16)$$

$$Y = H_v/3 \quad (\text{GPa}). \quad (17)$$

## 4 Mechanical Nature of Alloy Superconductors

### 4.1 Niobium-Titanium Nb–Ti

Since the discovery of superconductivity in 1911, the practical applications of superconductivity and the fabricating techniques of superconductors have been increasingly advanced over many decades. Niobium (Nb) is as an alloying element inserted to superalloys and melting steels in the form of Ni–Nb alloys or Fe–Nb. Nb-compounds ( $\text{Nb}_3\text{Ge}$ ,  $\text{Nb}_3\text{Sn}$ ,  $\text{Nb}_3\text{Ga}$ , and  $\text{Nb}_3\text{Al}$ ), Nb-alloys or pure Nb, have applications that are more particular, are formed in tinier quantities and expensive. Pure niobium shows a superconducting state at extremely low temperatures. High purity superconducting Nb can be employed to produce superconducting accelerator cavities to hasten charged particles. The effective accelerators necessitate that the microstructure of Nb be altered to obtain excellent physical and mechanical characteristics [28]. Nb shall be malleable enough that it deforms according to the geometry of the resulting conceived cavity, and shall elaborate, throughout the plastic deformation, a smooth internal surface in the cavity. It has been revealed that the Nb microstructure has a great influence on the mechanical and physical properties of the characteristic's niobium [29]. A heterogeneous microstructure conduces to an uneven surface in the resulting cavity which may reduce the cavity efficiency.

In 2006, a group from USA reported the mechanical characteristics of high pure niobium sheets, which are exploited in the manufacture of the superconducting accelerator cavity [30]. Several tests have been adopted to evaluate the mechanical behaviors of high pure niobium sheets. TT was managed based on the standard ASTM E517 with the strain rate of  $5 \times 10^{-3} \text{ s}^{-1}$ . TT samples were scratch in the sheet plane from five various directions of  $0^\circ$ ,  $22.5^\circ$ ,  $45^\circ$ ,  $67.5^\circ$ , and  $90^\circ$ , as compared to the rolling direction., Three tensile samples were employed for each direction. To accurately estimate the transversal and longitudinal strains, the longitudinal and transverse extensometers were integrated on tensile samples. The engineering strain–stress plots showed that high pure Nb showed a mean elongation of about 50%. Also, the yield stress variations versus of the direction of rolling was plotted. The results showed that the yield stress is maximum in the  $45^\circ$  and achieved its minimum value in the  $22.5^\circ$  direction.

Although pure niobium shows a superconductivity phenomenon at low temperature, there exist several Nb compounds and Nb solid solutions (Nb–Zr, Nb–Ti,) that have improved superconducting characteristics [31]. Since 1960, the niobium-titanium (Nb–Ti) alloy has been the leading commercialized superconductor employed for magnet windings owing to its high critical current density, ductility, and strength [32]. Besides, Nb–Ti remains the low-priced superconductor for applications in the liquid He temperature area, since the starting materials and prices are much lesser compared to other superconductors. The principal applications of NbTi are in MRI, NMR, superconducting magnetic energy storage and particle accelerators. Because of its good ductility, Nb–Ti alloy can be warped into long wires.

In almost all commercialized Nb-Ti wires, usually with Ti contents ranging from 45 to 65 (wt.) %, show an exceptional arrangement of  $T_c$ ,  $H_c$  and  $J_c$ . Generally, high content of Ti rises the hardness of Nb-Ti filaments and can lead to sausage filaments and even the rupture of the filament [33, 34]. Since the diameter of the filament is typically less than 10  $\mu\text{m}$  and even less than 1  $\mu\text{m}$ , it needs that the primary composition of alloy be regular on the whole casting alloy. Hence, no Ti-rich zone, or unfused niobium are allowed in the primary Nb-Ti alloy. Z Guo et al. [35] have studied the mechanical characteristics of fine Nb-Ti filament with heat processing treatment. The authors calculated the hardness using Vickers hardness tester. They showed that the hardness upsurges when the strain of the wire rises, and cold work constantly increases the hardness of the filament. The initial of treatments rise the filaments hardness by 6% to 12%. This is attributed to the precipitates of titanium. The extra heat treatments reduce slightly the filament hardness (around 2–4%), where Nb-Ti cold work solidifies, although precipitation continues to increase. By means of tensile testing, Z. Guo et al. have measured the stress-strain curve of Nb-Ti fiber having a diameter of 67  $\mu\text{m}$  down to 9  $\mu\text{m}$ . Around 400 Nb-Ti fiber samples have been measured. The result showed that the mechanical behavior of fibers were affected by heat treatment. It was found that the strength of fiber diminishes by around 6 to 11% in the final heat treatment. The higher the heat treatment, the lower the strength of fiber was. The authors ascribed this effect to the precipitates of titanium that were produced with high temperature. Yet, when the size of the fiber is small due to the large effect of strain hardening, the impact of heat treatment become trivial. The authors have also determined the Yong's modulus ( $E$ ) of 67  $\mu\text{m}$  fiber. Their results showed that as the temperature increases,  $E$  increases accordingly. The authors ascribed this effect to the formation of titanium precipitates that results in high atomic percent of niobium of the matrix. In another study, He Liu et al. [36] have studied the mechanical behavior of Nb-Ti superconducting wires and evaluated its evolution with the wire size, geometry and volume ratio of the components and the influence of heat treatment at last obtaining wire sizes. To comprehend the mechanical characteristics of the Nb-Ti composite, mechanical assessments of the copper matrix, individual composite components, and Nb-Ti filament were carried out. The results showed that for the mono filamentary composite, copper matrix and Nb-Ti filament, can be utilized as the expectation of the ultimate tensile strength (UTS) of the composite. For the multi filamentary composite, the three components bring about the composites; a low strength, a high strength Nb-Ti fiber, high ductility bulk copper matrix and a medium strength (between bulk copper matrix and the Nb-Ti fiber) inter-filamentary copper matrix. Besides, Nb-Ti alloys are employed in superconducting cables, and orthodontic/orthopedic grafts [37, 38].

Generally, manufacture of Nb-Ti alloys begins with melting and ultimately re-melting in a vacuum arc re-melting (VAR) oven. An alternate processing stage is EBM (electron beam melting). EBM has significant benefits: this process improved hardness, ductility, and superconducting characteristics, and relatively low resulting amounts of interstitial elements (N, H, O, and C) can be formed [39]. Though, EBM has some disadvantages because of the hard monitoring of the chemical compositions



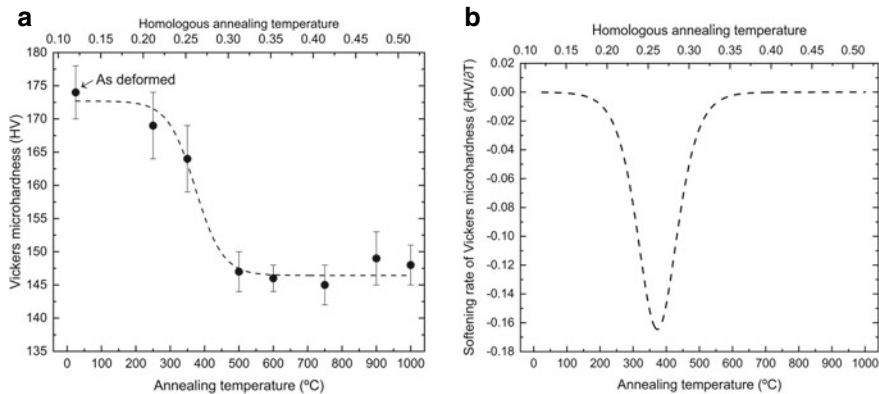


**Fig. 5** **a**  $H_v$  measurements of specimens exposed to annealing cycles of 1 h. **b** softening rate of  $H_v$  versus the homologous and annealing temperatures. Reproduced with permission from Ref. [39]

owing to the Ti evaporation under high vacuum during the melting and the accurate elements separation during solidification [39]. A probable following processing stage for the alloys of Nb-Ti is the plastic deformation of the cast alloys. Due to its high ductility and manufacturability, rods of these alloys with diameters of more than a few centimeters are plastically distorted onto micrometer filament to make superconducting cables [40]. Intermediate annealing cycles are frequently compulsory during mechanical treating, producing phase deposition, retrieval, and recrystallization, which may considerably alter the microstructure of warped alloys and their superconducting characteristics [41]. In a recent study, Andrei Marx Ferreira et al. [39] have examined the effect of recrystallization and recovery on texture and microstructure of a cold distorted Nb-50 (wt.) %Ti alloy superconducting. The measurements of Vickers microhardness were carried out with a load of 2 N.

Figure 5a displays the measurements of Vickers hardness versus the annealing temperatures and isotropic annealing. This figure showed a characteristic reduction as the temperatures are increased. The decrease is almost completed at 500 °C. The authors attribute this effect to recovery. The sigmoidal plot of  $H_v$  data was regulated (Fig. 5b). The rate of the decrease was computed, and the maximum decrease rate happened at around 380 °C.

## 4.2 A-15 Niobium-Tin $Nb_3Sn$

The niobium-tin  $Nb_3Sn$  is another important commercialized alloy with A-15 crystallographic structure. Getting  $Nb_3Sn$  superconductor that meet very stringent necessities regarding their properties and, in particular, their current transport capacity is one of the topical problems in creating magnetic systems for up-to-date elementary particle accelerators, like High Luminosity-Large Hadron Collider (HL-LHC) [42].

The upgrade of the LHC [43] at CERN involves replacing, at certain points, the main Nb–Ti-based dipole by two 11 T-based Nb<sub>3</sub>Sn dipoles [44]. Under the HL-LHC project, there are Nb<sub>3</sub>Sn coils impregnated with epoxy resin at the center of the 11 T magnet and other high-field magnets. In this status, it is verified that the Nb<sub>3</sub>Sn Rutherford cable that makes the coil, displays an irreversible deterioration in operation when exposed to too much loading [45, 46]. It is so compulsory to examine the mechanical features of the coils, to monitor and improve the stresses generated during assemblage and operation steps, involving the cooling period. Owing to its brittleness, Nb<sub>3</sub>Sn cannot be distorted directly into wires as performed for Nb–Ti alloys.

Numerous kinds of procedures can be adopted for wires manufacture involving bronze process (began with the bars of Nb alloy enveloped with ductile Cu–Sn bronze and then amassed within another Cu–Sn tube to get a multi-filament structure), Sn internal process (began by locating the core of Sn in the middle of the Nb strands implanted in the copper matrix), and the PIT process (began with by filling Nb–Sn powders rich in Sn such as NbSn<sub>2</sub>, and Nb<sub>6</sub>Sn<sub>5</sub> into niobium tubes). Through cold wire heat treatment, the Nb<sub>3</sub>Sn phase can be gotten by the reaction between Nb and Sn. The main to improving Nb<sub>3</sub>Sn wires is to enhance their trapping ability. Since the pinning of grain boundaries in Nb<sub>3</sub>Sn is neither as effective nor intense as  $\alpha$ -Ti pinning in the Nb–Ti alloy, fine-tuning of grain of and the artificial pinning cores are operative in the flux trapping. Owing to the increasing complexity of wire fabrication, the Nb<sub>3</sub>Sn superconducting wires commercialization was achieved after 1970, with a somewhat higher cost than that of Nb–Ti superconductors. Since that time, Nb<sub>3</sub>Sn has been widely studied by numerous researchers worldwide for practical applications. Magnets high-field Nb<sub>3</sub>Sn for the next generation of hadron colliders are recognized to have an elongated and restricted drill by 90% of the short specimen limit at best, implying that the current of conductor is at 60% or lower than its critical value. Monolithic finite element models are usually exploited for a complicated system that contains wedges, coils, yokes, shafts, fillers, bars, wrenches, shoes, casing, etc.

Measurements of mechanical properties allow for a well comprehension of strain and stress distributions. This is very necessary for the functioning of Nb<sub>3</sub>Sn since modern high-critical current wires are mostly sensitive to strain. Emanuela Barzi et al. [47] measured the mechanical properties of Nb<sub>3</sub>Sn cables, coils, and strands. For this purpose, tensile testing of cold-worked copper, unreacted Nb–Sn, and annealed copper wires were gauged at room temperature using an Instron machine. More than 15 specimens tested, the final average stress of the former was 630 MPa  $\pm$  5%, and above 11 tested samples, the Young's modulus of the latter was found to be 53 MPa  $\pm$  10%. Jose Luis Rudeiros Fernandez et al. [45] measured experimentally the mechanical properties of Nb<sub>3</sub>Sn Coils. Their findings demonstrated that the compression behavior of the entire conductor block, and the structure of the coil composite is nonlinear in the analyzed zone, while displaying high levels of nonlinear stress stiffness, even from moderately low stress levels. Furthermore, lasting plastic deformation was also detected from minimum levels of mid-level stress. Given that Nb<sub>3</sub>Sn is brittle, and its superconducting characteristics are sensitive to the stress,

a group from CERN, Austria, and Germany aimed to study the irreversible degradation of critical current with the mechanical prestressing, which is exerted to the interacting and saturated Nb<sub>3</sub>Sn coils for accelerator magnets at room temperature [46]. The reactive and impregnated cables of Nb<sub>3</sub>Sn were subjected to rising tangential compressive stress up to an extreme stress level of 200 MPa at room temperature. After each cycle of compression, the critical current of the cable samples was marked at 4.3 K at the FRESCA Cable Test Station. No serious degradation of the current was observed up to 150 MPa, tracked by a degradation of less than 4% after a nominal stress of 175 MPa. A lasting remarkable decline of the critical current arisen after an application of pressure of 200 MPa.

### 4.3 Niobium Aluminide (Nb<sub>3</sub>Al)

The advance of A15 high-current superconducting superconductors capable of carrying current in extremely high magnetic fields is known as an allowing technology for the design of second-generation NMR magnets functioning at frequencies above 1 GHz. The ternary metal alloy Nb<sub>3</sub>Al has been known as an exceptional source of future multi filamentary superconductors able of operating at magnetic fields well above 25 T and in severe irradiation and mechanical conditions [48]. NbAl<sub>3</sub> is stable up to elevated temperatures exceeding 1000 °C. Magnetic fields above 40 T have already been measured without defeat of superconductivity for some Nb<sub>3</sub>Al compounds [48]. If this type of inter-metallic material can be established in the form of wire, it will lead to a new invention of commercialized high-magnetic field magnets, like those needed for NMR spectrometers to operate in the 1000 MHz. Nb<sub>3</sub>Al are interesting owing to their high elasticity modulus, high melting point, outstanding oxidation resistance, and low density. Moreover, Nb<sub>3</sub>Al can be an alternate to Nb<sub>3</sub>Sn for high-magnetic field applications. However, it is extremely hard to exploit Nb<sub>3</sub>Al alloys as single-phase for applications due to the extreme brittleness at room temperature. The single-phase Nb<sub>3</sub>Al alloy exhibits a fracture toughness, K<sub>IC</sub> with a value as small of 1.1 MPa m<sup>1/2</sup>[49]. Therefore, inclusion of a tougher phase solid solution like Nb (Nb<sub>SS</sub>) can be one operative method to improving the K<sub>IC</sub> at room temperatures, even though it will lead to a reduction in the strength at higher temperatures. Accordingly, Nb-based in situ compounds like Nb/Nb<sub>3</sub>Al [50] have been established.

The development of Nb/Nb<sub>3</sub>Al as possible high-temperature structural material, in which solid metal particles are incorporated into Nb solid solution and there are no interfacial interactions due to interfacial stability even at extremely high temperatures. But, both the oxidation and fracture characteristics of these alloys are insufficient for high-temperature structural applications [51]. Hence, further improvement is required by alloying additives in Nb-based in situ composites. L.M. Peng have synthesized niobium aluminide-based composites and studied their mechanical behaviors at ambient temperature [52]. The mean value of flexural strength is 356 and 368 MPa for Al<sub>40</sub>Nb<sub>60</sub> (at.%)–TiO<sub>2</sub>20C8 (wt.%) and Al<sub>30</sub>Nb<sub>70</sub> (at.%)–Al<sub>2</sub>O<sub>3</sub>10TiC10 (wt.%)

based composites, respectively. Also, these composites displayed a corresponding value of  $K_{IC}$  of 5.3 and 5.6 MPa m<sup>1/2</sup>. From these results, the authors concluded that both the in-situ created and externally added fine Al<sub>2</sub>O<sub>3</sub> and TiC particles are efficient in improving both the fracture toughness and strength of the Nb<sub>3</sub>Al via interactions among the microstructure and crack tip. This improving effect could be ascribed to the protecting effect throughout crack spread through crack deflection and crack bridging under compressive stress, induced by the mismatch of lattice coefficients and thermal expansion coefficients between the second phase particles and the matrix.

## 5 Mechanical Properties of High T<sub>c</sub> Cuprate Superconductors

High T<sub>c</sub> superconductors (HTS) possess high T<sub>c</sub> above the LN<sub>2</sub> temperature (77 K). Owing to the very rich nitrogen abundance, the price of cooling with liquid nitrogen (LN<sub>2</sub>) is extremely inferior than liquid helium (LHe), which renders it achievable for large-scale industrial applications. The rare earth-based cuprates (REBCO) and bismuth-based cuprates (BSCCO) are among the well-known HTS. Although the T<sub>c</sub> of the REBCO and BSCCO is much superior than that of Nb<sub>3</sub>Sn and Nb–Ti alloys, they are very hard to treat with tapes and wires due to their ceramic fragility. HTS display great critical current density and good trapped magnetic field at cryogenic temperature [53–58]. Yet, practicable applications of these HTS are frequently limited. The weak mechanical characteristics of HTS stand in the avenue of a large range of real applications. This is due to the lack of slip planes in the oxide materials, which kills the ductility of HTS and increases their brittleness. During the discovery of HTS, great interest has been paid to the improvement of the mechanical behavior of these materials to expand their practical implementations. One of the most interesting characteristics to be enhanced for engineering applications of these materials, are the micro hardness, elastic modulus, creep behavior etc.

### 5.1 BSCCO Superconductor

Bismuth-based HTS class is epitomized by the common formula Bi<sub>2</sub>Sr<sub>2</sub>Ca<sub>x-1</sub>Cu<sub>x</sub>O<sub>2x+4</sub> (x = 1, 2, and 3, corresponding to Bi-2201, Bi-2212, and Bi-2223 phases, respectively). The former two phases are recognized to have some significant characteristics for the research development, and applications in industry and technology. Among these three phases, Bi-2223 looks to be the most talented candidate for power transmission cables application at the temperature of LN<sub>2</sub> owing to its high critical temperature, T<sub>c</sub> (110 K). Nevertheless, there are some main restrictions for the practicable applications of Bi-2223, which are

linked to their ceramic nature: they are relatively brittle, highly anisotropic, exhibits small critical current density ( $J_c$ ) at elevated temperatures and hard to form as a single-phase. The practical applications will necessitate, particularly, the assessment of mechanical characteristics.

The strength and plasticity of BSCCO can be rigorously influenced by numerous defects: twins, micro-cracks, dislocations, pores, and ordering defects. Consequently, enhancement of the mechanical features of BSCCO is a main research purpose. It is probable to restrain the intrinsic brittleness of these superconductors and disclose an apparent plastic flux with dislocation creation by distortion at high temperature, and at ambient temperature by applying a hydrostatic pressure, or by doping [59, 60]. S.M. Khalil showed an enhancement of the mechanical behavior of BSCCO by doping it with lead [61]. Microhardness investigations on chosen smooth surfaces of the samples studied were performed at room temperature by exposing the surface of sample to standing indentation tests. The load was ranging between 0.15 and 0.98 N. For all indentations, the duration of indentation was 15 s. Indentations were performed at various positions of the surface's sample so that the distance linked two indentations was greater than 3 times the diagonal of the inden mark to prevent the effects of surface because of neighboring indentations. For each sample, many attempts of indentation with each load were performed and then the mean value was calculated. The hardness  $H_v$  is around to 1.14 MPa for a load of 0.15. The hardness decreases as the load decreases. The authors attribute this behavior to many reasons: (i) at greater indentation loads, the  $H_v$  showed low values, this can be owing to the existence of weak links in the ceramics; (ii) at low indentation loads, the  $H_v$  presented high values, this is credited to the fact that the values of measured hardness were more suggestive of the mono-crystal case with the absence of overlap from the grain boundaries. Interestingly, the hardness showed an increase with increasing the content of Pb in the BSCCO and the maximum value of 3.25 MPa was obtained for  $x = 0.3$ . The Young's modulus as well as the yield strength increase with Pb addition. M. Anas studied the mechanical properties of BSCCO added with  $PbF_2$ . The results showed that a 0.1%  $PbF_2$  added to BSCCO phase enhance its mechanical property. The data of  $s$  micro hardness were analyzed by various approaches and a good concurrence with PSR model was demonstrated [62].

BSCCO wires can be implemented in power electric devices including NMR, MRI in high magnetic field. During magnet fabrication, a complex stress/strain is engendered during pulling and twisting, and during its activation, a great electromagnetic force is exerted to the superconducting wires due to their high  $J_c$ . Hence, it is interesting to have comprehensive awareness of mechanical and electromagnetic features of superconducting wires. Bi-2223 tapes have been effectively commercialized using monitored overpressure technology. To be exploited in high-magnetic field applications, enhancements in their current transport capacity are still required under significant stress/strain conditions as well as better mechanical characteristics. The tapes have been strengthened by means of sheet metal lamination including stainless steel, copper alloy, and nickel alloy, which improves both critical current stress tolerance and yield strength [63]. To properly comprehend these enhancements, mechanical

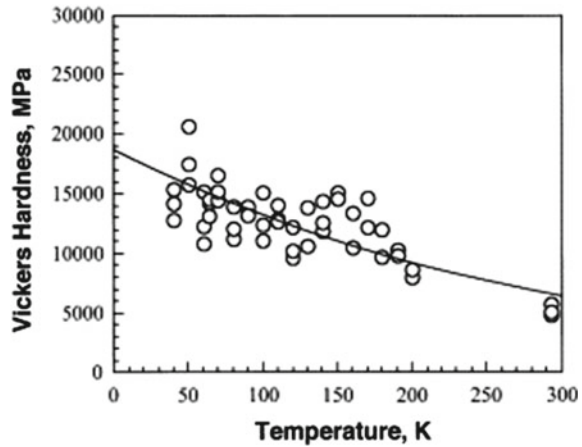
properties and the effect of the local strain applied on the BSCCO filaments themselves are required. For instance, Kozo Osamura et al. [64] studied the mechanical property of Bi-2223 wire laminated by stainless steel. It is found a linear decrease of  $J_c$  in BSCCO tapes in a small zone of tensile stress and a reversible return of  $J_c$  upon stress reduction. On increasing the tensile stress beyond the typical value,  $J_c$  dropped quickly because of the brittle breakage of the BSCCO filament. A Godeke et al. [65] have conducted systematic research of the appropriateness of the high strength DI-BSCCO type HT-NX (this type has been declared in 2014 by SEI which is covered with a high-strength nickel alloy) for high-field solenoid applications. The authors found strain limits of 0.92% and higher, flexibly calculated at the exterior border of the conductor. Thus, in coils subjected to single bending during twisting with loop stress, a strain limit of 0.92% appears to be relevant, which renders DI-BSCCO type HT-NX very appropriate for the input coils of high field solenoid magnets. Bi-2212, another correlated Bi-based HTS, can be made as a multi-filament round wire by using powder-in-tube method, nonetheless a high pressure (up to 100 bar) is needed during high temperature oxygen handling to attain highest critical currents. Bi-2212 is produced in an isotropic, circular, multi-filament form that can be coiled or bonded into random geometries including Rutherford cables. Bi-2212 will also enable high-field magnets that exceed the proton NMR current limit of 1 GHz (23.5 T) for Nb3Sn technology.

Tremendous progress has been made in its development for exploitation in high-field magnets since the demonstration of a multi-filament circular wire Bi-2212 by Oxford Instruments. The Chinese Fusion Engineering Test Reactor is a novel tokamak design whose magnet scheme contains a central solenoid (CS), toroidal field (TF), and poloidal field coils (PF) consisting of a cable-in-channel conductor (CICC). Bi-2212 HTS is a promising magnetic material for CICC because it displays good superconducting carrying capacity at low temperature of 4.2 K under magnetic field, particularly for high-pressure heat-treatment. Nevertheless, the Bi-2212 phase is a stress-sensitive ceramic. So, the mechanical property is of great significance for its application. In this context, Zhe-Hua Mao et al. [66] studied the mechanical property of Bi-2212 round wire using standard and high-pressure heat treatments at 300, 77 and 4.2 K. The authors found that the wires treated at 50 atm high-pressure heat treatment exhibited upper mechanical strength than that treated under 1 atm standard pressure. Hence, high-pressure heat-treating Bi-2212 could be ideal choice to enhance the performance and mechanical strength of wires, rendering them promising for conductor design and upcoming manufacture.

## 5.2 REBCO Superconductor

Contrasted to BSCCO superconductors, REBCO (RE: rare earth elements) exhibits lower anisotropy and higher  $J_c$  in the presence of field at 77 K. Yet, the uniaxial aligned grain structure (c-axis) attained in BSCCO wires by melting or rolling induced texture is insufficient for REBCO, so it is necessary to achieve high  $J_c$  and a bi-axial grain

**Fig. 6** Temperature dependency of Vickers hardness for bulk YBCO. Reproduced with permission from Ref. [67]



texture. REBCO superconductors fabricated by the usual sintering method are recognized to be mechanically extremely brittle and of concern in their practicable applications. The cause for the fragility is principally the existence of pores in the ceramics with a restricted plastic deformation extent. During the past years, the mechanical characteristics of YBCO have been examined at cryogenic temperature called work temperature ( $T_w$ ) or at room temperatures. The most chief characteristics evaluated have been the elastic modulus,  $E$ , the hardness,  $H$ , the toughness fracture,  $K_{IC}$ , and the yield stress. These parameters can be measured by different techniques. Yoshino et al. [67] measured the Vickers hardness  $H_v$  of bulk YBCO at temperatures ranging from 40 to 290 K by means of the cryocooled-type Vickers hardness tester.  $H_v$  was found to be  $5.2 \pm 500$  GPa at room temperature.  $H_v$  was boosted by about 3.5 times on decreasing the temperature. High hardness dispersion was observed at cryogenic temperatures (Fig. 6). Generally, hardness bulk YBCO are in the range of 5–8 GPa at room temperature [67, 68] and increases with decreasing the temperature [69].

Numerous efforts have already been done to surpass this drawback. For instance, silver-coated REBCO-sealed ceramic powders are pulled into a wire or a mixture of superconductor ceramic and gold or silver-metal powders sintered to produce composite materials. Matsumuro et al. [70] treated the mechanical characteristics of YBCO/Ag composites made at high pressures of 2.0 and 5.4 GPa. The YBCO/Ag composites were made by mixing Ag and YBCO powders in different volume ratios (0 to 100%). The mechanical characteristics typified by the maximum strain and the compressive strength were found to be improved 2 to 3 times, compared to the pure YBCO made under the normal pressure of lower than 1 GPa. C. E. Foerster et al. [71] investigated the mechanical characteristics of silver-doped top-seeded melt-grown YBCO pellets. The different contents of  $Ag_2O$  were in the range of 0.0–15 wt.%. Elastic modulus and hardness were gotten by fracture toughness and instrumented indentation by traditional Vickers indentation. The supreme values of elastic modulus and hardness were attained for a content of 5 wt.%  $Ag_2O$ . The hardness was around 9000 MPa for 5 wt.%  $Ag_2O$  content whereas it was about 8000 MPa for virgin YBCO.

With further increasing silver concentrations, the hardness reduced to 7000 MPa. The elastic modulus was also increased from 180,000 MPa for pure sample to reach its maximum value of 220,000 MPa for 5 wt.%  $\text{Ag}_2\text{O}$  concentration. The  $\text{Ag}_2\text{O}$  doping also improved the indentation  $K_{\text{IC}}$  from 1.43  $\text{MPa m}^{1/2}$  for virgin sample to 1.6  $\text{MPa m}^{1/2}$  for sample mixed with 10 wt. % of  $\text{Ag}_2\text{O}$ . Kölemen et al. [72] studied the impact of 1.0 wt.%  $\text{ZnO}$  on the mechanical behaviors of YBCO bulk. For pure sample, the hardness at ambient temperature was equal to 517 MPa and increasing with decreasing the temperature. For example, an enhancement by a factor  $\sim 3.5$  at  $T = 40$  K. Great scattering was found at cryogenic temperatures. For YBCO added with 1.0 wt%  $\text{ZnO}$  sample,  $H_v$  at ambient temperature was equal to 1075 MPa and increased at 40 K to 2316 MPa.

For numerous types of materials, apparent microhardness is dependent on applied load. Generally, hardness shows an almost decrease in parabolic behavior when increasing the load applied and tends at high applied loads to a plateau with nearly constant hardness values. According to U. Kölemen et al.' study, the hardness rises as  $\text{ZnO}$  content increases. The authors attribute this effect to  $\text{ZnO}$  addition that can rise the mechanical strength of ceramics by precipitation hardening mechanisms and solute solution. On the other hand, YBCO conductors can withstand high tensile stresses up to 0.7 GPa [5–7]. Hence, YBCO-coated tapes are suitable for NMR, accelerators and generators. For mechanical strengthening in defiance of giant Lorentz forces under elevated magnetic field, impregnating YBCO coils with epoxy resins are frequently employed. Nevertheless, epoxy resins exhibit dissimilar thermal expansion coefficients compared to YBCO HTS tapes. Naturally, at 77 K, epoxy resin dwindles around seven times more than metals. Over the cooling process, the shrinkage of the epoxy resin not only engenders tangential stress on the YBCO tape's surface, but also produces cleavage stress at the YBCO tape border. Due to the laminating structure, YBCO-coated tapes cannot withstand tangential stress beyond 10 MPa [73] and cleavage stress beyond 0.5 MPa [74].

Many researches indicated that thermal expansion mismatch led to conductor damage and critical current degradation in epoxy-impregnated YBCO HTS coils. Numerous methods have been anticipated to resolve the problematic, such as the usage of polyester thermal shrink tube (PTST) [75], no-insulation (NI) technique [76], paraffin impregnation [77]. Generally, the mechanical strength of paraffin is relatively low. At low temperatures, paraffin is brittle so it is not easy to offer the entire mechanical stability for the magnet in an elevated magnetic field. The PTST method although it gives good results under the application of high field magnets [75], it is complex which may constrain its applications. In NI technique, no critical current degradation was observed. Until now, an YBCO HTS magnet with no-insulation technique has effectively attained 26.4 T at low temperature of 4.2 K. But, if the magnetic field exceeds 30 T, the NI technique might not deliver sufficient mechanical strength for the YBCO magnets. Tomita et al. [78] showed an enhanced mechanical characteristic of YBCO bulk superconductor prepared with carbon fiber fabrics. Using a tensile tester, the authors measured the tensile strength of YBCO bulk. The tensile strength was significantly improved by coiling the bulk YBCO with a carbon fiber fabric before impregnating with resin. The mechanical characteristics of



YBCO large grains were examined by strain measures. The electromagnetic pressure was executed on the specimens at 65 K by decreasing the exterior field from 7 to 0 T. The bulk sample was cracked in the absence of resin throughout the field decrease process with a supreme stress of 150 MPa. However, the highest pressure was merely 40 MPa for the resin-impregnated specimen coated with carbon fiber fabrics. These findings showed that covering the bulk YBCO with carbon fiber fabrics could influence positively in steadying the mechanical characteristic and improving the tensile strength. In another study, Guangda Wang et al. [79] proposed to exploit, for the first time, ice to impregnate YBCO HTS coils for insulation and mechanical strength. This new method based on ice impregnated coil allowed to get superior mechanical strength than that of the paraffin impregnated coil. This is helpful for the appliance of YBCO HTS coils in the high magnetic field. In addition, this method is cost-effective and easy to process. Also, the YBCO tapes can be repetitively employed after impregnation. As a perspective for this study, the authors have proposed to quantify the insulation and mechanical strength of the ice impregnated YBCO and to further explain the avoidance of the critical current degradation in future studies.

Additionally, carbon-based compounds played a leading role in enhancing the mechanical features of REBCO due to their extraordinary hardness caused by SP2 bonds between the individually arranged carbon atoms. For example, a study performed by Anas et al. [80] showed that the microhardness  $H_v$  was improved by low addition of single and multi-walled carbon nanotubes into REBCO (RE = Gd). The microhardness measurements were performed at room temperature in air using a IN-412A Vickers microhardness tester. The load applied changes between 0.5 to 10 N for a loading duration of 40 s. For each load, the mean value of  $H_v$  was computed by considering five readings at various positions on the specimen's surface. The Vickers microhardness  $H_v$ , elastic modulus  $E$ , the yield strength  $Y$ , and the fracture toughness  $K_{IC}$  were determined and showed an enhancement with small addition of CNTs.  $H_v$  drops quickly when the applied load increases then it inclines to be saturated. This is due to ISE effect. Besides, this effect is associated with the indenter penetration depth; for low loads, the indenter enters only the surface layers, accordingly the surface effect is dominant. Though, when the penetration depth rises, the effect of internal layers is overlooked, for this reason, the value of  $H_v$  is unchanged for high load was occurred. The authors also demonstrated that  $H_v$  boosts when CNTs addition increases up to 0.08 wt.%. This enhancement is credited to the diminution of the degree of porosity and the improvement in inter-connectivity. REBCO (RE = Y) HTS can be combined with polymer matrix to fabricate composite materials with good mechanical characteristics, flexibility, and greater processing capacity. They can be simply modeled into several suitable forms by multipurpose polymer processing methods like extrusion, injection molding and, compression.

It is difficult to achieve an exceptional combination of good insulating and mechanical traits in a single-component material. Pure polymers are simple to treat as mechanically strong components but commonly suffer from a minimal dielectric constant [81]. Additionally, ceramics are fragile and need an elevated temperature [82] which is frequently incompatible with existing with integrator technologies. The perfect solution would be incorporated adequate polymer to the mechanically

robust materials to form polymer/ceramic composites that may meet the anticipated characteristics of the components [83]. Rosalin Abraham et al. [84] have studied the mechanical behavior of YBCO/polystyrene composites. Tensile properties were examined using ASTM D638. The Young's modulus of the composites increases on augmenting the filler YBCO concentration. However, tensile strength and elongation at break of the composites diminish with filler addition. Similarly, Kupchishin and co-workers [85] reported the impact of YBCO filler on mechanical characteristics of composites-based polyimide. Mechanical measurements were done on the tensile tester. Their findings showed that the introduction of YBCO filler into the polyimide induces an important change in strength and plastic characteristics of polymer matrix. Recent work performed in 2019 by Tomas Hlasek et al. [86] reported the mechanical behavior of single-domain YBCO bulk superconductor treated with artificial holes (Ahs). The samples were fabricated by a traditional top-seeded melt growth method. Ahs were included to the green sample before the process of heat treatment using a detailed "toothed" mold. Mechanical characteristics including Vickers hardness, tensile strength, compressive strength, and modulus of elasticity were measured. Their results showed that the hardness is somewhat higher for the sample holding Ahs. At 77 K, the hardness was increased from around 5.29 GPa for standard pellet to about 6.17 GPa for pellets with Ahs. The elastic modulus of the YBCO with Ahs was enhanced by more than 45% at temperatures of 77 and 295 K. At room temperature, the ultimate tensile strength was also enhanced from 360 to 460 GPa for YBCO with Ahs. The results showed that filling bulk YBCO with holes is potential for improving the mechanical characteristics. Such method will further allow the thermal conductivity to be regulated and enhance the stability and applications range of the material, particularly in pulsed field magnetization.

The growth success rate of single-grain superconductors YBCO bulk, which are typically useful for trapping field magnets, by melt-processing methods is frequently relatively low. To guarantee that RE elements consumed in these systems are not lost, and to recover the production economics, an efficient method of recycling these "non succeeded" materials is indispensable to the prolonged-term sustainability of the bulk process. This has encouraged scientists to expand new methods to recycle these failed materials in moderately large numbers. Top seed melt growth is the commonly used method for preparation single-grain superconductors YBCO bulk. A substitute approach to TSMG is the TSIG (top-seeded infiltration and growth) process [87]. In this context and based on this idea, Devendra K. Namburi et al. [88] studied the mechanical characteristics via recycling YBCO superconductor. The mechanical measurements were performed by using nano-indentation technique to determine the elastic modulus ( $E$ ) and hardness ( $H$ ), 3 points bend test for the flexural strength, and Brazilian tests for tensile strength determination [88]. The hardness measurements showed that the YBCO-211 phase (non-superconductor) is harder (with elevated elastic modulus) than the superconductor YBCO-123. Besides, both the YBCO-211 and YBCO-123 phases are stiffer and harder than the  $\text{BaCeO}_3$ . More importantly, the prime grown samples prepared through the TSMG method are considerably stiffer and harder than the recycled samples. The authors correlated this effect to the

distinctions in distribution and the dimension of the microstructural phases (specifically YBCO-211 and YBCO-123). During the recycling process, more stresses in the YBCO-123 matrix can be generated owing to the mismatch in thermal expansion of the YBCO-123 and YBCO-211 phases. This would diminish hardness (and ultimately elastic modulus) of the recycled samples comparative to the initial produced samples. However, the flexural strength showed an increase from  $\sim 50$  MPa for the initial produced samples to  $\sim 75$  MPa for recycled samples. In addition, the maximum tensile strength is around 20.2 MPa for the recycled YBCO sample, which somewhat higher than obtained in the initial produced YBCO sample ( $\sim 19.1$  MPa). All these results obtained indicated that the recycled bulk YBCO samples have important prospects for exploitation in industrial applications where the mechanical strength of the superconductor is a key concern and that the recycled samples may provide satisfactorily better superconducting traits.

## 6 Mechanical Properties of Non-cuprate High- $T_c$ Superconductors

### 6.1 Diboride of Magnesium $MgB_2$

$MgB_2$  is an intermetallic material with a moderately high- $T_c$  of  $\sim 40$  K [89], which produces an innovative  $T_c$  record in the metallic-type systems. Dissimilar from the HTS,  $MgB_2$  exhibits benefits of rather simple crystal structure and chemical composition, great coherence length, low anisotropy, and cost-effective of raw materials. These benefits render it a talented candidate for small or mediocre magnetic field applications in the 20–30 K temperature interval. Owing to its brittle character, it is compulsory for  $MgB_2$  to exhibit good mechanical behavior to resist the Lorentz force engendered by the magnetic field. The preparation method, doping effect can affect the mechanical behavior of  $MgB_2$ . Sintering processes under the high pressure, including spark plasma sintering SPS, the Reactive Liquid Mg Infiltration (RLMI) and hot isostatic pressing HIP, are operative in enhancing the packing ratio of bulk  $MgB_2$  superconductor [90, 91]. Akira Murakam et al. [91] reported the mechanical characteristics of  $MgB_2$  prepared by SPS at different temperatures of 950, 1000, and 1100 °C using bending tests. Strain–stress behaviors are nearly linear till the fracture. This linearity is usually observed for brittle materials. The Young's modulus and bending strength (stress at fracture) were enhanced by the rise of the SPS temperature. G. Giunchi et al. have adopted RLMI method for the synthesis of bulk  $MgB_2$  and have studied their mechanical characteristics [92]. RLMI led to dense  $MgB_2$  samples. The  $H_v$  measurements were carried out in micro indenter tester by using a load of 1.961 N. The authors have measured  $H_v$  in different regions of the samples. The results showed that  $H_v$  is different from one region to another. The average  $H_v$  value in inter-grain region is 1.9 GPa, lower than obtained in the large grains where the mean  $H_v$  value is 35 GPa. The authors ascribed this result to the existence of

impurity ( $\text{Mg}_2\text{B}_{25}$ ) within the large grains.  $\text{Mg}_2\text{B}_{25}$  is well known with its great hardness. In addition, the doping effect greatly affects the mechanical behavior of bulk  $\text{MgB}_2$ . Deeper information on this effect were discussed in REFs [93–96].

The extensive advance  $\text{MgB}_2$  in wires form is aimed at wide range implementation of superconductors beyond what is reasonably feasible with low-temperature superconductors, operating at the temperature of LHe. This wire type may attain industrial performance levels for multi-applications. To determine the necessitated wire characteristics and validate the potential, works on different applications is required.  $\text{MgB}_2$  conductors at CERN are exploited for the current connections to the LHC. Concentrating on the conductor  $\text{MgB}_2$ , there are many future applications, specifically in the mediocre magnetic field of 0.5–4 T range. Including these are induction heaters, high current cables, coils for MRI devices, engines and generators.  $\text{MgB}_2$ -based engines and generators are the basis for impulsion of ships, wind turbines (WT) and electric aircraft. Superconducting WT generators are driven by the relatively low size and weight that can be achieved when the magnetic field in the air gap is increased over 1 T [97], which is the maximum for long-lasting magnet-based generators. The central technology is the superconducting field coil of the rotor.

To evaluate technology and offer a wide range of engineering fabrication, various winding and wire methods must be evaluated and tested to get reliable coils at a depressed price. Practically,  $\text{MgB}_2$  wire commonly requires a diffusion barrier averting the probable reaction that can occur between superconducting filaments within a good conductive metallic sheath. PIT method is extensively employed for fabrication of  $\text{MgB}_2$  tapes and wires. In PIT process, the external sheath material (like Cu, Fe, stainless steel (SS)) plays a leading role in the densification of powder influencing the final the superconducting property especially  $J_c$  value [98]. In addition, the external sheath influences the tolerance to mechanical stresses [99]. Shielding barriers are frequently created of inert metals (like Ta, Ti or Nb) to minimize or prevent any reaction between the outer sheet and Mg. Furthermore, using diffusion barrier renders the superconductor composite more complex and pricier, and reduces the load factor of the superconducting phase of the wire. Groove rolling, drawing, or biaxial deformation rolling processes are employed for  $\text{MgB}_2$  wires with better performance [98]. An external sheath mechanically robust is particularly imperative for only drawing-deformed wires if a high density, and even filament structure is required [98]. I Husek et al. studied the mechanical behavior of multi-core  $\text{MgB}_2/\text{Ti}/\text{Cu}/\text{SS}$  wire treated at 500–850 °C [100]. The heat treatment has an impact on the mechanical behaviors of the prepared multi-core wire. A constant increase of hardness of filament with heat-treatment temperature was obtained. The hardness of the Ti barrier and Cu steadiness are unaffected for temperature annealing ranging between 500 and 650 °C. The  $H_V$  of the SS sheath annealed at 500 °C–550 °C is greater than that obtained for as-drawn wire ( $H_V = 560$  MPa) owing to probable transformation. Softening of the SS jacket contributed to annealing at temperatures exceeding 650 °C and the external jacket was less stiff than  $\text{MgB}_2$  filaments after annealing beyond 700 °C. The authors were also calculated the plasticity ( $\epsilon$ ) and the mechanical strength of as-drawn and annealed wire at 600 and 800 °C. Their results showed that the strength was equal to 1200 MPa for the as-drawn wire, such a value

is extremely high and its plasticity relatively low ( $\epsilon$  lower than 5%). The authors attribute this effect to high cold deformation of the SS sheath. A reduction by 24% in the strength of the wire and an almost variation in the plasticity was occurred when heat treating the wire at 600 °C. With further increase the heat treatment (800 °C), the strength was reduced by 57% and the plasticity was increased more than twofold owing to the changes of component and interface reactions.

On the other hand, many researchers have focused their works, in last decade, on  $\text{MgB}_2$  thin films since they can be used effectively in manufacturing of numerous superconducting devices as Josephson Junctions, tunnel junctions, and field sensors. These devices are usually reserved at 4.2 K during working, and heated up when not in operation. Permanent thermal cycling generates stresses on the thin films. Correct knowledge of these stresses and potential failure modes requires the mechanical characteristics of  $\text{MgB}_2$  thin films. In 2015, Ozmetin's group [101] reported the mechanical behavior of  $\text{MgB}_2$  thin films by means of nano indentation. At an applied indentation load of 150  $\mu\text{N}$ , the nano hardness is about 12.8 GPa. The values of nano hardness decrease with increasing the applied indentation load and become constant for high applied indentation load. This effect is due to ISE effect. To further explain the ISE effect, Ozmetin et al. used the PSR model for analyzing the experimental results. Reduced elastic modulus and nano hardness values were found to be equal to 178.13 GPa, and 11.72 GPa, respectively [101].

## 6.2 *Iron-Based Superconductors (IBSc)*

The discovery of superconductivity phenomenon in IBSc in 2008 [102] has endorsed a great interest in the applied research on superconducting materials. These materials belong to the second family HTSc after the cuprates. They exhibit high critical fields and low electromagnetic anisotropy. Among the most important ISc materials are 122 type. The unique properties of 122 type IBSc render them highly talented candidates for high-field applications, which require high-functioning and cost-effective tape and wire conductors with great current transport ability to produce giant magnetic fields, satisfactory mechanical strength to resist the thermal stress and electromagnetic during work, and superconducting filaments in metal matrix for shielding against flow jumps and thermal cooling.

The possibility of producing 122-type IBSc tapes and wires with high-strength metals like Monel alloy Fe, and Cu renders them interesting for high-field purposes. More significantly, they can be made by an easy and effective price PIT method, which is favorable to mass manufacture. In term of covering materials, Ag is frequently used as an inert wall between the metallic sheath and the superconductor in the fabrication of the IBS type 122 multifilaments. For instance, Yao et al. [103] fabricated high strength seven-filamentary  $\text{Sr122}/\text{Ag}/\text{Monel}$  tapes, demonstrating practically no  $J_c$  reduction under a compressive strain of 0.6% [10]. Xu Guangxian et al. [104] suggested a rolling method—bi-directional rolling for 7-filament 122 tape. The impact

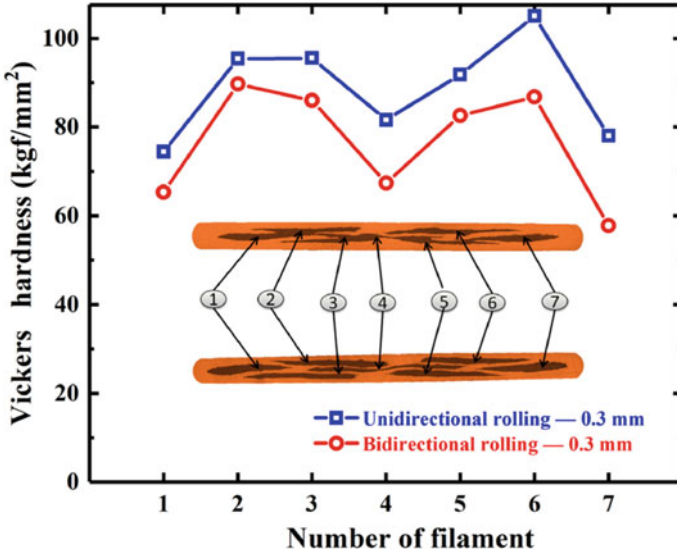


**Fig. 7**  $H_v$  measurement of uni-directional and bi-directional rolled tapes for 0.3 mm for the superconducting filaments. Reproduced with permission from Ref. [104]

of rolling direction on the Vickers micro-hardness of 7-filament 122 tapes was examined. Vickers micro-hardness was performed by a transverse cross-sectional micro hardness tester with 50 g load and duration of 10 s. The hardness of uni-directional rolled specimen is greater than that of the bi-directional rolled tape at the respective position of each filament, which indicates that the filament density is further improved by uni-directional rolling than by the bi-directional rolling (Fig. 7). For example, for a number of filaments of 4,  $H_v$  are about 0.88 and 0.60 GPa for uni- and bi- directional rolling, respectively. Since the direction of the force of the superconducting filament still steady for each track in the uni-directional rolling, the superconducting filament permanently distorts in the identical direction, which leads to an increase in the density of the core. Additionally, the central layer of superconducting filaments, whose positions are far from the surface, show relatively reduced values of stiffness, and filaments close to the surface displayed rather great hardness.

He Huang and co-workers [105] studied the influence of thickness of tape on the characteristics of silver-sheathed 122 superconducting tapes. The  $H_v$  of the tapes were gauged on the polished cross-section with a duration of 10 s and with 50 g load. Around 30 positions were gauged for each specimen by a Vickers hardness tester. The results showed that the mean  $H_v$  values rise with reducing the thickness of tapes until the tapes rolled to 0.5 mm. The relationship between  $H_v$  and  $J_c$  was studied, and the results showed that  $H_v$  values of 0.4 mm tapes is equivalent to that of 0.5 mm tapes ( $H_v = 0.88\text{GPa}$ ), however the values of  $J_c$  for tapes with 0.4 mm thickness are greater than that of for tapes with 0.5 mm thickness, indicating the saturation of the core density inside the Ag sheath. Shifa Liu et al. [106] fabricated

7-filamentary 122 tapes and wires via HIP. By performing Vickers measurements using the Wilson 402MVD tester with 10 s duration and 25 g load on well-polished samples, the authors assessed the mechanical property of 7-filamentary 122 tapes and wires. For IBSc, superconducting cores mass density can be estimated via Vickers hardness. Great  $H_v$  designates a dense IBSc phase and therefore is advantageous to the transport performances. The average value of  $H_v$  is above 1.96 GPa for 7-filamentary 122 wire. Such a value is higher than that obtained in Refs. [104, 105]. This indicates a significant enhancement in grain conductivity achieved by the HIP process.

## 7 Conclusion

The implementation of superconducting materials in different applications requires a clear understanding and extensive studies of their mechanical properties. The mechanical property of material is affected by different factor such as the preparation process, degree of heat treatment temperature, doping effect. In bulk superconductors, generally improved mechanical behavior appeared with the effect of doping or additives. The extensive progress of alloys superconductor (such as Nb-Ti, Nb<sub>3</sub>Sn, etc.), cuprates (REBCO or BSCCO), pnictides and MgB<sub>2</sub> wires and tapes open the way to wide-ranging applications needing a high magnetic field such cables, MRI, NMR, motors and generators and so on. These wire and tape types might achieve industrial performance levels for multi-applications. To outline the potential wire or tapes application, works on various mechanical properties is needed. Composite wires consist of a metal sheath tube, co-axial inner powder rod, which are wrapped into the space between the sheath tube and the rod. For wires and tapes fabrication, PIT process is one is the most common used processes due to its ease to scale up. Metal-sheathed superconducting tapes/wires are frequently made by the PIT method. Yet, sustained research and development centers in many countries yielded great achievement in the manufacture of wires and tapes by using other alternatives processes to further enhance their mechanical properties hence expand their deployment beyond what is economically feasible. Previous and current investigations on the mechanical properties of different types of superconductors, even if elementary, should be considered as the basis for further improvements in the future in view of better control of the material.

## References

1. P. Mukherjee, V.V. Rao, Design and development of high temperature superconducting magnetic energy storage for power applications—a review. *Phys. C: Supercond. Appl.* **563**, 67–73 (2019)
2. K.S. Haran, S. Kalsi, T. Arndt, H. Karmaker, R. Badcock, B. Buckley, E.W. Stautner,

- High power density superconducting rotating machines—development status and technology roadmap. *Supercond. Sci. Technol.* **30**(12), 123002
3. S. Zhao, S. Withington, D.J. Goldie, C.N. Thomas, Electromagnetic models for multilayer superconducting transmission lines. *Supercond. Sci. Technol.* **31**(8), 085012
  4. I. Faridmehr, M.H. Osman, A.B. Adnan, A.F. Nejad, R. Hodjati, M. Azimi, Correlation between engineering stress–strain and true stress–strain curve. *Am. J. Civ. Eng. Archit.* **2**(1), 53–59 (2014)
  5. J. Hay, Introduction to instrumented indentation testing. *Exp. Tech.* **33**(6), 66–72 (2009)
  6. M.L. Palacio, B. Bhushan, Depth-sensing indentation of nanomaterials and nanostructures. *Mater. Charact.* **78**, 1–20 (2013)
  7. S.R. Jian, G.J. Chen, W.M. Hsu, Mechanical properties of Cu<sub>2</sub>O thin films by nanoindentation. *Materials* **6**(10), 4505–4513 (2013)
  8. W.C. Oliver, G.M. Pharr, An improved technique for determining hardness and elastic modulus using load and displacement sensing indentation experiments. *J. Mater. Res.* **7**(6), 1564–1583 (1992)
  9. C. Ullner, A. Germak, H. Le Doussal, R. Morrell, T. Reich, W. Vandermeulen, Hardness testing on advanced technical ceramics. *J. Eur. Ceram. Soc.* **21**(4), 439–451 (2001)
  10. G.E. Dieter, D.J. Bacon, *Mechanical Metallurgy*, vol. 3 (McGraw-Hill, New York, 1976)
  11. B. Kaur, M. Bhat, F. Licci, R. Kumar, P.N. Kotru, K.K. Bamzai, Effect of 50 MeV Li<sup>3+</sup> ion irradiation on mechanical characteristics of pure and Ga–In substituted M-type strontium hexaferrite. *Nucl. Instrum. Methods Phys. Res., Sect. B* **222**(1–2), 175–186 (2004)
  12. O. Uzun, T. Karaaslan, M. Keskin, Hardness evaluation of Al–12Si–0.5 Sb melt–spun ribbons. *J. Alloys Compd.* **358**(1–2), 104–111 (2003)
  13. E. Martinez, J. Romero, A. Lousa, J. Esteve, Nanoindentation stress–strain curves as a method for thin-film complete mechanical characterization: application to nanometric CrN/Cr multilayer coatings. *Appl. Phys. A* **77**(3), 419–426 (2003)
  14. U. Kölemen, Analysis of ISE in microhardness measurements of bulk MgB<sub>2</sub> superconductors using different models. *J. Alloy. Compd.* **425**(1–2), 429–435 (2006)
  15. O. Uzun, T.U.N.C.A.Y. Karaaslan, M. Gogebakan, M.U.S.T.A.F.A. Keskin, Hardness and microstructural characteristics of rapidly solidified Al–8–16 wt.% Si alloys. *J. Alloys Compd.* **376**(1–2), 149–157
  16. J. Gong, J. Wu, Z. Guan, Examination of the indentation size effect in low-load Vickers hardness testing of ceramics. *J. Eur. Ceram. Soc.* **19**(15), 2625–2631 (1999)
  17. J. Gong, Z. Zhao, Z. Guan, H. Miao, Load-dependence of Knoop hardness of Al<sub>2</sub>O<sub>3</sub>–TiC composites. *J. Eur. Ceram. Soc.* **20**(12), 1895–1900 (2000)
  18. J. Gong, Y. Li, An energy-balance analysis for the size effect in low-load hardness testing. *J. Mater. Sci.* **35**(1), 209–213 (2000)
  19. M.B. Turkoz, S. Nezir, O. Ozturk, E. Asikuzun, G. Yildirim, C. Terzioglu, A. Varilci, Experimental and theoretical approaches on mechanical evaluation of Y123 system by Lu addition. *J. Mater. Sci.: Mater. Electron.* **24**(7), 2414–2421 (2013)
  20. A. Leenders, M. Mich, H.C. Freyhard, Influence of thermal cycling on the mechanical properties of VGF melt-textured YBCO. *Phys. C* **279**(3–4), 173–180 (1997)
  21. R. Awad, A.I. Abou Aly, M. Kamal, M. Anas, Mechanical properties of (Cu 0.5 Ti 0.5)–1223 substituted by Pr. *J. Supercond. Novel Magn.* **24**(6), 1947–1956
  22. H. Li, R.C. Bradt, The microhardness indentation load/size effect in rutile and cassiterite single crystals. *J. Mater. Sci.* **28**(4), 917–926 (1993)
  23. L. Sidjanin, D. Rajnovic, J. Ranogajec, E. Molnar, Measurement of Vickers hardness on ceramic floor tiles. *J. Eur. Ceram. Soc.* **27**(2–3), 1767–1773 (2007)
  24. B.R. Lawn, V.R. Howes, Elastic recovery at hardness indentations. *J. Mater. Sci.* **16**(10), 2745–2752 (1981)
  25. A. Toplu, I. Karaca, U. Kölemen, Calculation of true hardness value of Zn added (BiPb) SrCaCuO superconductor by different models. *Ceram. Int.* **41**(1), 953–960 (2015)
  26. H. Li, R.C. Bradt, The effect of indentation-induced cracking on the apparent microhardness. *J. Mater. Sci.* **31**(4), 1065–1070 (1996)



27. H. Li, Y.H. Han, R.C. Bradt, Knoop microhardness of single crystal sulphur. *J. Mater. Sci.* **29**(21), 5641–5645 (1994)
28. G. Myneni, *Mechanical Properties of High Purity Niobium-Novel Measurements* (No. JLAB-ACC-04-01; DOE/ER/40150-2617). Thomas Jefferson National Accelerator Facility, Newport News, VA (US)
29. H. Jiang, T.R. Bieler, C. Compton, T.L. Grimm, *Proceedings of the 12th International Workshop on RF Superconductivity* (Ithaca, New York, Cornell University, 2005)
30. A. Zamiri, F. Pourboghrat, H. Jiang, T.R. Bieler, F. Barlat, J. Brem, T.L. Grimm, On mechanical properties of the superconducting niobium. *Mater. Sci. Eng. A* **435**, 658–665 (2006)
31. R.M. Scanlan, A.P. Malozemoff, D.C. Larbalestier, Superconducting materials for large scale applications. *Proc. IEEE* **92**(10), 1639–1654 (2004)
32. M. Fischer, D. Joguet, G. Robin, L. Peltier, P. Laheurte, In situ elaboration of a binary Ti–26Nb alloy by selective laser melting of elemental titanium and niobium mixed powders. *Mater. Sci. Eng. C* **62**, 852–859 (2016)
33. G.P. Vedernikov, A.K. Shikov, L.V. Potanina, E.I. Plashkin, E.V. Nikulenkov, I.N. Gubkin, V.Y. Korpusov, Development of fine filament NbTi superconducting strands for magnet systems of fusion reactors. *Phys. C* **354**(1–4), 420–423 (2001)
34. H.C. Kanithi, P. Valaris, B.A. Zeitlin, A novel approach to make fine filament superconductors, in *Supercollider*, vol. 4 (Springer, Boston, MA, 1992), pp. 41–47
35. Z. Guo, W.H. Warnes, Mechanical behavior of fine filament Nb-Ti as a function of processing (composite superconductors). *IEEE Trans. Appl. Supercond.* **3**(1), 1022–1025 (1993)
36. H. Liu, Mechanical properties of Nb–Ti composite superconducting wires (1991)
37. A. Cremasco, W.R. Osorio, C.M. Freire, A. Garcia, R. Caram, Electrochemical corrosion behavior of a Ti–35Nb alloy for medical prostheses. *Electrochim. Acta* **53**(14), 4867–4874 (2008)
38. H. Yu, J.W. Levitan, J. Lu, Calibration of a superconducting transformer by measuring critical current of a NbTi Rutherford cable. *Supercond. Sci. Technol.* (2021)
39. A. M. Ferreira, M.A. Martorano, N.B. de Lima, A.F. Padilha, Effects of recovery and recrystallization on microstructure and texture during annealing of a cold deformed superconducting Nb-50 (wt.%) Ti alloy. *J. Alloys Comps.* **887**, 161334 (2021)
40. P.J. Lee, D.C. Larbalestier, Niobium-titanium superconducting wires: Nanostructures by extrusion and wire drawing. *Wire J. Int. (USA)* **36**(2), 61–66 (2003)
41. A.M. Campbell, J.E. Evetts, Flux vortices and transport currents in type II superconductors. *Adv. Phys.* **50**(8), 1249–1449 (2001)
42. A. Ballarino, L. Bottura, Targets for R&D on Nb 3 Sn conductor for high energy physics. *IEEE Trans. Appl. Supercond.* **25**(3), 1–6 (2015)
43. Rossi, L. (2011). LHC upgrade plans: options and strategy (No. IPAC-2011-TUYA02, p. TUYA02)
44. F. Savary, M. Bajko, B. Bordini, L. Bottura, L. Fiscarelli, J. Fleiter, A.V. Zlobin, Progress on the development of the Nb<sub>3</sub>Sn 11T dipole for the high luminosity upgrade of LHC. *IEEE Trans. Appl. Supercond.* **27**(4), 1–5 (2017)
45. J.L.R. Fernández, J.C. Perez, S.F. Troitino, M. Guinchard, P. Grosclaude, M.D. Crouvizier, F. Savary, Characterization of the mechanical properties of Nb<sub>3</sub>Sn Coils. *IEEE Trans. Appl. Supercond.* **29**(5), 1–5 (2019)
46. P. Ebermann, J. Bernardi, J. Fleiter, F. Lackner, F. Meuter, M. Pieler, E. Eisterer, Irreversible degradation of Nb<sub>3</sub>Sn Rutherford cables due to transverse compressive stress at room temperature. *Supercond. Sci. Technol.* **31**(6), 065009 (2018)
47. E. Barzi, C. Franceschelli, I. Novitski, F. Sartori, A.V. Zlobin, Measurements and modeling of mechanical properties of nb 3 sn strands, cables, and coils. *IEEE Trans. Appl. Supercond.* **29**(5), 1–8 (2019)
48. B.A. Glowacki, Niobium aluminide as a source of high-current superconductors. *Intermetallics* **7**(2), 117–140 (1999)
49. D.R. Bloyer, K.V. Rao, R.O. Ritchie, Resistance-curve toughening in ductile/brittle layered structures: behaviour in Nb/Nb<sub>3</sub>Al laminates. *Mater. Sci. Eng. A* **216**(1–2), 80–90 (1996)

50. C.D. Bencher, A. Sakaida, K.V. Rao, R.O. Ritchie, Toughening mechanisms in ductile niobium-reinforced niobium aluminide (Nb/Nb 3 Al) in situ composites. *Metall. and Mater. Trans. A* **26**(8), 2027–2033 (1995)
51. K.S. Chan, Alloying effects on fracture mechanisms in Nb-based intermetallic in-situ composites. *Mater. Sci. Eng., A* **329**, 513–522 (2002)
52. L.M. Peng, Synthesis and mechanical properties of niobium aluminide-based composites. *Mater. Sci. Eng., A* **480**(1–2), 232–236 (2008)
53. Y. Slimani, M.A. Almessiere, E. Hannachi, A. Baykal, A. Manikandan, M. Mumtaz, F.B. Azzouz, Influence of WO<sub>3</sub> nanowires on structural, morphological and flux pinning ability of YBa<sub>2</sub>Cu<sub>3</sub>O<sub>y</sub> superconductor. *Ceram. Int.* **45**(2), 2621–2628 (2019)
54. E. Hannachi, Y. Slimani, F.B. Azzouz, A.H.M.E.T. Ekicibil, Higher intra-granular and inter-granular performances of YBCO superconductor with TiO<sub>2</sub> nano-sized particles addition. *Ceram. Int.* **44**(15), 18836–18843 (2018)
55. E. Hannachi, M.A. Almessiere, Y. Slimani, A. Baykal, F.B. Azzouz, AC susceptibility investigation of YBCO superconductor added by carbon nanotubes. *J. Alloys Compd.* **812**, 152150 (2020)
56. R. Algarni, M.A. Almessiere, Y. Slimani, E. Hannachi, F.B. Azzouz, Enhanced critical current density and flux pinning traits with Dy<sub>2</sub>O<sub>3</sub> nanoparticles added to YBa<sub>2</sub>Cu<sub>3</sub>O<sub>7-d</sub> superconductor. *J. Alloys Compd.* **852**, 157019 (2021)
57. Y. Slimani, E. Hannachi, A.H.M.E.T. Ekicibil, M.A. Almessiere, F.B. Azzouz, Investigation of the impact of nano-sized wires and particles TiO<sub>2</sub> on Y-123 superconductor performance. *J. Alloy. Compd.* **781**, 664–673 (2019)
58. S.A. Alotaibi, Y. Slimani, E. Hannachi, M.A. Almessiere, G. Yasin, F.O. Al-qwairi, F.B. Azzouz, Intergranular properties of polycrystalline YBa<sub>2</sub>Cu<sub>3</sub>O<sub>7-δ</sub> superconductor added with nanoparticles of WO<sub>3</sub> and BaTiO<sub>3</sub> as artificial pinning centers. *Ceram. Int.* (2021)
59. N. El Ghouch, R. Al-Oweini, K. Habanjar, R. Awad, Comparative study on the effect of adding two transition-metal-substituted polyoxometalates on the mechanical properties of the (Bi, Pb)-2223 superconducting phase. *J. Phys. Chem. Solids* **151**, 109807 (2021)
60. N. Loudhaief, H. Labiadh, E. Hannachi, M. Zouaoui, M.B. Salem, Synthesis of CdS nanoparticles by hydrothermal method and their effects on the electrical properties of Bi-based superconductors. *J. Supercond. Novel Magn.* **31**(8), 2305–2312 (2018)
61. S.M. Khalil, Enhancement of superconducting and mechanical properties in BSCCO with Pb additions. *J. Phys. Chem. Solids* **62**(3), 457–466 (2001)
62. Anas, M. (2020). The effect of PbF<sub>2</sub> doping on the structural, electrical and mechanical properties of (Bi, Pb)-2223 superconductor. *Chem. Phys. Lett.* **742**, 137033
63. T. Nakashima, K. Yamazaki, S. Kobayashi, T. Kagiya, M. Kikuchi, S. Takeda, K. Osamura, Drastic improvement in mechanical properties of DI-BSCCO wire with novel lamination material. *IEEE Trans. Appl. Supercond.* **25**(3), 1–5 (2015)
64. K. Osamura, S. Machiya, T. Kawasaki, S. Harjo, T. Kato, S. Kobayashi, G. Osabe, Mechanical—electromagnetic property of stainless sheet laminated BSCCO-2223 wires. *Mater. Res. Express* **6**(2), 026001 (2018)
65. A. Godeke, D.V. Abraimov, E. Arroyo, N. Barret, M.D. Bird, A. Francis, J.M. White, A feasibility study of high-strength Bi-2223 conductor for high-field solenoids. *Supercond. Sci. Technol.* **30**(3), 035011 (2017)
66. Z.H. Mao, H. Jin, J.G. Qin, F. Liu, C. Dai, Q.B. Hao, C.S. Li, Axial tensile stress–strain characterization of Bi-2212 round wire with different heat treatments. *IEEE Trans. Appl. Supercond.* **27**(6), 1–5 (2017)
67. Y. Yoshino, A. Iwabuchi, K. Noto, N. Sakai, M. Murakami, Vickers hardness properties of YBCO bulk superconductor at cryogenic temperatures. *Phys. C* **357**, 796–798 (2001)
68. S.V. Lubenets, V.D. Natsik, L.S. Fomenko, H.J. Kaufmann, V.S. Bobrov, A.N. Izotov, Influence of oxygen content and structural defects on low-temperature mechanical properties of high-temperature superconducting single crystals and ceramics. *Low Temp. Phys.* **23**(8), 678–683 (1997)

69. N. Güçlü, U. Kölemen, O. Uzun, S.E.L.A.H.A.T.T.İN. Çelebi, Work of indentation approach for investigation of mechanical properties of YBCO bulk superconductor at cryogenic temperatures. *Phys. C* **433**(1–2), 115–122 (2005)
70. A. Matsumuro, K. Kasumi, U. Mizutani, M. Senoo, Superconducting and mechanical properties of YBCO/Ag composites fabricated at high pressures up to 5.4 GPa. *J. Mater. Sci.* **26**(3), 737–742
71. A.K. Najem, Physical and electrochemical properties of (Bi, Pb)-2223 prepared at different pressures (2020)
72. U. Kölemen, S.E.L.A.H.A.T.T.İN. Çelebi, Y. Yoshino, A. Öztürk, Mechanical properties of YBCO and YBCO+ ZnO polycrystalline superconductors using Vickers hardness test at cryogenic temperatures. *Phys. C* **406**(1–2), 20–26 (2004)
73. T.A.K.U.Y.A. Takematsu, R.U.X.I.N. Hu, T.O.M.O.A.K.I. Takao, Y.O.S.H.I.N.O.R.I. Yanagisawa, H. Nakagome, D. Uglietti, H. Maeda, Degradation of the performance of a YBCO-coated conductor double pancake coil due to epoxy impregnation. *Phys. C: Supercond. Appl.* **470**(17–18), 674–677 (2010)
74. Y. Yanagisawa, H. Nakagome, T. Takematsu, T. Takao, N. Sato, M. Takahashi, H. Maeda, Remarkable weakness against cleavage stress for YBCO-coated conductors and its effect on the YBCO coil performance. *Phys. C: Supercond. Appl.* **471**(15–16), 480–485 (2011)
75. U.P. Trociewitz, M. Dalban-Canassy, M. Hannion, D.K. Hilton, J. Jaroszynski, P. Noyes, D.C. Larbalestier, 35.4 T field generated using a layer-wound superconducting coil made of (RE) Ba<sub>2</sub>Cu<sub>3</sub>O<sub>7-x</sub> (RE= rare earth) coated conductor. *Appl. Phys. Lett.* **99**(20), 202506 (2011)
76. S. Hahn, D.K. Park, J. Bascuñán, Y. Iwasa, HTS pancake coils without turn-to-turn insulation. *IEEE Trans. Appl. Supercond.* **21**(3), 1592–1595 (2010)
77. S. Matsumoto, T. Kiyoshi, A. Otsuka, M. Hamada, H. Maeda, Y. Yanagisawa, H. Suematsu, Generation of 24 T at 4.2 K using a layer-wound GdBCO insert coil with Nb<sub>3</sub>Sn and Nb–Ti external magnetic field coils. *Supercond. Sci. Technol.* **25**(2), 025017 (2012)
78. M. Tomita, M. Murakami, K. Yoneda, Improvements in the mechanical properties of bulk YBCO superconductors with carbon fibre fabrics. *Supercond. Sci. Technol.* **15**(5), 803 (2002)
79. G. Wang, H. Ding, R. He, Z. Huang, H. Liu, J. Qin, Y. Tan, A new method for avoiding critical current degradation of YBCO coils using ice impregnation. *Supercond. Sci. Technol.* **32**(10), 105011 (2019)
80. M. Anas, S. Ebrahim, I.G. Eldeen, R. Awad, A.I. Abou-Aly, Effect of single and multi-wall carbon nanotubes on the mechanical properties of Gd-123 superconducting phase. *Chem. Phys. Lett.* **686**, 34–43 (2017)
81. N. Hameed, S.P. Thomas, R. Abraham, S. Thomas, Morphology and contact angle studies of poly (styrene-co-acrylonitrile) modified epoxy resin blends and their glass fibre reinforced composites. *Express Polym Lett* **1**(6), 345–355 (2007)
82. S. Yu, P. Hing, X. Hu, Dielectric properties of polystyrene–aluminum-nitride composites. *J. Appl. Phys.* **88**(1), 398–404 (2000)
83. C.B. Yoon, S.H. Lee, S.M. Lee, Y.H. Koh, H.E. Kim, K.W. Lee, Piezoelectric multilayer ceramic/polymer composite transducer with 2–2 connectivity. *J. Am. Ceram. Soc.* **89**(8), 2509–2513 (2006)
84. R. Abraham, P. Thomas, S., Kuryan, S., Issac, J., Nandakumar, K., & Thomas, S., Structural and mechanical properties of YBCO-polystyrene composites. *J. Appl. Polym. Sci.* **118**(2), 1027–1041 (2010)
85. A.I. Kupchishin, B.G. Taipova, N.A. Voronova, Study of the influence of filler on the mechanical properties of composites based on polyimide, in *IOP Conference Series: Materials Science and Engineering*, vol. 168, no. 1 (IOP Publishing, 2017), p. 012015
86. T. Hlášek, K.Y. Huang, J. Esnoz-Larraya, V. Plecháček, J. Durrell, I. Valiente-Blanco, D.A. Cardwell, Enhanced mechanical properties of single-domain YBCO bulk superconductors processed with artificial holes. *IEEE Trans. Appl. Supercond.* **29**(5), 1–4 (2019)
87. R. Cloots, T. Koutzarova, J.P. Mathieu, M. Ausloos, From RE-211 to RE-123. How to control the final microstructure of superconducting single-domains. *Superconduct. Sci. Technol.* **18**(3), R9 (2004)

88. D.K. Namburi, K. Singh, K.Y. Huang, S. Neelakantan, J.H. Durrell, D.A. Cardwell, Improved mechanical properties through recycling of Y-Ba-Cu-O bulk superconductors. *J. Eur. Ceram. Soc.* **41**(6), 3480–3492 (2021)
89. J. Nagamatsu, N. Nakagawa, T. Muranaka, Y. Zenitani, J. Akimitsu, Superconductivity at 39 K in magnesium diboride. *Nature* **410**(6824), 63–64 (2001)
90. T. Machi, S. Shimura, N. Koshizuka, M. Murakami, Fabrication of MgB<sub>2</sub> superconducting wire by in situ PIT method. *Phys. C* **392**, 1039–1042 (2003)
91. J.G. Noudem, Y. Xing, P. Bernstein, R. Retoux, M. Higuchi, S.S. Arvapalli, M. Murakami, Improvement of critical current density of MgB<sub>2</sub> bulk superconductor processed by Spark Plasma Sintering. *J. Am. Ceram. Soc.* **103**(11), 6169–6175 (2020)
92. G. Giunchi, T. Cavallin, P. Bassani, S. Guicciardi, The mechanical properties of the MgB<sub>2</sub> bulk materials obtained by reactive liquid Mg infiltration, in *AIP Conference Proceedings*, vol. 986, no. 1 (American Institute of Physics, 2008)
93. N. Kumar, S. Das, C. Bernhard, G.D. Varma, Effect of graphene oxide doping on superconducting properties of bulk MgB<sub>2</sub>. *Supercond. Sci. Technol.* **26**(9), 095008 (2013)
94. M. Muralidhar, K. Inoue, M.R. Koblishka, A. Murakami, M. Murakami, Effects of silver addition on critical current densities and mechanical properties in bulk MgB<sub>2</sub>. *Adv. Eng. Mater.* **17**(6), 831–838 (2015)
95. K.M. Elsabay, Narrow range of hafnium doping for promoted mechanical properties and critical current density (J<sub>c</sub>) values of Mg<sub>1-x</sub>Hf<sub>x</sub>B<sub>2</sub> superconductor. *J. Supercond. Novel Magn.* **24**(6), 1853–1861 (2011)
96. N. Kaya, Ş. Çavdar, Ö. Öztürk, H. Ada, H. Koralay, Investigation of microhardness properties of the multi-walled carbon nanotube additive MgB<sub>2</sub> structure by using the vickers method. *Cryogenics* **116**, 103295 (2021)
97. A.B. Abrahamsen, D. Liu, N. Magnusson, A. Thomas, Z. Azar, E. Stehouwer, H. Polinder, Comparison of leveled cost of energy of superconducting direct drive generators for a 10-MW offshore wind turbine. *IEEE Trans. Appl. Supercond.* **28**(4), 1–5 (2018)
98. P. Kováč, I. Hušek, T. Melišek, L. Kopera, M. Reissner, Stainless steel reinforced multi-core MgB<sub>2</sub> wire subjected to variable deformations, heat treatments and mechanical stressing. *Supercond. Sci. Technol.* **23**(6), 065010 (2010).
99. P. Kovac, L. Kopera, Electromechanical properties of filamentary MgB<sub>2</sub> wires. *IEEE Trans. Appl. Supercond.* **22**(1), 8400106–8400106 (2011)
100. I. Hušek, P. Kováč, Mechanical properties, interface reactions and transport current densities of multi-core MgB<sub>2</sub>/Ti/Cu/SS wire. *Supercond. Sci. Technol.* **23**(7), 075012 (2010)
101. A.E. Ozmetin, O. Sahin, E. Ongun, M. Kuru, Mechanical characterization of MgB<sub>2</sub> thin films using nanoindentation technique. *J. Alloy. Compd.* **619**, 262–266 (2015)
102. H. Hosono, Layered iron pnictide superconductors: discovery and current status. *J. Phys. Soc. Jpn.* **77**(Suppl. C), 1–8 (2008)
103. C. Yao, H. Lin, Q. Zhang, X. Zhang, D. Wang, C. Dong, K. Watanabe, Critical current density and microstructure of iron sheathed multifilamentary Sr<sub>1-x</sub>K<sub>x</sub>Fe<sub>2</sub>As<sub>2</sub>/Ag composite conductors. *J. Appl. Phys.* **118**(20), 203909 (2015)
104. G. Xu, X. Zhang, C. Yao, H. Huang, Y. Zhu, L. Li, Y. Ma, Effects of different directional rolling on the fabrication of 7-filament Ba<sub>1-x</sub>K<sub>x</sub>Fe<sub>2</sub>As<sub>2</sub> tapes. *Phys. C: Supercond. Appl.* **561**, 30–34 (2019)
105. H. Huang, C. Yao, Y. Zhu, X. Zhang, C. Dong, D. Wang, Y. Ma, Influences of tape thickness on the properties of Ag-Sheathed Sr<sub>1-x</sub>K<sub>x</sub>Fe<sub>2</sub>As<sub>2</sub> superconducting tapes. *IEEE Trans. Appl. Supercond.* **28**(4), 1–5 (2017)
106. S. Liu, C. Yao, H. Huang, C. Dong, W. Guo, Z. Cheng, Y. Ma, Enhancing transport performance in 7-filamentary Ba<sub>0.6</sub>K<sub>0.4</sub>Fe<sub>2</sub>As<sub>2</sub> wires and tapes via hot isostatic pressing. *Phys. C: Supercond. Appl.* **585**, 1353870 (2021)

# Type I and Type II Superconductivity



Siti Fatimah Saipuddin, Azhan Hashim, and Nurbaisyatul Ermiza Suhaimi

**Abstract** Superconductors may be categorized into many classes based on their critical temperature,  $T_c$ , crystal structure, and the nature of their superconductivity. The magnetic fields and current densities must be kept below the critical values  $B_c$ , and  $J_c$  respectively to remain in a superconducting state. One of the classifications is based on how the superconducting materials behaved when exposed to weak, external magnetic fields  $B_a$ . According to the Meissner Effect, as weak magnetic fields are exposed to a superconducting material, no magnetic field will penetrate the material,  $B_{in}$  except for a small region surrounding it,  $B_{out}$  creating perfect diamagnetism. However, the superconductivity may break up when  $B_a$  increases which classify the materials into Type I and Type II superconductors. In Type I superconductors, there is only one critical magnetic field  $B_c$  which separates the superconducting and non-superconducting states of the materials. The BCS theory has successfully explained the superconductivity in low-temperature superconductors based on the formation of the electron Cooper pairs, enabling them to occupy the same ground energy level. In Type II superconductors, the formation of two critical magnetic fields,  $B_{c1}$  and  $B_{c2}$  creates the Vortex or Mixed State in the between. Below  $B_{c1}$ , the materials behaved as a superconductor and lost their superconductivity above  $B_{c2}$ . The differences between Type I and Type II superconductors may well be explained based on their changes between resistance and critical temperature, magnetization, and Ginzburg-Landau parameters,  $\kappa$ .

**Keywords** Type I superconductor · Type II superconductor · Mixed state · Vortex state

---

S. F. Saipuddin (✉) · A. Hashim  
Faculty of Applied Sciences, Universiti Teknologi MARA (UiTM) Jengka Campus, Bandar Tun Abdul Razak, 26400 Pahang, Malaysia  
e-mail: [sitifatihmah7020@uitm.edu.my](mailto:sitifatihmah7020@uitm.edu.my)

S. F. Saipuddin · N. E. Suhaimi  
Faculty of Applied Sciences, Universiti Teknologi MARA (UiTM), 40200 Shah Alam, Selangor, Malaysia

## 1 Introduction

In 1911, Kamerlingh Onnes has discovered superconductivity in mercury, Hg soon after his success in liquefying helium at  $T_c < 4.2$  K which had dramatically drop resistivity,  $\rho$  from  $0.03 \Omega$  to  $3 \times 10^{-6} \Omega$ , and was thought to be simply the disappearance of electrical resistance ( $\rho = 0$ ) below a transition temperature [1, 2]. Since the discovery, many scientists around the world have conducted various researches in finding more materials exhibiting superconducting properties and reasons why the transition temperature,  $T_c$  to become superconducting, was so low than in other phase transitions. Other than Hg, Onnes and his research team discovered pure metals such as Sn and Pb to exhibit zero resistivity at low temperatures of 3.8 K and 6 K respectively while having the magnetic field expelled from the interior, hence becoming superconducting [1]. Since the 1930's, superconductivity has been found in numbers of A15 alloy compounds with higher critical temperatures and magnetic fields [3–5]. Much higher critical fields carry higher critical current densities in the superconducting state. Early theories on quantum mechanical ordering were first suggested in the 1930's but in 1957, the first microscopic theory of superconductivity, the BSC theory by John Bardeen, Leon Cooper, and Robert Schrieffer was published. It has been suggested that the electron Cooper pairs are formed through the electron-phonon interaction with the crystal lattice in superconductor materials and their phase coherence [5]. At low temperatures, the current of electron pairs flows without experiencing any resistance. It results from the slight attraction of a singly negatively charged electron that distorts the superconductor crystal lattice causing lattice vibrations hence producing phonon interactions. The small excess positive charge created attracts the second electrons creating electron Cooper pairs with opposite spins and momenta. Instead of behaving like fermions obeying the Pauli exclusion principle as in a single electron, the Cooper pairs exhibit boson-like behavior, enabling them to condense into the same energy level. An energy gap at the order of  $10^{-3}$  eV at the Fermi level suggests the phase condensation-like transition as implied by Bose-Einstein condensation for boson-like electron behavior when it condenses to its lowest energy level, losing its electrical resistance below the critical temperature [6].

In 1957, instead of assuming that all superconductors, elements, and alloys behaved similarly unless there were impurities and defects, A. A. Abrikosov has classified different 'generations' of superconductors into Type I of Low-Temperature Superconductors (LTS) and Type II of High-Temperature Superconductors (HTS) or also known as *soft* and *hard* superconductors respectively. The terms *soft* and *hard* refers to the ability in losing their superconductivity. The classification was made based on their behavior while transiting from the superconducting state to the normal state when the applied magnetic field exceeds its critical field,  $B_c$ . In general, Type II superconductors have higher critical magnetic fields compared to Type I superconductors. More details on their differences are described in the following subchapters.

The BCS theory however only perfectly explains the superconductivity of Type I superconductor that operates at low temperatures, between 0 and 10 K, and some Type

II conventional superconductors such as Niobium (Nb), Vanadium (V), and Technetium (Tc). The Type I superconductors generally consist of pure metal elements such as Mercury (Hg), Zinc (Zn), and Lead (Pb).

In 1986, the first high-temperature cuprates of La-(Sr, Ba)-Cu-O by J.G. Bednorz and K. A. Muller was studied with a critical temperature,  $T_c$  above the boiling point of liquid nitrogen (77 K) and since that, many possibilities of superconductor applications were discovered [7–9]. The mechanism of Type II superconductivity at high temperatures has been affected by many factors such as planar layering within the crystal structure, the charge carried by oxygen at charge reservoirs, slight impurity doping, and many others. Alloys and more complex ceramic oxides are mostly Type II superconductors.

Many industrial applications benefit from the superconducting properties based on their practicality and excellent performances. For example, the high-speed train, applying magnetic levitation using the persistent current due to its ability to reach zero resistance when applied with an external magnetic field below its critical temperature. Maglev trains have the ability to reach the speed of 600 km/h, currently the fastest ground vehicle in the world. In medicine, The Magnetic Resonance Imaging (MRI) machines used in hospitals and medical research centers applied the superconducting magnets to generate the magnetic fields 1.5–3.0 T, a maximum of 60 000 times stronger than the magnetic field of the Earth. The Superconducting Quantum Interference Device (SQUID) can detect voltages and magnetic fields of the order  $10^{-14}$  V and  $10^{-10}$  G respectively, making it useful in brain scans and heart detectors. The SQUID magnetometer also can detect tiny earth variations before the occurrence of earthquakes. Superconductors producing very high voltages produce strong electromagnetic pulses, disabling the electronic communication used in a war setting. The Large Hadron Collider (LHC) in CERN used thousands of lattice magnets of very high power and efficiency in detecting Higgs boson experiments on Earth. In telecommunication and potential defense applications, Josephson junctions are used to produce fast information exchange applying quantum computing.

The future anticipates many other superconducting abilities. The continuously improved experimental techniques and theoretical methods in many-body physics and quantum fields theory sparks excitement in anticipating more concepts on superconductivity electronic mechanisms.

## 2 Introduction to BCS Theory

In describing superconductivity, the basis of quantum theory related to it must first be grasped. The theory was based on the ideas presented by Bardeen, Cooper, and Schrieffer through their presented research paper in 1957, which led to earning the Nobel Prize in 1972 on microscopic (BCS) theory of conventional superconductors. The theoretical findings were very useful in explaining the electron motion in superconducting materials and how it differs from other types of materials—metal, insulator, and semiconductor. Before 1911, electrical conductivity was well explained

using the classical theory of electron motion in materials. Based on the free electron model, the electrical properties in any material react towards electron scattering due to imperfections and impurities present in it. The electron scattering due to lattice vibrations at high temperature results in electron-phonon interaction which increases its electrical resistance. Different materials exhibit different temperature-resistivity behavior and previously only be explained using the band theory of solids.

## 2.1 Temperature Dependence on Resistivity

From Ohm's law, resistivity for a sample of the material may be described as:

$$\rho = \frac{E}{J} = \frac{RA}{l} = \frac{m}{ne^2\tau} \quad (1)$$

The first part of the resistivity equation in (1) shows its dependence on the electric field,  $E$ , and current density,  $J$  while the second part may be used in determining resistivity for samples of materials with electrical resistance,  $R$ , cross-sectional area,  $A$  and length,  $l$ . When dealing with electron movement, the third part was applied where the resistivity depends on the mass of the electron,  $m$ , charge density,  $n$ , electron charge,  $e$ , and relaxation time of the electron,  $\tau$ .

The resistivity of material also depends on the temperature and is given by Eq. (2):

$$\rho_t = \rho_o[1 + \alpha(T - T_o)] \quad (2)$$

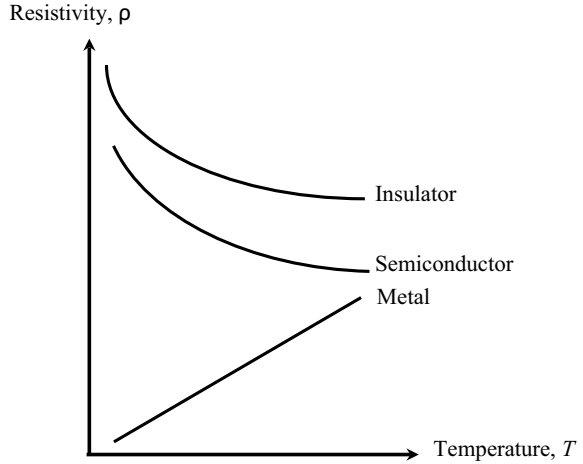
where  $\rho_t$  is the resistivity at temperature,  $t$  in °C,  $\rho_o$  is the resistivity at standard temperature,  $T_o$  is the reference temperature and  $\alpha$  is the temperature coefficient of resistivity. Using Eq. (2) and band theory of solids, variation of resistivity in metals, insulators, and semiconductors may well be explained.

In metallic conductors, no energy gap exists between the conduction band and valence band, with many overlapping of each other. With its low ionization energy, metals tend to lose their electrons easily and the delocalized electrons are free to move within the structure when electric current is applied to it. As temperature increases, metal ions and atoms vibrate at a higher amplitude. More frequent vibrations between the electrons restrict the movement causing drift velocity to decrease. Decrement in electron movement due to decrement in relaxation time,  $\tau$  results in decreased conductivity, hence increasing its resistivity. Having a positive value of  $\alpha$  resistivity in most metals increases linearly with temperature for a range of 500 K.

As for insulators, the energy gap between the conduction band and valence band is high, reaching more than 3 eV. A high amount of energy is required to move an electron from the valence band to the conduction band because the electrons are tightly bound to the nucleus. When temperature increases, atoms within the materials vibrate. As energy increases more than the value of the energy gap, electrons from



**Fig. 1** Temperature dependence on resistivity for insulator, semiconductor, and metal



the valence band get promoted to the conduction band hence conduct electricity. At high temperatures, some insulators change their conductivity into metals. With  $\alpha$  value negative, resistivity decreases as temperature increases.

The energy gap for semiconductors is in the range between metal and insulator. When small energy is applied to the material, electrons are easily being promoted from the filled valence band to the empty conduction band. As temperature increases, the energy gap gets smaller, increasing its conductivity. Having value negative, its resistivity decreases with temperature increment.

For both insulator and semiconductor, as temperature increases charge density,  $n$  increases more significantly than the decrement in relaxation time,  $\tau$ . These changes cause the resistivity for both types of materials to increase as temperature increases.

The graph in Fig. 1 summarizes the temperature dependence on resistivity for metal, insulator, and semiconductor.

## 2.2 Conductivity in Superconductors

In normal metals, energy is dissipated as the current passes through depending on the resistance of the material. The higher the resistance, the higher the energy dissipated, resulting in less current flown. In 1911 when a sample of pure metal mercury, Hg, was liquified at 4.2 K, its resistance dropped to zero like a superconductor. At zero resistance the material can conduct without energy loss. This is due to the absence of energy dissipated by electron collision at very low temperatures known as the critical temperature,  $T_c$  resulting in zero resistance. The same superconductor when placed in a magnetic field will bend the fields around it. perfect diamagnetism is achieved as no magnetic field can penetrate the material behaving in a superconducting state. However, when the magnetic fields are increased to a certain critical value,  $B_c$  the

magnetic fields can now penetrate the material, destroying the superconductivity. At this point, the superconductor properties have changed into normal metal. When an electric current is passed through a superconductor below a certain critical current density value,  $J_c$  superconductivity may also be destroyed.

Superconductor behavior ends when temperature, magnetic fields, and current density are high exceeding the critical values  $T_c$ ,  $B_c$ , and  $J_c$ . The values are different for different materials. All Type I and some Type II superconductors exist at low temperatures. Many kinds of research were conducted in determining materials that can behave as superconductors in high-temperature states.

### **2.3 Origin of BCS Theory**

The superconductivity was first described using BCS theory to envision zero resistance and perfect diamagnetism behaviors. In reaching the theory, there are events that have driven researchers towards it. When transiting from superconducting to the normal state, there should have been a certain amount of energy band gap to separate the charge carriers. This is because as the temperature reaches its critical value, the specific heat of the material has increased exponentially. This suggests that thermal energy carries charge carriers in bridging the gap, hence transiting the state from superconducting to normal through condensation as implied by Bose-Einstein condensation. Its critical temperature has shown to be a measure of the bandgap which was later found to depend on its isotope mass, hence suggesting the involvement of interaction between the free electrons and crystal lattice. The properties of the electrons as fermions disables the idea of the energy gap, eliminating a single electron as a charge carrier. Electrons behaving as bosons enable the idea of having electron pairs with opposite spin and momentum, named as the Cooper pair.

### **2.4 BCS Theory**

In BCS theory, it is assumed that there is a net attractive Coulombic force between the electrons, compensating the conventional electrostatic repulsive force between two electrons. For Type I superconductors, when interacting with the crystal lattice, the electrons create Cooper pairs close to the Fermi level resulting in the slight attraction between the electrons and lattice vibrations. The existence of free electrons in lattices creates slightly positive charges around it, hence attracting another electron. These electron Cooper pairs will remain inbound as long as the temperature is kept low since the energy binding them together is less than the thermal energy produced from the lattice vibrations. Almost all Type I superconductors exhibit superconductivity at low temperatures, where current is carried by Cooper pairs, unlike in normal such as metal, insulator, and semiconductor the currents are made up by individual electrons. In series of experimental setups investigating the isotope effect in Type I

superconductors, it has been proven that there is an interaction between the Cooper pairs with the crystal lattice. The critical temperature of each material depends on the atomic nucleus mass. When neutrons are added to each isotope, the critical temperature increases since it becomes more massive. However, unlike the elemental Type I superconductors where it is nearly independent of the shape of the phonon spectrum the isotope effect experiment was weakly shown for Type II perovskite superconductors as it depends on which subset of phonon modes is affected by subset substitution [10].

## 2.5 Bose–Einstein Condensation

When Bose derived the Planck law for black-body radiation, photons were treated as a gas of identical particles, leading Einstein to generalize the theory into an ideal gas of identical atoms or molecules where the number of particles remains conserved. At the Bose-Einstein condensate (BEC) state, the matters are mostly consisting of a very large number of particles and bosons with the same lowest energy level with a total spin of an integer multiple of  $\frac{h}{2\pi}$ . The Cooper pairs were made of electrons of opposite spin. The electrons are fermions, with spin  $\pm\frac{1}{2}$  to comply with the Pauli exclusion principle while Cooper pairs in superconductors act as the bosons of zero net spin with charge  $2e$ . At sufficiently low temperatures, the Cooper pairs clamped together in the lowest quantum state. From the Schafroth model, above  $T_c$ , the pairing has already existed and its energy  $\Delta_s > k_B T$  where  $T$  is the temperature when the Bose-Einstein starts to appear.

## 3 The Meissner Effect

The critical temperature,  $T_c$ , distinctly defines how a superconductor behaves since its properties are different below and above the temperature. Below  $T_c$ , the expulsion of magnet fields happens due to the Meissner Effect, creating the perfect diamagnetic condition. As a magnetic field is applied to a superconducting material below its critical temperature, by Lenz's law the change of flux induces current as well as the magnetic field that opposes the origin fields. With the absence of applied magnetic field, surface current flows without resistance creating internal magnetization within the superconductor hence no magnetic field can penetrate the material since the magnetic susceptibility equals  $-1$ . Magnetic levitation is one of the observations in demonstrating the Meissner Effect in superconductors. The effect may be disabled by increasing temperature above its critical value or removing the magnetic field hence the surface current and magnetization disappear. The absence of the internal magnetic fields does not depend on the order of the applied fields, be it after the material becomes a superconductor or before it is cooled to its superconducting

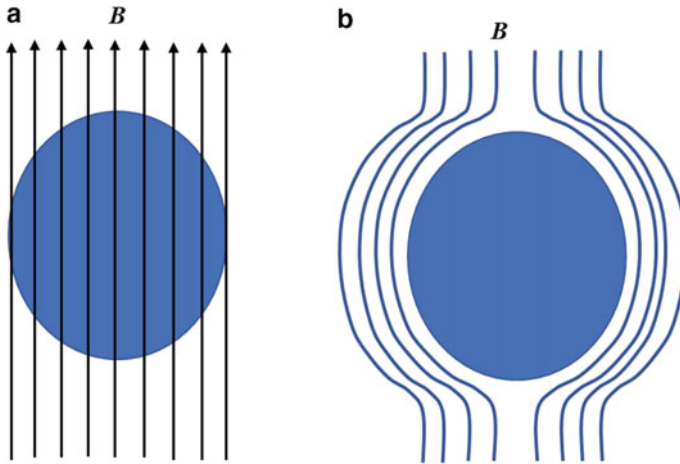


**Fig. 2** Meissner Effect when **a**  $T > T_c$  and **b**  $T < T_c$

state. Both situations expelled the applied magnetic field from the interior of the material. Figure 2a and b illustrate the Meissner Effect for temperature above and below the critical temperature of the material respectively. It shows the magnetic expulsion from the interior of the superconductor when temperature is cooled down to below  $T_c$ . The Meissner Effect being discussed in more detail in subchapter 6 on Magnetization.

## 4 Electrical Resistance Versus Critical Temperatures

Superconductivity occurs with two classifying characteristics: having zero dc resistivity ( $\rho = 0$ ) below a critical temperature and perfect diamagnetism or interior magnetic field expulsion ( $B_{in} = 0$  T). The first characteristic of superconductor materials is the ability to reach zero resistivity at certain critical temperature values where direct current is able to flow through the material freely. The resistivity of a superconductor is so small that it is less than  $10^{-26}$  m $\Omega$ , 18 times smaller than the resistivity of a copper at room temperature,  $\rho \cong 10^{-8}$  m $\Omega$  [1]. Many experiments were conducted over years of research to prove electrical resistance in a superconductor—whether or not there is any small residual resistance that occurs in the superconducting state. The experiments involved current flowing around a superconducting ring and observations are made to see any current decays. It shows through the experiments that constant magnetic fields and superconducting currents within the measuring equipment precision are produced. The persistent current produced characterizes superconductivity behavior, causing the magnetic flux that passes through the continuous ring to remain constant [2]. Infinite conductivity ( $\sigma = \infty$ ) is simply the other way of describing zero resistivity ( $\rho = 0$ ) because they are reciprocal of each other.

As described by BCS theory, despite the Pauli Principle which states that no two electrons can share the same quantum numbers, large numbers of electrons were able to conduct due to the attractive attraction between them, creating pairs of opposite momentum and spin known as the Cooper pairs. The boson-like behavior disabled the limitations of the Pauli Principle. The vibrations in the crystal lattice produced quantized lattice-vibrational energy called a phonon. As the strength and dynamics of the electron polarization with the positively charged lattice become conducive, the second electron will be attracted to the same region. The electron Cooper pairs are also regarded as quasiparticles [5] with two charges and mass with its velocity given by Eq. (3):

$$v = \frac{\hbar}{2m} \nabla\varphi \tag{3}$$

where  $\hbar$  represents the reduced-Planck constant,  $2m$  as the mass of Cooper pair and  $\varphi$  its wavefunction.

Figure 3 shows the changes of resistance as temperature increases and reaching the critical temperature point for a superconductor and non-superconducting metal. Referring to Eq. (1) on the direct relationship between resistance,  $R$  and resistivity,  $\rho$ , the graph in Fig. 3 is also applicable for resistivity versus temperature for both superconductor and non-superconducting materials.

All Type I and some Type II conventional superconductors are classified as the Low-Temperature Superconductor where they exhibit zero resistivity at low critical temperature values. BCS theory successfully explained the mechanism of electron pairs while coupled with lattice phonon interactions. Table 1 shows the critical temperature,  $T_c$  and critical magnetic field strength,  $B_c(0)$  values for Type I conventional superconductor elements. As the BSC theory successfully explains the electron–phonon conductivity in Type I superconductors, it failed to be solely applied for Type II superconductors. The electron–phonon interaction above the critical temperature of 30–40 K gives off too high energy to allow the formation of or to sustain

**Fig. 3** Resistance versus Temperature for superconductor and non-superconducting metal

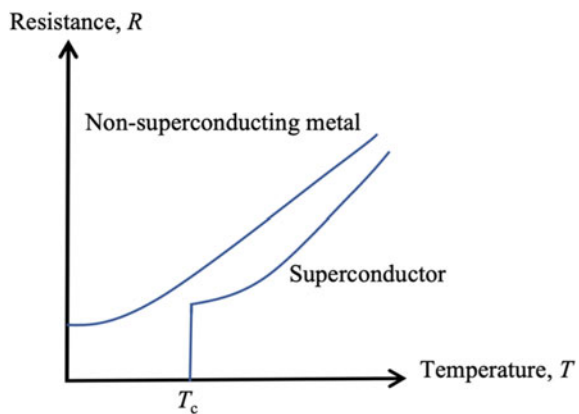


**Table 1** The critical temperature,  $T_c$  and critical magnetic field strength,  $B_c(0)$  values for Type I conventional superconductor elements

Type I conventional superconductors		
Element	$T_c/K$	$B_c(0)/mT$
Rhodium, Rh	0.00033	0.005
Tungsten, W	0.016	0.12
Beryllium	0.024	0.108
Lutecium, Lu	0.1	35
Iridium, Ir	0.11	1.6
Hafnium, Hf	0.13	1.27
Protactinium, Pa	1.4	–
Titanium, Ti	0.4	5.6
Ruthenium, Ru	0.5	–
Cadmium, Cd	0.52	2.8
Uranium, U	0.6	–
Osmium, Os	0.7	6.3
Molybdenum, Mo	0.9	9.8
Zinc, Zn	0.85	5.4
Zirconium, Zr	0.8	4.7
Gallium, Ga	1.1	5.1
Aluminium, Al	1.2	10
Thorium, Th	1.4	16.2
Rhenium, Re	1.7	20.1
Thallium, Tl	2.4	18
Indium, In	3.41	28
Tin, Sn	3.7	31
Mercury, Hg	4.2	41
Tantalum, Ta	4.47	83
Lanthanum, Ln	4.8	79.8
Lead, Pb	7.2	80

the Cooper pairs. Some of the examples of Type II conventional and unconventional superconductors with their respective critical temperatures are shown in Table 2. The conventional superconductors classified under the Type II are mainly due to their mechanism which may be described using BCS theory, unlike the unconventional superconductors which mostly consist of compounds and alloys. The mechanisms used in describing Type II superconductors are still unclear as major modifications are required in BCS theory for it to be used in explaining high-temperature superconductors.

**Table 2** Type II conventional and unconventional superconductors with different critical temperature,  $T_c$

Type II conventional superconductor			
Material		$T_c/K$	
Vanadium, V		5.4	
Technetium, Tc		7.9	
Niobium, Nb		9.3	
Type II unconventional superconductors			
Compound	$T_c/K$	Compound	$T_c/K$
NbTi	9.2	V <sub>3</sub> Al	9.6
NbN	16.0	V <sub>3</sub> Ga	16.5
Nb <sub>3</sub> Si	18.0	V <sub>3</sub> Si	17.1
Nb <sub>3</sub> Sn	18.3	MgB <sub>2</sub>	39.0
Nb <sub>3</sub> Al	18.6	YBa <sub>2</sub> Cu <sub>3</sub> O <sub>7</sub>	93.0
Nb <sub>3</sub> Ga	20.3	(Bi, Pb) <sub>2</sub> Sr <sub>2</sub> Ca <sub>2</sub> Cu <sub>3</sub> O <sub>x</sub>	110.0
Nb <sub>3</sub> Ge	23.0	Tl <sub>2</sub> Ba <sub>2</sub> Ca <sub>2</sub> Cu <sub>3</sub> O <sub>x</sub>	127.0
V <sub>3</sub> Sn	4.3	HgBa <sub>2</sub> CaCu <sub>2</sub> O <sub>x</sub>	128.0
V <sub>3</sub> Ge	7.0	HgBa <sub>2</sub> Ca <sub>2</sub> Cu <sub>3</sub> O <sub>x</sub>	138.0

## 5 Critical Current Density, $J_c$

Critical current density,  $J_c$  also describes superconducting behavior where it is defined as the maximum current that can flow from the superconductor before it turns into normal material. For a normal state material with a steady current flowing through a wire, the current density is uniform over its cross-section area. Due to this, the magnetic field strength within the wire increases linearly with distance from its center to the surface of the wire. However, the magnetic field is zero for material in the superconducting state. According to Ampere’s Law, a non-zero current density flowing in the surface of the wire will produce a magnetic field hence, the current density within the wire must be zero.

In generating high magnetic fields for industrial purposes, many of the Type II superconductor alloys need to have high critical currents at high upper critical magnetic fields. These may be achieved from the interaction between the current flowing through the superconductor while in a mixed state with the ‘tubes’ of magnetic flux, threading into the normal state. The Lorentz force formed on the electrons with the perpendicular current density and magnetic fields. It creates mutual interaction between the electrons and flux in the normal state, producing opposite direction force to Lorentz force on electrons in the normal core.

Applying the theory of the electromagnetic fields, the Lorentz force behaves like an eddy current. It causes the core and its magnetic flux to move, inducing an emf that drives current into the normal cores. The formation of eddy current causes energy dissipation in the normal cores, impeding the movement of the electrons hence producing resistance in the current flow.

One of the methods used to overcome flux motion is by introducing defects and impurities into the crystalline structure. Through this method, many small crystalline grains with different orientations and small precipitates of different compositions may be developed. The defects pinned the normal cores in their positions by providing potential barriers where they must exceed certain force values for the cores to move. The amount of potential barrier created depends on the number of flux pinning introduced into the cores. With the increment, more currents are needed to move it, hence the greater their critical currents. Flux pinning will be discussed in more detail in subchapter 6.2.

## 6 Magnetization

Superconductor materials show responses towards the magnetic and current-carrying properties. For diamagnetism to occur, currents must be induced by an applied magnetic field into the atomic orbitals hence producing magnetization within the material. When the applied field is removed, the opposed magnetization produced will disappear. For a normal diamagnetic material the magnetic field is given by Eq. (4):

$$B = \mu_r \mu_o H \quad (4)$$

where the relative permeability,  $\mu_r$  is slightly less than 1. This is due to the very small magnetization effect which reduces the applied field by less than one part in  $10^5$  within the material. For a superconducting material, however since the internal field becomes zero, the diamagnetism effect is more obvious hence the relative permeability,  $\mu_r$  for a superconductor is zero.

The most outstanding difference between Type I and Type II superconductors are in their magnetic behaviors when applied magnetic field exceeds the critical fields,  $B_c$ . For Type I superconductor, as the applied field increases, assuming the material has relative permeability  $\mu_r = 0$ , perfect diamagnetism occurs as it perfectly obeys the Meissner Effect. At this stage, the material becomes normal where electrical resistivity will no longer show zero value. According to the Meissner Effect, below the critical magnetic field,  $B_c$  total expulsion occurs in superconducting materials, hence the internal magnetic field,  $B_{in} = 0$ , reducing its resistivity to zero. The difference between the magnetization effect in a perfect conductor and a superconductor is from the exclusion ability of the magnetic field. In a perfect conductor, the magnetization state depends on the temperature, applied magnetic field, and the previous state of the material. If the material which was previously in certain magnetic fields is being cooled to its critical temperature, the magnetic fields within the conductor remain uniform. Unlike a superconductor, the magnetic fields are always internally expelled whether the material is cooled below its critical temperature,  $T_c$  in zero  $B_a = 0$ , or a finite applied magnetic field  $B_a = B_a$ . The current produced on the superconducting



material surface creates a magnetic field in such a way that it opposes the direction of the applied field in the material hence actively excluding the magnetic fields as described by the Meissner Effect.

Figures 4 and 5 illustrate the changes in the magnetic field as temperature increases for Type I and Type II superconductors respectively.

As shown in Fig. 4, above the critical point,  $B_c$ , Type I superconductors which are mostly metallic materials will no longer exhibit a superconducting state, hence turning into a normal conductor. At a normal conductor state, its resistivity starts to increase as it obeys the free electron model. The diamagnetic moment becomes zero and demonstrates an equal magnetic field inside and outside of the material. For Type II superconductors, below  $B_{c1}$ , the superconductor behaves exactly as the Type I superconductors which is also known as the Meissner state and above  $B_{c2}$ , the normal state occurred with the mixed state in between both critical magnetic fields,  $B_{c1}$  and  $B_{c2}$  as shown in Fig. 5.

Figures 6 and 7 describe the magnetization behavior over magnetic fields increment for Type I and Type II superconductors respectively. From Fig. 6, when applied

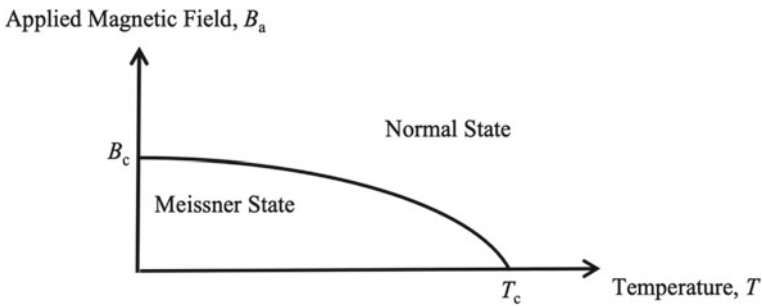


Fig. 4 Applied magnetic field versus temperature for Type I superconductor

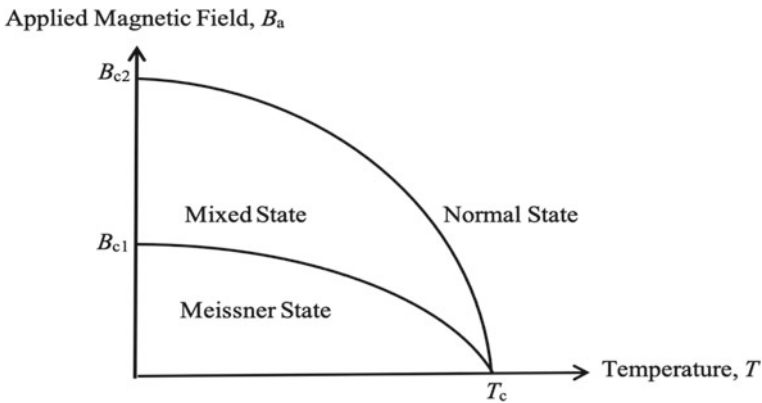


Fig. 5 Applied magnetic field versus temperature for Type II superconductor

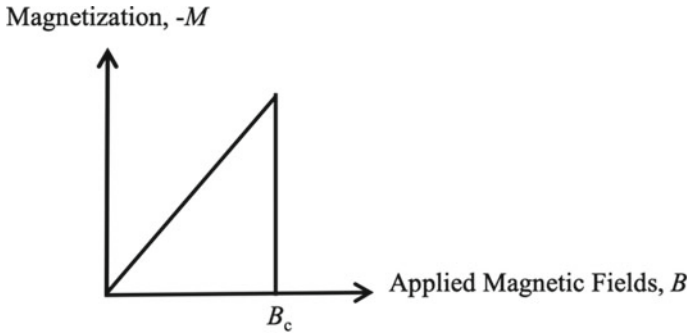


Fig. 6 Magnetization versus Applied Magnetic Fields for Type I superconductors

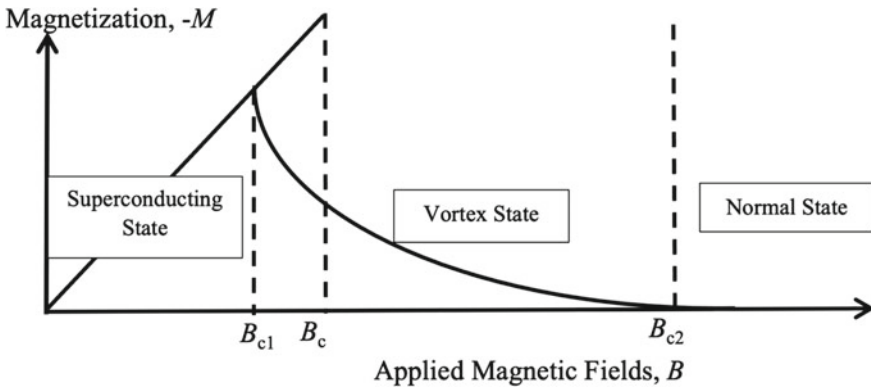


Fig. 7 Magnetization versus Applied Magnetic Fields for Type II superconductors

magnetic field,  $B$  exceeds  $B_c$ , magnetization drops abruptly to zero and becomes a normal conductor. Its single, low critical magnetic fields at the range of  $4.9 \times 10^{-5}$  T to 1 T have limited its technical applications especially in many industrial needs [11]. There are two ways to describe perfect diamagnetism in Type I superconductors. Firstly, by assuming that there is zero relative permeability,  $\mu_r$  property of the bulk diamagnet material where flux density becomes zero due to the flux density induced at the interior of the material,  $\mu_r B_a$  equals zero, hence said to be in perfect diamagnetism.

The second way of determining perfect diamagnetism in Type II superconductors is by the surface current that screens the magnetic fields where it will generate the interior magnetic field that cancels the applied fields.

Some difficulties were faced in applying it to practical applications due to the insignificant current it carries.

For Type II superconductors, permeability happens until the first critical field,  $B_{c1}$  is reached. As shown in Fig. 7 on the magnetization,  $-M$  behavior of a Type II superconductor when given applied magnetic fields,  $B$ , at a lower critical magnetic field,

$B_{c1}$ , the appearance of vortices, the magnetic flux quantum that penetrates superconductors are more obvious. The superconducting state changes to a vortex state or intermediate state where it gradually loses its superconductivity. Partial magnetic field penetration happens in between lower and upper critical fields,  $B_{c1}$  and  $B_{c2}$  as it partly obeys the Meissner Effect, unlike the Type I superconductors hence are not perfectly diamagnetic. The transition from superconducting to normal state is known as the mixed state, where fine filaments of vortices start to circulate. The Type II superconductors with magnetic fields below  $B_{c1}$  exhibit the same behavior as the Type I superconductor materials while above  $B_{c2}$ , it becomes a normal conductor. Alloys and high critical temperature ceramics are all Type II superconductors such as the YBCO, NbTi, Nb<sub>3</sub>Sn, and many others. Many technical applications were governed due to its high critical magnetic fields which are more than 1 T value such as the strong field superconducting magnets. Examples of Type II superconductor alloys that exhibit high upper critical field strength,  $B_{c2}$  values are Niobium-Titanium (NbTi<sub>2</sub>) with about 10 T and Niobium-Tin (Nb<sub>3</sub>Sn) of 20 T makes them very reliable in industrial applications especially those which requires generating high magnetic fields. Compared to Type I superconductor Lead, Pb with only 0.08 T, fewer industrial applications may be governed by its weak material magnetic performance.

When considering exponential decrement in transitional behavior of Type II superconductors, the interface separating both states—normal and superconducting must also be considered. As applied magnetic fields are increased onto the superconducting material, the surface energy on the interface decreases. As the applied magnetic field increases, Type I superconductors always exhibit positive surface energy and negative on the interface of Type II superconductors.

As the magnetic field is expelled, the free energy of a bulk superconductor also increases except on a very thin superconducting film where parallel fields may uniformly penetrate. For the thin film, only a small part of the flux is expelled. As the magnetic field increases its energy also increases, hence the high field intensity is required in transiting from superconducting to normal state.

## 6.1 Vortex State

At a mixed state, Type II superconductors exhibit both superconducting and normal behaviors. The superconducting normal cores are surrounded by vortices which allows gradual magnetic field penetration to happen. In the vortex state, the superconducting currents circulate in vortices throughout the bulk superconductor. The normal core size of about 300 nm becomes more closely packed as the critical temperatures are approached and overlap as it loses its superconducting state. More increment of temperature or the external magnetic fields to the superconductor material affects the normal cores to be more closely packed together. As the current flows, the vortices surrounding it feel a force to move and if they do which will cause them to lose their superconducting state. Fixed or pinned vortices permit the magnetic field to

penetrate with zero resistivity. The vortex state is so stable that no significant differences in chemical and crystallographic properties were detected when compared to the superconducting and normal state.

Introduction of microscopic defects through alterations in superconductor fabrication techniques may pin the vortices and hence maintain the superconducting state at higher critical temperatures.

## 6.2 Flux Pinning

Also known as Quantum Locking, Flux Pinning happens due to magnetic field lines penetration in Type II superconductors. It is believed that the flux pinning interaction between the flux lines and defects induces high critical current density in superconductors. The magnetization analysis of magnetic flux pinning of GdBCO with two types of ferromagnetic LSMO buffers deposited on STO substrate shows the presence of multiple flux pinning mechanisms which has improved the critical current of GdBCO [12]. Some of the ways to create flux pinning are by introducing impurities and defects [13]. The impurities additional however must be carefully identified before being added to prevent the destruction of Cooper pairs, hence breaking their superconductivity. Flux pinning centers are created as nanoparticles being added which creates planar defects, strain subgrain boundaries, and twins, contributing to higher current densities when applied with external magnetic fields [14, 15]. The critical temperature,  $T_c$ , may also be increased when flux pinning is introduced into the crystal structure such as in  $Mn_3O_4$  addition into YBCO superconductors [16].

## 7 London Equations

The theory of superconductivity was further explained using London equations, explaining the penetration depth and coherence length – the two characteristic distances in superconductors. The values of penetration depth and coherence length of most high-temperature superconductors are of the order of 100 Å and 10 Å respectively. In a superconducting state, no magnetic field exists in the interior of the material as previously described by the Meissner Effect, hence the current is only restricted to flow on its surface. In 1935, soon after the discovery of the Meissner Effect, Fritz and Heinz London proposed equations to predict the magnetic field and surface current variation with the distance to the surface of a superconductor.

The first and second London equations are shown in Eqs. 5 and 6 respectively:

$$\frac{d\mathbf{J}_s}{dt} = \frac{n_s e^2}{m} E \quad (5)$$

$$\text{curl} J_s = -\frac{n_s e^2}{m} B \quad (6)$$

The equations are used to restrict Maxwell's equations hence making the superconductor behaviors as deduced by the equation, to be consistent with the experimental findings and Meissner Effect.

Ampere's law is applied in Eq. (7) into (6) as shown in Eq. (8) to deduce theoretical observation on Meissner Effect:

$$\text{curl} B = -\mu_o J_s \quad (7)$$

$$\text{curl}(\text{curl} B) = -\frac{\mu_o n_s e^2}{m} B = -\frac{1}{\lambda^2} B \quad (8)$$

Since  $\text{curl}(\text{curl} B) = \text{grad}(\text{div} B) - \nabla^2 B$  and  $\text{div} B = 0$ ,

$$\nabla^2 B = -\frac{1}{\lambda^2} B \quad (9)$$

From Eq. (9), the field is identically zero inside the material for the Meissner Effect to take place. If magnetic field,  $B$  has certain values,  $\nabla^2 B$  also consists of a certain amount, making  $B$  position dependent.

If the uniform external field moves in the  $x$ -direction of the superconductor, the inside fields will also be in the  $x$ -direction and its strength depends on  $z$ -direction as shown in Eq. (10).

$$\frac{\partial^2}{\partial z^2} \left( \frac{\partial B_x(z, t)}{\partial t} \right) = \frac{1}{\lambda^2} \frac{\partial B_x(z, t)}{\partial t} \quad (10)$$

The internal field is hence given by Eq. (11).

$$\left( \frac{\partial B_x(z, t)}{\partial t} \right) = \frac{\partial B_o(t)}{\partial t} e^{-\frac{z}{\lambda}} \quad (11)$$

The equation is further simplified into Eq. (12).

$$B_x(z) = B_o e^{-\frac{z}{\lambda}} \quad (12)$$

The exponential decay of magnetic field reduction in Type II superconductors agrees with the experimental findings. One of the important differences between Type I and Type II superconductors is in terms of the conduction electrons mean free path in the Normal State. Long mean free path causes the penetration depth to decrease and the coherence length to increase, resulting in the properties of Type I superconductors and vice versa for Type II superconductors. The theory was developed by Ginzburg, Landau, Abrikosov, and Gorkov in classifying the superconductors.

## 7.1 Penetration Depth

As proposed by the London brothers on one of the characteristic lengths,  $\lambda$  or also known as penetration depth, the value depends on the number density of superconducting electrons,  $n_s$ . The magnetic field at the interior surface on the transition between superconducting state into normal state decays gradually within a thin layer of thickness less than  $1 \mu\text{m}$  [17]. From Eq. (8) the penetration depth,  $\lambda$  is defined by Eq. (13):

$$\lambda = \left( \frac{m}{\mu_o n_s e^2} \right)^{\frac{1}{2}} \quad (13)$$

where  $m$  = mass,  $\mu_o$  = permeability in the free space,  $n_s$  = density of superconducting electrons, and  $e$  = electron charge.

In estimating the  $\lambda$  value, all free electrons are assumed to be superconducting and the value of typical free electron density in a metal,  $n_s = 10^{29} \text{ m}^{-3}$  were substituted in Eq. (9), resulting in the very small size of penetration depth as shown in Eq. (14).

$$\lambda = 1.7 \times 10^{-8} \text{ m} \cong 20 \text{ nm} \quad (14)$$

This theoretical approach explains the Meissner Effect where the magnetic field inside the superconductor must be identically zero. Otherwise, the penetration depth will give infinite values, hence not exhibit superconductivity. These observations show agreement with the experimental findings of the Meissner Effect. Experimental studies show that the penetration depth depends on the film thickness by considering experimental dependence on critical temperature or residual resistivity. As an example, for Niobium thin films, the penetration length ranges from 80 nm for thick films ( $t = 200\text{--}300 \text{ nm}$ ) to 230 nm for thin films ( $t = 8 \text{ nm}$ ) [18].

## 7.2 Coherence Length

Coherence length is an independent characteristic length that relates to the Fermi velocity of the material and energy gap due to the condensation of electron pairs to the superconducting state. Some amount of minimum length must be penetrated in destroying its superconducting state. The coherence length is shown by Eq. (15), describing the finite thickness required in making the transition happen.

$$\xi = \frac{-2\hbar v_F}{\pi E_g} \quad (15)$$

The  $v_F$  and  $E_g$  in the equation represent Fermi velocity and superconducting band gap respectively.

In experimental work of interfacial lattice mismatch of  $\text{YBa}_2\text{Cu}_3\text{O}_{7-\delta}$ , the atomic structure of thickness less than its coherence length has been distorted due to electron screening [19].

Table 3 shows some of the examples of calculated penetration depth and coherence length for Type I and Type II superconductors. Most of the Type I superconductors have a ratio of the Ginzburg–Landau parameter,  $\kappa$  values of  $0 < \frac{\lambda}{\xi} < \frac{1}{\sqrt{2}}$  while Type II superconductors have values of  $\frac{\lambda}{\xi} > \frac{1}{\sqrt{2}}$ . Extreme Type II superconductors exhibit  $\kappa \approx 100$ . The coherence length is usually shorter than the penetration depth ( $\xi < \lambda$ ) for Type II superconductors which energetically enables the appearance of vortices in the mixed state. For Type I superconductors, no vortices are created hence  $\xi < \lambda$  which are mostly pure metals. There are negligible fluctuations in superconducting order parameters for low-temperature superconductors but large in high-temperature superconductors. This is due to the short coherence length,  $\xi$  and large penetration depth,  $\lambda$  properties in high-temperature superconductors which are mostly of Type II [20]. The short coherence length could have been contributing to the cross-over between the BCS theory and Bose–Einstein condensation as local Cooper pair formation which is driven by a gain in potential energy can form above the condensation temperature [21].

The number of superelectrons density is zero at the center of a normal core of a superconductor and it rises over coherence length,  $\xi$ . Its magnetic field also spread over a region over a quantized superconducting loop of quantum magnetic flux given by the Eq. (16):

**Table 3** Examples of penetration depth,  $\lambda$ , coherence length,  $\xi$  and Ginzburg-Landau parameters,  $\kappa$  for Type I and Type II superconductors

Superconductor	Materials	Penetration depth, $\lambda$ (nm)	Coherence length, $\xi$ (nm)	$\kappa \left( \frac{\lambda}{\xi} \right)$
Type I <sup>a</sup>	Sn	34	230	0.15
	In	50	1600	0.03
	Al	16	1600	0.01
	Pb	37	83	0.45
	Cd	110	760	0.14
Type II <sup>b</sup>	Nb	39	38	1.02
	NbTi	60	40	1.50
	NbN	250	4	62.50
	Nb <sub>3</sub> Sn	80	3	26.67
	V <sub>3</sub> Ga	90	3	30.00
	V <sub>3</sub> Si	60	3	20.00

Source <sup>a</sup>R. Meservey and B. B. Schwartz in Kittel Chap. 12 [22], <sup>b</sup>Introduction to Superconductivity[23]

$$\frac{h}{2e} = 2.07 \times 10^{-15} Tm^2 \quad (16)$$

where  $h$  is the Planck constant and charge of  $2e$  represents the electron pairs due to their coupling and condensation into a superconducting ground state.

The superconducting Quantum Interference Devices (SQUID) applied flux quantization of a superconductor in its application. The device, which consists of a small superconducting loop with weakly superconducting links, is being used in measuring the magnetic fields by currents in the brain. The flux quantization in the loop causes its electrical properties to depend on applied flux of periodicity equal to the very small magnitude flux quantum which determines the sensitivity of the device towards very small magnetic fields.  $Nb_3Sn$  wires have abilities in carrying large supercurrents, making them reliable for the commercial development of strong field superconducting magnets. There are also conceptual HTS composites being developed for applications involving large current-carrying capacities magnet with high fields [24].

## 8 Timeline in Superconductivity Discoveries

Findings in superconductivity have emerged from the discoveries of conventional low-temperature superconductors to non-conventional high-temperature superconductors and lately, the novel superconductors. In 1911, Mercury, Hg became the first conventional superconductor when found to exhibit sudden zero resistance at the critical temperature,  $T_c = 4.2$  K by H. K. Onnes, gaining him Nobel Prize in 1913 for describing the properties of materials at low temperatures [1]. The Meissner Effect phenomenon was discovered by Meissner and Ochsenfeld in 1933, further explaining the perfect diamagnetism in superconductivity behavior [25]. Prediction on magnetic penetration depth,  $\lambda$  using two-fluid model using London theory able to describe the Meissner Effect flux repulsion later in 1935 [26]. In 1950, Maxwell observed the isotope effect for Hg suggesting the electron–phonon coupling in superconductivity and later verified the BCS theory [27]. Ginzburg-Landau theory was then introduced, extending the London theory and introduced the order parameter within the same year [28]. In 1957, superconductors were classified into Type I and Type II by Abrikosov [29] and BCS theory by Bardeen, Cooper, and Schrieffer has electronically explained the microscopic behavior of superconductivity using Cooper pairs in energy shell  $\hbar\omega$  around the Fermi surface due to the electron–phonon interaction. The theory won the Nobel Prize in 1972 [2].

The BCS theory applies well for conventional superconductors, but for unconventional superconductors it fails to compromise between the density of states at the Fermi surface and the lattice vibration strength of the materials [30]. In 1962, Josephson tunneling theory by I. Giaever and B. Josephson further described the Cooper pair using tunneling effect through a thin insulating barrier between two superconductors known as the Josephson tunneling which won the Nobel Prize in



1973 [31]. Two years later, Ginzburg proposed the idea of interface structures in avoiding the conflict between the density of states and lattice vibration strength [30]. The highest-temperature conventional superconductor was discovered in the  $\text{Nb}_3\text{Ge}$  superconductor in 1973 with  $T_c$  above 22 K [4]. It remained highest until the  $\text{MgB}_2$  superconductor with  $T_c$  39 K was discovered in 2001 [32].

For non-conventional superconductors, J. G. Bednorz and K. A. Muller discovered  $\text{La}(\text{Sr}, \text{Ba})\text{CuO}$  with superconductivity at  $T_c = 35$  K in 1986, marked as the first high-temperature cuprate superconductor, gaining the Nobel Prize in 1986 [3]. A year later, M. K. Wu and his team have synthesized the  $\text{YBaCuO}$  superconductor with  $T_c = 92$  K [33]. In 1988,  $\text{BiSrCaCuO}$  was synthesized by H. Maeda, Y. Tanaka, and T. Asano and  $\text{TlBaCuCuO}$  superconductors were discovered by Z. Z. Sheng and A. M. Hermann, both with  $T_c$  more than 100 K [34] which is above the boiling point of liquid nitrogen (77 K). Hg system of copper oxide high-temperature superconductors was discovered in 1933 by Putilin and Shilling [35, 36].

Between 2007 and 2008, superconductivity behavior was found in the iron-based compound,  $\text{LaFeAsO}$  with critical temperature,  $T_c = 26$  K [37]. Later in 2008, the  $T_c$  was improved to 55 K. However, the weak phonon mode disabled BCS theory to be applied in explaining its superconductivity. In 2012, the single-layer  $\text{FeSe}/\text{SrTiO}_3$  films fabricated using Molecular Beam Epitaxy (MBE) were said to be the first significantly enhanced superconductor [38].

The questions inquired by Wigner and Huntington in 1934, predicting the metallic hydrogen [39] have led Ashcroft to foresee the ability of room-temperature superconductivity for metallic hydrogen in 1968 [40]. Failure attempts were faced by researchers in finding room-temperature superconductors using pure hydrogen. The attempts of applying high pressure went on until the binary hydrogen-rich system suggested by Ashcroft showed promising room temperature superconductivity. In October 2020, Carbon–Sulphur Hydrogen (C-S-H) was discovered under very high pressure and became the first room temperature superconductor, proved by the resistance measurement and magnetic properties. When put under the pressure of 148 Gpa,  $T_c$  obtained at 147 K and further increment pressure of 267 Gpa,  $T_c$  reached 287 K, the highest  $T_c$  achieved to date [41]. The year of 2020 remarks the important discoveries in superconductivity by the finding of metallic hydrogen and the first room-temperature superconductor [42]. The milestone in the discoveries of room-temperature superconductors is shown in Table 4.

## 9 Conclusion

A superconductor has always been described as a material that demonstrates infinite conductivity at its critical temperature,  $T_c$ . Below  $T_c$  values, the material behaves as a superconductor and transits into normal metal once exceeded the temperature. The absence of resistivity in a bulk metal specimen behaving in a superconducting state is explained using the Meissner Effect where zero magnetic induction happens, and the material exhibits perfect diamagnetism. In low-temperature superconductors, the

**Table 4** Milestone in room temperature discoveries

Material	Critical temperature, $T_c$ (K)	Year
SiH <sub>x</sub>	17	2008
BaReH <sub>9</sub>	7	2014
H <sub>3</sub> S	200	2015
PH <sub>3</sub>	100	2015
LaH <sub>10</sub>	250	2018
ThH <sub>10</sub>	160	2019
YH <sub>6</sub>	220	2019
YH <sub>9</sub>	240	2019
C-S-H	287	2020

Source R. Asokamani, "March towards Room Temperature Superconductivity," vol. 38, pp. 27–38, 2021 [42]

Cooper pairs are bound with the crystal lattices due to the electron–phonon interactions where they can conduct electricity at zero resistance. In the BCS theory, the attractive attraction forces between the electrons create the electron pairs of opposite momentum and spin, disabling the Pauli Principle where no two electrons can share the same quantum numbers. The BCS theory best describes the conductivity of superconductors in low temperature, but major additions are essential to explain the superconductivity at high temperature conditions. For a Type II superconductor to remain in superconducting state, high critical current density,  $J_c$  is required at high upper critical magnetic fields. Another way in classifying superconductors is through their response towards magnetization. There are Type I of mostly conventional, low-temperature superconductors and Type II of mostly unconventional high-temperature superconductors. Most of the Type I superconductors consist of pure elements while Type II superconductors are mostly the alloys and more complex ceramic oxides. The superconducting state in Type I and Type II superconductors is destroyed and becomes normal metal when exceeded a certain amount of applied critical magnetic fields. For a Type I superconductor, only one critical magnetic field,  $B_c$  value, separates between the superconducting state and the normal state. In Type II superconductors there are two critical field strengths,  $B_{c1}$  and  $B_{c2}$  where  $B_{c1} < B_c < B_{c2}$  and the vortex state exists in the range between the two fields. Type I and Type II superconductors may be differed using the penetration depth,  $\lambda$ , and coherence length,  $\xi$ . The penetration depth of each specimen determines the magnetic field penetration through its surface over distances while coherence length measures the path it takes for superconducting electron concentration to drastically disappear in spatially varying magnetic fields. Both lengths were related into the Ginzburg–Landau parameters,  $\kappa$  with  $\kappa = \frac{\lambda}{\xi}$ . Type I superconductors normally exhibit  $\xi < \lambda$ , hence  $0 < \frac{\lambda}{\xi} < \frac{1}{\sqrt{2}}$  while Type II superconductor having  $\xi > \lambda$  with  $\frac{\lambda}{\xi} < \frac{1}{\sqrt{2}}$ . GL theory best describes Type II superconductors compared to Type I because only near  $T_c$  the theory is valid, and the non-local interaction of electronic qualities become less significant. Since 1911, the discoveries of superconductors

have emerged so rapidly with ever-increasing critical temperature,  $T_c$  and current density,  $J_c$  values while maintaining the perfect diamagnetism ability. The needs in various applications involving high magnetic fields encouraged researchers around the world to further explore in finding the best superconductor to cater every industrial demand.

## References

1. D. Van Delft, History and significance of the discovery of superconductivity by Kamerlingh Onnes in 1911. *Phys. C Supercond. Appl.* **479**, 30–35 (2012)
2. J. Bardeen, L.N. Cooper, J.R. Schrieffer, Theory of superconductivity. *Theory Supercond.* **108**(5), 1175–1204 (1957)
3. J.G. Bednorz, M. Takashige, K.A. Müller, Possible High- $T_c$  Superconductivity in the Ba-La-Cu-O system. *Prop. Perovskites Other Oxide.* **64**, 189–193 (1986)
4. J.R. Gavaler, Superconductivity in NbGe films above 22 K. *Appl. Phys. Lett.* **23**(8), 480–482 (1973)
5. H.U. Habermeier, Science and technology of cuprate-based high temperature superconductor thin films, heterostructures and superlattices-the first 30 years. *Low Temp. Phys.* **42**(10), 840–862 (2016)
6. G.L. Zhao, Sharp electronic structure and anomalous isotope effect in Zr, Nb<sub>3</sub>Sn, and YBa<sub>2</sub>Cu<sub>3</sub>O<sub>7</sub>. *Phys. Status Solid. Basic Res.* **251**(8), 1531–1538 (2014)
7. B. Prabhakar, Mechanical properties of YBCO superconductor under high-pressure. *Indian J. Sci. Technol.* **13**(22), 2264–2271 (2020)
8. D. Koelle, R. Kleiner, F. Ludwig, E. Dantsker, J. Clarke, High-transition-temperature superconducting quantum interference devices. *Rev. Mod. Phys.* **71**(3), 631–686 (1999)
9. A.B. Karci, M. Tepe, H. Sozeri, Dependence of the structural, electrical and magnetic properties of the superconductive YBCO thin films on the deposition rate. *J. Phys. Conf. Ser.* **153**, 0–8 (2009)
10. P. Bussmann-Holder, H. Büttner, The isotope effect in ferroelectric and superconducting oxides. *Ferroelectrics* **105**(1), 21–26 (1990)
11. J.E. Hirsch, F. Marsiglio, Meissner effect in nonstandard superconductors. *Phys. C Supercond. Appl.* **587**, 1353896 (2021)
12. J.Y. Oh et al., Strong correlation between flux pinning and epitaxial strain in the GdBa<sub>2</sub>Cu<sub>3</sub>O<sub>7-x</sub>/La<sub>0.7</sub>Sr<sub>0.3</sub>MnO<sub>3</sub>nanocrystalline heterostructure. *RSC Adv.* **10**(64), 39102–39108 (2020)
13. R.M. Scanlan, A.P. Malozemoff, D.C. Larbalestier, Superconducting materials for large scale applications. *Proc. IEEE* **92**(10), 1639–1654 (2004)
14. Y. Slimani, E. Hannachi, A. Ekicibil, M. A. Almessiere, F. Ben Azzouz, Investigation of the impact of nano-sized wires and particles TiO<sub>2</sub> on Y-123 superconductor performance. *J. Alloys Compd.* **781**, 664–673 (2019)
15. A.K. Jha, K. Matsumoto, Superconductive REBCO thin films and their nanocomposites: the role of rare-earth oxides in promoting sustainable energy. *Front. Phys.* **7**, 1–21 (2019)
16. Y.S. Rammah, A.H. Salama, M. Elkhatib, Magnetic moment and its correlation with the critical temperature in YBCO. *Int. Ceram. Rev.* **68**(5), 34–41 (2019)
17. C. Egloff, A.K. Raychaudhuri, L. Rinderer, Penetration of a magnetic field into superconducting lead and lead-indium alloys. *J. Low Temp. Phys.* **52**(1–2), 163–185 (1983)
18. A.I. Gubin, K.S. Il'in, S.A. Vitusevich, M. Siegel, N. Klein, Dependence of magnetic penetration depth on the thickness of superconducting Nb thin films. *Phys. Rev. B Condens. Matter Mater. Phys.* **72** (6), 1–8 (2005)
19. T. Horide, F. Kametani, S. Yoshioka, T. Kitamura, K. Matsumoto, Structural evolution induced by interfacial lattice mismatch in self-organized YBa<sub>2</sub>Cu<sub>3</sub>O<sub>7- $\delta$</sub>  Nanocomposite Film. *ACS Nano* **11**(2), 1780–1788 (2017)

20. G. Deutscher, Coherence and single-particle excitations in the high-temperature superconductors. *Nature* **397**(6718), 410–412 (1999)
21. B. Lu, W.A. Van Wijngaarden, Bose-Einstein condensation in a QUIC trap. *Can. J. Phys.* **82**(2), 81–102 (2004)
22. C. Kittel, *Introduction to Solid State Physics/Charles Kittel* (1986), p. 646
23. R. Abd-Syukor, *Introduction to Superconductivity: in Metals, Alloys and Cuprates* (Universiti Pendidikan Sultan Idris, 2004)
24. Z. Chen, G. Geng, J. Fang, S. Dai, Design and characteristics analysis of a new high-temperature superconducting composite conductor. *IEEE Trans. Appl. Supercond.* **29**(2), 1 (2019)
25. W. Meissner, R. Ochsenfeld, Ein neuer Effekt bei Eintritt der Supraleitfähigkeit. *Naturwissenschaften* **21**(44), 787–788 (1933)
26. F. London, H. London, the electromagnetic equations of the supraconductor. **85**(1933) (1934)
27. K.H. Bennemann, J.B. Ketterson, History of superconductivity: conventional-, high-transition temperature and novel superconductors. *Phys. Supercond.* 1–21, May 2014 (2003)
28. L.P.G.O.R. Kov, Microscopic Derivation of Ginzburg-Landau Equations in th. *J. Exptl. Theor. Phys.* **36**(6), 1364–1367 (1959)
29. A.A. Abrikosov, On the magnetic properties of superconductors of the second group. *Sov. Phys.* **5**(6), 1174–1182 (1957)
30. Z. Li et al., Atomically thin superconductors. *Small* **17**(9), 1–15 (2021)
31. B.D. Josephson, Possible new effects in superconductive tunneling. *arXiv.* **1**(7), 251–253 (1962)
32. J. Nagamatsu, N. Nakagawa, T. Muranaka, Y. Zenitani, J. Akimitsu, Superconductivity at 39 K in magnesium diboride. *Nature* **410**(6824), 63–64 (2001)
33. M.K. Wu et al., Superconductivity at 93 K in a new mixed-phase Yb-Ba-Cu-O compound system at ambient pressure. *Phys. Rev. Lett.* **58**(9), 908–910 (1987)
34. A. Toshihisa, T. Yoshiaki, F. Masao, J. Kazunori, M. Junichi, M. Hiroshi, Preparation of highly oriented microstructure in the (Bi, Pb)<sub>2</sub>Sr<sub>2</sub>Ca<sub>2</sub>Cu<sub>3</sub>O<sub>x</sub>Sintered oxide superconductors. *Jpn. J. Appl. Phys.* **29**(4), L576–L579 (1990)
35. L.T.O. Nature, HgBa<sub>2</sub>Cu<sub>04+o</sub>. **362**, 1990–1992 (1993)
36. A. Schilling, M. Cantoni, J.D. Guo, H.R. Ott, Superconductivity above 130 K in the Hg-Ba-Ca-Cu-O system. *Nature* **363**(6424), 56–58 (1993)
37. Y. Kamihara, T. Watanabe, M. Hirano, H. Hosono, Iron-based layered superconductor La[O<sub>1-x</sub>F<sub>x</sub>]FeAs (x= 0.05-0.12) with T<sub>c</sub> = 26 K. *J. Am. Chem. Soc.* **130**(11), 3296–3297 (2008)
38. G. Zhou et al., Interface induced high temperature superconductivity in single unit-cell FeSe on SrTiO<sub>3</sub>(110). *Appl. Phys. Lett.* **108**(20), 1–14 (2016)
39. E. Wigner, H.B. Huntington, On the possibility of a metallic modification of hydrogen. *J. Chem. Phys.* **3**(12), 764–770 (1935)
40. N.W. Ashcroft, Metallic hydrogen: a high-temperature superconductor? *Phys. Rev. Lett.* **21**(26), 1748–1749 (1968)
41. E. Snider et al., Room-temperature superconductivity in a carbonaceous sulfur hydride. *Nature* **586**(7829), 373–377 (2020)
42. R. Asokamani, *March Towards Room Temperature Superconductivity*, vol. 38, (2021), pp. 27–38

# Classical Superconductors Materials, Structures and Properties



Michael R. Koblishka and Anjela Koblishka-Veneva

**Abstract** In this chapter, we discuss the structures and properties of classical (or conventional) superconductors, often dubbed also low- $T_c$  materials (LTSc). Among them are elemental superconductors, being superconductors at ambient conditions or under pressure, and several metallic alloys. Among them are the systems NbTi, NbN, and Nb<sub>3</sub>Sn, which are the so-called workhorses of superconductivity for nearly all types of applications, even today. Then, there are several families of materials with interesting outstanding superconducting and/or crystallographic properties like the heavy-fermion superconductors, the Chevrel phases, borocarbides, 2D materials or layered superconductors. For basic research questions, the metallic superconductors are ideal materials when preparing mesoscopic superconductor structures for the investigation of superconductivity in reduced dimensions. With the discovery of MgB<sub>2</sub> with a  $T_c$  of 38 K in 2001, the border to the high- $T_c$  materials was crossed, thus triggering a lot of research efforts in the field. Besides this big push, the field of conventional superconductors is still progressing—new materials like the superconducting high entropy alloys (HEAs) and new families like the LaBi<sub>3</sub> superconductors or superconducting magic-angle graphene were discovered—stimulating the research in the field of superconductivity even further. Among the new experiments carried out are high-pressure experiments on the HEAs and even on NbTi, which was never done before. These experiments gave remarkable results showing NbTi being a superconductor with increased  $T_c \sim 19$  K even up to 261 GPa. And finally, the high-pressure research on H<sub>3</sub>S and LaH<sub>10</sub> led to record, nearly room-temperature  $T_c$ 's for materials belonging to the conventional superconductors.

**Keywords** Superconductors · Conventional superconductivity · Metals · Alloys · Chevrel phases · Heavy fermions · 2D superconductors · High entropy alloys · High pressure

---

M. R. Koblishka (✉) · A. Koblishka-Veneva  
Experimental Physics, Saarland University, P.O. Box 151150, 66041 Saarbrücken, Germany  
e-mail: [m.koblishka@ieee.org](mailto:m.koblishka@ieee.org); [m.koblishka@gmail.com](mailto:m.koblishka@gmail.com)

A. Koblishka-Veneva  
e-mail: [a.koblishka@gmail.com](mailto:a.koblishka@gmail.com)

## 1 Introduction

Superconductivity was discovered in Hg by H. Kamerlingh Onnes in 1911 [1, 2] by accident when trying to answer the question what the resistance will do at ultralow temperatures after having established the liquefaction of He. Mercury (Hg), being a liquid at ambient conditions, was the best choice to obtain very pure samples by multiple distillation. Hg was found to be a superconductor below  $T_c = 4.15$  K, just below the temperature of liquid Helium (4.2 K). It took then some time to find other metallic elements showing the same superconducting transition, including the metals Sn and Pb with  $T_c = 7.2$  K [3–8], being well above 4.2 K, followed by Nb with a  $T_c$  of 9.15 K, which is the highest one of all elements in ambient conditions. However, all these materials did not allow to produce a superconducting coil to generate magnetic fields without losses, which already Onnes had planned. The next step forward was NbN with a  $T_c$  of 16 K, followed by the alloys NbTi and V<sub>3</sub>Si in the 1950s, which set the base for the development of real conductors with improved high-field properties [3, 7]. In this period, also fruitful empirical rules like the Matthias' rules were developed to enable the search for new superconductors, especially among the metallic alloys [9, 10]. The A15-alloys like Nb<sub>3</sub>Sn, and the long-time  $T_c$ -record holder, Nb<sub>3</sub>Ge with  $T_c = 23.2$  K [11], were then developed in a quest to improve  $T_c$  further. Besides this, new families of superconductors were discovered from the 1960s onwards like the Chevrel phases [12], the heavy-fermion superconductors [13] and the borocarbides [14]. All the main development in this field then focused on the conductor development and some other applications like superconducting sensor elements, Josephson circuits including super-computers [4, 6]. Besides the big push with the upcoming of the high- $T_c$  superconductors in 1986 [15], the field of conventional superconductivity did not die out, however,  $T_c$  could only be improved in 2001 [16] when MgB<sub>2</sub> was found to be a superconductor. As the conventional superconductors are metals, the samples could always be produced with high purity, making these systems most interesting for basic research questions. This opened up new fields like layered superconductors and mesoscopic superconductors, which are most interesting to investigate superconductivity in reduced dimensions like in nanowires or nanoparticles [17, 18]. Also, the search for new superconductors has never stopped, and so new systems like the ones with AuCl<sub>3</sub>-structure [19] and the high-entropy alloys (HEAs) [20] were found. This quest for new superconductors is nowadays pushed forward by machine-learning search of databases [21–23]. Moreover, the recent high-pressure experiments on the HEAs [24], on NbTi [25], H<sub>3</sub>S [26] and the La (super)hydrides (LaH<sub>10</sub>) [27] brought out very interesting and remarkable results, with  $T_c$  reaching practically room-temperature. This further stimulated the research on the question if metallic hydrogen could be a superconductor [28, 29]. Thus, there are still many open questions to be answered, and so the field of conventional superconductivity remains to be very important.

## 2 Superconducting Elements

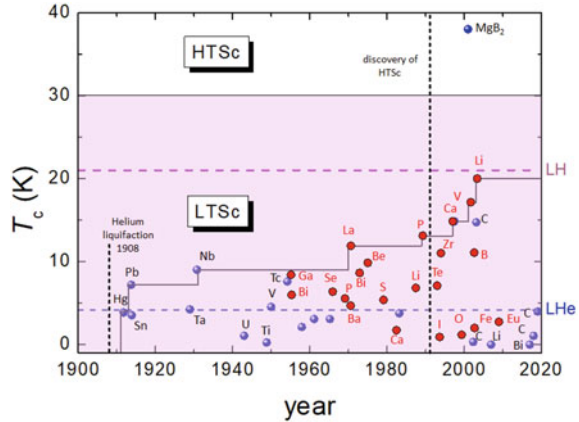
All superconductors marked green in Fig. 1 are metals, whereas also semimetals and non-metals can become superconductors under high pressure conditions (violet). There are some remarkable elements like carbon, which can be a superconductor with  $T_c = 15$  K in form of carbon nanotubes [30], Boron-doped diamond films with  $T_c = 4$  K [31], and recently as magic-angle bi-layered graphene with  $T_c$  ranging between 0.5 and 3 K [32–34]. Cr can be a superconducting material only as thin film [35], and Pd is a superconductor when being irradiated with  $\text{He}^+$ -ions [36]. Recently, also for Bi a  $T_c$  was obtained in ambient conditions, although very low ( $T_c = 0.53$  mK, [37]) as compared to the several high-pressure phases of Bi, reaching 8.7 K (9 GPa). The same applies for Li, which was found to be superconductor at ambient conditions with  $T_c = 4$  mK, but having  $T_c = 20$  K at 50 GPa pressure [38]. Remarkable is further that even Fe may be a superconductor at  $T_c = 2$  K under pressure [39]. Note also the very high  $T_c$ 's for the non-metals B, O, S, P, and Se. Superconductivity for metallic hydrogen is still an open question (“??”), but with remarkable predictions to be a room-temperature superconductor [28, 29].

Nb is the element with the highest  $T_c = 9.2$  K in ambient conditions, closely followed by the radioactive element, Tc, with  $T_c = 7.8$  K [40]. Figure 2 presents  $T_c$  as a function of the year of discovery following Refs. [41, 42]. The blue symbols denote the elements superconducting at ambient conditions, and the red symbols such being superconducting only under pressure.

H ??																	He																														
Li 0.0004	Be 0.026 <small>thin film</small>											B 11 250 GPa	C 15 nanotube	N 7	O 0.6 120 GPa	F	Ne																														
Na	Mg											Al 1.19 <small>thin film</small>	Si 8.5 250 GPa	P 6 7 GPa	S 17 180 GPa	Cl	Ar																														
K	Ca 15 150 GPa	Sc 0.3 21 GPa	Ti 0.4	V 5.3	Cr 3.2 <small>thin film</small>	Mn	Fe 2 21 GPa	Co	Ni	Cu	Zn 0.9	Ga 1.1 <small>nanos-R&amp;K</small>	Ge 5.4 11.9 GPa	As 2.7 24 GPa	Se 7 160 GPa	Br 1.4 150 GPa	Kr																														
Rb	Sr 4 50 GPa	Y 2.8 15 GPa	Zr 0.6	Nb 9.2	Mo 0.92	Tc 7.8	Ru 0.5	Rh 0.0003	Pd 3.2 <small>irradiated</small>	Ag	Cd 0.55	In 3.4	Sn 3.7 <small>thin film</small>	Sb 3.6 8.6 GPa	Te 7.4 11 GPa	I 1.2 10 GPa	Xe																														
Cs 1.5 5 GPa	Ba 5 15 GPa	(La)	Hf 0.13	Ta 4.4	W 0.01 <small>thin film</small>	Re 1.7	Os 0.65	Ir 0.14	Pt	Au	Hg 4.15	Tl 2.39	Pb 7.2	Bi 0.00053	Po	At	Rn																														
Fr	Ra	(Ac)	Rf	Db	Sg	Bh	Hs	Mt	Ds	Rg	Cn	Nh	Fl	Mc	Lv	Ts	Og																														
<table border="1"> <tr> <td>La 5.9</td> <td>Ce 1.7 5 GPa</td> <td>Pr</td> <td>Nd</td> <td>Pm</td> <td>Sm</td> <td>Eu 2.7 80 GPa</td> <td>Gd</td> <td>Tb</td> <td>Dy</td> <td>Ho</td> <td>Er</td> <td>Tm</td> <td>Yb</td> <td>Lu 0.1</td> </tr> <tr> <td>Ac</td> <td>Th 1.4</td> <td>Pa 1.4</td> <td>U 0.2</td> <td>Np 0.075</td> <td>Pu</td> <td>Am 0.8</td> <td>Cm</td> <td>Bk</td> <td>Cf</td> <td>Es</td> <td>Fm</td> <td>Md</td> <td>No</td> <td>Lr</td> </tr> </table>																		La 5.9	Ce 1.7 5 GPa	Pr	Nd	Pm	Sm	Eu 2.7 80 GPa	Gd	Tb	Dy	Ho	Er	Tm	Yb	Lu 0.1	Ac	Th 1.4	Pa 1.4	U 0.2	Np 0.075	Pu	Am 0.8	Cm	Bk	Cf	Es	Fm	Md	No	Lr
La 5.9	Ce 1.7 5 GPa	Pr	Nd	Pm	Sm	Eu 2.7 80 GPa	Gd	Tb	Dy	Ho	Er	Tm	Yb	Lu 0.1																																	
Ac	Th 1.4	Pa 1.4	U 0.2	Np 0.075	Pu	Am 0.8	Cm	Bk	Cf	Es	Fm	Md	No	Lr																																	

**Fig. 1** Superconducting elements in the periodic table. The green color denotes elements being superconducting in ambient conditions, violet color denotes elements being superconductors under pressure. Light blue indicates elements being superconducting only under special conditions, see text. For some elements, a second  $T_c$  is given when in thin film or nanosized form. Hydrogen is marked orange with “??” for  $T_c$ , pointing to the big challenge for future investigations (“metallic H”). Drawn using data collected from Refs. [3–8, 30–43]

**Fig. 2**  $T_c$  as a function of the year of discovery of the superconducting elements (blue—ambient conditions, red—under pressure). Note the highest  $T_c$  of all elements at 20 K for Li under pressure. Also presented are the borderlines for liquid He and liquid H. The 30 K-line marks the border between LTSc and HTSc materials, crossed by  $MgB_2$ , which is given for comparison



The bold line shows the upper  $T_c$ -limit as function of time. Table 1 gives a compilation of the superconducting properties (London penetration depth,  $\lambda_L$ , the coherence length,  $\xi_L$  and the critical field,  $B_c$ , of some elemental superconductors, together with the respective crystal structure and the Debye temperature,  $\Theta_D$ , which describes the lattice vibrations and the melting point. Note that all superconducting elements are type-1 superconductors (see chapter “[Magnetic Properties of Superconducting Materials](#)”), except Nb, which has a  $\kappa$  being very close to the borderline between type-1 and type-2 superconductors, so pure Nb is ‘just’ a type-2 superconductor. Table 2 presents the  $T_c$ -values of some of the elements being superconductors under pressure, including the latest element found to be a superconductor, Eu [43]. It is remarkable that the  $T_c$ -values obtained can be relatively high as compared to the elements at ambient conditions, and are exceptionally high for Li (20 K at 50 GPa, but 0.4 mK ambient), which holds the  $T_c$ -record of all elements, followed closely by P (18 K). Buzea and Robbie have reviewed the so-called puzzle of superconducting elements, as it is not straightforward to determine a clear rule if a material will be a superconductor or not [41]. The data presented in Tables 1 and 2 clearly reveal further that there is no simple relation between  $T_c$  and the respective crystal structure or the Debye temperature,  $\Theta_D$ , but as described in Refs. [44, 45], a relation between a characteristic crystallographic length,  $x$ , and  $T_c$  does exist which enables a simple calculation of  $T_c$  with the only knowledge of the electronic structure and the crystallographic data [46, 47]. This approach, called Roeser-Huber formula, can directly be proven using superconducting elements being superconducting with more than one crystal structure, also called polymorphs (Fig. 3).

Such cases can indeed be found for Hg (see Table 1), and especially, for La with the two structures *fcc* ( $T_c = 6$  K) and *dhcp* (double hexagonal close-packed, with  $T_c = 4.8$  K) [41]. The application of the Roeser-Huber formula and the search principles for the characteristic length  $x$  in the crystal structure brings out the correct values for the respective  $T_c$  values.



**Table 1**  $T_c$  of some superconducting elements in alphabetical order, together with their crystal lattice, melting point and some superconducting properties. Data were collected from Refs. [3, 30–43]. The crystal structures are *fcc*—face-centered cubic, *bcc*—body-centered cubic, *hex.* —hexagonal, *dhcp*—double hexagonal close packed, *rhomb.*—rhombohedral, *tetr.*—tetragonal and *orth.*—orthorhombic

Element	$T_c$ (K)	Crystal structure	Melting point (°C)	$\Theta_D$ (K)	$\lambda_L$ (nm)	$\xi_{GL}$ (nm)	$B_c$ (mT)
Al	1.18	<i>fcc</i>	660	420	50	1600	10
Bi	0.00053	<i>trigonal</i>	271.4	112	0.16	96,000	0.0052
Cd	0.52	<i>hex</i>	321	300	130	760	3
Ga	1.08	<i>orth</i>	29.8	317	120		5.9
Hg	4.15 3.95	<i>rhomb</i> <i>tetr</i>	−38.9 −	90 −	− −	55 −	40 34
In	3.4	<i>tetr</i>	156	109	24–64	360–440	28
La	5.9 4.8	<i>fcc</i> <i>dhcp</i>	− −	− −	− −	− −	− −
Nb	9.2	<i>fcc</i>	2500	240	32–44	39–40	195
Pb	7.2	<i>fcc</i>	327	96	32–39	51–83	80
Re	1.7	<i>hex</i>	3180	430	−	−	19
Ru	0.5	<i>hex</i>	2500	600	−	−	6.6
Sn	3.7	<i>tetr</i>	231.9	195	25–50	120–320	30.5
Ta	4.4	<i>bcc</i>	3000	260	35	93	80
Th	1.4	<i>fcc</i>	1695	170			15
V	5.4	<i>bcc</i>	1730	340	39.8	45	120
W	0.01	<i>bcc</i>	3380	390	−	−	0.124
Zn	0.85	<i>hex</i>	419	310		25–32	5.2

**Table 2**  $T_c$  of elements being superconducting only under pressure. Data were collected from Refs. [3, 30–43]

Element	$T_c$ (K)	Pressure (MPa)
As	2.7	24
Ba	5.1	20
Bi-II	3.9	2.6
Bi-III	7.2	>2.7
Bi-V	8.7	>9
Eu	2.7	142
Fe	2	21
Ge	5.4	11.5
Li	20	50
P	18	30
Se	6.9	13
Si	8.5	12
Te	7.4	35

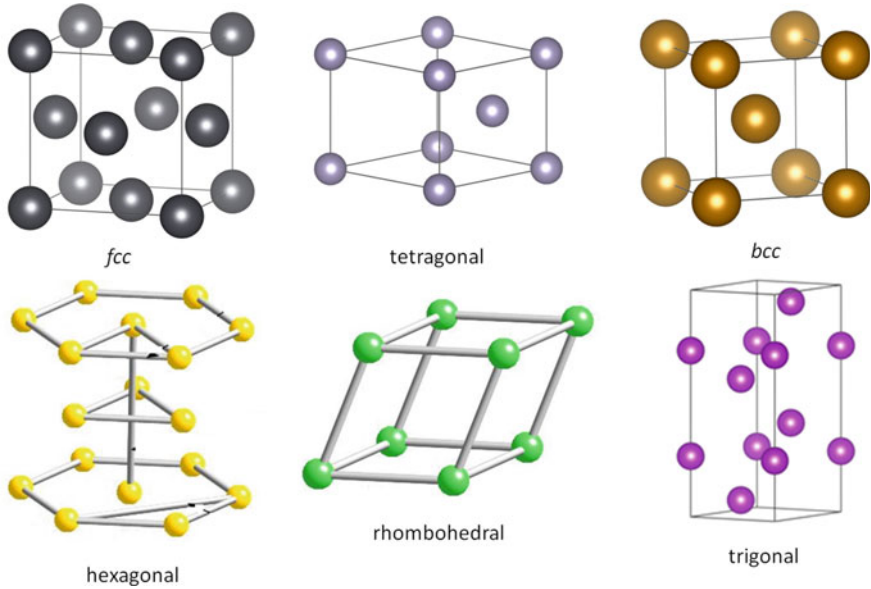


**Fig. 3** Typical crystal structures of the superconducting elements (see also Table 1). Crystal structures were drawn using VESTA software [48] and the data files were performed based on X-ray databases [49–51]

The puzzle of the superconducting elements gets an additional complication when preparing superconductors in reduced dimensions (e.g., as nanostructured thin films (2D/1D), as nanowires (1D) or nanowire arrays or even nanoparticles (0D)). In thin film form, which acts as a platform for geometrically confined, strongly interacting electrons, several superconductors exhibit higher  $T_c$ 's (the most famous example are here Al thin films with  $T_c$  raising from 1.2 K up to 4 K [52]), and other materials follow the more common understanding showing their  $T_c$  being reduced with decreasing the film thickness. All such experiments were summarized by Ivry et al. [53], which certainly contributes to gain better understanding of these effects.

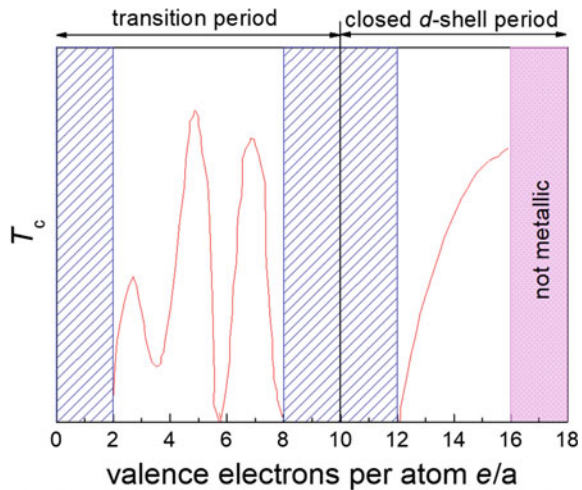
Another complication is offered when approaching 1D or 0D dimensions with nanowires and nanoparticles prepared from superconducting materials. Several observations of unexpected phenomena were reported in the literature, e.g., Pb films with thickness-dependent oscillating behavior of  $T_c$  [54], and Al-nanowires exhibiting size-dependent breakdowns of superconductivity [55].

A recent example should be mentioned here in more detail: Samples of nanostructured  $\beta$ -Ga wires were recently prepared by a novel method of metallic-flux nanonucleation in alumina templates [56] allowing the determination of several superconducting parameters via magnetic measurements. The Ga nanowires could be described as a weak-coupling type-2 superconductor with  $\kappa = 1.18$ , favored by the nanoscopic scale of the Ga nanowires. This result and the relatively high  $T_c$

of 6.2 K reported is in stark contrast to pure bulk Ga, which is a type-I superconductor with  $T_c \sim 1.1$  K [57, 58]. The fabrication techniques of such 1D-nanowires were recently reviewed by Koblischka and Koblischka-Veneva [59], and similar effects were observed also in other superconducting materials when being prepared in nanowire form. The topic of superconductivity in reduced dimensions and the possible increase of  $T_c$  will certainly deliver new surprises in the future.

A set of empirical rules was established in 1957 by Matthias [9, 10], which is commonly referred to as Matthias’ rule. Although there is no apparent regularity in the occurrence of super-conductivity and the placement of the element in the periodic table, the rules provide certain useful traits for the search of new superconducting materials. The main idea is to qualitatively relate the superconducting transition temperature,  $T_c$ , to the valence electrons per atom,  $e/a$ . When looking at this relation for non-transition elements (e.g., closed  $d$ -shell),  $T_c$  is a smooth increasing function of the  $e/a$ , while for the transition metals, when being in stable crystalline form, the resulting function shows peaks in  $T_c$  for  $e/a$  values of 3, 5, and 7. This function is shown in Fig. 4, indicating the transition period and the period of closed  $d$ -shell. Another rule concerns the crystal symmetry, saying ‘high symmetry is good, cubic symmetry is the best’. Other rules contain recommendations like ‘Stay away from magnetism’, which is a quite understandable advice, or ‘Stay away from oxygen and insulators’, but many new unconventional superconductors have broken these rules. For most metals, and especially for the main superconducting alloys and intermetallic compounds, the rules have worked fairly well, helping researchers a lot to find new superconducting materials.

**Fig. 4** Matthias’ rule, showing  $T_c$  as function of the valence electron count,  $e/a$ . 3 peaks appear in the transition period, whereas a smooth curve is obtained in the closed  $d$ -shell period



### 3 Metallic Alloys and Intermetallic Compounds

The metallic alloys and intermetallic compounds are the largest group of all superconducting materials with more than 1000 members, reflecting the numerous combinations of metallic elements possible. In this chapter, we will therefore only focus on the five alloys and intermetallic compounds, which are the most important ones for applications, that is, NbN, NbTi, the A15-compounds with the most prominent member, Nb<sub>3</sub>Sn, the Chevrel phases plus the newest member with the highest  $T_c$  of all metal alloys, the MgB<sub>2</sub> compound. Especially when considering superconductivity in the metallic alloys, the Matthias' rule proved its usefulness to find new superconducting materials.

#### 3.1 NbN

The NbN material was the first binary compound with a  $T_c$  above 10 K discovered by Aschermann [60] in 1941. The optimum  $T_c$  is obtained to be 16 K, being much higher than that of the superconducting elements. NbN has a crystal structure of the rock-salt type (B1), and the lattice parameter and the achievable  $T_c$  depend strongly on the N content [61–63]. The material is attractive for applications especially in form of thin films [4, 64] for use in radio frequency cavities or as active element in single-photon detectors [65, 66]. NbN is typically sputtered (reactive DC magnetron sputtering) from Nb targets in controlled N<sub>2</sub>-atmosphere on Si/SiO<sub>2</sub>-substrates, and the heating of the substrate material is an important issue for the performance as it influences directly the sample resistance and the upper critical fields. As thin film material, nanostructuring with modern technologies like e-beam lithography or focused ion-beam milling is an important issue for further development.

#### 3.2 NbTi

The alloy NbTi is the classical workhorse of superconductivity. Since its discovery in 1960, this material proved that it can be easily produced in wire form, even as multi-filaments. The superconducting parameters including a  $T_c$  of approximately 10 K and an upper critical field of  $B_{c2}(0) \sim 11.5$  T made it the material of choice for MRI applications and most laboratory equipment [67–69]. The Ti content in commercial NbTi conductors varies between 30 and 49%, and additions of, e.g., 20% Zr (for Ti) further strengthen the high field properties. The NbTi material has a *bcc* structure [70], which corresponds to that of Nb, whereas Ti has a hexagonal, close packed (*hcp*) crystal structure (P63/mmc). The size difference of Nb and Ti is only 2%, so the resulting lattice parameter,  $a$ , of NbTi is 0.3285 nm, slightly smaller than that of pure Nb. The component Ti itself is not superconducting down to 0.39 K at ambient

pressure [71]. Thus, the superconductivity depends mainly on the Nb component, and the bcc crystal structure must be maintained to keep up the  $T_c$ , which defines the limits of Ti and Zr additions. The effects of the metallurgical treatments and details of the composition on the flux pinning properties were discussed by Hillmann [72]. The development of NbTi wires for magnet applications is still ongoing [67], and also thin films of NbTi are of interest in the development of superconducting joints for HTSc conductors [73].

Very recently, high-pressure resistance measurements were performed as function of temperature and applied magnetic field on commercial NbTi alloy samples with the nominal composition  $\text{Nb}_{0.44}\text{Ti}_{0.56}$ , showing a  $T_c$  at ambient conditions of 9.6 K. Interestingly enough, such experiments were not carried out in all the years before. The interest in such experiments was now sparked by similar experiments carried out on the superconducting high-entropy alloys (HEA), which are based on the NbTi system. The properties of the HEA superconductors will be discussed in Sect. 2 below.

The high-pressure experiments on NbTi conducted in a non-magnetic diamond anvil cell by Guo et al. [25] showed an extraordinary robustness of superconductivity against pressure up to the very high pressure of 261 GPa. As illustrated in Fig. 5, this pressure corresponds to the outer core of Earth. The high-pressure experiments made NbTi now holding the record  $T_c$  and the record upper critical field,  $B_{c2}$ , for an alloy composed solely from transition elements. The high-pressure measurements also included XRD analysis, so Fig. 6 presents  $T_c$  as a function of the volume change ( $-\Delta V/V_0$ ) of the unit cell caused by the applied pressure. Both NbTi and the HEA alloy  $(\text{Tb}, \text{Nb})_{0.67}(\text{Hf}, \text{Zr}, \text{Ti})_{0.33}$  with the same crystal structure (*bcc*) show a similar behavior, although with clearly different magnitude, as compared to the pure element Nb. The remarkable findings presented in [25] thus not only reveal the extraordinary high-pressure superconducting properties of a commercially fabricated NbTi alloy, but also give a new push forward to a better understanding of the mechanism of superconductivity in general.

### 3.3 A15-Compounds

The other big group of superconducting alloys important for applications are the so-called A15 superconductors. The A15-type superconductors ( $\text{V}_3\text{Si}$  and  $\text{Nb}_3\text{Sn}$ ) were found by Hardy and Hulm [74] and Matthias [10, 75] in 1954. The history of these materials, which were since then the materials with the highest  $T_c$  known until the HTSc era, was recently reviewed by Stewart [76]. There are 69 distinct members of A15 compounds, from which 53 are superconductors, and 15 of them show a superconducting transition temperature of 10 K or higher. All the superconductors with the A15 structure are extreme type-2 superconductors and thus very important for the generation of large magnetic fields.

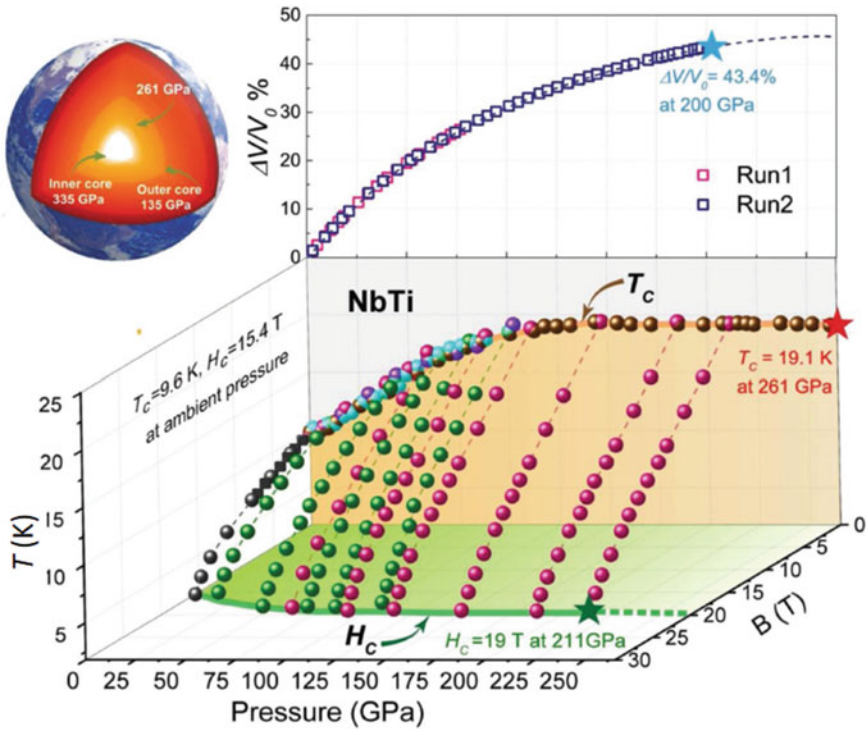


**Fig. 5** High-pressure resistance measurements as function of applied magnetic field and temperature on NbTi. Data are taken in different experimental runs as indicated by the colors used. The red star marks the record  $T_c$  of 19.1 K at 261 GPa, the green one the highest critical field,  $B_{c2}$ , recorded at 19 T. The inset presents the pressures around Earth’s core for comparison. Reproduced with permission from Ref. [25]

**Fig. 6** High-pressure experiment showing  $T_c$  as function of the volume change for NbTi, the HEA alloy  $(\text{Ta,Nb})_{0.67}(\text{Hf,Zr,Ti})_{0.33}$  and that of elemental Nb for comparison. Reproduced with permission from Ref. [25]

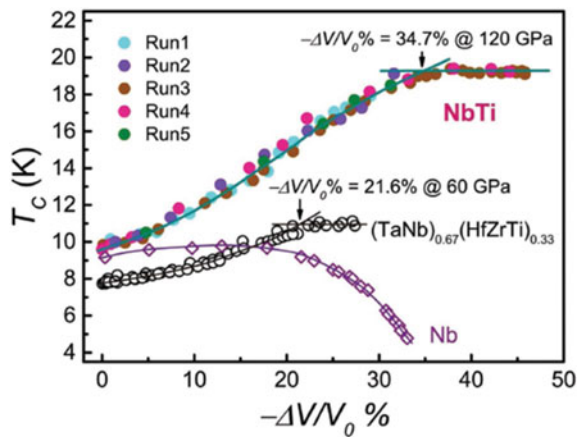
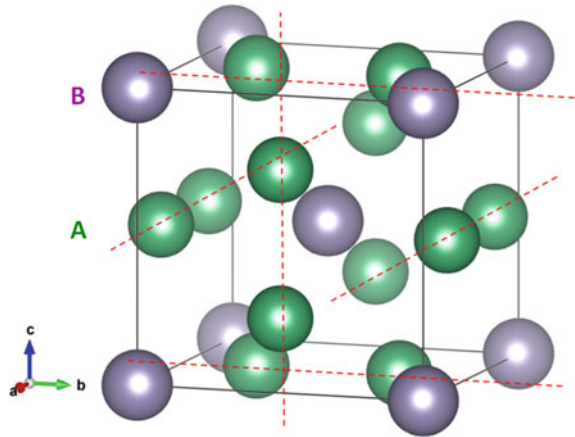


**Fig. 7** Crystal structure of the A15-compounds. The dashed red lines indicate the chain directions, formed by the A-elements



The crystal structure of the A15 compounds is the  $\beta$ -tungsten structure. The prototype material of the A15-class is  $\text{Cr}_3\text{Si}$  (or abbreviated  $\text{A}_3\text{B}$ ). The B-component occupies a *bcc* lattice, and on each crystal face, there are two atoms of the A-component. The crystal structure is depicted in Fig. 7. The lattice parameters are  $a = b = c$  and  $\alpha = \beta = \gamma = 90^\circ$ .

The superconducting transition temperatures were steadily increased from 18 K ( $\text{Nb}_3\text{Sn}$ , 1954) [74, 75], to 20 K ( $\text{Nb}_3\text{Al}_{0.2}\text{Ge}_{0.8}$ , 1967) [76], 20.3 K ( $\text{Nb}_3\text{Ga}$ , 1971) [77] and, finally,  $\text{Nb}_3\text{Ge}$  with a  $T_c$  of 22.3 K (1973) and further optimized in thin film form to the record value of 23.2 K in 1974 [78, 79]. The biggest problem is that the fabrication of wires from the A15 superconductors is a very complicated procedure as  $\text{Nb}_3\text{Sn}$  is a brittle intermetallic compound [4], but with a well-defined stoichiometry. The wire form is typically prepared by long term reactive diffusion, using Nb and Sn rods as the starting materials. To further improve the fabrication process and to prepare the required multifilamentary wires, several routes have been developed in the literature like the bronze route, the internal tin and the powder-in-tube technique [4, 5]. The production of the A15 conductors is mainly driven by the large projects on particle accelerators and fusion reactors, demanding high magnetic fields [80]. Therefore, many new developments are reported in this field still today, and the achieved progress concerning the critical current density is remarkable [81–83].

Another direction of research is the preparation of thin films of the A15 materials to be used in superconducting cavities. It is remarkable that the highest  $T_c$  of all A15 compounds was reached in the thin film state, where the substrate contributes to stabilizing the metastable  $\text{Nb}_3\text{Ge}$  compound. Also, in this branch of research, the work is still ongoing to further optimize the microstructures and the resulting superconducting properties [84].

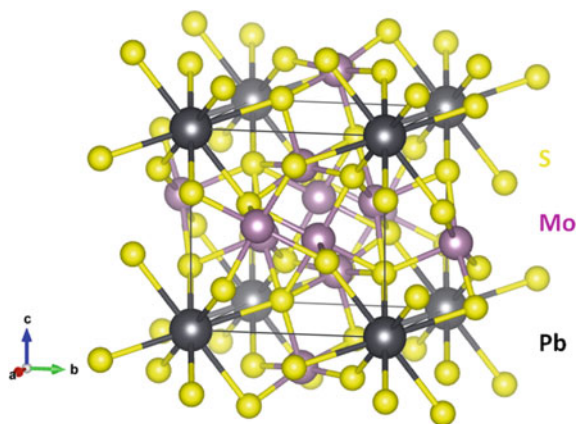
### 3.4 Chevrel Phases

The intermetallic compounds known as Chevrel phases are ternary molybdenum chalcogenides, with the general formula  $M_y\text{Mo}_6\text{X}_8$ , where  $M$  is a metal ion and  $X$  a chalcogen (S, Se, or Te). The Chevrel phases form a very interesting family of materials, and their unusual crystal structures were discovered by Chevrel et al. in 1971 [13, 85]. The superconductivity of these materials, with  $T_c$  values ranging up to 15 K, was first reported by Matthias et al. in 1972 [86]. In the following years, it was found that many members of this Chevrel phase family exhibited exceptionally high upper critical fields, which were clearly higher than the 20–40 T range of the A-15 superconductors [87, 88]. This observation made the Chevrel phase superconductors very unique, and very interesting for possible high-field applications [89]. In general, superconductivity is observed for compounds containing  $M = \text{Li}, \text{Na}, \text{Sc}, \text{Pb}, \text{Sn}, \text{Cu}, \text{Ag}, \text{Zn}, \text{Cd}$ , and almost all lanthanides, except Ce, Pm, and Eu [7]. Among the ternary compounds, the material  $\text{PbMo}_6\text{S}_8$  (abbreviated as PMS) shows the highest  $T_c$  of 15 K and the upper critical field at  $T = 4.2$  K reaches 60 T [4, 90, 91]. Thus, PMS is a material for high-field applications at low temperatures with an upper critical field clearly above that of  $\text{Nb}_3\text{Sn}$ .

The characteristic of all Chevrel-phase compounds with the chemical formula  $M_y\text{Mo}_6\text{X}_8$  contain  $\text{Mo}_6\text{X}_8$  octahedra as basic building blocks of the rhombohedral-hexagonal structure with space group  $R(-3)$  as presented in Fig. 8. Each unit has in the form of a distorted cube or pseudo-cube with the  $X$ -atoms being located at the corners. The six Mo atoms are placed near the centers of each of its six faces, thus forming a dense cluster with the shape of a distorted Mo octahedron.

Looking at the various compositions possible, the intra-cluster distance varies from 0.267 nm for  $\text{Cu}_{3.6}\text{Mo}_6\text{S}_8$  to 0.276 nm for  $\text{Mo}_6\text{S}_8$  and the inter-cluster distance ranges from 0.308 nm for  $\text{Mo}_6\text{S}_8$  to 0.366 nm for  $\text{PbMo}_6\text{Se}_8$ . The Mo-3d-orbitals are sufficiently extended allowing strong metallic bonding. The pseudo-cubes are stacked in an almost-cubic unit cell, with each of its one-eighth unit cells being occupied

**Fig. 8** Crystal structure of Chevrel phase compound  $\text{PbMo}_6\text{S}_8$  (PMS)





by a  $\text{Mo}_6\text{X}_8$  cluster. The side length of the unit cell is typically about 0.65 nm, and the extension of the embedded  $\text{Mo}_6\text{S}_8$  cluster is about 0.38 nm. Both the intra- and inter-cluster distances were found in the literature to be important in controlling the  $T_c$  of the compound.

The superconducting parameters of the Chevrel phase compounds are quite special (see Fig. 9 and Table 3), placing these materials between the conventional metal systems and the HTSc materials. The anisotropy is  $>2$ , whereas the coherence length is  $\sim 2.5$  nm, which is smaller than that of  $\text{Nb}_3\text{Sn}$  (3 nm), but larger as for the HTSc. Superconductivity in Chevrel-phase compounds was previously thought to be of conventional singlet  $s$ -wave type, although experimental data exhibit features of both conventional and unconventional superconductivity. Interestingly, recent studies have found them to be  $d$ -wave superconductors, and even multiband superconductivity has been manifested in PMS and SMS compounds in STS studies [7]. A full understanding of these unusual materials is still not reached yet. Nevertheless, Chevrel-phase superconductors are potential materials for ultrahigh-field applications due to their extremely high critical fields [4].

**Fig. 9** Comparison of the upper critical fields,  $B_{c2}(T)$ , of  $\text{PbMo}_6\text{S}_8$  (PMS) with  $\text{Nb}_3(\text{Al, Ge})$ ,  $\text{Nb}_3\text{Ge}$ ,  $\text{Nb}_3\text{Sn}$ ,  $\text{NbTi}$ ,  $\text{MgB}_2$  and the HTSc material Y-123 in the field directions  $B \parallel c$  and  $B \parallel (a, b)$ . Data were collected from Ref. [91]

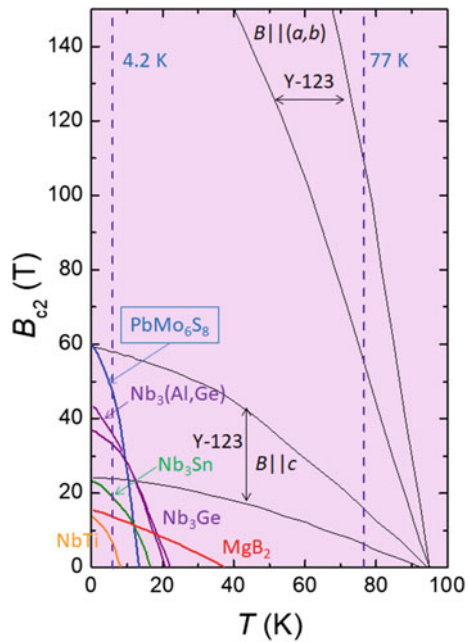


**Table 3** Superconducting parameters of various Chevrel phase compounds. Data were collected from Refs. [3, 7]

Material	$T_c$ (K)	$B_{c2}$ (T)	$\lambda_L$ (nm)	$\xi_{GL}$ (nm)
PbMo <sub>6</sub> S <sub>8</sub>	15	60	240	2.3
SnMo <sub>6</sub> S <sub>8</sub>	12	34	240	3.5
LaMo <sub>6</sub> S <sub>8</sub>	7	45	–	3.1
TbMo <sub>6</sub> S <sub>8</sub>	1.65	0.2	–	45
PbMo <sub>6</sub> Se <sub>8</sub>	3.6	3.8	–	11
LaMo <sub>6</sub> Se <sub>8</sub>	11	5	–	9

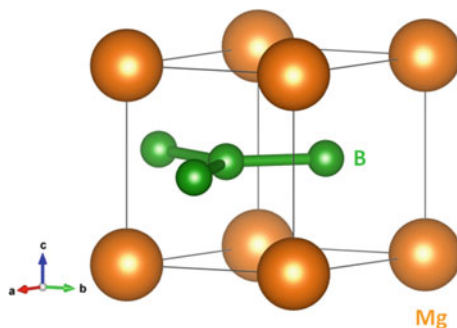
### 3.5 Magnesium Diboride, MgB<sub>2</sub>

Superconductivity in the MgB<sub>2</sub> system was found by Nagamatsu et al. in 2001 [16], showing a  $T_c$  of 38 K. This finding nearly doubled the previous record for the highest  $T_c$  of a metallic compound, crossing into the HTSc regime above 30 K. The material itself was not new, but never tested for superconductivity before. A reason for this may be the fact that neither element Mg nor B is superconducting itself, and both constituents are light metals without d-electrons, which were thought to be necessary for superconductors.

The crystal structure of MgB<sub>2</sub> is hexagonal of the type AlB<sub>2</sub> (space group C32, P6/mmm). The magnesium and boron atoms are arranged in sequent layers (see Fig. 10). The lattice parameters are  $a = 0.3047$  nm and  $c = 0.3421$  nm. The shortest distance between atoms is the B-B-spacing within the B-layer with  $d = 0.176$  nm [92, 93].

The MgB<sub>2</sub> compound shows several remarkable properties including extreme type-2 superconductivity with high critical fields up to 14 T (bulks) and 74 T for thin films [7]. MgB<sub>2</sub> is the first established example of a multiband superconductor, possessing two distinct energy gaps of about 2 and 7 meV [94]. Owing to the close relation to the metallic superconductors, polycrystalline samples of MgB<sub>2</sub> were quickly found to show transparency of transport currents to the grain boundaries,

**Fig. 10** Crystal structure of the MgB<sub>2</sub>-compound showing the two different structures of Mg and the boron layer



which implies that the grain boundaries are not acting as weak links to degrade the critical currents as is the case for the cuprate HTSc superconductors [95, 96]. This observation sparked the interest in applications of  $\text{MgB}_2$ , as a much cheaper production route could lead to wires and bulk samples, even though the  $T_c$  is clearly below 77 K.

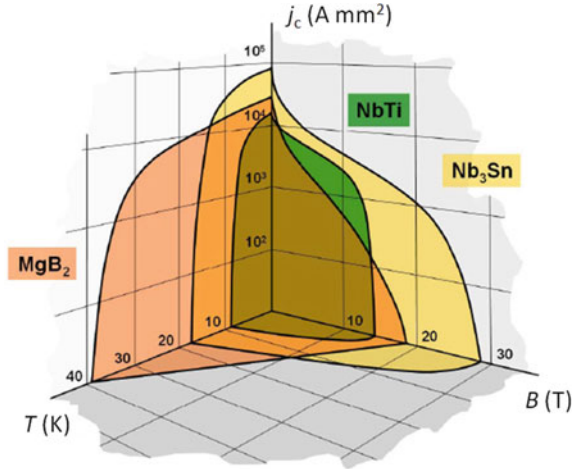
The  $\text{MgB}_2$  crystal lattice shows two different atomic bindings, the covalent ones which are mostly typical for semiconductors and also metallic binding, being typical for conductive materials. These covalent bindings are strong, whereas the coupling between B and Mg between the layers is formed by metallic 3D  $\pi$ -bindings, which provide a weak coupling only [93]. Furthermore, the bindings within the Mg-plane are much stronger than the Mg-B-bindings [92]; thus, cleaving of the crystal can take place at this position [94]. The electronic structure of  $\text{MgB}_2$  shows 4 bands crossing the Fermi niveau [97, 98]. Two  $\pi$ -bands, which result from the  $p_z$ -orbitals of the B-atoms and are weakly coupled with the phonon-modes (3D character). The two  $\sigma$ -bands result from the  $p_{x,y}$ -orbitals of the B-atoms. These are weakly coupled to the phonon-modes exhibiting 2D character [97, 99, 100]. Furthermore, there have been recently speculations that  $\text{MgB}_2$  could belong to a new type of superconductivity, the type-1.5 superconductivity (see also chapter “[Magnetic Properties of Superconducting Materials](#)”), exhibiting similarities between type-1 and type-2 superconductivity, based on observations of the flux-line lattice [101]. This is a direct consequence of the multiband character of superconductivity in  $\text{MgB}_2$ . The  $\text{MgB}_2$  compound is now considered as a strong competitor to the other metallic superconductors NbTi and  $\text{Nb}_3\text{Sn}$ , but offers also the possibility to operate at more elevated temperatures like 20K, which can be cost-effectively generated by modern cryo-cooling systems. The fact that both ingredients abundantly available, and no expensive rare earth materials are involved, makes  $\text{MgB}_2$  a cost-effective superconducting material, which can also compete with the HTSc for some applications. Thus, the development of fabrication processes of  $\text{MgB}_2$  wires is strongly pushed forward [102], also benefitting from the lessons learned in the HTSc wire development.

## 4 Critical Currents and Fields, Conductor Development

### 4.1 Comparison of Critical Currents and Fields of Different Materials

The starting point for choosing an appropriate material for a given application is, of course, a proper choice of the superconducting properties of the respective material. Thus, it is very informative to have a look at the  $j_c(T, B)$ -diagram and compare the common wire materials NbTi,  $\text{Nb}_3\text{Sn}$  and the new  $\text{MgB}_2$  with each other. Such a comparison of the  $j_c(B, T)$ -surfaces of  $\text{MgB}_2$ , NbTi and  $\text{Nb}_3\text{Sn}$  is depicted in Fig. 11.  $\text{Nb}_3\text{Sn}$  reveals the best high-field properties among these materials, but  $\text{MgB}_2$  competes mostly well with NbTi—with the critical field being a bit low—but

**Fig. 11** Comparison of the 3D-surfaces  $j_c(B, T)$  for the compounds  $\text{MgB}_2$ ,  $\text{NbTi}$  and  $\text{Nb}_3\text{Sn}$ , following Ref. [103]



has the advantage of a possible operation at 20 K due to the much higher  $T_c$ . The data for the critical current density,  $j_c$ , at 4.2 K, the upper critical fields,  $B_{c2}$  at 4.2 K, the irreversibility fields,  $B_{irr}$  at 4.2 K and the superconducting parameters  $\lambda(0)$  and  $\xi(0)$  are given in Table 3 together with the electrical resistivity obtained at  $T_c$ .

Table 4 reveals that the critical fields of the HTSc compounds at 4.2 K are unbeatably high, whereas the size of the critical currents is comparable of all materials. The metallic alloys have the advantage of having no anisotropy effects, which makes them the best choice for applications at low temperatures and in their respective field range. It is also obvious from the data that  $\text{MgB}_2$  belongs to the metallic alloys, showing a small anisotropy. However, the critical fields of  $\text{MgB}_2$  at 4.2 K are relatively low, but when considering applications operating at 20 K,  $\text{MgB}_2$  has a unique position among all superconducting materials.

**Table 4** Comparison of the superconducting properties of  $\text{NbTi}$ ,  $\text{Nb}_3\text{Sn}$  and  $\text{MgB}_2$  with those of the HTSc compounds  $\text{YBa}_2\text{Cu}_3\text{O}_x$  (YBCO) and  $\text{Bi}_2\text{Sr}_2\text{Ca}_2\text{Cu}_3\text{O}_{10}$  (Bi-2223) (see also chapter “Noncuprate Superconductors: Materials, Structures and Properties”)

Parameter	NbTi	Nb <sub>3</sub> Sn	MgB <sub>2</sub>	YBCO	Bi-2223
$T_c$ (K)	9	18	39	92	110
anisotropy	Negligible	Negligible	1.5–5	5–7	50–200
$j_c$ at 4.2 K ( $\text{A}/\text{cm}^2$ )	$\sim 10^6$	$\sim 10^6$	$\sim 10^6$	$\sim 10^6$	$\sim 10^7$
$B_{c2}$ (T) at 4.2 K	11–12	25–29	15–20	>100	>100
$B_{irr}$ (T) at 4.2 K	10–11	21–24	6–12	5–7 (77 K)	0.2 (77 K)
$\xi(0)$ (nm)	4–5	3	4–5	1.5	1.5
$\lambda(0)$ (nm)	240	65	100 ~ 140	150	150
Resistivity $\rho(T_c)$ ( $\mu\Omega$ cm)	60	5	0.4	150–800	40–60

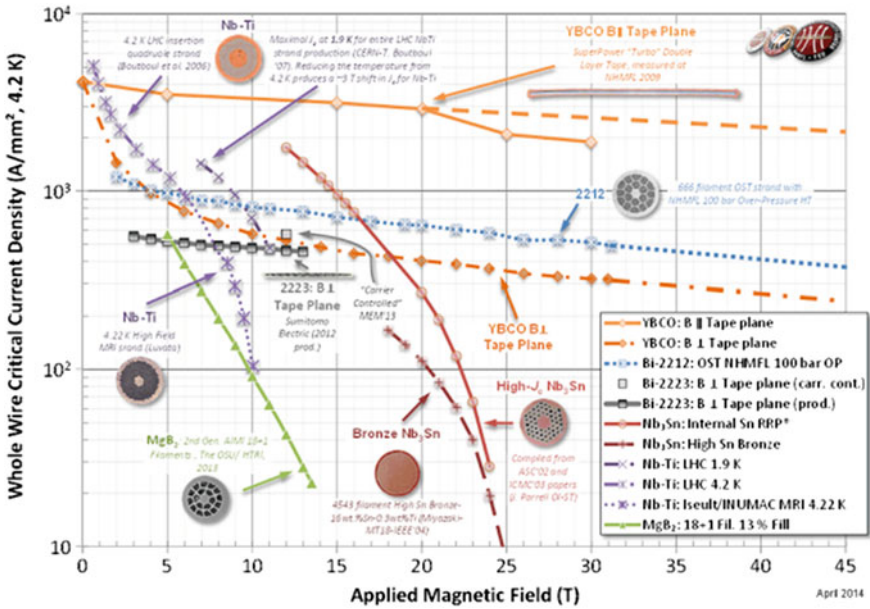


**Fig. 12** Results of the critical current density (whole wire,  $T = 4.2$  K) from various types of wire samples, including  $MgB_2$ -wires, NbTi,  $Nb_3Sn$  and the HTSc-compounds Bi-2212, Bi-2223 and YBCO [104]

Figure 12 presents data of the whole wire critical current density at  $T = 4.2$  K (liquid Helium temperature) as function of the applied magnetic field. At the given low temperature, the HTSc materials show their ultimately high critical fields, but the critical currents of the nowadays well-developed  $Nb_3Sn$  and NbTi-wires can surpass the ones of the HTSc in an appropriate field range.

The critical current data of the  $MgB_2$ -wire are still the lowest ones, but of course, the  $MgB_2$ -wire production is still not as mature as that of NbTi, so there is hope for future developments improving the flux pinning properties.

### 4.2 Fabrication of Wires for Applications

Careful design is required to develop superconducting wires and cables as detailed in the reviews of wire manufacturing in Refs. [4, 5]. For different types of applications, the wire design needs to be adapted accordingly, which adds complexity to the wire architecture in the sense that also the outer shell and the manufacturing route have to be selected carefully to achieve the demanded superconducting properties.

NbTi is practically an ideal material for conductor fabrication, with no anisotropy (cubic crystal structure), the only metallic superconductor being ductile and being composed of only two constituents [5]. Figure 13 presents cross-section views of

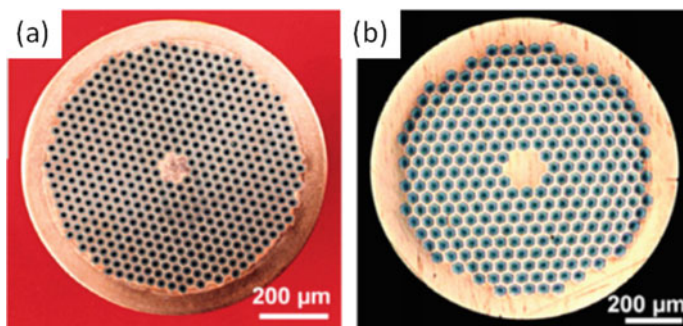


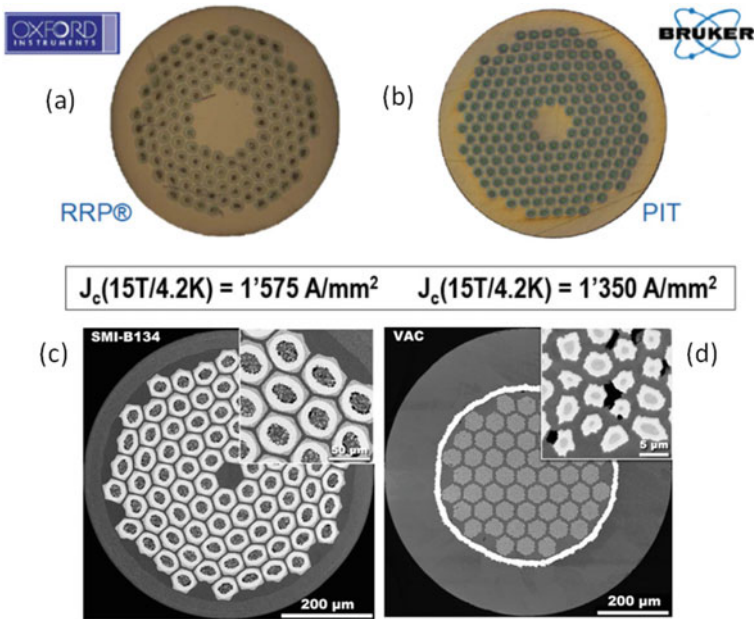
**Fig. 13** Modern 504 filament (left) and 288 filament (right) PIT wires, manufactured by Shape Metal Innovations (SMI, Enschede, The Netherlands). Reproduced with permission from Ref. [105]

(a) a 504 filament and (b) 288 filament powder-in-tube (PIT) NbTi wires fabricated by Shape Metal Innovations (SMI). The properties of these wires were discussed in detail in Ref. [105]. However, as shown before in Fig. 12, the applicable field range for NbTi is limited up to 9 T, so for the high-field applications in laboratory magnets and the large particle colliders, Nb<sub>3</sub>Sn wires are required for the magnet design [106]. In Ref. [107], the properties of Nb<sub>3</sub>Sn wires for applications at CERN (Large Hadron Collider, LH-LHC quadrupoles) were discussed and the wires stemming from different manufacturers were compared to each other. This illustrated in Fig. 14a, b. Figure 14c, d present Nb<sub>3</sub>Sn wires with different manufacturing processes from SMI (reinforced ternary PIT wire) and a wire fabricated by the ternary bronze route from Vacuumschmelze, respectively. A comprehensive discussion of the Nb<sub>3</sub>Sn wire fabrication was presented by Godeke [108].

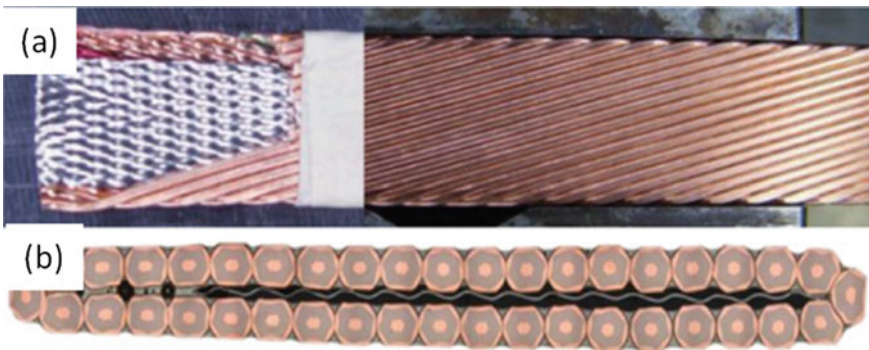
Accelerator magnets use high-current, multi-strand superconducting cables to reduce the number of turns in the coils, and thus magnet inductance [106]. A face view and the cross-sections of such a 40-strand Nb<sub>3</sub>Sn cable are presented in Fig. 15.

Figure 16 presents the steps made towards an MgB<sub>2</sub>-wire fabrication, which can profit from the existing knowledge of the other metallic compounds, but also from the lessons learned from the HTSc wires of the first generation. The images of Fig. 16 present a MgB<sub>2</sub> monofilament, the strand architecture, shaped wires and 3 × 3 and 12-strand cables. Even though the MgB<sub>2</sub> material is relatively new as compared to the metal alloys of the 1960s, multifilament wires and cables of MgB<sub>2</sub> can already be manufactured, but there are still lot of efforts required to bring the MgB<sub>2</sub> wires to a similar stage like the metal alloys NbTi and Nb<sub>3</sub>Sn. The current status of European MgB<sub>2</sub>-wire manufacturing was recently reviewed in [105].

Finally, Fig. 17 illustrates the conductor development of the Chevrel phase superconductor, TMC (ternary Mo chalcogenides, i.e., the compound PbMo<sub>6</sub>S<sub>8</sub>). The superconducting material is packed in a Mo shell, and then into a stainless-steel tube to improve the mechanical properties as the final conductor is foreseen for high-field experiments [110, 111]. The extrusion billet shown weighs 1.5 kg. The TMC wires are not only working at much higher fields as those of Nb<sub>3</sub>Sn, but may also have an



**Fig. 14** Nb<sub>3</sub>Sn wire development. **a** Restacked-rod process (RRP)-wires from Oxford Instruments (USA) and **b** PIT-wires from Bruker (Hanau, Germany). Reprinted from Ref. [107]. **c** Reinforced ternary PIT wire from SMI and **d** wires using the ternary bronze route from Vacuumschmelze (Hanau, Germany). Reprinted from Ref. [108]



**Fig. 15** Nb<sub>3</sub>Sn Rutherford cables: **a** large face view of cable with stainless-steel (SS) core; **b** cross-sections of 40-strand cable. Reprinted from Ref. [109]

advantage of lower fabrication and material costs involved [111]. Wires of this type are manufactured by Plansee SE (Austria) [110].

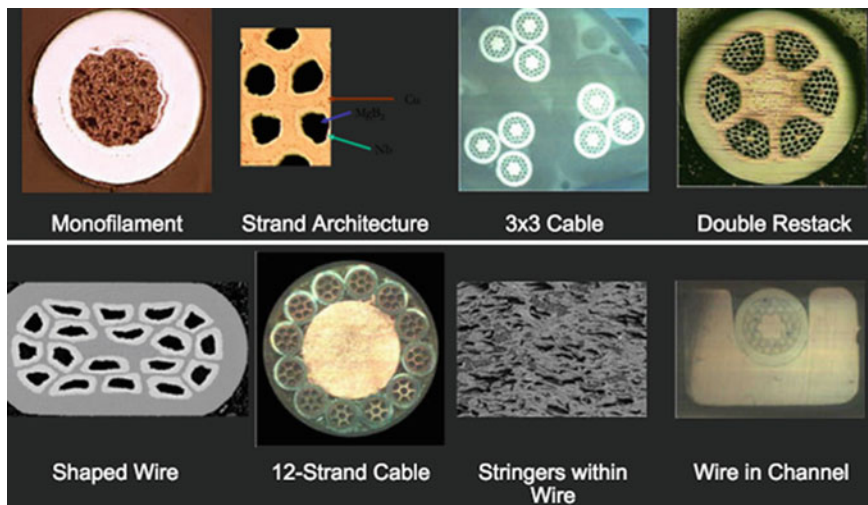
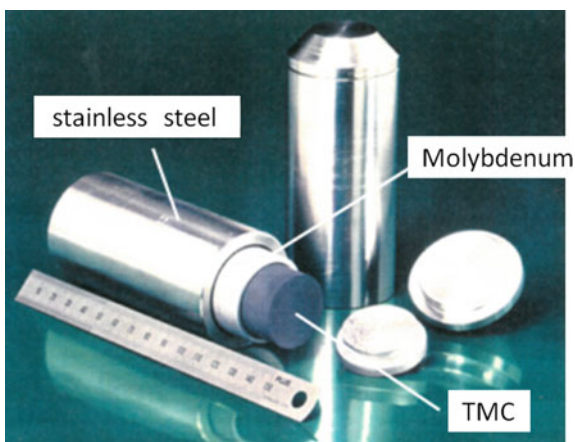


**Fig. 16**  $\text{MgB}_2$ -wire development [109], showing the steps towards useful wire architecture

**Fig. 17** Development of Chevrel-phase conductors of the TMC-type, showing an extrusion billet (~1.4 kg) for a 1 km long wire. Reinforcement by stainless steel is required for the foreseen high-field applications, Image from Plansee SE, courtesy B. Seeber [110]



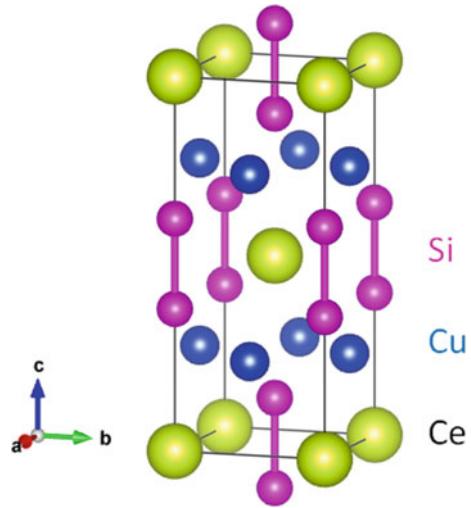
## 5 Other Superconducting Materials

### 5.1 Heavy Fermions

The prerequisite for heavy fermion (HF) compounds is a high concentration of magnetic ions which build up periodic lattice sites. As consequence, it seemed to be remote to find superconductivity as the presence of strong magnetism prohibits in principle the formation of Cooper pairs. However, Steglich et al. [112] have found the superconductor  $\text{CeCu}_2\text{Si}_2$ , exhibiting unconventional superconductivity in ambient



**Fig. 18** Crystal structure of the heavy-fermion superconductor  $\text{CeCu}_2\text{Si}_2$



conditions; the crystal structure is presented in Fig. 18. Since this time, superconductivity was discovered in more than 30 HF materials mainly containing Ce and U, and many more of their substituted phases, building up an entire class of materials with ferromagnetic and antiferromagnetic order. The superconductivity takes place mostly at  $T_c$  values below  $2\text{K}$ , but the most recently found materials  $\text{NpPd}_5\text{Al}_2$  with  $T_c = 4.9\text{ K}$  [113] and  $\text{PuCoGa}_5$  [114] with a  $T_c$  of even  $18.5\text{ K}$  exhibit an even more strange behaviour (Table 5).

The unique properties of the HF superconductors were reviewed by Stewart [115] and Steglich [12, 116, 117]. Some superconducting parameters are listed in Table 4. The HF materials are strongly correlated materials with an effective charge carrier being 10–1000 larger than that of a free electron, with the direct consequence that the pairing mechanism is unconventional. These materials are still a big puzzle concerning the coexistence of magnetism and superconductivity [118], and so a recent article concludes that the superconducting state may arise due to the magnetism rather than in spite of it [119]. These observations on the HF systems, being classified

**Table 5** Properties of selected heavy-fermion compounds. Data were collected from Refs. [12, 115]

Material	$T_c$ (K)	Eff. mass ( $e_m$ )	$B_{c2}$ (T)	$\lambda_L$ (nm)	$\xi_{GL}$ (nm)
$\text{URu}_2\text{Si}$	1.5	140	8	1000	10
$\text{CeCu}_2\text{Si}_2$	1.5	380	1.5–2.5	500	9
$\text{UPt}_3$	1.5	180	1.5	>1500	20
$\text{UBe}_{13}$	0.85	260	10	1100	9.5
$\text{UNi}_2\text{Al}_3$	1	48	<1	330	24
$\text{UPd}_2\text{Al}_3$	2	66	2.5–3	400	8.5

as unconventional superconductors, may also shed light on the pairing mechanism leading to high- $T_c$  superconductivity ( $d$ -wave superconductivity), where a similar phase diagram with a coexistence of magnetism (antiferromagnetism) exists.

## 5.2 Borocarbides

At the same time as the Chevrel phases, ternary borides and stannides were discovered, all of which show also an interplay between magnetism and superconductivity. The formulae of these compounds are  $RERh_4B_4$  (where  $RE = Nd, Sm, Er,$  or  $Tm$ ) and the stannides are described by  $RERh_xSn_y$  (where  $RE = La$  or  $Er$  with  $x \approx 1-1.5$  and  $y \approx 3.5-4.5$ ) [7]. The magnetic order in these materials can be ferromagnetic, antiferromagnetic, spin glass-type, oscillatory, as well as weakly ferromagnetic.

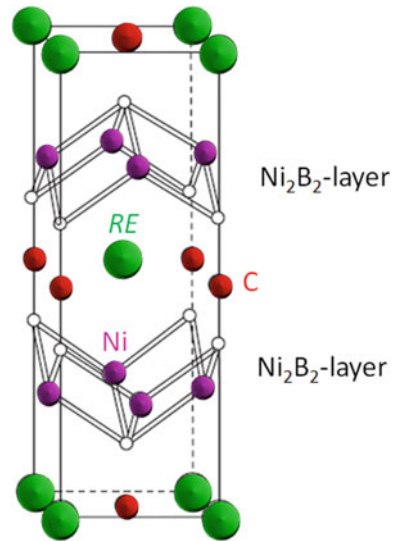
The most recent addition to this class of materials are the quaternary borides, which show an interplay with antiferromagnetism [3, 7]. The Ni-based borocarbides with the chemical formula  $RENi_2B_2C$  ( $RE = Dy, Ho, Er, Tm,$  or  $Lu$ ) exhibit superconducting transitions in the range between 6 and 17 K, with the most prominent member,  $YNi_2B_2C$ , becoming superconducting at 15.5 K (see Table 6). The  $T_c$ -value is found to increase up to 23 K, when Ni is replaced by Pd. The crystal structure (see Fig. 19) is body-centered tetragonal, with the electrical conduction taking place in the  $Ni_2B_2$  layers. The  $T_c$  and the Néel temperature,  $T_N$ , values are very close to each other, exhibiting all possible combinations  $T_c > T_N$ ,  $T_c < T_N$ , and  $T_c \approx T_N$ .

The superconducting properties in these compounds were reviewed in [120–123] and are considered as conventional superconductors, but similar to  $MgB_2$ , different energy bands contribute in different fashion to superconductivity. Borocarbides are type-2 superconductors with  $\kappa \sim 15$  ( $\xi \sim 10$  nm,  $\lambda \sim 150$  nm and  $B_{c2}$  up to  $10_T$ ). Furthermore, in this family also antiferromagnetism and superconductivity can coexist, with the compound  $YbNi_2B_2C$  exhibiting a heavy-fermion behavior. Furthermore, it was shown in [124] that the grain boundaries of polycrystalline borocarbide samples act as weak links like in the case of the HTSc cuprates, which makes them uninteresting for possible applications.

**Table 6** Properties of selected borocarbide compounds. Data were collected from Refs. [3, 120–123]

Material	$T_c$ (K)	$B_{c2}$ (T)	$\lambda_L$ (nm)	$\xi_{GL}$ (nm)
YPd <sub>2</sub> B <sub>2</sub> C	23	–	–	–
LuNi <sub>2</sub> B <sub>2</sub> C	16.6	7	70–130	7
YNi <sub>2</sub> B <sub>2</sub> C	15.5	6.5	120–350	6.5
TmNi <sub>2</sub> B <sub>2</sub> C	11	–	–	–
ErNi <sub>2</sub> B <sub>2</sub> C	10.5	1.4	750	15
HoNi <sub>2</sub> B <sub>2</sub> C	7.5	–	–	–

**Fig. 19** Crystal structure of the quaternary borocarbide  $RENi_2B_2C$  ( $RE$  = rare earths)

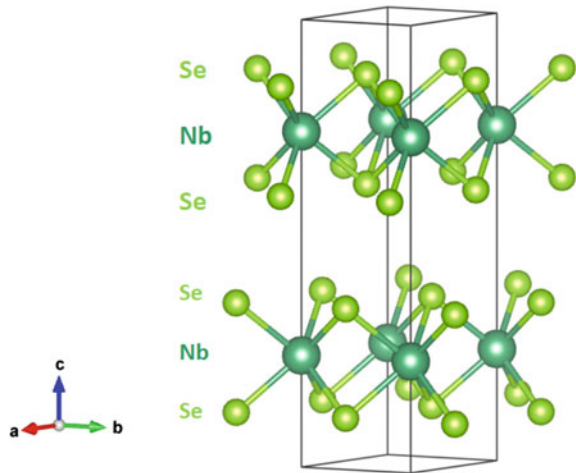


### 5.3 Layered Superconductors

The thin film preparation technology enabled the growth of multilayered systems consisting of, e.g., a metal and a superconductor, an insulator and a superconductor or two superconductors with different superconducting properties. As the thicknesses of the constituents can be varied, artificial multilayers with a variety of properties can be fabricated. Such materials were reviewed in [125, 126]. Even more interesting are materials with an internal layer structure or real 2D superconductors. If the coherence length gets smaller than the interlayer distance, the superconducting state will vary spatially, and in the extreme case, there will be an atomic sequence of superconducting and non-superconducting layers, where superconducting current perpendicular to the layers will flow as Josephson currents. Beginning in the 1960s, such natural layered superconductors were investigated. The general formula of these systems can be written as  $MX_2$  with  $M$  being a transition metal and  $X$  a chalcogenide Se, S or Te [3, 7]. A typical crystal structure of this material class is shown in Fig. 20 for the case of niobium diselenide ( $NbSe_2$ ), which was described first in [127].

This material is very interesting for low-temperature STM investigations as a calibration material, as the structure can readily be cleaved. With the upcoming of van der Waals-coupled multilayer engineering [128, 129],  $NbSe_2$  is best suited to provide a superconducting contribution for such 2D-vdW-architectures.

**Fig. 20** Crystal structure of  $\text{NbSe}_2$  as an example of layered or 2D-superconductors



## 6 New Developments

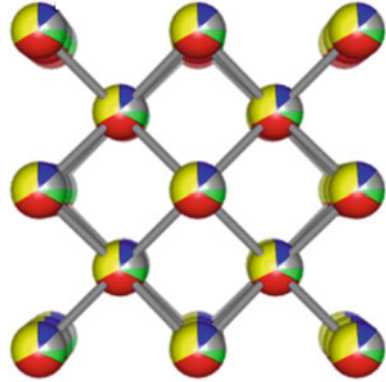
### 6.1 New Materials

New superconducting materials are still searched for, and the Matthias' rule is still an important guide to do so [130]. Recently, the Matthias' rules helped to find a new class of superconductors, which crystallize in the  $\text{AuCu}_3$ -type lattice, that is, the compounds of  $\text{LaBi}_3$  [19]. The finding of superconducting high-entropy alloys is also strongly guided by the valence electron count,  $e/a$ . This demonstrates that there are still many more superconducting materials to discover, and the help of machine learning to search databases and to perform band structure calculations [21–23] will certainly contribute to these efforts in the future.

### 6.2 High-Entropy Alloys (HEA) Compounds

A new field for research opened up when the high-entropy alloys (HEA) were found to contain also superconducting members. Based on the overall structure of the Nb-Ti-system, a total of 5 elements were composed to achieve the HEA effect as illustrated in Fig. 21. All atoms may occupy any lattice site with the same probability. The first such alloy was  $\text{Ta}_{34}\text{Nb}_{33}\text{Ti}_{11}\text{Zr}_{14}\text{Hf}_8$ , found by Kozelj et al. [20] with a  $T_c$  of 7.3 K. The basic idea of the HEA compound is depicted in Fig. 20. All atoms involved may take any position in the unit cell, in this case a  $bcc$  one. In the meantime, other HEA compounds including Nb-Re-Hf-Zr-Ti, Hf-Nb-Ti-V-Zr, Mo-Re-Ru-Rh-Ti [131, 132] and such containing U were found to be superconductors [133].

**Fig. 21** Composition scheme of the HEA alloys in the *bcc* structure. All atoms involved may occupy each lattice site as indicated by the different colors



It was later shown that HEA is not limited to the *bcc* unit cell as a superconducting hexagonal HEA alloy ( $\text{Re}_{56}\text{Nb}_{11}\text{Ti}_{11}\text{Zr}_{11}\text{Hf}_{11}$ ) with a  $T_c$  of 4.4 K was found [134], and the HEA  $\text{AgInSnPbBiTe}_5$  crystallizes in a NaCl-structure (space group  $Fm\bar{3}m$ ), with the metals on the cation site and Te on the anion site. The  $T_c$  of this system is 2.8 K [135]. V-Nb-Mo-Al-Ga shows polymorphism and crystallizes for some mixing ratio in the *bcc* structure but upon annealing, an A15-structure is obtained [136].

While in the A15-structure, the highest upper critical field for all HEAs of 20.1 T was measured. All the superconducting HEAs are type-2 superconductors with critical fields up to 8–10 T. The remarkable behavior of the electron system of the HEA compounds became visible in high-pressure experiments as shown in Fig. 6, which indicates that the electronic character of the HEA is different from that of the single constituents. The consequences this may have for the fabrication of wires is still not yet explored. Thus, there will be for sure more interesting physics coming out from such systems in the future.

### 6.3 Magic-Angle Bi-layered Graphene

Carbon becomes superconducting in various forms, including the carbon-doped diamond films and carbon nanotubes [30, 31]. Another interesting carbon material is graphene, and superconductivity in such systems was discovered recently in magic-angle, twisted bi-layered graphene (MA-tblG) [32–34]. Placing two graphene layers together under an angle of  $1.1^\circ$  forms a Moiré pattern as shown in Fig. 22. This observation leads to a new type of superconducting material, being the start of the so-called Moiré superconductivity, where superconductivity depends on the Moiré pattern formed between two or more atomically flat layers with a much larger lattice parameter. The  $T_c$  of MA-tblG is low with  $T_c$  ranging between 0.5 and 1.4 K, but it could be shown that adding hexagonal boron nitride (h-BN) layers of different thickness improves  $T_c$  up to 4 K [34].

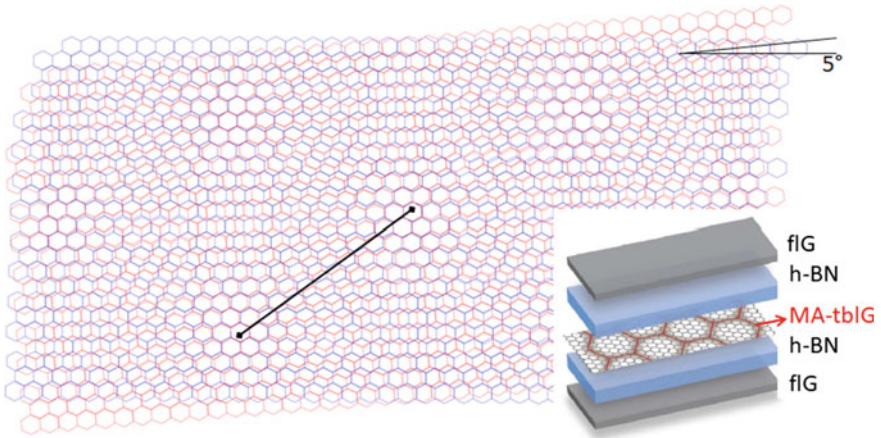


**Fig. 22** Magic-angle bi-layered graphene (MA-tblG), presented as Moiré-pattern of two  $5^\circ$ -tilted graphene layers for clarity. The bold line shows the new Moiré lattice parameter. The inset presents the arrangement for measurements, where the sample is covered by few layers of graphite flakes (fIG) acting as gates

The superconductivity of the MA-tblG layers is on the way to be understood in detail [137], even though more careful experiments on the Moiré superconductors, which include also other 2D-layers with similar structure like e.g.,  $\text{WSe}_2$  [138], regarding their superconducting properties are still required.

#### 6.4 Metal Hydrides Under Pressure

Superconductivity in metal-hydrides was found in 1972 by Skoskiewicz in the Pd-H system [139]. A maximum  $T_c$  of  $\sim 4$  K was obtained for a ratio H/Pd  $\sim 0.9$  in ambient conditions. However, if the pressure is sufficiently high, hydrogen is believed to become a monatomic metal with exotic electronic properties owing to the quantum nature of this low- $Z$  system [28, 140]. Due to the fact that very high pressures are required to create such states, hydrogen-rich metal compounds, in which the hydrogen is chemically pre-compressed, have been considered as an alternative for experimental work.

In recent experiments, X-ray diffraction and optical studies have demonstrated that super-hydrides of lanthanum can be synthesized with La atoms in an *fcc* lattice at 170 GPa upon heating to about 1000 K. The results obtained in [27, 141, 142] match the predicted cubic metallic phase of  $\text{LaH}_{10}$  [143] having cages of thirty-two hydrogen atoms surrounding each La atom. This configuration is up to now the closest one to pure metallic hydrogen. Four-probe electrical transport measurements were

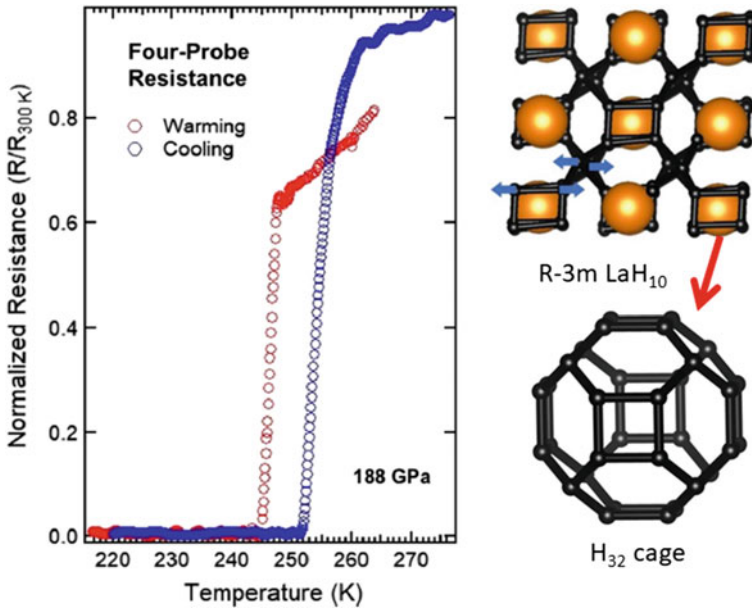


**Fig. 23** Resistance measurements under high pressure (188 GPa) on LaH<sub>10</sub>. Reproduced with permission from Ref. [141]. On the right, the crystal structure of R-3 m-LaH<sub>10</sub> is shown, with the blue arrows indicating displacements of the H-cluster. Below the H<sub>32</sub>-cluster which surrounds each La atom in the structure is presented. Reproduced with permission from Ref. [143]

performed in the high-pressure environment that display significant drops in resistivity on cooling up to 260 K and 180–200 GPa. These measured transitions represent signatures of superconductivity at near room temperature, which is a remarkable result, initiating a new area in superconductivity [42]. The underlying mechanism is, however, that of conventional superconductivity based on electron–phonon interaction (Fig. 23).

## 7 Conclusion

The conventional or low- $T_c$  superconductors are by no means dead as one could think during the hype around the various high- $T_c$  materials: The LTSs still serve as model systems in basic physics, e.g., for creating mesoscopic superconducting samples, 2D superconductors or model systems to investigate flux pinning properties. Concerning the fabrication of superconducting wires, there is still a lot of development required to design and produce the wires and cables for the current big projects like ITER and the planned fusion reactors. And, very important, there are new and unexpected results reported in the literature, which give the entire field a new push. This concerns mainly the discovery of new superconducting materials like

the discovery of the high-entropy alloys (HEA), which was based on the Matthias' rules. These materials show up with interesting new properties. This is especially the case for the high-pressure dependence of  $T_c$ , which exhibited superconductivity up to 190 GPa pressure. This result points out that the electron system of a HEA is truly different from its individual components like Nb or Ta. Very remarkably, it was found that the parent compound of the HEA, NbTi, was never investigated before at high pressures, carrying out this experiment recently, brought out the striking result that  $T_c$  of NbTi can be increased up to 19 K, and the superconductivity persists also up to 261 GPa, the highest pressure which can be applied experimentally. Furthermore, superconductivity was found in magic-angle, bi-layered graphene, creating a new class of superconducting materials, the Moiré-type superconductors. And, the high-pressure experiments on LaH<sub>10</sub> reaching room-temperature superconductivity put the research on metallic superconductors to the forefront of interest. Thus, there is a lot of exciting new physics in this field, coming up certainly with new and important results in the near future.

## References

1. H.K. Onnes, The superconductivity of mercury. Commun. Phys. Lab. Univ. Leiden 120b, 122b, 124c (1911)
2. D. van Delft, P.H. Kes, The discovery of superconductivity. Phys. Today **63**, 38–43 (2010)
3. W. Buckel, R. Kleiner, *Supraleitung. Grundlagen und Anwendungen*, 7th edn. (Wiley-VCH, Weinheim, 2013)
4. B. Seeber (ed.), *Handbook of Applied Superconductivity* (IOP Publishing, Bristol, UK, 1999)
5. D.A. Cardwell, D.S. Ginley (eds.), *Handbook of Superconducting Materials* (CRC Press, Boca Raton, USA, 2002)
6. P. Seidel (ed.), *Applied Superconductivity* (Wiley-VCH, Weinheim, Germany, 2015)
7. A.V. Narlikar, *Superconductors* (Oxford University Press, Oxford, U.K., 2014)
8. K.H. Bennemann, J.B. Ketterson (eds.), *Superconductivity* (Springer, Berlin, Heidelberg, Germany, 2008)
9. B.T. Matthias, Chapter V superconductivity in the periodic system. Prog. Low Temp. Phys. **2**, 138–150 (1957)
10. B.T. Matthias, T.H. Geballe, V.B. Compton, Superconductivity. Rev. Mod. Phys. **35**, 1–22 (1963)
11. J.R. Gavaler, M.A. Janocko, C.K. Jones, Preparation and properties of high  $T_c$  Nb-Ge thin films. J. Appl. Phys. **45**, 3009–3012 (1974)
12. R. Chevrel, M. Sergent, J. Prigent, Sur de nouvelles phases sulfurées ternaires du molybdène. J. Solid State Chem. **3**, 515–519 (1971)
13. F. Steglich, S. Wirth, Foundations of heavy-fermion superconductivity: lattice Kondo effect and Mott physics. Rep. Prog. Phys. **79**, 084502 (2016)
14. H. Takagi, M. Nohara, R.J. Cava, Borocarbide superconductors: materials and physical properties. Phys. B **237–238**, 292–295 (1997)
15. K.A. Müller, J.G. Bednorz, Possible high  $T_c$  superconductivity in the Ba-La-Cu-O system. Z. Phys. B **64**, 189–193 (1986)
16. J. Nagamatsu, N. Nakagawa, T. Muranaka, Y. Zenitani, J. Akimitsu, Superconductivity at 39 K in magnesium diboride. Nature **410**, 63–64 (2001)
17. A. Bezryadin, *Superconductivity in Nanowires* (Wiley-VCH, Weinheim, Germany, 2013)



18. F. Altomare, A.M. Chang, *One-Dimensional Superconductivity in Nanowires* (Wiley-VCH, Weinheim, Germany, 2013)
19. T. Kinjo, S. Kajino, T. Nishio, K. Kawashima, Y. Yanagi, I. Hase, T. Yanagisawa, S. Ishida, H. Kito, N. Takeshita, K. Oka, H. Eisaki, Y. Yoshida, A. Iyo, Superconductivity in  $\text{LaBi}_3$  with  $\text{AuCu}_3$ -type structure. *Supercond. Sci. Technol.* **29**, 03LT02 (2016)
20. P. Kozelj, S. Vrtnik, A. Jelen, S. Jazbec, Z. Jaglicic, S. Maiti, M. Feuerbacher, W. Steurer, J. Dolinsek, Discovery of a superconducting HEA alloy. *Phys. Rev. Lett.* **113**, 107001 (2014)
21. K. Matsumoto, T. Horide, An acceleration search method of higher  $T_c$  superconductors by a machine learning algorithm. *Appl. Phys. Express* **12**, 073003 (2019)
22. M.J. Hutcheon, A.M. Shipley, R.J. Needs, Predicting novel superconducting hydrides using machine learning approaches. *Phys. Rev. B* **101**, 144505 (2020)
23. S. Zeng, Y. Zhao, G. Li, R. Wang, X. Wang, J. Ni, Atom table convolutional neural networks for an accurate prediction of compounds properties. *npj Comput. Mater.* **5**, 84 (2019)
24. J. Guo, H. Wang, F. von Rohr, Z. Wang, S. Cai, Y. Zhou, K. Yang, S. Jiang, Q. Wu, R.J. Cava, L. Sun, Robust zero resistance in a superconducting high-entropy alloy at pressures up to 190 GPa. *Proc. Nat. Acad. Sci.* **114**, 13144–13147 (2017)
25. J. Guo, G. Lin, S. Cai, C. Xi, C. Zhang, W. Sun, Q. Wang, K. Yang, A. Li, Q. Wu, Y. Zhang, T. Xiang, R.J. Cava, L. Sun, Record-high superconductivity in Niobium-Titanium alloy. *Adv. Mater.* **31**, 1807240 (2019)
26. A.P. Drozdov, M.I. Eremets, I.A. Troyan, V. Ksenofontov, S.I. Shylin, Conventional superconductivity at 203 kelvin at high pressures in the sulfur hydride system. *Nature* **525**, 73–76 (2015)
27. A.P. Drozdov, P.P. Kong, V.S. Minkov, S.P. Besedin, M.A. Kuzovnikov, S. Mozaffari, L. Balicas, F.F. Balakirev, D.E. Graf, V.B. Prakapenka, E. Greenberg, D.A. Knyazev, M. Tkacz, M.I. Eremets, Superconductivity at 250 K in lanthanum hydride under high pressures. *Nature* **569**, 528–533 (2019)
28. N.W. Ashcroft, Metallic hydrogen: a high- temperature superconductor? *Phys. Rev. Lett.* **21**, 1748–1749 (1968)
29. K.J.B. Ghosh, S. Kais, D.R. Herschbach, Dimensional interpolation for metallic hydrogen. *Phys. Chem. Chem. Phys.* **23**, 7841–7848 (2021)
30. Z.K. Tang, L. Zhang, N. Wang, X.X. Zhang, G.H. Wen, G.D. Li, J.N. Wang, C.T. Chen, P. Sheng, Superconductivity in 4 angstrom single-walled carbon nanotubes. *Science* **292**, 2462–2465 (2001)
31. A. Bhaumik, R. Sachan, J. Narayan, High-temperature superconductivity in boron-doped Q-carbon. *ACS Nano* **11**, 5351–5357 (2017)
32. Y. Cao, V. Fatemi, S. Fang, K. Watanabe, T. Taniguchi, E. Kaxiras, P. Jarillo-Herrero, Unconventional superconductivity in magic-angle graphene superlattices. *Nature* **556**, 43–50 (2018)
33. M. Yankowitz, S. Chen, H. Polshyn, Y. Zhang, K. Watanabe, T. Taniguchi, D. Graf, A.F. Young, C.R. Dean, Tuning superconductivity in twisted bilayer graphene. *Science* **363**, 1059–1064 (2019)
34. Y. Saito, J. Ge, K. Watanabe, T. Taniguchi, A.F. Young, Independent superconductors and correlated insulators in twisted bilayer graphene. *Nature Phys.* **16**, 926–930 (2020)
35. M. Sawabu, M. Ohashi, K. Ohashi, M. Miyagawa, T. Kubota, K. Takanashi, The electrical resistivity of epitaxially deposited chromium films. *IOP Conf. Ser.* **871**, 012002 (2017)
36. B. Stritzker, Superconductivity in irradiated palladium. *Phys. Rev. Lett.* **41**, 1769–1773 (1979)
37. O. Prakash, Anil Kumar, A. Thamizhavel, S. Ramakrishnan, Evidence for bulk superconductivity in pure bismuth single crystals at ambient pressure. *Science* **355**, 52–55 (2017)
38. J. Tuoriniemi, K. Juntunen-Nurmilaukas, J. Uusvuori, E. Pentti, A. Salmela, and A. Sebedash, Superconductivity in lithium below 0.4 millikelvin at ambient pressure. *Nature* **447**, 187–189 (2007)
39. K. Shimizu, T. Kimura, S. Furomoto, K. Takeda, K. Kontani, Y. Onuki, K. Amaya, Superconductivity in the non-magnetic state of iron under pressure. *Nature* **412**, 316–318 (2001)

40. K. Schwochau, *Technetium: Chemistry and Radiopharmaceutical Applications* (Wiley-VCH, Weinheim, Germany, 2000)
41. C. Buzea, K. Robbie, Assembling the puzzle of superconducting elements: a review. *Supercond. Sci. Technol.* **18**, R1–R8 (2005)
42. J.A. Flores-Livas, L. Boeri, A. Sanna, G. Profeta, R. Arita, M. Eremets, A perspective on conventional high-temperature superconductors at high pressure: methods and materials. *Phys. Rep.* **856**, 1–78 (2020)
43. M. Debessai, T. Matsuoka, J.J. Hamlin, J. S. Schilling, K. Shimizu, Pressure-induced superconducting state of Europium metal at low temperatures. *Phys. Rev. Lett.* **102**, 197002 (2009)
44. H.P. Roeser, D.T. Haslam, J.S. Lopez, M. Stepper, M.F. von Schoenermark, F.M. Huber, A.S. Nikoghosyan, Correlation between transition temperature and crystal structure of niobium, vanadium, tantalum and mercury superconductors. *Acta Astronaut.* **67**, 1333–1336 (2010)
45. M.R. Koblischka, S. Roth, A. Koblischka-Veneva, T. Karwoth, A. Wiederhold, X.L. Zeng, S. Fasoulas, M. Murakami, Relation between crystal structure and transition temperature of superconducting metals and alloys. *Metals* **10**, 158 (2020)
46. A. Moritz, Calculation of the transition temperature of one-component-superconductors (in German). Master thesis IRS 09-S33, Institute of Space Systems, University of Stuttgart, Stuttgart, Germany (2009)
47. M. Stepper, Calculation of the transition temperature of two-component-superconductors (in German). Master thesis IRS 08-S23, Institute of Space Systems, University of Stuttgart, Stuttgart, Germany (2008)
48. K. Momma, F. Izumi, VESTA 3 for three-dimensional visualization of crystal, volumetric and morphology data. *J. Appl. Crystallogr.* **44**, 1272–1276 (2011)
49. ICDD PDF Data Base, ICDD: 12 Campus Blvd, Newtown Square, PA 19073, USA. Accessed 22 Aug 2021
50. Materials Project Database V2019.05. <https://materialsproject.org/>. Accessed 22 Aug 2021
51. Crystallography Open Database (COD). <http://www.crystallography.net/cod/>. Accessed 22 Aug 2021
52. R.W. Cohen, B. Abeles, Superconductivity in granular aluminum films. *Phys. Rev.* **168**, 444–450 (1968)
53. Y. Ivry, C.-S. Kim, A.E. Dane, D. De Fazio, A.N. McCaughan, K.A. Sunter, Q. Zhao, K. Berggren, Universal scaling of the critical temperature for thin films near the superconducting-to-insulating transition. *Phys. Rev. B* **90**, 214515 (2014)
54. Y. Guo, Y.-F. Zhang, X.J. Bao, T.Z. Han, Z. Tang, L.X. Zhang, W.G. Zhu, E. Wang, Q. Niu, Z.Q. Qiu, J.-F. Jia, Q.-K. Xue, Superconductivity modulated by quantum size effects. *Science* **306**, 1915–1917 (2004)
55. M. Zgirski, K.P. Riikonen, V. Touboltsev, K. Arutyunov, Size dependent breakdown of superconductivity in ultranarrow nanowires. *Nano Lett.* **50**, 1029–1033 (2005)
56. K.O. Moura, K.R. Pirota, F. Béron, C.B.R. Jesus, P.F.S. Rosa, D. Tobia, P.G. Pagliuso, O.F. de Lima, Superconducting properties in arrays of nanostructured  $\beta$ -gallium. *Sci. Rep.* **7**, 15306 (2017)
57. W.J. de Haas, J. Voogd, On the superconductivity of the gallium. *Commun. Phys. Lab. Univ. Leiden* **199d**, 733–734 (1929)
58. B.W. Roberts, Survey of superconductive materials and critical evaluation of selected properties. *J. Phys. Chem. Ref. Data* **5**, 581–821 (1976)
59. M.R. Koblischka, A. Koblischka-Veneva, Fabrication of superconducting nanowires using the template method. *Nanomaterials* **11**, 1970 (2021)
60. G. Aschermann, E. Friedrich, E. Justi, J. Kramer, Superconductive connections with extremely high cracking temperatures (NbH and NbN). *Phys. Z.* **42**, 349–360 (1941)
61. G. Horn, E. Saur, Preparation and superconductive properties of niobium nitride and niobium nitride with admixtures of titanium, zirconium and tantalum. *Z. Phys.* **210**, 70–79 (1968)
62. H. Rögner, Zur Supraleitung des Niobnitrids. *Z. Phys.* **132**, 446–467 (1952)

63. K. Hechler, G. Horn, G. Otto, E. Saur, Measurements of critical data for some type II superconductors and comparison with theory. *J. Low Temp. Phys.* **1**, 29–43 (1969)
64. S. Leith, M. Vogel, J. Fan, E. Seiler, R. Ries, and X. Jiang, Superconducting NbN thin films for use in superconducting radio frequency cavities. *Supercond. Sci. Technol.* **34**, 025006 (2021)
65. L. You, Superconducting nanowire single-photon detectors for quantum information. *Nanophotonics* **9**, 2673–2692 (2020)
66. S. Steinhauer, S. Gyger, and V. Zwiller, Progress on large-scale superconducting nanowire single-photon detectors. *Appl. Phys. Lett.* **118**, 100501 (2021)
67. B.A. Glowacki, Development of Nb based conductors, in *Frontiers of Superconducting Materials*. ed. by A.V. Narlikar (Springer, Berlin, Heidelberg, Germany, 2005), pp. 697–738
68. D. Gajda, Analysis method of high-field pinning centers in NbTi wires and MgB<sub>2</sub> wires. *J. Low Temp. Phys.* **194**, 166–182 (2019)
69. C. Meingast, D.C. Larbalestier, Quantitative description of a very high critical current-density Nb-Ti superconductor during its final optimization strain. 2. Flux pinning mechanism. *J. Appl. Phys.* **66**, 5971–5983 (1989)
70. T.S. Hutchinson, G. Ocampo, G.J.C. Carpenter, Crystal structure and morphology in commercial NbTi (46.5 wt.-% Ti) superconducting fibers. *Scr. Metall.* **19**, 635–638 (1985)
71. M.C. Steele, R.A. Hein, Superconductivity of titanium. *Phys. Rev.* **92**, 243–247 (1953)
72. H. Hillmann, Interaction of metallurgical treatment and flux pinning of NbTi superconductors. *Supercond. Sci. Technol.* **12**, 348–355 (1999)
73. J. Shimizu, K. Tonooka, Y. Yoshida, M. Furuse, H. Takashima, Growth and superconductivity of niobium titanium alloy thin films on strontium titanate (001) single crystal substrates for superconducting joints. *Sci. Rep.* **8**, 15135 (2018)
74. G.F. Hardy, J.K. Hulm, The superconductivity of some transition metal compounds. *Phys. Rev.* **93**, 1004–1016 (1954)
75. B.T. Matthias, T.H. Geballe, S. Geller, E. Corenzwit, Superconductivity of Nb<sub>3</sub>Sn. *Phys. Rev.* **95**, 1435
76. G.A. Stewart, Superconductivity in the A15 structure. *Phys. C* **514**, 28–35 (2015)
77. B.T. Matthias, T.H. Geballe, L.D. Longinotti, E. Corenzwit, G.W. Hull, R.H. Willens, J.P. Maita, Superconductivity at 20 degrees Kelvin. *Science* **156**, 645–646 (1967)
78. G.W. Webb, L.J. Vieland, R.E. Miller, A. Wicklund, Superconductivity above 20 degrees K in stoichiometric Nb<sub>3</sub>Ga. *Solid State Commun.* **9**, 1769–1773 (1971)
79. L.R. Testardi, J.H. Wernick, W.A. Royer, Superconductivity with onset above 23 K in Nb-Ge sputtered films. *Solid State Commun.* **15**, 1–4 (1974)
80. Y. Hishinuma, H. Taniguchi, A. Kikuchi, Development of the internal matrix reinforcement bronze processed Nb<sub>3</sub>Sn multicore wires using Cu-Sn-In ternary alloy matrix for fusion magnet application. *Fusion Eng. Des.* **148**, 111269 (2019)
81. S. Kawashima, T. Kawarada, H. Kato, Y. Murakami, M. Sugano, H. Oguro, S. Awaji, Development of a high current density distributed Tin method Nb<sub>3</sub>Sn wire. *IEEE Trans. Appl. Supercond.* **30**, 6000105 (2020)
82. A. Ballarino, S.C. Hopkins, C. Simon, B. Bordini, D. Richter, D. Tommasini, L. Bottura, M. Benedikt, M. Sugano, T. Ogitsu, S. Kawashima, K. Saito, Y. Fukumoto, H. Sakamoto, H. Shimizu, V. Pantsyrny, I. Abdyukhanov, M. Shlyakov, S. Zernov, F. Buta, C. Senatore, I. Shin, J. Kim, J. Lachmann, A. Leineweber, S. Pfeiffer, T. Baumgartner, M. Eisterer, J. Bernardi, A. Malagoli, V. Braccini, M. Vignolo, M. Putti, C. Ferdeghini, The CERN FCC conductor development program: a worldwide effort for the future generation of high-field magnets. *IEEE Trans. Appl. Supercond.* **29**, 6000709 (2019)
83. J.R. Gavaler, M.A. Janocko, C.K. Jones, Preparation and properties of high-*T<sub>c</sub>* Nb-Ge thin films. *J. Appl. Phys.* **45**, 3009–3012 (1974)
84. M.N. Sayeed, U. Pudasaini, C.E. Reece, G. Ereemeev, H.E. Elsayed-Ali, Structural and superconducting properties of Nb<sub>3</sub>Sn films grown by multilayer sequential magnetron sputtering. *J. Alloys Compounds* **800**, 272–278 (2019)

85. R. Chevrel, M. Hirrien, M. Sergent, Superconducting Chevrel phases: prospects and perspectives. *Polyhedron* **5**, 87–94 (1986)
86. B.T. Matthias, M. Marezio, E. Corenzwit, A.S. Cooper, H.E. Barz, High-temperature superconductors, the first ternary system. *Science* **175**, 1465–1466 (1972)
87. Ø. Fischer, A. Treyvaud, R. Chevrel, M. Sergent, Superconductivity in the  $RE_xMo_6S_8$ . *Solid State Commun.* **17**, 721–724 (1975)
88. R. Odermatt, Ø. Fischer, H. Jones, G. Bongi, Upper critical fields of some ternary molybdenum sulphides. *J. Phys.* **C7**, L13–L15 (1974)
89. S. Foner, E.J. McNiff Jr., E.J. Alexander, 600 kG superconductors. *Phys. Lett.* **49A**, 269–270 (1974)
90. B. Seeber, N. Cheggour, J.A.A.J. Perenboom, R. Grill, Critical current distribution of hot isostatically pressed  $PbMo_6S_8$  wires. *Physica C* **234**, 343–354 (1994)
91. B. Seeber, M. Decroux, O. Fischer, Status and prospects of superconducting Chevrel phase wires for high magnetic field applications. *Physica B* **155**, 129–135 (1989)
92. C. Buzea, T. Yamashita, Review of the superconducting properties of  $MgB_2$ . *Supercond. Sci. Technol.* **14**, R115–R146 (2001)
93. T. Muranaka, J. Akimitsu, Superconductivity in  $MgB_2$ . *Z. Kristallogr.* **226**, 385–394 (2011)
94. S. Souma, Y. Machida, T. Sato, T. Takahashi, H. Matsui, S.-C. Wang, H. Ding, A. Kaminski, J. C. Campuzano, S. Sasaki, K. Kadowaki, The origin of multiple superconducting gaps in  $MgB_2$ . *Nature* **423**, 65–67 (2003)
95. M. Kambara, N. Hari Babu, E.S. Sadki, J.R. Cooper, H. Minami, D.A. Cardwell, A.M. Campbell, I.H. Inoue, High intergranular critical currents in metallic  $MgB_2$  superconductor. *Supercond. Sci. Technol.* **14**, L5–L7 (2001)
96. P. Mikheenko, E. Martinez, A. Bevan, J.S. Abell, J.L. MacManus-Driscoll, Grain boundaries and pinning in bulk  $MgB_2$ . *Supercond. Sci. Technol.* **20**, S264–S272 (2007)
97. K.D. Belashenko, M. van Schilfgaarde, V.P. Antropov, Coexistence of covalent and metallic bonding in the boron intercalation superconductor  $MgB_2$ . *Phys. Rev. B* **64**, 092503 (2001)
98. S.K. Das, A. Bedar, A. Kannan, K. Jasuja, Aqueous dispersions of few-layer-thick chemically modified magnesium diboride nanosheets by ultrasonication assisted exfoliation. *Sci. Rep.* **5**, 10522 (2015)
99. I. Pallecchi, V. Ferrando, E. Galleani D’Agliano, D. Marré, M. Monni, M. Putti, C. Tarantini, F. Gatti, H.U. Aebersold, E. Lehmann, X.X. Xi, E.G. Haanappel, C. Ferdeghini, Magnetoresistivity as a probe of disorder in the  $\pi$  and  $\sigma$  bands of  $MgB_2$ . *Phys. Rev. B* **72**, 184512 (2005). Erratum in *Phys. Rev. B* **73**, 029901 (2006)
100. R.S. Gonnelli, D. Daghero, G.A. Ummarino, V.A. Stepanov, J. Jun, S.M. Kazakov, J. Karpinski, Direct evidence for two-band superconductivity in  $MgB_2$  single crystals from directional point-contact spectroscopy in magnetic fields. *Phys. Rev. Lett.* **89**, 247004 (2002)
101. V. Moshchalkov, M. Menghini, T. Nishio, Q.H. Chen, A.V. Silhanek, V.H. Dao, L.F. Chibotaru, N.D. Zhigadlo, J. Karpinski, Type-1.5 superconductivity. *Phys. Rev. Lett.* **102**, 117001 (2009)
102. A. Ballarino, R. Flükiger, Status of  $MgB_2$  wire and cable applications in Europe. *J. Phys. Conf. Ser.* **871**, 012098 (2017)
103. H. ten Kate, ESIPAP-CERN lecture, [https://indico.cern.ch/event/301339/contributions/688973/attachments/568795/783412/TenKate\\_-\\_ESIPAP\\_-\\_Lecture\\_1\\_-\\_Superconductors\\_for\\_Magnets\\_3Mar14.pdf](https://indico.cern.ch/event/301339/contributions/688973/attachments/568795/783412/TenKate_-_ESIPAP_-_Lecture_1_-_Superconductors_for_Magnets_3Mar14.pdf). Accessed 22 Aug 2021
104. P.J. Lee, <https://fs.magnet.fsu.edu/~lee/plot/plot.htm>. Accessed 22 Aug 2021
105. A. Godeke, A. den Ouden, A. Nijhuis, H.H.J. ten Kate, State of the art powder-in-tube niobium–tin superconductors. *Cryogenics* **48**, 308–316 (2008)
106. E. Barzi, A.V. Zlobin, in *Nb<sub>3</sub>Sn Accelerator Magnets Designs, Technologies and Performance* ed. by D. Schoerling, A.V. Zlobin (Springer Open, Cham, Switzerland, 2019), p. 39
107. R. Flükiger, Superconductivity for magnets, in *Proceedings of the CAS–CERN Accelerator School: Superconductivity for Accelerators*, Erice, Italy, 24 April–4 May 2013, ed. by R. Bailey, CERN-2014–005 (CERN, Geneva, 2014), pp. 247–267
108. A. Godeke, Performance boundaries in  $Nb_3Sn$  superconductors. PhD thesis, University of Twente, Enschede, The Netherlands (2005)

109. <https://www.nextbigfuture.com/2015/08/magnesium-diboride-superconductors-can.html>. Accessed 22 Aug 2021
110. R. Grill, E. Kny, B. Seeber, Anwendung von Refraktärmetallen in Keramik Supraleiter, in *Proceedings of 12th Plansee Seminar*, Reutte, Austria (1989), pp. 989–1006
111. B. Seeber, Ternary molybdenum chalcogenide superconducting wires for ultrahigh field applications. *IEEE Trans. Appl. Supercond.* **28**, 6900305
112. F. Steglich, J. Aarts, C.J. Bredl, W. Lieke, D. Meschede, W. Franz, H. Schäfer, *Phys. Rev. Lett.* **43**, 1892–1895 (1979)
113. D. Aoki, A. Nakamura, F. Honda, D. Li, Y. Homma, Y. Shimizu, Y.J. Sato, G. Knebel, J. Brison, A. Pourret, D. Braithwaite, G. Lapertot, Q. Niu, M. Vališka, H. Harima, J. Flouquet, Unconventional superconductivity in heavy fermion UTe<sub>2</sub>. *J. Phys. Soc. Jpn.* **88**, 043702 (2019)
114. J.L. Sarrao, L.A. Morales, J.D. Thompson, B.L. Scott, G.R. Stewart, F. Wastin, J. Rebizant, P. Boulet, E. Colineau, G.H. Lander, Plutonium-based superconductivity with a transition temperature above 18 K. *Nature* **420**, 297–299 (2002)
115. G.R. Stewart, Heavy-fermion systems. *Rev. Mod. Phys.* **56**, 755–787 (1984)
116. F. Steglich, J. Arndt, S. Friedemann, C. Krellner, Y. Tokiwa, T. Westerkamp, M. Brando, P. Gegenwart, C. Geibel, S. Wirth, O. Stockert, Superconductivity versus quantum criticality: what can we learn from heavy fermions? *J. Phys. Cond. Mat.* **22**, 164202 (2010)
117. F. Steglich, O. Stockert, S. Wirth, C. Geibel, H. Q. Yuan, S. Kirchner, Q. Si, Routes to heavy-fermion superconductivity. *J. Phys. Conf. Ser.* **449**, 012028 (2013)
118. A. Amato, E. Bauer, C. Baines, On the coexistence magnetism/superconductivity in the heavy-fermion superconductor CePt<sub>3</sub>Si. *Phys. Rev. B* **71**, 092501 (2005)
119. N.D. Mathur, F.M. Grosche, S.R. Julian, I.R. Walker, D.M. Freye, R.K.W. Haselwimmer, G.G. Lonzarich, Magnetically mediated superconductivity in heavy fermion compounds. *Nature* **394**, 39–43 (1998)
120. C. Mazumdar, R. Nagarajan, C. Godart, L.C. Gupta, M. Latroche, S.K. Dhar, C. Levy, B.D. Padalia, R. Vijayaraghavan, Superconductivity at 12 K in the Y-Ni-B system. *Solid State Commun.* **87**, 413–416 (1993)
121. R. Nagarajan, C. Mazumdar, Z. Hossain, S.K. Dhar, K.V. Gopalakrishnan, L.C. Gupta, C. Godart, B.D. Padalia, R. Vijayaraghavan, Bulk superconductivity at an elevated temperature ( $T_c \sim 12$  K) in a nickel containing alloy system Y-Ni-B-C. *Phys. Rev. Lett.* **72**, 274–277 (1994)
122. L.C. Gupta, Quaternary borocarbide superconductors. *Phil. Mag. B* **77**, 717–726 (1998)
123. H. Schmidt, H.F. Braun, in *Studies of High Temperature Superconductors*, vol. 26, ed. by A.V. Narlikar (Nova Science, Commack, New York, 1998), p. 47
124. N. Khare, A.K. Gupta, S. Khare, L.C. Gupta, R. Nagarajan, Z. Hossain, R. Vijayaraghavan, Radio frequency-SQUID effect in YNi<sub>2</sub>B<sub>2</sub>C due to natural grain boundary weak links. *Appl. Phys. Lett.* **69**, 1483–1485 (1996)
125. S. Brongersma, J. Pothuizen, E. Verweij, N. Koeman, D.G. Groot, R. Griessen, Multiple maxima in the field dependent magnetisation of superconducting Nb/Cu multilayers. *J. Alloys Compounds* **195**, 443–446 (1993)
126. M. Ziese, P. Esquinazi, P. Wagner, H. Adrian, S.H. Brongersma, R. Griessen, Matching and surface barrier effects of the flux-line lattice in superconducting films and multilayers. *Phys. Rev. B* **53**, 8658–8670 (1996)
127. M. Marezio, P.D. Dernier, A. Menth, G.W. Hull, jr., The crystal structure of NbSe<sub>2</sub> at 15 °K. *J. Solid State Chem.* **4**, 425–429 (1972)
128. K. Tahara, S. Lei, J. Adisojoso, S. De Feyter, Y. Tobe, Supramolecular surface-confined architectures created by self-assembly of triangular phenylene–ethynylene macrocycles *via* van der Waals interaction. *Chem. Commun.* **46**, 8507–8525 (2010)
129. L. Wang, Y. Shi, M. Liu, A. Zhang, Y.-L. Hong, R. Li, Q. Gao, M. Chen, W. Ren, H.-M. Cheng, Y. Li, X.-Q. Chen, Intercalated architecture of MA<sub>2</sub>Z<sub>4</sub> family layered van der Waals materials with emerging topological, magnetic and superconducting properties. *Nature Commun.* **12**, 2361 (2020)
130. K. Conder, A second life of the Matthias' rules. *Supercond. Sci. Technol.* **29**, 080502 (2016).

131. L. Sun, R.J. Cava, High-entropy alloy superconductors: status, opportunities, and challenges. *Phys. Rev. Mater.* **3**, 090301 (2019)
132. J. Kitagawa, S. Hamamoto, N. Ishizu, Cutting edge of high-entropy alloy superconductors from the perspective of materials research. *Metals* **10**, 1078 (2020)
133. W.L. Nelson, A.T. Chemey, M. Hertz, E. Choi, D.E. Graf, S. Latturmer, T.E. Albrecht-Schmitt, K. Wei, R.E. Baumbach, Superconductivity in a uranium containing high entropy alloy. *Sci. Rep.* **10**, 4717 (2020)
134. S. Marik, K. Motla, M. Varghese, K.P. Sajilesh, D. Singh, Y. Breard, P. Boullay, R.P. Singh, Superconductivity in a new hexagonal high-entropy alloy. *Phys. Rev. Mater.* **3**, 060602(R) (2019)
135. Y. Mizuguchi, Superconductivity in high-entropy-alloy telluride  $\text{AgInSnPbBiTe}_5$ . *J. Phys. Soc. Jpn.* **88**, 124708 (2019)
136. J. Wu, B. Liu, Y. Cui, Q. Zhu, G. Xiao, H. Wang, S. Wu, G. Cao, Z. Ren, Polymorphism and superconductivity in the V-Nb-Mo-Al-Ga high-entropy alloys. *Sci. China Mater.* **63**, 823–831 (2020)
137. E.F. Talantsev, R.C. Mataira, W.P. Crump, Classifying superconductivity in Moiré graphene superlattices. *Sci. Rep.* **10**, 212 (2020)
138. L. An, X. Cai, D. Pei, M. Huang, Z. Wu, Z. Zhou, J. Lin, Z. Ying, Z. Ye, X. Feng, R. Gao, C. Cacho, M. Watson, Y. Chen, N. Wang, Interaction effects and superconductivity signatures in twisted double-bilayer  $\text{WSe}_2$ . *Nanoscale Horiz.* **5**, 1309 (2020)
139. T. Skoskiewicz, Superconductivity in the palladium-hydrogen and palladium-nickel-hydrogen systems. *Phys. Stat. Sol. A* **11**, K 123–K126 (1972)
140. J.M. McMahon, M. Morales, C. Pierleoni, D.M. Ceperley, The properties of hydrogen and helium under extreme conditions. *Rev. Mod. Phys.* **84**, 1607–1653 (2012)
141. M. Somayazulu, M. Ahart, A.K. Mishra, Z.M. Geballe, M. Baldini, Y. Meng, V.V. Struzhkin, R.J. Hemley, Evidence for superconductivity above 260 K in lanthanum superhydride at megabar pressures. *Phys. Rev. Lett.* **122**, 027001 (2019)
142. Z.M. Geballe, H. Liu, A.K. Mishra, M. Ahart, M. Somayazulu, Y. Meng, M. Baldini, R.J. Hemley, Synthesis and stability of lanthanum superhydrides. *Angew. Chem. Int. Ed.* **57**, 688–692 (2018)
143. I. A. Kruglov, D.V. Semenov, H. Song, R. Szcześniak, I.A. Wrona, R. Akashi, M. Mahdi Davari Esfahani, D. Duan, T. Cui, A.G. Kvashnin, A.R. Oganov, Superconductivity of  $\text{LaH}_{10}$  and  $\text{LaH}_{16}$  polyhydrides. *Phys. Rev. B* **101**, 024508 (2020)

# High- $T_c$ Cuprate Superconductors: Materials, Structures and Properties



Anjela Koblischka-Veneva and Michael R. Koblischka

**Abstract** The cuprate superconductors are the first and the most important high- $T_c$  superconducting materials, as still today applications of superconductivity at the temperature of liquid nitrogen (77 K) are only possible with cuprate superconductors (and here, especially the three compositions  $\text{YBa}_2\text{Cu}_3\text{O}_{7-\delta}$  (abbreviated as Y-123 or YBCO),  $\text{Bi}_2\text{Sr}_2\text{CaCu}_2\text{O}_{8+\delta}$  (Bi-2212) and  $\text{Bi}_2\text{Sr}_2\text{Ca}_2\text{Cu}_2\text{O}_{10+\delta}$  (Bi-2223)). In this chapter, we present the crystal structures of the main 5 HTSc cuprate families ( $\text{Ln-Cu-O}$  (Ln-214), Y-Ba-Cu-O (YBCO), Bi-Sr-Ca-Cu-O (BSCCO), Tl-Ba-Ca-Cu-O (TlBCCO), and Hg-Ba-Ca-Cu-O (HgBCCO)) and their specific crystallographic features and discuss the resulting superconducting properties and the electric and magnetic characteristics being important for the applications, including the normal state properties, the grain boundary problem, the irreversibility lines, and issues of creating flux pinning sites to increase the critical current density,  $j_c$ . We further point out the progress in the material development in the direction for applications concerning the microstructure and texture and present the typical sample shapes.

**Keywords** High- $T_c$  superconductors · Cuprates · Crystal structures · Phase diagram · Doping · Oxygen content · Irreversibility lines · Microstructure · Applications

## 1 Introduction

The cuprate high-temperature superconductors (HTSc) were the first materials with a superconducting transition temperature,  $T_c$ , above 30 K, being clearly above that of the previous record holder,  $\text{Nb}_3\text{Ge}$  films with  $T_c = 23.2$  K [1–3]. In their pioneering paper, Bednorz and Müller (Nobel prize 1989) presented the compound  $\text{LaBaCuO}$  (the stoichiometric composition turned out to be  $\text{La}_{1.85}\text{Ba}_{0.15}\text{CuO}_4$ , now abbreviated as La-214) as a possible HTSc material [4]. The striking difference to all previous superconductors being metals and metal alloys was the fact that this material was a

---

A. Koblischka-Veneva (✉) · M. R. Koblischka  
Experimental Physics, Saarland University, P.O. Box 151150, 66041 Saarbrücken, Germany  
e-mail: [a.koblischka@gmail.com](mailto:a.koblischka@gmail.com)

ceramic, which was thought to be impossible as ceramics are normally insulators. Soon after the results could be reproduced by other groups, a race for even higher  $T_c$ 's set in, the early stages of which are nicely narrated in the book by Hazen [5] and in very short times after, the compound  $(\text{La,Sr})_2\text{CuO}_4$  was found with  $T_c = 38$  K [6]. By high-pressure experiments on  $\text{La-Ba-Cu-O}$ , the idea came up to replace La by the smaller ion of Y, and so the YBCO compound with a  $T_c$  of 91...93 K was found by Wu et al. [7] and Chu et al. [8]. This was the first time to raise  $T_c$  above the temperature of liquid nitrogen (77 K), so superconductivity was no longer a phenomenon which could take place only behind the steel walls of cryostats, but could now be demonstrated easily to the public or even in class rooms. Following this progress, about a year later the first members of the BSCCO-family were announced by Maeda et al. [9] and Zandbergen et al. [10], raising  $T_c$  from 85 K in  $\text{Bi}_2\text{Sr}_2\text{CaCu}_2\text{O}_{8+\delta}$  (Bi-2212) to 105 K in  $\text{Bi}_2\text{Sr}_2\text{Ca}_2\text{Cu}_3\text{O}_{10+\delta}$  (Bi-2223). The next steps of the quest to find materials with even higher  $T_c$  were the finding of the Tl-based superconducting family [11–13] and the Hg-based family [14, 15], which brought up  $T_c$  to 138 K in slightly Tl-doped  $\text{HgSr}_2\text{Ca}_2\text{Cu}_3\text{O}_9$  (Hg-1223). This material still holds today the  $T_c$  record for a material in ambient conditions [1]. Under pressure, the  $T_c$  of Hg-1223 could be raised further to 165 K [16, 17], which is now surpassed by reaching nearly room temperature in  $\text{H}_3\text{S}$  [18] and then in  $\text{LaH}_{10}$  [19]. Even though now more than 100 HTSc superconductors are known with  $T_c$ 's above the HTSc limit of 30 K, none of these materials could further improve the maximum  $T_c$  [20]. The main HTSc families and their maximum  $T_c$  are plotted in Figs. 1 and 2 below.

The La-124 system was developed further with family members doped with electrons, instead of hole-doping like for all other cuprate HTSc, making up the general

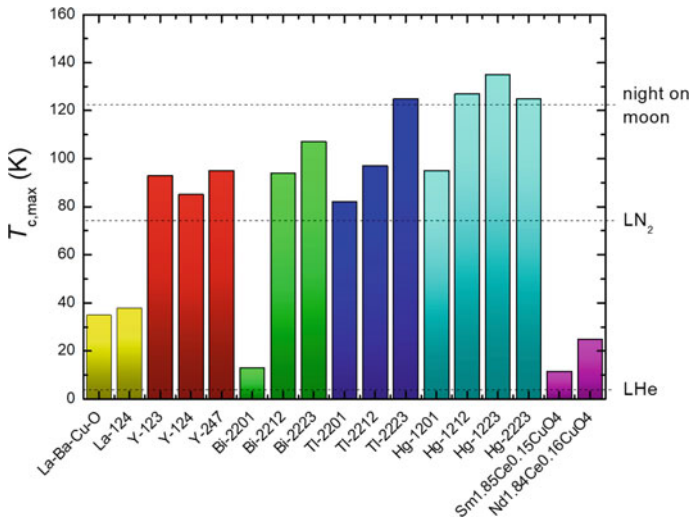
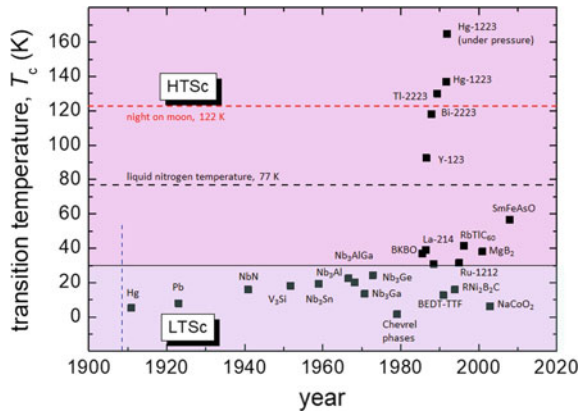


**Fig. 1** Superconducting transition temperature,  $T_c$ , of various cuprate HTSc. Different HTSc families are indicated by different colors. Data were collected from Refs. [1–3]



**Fig. 2** The raise of  $T_c$  as a function of time, starting from the first superconductor, Hg, discovered in 1911. The borderline between LTSc and HTSc is defined at  $T = 30$  K, and several other superconducting materials discovered since 1960 are also shown for comparison. Data were collected from Refs. [1–3]



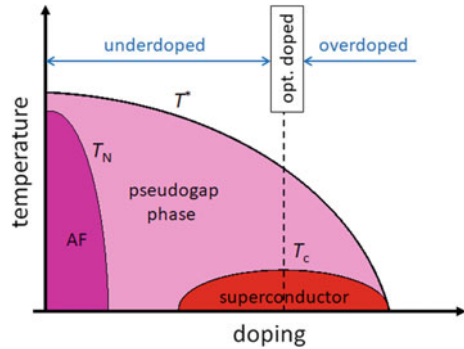
formula  $Ln_{2-x}M_xCuO_{4-\delta}$  (with  $Ln =$  rare earths  $Pr^{3+}$ ,  $Nd^{3+}$ ,  $Sm^{3+}$ , or  $Eu^{3+}$  and  $M = Ce^{4+}$  or  $Th^{4+}$  where  $x \approx 0.1-0.18$  and  $\delta \approx 0.02$ ), yielding the highest  $T_c$  of about 25 K for NCCO (i.e.  $Nd_{2-x}Ce_xCuO_{4-\delta}$ ) [21, 22]. These materials are especially important to test theories of the Cooper pair formation in HTSc materials.

From the applications' point of view, only the three systems, (*RE*)-BCO with *RE* denoting light rare earth elements, i.e., Nd, Eu, Sm and Gd, and the Bi-2212 and Bi-2223 systems, are really useful materials to be produced in a variety of shapes, ranging from epitaxial thin films, thick films, coated conductors, powder-in-tube wires and tapes, and bulk materials [23–25]. Very recently, even superconducting foams [26, 27] and nanofiber mats [28, 29] could be produced. Most attractive for many applications are such with cooling by liquid nitrogen ( $T = 77$  K), even though nowadays the development of cryocooling systems [30] has largely advanced allowing to reach even low temperatures in a cryogen-free manner.

Figure 2 gives the superconducting transition temperatures,  $T_c$ , as function of the year of discovery, starting from 1911 with Hg discovered by Kammerlingh Onnes [31]. A borderline at 30 K separates the conventional, low- $T_c$  superconductors (LTSc) from the HTSc compounds [1].

The common feature of all the cuprate HTSc crystal structures is the layered structure consisting of several different plane layers. The most important one are the Cu–O-planes, which are considered to be the main superconducting highways. All other layers in the crystal structure serve as charge carrier reservoirs. The layered structure leads in turn to a high anisotropy of the superconducting properties [1–3], which causes interesting magnetic properties as discussed in Chap. 3. Another common issue for all cuprate superconductors is the fact that they are ceramic oxidic materials, and as consequence, the oxygen loading and oxygen distribution within the Cu–O-planes is an important issue for the resulting superconducting performance. A generic phase diagram of the HTSc materials is presented in Fig. 3 below. Depending on the hole concentration  $p$ , the material can be driven from an antiferromagnet (AF, with the corresponding Néel temperature  $T_N$ ) via a spin glass state to a superconductor, SC.

**Fig. 3** Generic phase diagram for cuprate HTSc showing temperature versus the charge carrier concentration (doping)



At temperatures above  $T_N$  or  $T_c$ , the compound may behave as “normal” metal, mostly as semiconductor [32, 33]. This coexistence of an antiferromagnetic state with superconductivity may be the key for the underlying pairing mechanism in the cuprate HTSc [34].

In this chapter, we discuss the crystal structures of the cuprate HTSc families and the resulting consequences, the microstructures and the important superconducting properties. Furthermore, we discuss the use of the cuprate HTSc in applications of superconductivity.

## 2 Crystal Structures of the Cuprate HTSc Families

The HTSc cuprate superconductors have either tetragonal or orthorhombic crystal structures, and their unit cells are formed by stacking various layers together along the  $c$ -direction, which causes the  $c$ -axis parameter to be much longer than the  $a$ - and  $b$ -axes. One or more Cu–O-planes that are present are particularly important, as they constitute the superconducting layers, where the mobile charge carriers (electrons or holes) reside and that undergo superconducting condensation when cooled below  $T_c$ . Other intervening metal oxide and pure metal layers are present as well, namely Tl–O, Bi–O, Hg–O, Ba–O, and Sr–O layers. Furthermore, Cu–O chains, and Y and Ca layers appear in the HTSc unit cells, which provide the necessary structural framework for the pertinent number of Cu–O-planes to exist. Several of the oxide layers (e.g., Tl–O, Bi–O, Hg–O layers and the Cu–O chains) exhibit a mixed-valence character, which makes them serve as charge reservoir layers supplying mobile carriers to the superconducting Cu–O-planes. At the same time, these layers render a low dimensionality to their electronic structure by serving as blocking or spacer layers between the superconducting layers. A negative consequence of the presence of such additional layers is that they weaken the electronic coupling along the  $c$ -direction to make the material quasi-two-dimensional, and thus promote a significant anisotropy in both the superconducting and normal states. The ratio of the normal-state resistivities along and perpendicular to the  $c$ -direction,  $\rho_c/\rho_{ab}$ , ranges from the order of  $10^2$

to the order of  $10^5$  and the critical current across the layers in the superconducting state can be orders of magnitude lower than in the  $(a,b)$ -plane [20, 35]. This poses a serious constraint and a challenge for material science to prepare HTSc conductors achieving the high critical current densities,  $j_c$ , required for practical applications [36].

## 2.1 YBCO

We will start with the YBCO compound, which is the most important HTSc material for present-day's applications [23–25]. Interestingly enough, YBCO was the first HTSc material with  $T_c$  at 91 K, which is well above 77 K, the temperature of liquid nitrogen, allowing the operation of applications at this temperature. Starting from high pressure studies on LBCO, Chu et al. [8] noted a large and positive pressure coefficient of  $T_c$ , with the onset of superconductivity occurring at 52.5 K [37]. So, the idea was born to simulate this pressure in a chemical way (i.e., internal pressure) by replacing  $\text{La}^{3+}$  with the smaller  $\text{Y}^{3+}$  ion. The resulting material was a mixture of two phases, the superconducting (black) YBCO and the green (insulating)  $\text{Y}_2\text{BaCuO}_5$  (Y-211) phase [5]. This phase mixture is still an important issue to create a reasonable amount of flux pinning sites in the 123-compounds today [38].

The unit cell of  $\text{YBaCuO}_{6+y}$  possesses double Cu–O-planes and a single plane with Cu–O-chains as shown in Fig. 4 for  $y = 0.5$  (double unit cell),  $y = 0.7$  and  $y = 1.0$ . YBCO has an orthorhombic unit cell (i.e.,  $a \neq b$ ) for  $y = 0.5$  to 1.0, and a tetragonal one ( $a = b$ ) below 0.5. The material is optimally doped at  $y = 1.0$  (that is,  $\text{O}_7$ ), and is underdoped for all other  $y$  [39–41]. This is further illustrated in Fig. 5

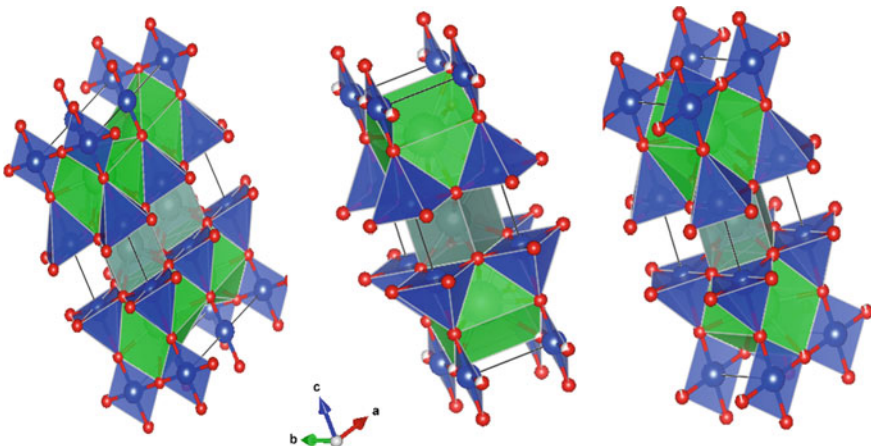
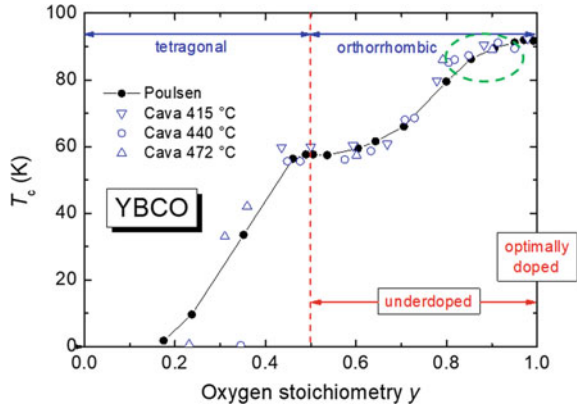


**Fig. 4** Crystal structures of YBCO compounds depending on the oxygen content,  $y$ , ranging from  $y = 0.5$  (half doped) via  $y = 0.7$  (underdoped) to  $y = 1.0$  (optimally doped)

**Fig. 5**  $T_c$  as function of the oxygen content (redrawn with permission from Ref. [40]). Below  $y = 0.5$ , YBCO is tetragonal, above orthorhombic. YBCO is optimally doped at  $y = 1$ , otherwise only underdoped. The green circle marks the range where  $\delta T_c$ -pinning can appear (fishtail effect in the MHLs)



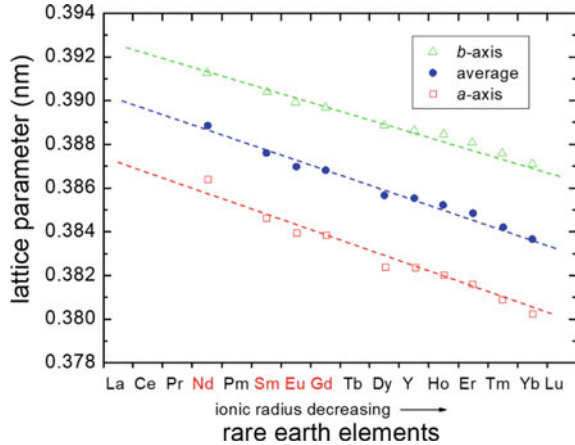
below. Practically, to reach full oxygen loading, long times are required (diffusion), so this poses a problem when fabricating large sample sizes like YBCO bulks [42]. Note also that it is not possible to create an overdoped YBCO superconductor by oxygen loading.

The consequence of all this is a strong dependence of YBCO on the oxygen loading achieved. In [40], Poulsen et al. have shown by experimental neutron scattering data and simulations that the oxygen atoms have a strong tendency to form chains in the Cu–O-planes. In the state  $y = 0.5$ , every second row of oxygen atoms is unoccupied, thus the doubling of the unit cell to describe this situation properly. A slight oxygen deficiency is already sufficient to reduce  $T_c$ , which poses a big problem when investigating the surface of an YBCO crystal under UHV conditions, e.g., by STM [43, 44]. For  $y < 1$ , regions with lower  $T_c$  (= broken chains) are embedded in the YBCO<sub>7</sub> matrix when being close to optimal doping. If these regions are of similar size to  $\xi$ , then the order parameter only varies slightly, but if the regions are larger than  $2\xi$ , so-called  $\delta T_c$ -pinning sites [45, 46] may be formed, and the corresponding magnetization loops may show the so-called fishtail effect [45, 47]. The resulting fishtail effect is only weak, and further oxygen loading may completely remove this peculiar shape of the MHLs again in ultrapure single crystals [48]. The region, where this can happen, is marked by the green dashed circle in Fig. 5 below. In this sense, an YBCO crystal with  $y < 1$  can be seen as a granular material on the nanoscale, which confirms the early observations of Däumling et al. [49].

In subsequent experiments, it was soon realized that the formation of the high- $T_c$  phase was not confined to  $Y^{3+}$  alone, but, a superconducting RE-123 family could be created [50] with nearly all lanthanides RE, except Ce and Tb, resulting in non-superconducting multi-phases. This is commonly attributed to their relatively bigger ion size (see also Fig. 6). The case of Pr was long debated in the literature, but the final conclusion is that also Pr does not yield a superconducting material [51, 52].

Figure 6 presents the lattice parameter of the RE-BCO unit cells for the rare earth elements in the order of their ionic radius, compiled from literature data. Erbe et al. [53] also showed recently the lattice parameter of the two most important

**Fig. 6** Lattice parameter of RE-BCO depending on the ionic radius of the RE ions, (data were collected from Ref. [53]). The four *LRE* elements are marked in red. Pr, Tb and Ce do not form HTSc materials, Pm is radioactive



substrates for thin film production, SrTiO<sub>3</sub> (STO) and LaAlO<sub>x</sub> (LAO), which are just engulfing the *RE*-BCO compounds, thus leading to some stress/strain in the thin film samples. The quest to further enhance the critical currents in the *RE*-BCO compounds, especially for large bulk samples, lead to interesting combinations of more than one *RE* element, leading to binary [54, 55], ternary [56, 57], and even to HEA-inspired (see Chap. 6) *RE*-BCO compounds with five *RE* elements [58], where the increased disorder on the Y-site provides new possibilities to design an appropriate material for applications with high current densities.

For the set of light rare earth elements (*LRE* = Nd, Sm, Eu and Gd), the ion size of the  $LRE^{3+}$ -ion becomes comparable to that of  $Ba^{2+}$ -ion. As result, the  $LRE^{3+}$ -ion can substitute  $Ba^{2+}$ , thus forming a *LRE*-rich compound with reduced superconducting properties ( $T_c \sim 65$  K) [59]. A controlled mixture of these two phases by dedicated processing steps enables increased flux pinning, at low temperatures by variation of the order parameter  $\xi$  ( $\delta T_c$ -pinning) and at elevated temperatures by magnetic-field induced pinning of the *LRE*-rich sites rendered normal. The final result are magnetization curves with a large secondary peak, i.e., strongly increased critical currents at elevated magnetic fields [46, 60]. In contrast to the fishtail effect caused by oxygen vacancies, this *LRE*-induced fishtail effect is very strong and also not reversible. All these observations nicely illustrate the importance of nanoengineering of flux pinning sites in the *RE*-BCO compounds to tailor the flux pinning properties and the resulting critical current densities [61].

The surface of NdBCO is reported to be much more stable as that of YBCO, so measurements within an UHV environment are possible [63]. Low-temperature scanning tunnelling spectroscopy (STS) was performed on high-quality, doped Nd-123 single-crystal samples [62] as shown in Fig. 7 with  $T_c$  values of 76 K (highly underdoped), 93.5 K (underdoped) and 95.5 K (optimally doped), respectively. The measurements were taken on an (*a*, *b*)-plane for the underdoped samples and on a (*b*, *c*)-plane for the optimally doped sample. From the  $dI/dV$ -curves obtained showing features like the conductance peaks (marked as P), dips (D) and humps (H), the

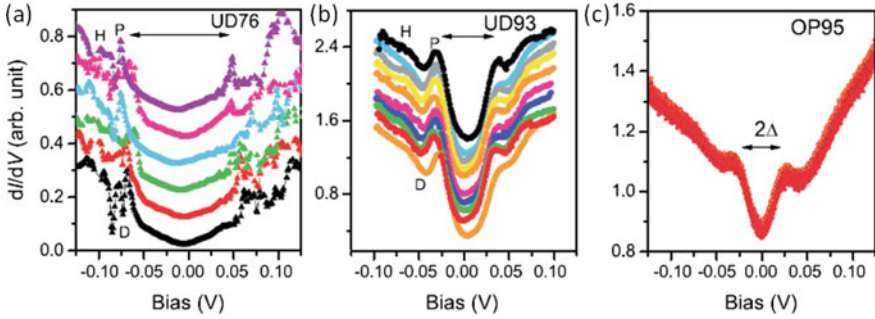


**Fig. 7** Representative  $dI/dV$ -curves obtained at  $T = 4.2$  K on NdBCO single crystals with  $T_c$  values of 76 K (highly underdoped, UD76, **a**), 93.5 K (underdoped, UD93, **b**) and 95.5 K (optimally doped, OP95, **c**). Spectra shown for UD76 were obtained along a 5 nm scan line and for UD93 they were obtained along a 20 nm scan line. The spectra shown for OP95 were obtained at the same location. The curves observed at different locations are staggered for clarity. Reproduced with permission from Ref. [62]

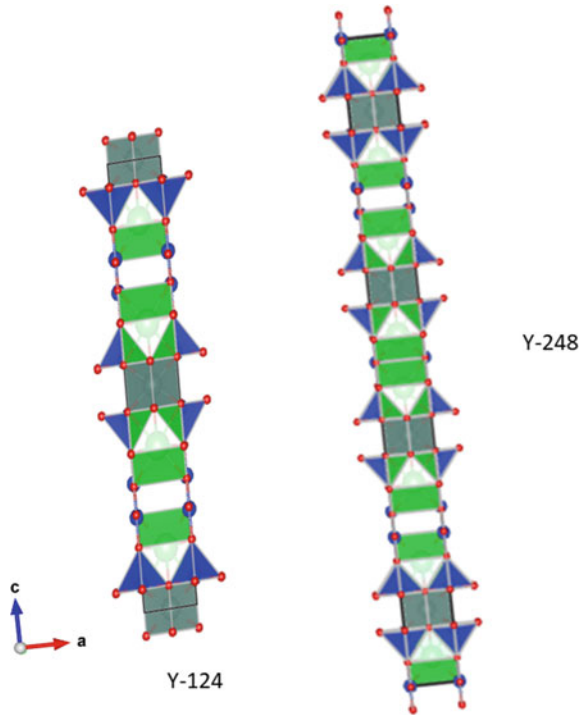
energy gap ( $2\Delta$ ) measured from peak-to-peak separation monotonically increases as the  $T_c$  values decrease monotonically due to underdoping. In detail, values of  $56 \pm 4$  meV for OP95,  $70.6 \pm 1.5$  meV for UD93 and  $117 \pm 25$  meV for UD76 were obtained. These values are in the range reported for both Bi-2212 and YBCO compounds [64].

The YBCO-family has two more members by created by adding additional layers to the original composition. The compound  $REBa_2Cu_4O_8$  (i.e., RE-124, where RE denotes any lanthanide other than Ce, Tb, or Pr) with  $T_c \sim 80$  K was subsequently discovered, which is an analogue of RE-123, but with an extra plane containing Cu–O chains [65], whereas a combination of the 123 and 124 systems turned out to be an ordered inter-growth in the form of the  $Y_2Ba_4Cu_7O_{15}$  (Y-247) system, which has a  $T_c$  of 95 K [66]. The crystal structures of Y-124 and Y-247 are presented in Fig. 8. Y-124 was found to appear as stacking fault in Y-123 crystals. The more complicated preparation route to achieve pure materials has excluded them from applications.

## 2.2 BSCCO Family

Starting from the LaSrCuO compound, Michel et al. [67] had found the  $T_c$  of several Bi–Sr–Cu–O compounds to range between 7 and 22 K, which later was raised even to 34 K. These findings suggested the replacement of the La-ion by Bi in LSCO, although the resulting crystal structure was found to be different from the original  $K_2NiF_4$  structure. The crystal structures of the BSCCO family are illustrated in Fig. 9, starting with the single CuO-layer ( $n = 1$ ) compound  $Bi_2Sr_2CuO_6$  (Bi-2201), having a  $T_c$  of  $\sim 25$  K. Subsequently Maeda et al. [9] found a substantially enhanced  $T_c$  of the order of 80–110 K for Bi–Sr–Ca–Cu–O (BSCCO), and the generic formula of

**Fig. 8** Crystal structures of the YBCO-family members, Y-124 and Y-247. Y-124 has an extra chain layer as compared to Y-123, and Y-247 is an intergrowth of both Y-123 and Y-124 phases



the BSCCO family turned out as  $\text{Bi}_2\text{Sr}_2\text{Ca}_{n-1}\text{Cu}_n\text{O}_{2n+4}$ . For the  $\text{Bi}_2\text{Sr}_2\text{CaCu}_2\text{O}_{8+d}$  (Bi-2212) compound with two ( $n = 2$ ) Cu-O-layers,  $T_c$  ranged from 85 to 95 K, while for  $\text{Bi}_2\text{Sr}_2\text{Ca}_2\text{Cu}_3\text{O}_{10+d}$  (Bi-2223) containing three ( $n = 3$ ) Cu-O-planes,  $T_c$  was up to 110 K [10]. A partial substitution of Bi by Pb,  $(\text{Bi,Pb})_2\text{Sr}_2\text{Ca}_2\text{Cu}_3\text{O}_{10+d}$ , was found to contribute to the phase stability in the processing steps [68]. Among the BSCCO family, the Bi-2212 compound has the highest anisotropy, which is the highest one of all HTSc compounds [20]. This leads, of course, to interesting consequences concerning the magnetic properties as discussed in Chap. 3.

Many of the superconducting and normal state properties of the BSCCO compounds were discussed in [70]. Important is here that in the BSCCO system underdoped, optimally doped and overdoped superconductors may be created, which enables to test the prediction of the phase diagram. Figure 10 illustrates how the resistivity curves will vary upon doping for the two situations, in-plane and out-of-plane. Thus, one can recognize, e.g., the optimally-doped situation directly from the resistivity measurement.

Figure 11 presents resistivity measurements carried out on optimally doped Bi-2212 as well as on underdoped material [71, 72]. The resistivity curve of the underdoped material is assumed to approach the pseudogap temperature,  $T^*$ , visualized by the first deviation from the otherwise linear behavior.

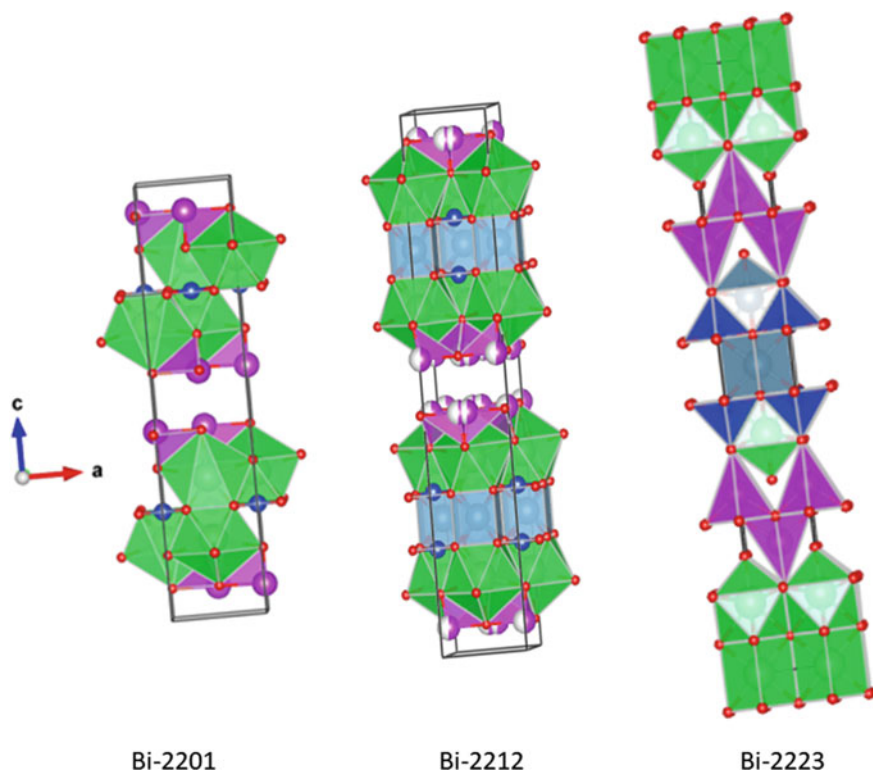


**Fig. 9** Crystal structures of members of the BSCCO HTSc family, Bi-2201, Bi-2212 and Bi-2223

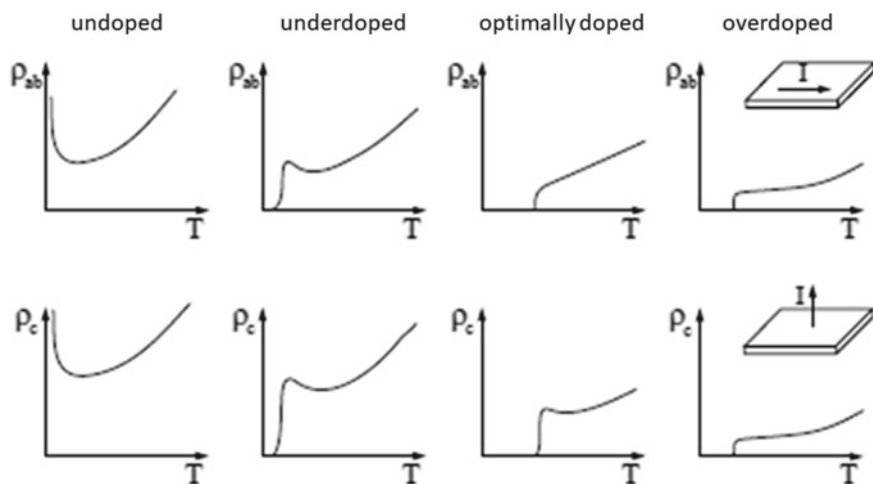
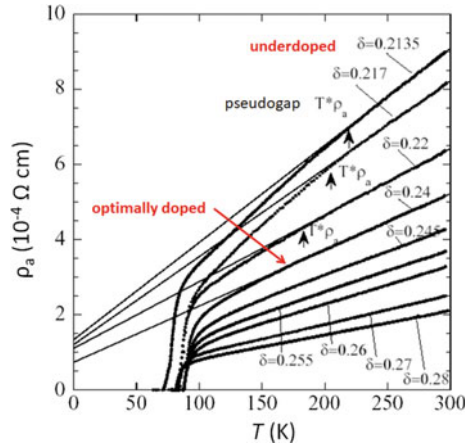


**Fig. 10** Schematic overview of the dependence of the measured resistivity on doping effects. The top row shows the in-plane resistivity, and the lower row the out-of-plane resistivity. The two insets illustrate the direction of the current,  $I$ . Reproduced with permission from Ref. [69]



**Fig. 11** Resistivities along the  $a$ -axis measured on Bi-2212 single crystals for various oxygen dopings,  $\delta$ . Optimally doped material ( $\delta = 0.24$ ) shows no extra kink at high  $T$  indicating the pseudogap temperature  $T^*$  (see also the phase diagrams), whereas underdoped material ( $\delta = 0.22-0.2135$ ) does. Reproduced from Ref. [72]



Furthermore, the BSCCO material is less sensitive to oxygen loss, so proper surfaces may be prepared by cleaving under UHV conditions, so high-resolution STM measurements became possible especially on the Bi-2212 system, revealing interesting physics. Figure 12 shows two so-called gap-maps as determined by STM/STS [73], where the superconducting gap is determined from  $I/V$ -curves measured locally by STS (see also Fig. 7) and then plotted as a function of position. These maps reveal the local variation of the superconducting gap size, and it is clearly visible that regions with similar gap sizes form clusters in both cases (a—underdoped) and (b—as grown, which is slightly overdoped). As seen before in the case of NdBCO, the

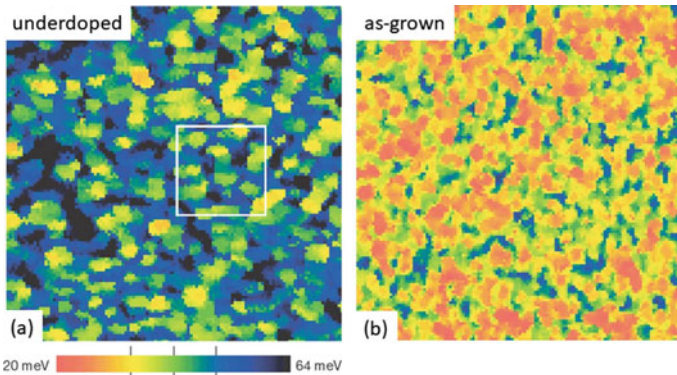


**Fig. 12** STM images (“gap maps”) of a Bi-2212 single crystal. **a** Shows an underdoped crystal, and **b** the as-grown state (which is, i.e., slightly overdoped). The color code for the superconducting gap is chosen to be the same for both images. The observation temperature was  $T = 4.2$  K; the image size is  $56 \times 56 \text{ nm}^2$ . The points in the white rectangle were further analyzed in [63]. Note that the gaps in (a) and (b) are quite different from each other, but in both cases, nanometer-sized areas of different gaps are visible in the images. Reproduced with permission from Ref. [73]

superconducting gaps of the underdoped samples are much larger as compared to the optimally doped or overdoped cases, the two maps differ in the size of the measured gaps, but show the same clustering.

The gap maps clearly demonstrate that oxygenation is creating a kind of internal granularity (i.e., a spatial variation of the superconducting gaps due to different oxygen content) on the nanometer scale even in high-quality single crystals. This important result should always be kept in mind when interpreting results of electric or magnetic measurements of superconducting properties of HTSc samples.

### 2.3 TIBCCO Family

By completely replacing Bi by Tl and Sr by Ba, that is, forming the Tl–Ba–Ca–Cu–O family (in short TBCCO), one may have single- or double-Tl-layered compounds [11] with the generic chemical compositions  $\text{TlBa}_2\text{Ca}_{n-1}\text{Cu}_n\text{O}_{2n+3}$  and  $\text{Tl}_2\text{Ba}_2\text{Ca}_{n-1}\text{Cu}_n\text{O}_{2n+4}$ , respectively. Crystal structures of the compounds Tl-1212, Tl-1223 and Tl-2212 are presented in Fig. 13.

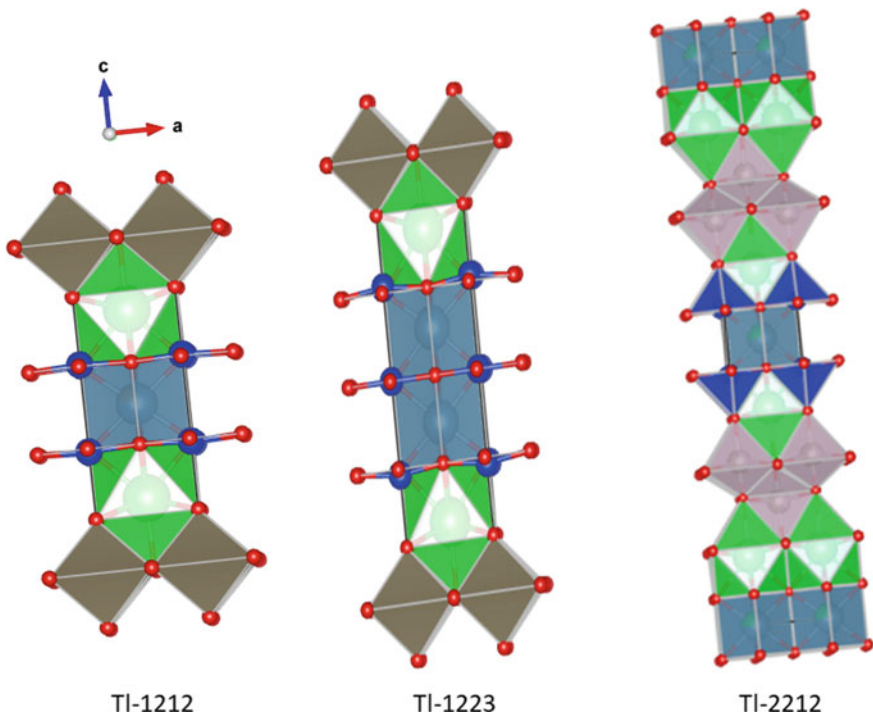


**Fig. 13** Crystal structures of the Tl-based HTSC family, showing the compounds Tl-1212, Tl-1223 and Tl-2212

As already seen in case of the BSCCO compounds, the nominal composition and the processing schedule influence the resulting  $T_c$  and the structural details of the synthesized phases of the TBCCO system. Most notable is here that among the single-Tl-layer compounds, Tl-1223 and Tl-1234 exhibit the highest  $T_c$  values of 133 K [12] and 127 K [74], respectively. Among the double-Tl-layer compounds, the two compositions Tl-2223 and Tl-2234 possess  $T_c$  values of 128 K [13] and 119 K [75], respectively. The structural, chemical and mechanical properties of the TIBCCO family were summarized by Bellingeri and Flükiger [76], including also the less common members of the family like Tl-1222, Tl-1234 and Tl-2234. The last two compounds exhibit even four Cu–O-layers per unit cell. The pressure dependence of  $T_c$  of the two compounds Tl-2223 (3 Cu–O-layers) and Tl-2234 exhibited a clear kink at  $\sim 12$  GPa [12], suggesting that the inner and outer Cu–O-layers, which are inequivalent (the inner layer has fourfold oxygen coordination, the outer ones fivefold), also behave differently under pressure. In ambient conditions, due to the only proximity weak coupling between the Cu–O-layers,  $T_c$  is determined by the Cu–O-layer with the highest intrinsic  $T_c$ .

Due to the high  $T_c$  and the lower anisotropy as compared to Bi-2212, it was attempted to fabricate powder-in-tube tapes, especially with the compound Tl-1223, which presented reasonably high irreversibility fields. However, the grain boundary weak link problem, which is essential for all HTSc compounds [77–79], led only to reduced critical current densities of these tapes [80], making them obsolete for applications. Furthermore, the compounds Tl-1212 and Tl-2212 were used for the fabrication of microwave devices, showing a low surface resistance in frequencies up to 10 GHz [81]. Another important obstacle is the toxicity and volatility of Tl, which is according to [76] controllable by taking specific measures and encapsulating the superconducting material like as is done in the Ag-sheathed tapes. However, extra costs caused by these procedures are hindering the applications of the TIBCCO compounds.

## 2.4 HgSCCO Family

The HgSCCO HTSc family is rich of members following the basic compositions  $\text{HgBa}_2\text{Ca}_{n-1}\text{Cu}_n\text{O}_{2n+3}$  and  $\text{Hg}_2\text{Ba}_2\text{Ca}_{n-1}\text{Cu}_n\text{O}_{2n+4}$  [14–16] describing single- and double-layered Hg systems. Figure 14 presents the crystal structures of the Hg-1201, Hg-1212 and Hg-1223 compounds. As pointed out already before, the single-Hg-layered compound Hg-1223 exhibiting three Cu–O planes ( $n = 3$ ) has a  $T_c$  of 134 K, but has manifested the highest  $T_c = 138$  K of all cuprate HTSc, when Hg is marginally replaced by 0.2% Tl. Now other material showed a higher  $T_c$  at ambient conditions, even to date.

Schwartz and Sastry [82] summarized the properties of the HgBCCO family members, and also the efforts made with the fabrication of thin films, thick films and tapes of the Hg-based compounds. Although the irreversibility lines of the undoped

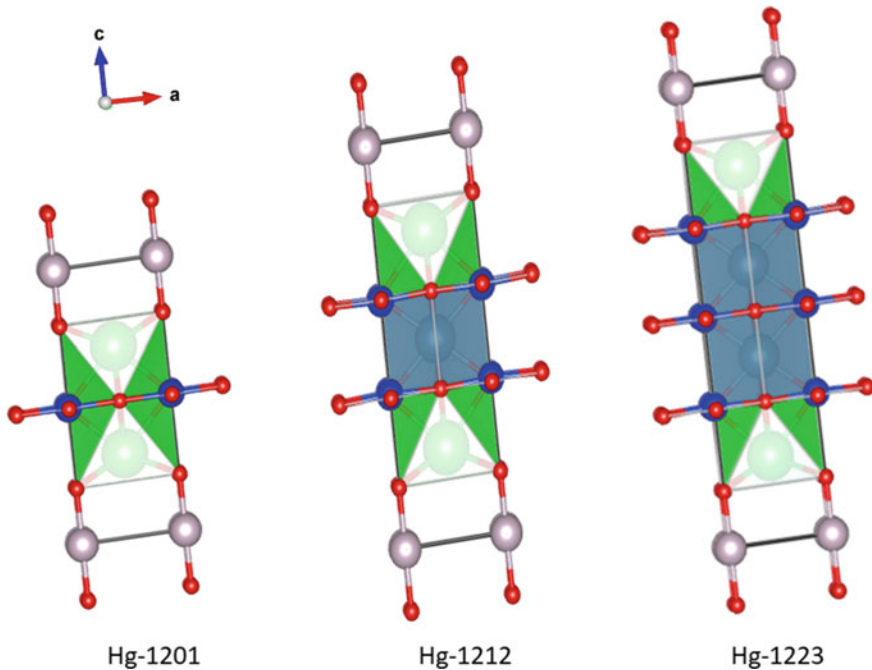


**Fig. 14** Crystal structures of the Hg-based HTSC family, showing the compounds Hg-1201, Hg-1212 and Hg-1223, the  $T_c$ -record holder for the cuprate HTSc

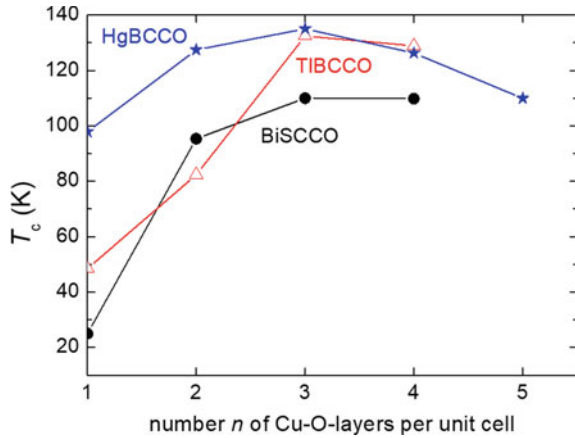
and doped  $\text{HgBa}_2\text{Ca}_{n-1}\text{Cu}_n\text{O}_{2n+2}$  compounds show the highest values for the irreversibility field at high temperatures of any known superconductor, it is only comparable to that of YBCO at 77 K. Furthermore, it was found that the position of  $B_{\text{irr}}(T)$  is strongly dependent upon added dopants, which is an important issue from both fundamental and technological points-of-view, offering possibilities to tailor the magnetic properties.

Plotting the irreversibility field,  $B_{\text{irr}}$ , versus the reduced temperature,  $T/T_c$ , it was shown that  $B_{\text{irr}}$  is above that of the Bi–Sr–Ca–Cu–O double layer compounds, but below the one of the YBCO compound [83]. This observation is thus consistent with the model that the irreversibility field as a function of normalized temperature is inversely proportional to the separation of the Cu–O-layer in the unit cell. As a consequence of the record-high  $T_c$ , the absolute value of  $B_{\text{irr}}(T)$  is as high as that of YBCO at 77 K, and consequently, above it for higher temperatures [84].

There have been several efforts in the literature to produce especially thin film materials of the HgBCCO family members, but overall, the fact that HgBCCO materials are not considered for practical applications demonstrates that  $T_c$  is not the decisive criterion for the use in applications, but the achievable critical current density,  $j_c$ .

Figure 15 shows the superconducting transition temperature,  $T_c$ , as a function of  $n$ , the number of Cu–O-layers per unit cell for the BSCCO, TIBCCO and HgBCCO

**Fig. 15**  $T_c$  as function of the layer number  $n$  of Cu–O-layers per unit cell of the BSCCO, TIBCCO and HgBCCO HTSc families. Data were collected from Ref. [85]



families. The highest  $T_c$ 's are obtained at  $n = 3$ , whereas an increase to 4 Cu–O-layers reduces  $T_c$  again, which is also a consequence of the inequality of the inner and outer Cu–O-layers as observed in the pressure experiments [12]. Nevertheless, it was attempted to create a so-called infinite layer compound,  $(\text{Sr}_{1-x}\text{Ca}_x)_{1-y}\text{CuO}_2$ , consisting of only Cu–O-layers in the literature, but the resulting  $T_c$  reached in first experiments hardly 45 K, but was reported to achieve 110 K in later experiments [86]. The fact that the infinite layer compound does not achieve a very high  $T_c$  proves the importance of the charge carrier reservoirs and spacer layers for the high- $T_c$  superconductivity in the other cuprate HTSc materials.

## 2.5 RE-214 Family

The general formula of the RE-214 family is  $\text{La}_{2-x}\text{M}_x\text{CuO}_4$  ( $M = \text{Ba}, \text{Sr}, \text{Ca}, \text{or Na}$ ; with  $x = 0.15\text{--}0.17$ ). This family was developed on the base of the first experiments by Bednorz and Müller [4], reaching a maximum  $T_c$  value of 38 K [6]. However, this was only the start of this HTSc family, which developed further into the most complete HTSc family with both hole-doped and electron-doped members. As the basic pairing mechanism for high- $T_c$  superconductivity is still unknown, the common opinion is that the Cu–O-planes play the key role, and these planes can be obtained by electron- or hole doping of the parent Mott insulator system. Thus, the finding in 1989 of true electron superconductors among the cuprate HTSc has significant implications for the understanding of HTSc superconductivity, allowing to test new and existing theories experimentally [21, 87, 88]. The first electron-doped analogue of the LSCO cuprate system was  $\text{RE}_{2-x}\text{M}_x\text{CuO}_{4-\delta}$  ( $\text{RE} = \text{rare earth elements Pr}^{3+}, \text{Nd}^{3+}, \text{Sm}^{3+}, \text{or Eu}^{3+}$ ; and  $M = \text{Ce}^{4+} \text{ or Th}^{4+}$ ; with the parameters  $x \approx 0.1\text{--}0.18$  and  $\delta \approx 0.02$ ). The highest  $T_c$  of this group was 25 K for the NCCO compound (i.e.,  $\text{Nd}_{2-x}\text{Ce}_x\text{CuO}_{4-\delta}$ ).

The electron-doped cuprate family does have the Cu–O-planes like the other cuprate HTSc, but the oxygen coordination is different. Figure 16 presents the crystal structure of NCCO (called T'-phase) in comparison with the other crystal structures (T-phase showing Cu–O octahedra) and the T\*-phase (showing Cu–O pyramids). While the hole-doped HTSc are either of the T or the T\*-phase type, the T'-phase is composed of sheets of Cu–O squares and has no apical oxygen atoms. As result, the T'-phase can only be doped by electrons [89]. Figure 17 gives the phase diagram for the RE-214 family, which is the most complete one of all cuprate HTSc families. There are two superconducting domes (SC) on each side of the diagram, separated by the antiferromagnetic (AF) phase. The resulting  $T_c$  values of the NCCO compounds are ranging only between 13 and 25 K, while the highest  $T_c$  of LaCCO of 30 K can only be stabilized in thin film form. These low  $T_c$ 's do not pose a problem for the basic research, but there are no envisaged applications of this cuprate HTSc family to date.

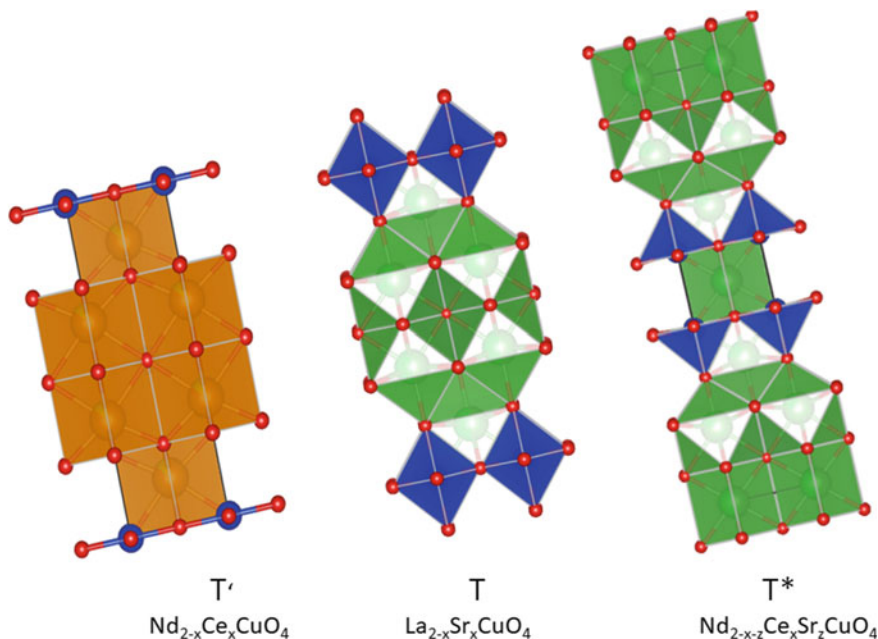
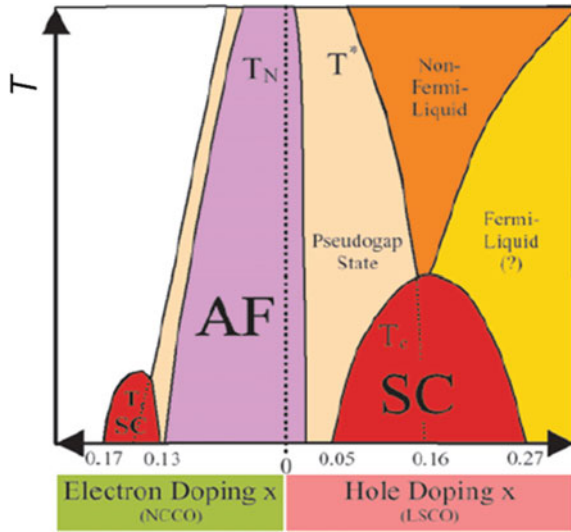


**Fig. 16** Crystal structures of the 214 HTSc family with the three compounds  $Nd_{2-x}Ce_xCuO_4$  (T'),  $La_{2-x}Sr_xCuO_4$  (T) and  $Nd_{2-x-z}Ce_xSr_zCuO_4$  (T\*)

**Fig. 17** Phase diagram of the RE-214 HTSc family with both hole-doping and electron doping. Superconducting states are obtained in the two red domes on both sides of the diagram, separated by the antiferromagnetic state. Reproduced with permission from Ref. [88]



### 3 Important Superconducting Properties and Typical Microstructures

The most important property for applications of superconductors is the achievable critical magnetic fields as those define in which fields the superconductor stays superconducting. However, as discussed in Chap. 3, the irreversibility fields are the ones limiting the superconducting performance of the HTSc materials. Thus, Fig. 18 presents the irreversibility fields,  $B_{irr}(T)$ , together with the  $B_{c2}(T)$ -lines for various HTSc materials. The  $B_{irr}(T)$ -line or often called irreversibility line (IL) gives the upper limit for possible applications as the flux pinning, and thus the critical currents, goes to zero at this line, but the material stays superconducting up to the upper critical field,  $B_{c2}(T)$ . The data presented are collected from various literature data [90, 91]. Here, one should note that the IL is always located much lower than the corresponding  $B_{c2}(T)$ , which is due to thermally activated flux creep, and the principal temperature dependence of both lines is supposed to be similar [45]. An exception to this rule occurs if there are anisotropy effects present, i.e., the rigid vortex lines are dissociating into vortex pancakes which only exist within the Cu–O-planes [92]. In this case, the temperature dependencies of the vortex state and the pancake state can be clearly different from each other, whereby the low temperature part corresponds to the ones of the less anisotropic samples.

This is, e.g., realized in the case of Bi-2212, where a clear change of shape of the IL below 20 K is visible in the diagram [91]. The effect is less pronounced in Bi-2223, which is accordingly also less anisotropic than Bi-2212. The  $B_{c2}(T)$ -lines of both materials are not shown, but  $B_{c2}(T)$  of Bi-2212 is almost similar to that of YBCO but reaching even higher fields at low  $T$ , so there is a huge differences between

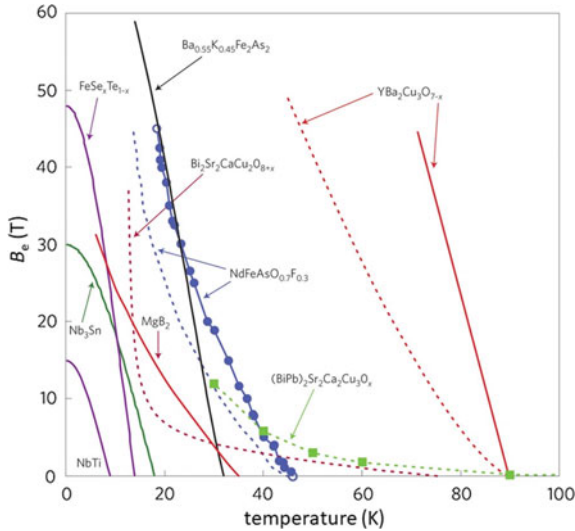


**Fig. 18** Diagram comparing the irreversibility fields,  $B_{irr}(T)$  and the upper critical fields,  $B_{c2}(T)$ , of various HTSc materials. The conventional LTSc alloys NbTi, Nb<sub>3</sub>Sn and MgB<sub>2</sub> are also included for comparison, and also NdFeAsO<sub>0.7</sub>F<sub>0.3</sub> and FeSe<sub>1-x</sub>Te<sub>x</sub>, which are two different types of iron-based superconductors. The full lines indicate the  $B_{c2}(T)$ -lines of a superconductor, and the dashed lines represent the irreversibility lines. Note the difference between  $B_{c2}(T)$  and  $B_{irr}(T)$  of Y-123, which reflects the effect of thermal fluctuations. The BSCCO materials show the effect of dimensionality. Reproduced with permission from Ref. [90]

the two lines. The ILs strongly depend on the experimental conditions, that is, the sweep rate of the external magnetic field or the current criterion employed in the measurements due to the thermally activated flux creep. Therefore, an analysis of the underlying pinning mechanism(s) by only measuring the IL is not straightforward. Table 1 presents the superconducting parameters of several HTSc materials [92], including the upper critical fields,  $B_{c2}$ , measured parallel ( $B_{c2}^{ab}$ ) and perpendicular ( $B_{c2}^c$ ) to the ( $a,b$ )-plane.

**Table 1** Superconducting parameters of several HTSc compounds. Data were collected from Ref. [69]

Cuprate	$T_c$ (K)	$\xi_{ab}$ (nm)	$\xi_c$ (nm)	$\lambda_{ab}$ (nm)	$\lambda_c$ (nm)	$B_{c2}^{ab}$ (T)	$B_{c2}^c$ (T)	$\kappa_{ab}$
LSCO	38	3.3	0.25	200	2000	80	15	61
NCCO	25	7–8	0.15	120	2600	7	–	15
YBCO	92	1.3	0.2	145	600	150	40	115
Bi-2212	95	1.5	0.1	180	700	120	30	120
Bi-2223	110	1.3	0.1	200	1000	250	30	150
Tl-1223	133	1.4	0.1	150	–	160	–	110
Hg-1223	134	1.3	0.2	177	3000	190	–	136



The data of Fig. 18 and of Table 1 now reveal that applications operating at 77 K demand the use of the RE-123 compounds, whereas tapes or wires of the BSCCO family require to be cooled down to at least 20 K [93], if not to 4.2 K, where the so much higher  $B_{c2}$  is justifying their use even as inset coils into conventional  $Nb_3Sn$  magnets.

To discuss the problems appearing for the use of RE-123 in applications, it is essential to have a closer look on the characteristic microstructure of the superconducting samples. When preparing HTSc superconductors in a solid-state reaction, the resulting material will be polycrystalline consisting of superconducting grains with typical sizes ranging between 1 and 20  $\mu\text{m}$ . When sending electric currents through such samples, one immediately realizes that only small currents can be sent without showing a too high resistance. The problems are due to the grain boundaries (GBs), which act as weak links for the current flow. Thus, to avoid the GBs, texture of the material is required, which is very demanding for the sample preparation, and lot of work in the field of HTSc was devoted to develop preparation techniques to achieve a good texture [76–78].

A first stage of microstructures is presented in Fig. 19, where single crystals and melt-textured RE-123 samples are shown [94–96]. The typical structure is caused by the twin boundaries, which appear in the sample preparation when cooling down the sample from close to the melting temperature. In this stage, RE-123 has the tetragonal crystal structure and is converted to orthorhombic by oxygen uptake, which is done

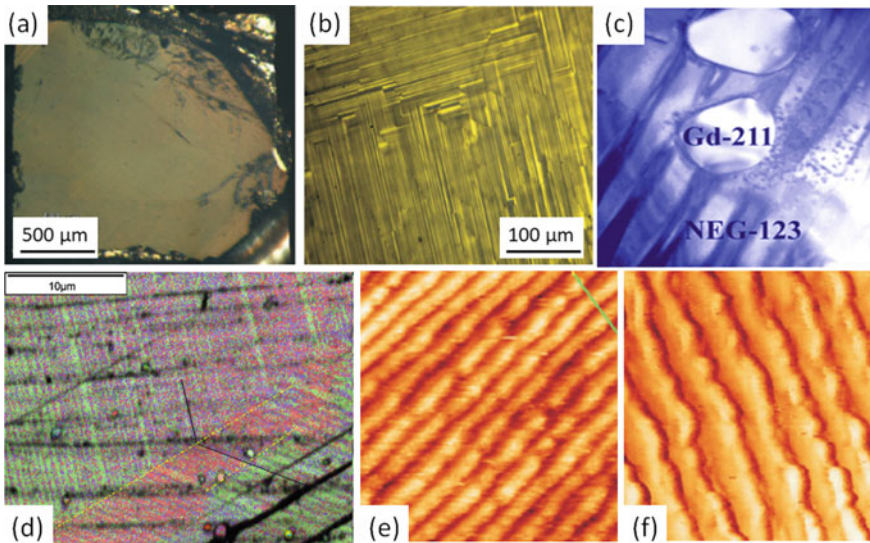


**Fig. 19** Various microstructures of YBCO samples. **a** Typical RE-123 single crystal, optical image [91]. **b** Polarization image of an  $(a,b)$ -surface revealing the twin structure [91]. **c** Twins and embedded Gd-211 particles in the superconducting matrix of NEG-123. **d** Analysis of the twin structure by means of EBSD. (Image **d**) was reproduced from Ref. [95]. **e** Nanostripes of SmBCO showing a regular pattern and **f** irregular pattern [91]

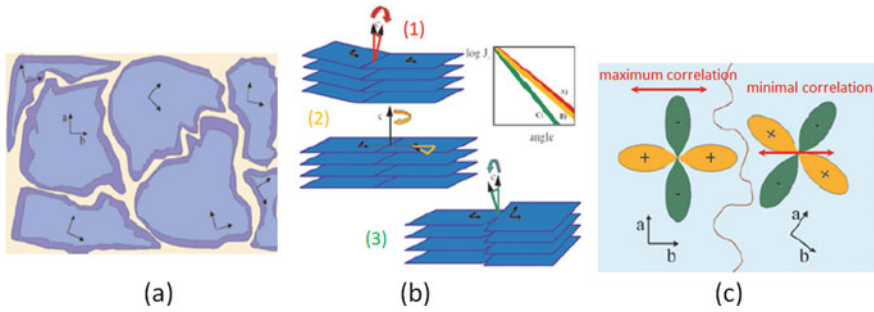


**Fig. 20** Illustrations to the GB problem of HTSc. **a** Gives a schematic view of a polycrystalline sample with grains of different orientations in blue. The border area of the grain (violet) can be oxygen-depleted. **b** Shows possible grain boundaries, (1) tilted, (2) rotated in plane and (3) distorted. The small graph indicates that currents are lowest for case (3). **c** Shows the cancelling effect as a reason for the weak link effect of the GBs regarding the superconducting phase (*d*-wave-symmetry). Reproduced with permission from Ref. [88]

mostly in a separate oxygen-loading step. The twins are  $90^\circ$ -twins by interchanging the *a*- and *b*-axis of the material, and form twin domains [90]. The twin boundaries are guiding the vortex motion in a superconducting sample, as moving along the twins is easier as crossing them. The border area of such twin domains is also a weak section, allowing penetrating flux to rush along there [97]. Thus, the twin pattern does have an influence on the magnetic properties of the RE-123 compounds. The nanostripes of some RE-BCO compounds are observable using AFM or STM at ambient conditions [96] and are created during the growth of the superconducting matrix, especially in the melt-growth techniques, which are applied to grow bulk samples. Also these nanostripes can influence the vortex motion as demonstrated in dedicated transport measurements [98].

The basic character of the GBs in all HTSc materials was topic of many research reports in the literature, and the output is summarized in [76–78]. Figure 20 gives a short overview of the GB problem. In (a), a typical polycrystalline sample is sketched schematically. The grains may have different orientations, and their border areas may be oxygen-depleted. Furthermore, some impurities or secondary phases may be found along the GBs. (b) shows three cases (1–3) of GBs, and the small inset indicates that the situation (3) is the worst for a transport current. Finally, (c) illustrates a possible explanation for the weak link character regarding the superconducting phase in each grain (*d*-wave character). The interaction between the two different phases reduces the currents through the GB as indicated; maximum correlation yields the highest current through the boundary, the minimal configuration the lowest.

Figure 21 presents a magneto-optical (MO) analysis of the flux penetration along GBs with different angles, which were obtained in YBCO thin films, deposited on respective bicrystal substrates [99]. The MO images demonstrate clearly that flux can easily rush along a GB if the misorientation is higher than  $5^\circ$ . Thus, it is obvious that achieving a good texture is essential to reach high critical current densities in HTSc samples.

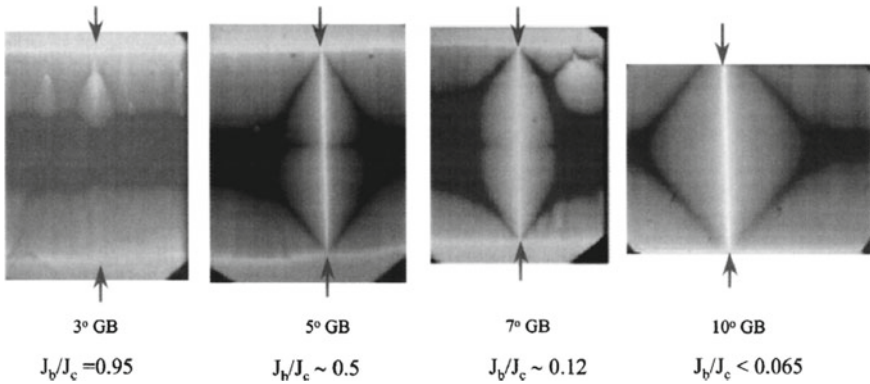


**Fig. 21** Magneto-optic observations of flux penetration a thin film along a GB with different angles. The current ratio,  $J_b/J_c$ , strongly reduces on increasing the angle. Reproduced with permission from Ref. [99]

### 4 HTSc Cuprates and Applications

Several new preparation techniques and approaches were developed since the discovery of the HTSc, with the main demand to achieve a good sample texture. Figure 22 presents several samples for applications of the RE-123 family. Image

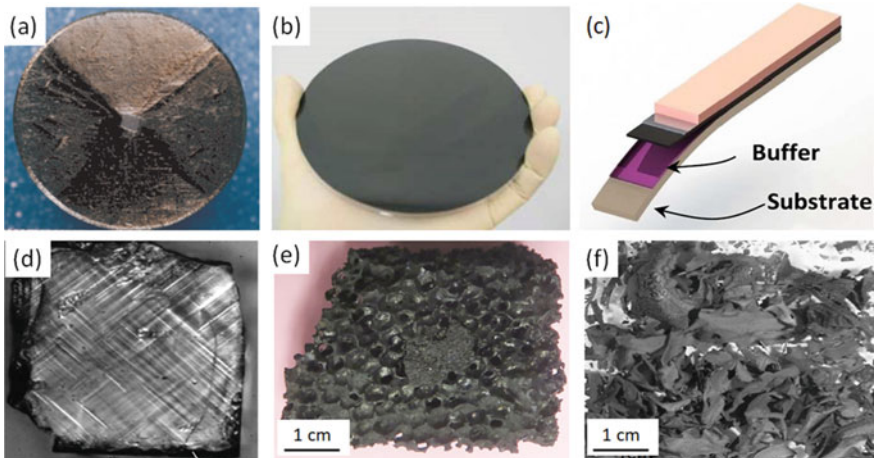


**Fig. 22** Typical samples of the RE-123 HTSc family for applications. **a** Melt-textured Gd-123 bulk (see the seed crystal in the sample center) [91]. **b** 15 cm-diameter YBCO thin film (Ceraco) [103]. **c** Sketch of YBCO coated conductor [104]. **d** Large twinned single crystal of NdBCO for basic research [105]. **e** Superconducting YBCO foam (details described in open accessed Ref. [106]), and **f** YBCO nanofiber mat [28]. Images c, d, and f were reproduced from Refs. [104, 105], and [28], respectively

(a) shows a melt-textured, bulk RE-123 sample with a typical diameter of 2 cm for laboratory use. This type of sample processing was discussed in Refs. [100, 101]. Nowadays, batch-processed samples with diameters up to 10 cm can be fabricated [102]. (b) presents a YBCO thin film sample with a diameter of 15 cm, fabricated by Ceraco [103]. (c) shows an YBCO coated conductor in uncovered state. The YBCO thick film is prepared by CVD on a metal substrate, requiring some intermediate buffer layers to get a suitable base for the growth of YBCO [104]. (d) presents a large, twinned single crystal of NdBCO [105] which is interesting for basic research, and (e) gives a superconducting, open-cell porous YBCO foam [106] and finally, (f) a solution-spun YBCO nanofiber mat [28, 107].

The last two sample types are porous materials, the advantages of which were discussed in Refs. [107, 108, 109]; the materials are light weight and exhibit improved oxygenation and cooling properties, avoiding the problems appearing when trying to increase to sample diameters further.

Figure 23 shows samples for applications from the BSCCO HTSc family. As it was most straightforward to use the powder-in-tube technique from the  $Nb_3Sn$ -fabrication also for HTSc, the Bi-2223 compound turned out to be more useful in tape form as YBCO due to the easier alignment of the elongated Bi-2223 grains during rolling and wire drawing. Tapes of this type could reach 1 km in length (a), and were thus the first choice for demonstrators for energy applications [110]. Bi-2212 wires

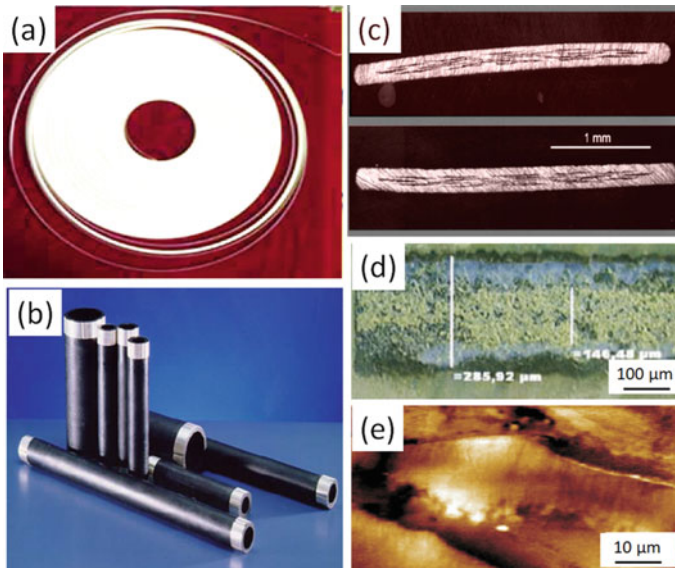


**Fig. 23** Samples and microstructures of the BSCCO family for applications. **a** First-generation silver-sheathed Bi-2223 tape [110], **b** melt-cast Bi-2212 samples for current leads (Nexans, [112]). **c** presents the cross-sections of multifilamentary Bi-2223 tapes, image from [113], **d** an extracted filament, and **e** an AFM topography image of the Bi-2223 grains. Images (d) and (e) were reproduced from Ref. [114]

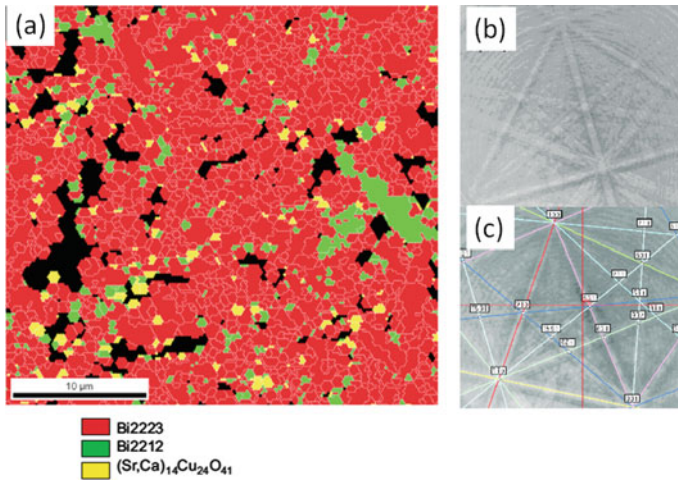


**Fig. 24** **a** EBSD-analysis of a section of a Bi-2223 tape, showing the phase map (color code below the map) together with the EBSD-detected GBs (marked white). Reproduced with permission from Ref. [116]. **b** Kikuchi pattern of the Bi-2223 phase and **c** indexation

were also fabricated in the same way for high-field applications at low temperatures [111], and melt-cast Bi-2212 samples (b) could be used for current leads [112]. Image (c) gives two cross-sections of Bi-2223 multifilamentary tape [113], (d) presents an optical image of an extracted filament and an AFM topography image [114].

Here, it must be mentioned that the microstructure of the HTSc samples requires nanoengineering, as the flux pinning sites should be of a size comparable to  $2\xi$ , and thus, the size of the optimum flux pinning sites is about 10 nm [61, 115]. The consequence of this is that also the required analysis techniques are pushed to their limits. A typical example for a dedicated sample analysis is presented in Fig. 24 as performed in [116].

The electron backscatter diffraction (EBSD) technique developed into a routine tool to investigate the nanostructures of ceramic materials during the development of the HTSc conductors and could thus deliver important contributions to it [116–118]. The main problem for the fabrication of HTSc wires or tapes is now to maintain control on the nanoscale while preparing meter-long materials. All the efforts made are summarized in [119–123]. Thus, the preparation of HTSc samples for applications is still a demanding challenge for further research and development.

## 5 Conclusion

The present chapter has shown the crystal structures of all the important HTSc family members and discussed the respective properties due to the nature of being ceramic oxidic materials. Thus, effects of doping, oxygen-loading and –depletion play an

important role for the superconducting performance of the cuprate HTSc samples. The cuprate HTSc are still the only superconducting materials enabling applications of superconductivity at 77 K with liquid nitrogen as coolant. Samples for applications come mainly from the RE-123 family and of the BSCCO family, whereas the TlBCCO and HgBCCO families are not considered for applications despite their much higher  $T_c$ -values. The main reason for this is the grain boundary problem, from which all cuprate HTSc suffer. This also lines out that achieving good sample textures in the sample fabrication is an essential task to obtain high critical current densities demanded for the applications. To do so, not only the preparation techniques had to be developed or to be improved, but also the required analysis and characterization techniques required further development in order to enable nanoengineering of the flux pinning sites within the HTSc materials.

All the images of crystal structures were prepared using the software VESTA [124].

## References

1. A.V. Narlikar, *Superconductors* (Oxford University Press, Oxford, U.K., 2014)
2. W. Buckel, R. Kleiner, *Supraleitung. Grundlagen und Anwendungen*, 7th edn (Wiley-VCH, Weinheim, 2013)
3. K.H. Bennemann, J.B. Ketterson (eds.), *Superconductivity* (Springer, Berlin, Heidelberg, Germany, 2008)
4. K.A. Müller, J.G. Bednorz, Possible high  $T_c$  superconductivity in the Ba-La-Cu-O system. *Z. Phys. B* **64**, 189–193 (1986)
5. R. Hazen, *Superconductors: The Breakthrough* (Summit Books, N.Y., USA, 1988)
6. H. Takagi, S. Uchida, K. Kitazawa, S. Tanaka, High- $T_c$  Superconductivity of La-Ba-Cu Oxides. II.—Specification of the Superconducting Phase. *Jpn. J. Appl. Phys.* **26**, L123–L124 (1987)
7. M.K. Wu, J.R. Ashburn, C.J. Torng, P.H. Hor, R.L. Meng, L. Gao, Z.J. Huang, Y.Q. Wang, C.W. Chu, Superconductivity at 93 K in a new mixed-phase Y-Ba-Cu-O compound system at ambient pressure. *Phys. Rev. Lett.* **58**, 908–910 (1987)
8. C.W. Chu, P.H. Hor, R.L. Meng, L. Gao, Z.J. Huang, Y.Q. Wang, Evidence for superconductivity above 40 K in the La-Ba-Cu-O compound system. *Phys. Rev. Lett.* **58**, 405–407 (1987)
9. H. Maeda, Y. Tanaka, M. Fukutomi, T. Asano, A new high- $T_c$  oxide superconductor without a rare earth element. *Jpn. J. Appl. Phys.* **27**, L209–L210 (1988)
10. H.W. Zandbergen, Y.K. Huang, M.J.V. Menken, J.N. Li, K. Kadowaki, A.A. Menovsky, G. van Tendeloo, S. Amelinckx, Electron microscopy on the  $T_c = 110$  K (midpoint) phase in the system  $\text{Bi}_2\text{O}_3\text{-SrO-CaO-CuO}$ . *Nature* **332**, 620–623 (1988)
11. Z.Z. Sheng, A.M. Hermann, Bulk superconductivity at 120 K in the Tl-Ca/Ba-Cu-O system. *Nature* **332**, 138–139 (1988)
12. D. Tristan Jover, R.J. Wijngaarden, R. Griessen, E.M. Haines, J.L. Tallon, R.S. Liu, Pressure dependence of the superconducting critical temperature of  $\text{Tl}_2\text{Ba}_2\text{Ca}_2\text{Cu}_3\text{O}_{10+y}$  and  $\text{Tl}_2\text{Ba}_2\text{Ca}_3\text{Cu}_4\text{O}_{12+y}$  up to 21 GPa. *Phys. Rev. B.* **54**, 10175–10185 (1996)
13. A. Iyo, Y. Tanaka, Y. Ishiura, M. Tokumoto, K. Tokiwa, T. Watanabe, H. Ihara, Study on enhancement of  $T_c$  ( $\geq 130$  K) in  $\text{TlBa}_2\text{Ca}_2\text{Cu}_3\text{O}_y$  superconductors. *Supercond. Sci. Technol.* **14**, 504–510 (2001)
14. S.N. Putilin, E.V. Antipov, O. Chrnaissem, M. Marezio, Superconductivity at 94 K in  $\text{HgBa}_2\text{CuO}_{4+\delta}$ . *Nature* **362**, 226–228 (1993)

15. A. Schilling, M. Cantoni, J.D. Guo, H.R. Ott, Superconductivity above 130 K in the Hg–Ba–Ca–Cu–O system. *Nature* **363**, 56–58 (1993)
16. K.A. Lokshin, D.A. Pavlov, S.N. Putilin, E.V. Antipov, D.V. Sheptyakov, A.M. Balagurov, Enhancement of  $T_c$  in  $\text{HgBa}_2\text{Ca}_2\text{Cu}_3\text{O}_{8+\delta}$  by fluorination. *Phys. Rev. B* **63**, 064511 (2001)
17. L. Gao, Superconductivity up to 164 K in  $\text{HgBa}_2\text{Ca}_{m-1}\text{Cu}_m\text{O}_{2+2+\delta}$  ( $m = 1, 2, \text{ and } 3$ ) under quasihydrostatic pressures. *Phys. Rev. B* **50**, 4260–4263 (1994)
18. A.P. Drozdov, M.I. Eremets, I.A. Troyan, V. Ksenofontov, S.I. Shylin, Conventional superconductivity at 203 kelvin at high pressures in the sulfur hydride system. *Nature* **525**, 73–76 (2015)
19. A.P. Drozdov, P.P. Kong, V.S. Minkov, S.P. Besedin, M.A. Kuzovnikov, S. Mozaffari, L. Balicas, F.F. Balakirev, D.E. Graf, V.B. Prakapenka, E. Greenberg, D.A. Knyazev, M. Tkacz, M.I. Eremets, Superconductivity at 250 K in lanthanum hydride under high pressures. *Nature* **569**, 528–533 (2019)
20. A.V. Narlikar (ed.), *Frontiers in Superconducting Materials* (Springer, Berlin, Heidelberg, Germany, 2005)
21. Y. Tokura, H. Takagi, S. Uchida, A superconducting copper oxide compound with electrons as the charge carriers. *Nature* **337**, 345–347 (1989)
22. J.T. Markert, M.B. Maple, High temperature superconductivity in Th-doped  $\text{Nd}_2\text{CuO}_{4-y}$ . *Solid State. Commun.* **70**, 145–147 (1989)
23. B. Seeber (ed.), *Handbook of Applied Superconductivity* (IOP Publishing, Bristol, UK, 1999)
24. D.A. Cardwell, D.S. Ginley (eds.), *Handbook of Superconducting Materials* (CRC Press, London, U.K., 2002)
25. P. Seidel (ed.), *Applied Superconductivity* (Wiley-VCH, Weinheim, Germany, 2015)
26. E.S. Reddy, G.J. Schmitz, Superconducting foams. *Supercond. Sci. Technol.* **15**, L21–L24 (2002)
27. M.R. Koblishka, S. Pavan Kumar Naik, A. Koblishka-Veneva, M. Murakami, D. Gokhfeld, E.S. Reddy, G.J. Schmitz, Superconducting YBCO foams as trapped field magnetis. *Materials* **12**, 853 (2019)
28. X.L. Zeng, T. Karwoth, M.R. Koblishka, U. Hartmann, D. Gokhfeld, C. Chang, T. Hauet, Analysis of magnetization loops of electrospun nonwoven superconducting fabrics. *Phys. Rev. Mater.* **1**, 044802 (2017)
29. M. Rotta, L. Zadorosny, C.L. Carvalho, J.A. Malmonge, I.F. Malmonge, R. Zadorosny, YBCO ceramic nanofibers obtained by the new technique of solution blow spinning. *Ceram. Int.* **42**, 16230–16234 (2016)
30. L. Duband, Space cryocooler development. *Phys. Proc.* **67**, 1–10 (2015)
31. D. van Delft, P.H. Kes, The discovery of superconductivity. *Phys. Today* **63**, 38–43 (2010)
32. J.L. Tallon, Oxygen in high- $T_c$  cuprate superconductors, in *Frontiers in Superconducting Materials*, ed. by A.V. Narlikar (Springer, Berlin, Heidelberg, Germany, 2005)
33. Ø. Fischer, M. Kugler, I. Maggio-Aprile, C. Berthod, Scanning tunneling spectroscopy of high-temperatur superconductors. *Rev. Mod. Phys.* **79**, 353–419 (2007)
34. A. de Visser, Magnetic field–boosted superconductivity. *Phys. Today* **73**, 44–50 (2020)
35. A. Koblishka-Veneva, N. Sakai, S. Tajima, M. Murakami, YBCO, in *Handbook of Superconducting Materials*, ed. by D.A. Cardwell, D.S. Ginley (CRC Press, Boca Raton, USA, 2002)
36. D.C. Larbalestier, A. Gurevich, D.M. Feldmann, A. Polyanskii, High- $T_c$  superconducting materials for electric power applications. *Nature* **414**, 368–377 (2001)
37. C.W. Chu, P.H. Hor, R.L. Meng, L. Gao, Z.J. Huang, Superconductivity at 52.5 K in the lanthanum-barium-copper-oxide system. *Science* **235**, 567–569 (1987)
38. D.A. Cardwell, N. Hari Babu, Improved magnetic flux pinning in bulk RE(BCO) superconductors. *AIP Conf. Proc.* **986**, 543–550 (2008)
39. R.J. Cava, B. Batlogg, C.H. Chen, E.A. Rietman, S.M. Zahurak, D. Werder, Oxygen stoichiometry, superconductivity and normal state properties of  $\text{YBa}_2\text{Cu}_3\text{O}_{7-\delta}$ . *Nature* **329**, 423–425 (1987)

40. H.F. Poulsen, N.H. Andersen, J.V. Andersen, H. Bohr, O.G. Mouritsen, Relation between superconducting transition temperature and oxygen ordering in  $\text{YBa}_2\text{Cu}_3\text{O}_{6+x}$ . *Nature* **349**, 594–596 (1991)
41. N.H. Andersen, M. von Zimmermann, T. Frello, M. Käll, D. Mønster, P.-A. Lindgard, J. Madsen, T. Niemöller, H.F. Poulsen, O. Schmidt, J.R. Schneider, T. Wolf, P. Dosanjh, R. Liang, W.N. Hardy, Superstructure formation and the structural phase diagram of  $\text{YBa}_2\text{Cu}_3\text{O}_{6+x}$ . *Physica C* **317–318**, 259–269 (1999)
42. P. Diko, M. Kaňuchová, X. Chaud, P. Odier, X. Granados, X. Obradors, Oxygenation mechanism of TSMG YBCO Bulk Superconductor. *J. Phys. Conf. Ser.* **97**, 012160 (2008)
43. I. Maggio-Aprile, C. Renner, A. Erb, E. Walker, O. Fischer, Direct vortex lattice imaging and tunneling spectroscopy of flux lines on  $\text{YBa}_2\text{Cu}_3\text{O}_{7-\delta}$ . *Phys. Rev. Lett.* **75**, 2754–2757 (1995)
44. M. Maki, T. Nishizaki, K. Shibata, T. Sasaki, N. Kobayashi, Low temperature STM/STS of high- $T_c$  superconductors. *Physica C* **357–360**, 291293 (1995)
45. G. Blatter, M.V. Feigel'man, V.B. Geshkenbein, A.I. Larkin, V.M. Vinokur, Vortices in high-temperature superconductors. *Rev. Mod. Phys.* **66**, 1125–1388 (1994)
46. M.R. Koblischka, M. Murakami, Pinning mechanisms in bulk high- $T_c$  superconductors. *Supercond. Sci. Technol.* **13**, 738–744 (2000)
47. M. Jirsa, L. Püst, D. Dlouhy, M.R. Koblischka, Fishtail shape in the magnetic hysteresis loop for superconductor: Interplay between different pinning mechanisms. *Phys. Rev. B* **55**, 3276–3284 (1997)
48. A. Erb, J.-Y. Genoud, F. Marti, M. Däumling, E. Walker, R. Flükiger, Reversible suppression of the so-called fishtail effect in ultra pure single crystals of  $\text{YBa}_2\text{Cu}_3\text{O}_{7-\delta}$  achieved by proper oxygenation. *J. Low Temp. Phys.* **105**, 1023–1028 (1996)
49. M. Däumling, J.M. Seuntjens, D.C. Larbalestier, Oxygen-defect flux pinning, anomalous magnetization and intra-grain granularity in  $\text{YBa}_2\text{Cu}_3\text{O}_{7-\delta}$ . *Nature* **346**, 332–335 (1990)
50. P.H. Hor, R.L. Meng, Y.Q. Wang, L. Gao, Z.L. Huang, J. Bechtold, K. Forster, C.W. Chu, Superconductivity above 90 K in the square-planar compound system  $\text{ABa}_2\text{Cu}_3\text{O}_{6+x}$  with  $A = \text{Y, La, Nd, Sm, Eu, Gd, Ho, Er and Lu}$ . *Phys. Rev. Lett.* **58**, 1891–1894 (1987)
51. H.A. Blackstead, J.D. Dow, Implications of superconductivity of  $\text{PrBa}_2\text{Cu}_3\text{O}_7$ . *Solid State Commun.* **115**, 137–140 (2000)
52. P. Pęczkowski, P. Zachariasz, C. Jastrzębski, J. Piętosa, E. Drzymała, Ł. Gondek, On the superconductivity suppression in  $\text{Eu}_{1-x}\text{Pr}_x\text{Ba}_2\text{Cu}_3\text{O}_{7-\delta}$ . *Materials* **14**, 3503 (2021)
53. M. Erbe, P. Cayado, W. Freitag, K. Ackermann, M. Langer, A. Meledin, J. Hänisch, B. Holzapfel, Comparative study of CSD-grown REBCO films with different rare earth elements: processing windows and  $T_c$ . *Supercond. Sci. Technol.* **33**, 094002 (2020)
54. H.S. Chauhan, M. Murakami, Temperature-controlled tailoring of  $J_c(B)$ -properties in the Nd-Ba-Cu-O system. *Appl. Supercond.* **6**, 169–174 (1998)
55. T. Saitoh, K. Segawa, K. Kamada, N. Sakai, T. Segawa, S.I. Yoo, M. Murakami, Microstructures and superconducting properties of melt processed (RE,RE<sup>+</sup>)-Ba-Cu-O. *Physica C* **288**, 141–147 (1997)
56. M.R. Koblischka, M. Muralidhar, M. Murakami, Flux pinning in ternary ( $\text{Nd}_{0.33}\text{Eu}_{0.33}\text{Gd}_{0.33}$ ) $\text{Ba}_2\text{Cu}_3\text{O}_y$  melt-processed superconductors. *Appl. Phys. Lett.* **73**, 2351–2353 (1998)
57. M. Muralidhar, K. Suzuki, Y. Fukumoto, A. Ishihara, M. Tomita, Recent progress on batch processed large size LRE-123 bulk. *Physica C* **484**, 108–111 (2013)
58. Y. Shukunami, A. Yamashita, Y. Goto, Y. Mizoguchi, Synthesis of RE123 high- $T_c$  superconductors with a high-entropy-alloy-type RE site. *Physica C* **572**, 1353623 (2020)
59. M.J. Kramer, A. Karion, K.W. Dennis, M. Park, R.W. Mc Callum, Enhanced superconductivity in  $\text{Nd}_{1-x}\text{Ba}_2\text{-x}\text{Cu}_3\text{O}_{7-\delta}$  by low oxygen partial pressure annealing. *J. Electron. Mater.* **23**, 1117–1120 (1994)
60. M.R. Koblischka, Nanoengineering of flux pinning sites in high- $T_c$  superconductors. *Tsinghua Sci. Technol.* **8**, 280–291 (2003)
61. M.R. Koblischka, A. Koblischka-Veneva, M. Murakami, Nanosized pinning sites in HTSc compounds. *J. Supercond.* **17**, 373–377 (2004)



62. P. Das, M.R. Koblischka, T. Wolf, P. Adelman, U. Hartmann,  $T_c$ -dependence of energy gap and asymmetry of coherence peaks in  $\text{NdBa}_2\text{Cu}_3\text{O}_{7-\delta}$  superconductors. *Europhys. Lett.* **84**, 47004 (2008)
63. W. Ting, N. Koshizuka, S. Tanaka, Highly stable surfaces of  $\text{NdBa}_2\text{Cu}_3\text{O}_y$  single crystals. *Appl. Phys. Lett.* **72**, 2035–2037 (1998)
64. G. Deutscher, Coherence and single-particle excitations in the high temperature superconductors. *Nature* **397**, 410–412 (1999)
65. J.L. Tallon, D.M. Pooke, R.G. Buckley, M.R. Presland, F.J. Blunt,  $\text{R}_2\text{Ba}_4\text{Cu}_7\text{O}_{15-\delta}$ : A 92-K bulk superconductor. *Phys. Rev. B* **41**, 7220–7223 (1990)
66. J.-Y. Genoud, G. Triscone, A. Junod, J. Muller, Stability, superconducting and magnetic properties of  $\text{Y}_2\text{Ba}_4\text{Cu}_7\text{O}_x$  annealed under high oxygen pressure. *Physica C* **235–240**, 443–444 (1994)
67. C. Michel, M. Hervieu, M.M. Borel, A. Grandin, F. Deslandes, J. Provost, B. Raveau, Superconductivity in the Bi-Sr-Cu-O system. *Z. Phys. B* **68**, 421–423 (1987)
68. S.A. Sunshine, T. Siegrist, L.F. Schneemeyer, D.W. Murphy, R.J. Cava, B. Batlogg, R.B. van Dover, R.M. Fleming, S.H. Glarum, S. Nakahara, J.J. Krajewski, S.M. Zahurak, J.V. Waszczak, J.H. Marshall, L.W. Rupp, Jr., W.F. Peck, Structure and physical properties of single crystals of the 84-K superconductor  $\text{Bi}_{1.2}\text{Sr}_2\text{Ca}_{0.8}\text{Cu}_2\text{O}_{8+\delta}$ . *Phys. Rev. B* **38**, 893–896 (1988)
69. A. Mourachkine, *High Temperature Superconductivity in Cuprates. The Non-linear Mechanism and Tunneling Measurements* (Kluwer, London, U.K., 2002)
70. P.N. Mikheenko, K.K. Uprety, S.X. Dou, BSCCO, in *Handbook of Superconducting Materials*, ed. by D.A. Cardwell, D.S. Ginley (CRC Press: Boca Raton, USA, 2002)
71. T. Fujii, I. Terasaki, T. Watanabe, A. Matsuda, In-plane anisotropy on the transport properties in the modulated  $\text{Bi}_2\text{O}_2$ -based conductors Bi-2212 and Bi-Sr-Co-O. *Physica C* **378–381**, 182–186 (2002)
72. T. Watanabe, T. Fujii, A. Matsuda, Crystal growth and anisotropic transport properties of high- $T_c$  superconductors  $\text{Bi}_2\text{Sr}_2\text{Ca}_{n-1}\text{O}_{2n+4+\delta}$  ( $n = 2, 3$ ). arXiv:cond-mat/0401448v3 (2004)
73. K.M. Lang, V. Madhavan, J.E. Hoffman, E.W. Hudson, H. Eisaki, S. Uchida, J.C. Davis, Imaging the granular structure of high- $T_c$  superconductivity in underdoped  $\text{Bi}_2\text{Sr}_2\text{CaCu}_2\text{O}_{8+\delta}$ . *Nature* **415**, 412–416 (2002)
74. A. Iyo, Y. Aizawa, Y. Tanaka, Y. Ishiura, M. Tokumoto, K. Tokiwa, T. Watanabe, and H. Ihara, High-pressure synthesis of  $\text{Tl}_2\text{BaCa}_{n-1}\text{Cu}_n\text{O}_y$  ( $n = 3$  and 4) with  $T_c = 133.5$  K ( $n = 3$ ) and 127 K ( $n = 4$ ). *Physica C* **357–360**, 324–328 (2001)
75. X. Chen, C. Gong, Dependence of the superconducting transition temperature on the type and number of  $\text{CuO}_2$  layers in  $\text{Tl}_2\text{Ba}_2\text{Ca}_{n-1}\text{Cu}_{n2n+4-y}$ . *Phys. Rev. B* **59**, 4513–4523 (1999)
76. E. Bellingeri, R. Flükiger, TIBCCO, in *Handbook of Superconducting Materials*, ed. by D.A. Cardwell, D.S. Ginley (CRC Press: Boca Raton, USA, 2002)
77. S.E. Babcock, J.L. Vargas, Boundaries in the high- $T_c$  superconductors. *Annu. Rev. Mater. Sci.* **25**, 193–222 (1995)
78. H. Hilgenkamp, J. Mannhart, Grain boundaries in high- $T_c$  superconductors. *Rev. Mod. Phys.* **74**, 485–549 (2002)
79. J. Ayache, Grain boundaries in high temperature superconducting ceramics. *Phil. Mag.* **86**, 2193–2239 (2006)
80. R. Flükiger, R. Gladyshevskii, E. Bellingeri, Methods to produce Tl(1223) tapes with improved properties. *J. Supercond.* **11**, 23–26 (1998)
81. A. Sundaresan, H. Asada, A. Crisan, J.C. Nie, H. Kito, A. Iyo, Y. Tanaka, M. Kusunoki, S. Ohshima, Preparation of Tl-2212 and Tl-1223 superconductor thin films and their microwave surface resistance. *IEEE Trans. Appl. Supercond.* **13**, 2913–2916 (2003)
82. J. Schwartz, P.V.P.S.S. Sastry, TIBCCO, in *Handbook of Superconducting Materials*, ed. by D.A. Cardwell, D.S. Ginley (CRC Press: Boca Raton, USA, 2002)
83. U. Welp, G.W. Crabtree, J.L. Wagner, D.G. Hinks, Flux pinning and the irreversibility lines in the  $\text{HgBa}_2\text{CuO}_{4+\delta}$ ,  $\text{HgBa}_2\text{CaCu}_2\text{O}_{6+\delta}$  and  $\text{HgBa}_2\text{Ca}_2\text{Cu}_3\text{O}_{8+\delta}$  compounds. *Physica C* **218**, 373–378 (1993)

84. Z.J. Huang, Y.Y. Xue, R.L. Meng, C.W. Chu, Irreversibility line of the  $\text{HgBa}_2\text{CaCu}_2\text{O}_{6+\delta}$  high-temperature superconductors. *Phys. Rev. B* **49**, 4218–4221 (1994)
85. R. Hott, Material aspects of high temperature superconductors for applications, in *High Temperature Superconductivity I-Materials*, ed. by A.V. Narlikar (Springer, Berlin, Germany, 2004)
86. M. Azuma, Z. Hiroi, M. Takano, Y. Bando, Y. Takeda, Superconductivity at 110 K in the infinite-layer compound  $(\text{Sr}_{1-x}\text{Ca}_x)_{1-y}\text{CuO}_2$ . *Nature* **356**, 775–776 (1992)
87. B. Stadlober, G. Krug, R. Nemetschek, R. Hackl, J.L. Cobb, J.T. Markert, Is  $\text{Nd}_{2-x}\text{Ce}_x\text{CuO}_4$  a high-temperature superconductor? *Phys. Rev. Lett.* **74**, 4911–4914 (1995)
88. R. Hott, R. Kleiner, T. Wolf, G. Zwirgagl, Superconducting materials—a topical overview, in *Frontiers in Superconducting Materials*, ed. by A.V. Narlikar (Springer, Berlin, Heidelberg, 2005)
89. D. Lindner, Electron doped cuprates. [https://guava.physics.uiuc.edu/~nigel/courses/569/Essays\\_Spring2006/files/Lindner.pdf](https://guava.physics.uiuc.edu/~nigel/courses/569/Essays_Spring2006/files/Lindner.pdf). Accessed 22 Aug 2021
90. A. Gurevich, To use or not to use cool superconductors. *Nat Mater.* **10**, 255–259 (2011)
91. M.R. Koblischka, *Habilitation Thesis* (Saarland University, Saarbrücken, 2012)
92. J.R. Clem, Pancake vortices. *J. Supercond.* **17**, 613–629 (2004)
93. M.R. Koblischka, J. Sosnowski, Temperature-dependent scaling of pinning force data in Bi-based high- $T_c$  superconductors. *Eur. Phys. J. B* **44**, 277–280 (2005)
94. M. Muralidhar, M.R. Koblischka, M. Murakami, Embedding of 211 particles in NEG-123 superconductors. *Supercond. Sci. Technol.* **12**, 555–562 (1999)
95. A. Koblischka-Veneva, M.R. Koblischka, Analysis of twin boundaries using the electron backscatter diffraction (EBSD) technique. *Mat. Sci. Eng. B* **151**, 60–64 (2008)
96. M.R. Koblischka, M. Winter, U. Hartmann, Nanostripe structures in  $\text{SmBa}_2\text{Cu}_3\text{O}_x$  superconductors. *Supercond. Sci. Technol.* **20**, 681–686 (2007)
97. T. Schuster, M.R. Koblischka, H. Kronmüller, Magneto-optical imaging of Shubnikov phase. *J. Alloy Comp.* **195**, 483–490 (1993)
98. M.R. Koblischka, U. Hartmann, Evidence for a directed  $\delta T_c$ -type flux pinning by means of nanostripes in  $(\text{Sm}_{0.33}\text{Eu}_{0.33}\text{Gd}_{0.33})\text{Ba}_2\text{Cu}_3\text{O}_y$  high- $T_c$  superconductors. *Europhys. Lett.* **89**, 47002 (2010)
99. A.A. Polyanskii, A. Gurevich, A.E. Pashitski, N.F. Heinig, R.D. Redwing, J.E. Nordman, D.C. Larbalestier, Magneto-optical study of flux penetration and critical current densities in  $[001]$  tilt  $\text{YBa}_2\text{Cu}_3\text{O}_{7-\delta}$  thin-film bicrystals. *Phys. Rev. B* **53**, 8687–8697 (1996)
100. M. Murakami (ed.), *Melt Processed High Temperature Superconductors* (World Scientific, Singapore, 1991)
101. R. Tournier, E. Beaunon, O. Belmont, Processing of large  $\text{YBa}_2\text{Cu}_3\text{O}_{7-x}$  single domains for current-limiting applications. *Supercond. Sci. Tech.* **13**, 886–896 (2000)
102. D.K. Namburi, Y. Shi, D.A. Cardwell, The processing and properties of bulk (RE)BCO high temperature superconductors: current status and future perspectives. *Supercond. Sci. Technol.* **34**, 053002 (2021)
103. Ceraco ceramic coating. <https://www.ceraco.de>. Accessed 22 Aug 2021
104. V. Solovyov, P. Farrell, Exfoliated YBCO filaments for second-generation superconducting cable. *Supercond. Sci. Technol.* **30**, 014006 (2017)
105. M. Jirsa, M.R. Koblischka, T. Higuchi, M. Murakami, Effect of twin planes in the magnetization hysteresis loops of  $\text{NdBa}_2\text{Cu}_3\text{O}_7$  single crystals. *Phys. Rev. B* **58**, R14771–R14774
106. M.R. Koblischka, S. Pavan Kumar Naik, A. Koblischka-Veneva, M. Murakami, D. Gokhfeld, E.S. Reddy, G.J. Schmitz, Superconducting YBCO foams as trapped field magnets. *Materials* **12**, 853 (2019)
107. M.R. Koblischka, A. Koblischka-Veneva, Fabrication of superconducting nanowires using the template method. *Nanomaterials* **11**, 1970 (2021)
108. M.R. Koblischka, A. Koblischka-Veneva, Porous high- $T_c$  superconductors and their applications. *AIMS Mater. Sci.* **5**, 1199–1213 (2018)
109. D.M. Gokhfeld, M.R. Koblischka, A. Koblischka-Veneva, High-porous superconductors: synthesis, investigations and perspectives. *Phys. Met. Metall.* **121**, 1026–1038 (2020). ((in Russian))

110. L. Xiao, D. Zheng, P. Zhang, L. Lin, Recent research activities of applied superconductivity in China. Available at: [https://snf.ieeecsc.org/sites/ieeecsc.org/files/documents/snf/abstracts/ed3\\_XIAO-Presentation%20at%20ASC2016%20annotated\\_0.pdf](https://snf.ieeecsc.org/sites/ieeecsc.org/files/documents/snf/abstracts/ed3_XIAO-Presentation%20at%20ASC2016%20annotated_0.pdf). Accessed 01 Sept 2021
111. F. Kametani, J. Jiang, M. Matras, D. Abaimov, E.E. Hellstrom, D.C. Larbalestier, Comparison of growth texture in round Bi2212 and flat Bi2223 wires and its relation to high critical current density development. *Sci. Rep.* **5**, 8285 (2015)
112. J. Bock, F. Breuer, C.-E. Bruzek, N. Lallouet, M.O. Rikel, H. Walter, NEXANS activities and plans on HTS materials. High-performance Bi2212 tape and bulk conductors for magnet technology. Proc. WAMS 2004, 22–24.03.2004, Archamps, France. Available at: <https://www.yumpu.com/en/document/read/46876933/here-accelerator-magnet-technology-home-page-cern>. Accessed 01 Sept 2021
113. M.R. Koblishka, T.H. Johansen, H. Bratsberg, P. Vase, Study of flux entry and exit into Bi-2223 multifilamentary tapes. *Supercond. Sci. Technol.* **11**, 479–484 (1998)
114. A. Koblishka-Veneva, M.R. Koblishka, Surface preparation of high- $T_c$  superconductors for MO-imaging, in *Magneto-optical imaging*, ed. by T.H. Johansen, D.V. Shantsev (Kluwer academic Publishers, Dordrecht, The Netherlands, 2004), pp. 242–246
115. M.R. Koblishka, A. Koblishka-Veneva, Investigation of melt-textured superconductors on the nanoscale. *Mat. Sci. Eng. B* **151**, 47–52 (2008)
116. A. Koblishka-Veneva, M.R. Koblishka, T. Qu, Z. Han, F. Mücklich, Texture analysis of monofilamentary, Ag-sheathed (Pb, Bi)<sub>2</sub>Sr<sub>2</sub>Ca<sub>2</sub>Cu<sub>3</sub>O<sub>x</sub> tapes by electron backscatter diffraction (EBSD). *Physica C* **468**, 174–182 (2008)
117. A. Koblishka-Veneva, M.R. Koblishka, J. Schmauch, Y. Wan, J. Qian, X. Yao, EBSD characterization of specific microstructures in RE-BCO superconductors. *IEEE Trans. Appl. Supercond.* **29**, 6800504 (2019)
118. A. Koblishka-Veneva, M.R. Koblishka, J. Schmauch, M. Murakami, Secondary phase particles in bulk, infiltration-growth processed YBCO investigated by transmission Kikuchi diffraction and TEM. *Supercond. Sci. Technol.* **33**, 034010 (2020)
119. R.M. Scanlan, A.P. Malozemoff, D.C. Larbalestier, Superconducting materials for large scale applications. *Proc. IEEE* **92**, 1639–1654 (2004)
120. S.R. Foltyn, L. Civale, J.L. MacManus-Driscoll, Q.X. Jia, B. Maiorov, H. Wang, M. Maley, Materials science challenges for high-temperature superconducting wire. *Nature Mater.* **6**, 631–642 (2007)
121. M. Eisterer, S.H. Moon, H.C. Freyhardt, Current developments in HTSC coated conductors for applications. *Supercond. Sci. Technol.* **29**, 060301 (2016)
122. J.H. Durrell, M.D. Ainslie, D. Zhou, P. Vanderbemden, T. Bradshaw, S. Speller, M. Filipenko, D.A. Cardwell, Bulk superconductors: a roadmap to applications. *Supercond. Sci. Technol.* **31**, 103501 (2018)
123. A. Bussmann-Holder, H. Keller, High-temperature superconductors: underlying physics and applications. *Z. Naturforschung* **75**, 3–14 (2020)
124. K. Momma, F. Izumi, VESTA 3 for three-dimensional visualization of crystal, volumetric and morphology data. *J. Appl. Crystallogr.* **44**, 1272–1276 (2011)

# Noncuprate Superconductors: Materials, Structures and Properties



Soubhik Bhattacharyya and P. M. Sarun

**Abstract** This chapter briefly deals with the structures, properties, and applications of some of the well-studied classes of non-cuprate superconductors. The chapter begins with a brief discussion on low- $T_c$  superconductors, such as superconducting elements, A-15 superconductors, superconducting binary compounds, etc. In the next part of the chapter, two important classes of superconductors have been discussed— $MgB_2$  and iron-based superconductors. These two classes are probably the most widely studied non-cuprate superconductors around the globe in the last two decades. Electronic bandstructure, the impacts of doping on superconducting characteristics of  $MgB_2$ , etc., have been dealt with in detail. Structural, magnetic, superconducting properties at ambient and non-ambient pressures of various iron-based superconductors have been reviewed on iron-based superconductors. Subsequently, other classes of superconductors like superconducting nickelates, oxide superconductors, organic superconductors, Chevrel phases, heavy-fermion superconductors, etc., have been included. Among them, nickelate superconductors are the most recently discovered class of superconductors. In the last section, a brief history of the invention of superconductivity near ambient temperature in the metal hydrides has been discussed.

**Keywords** Superconductors · Non-cuprate ·  $MgB_2$  · Iron-based superconductors · Superconducting properties · Crystal structure

## 1 Introduction

The complete absence of electrical resistance in pure metal was first discovered in 1911 by Heike Kamerlingh Onnes [1] and his research group. They successfully investigated the properties of matter at low temperatures, which led to the liquefaction of liquid Helium. They detected a sharp drop of resistance of mercury at 4.2 K. The new phenomenon was termed superconductivity. Hence, the state of matter is known as the superconducting state. The temperature at which the phase transition

---

S. Bhattacharyya · P. M. Sarun (✉)  
Department of Physics, Indian Institute of Technology (Indian School of Mines), Dhanbad,  
Jharkhand 826004, India  
e-mail: [sarun@iitism.ac.in](mailto:sarun@iitism.ac.in)

occurs from the normal state to the superconducting state is the critical temperature or transition temperature ( $T_c$ ). Indeed, this disagrees with the postulate that the resistance in metal would stay finite at zero Kelvin. Meissner and Ochsenfeld [2] discovered perfect diamagnetism in the superconducting state in 1933, which is unique in elemental superconductors. The external weak magnetic field is expelled in the superconducting state, which is later known as the Meissner effect.

Numerous theories developed to explain the phenomenon of superconductivity. Most prominent among them are phenomenology theory by F. and H. London [3], semi phenomenology theory by Ginzburg and Landau [4], and the microscopic theory, known as BCS theory, hypothesized by Bardeen, Cooper, and Schrieffer [5] in 1957. Ginzburg–Landau’s (GL) theory divides the superconductors into type-I and type-II based on their behavior in an external magnetic field. BCS theory explains the mechanism of superconductivity in the elemental superconductors and few classes of the low- $T_c$  superconductors. These are known as conventional superconductors or BCS superconductors. Nevertheless, most of the superconductors, especially the high- $T_c$  superconductors, are unconventional superconductors. The BCS theory can not explain the mechanism of superconductivity in these compounds.

After discovering superconductivity, many new families of superconductors have been discovered in the last century. At present, there are several thousands of known superconducting compounds exist. In this chapter, only a few well-studied and technologically essential classes of non-cuprate superconductors have been discussed briefly.

## 2 Low- $T_c$ Superconductors

### 2.1 *Superconducting Elements*

After almost two years of discovering elemental superconductivity in mercury in 1911 [1], another two elements, Sn and Pb, were found to be superconducting at 3.7 K and 7.2 K, respectively [6]. Today, 31 elements are known to be superconducting at ambient pressure (the elements are shown in yellow color in the periodic table of Fig. 1). Several elements (around 21 at the moment of writing) superconduct under high pressure or when made into thin films (The elements shown in blue in the periodic table). However, noble metals—copper, silver, gold—which are excellent conductors of electricity at room temperature never become superconducting.

The mechanism of superconductivity in the elements can be explained based on the electron–phonon interaction described in conventional BCS theory, i.e., the cooper pairs form via electron–phonon coupling. Most of the elemental superconductors are type-I superconductors. None of the pure elemental superconductors is suitable for large-scale practical applications.

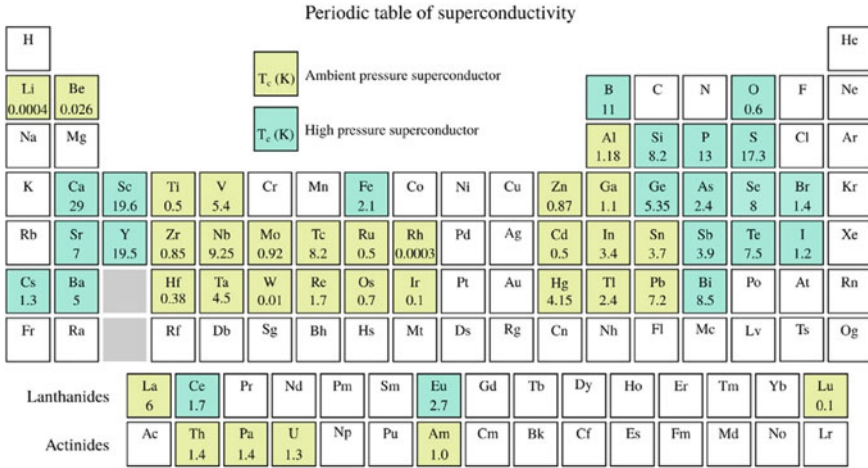


**Fig. 1** Periodic table showing the elements exhibiting superconductivity and their  $T_c$ . Reproduced from Ref. [7]

## 2.2 Binary Alloys and Stoichiometric Compounds

### 2.2.1 A-15 Superconductors

The compounds, having the structure  $A_3B$ , where A is a transition metal, namely, Ta, V, Nb, Zr, etc., and B is a non-transition element, namely, Sn, Ge, Al, Si, etc., are denoted as A-15 in crystallography. In 1953, Hardy and Hulm discovered superconductivity in a compound with an A-15 structure in  $V_3Si$  with  $T_c$  at 17.1 K [8]. Table 1 shows the superconducting characteristics of some A-15 compounds. Until discovering high- $T_c$  cuprates, the record for the highest  $T_c$  transition temperature was claimed by A-15 superconductors. The transition temperature of A-15 compounds is highly susceptible to the change in 3:1 stoichiometry [9].

Figure 2a shows the typical crystal structure of  $A_3B$  compounds. The structure is elucidated with the formation of one-dimensional chains by the A-atoms in the

**Table 1** Basic superconducting properties of some A-15 compounds. Data were taken from Refs. [8, 10–16]

Materials	$T_c$ (K)	$H_{c2}$ (T)	Gap ratio ( $2\Delta/KT_c$ )
$V_3Si$	17.1	22	$3.5 \pm 0.2$
$Nb_3Sn$	18	21.5 at 1.5 K	4.2–4.4
$Nb_3Ge$	21.8	38	4.2
$Nb_3Al$	18.7	35	–
$Nb_3Ga$	19.8	35	–
$Nb_3Al_{0.8}Ge_{0.2}$	20	43	–

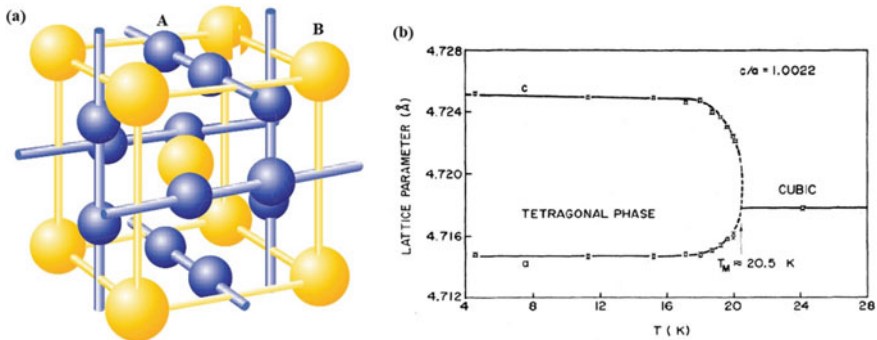


**Fig. 2** a Crystal structure of A-15 compounds. b Cubic-to-tetragonal structural transformation of  $V_3Si$  at  $T_M \sim 20.5$  K. Reproduced with permission from Ref. [18]

three orthogonal directions, with each chain bisecting the faces of the cubic structure. B-atoms arrange in the sublattice of the body-centered cubic structure [17].

BCS theory is well suited to describe the mechanisms of superconductivity in A-15 compounds. The one-dimensional chains of transition metal atoms increase the electronic density of states  $N(0)$  at the Fermi energy. The high critical temperature of A-15 compounds is because of the high  $N(0)$  value at the Fermi energy.

A-15 compounds have incredibly soft acoustic and optical phonon modes.  $Nb_3Sn$  and  $V_3Si$ , exhibited extreme phonon softening in few modes where the elastic modulus ( $c_{11}-c_{12}$ ) becomes zero [18]. This leads to structural phase transition from cubic to tetragonal, called martensite phase, and the process is volume-conserving in nature. The phase transition temperature  $T_M$  is close or above  $T_c$ . Such structural transition for the  $V_3Si$  compound is shown in Fig. 2b.

A-15 superconductors have large  $H_{c2}$  and  $J_c$  [19], which is useful for practical applications. Nevertheless, these materials are too brittle and quite sensitive to strains. Hence, for making magnet coils, the wind and react method is used. Generally, the powder-in-tube (PIT) method or internal bronze or tin processes are used to fabricate multifilamentary strands of  $Nb_3Sn$  wires [19, 20].

## 2.2.2 Transition Metal Nitrides and Carbides

Transition metal nitrides (TMN) and transition metal carbides (TMC) are fascinating materials because of their outstanding thermal, physical, and superconducting properties. They are binary compounds AB with NaCl-type structure. In crystallography, such structure is denoted as B1. In the structure shown in Fig. 3, A-atom is a transition element of III, IV, V, and VI subgroups, and B-atom is a non-transitional element.

The combination of transition metals with lighter covalent bonds forming elements like N or C often leads to materials with a high melting point, high hardness, and very low compressibility compared with pure metals [21]. Table 2 shows some of the binary nitrides and carbides and their  $T_c$  values.

**Fig. 3** Crystal structure of AB compounds (Example, NaCl-type structure)

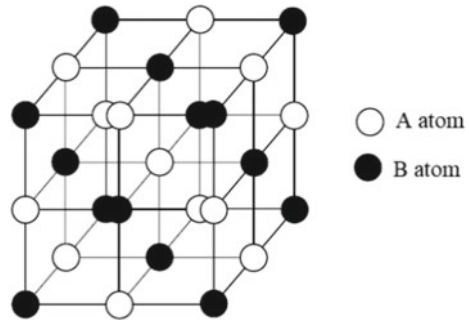


**Table 2** The critical temperature for some nitrides and carbides compounds. Data were taken from Refs. [22–24]

Nitrides	$T_c$ (K)	Carbides	$T_c$ (K)
NbN	17.0	TaC	10.3
ZrN	10.7	NbC	11.1
HfN	6.2	MoC	14.3
TiN	5.6	WC	10.0

The tunneling measurements in superconducting nitrides and carbides revealed that superconductivity in these materials is mainly due to the electron–phonon interaction [25]. From the study on the effect of neutron irradiation upon superconducting B1 compounds, it is seen that these compounds are much more resistant to radiation than the A-15 compounds [26]. Despite the extreme hardness and very high melting point of these compounds, the nitrides and carbides are pretty brittle, and that is why fabricating wires using the B1 compounds is very difficult.

### 2.2.3 Laves Phases

Laves phases are metallic  $AB_2$  type compounds having a cubic or hexagonal crystal structure. Laves phases form a vast class of intermetallic compounds, in which few superconducting laves phases have transition temperatures above 10 K and a high upper critical field,  $H_{c2}$ . The critical temperature of laves phases  $ZrV_2$  and  $HfV_2$  are 9 K and 2 K, respectively, and their upper critical fields measured at 4.2 K are 10.3 T and 20 T, respectively [22].  $Hf_xZr_{1-x}V_2$  is an interesting pseudobinary laves phase with  $T_c$  at 10.1 K [27]. It has high  $H_{c2}$ , and  $J_c$  is less brittle than the A-15 compounds and shows high resistance to neutron irradiation. These spectacular properties make (Hf, Zr)  $V_2$  superconductors well suited for high-field applications like fusion reactors [28].



### 3 MgB<sub>2</sub> Superconductor

Magnesium diboride, MgB<sub>2</sub>, has been a known material since the 1950s. Still, the discovery of superconductivity in MgB<sub>2</sub> by Jun Akimitsu's group in 2001 [29] surprised the field of material science because of its unusually high critical temperature ( $T_c$ ) of 39 K. Soon after the discovery of the MgB<sub>2</sub> superconductor; it drew significant attention from both theorists and experimentalists. Because its high critical temperature made people suspect the mechanism of superconductivity in MgB<sub>2</sub>. Also, its simple structure with lower anisotropy [30], nearly transparent grain boundary [31], and relatively high  $T_c$  [29] made experimentalists interested in this material.

According to BCS theory,  $T_c \sim \theta_D \exp(-1/\lambda_{\text{eff}})$  is the relationship of the critical temperature in terms of the Debye temperature ( $\theta_D$ ) of metal and coupling constant between phonons and electrons [ $\lambda_{\text{eff}} = \lambda = V \times N(E_F)$ ].  $N(E_F)$  is the density of states of electrons near the Fermi surface,  $V$  is the average matrix element of electron interaction. For MgB<sub>2</sub>, the Debye temperature ( $\theta_D$ ) is high but only comparable to the other light materials and diborides. Also, MgB<sub>2</sub> has low  $N(E_F)$  because of the absence of d-electrons. Thus, the exceptionally higher  $T_c$  of the MgB<sub>2</sub> superconductor made people initially think of an unconventional mechanism of superconductivity in MgB<sub>2</sub>. Besides these, the MgB<sub>2</sub> superconductor is different from other conventional BCS superconductors in another aspect, i.e., the presence of two distinct energy gaps in the superconducting state [32]. After much experimental and theoretical work, it is now widely accepted that MgB<sub>2</sub> is a phonon-mediated BCS superconductor. It is also evident that the unusually high transition temperature is due to the strong anharmonicity of the phonons involved. Evidence of the isotope effect also indicates the importance of phonons in the pairing mechanism in the MgB<sub>2</sub> superconductor. Figure 4a shows superconducting transitions for the isotopically substituted MgB<sub>2</sub>. The partial isotope effect coefficient of boron is 0.3 [33], a pretty significant value

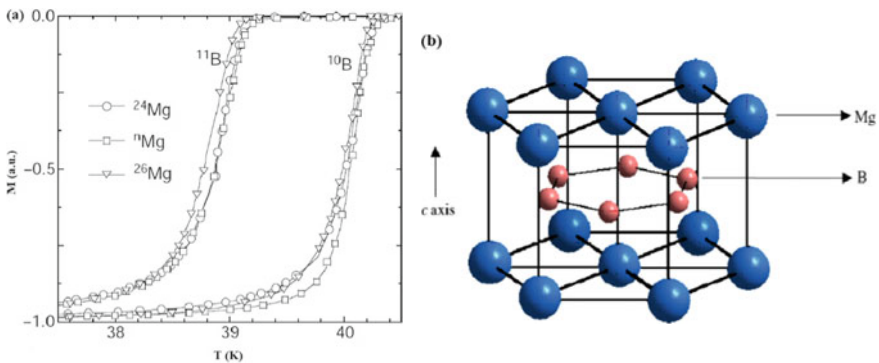


**Fig. 4** **a** The relative magnetization versus  $T$  (K) for isotopically substituted MgB<sub>2</sub> sample.  $^n\text{Mg}$  indicates samples with natural Mg (Reproduced with permission from Ref. [33]). **b** Crystal structure of MgB<sub>2</sub>

indicating the crucial role in the superconductivity of the phonons associated with boron atoms in  $\text{MgB}_2$ . While the isotope effect coefficient for Mg is small, 0.02, indicating the negligible effect of the vibrational frequencies of Mg on its  $T_c$  [33].

### Crystal Structure

$\text{MgB}_2$  is a type-II superconductor with layered structure. Its atoms, Mg and B arranged in the layers of hexagonal closed packed structure, with space group  $P6/mmm$  (Fig. 4b) [34, 35]. The structure is comprising of layers of magnesium and boron, alternating along the c-axis. Each boron layer is a graphite-like hexagonal lattice. The magnesium atoms reside between the boron layers and at the center of the hexagons. The typical values of the a- and c-lattice parameter of  $\text{MgB}_2$  are obtained as 3.084 Å and  $c = 3.524$  Å, respectively.

### Band Structure

In  $\text{MgB}_2$  crystal, Mg and B atoms form an ionic bond when Mg atoms share the valence electron to the boron atoms arranged in a planar lattice. There are 2D covalent bonds between the in-plane boron atoms and 3D metallic bonding between the layers. The partially filled 2D covalent  $\sigma$  bands are formed by the  $sp^2$  hybrids of boron 2s and  $p_{x,y}$  orbitals. These bands are localized on boron planes and act as hole bands. The  $p_z$  orbitals in boron atoms form the localized 3D metallic type  $\pi$  band, containing both holes and electrons as charge carriers [36]. The dynamics of the electrical conductivity at the normal state and the electronic density of states at the Fermi level of  $\text{MgB}_2$  are mainly governed by these  $\sigma$  and  $\pi$  bands. The occurrence of superconductivity is ascribed to the  $\sigma$  band on the boron layer in the  $\text{MgB}_2$ . Figure 5a shows the electronic band structure of  $\text{MgB}_2$ .

Boron  $p_{\sigma,\pi}$  bands, mainly form the valence bands in  $\text{MgB}_2$ . Both the  $\sigma_{p_{x,y}}$  and  $\pi_{p_z}$  bands have strong in-plane dispersion due to considerable overlap between all p-orbitals for neighboring boron atoms [39]. Figure 5b shows the pictorial representation of the Fermi surface of  $\text{MgB}_2$ . The two nearly cylindrical hole-type Fermi surfaces represent the degenerate  $\sigma$  bands which are mainly flat and lie above the

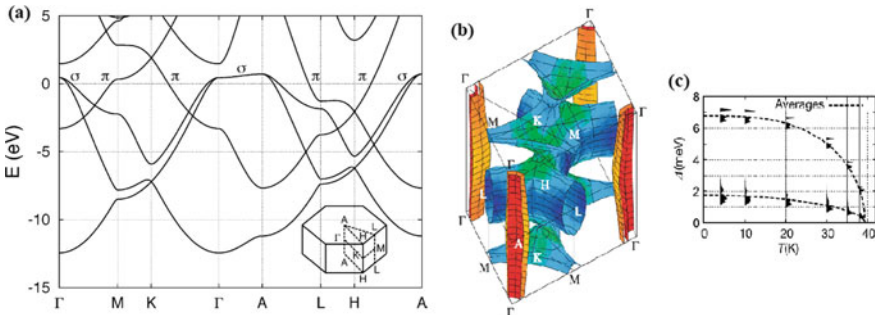


**Fig. 5** a Electronic structure of  $\text{MgB}_2$ . Inset: Brillouin zone of the simple hexagonal structure. b Fermi surface of  $\text{MgB}_2$ . c Temperature dependence of the superconducting gaps. Reproduced with permission from Refs. [37, 38]

Fermi level. The Fermi surface split into eight pieces around the four vertical  $\Gamma$ – $\Gamma$  lines. The  $\pi$  bands are represented by the two webbed tunnels ( $\pi$  sheets) along H–L and K–M lines, where the lower and upper K–M lines are equivalent [38, 39].

In the superconducting state,  $\text{MgB}_2$  exhibits two energy gaps. One is a large gap (5.5–8.0 meV at 4 K), and another one is a small gap (1.5–3.5 meV at 4 K) [40, 41]. Both the gaps have s-wave symmetry. The  $\sigma$ -orbital band is responsible for a larger energy gap. In comparison, the  $\pi$ -orbital band is responsible for a smaller energy gap [38]. Figure 5c shows the calculated energy gap at different temperatures below the transition temperature. It is evident from the graph that the temperature dependence of the  $\sigma$ -bonding energy gap (Larger gap) and the  $\pi$ -bonding energy gap (smaller gap) are different. At low temperatures, the values of the two superconducting energy gaps are significantly different. Moreover, both the energy gaps disappear simultaneously at the superconducting transition temperature [42].

It is observed from the Hall coefficient measurements (in-plane and out-of-plane) that the dominant charge carriers along the ab-plane and c-direction are holes and electrons, respectively. The results indicate that the transport properties of  $\text{MgB}_2$  are governed by the multi-band characteristics [43].

### ***Superconducting Properties of $\text{MgB}_2$***

$\text{MgB}_2$  is metallic at normal temperatures. It has much lower room temperature resistivity than the normal state resistivities of other superconducting materials [44].  $\text{MgB}_2$  has a distinct and sharp  $T_c^{\text{onset}}$  of 39 K. Also, the width of the superconducting transition is very narrow, which is less than 1 K [29]. The doping studies on  $\text{MgB}_2$  to increase its transition temperature give disappointing results. When different dopants are substituted at B- or Mg-site, in all the cases,  $T_c$  decreases, and the rate of decrease is different for different dopants. In  $\text{MgB}_2$ ,  $T_c$  is mainly influenced by the interband scattering, Fermi surface geometry, lattice parameter, charge density at the Fermi level, and lattice microstructure in the B-B layer [45].

The irreversibility field  $H_{\text{irr}}$  and the critical magnetic field  $H_{c2}$  of pure  $\text{MgB}_2$  samples are about 6–12 T and 15–25 T, respectively.  $H_{c2}$  decreases with the increase in coherence length,  $\xi$ . The dopants added in  $\text{MgB}_2$  act as electron scatterers. Hence, the mean free path of the electrons decreases, which in turn decreases the coherence length and subsequently improves the  $H_{c2}$ . Carrier scattering within the two bands of  $\text{MgB}_2$  (2D  $\sigma$  and 3D  $\pi$ ) strongly affects  $H_{c2}$  and  $H_{\text{irr}}$ . It is found that when the synthesized  $\text{MgB}_2$  samples show higher normal state resistivity, then the critical magnetic field is also higher. Besides this, the  $H_{c2}$  can be improved by doping at the Mg and B-sites with suitable dopants. The doping tunes the extent of the interband and intraband scattering rates, which affects the two energy gaps in the  $\text{MgB}_2$  superconductor. A comparison of superconducting properties of  $\text{MgB}_2$  and few other classes of non-cuprates superconductors is shown in Table 3.

### ***Applications of $\text{MgB}_2$ Superconductor***

$\text{MgB}_2$  superconductor is a promising material for superconducting applications due to its relatively high transition temperature, large in-field critical current density, and high upper critical field [46]. Physically  $\text{MgB}_2$  is a brittle material. The large value of

**Table 3** Basic superconducting properties of some non-cuprate compounds. Data were taken from Refs. [47, 48]

Material	$T_c$ (K)	$H_{c2}$ (T)	Coherence length (nm)
MgB <sub>2</sub>	39	15–20 at 4.2 K	4–5
NbTi	9	11–12 at 4.2 K	4–5
Nb <sub>3</sub> Sn	18	25–29 at 4.2 K	3
BKBO	34	30 at 2 K	3.5–5

$J_c$  makes MgB<sub>2</sub> suitable for superconducting wire formation. Various techniques are being used for the superconducting MgB<sub>2</sub> wires, such as diffusion method, coating technique, powder in tube (PIT) method, etc.

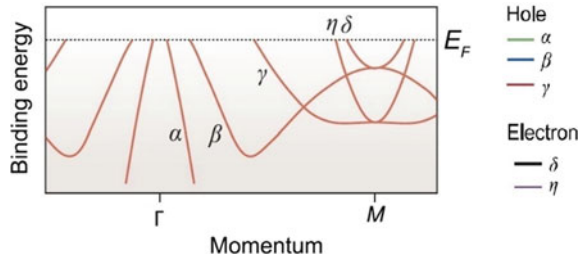
## 4 Iron-Based Superconductors

A new class of superconductors emerged when superconductivity was discovered in LaFePO at 4 K in 2006 [49]. In 2008, an analogous material LaFeAs(O, F), was discovered, superconducting at 26 K [50]. This discovery surprised physicists and material scientists because the compounds contained Iron, a ferromagnetic element. Until then, Iron was considered deleterious to superconductivity due to its strong local magnetic moment. The highest  $T_c$  in bulk iron-based superconductors was reported in SmFeAsO<sub>1-x</sub>F<sub>x</sub> at 55 K by Ren et al. [51]. Iron-based superconductors can be categorized mainly into four families—Iron pnictides 1111 (e.g., LnFeAsO, Ln = All lanthanides), 122 (e.g., BaFe<sub>2</sub>As<sub>2</sub>), 111 (e.g., NaFeAs), Iron chalcogenides 11 (e.g. FeSe). There are two newer families, such as iron pnictide of 21,311, Sometimes called 42,622 (e.g., Sr<sub>2</sub>ScO<sub>3</sub>FeP) and iron chalcogenides of 122-type, also called 122\* (e.g., A<sub>x</sub>Fe<sub>2-y</sub>Se<sub>2</sub>; A = Tl, Rb, Cs, K).

Semimetallic properties are observed in Iron-based superconductors [52]. There are many common features in iron-based superconductors and high- $T_c$  cuprates; both are unconventional superconductors, i.e., the mechanism of superconductivity in these materials is not explained by electron–phonon interactions in conventional BCS theory. Superconductivity in both of these classes (quasi 2D systems) is believed to be originated from the repulsive interaction of electron–electron systems, which induces fluctuations in the antiferromagnetic domain structure. Nevertheless, the actual mechanism of superconductivity in iron-based superconductors and high- $T_c$  cuprates remains an unsolved problem.

The low-energy electronic structure is dominated by the Fe 3d states in the iron-based superconductors [53]. The presence of multiple Fermi surfaces in the normal states, including the hole Fermi pockets and electron Fermi pockets, are confirmed for the Fe-based superconductors from polarization-dependent ARPES experiment and DFT calculations. The typical band structure along the  $\Gamma$ -M direction is shown in Fig. 6.

**Fig. 6** Band structure of iron pnictides. Reproduced from Ref. [54]



Multiple orbitals like  $d_{xy}$ ,  $d_{xz}$ , and  $d_{yz}$  contribute to the states near the Fermi energy [55]. The hole Fermi and nested electron surfaces indicate the itinerant origin of antiferromagnetism in iron-based superconductors [56].

### Phase Diagram

The crystal structure of the iron-based superconductors is of tetragonal symmetry at room temperature. The crystal symmetry changes from tetragonal to orthorhombic symmetry at the structural transition temperature,  $T_s$ , as the temperature is gradually lowered. Below the  $T_s$ , the material exists with a long-range antiferromagnetic ordering. Such structural transition originates not because of the structural effects but from electron-driven phase transition. The antiferromagnetic transition is strongly coupled with the electron-driven phase transition. The origin of antiferromagnetism is associated with the spin-density-wave (SDW) ordering of itinerant electrons [57].  $T_{SDW}$  is usually equal to or slightly lower to  $T_s$ . Phase diagrams for different classes of Fe-based superconductors are shown in Fig. 7. The superconductivity in the iron-based compounds starts to emerge after doping electron- or hole-type charge carriers above a critical doping level beyond with a maximum  $T_c$  is observed at the optimum doping concentration. Both structural and antiferromagnetic transitions are continuously suppressed with the increasing charge carriers due to doping beyond the optimal concentration.

In the phase diagram of  $Ba(Fe_{1-x}Co_x)_2As_2$  (Fig. 7c), it is observed that the antiferromagnetic transition temperature,  $T_N$  and the structural transition temperature,  $T_s$  split with co-doping. At the same time, in the case of  $Ba_{1-x}K_xFe_2As_2$  (Fig. 7b), they remain coincident with K-doping. For doped  $BaFe_2As_2$  compounds (Figs. 7b–d), the superconducting states coexist with the suppressed SDW order. However, for  $Fe_{1-y}Se_xTe_{1-x}$  there is no such coexistence prevails (Fig. 7e). For  $LaFeAsO_{1-x}F_x$  compounds, these two states do not coexist under normal pressure (see Fig. 7a). However, hydrostatic pressure experiments demonstrate that these two states can coexist in this material under pressure [58].

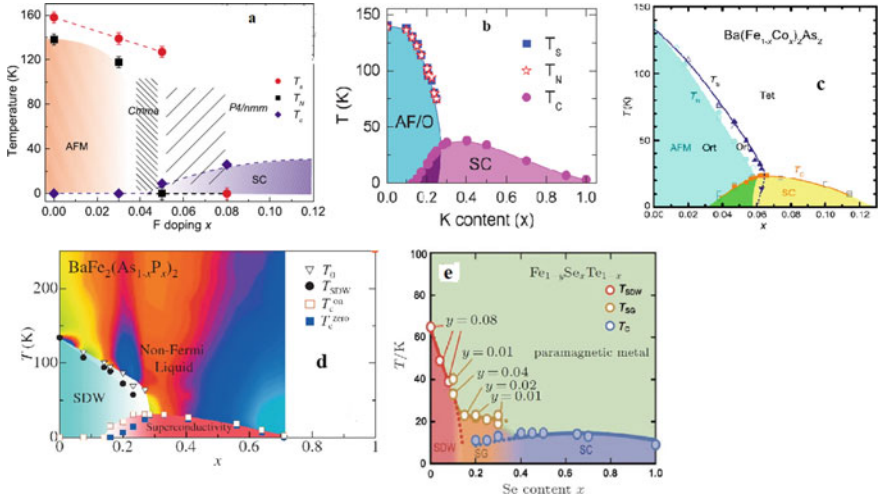


**Fig. 7** Phase diagrams of Fe-based materials:  $\text{LaFeAsO}_{1-x}\text{F}_x$  (a),  $\text{BaFe}_2\text{As}_2$  material with doping at three sites—Ba (b), Fe (c), As (d), and  $\text{Fe}_{1-y}\text{Se}_y\text{Te}_{1-x}$  (e). Reproduced with permission from Refs. [59–63]

*Crystal Structure and Properties of Iron-Based Superconductors*

*1111-Type Iron-Based Superconductors*

The general structure of iron-based materials of 1111-type is  $\text{LnT}_M\text{PnO}$ , where Ln = Rare-earth metal atoms like La, Sm, Gd, etc.,  $T_M$  = Transition metals like Ni, Co, Fe, etc., Pn = Pnictogen anions like As, P, etc.

$\text{LnFeAsO}$  has tetragonal, tP8 (“8” atoms per unit cell, “t” means tetragonal, and “P” means primitive unit cell)  $\text{ZrCuSiAs}$ -type structure, and they belong to  $P4/nmm$  space group. Figure 8a shows the crystal structure of the  $\text{LaFeAsO}$ . In the structure,

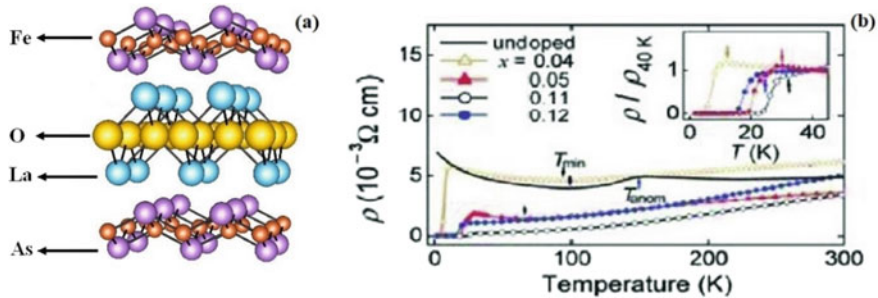


**Fig. 8** a Crystal structure of 1111-type iron pnictide. b Resistivity ( $\rho$ ) versus temperature (T) for undoped and  $\text{LaFeAsO}_{1-x}\text{F}_x$ :  $x = 0.04, 0.05, 0.11, \text{ and } 0.12$ . Inset shows zoomed  $\rho$ -T curves at low temperatures. Reproduced from Ref. [50]

**Table 4** A list of iron-based superconductors and their corresponding critical temperatures. Data were taken from Refs. [50, 51, 64, 69–75]

Compound	$T_c$ (K)	Compound	$T_c$ (K)
LaFeAsO <sub>0.89</sub> F <sub>0.11</sub>	26	Ba <sub>0.6</sub> K <sub>0.4</sub> Fe <sub>2</sub> As <sub>2</sub>	38
NdFeAsO <sub>0.88</sub> F <sub>0.12</sub>	50	BaFe <sub>2</sub> (As <sub>0.65</sub> P <sub>0.35</sub> ) <sub>2</sub>	30
SmFeAsO <sub>0.8</sub> F <sub>0.2</sub>	52	LiFeAs	18
PrFeAsO <sub>0.89</sub> F <sub>0.11</sub>	52	NaFeAs	9
La(Fe <sub>0.85</sub> Co <sub>0.15</sub> )AsO	14.3	$\alpha$ -FeSe	8
SmFe(As <sub>0.7</sub> P <sub>0.3</sub> )O	10.5	FeSe <sub>0.5</sub> Te <sub>0.5</sub>	14
BaFe <sub>1.85</sub> Co <sub>0.15</sub> As <sub>2</sub>	25	(Fe <sub>0.95</sub> Co <sub>0.05</sub> )Se	10
BaFe <sub>1.9</sub> Ni <sub>0.1</sub> As <sub>2</sub>	20	FeTe <sub>0.8</sub> S <sub>0.2</sub>	10

there is a negatively charged 2D Fe-As layer along the c-axis, and an alternating positively charged Ln–O layer.

At room temperature, the parent compounds of 1111 pnictides have tetragonal crystal structures [64]. The structural phase transition occurs in LnFeAsO compounds from the tetragonal  $P4/nmm$  to the orthorhombic structures by reducing the temperature. The orthorhombic form of LnFeAsO has space group  $P112/n$  or  $P2/c$  or  $Cmma$ .

The Ln–As bond length and the Fe–As–Fe bond angle are two essential parameters to be controlled to enhance superconductivity in 1111 pnictides [65]. Shirange et al. revealed that the a-axis length, which corresponds to the inter-atomic distance of Iron atoms, strongly correlates with  $T_c$  [66]. Again,  $T_c$  strongly depends on the As–Fe–As bond angle in LnFeAsO<sub>1-y</sub> due to the tetragonal distortion.  $T_c$  becomes maximum when a regular tetrahedron is formed by the As–Fe–As bond [67].

At high temperatures, the parent compound ( $x = 0$ ) of LaFeAsO<sub>1-x</sub>F<sub>x</sub> is a Pauli paramagnetic metal. a drastic decrease in magnetic susceptibility and resistivity is observed at 160 K as temperature decreases and reaches a minimum value and after that increases (see Fig. 8b). When fluorine is doped at the oxygen site for  $x = 0.04$ , zero-resistivity is observed at  $T > 4$  K. Table 4 shows the critical temperatures of some iron-based superconductors.

In iron pnictides/chalcogenides, external pressure has a significant effect on the superconducting properties of the compounds. Takahashi et al. [68] reported an enhanced  $T_c$  of 43 K in the LaFeAsO<sub>1-x</sub>F<sub>x</sub> superconductor under 4 GPa of pressure. External pressure increases the charge transfer between the conducting (FeAs) and insulating (LnO) layers. Also, the main reason for the enhancement of  $T_c$  is that the pressure induces an anisotropic shrinkage.  $T_c$  gradually increases to a maximum value and after which the  $T_c$  decreases with the progressive increase of external pressure.

### 122 and 111-Type Iron-Based Superconductor

122-type iron pnictides have general structure AFe<sub>2</sub>As<sub>2</sub>, where A corresponds to a divalent ion (A = Ca, Ba, Sr, etc.). The iron pnictides of 122 families are most widely studied and probably have the largest number of members as one can dope on any

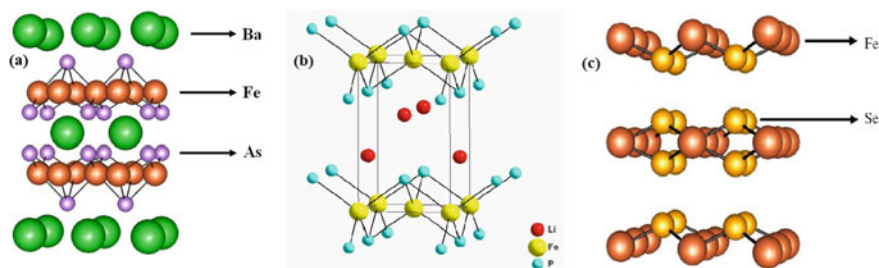


**Fig. 9** Crystal structures of **a** 122  $\text{BaFe}_2\text{As}_2$ , **b** 111  $\text{LiFeP}$ , and **c** 11  $\text{FeSe}$

of the three sites. The first reported 122-type compound was  $\text{BaFe}_2\text{As}_2$ . The crystal structure of  $\text{BaFe}_2\text{As}_2$  is shown in Fig. 9a [64]. 122 compounds have tetragonal with  $I10$  (“t” refers to tetragonal, “I10” means there is an atom at the center of 10 atom unit cell), standard  $\text{ThCr}_2\text{Si}_2$  structure. The Single Ba atom separates the FeAs layers in the structure.

111-type iron pnictide superconductors are highly reactive in air, and this property makes these compounds challenging to investigate. The 111 compounds have a  $\text{Cu}_2\text{Sb}$ -type structure with  $P4/nmm$  symmetry. The crystal structure of the  $\text{LiFeP}$  compound is shown in Fig. 9b [76]. Li layer and iron pnictide are stacked alternately, forming the layered structure.  $\text{FeP}_4$  tetrahedron is formed from the four-fold coordination of Fe atoms.

### **11-Type Iron-Based Superconductor**

The 11 compounds among the iron-based superconductors have the simplest crystal structure. Hsu et al. discovered the superconductivity in anti- $\text{PbO}$ -type  $\text{FeSe}$  at 8 K [70]. The crystal structure of an 11 compound ( $\text{FeSe}$ ) is shown in Fig. 9c.  $\text{FeSe}$  contains only the  $\text{FeSe}$  layers. It has a tetragonal crystal structure with  $P4/nmm$  symmetry. The lowest  $T_c$  has been observed for these types of superconductors among the iron-based superconductors. 11 compounds are very reactive with air and moisture. In solid-state-reacted  $\text{FeTe}_{0.8}\text{S}_{0.2}$  samples, moisture-induced superconductivity was observed. Surprisingly, superconducting properties improved dramatically by exposing the samples to the air [77]. Similar to 1111 superconductors, external pressure significantly influences the superconducting properties of 11-type chalcogenide superconductors. At ambient pressure,  $\text{FeSe}$  has the  $T_c$  of 8 K, which goes up to 37 K at an external pressure of 7–9 GPa [78]. In the  $\text{FeSe}$  system, the grains in the system are tightly packed at low pressures, and hence, the  $T_c$  increases. As the pressure is continued to increase, the DOS increases, and as a result,  $T_c$  increases. However, after a particular value of external pressure,  $T_c$  decreases because of the lattice stiffening effect [79].

The newer families of Fe-based superconductors are iron pnictide of 21,311 and iron chalcogenides of 122-type. The crystal structures of two representative materials from these two families are shown in Fig. 10. The crystal structure of 21,311



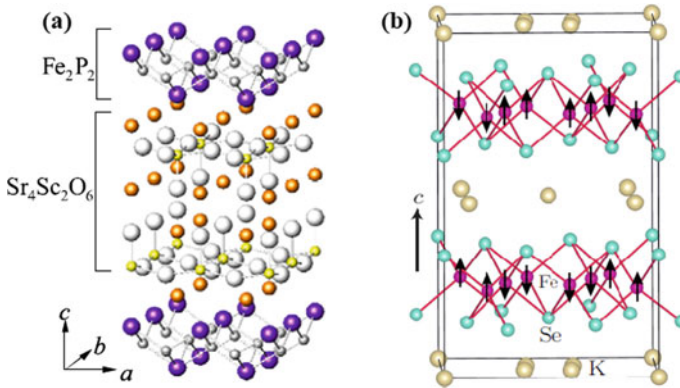


**Fig. 10** **a** Crystal structure of  $21,311$   $\text{Sr}_2\text{ScO}_3\text{FeP}$  and **b**  $122^*$   $\text{K}_{0.8}\text{Fe}_{1.6}\text{Se}_2$

compound  $\text{Sr}_2\text{ScO}_3\text{FeP}$  (Fig. 10a) has  $P4/nmm$  symmetry. This structure is visualized as the layer of perovskite  $\text{Sr}_4\text{Sc}_2\text{O}_6$  oxide alternating with the  $\text{Fe}_2\text{P}_2$  layer. The transition temperature of this family of iron-based superconductors has been increased up to  $\sim 47$  K by the intercalation of further layers of atoms between the FeAs layers [80]. Figure 10b shows the crystal structure of the most recently discovered class of iron-based superconductors. Its structure is an ordered defect alteration of the 122  $\text{BaFe}_2\text{As}_2$  structure (called 122\* also), written as  $\text{A}_{0.8}\text{Fe}_{1.6}\text{Se}_2$  or sometimes  $\text{A}_x\text{Fe}_{2-y}\text{Se}_2$  ( $\text{A} = \text{Tl}, \text{K}, \text{Rb}, \text{Cs}$  etc.). These materials have an exceptionally high magnetic moment of  $\sim 3 \mu_B$  per Fe atom and high Neel temperature ( $T_N > 500$  K) [81]. Further details on the structures and properties could be found in references [82, 83].

### *Applications of Iron-Based Superconductors*

Nowadays, iron-based superconductors are promising for technological applications due to their relatively large  $H_{c2}$  and high critical temperature. Generally, the powder-in-tube (PIT) technique is widely used to make superconducting wires. Gao et al. [84] reported using the PIT technique to make F-La1111 and F-Sm1111 superconducting wires with high  $T_c$  and  $J_c$  values.

## 5 Nickelate Superconductors

In August 2019, superconductivity was observed in Sr doped  $\text{NdNiO}_2$  thin film by Li et al., the first candidate in the nickel-oxide superconductor [85]. Rare-earth infinite layer nickelate  $\text{RNiO}_2$  are visualized as the series  $\text{R}_{n+1}\text{Ni}_n\text{O}_{2n+2}$  compound with each member in the series contains  $n$ - $\text{NiO}_2$  layers, where  $n = \infty$  number. The first nickelate superconductor was an epitaxial thin film of  $\text{Nd}_{0.8}\text{Sr}_{0.2}\text{NiO}_2$  (001), and it was grown on  $\text{SrTiO}_3$  (001) substrate using  $\text{CaH}_2$  as a reducing agent by pulsed laser

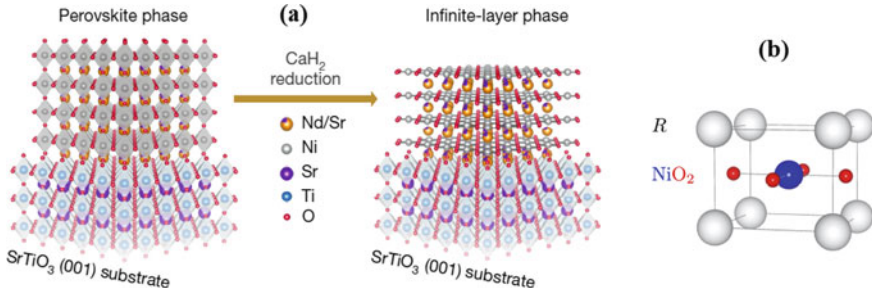


**Fig. 11** **a** Topotactic reduction of nickelate thin films (Reproduced with permission from Ref. [85]). **b** Ball and stick model of the unit cell of the RNiO<sub>2</sub> infinite layer nickelate superconductor

deposition (PLD) [85]. Figure 11a describes the topotactic reduction of nickelate thin film. Figure 11a shows the crystal structure of Nd<sub>0.8</sub>Sr<sub>0.2</sub>NiO<sub>3</sub> (left-hand side) and the crystal structure of Nd<sub>0.8</sub>Sr<sub>0.2</sub>NiO<sub>2</sub> thin films grown on SrTiO<sub>3</sub> (001) single-crystal substrate (right-hand side). The films undergo a topotactic transition to the infinite-layer phase from the perovskite phase upon low-temperature reduction.

The infinite layer nickelates, RNiO<sub>2</sub> (R = Rare-earth), have a crystal structure similar to the cuprates. The rare-earth spacer layer separates the NiO<sub>2</sub> layers in the crystal structure of nickelates. These materials have Ni-3d electrons. The weakly-interacting three-dimensional 5d metallic states are supported by the rare-earth spacer layer in the infinite layer nickelate. This three-dimensional 5d state of rare-earth hybridizes with a 3d<sub>x<sup>2</sup>-y<sup>2</sup></sub> state in the NiO<sub>2</sub> layer, a quasi-two-dimensional and strongly correlated state, resulting in the multi-band character of the Nickelates. In addition to that, the rare-earth 5d state also hybridizes with Ni-3d<sub>z<sup>2</sup></sub>, and thus the full, e<sub>g</sub> = {d<sub>x<sup>2</sup>-y<sup>2</sup></sub>, d<sub>z<sup>2</sup></sub>} sector of Ni-3d states becomes active in infinite layer nickelates [86]. In the normal state, the infinite layer nickelates show a weak-insulating or bad-metal behavior, which means that no superconductivity is observed in the pristine nickelate compound. Superconductivity is only observed in the nickelate thin films doped with charge carriers. Moreover, the doped bulk nickelates have not yet shown any superconductivity [87, 88].

The mechanism of superconductivity in the infinite layer nickelates can not be explained via electron–phonon interaction in the conventional BCS theory. Instead, Cooper pair formation in these systems is thought to be because of the repulsive interactions mediated by spin-fluctuations [89, 90]. From the fluctuation exchange (FLEX) and the random phase approximation (RPA) calculations for the many-body multi-orbital Hamiltonian, it is concluded that d-wave superconductivity is observed in nickelates.

Figure 12a shows the temperature-dependent resistivity for Nd<sub>1-x</sub>Sr<sub>x</sub>NiO<sub>2</sub> thin films for the various concentration of Sr-doping [91]. The resistivity curves of the parent compound (x = 0) and that of the underdoped and overdoped samples (x = 0.1, 0.125, and 0.25) show a rise in resistivity at lower temperatures. This rise in resistivity is due to weak localization or the onset of the Kondo effect at low

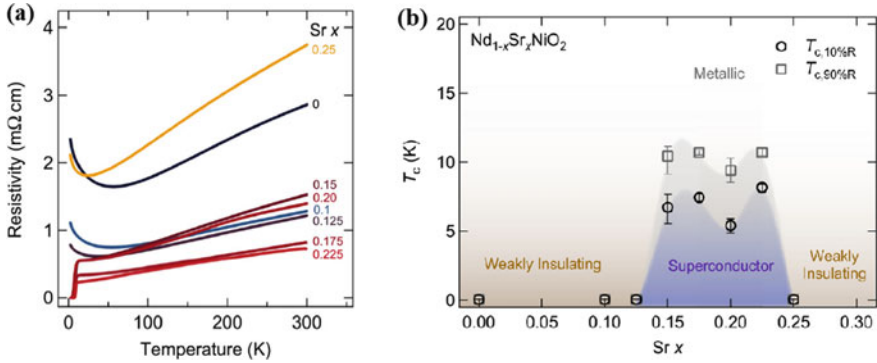


**Fig. 12** **a** Temperature-dependent resistivity was measured for  $\text{Nd}_{1-x}\text{Sr}_x\text{NiO}_2$  samples with different doping levels. **b** Phase diagram of  $\text{Nd}_{1-x}\text{Sr}_x\text{NiO}_2$  samples.  $T_{c,10\%R}$  ( $T_{c,90\%R}$ ) denotes the temperature at which the resistivity is 10% (90%) of the resistivity value at 20 K. Reproduced with permission from Ref. [91]

temperatures [92]. The resistivity curves show metallic nature in the normal state. The thin films with  $x = 0.15, 0.175, 0.2,$  and  $0.225$  show superconducting transition at low temperature with different  $T_c$ .

The phase diagram clearly shows the superconducting dome (Fig. 12b). This system is a bad metallic or weak insulating at all ranges in the phase diagram. A slight dip in  $T_c$  is observed at  $x=0.2$ , but its significance is still unknown. A recent NMR study has reported the presence of quasi-static antiferromagnetic order and antiferromagnetic fluctuations in  $\text{Nd}_{0.85}\text{Sr}_{0.15}\text{NiO}_2$  below 40 K. However, long-range magnetic order has not been reported yet for the undoped infinite layer nickelates [93].

From the Hall coefficient measurements performed in  $\text{Nd}_{1-x}\text{Sr}_x\text{NiO}_2$ , it is observed that the electrons are the primary charge carriers in the parent compound. For the superconducting and the overdoped samples, the main charge carriers change from electron to hole at low temperatures [91]. This indicates the multi-band character in the infinite layer nickelates.

## 6 Non-Cuprate Oxide Superconductors

### 6.1 Metal Oxide BKBO

In 1975, superconductivity was discovered in the metal oxide  $\text{BaPb}_{1-x}\text{Bi}_x\text{O}_3$  (BPBO) by Sleight et al. [94]. The maximum  $T_c$  was obtained at  $\sim 13.7$  K for  $x = 0.25$ . Mattheiss et al. [95] substituted K on Ba site, and  $T_c$  increased to greater than 20 K in  $\text{Ba}_{1-x}\text{K}_x\text{BiO}_3$  (BKBO) compound. Later, Cava et al. has reported a transition temperature of 30 K [96] and finally to 34 K [97] for this compound.

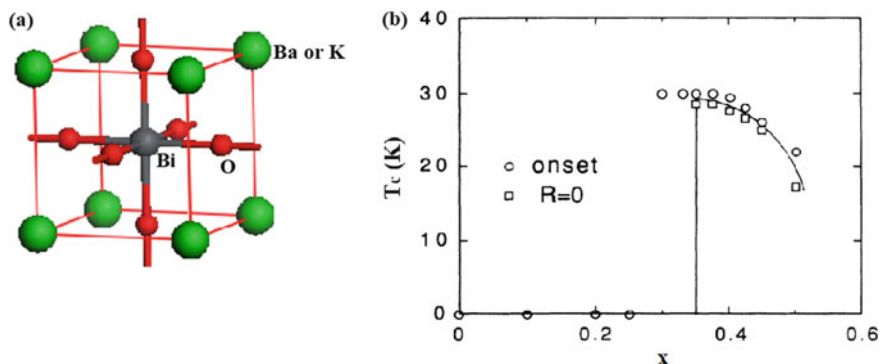


**Fig. 13** **a** Cubic perovskite unit cell of BKBO. **b** Critical temperature  $T_c$  versus  $x$  for  $\text{Ba}_{1-x}\text{K}_x\text{BiO}_3$ . Reproduced from Ref. [98]

Figure 13a shows the crystal structure of  $\text{Ba}_{1-x}\text{K}_x\text{BiO}_3$ . BKBO has a cubic perovskite structure for the potassium concentration  $x \geq 0.37$ . The parent compound  $\text{BaBiO}_3$  is semiconducting and has monoclinic symmetry [98–100]. Electronic structure calculations of  $\text{BaBiO}_3$  indicate a half-filled band system, i.e., a metallic system. Superconductivity in BKBO is found to occur near a metal–insulator transition. In the cubic perovskite phase, the bulk superconductivity exists for  $x \geq 0.37$ . Initially, the cubic structure distorts because of the tilting of  $\text{BiO}_6$  octahedral, and then distortion occurs by symmetric oxygen breathing-mode at room temperature as K-concentration is decreased.  $\text{Ba}_{1-x}\text{K}_x\text{BiO}_3$  becomes semiconducting and has monoclinic symmetry at low doping ranges ( $0.0 \leq x \leq 0.1$ ). This semiconducting behavior can be explained based on a commensurate charge-density wave [98]. Various studies suggest that the mechanism responsible for the superconductivity in BKBO is the electron–phonon coupling which is also justified by the isotope shift of  $T_c$  with relatively high values of isotope exponent  $\alpha$  obtained in measurements of oxygen isotope effect [99].

Figure 13b shows the variation of transition temperature for the bulk  $\text{Ba}_{1-x}\text{K}_x\text{BiO}_3$  with potassium content  $x$ . Sharp resistive transitions were observed for the K-concentration  $0.35 \leq x \leq 0.45$ . Samples with potassium concentration  $x < 0.3$  are semiconducting. The maximum  $T_c$  was observed at  $x = 0.37$ , which decreases further with the increasing K-doping concentration.

Semiconductor-like behavior is often observed in BKBO thin films. Few researchers [101] suggest that the BKBO sample is a mixture of both and can be modeled by a semiconductor and a metal in series. The rise of resistivity with the decrease in temperature indicates the variable-range hopping conduction (VRH) in BKBO films and follows a  $T^{-1/4}$  dependence [102]. Muon spin resonance studies on  $\text{BaBiO}_3$ ,  $(\text{Ba},\text{K})\text{BiO}_3$ , and  $\text{Ba}(\text{Pb},\text{Bi})\text{O}_3$  suggest that these materials are non-magnetic [103].

## 6.2 Some Other Non-Cuprate Oxide Superconductors

The oxide superconductor is probably the most extensive family among all superconducting materials. In 1964, superconductivity was observed in an oxide semiconductor,  $\text{SrTiO}_3$ , at 0.3 K [104]. This was the first example of an unconventional superconductor. After that, many more oxides were discovered which exhibit superconductivity, namely, NbO, TiO. They have transition temperatures in the vicinity of 1 K [105]. Superconductivity was observed in different tungsten bronzes such as  $\text{Na}_x\text{WO}_3$ ,  $\text{Ca}_x\text{WO}_3$ ,  $\text{Ba}_x\text{WO}_3$ ,  $\text{Sr}_x\text{WO}_3$ ,  $\text{K}_x\text{WO}_3$ ,  $\text{Rb}_x\text{WO}_3$ ,  $\text{Cs}_x\text{WO}_3$ , etc. They have  $T_c$ 's in the 2–6 K range [106]. Besides these, superconducting transitions have been found in  $\text{K}_x\text{ReO}_3$  and  $\text{K}_x\text{MoO}_3$  at 3.6 K and 4.2 K, respectively [107].  $\text{LiTi}_2\text{O}_4$  was found to be superconducting at the  $T_c$  of 13.7 K [108]. In 1994, superconductivity was first observed in a layered perovskite without copper  $\text{Sr}_2\text{RuO}_4$  with a  $T_c$  value of 0.93 K [109]. The development of more new oxide superconductors continues till now and in the future.

## 7 Organic Superconductors

### 7.1 Charge Transfer Organic Salts

Research on electronically conductive organic materials was started in the 1940s. In 1973, a pronounced conductivity peak was observed in the TTF-TCNQ compound near 60 K [110], the first stable quasi-1D organic conductor. Superconductivity in an organic compound was first observed in 1979 when Bechgaard and Jerome found a molecular salt  $(\text{TMTSF})_2\text{PF}_6$ , which becomes a superconductor under a pressure of 1.2 GPa and has  $T_c$  of 0.9 K [111]. The transition temperatures of most organic superconductors are very low.

The crystal structures of some organic compounds that form superconductors are shown in Fig. 14 [112]. In general, the organic molecules are flat, planar molecules. These molecules form their crystals by arranging them in stacks. These molecular crystals then aligned parallel to the chains of other atoms (Br, I, etc.) or molecules ( $\text{PF}_6$ ,  $\text{FeCl}_4$ , etc.). In organic superconductors, unpaired electrons are created by a partial charge transfer between an acceptor and a donor molecule. An inorganic (in most cases) electron-acceptor complex X combines with the organic donor molecule D according to the reaction  $[\text{X}_n] + [\text{D}_m] \rightarrow [\text{X}_n]^{-\delta} + [\text{D}_m]^{+\delta}$ . Mainly, the  $\pi$ -electrons of the D molecules take part in the charge transfer process, and the anions act mainly as charge-compensating spacers. The delocalization of charge carriers is obtained by overlapping the  $\pi$ -orbitals of the partially filled outer molecular shells of the densely packed donor molecules.

In the section below, the properties of few classes of organic superconductors are discussed briefly.

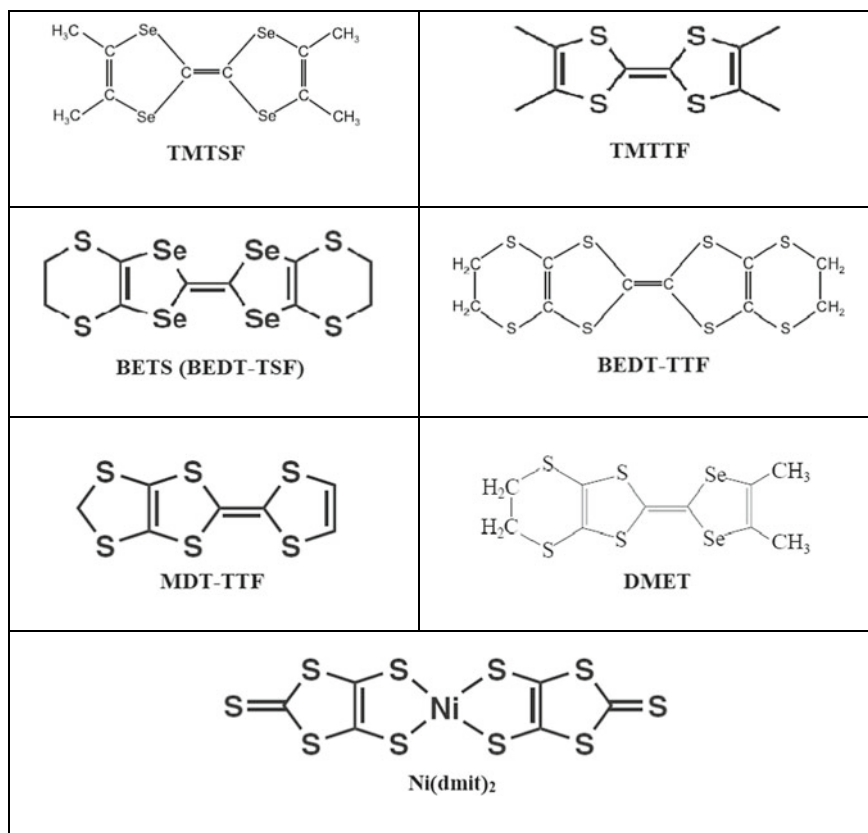


**Fig. 14** Structure of organic molecules that form superconductors

### *TMTSF and TMTTF salts*

Soon after discovering conductivity in organic compounds, the TMTSF salts became an area of interest for material scientists. Figure 15a shows the resistivity-temperature plot for the  $(\text{TMTSF})_2\text{PF}_6$  superconductor at ambient pressure. It is observed that a metal-insulator transition occurs at a temperature below 20 K as the temperature is gradually decreased. The observed rapid rise in resistivity at low temperature indicates a transition into an insulating SDW ground state.

Due to the minor transfer energy between one-dimensional columns in the molecule, TMTTF salts are more one-dimensional. As seen in the resistivity-temperature plot of Fig. 15a, the resistivity minima occur for  $(\text{TMTTF})_2\text{PF}_6$  at 250 K [115]. Charge-order (CO) transition for  $\text{PF}_6$  salts occurs at 70 K [116], then at 15 K, the spin Peierls (SP) transition occurs to be a non-magnetic insulating state [117].  $(\text{TMTTF})_2\text{PF}_6$  becomes superconducting at 1.8 K under 5.4 GPa [118]. The universal phase diagram of TMTSF and TMTTF salts is shown in Fig. 15b.

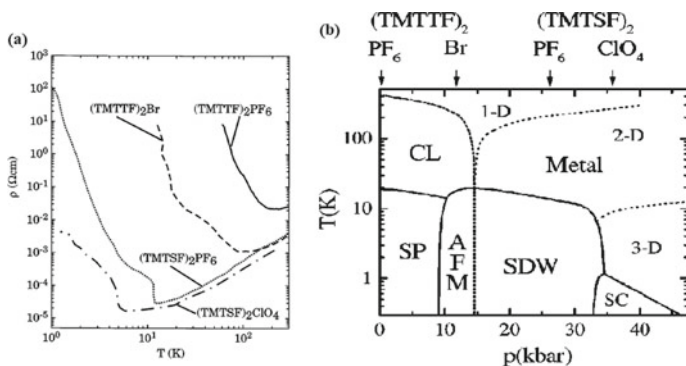


**Fig. 15** **a** Resistivity vs temperature for various  $(\text{TMTSF})_2\text{X}$  and  $(\text{TMTTF})_2\text{X}$  salts at ambient pressure. **b** Electronic phase diagram of TMTSF and TMTTF salts. Reproduced with permission from Refs. [113, 114]

### BEDT-TTF salts

Superconductivity was first observed in a BEDT-TTF salt was in  $\beta$ - $(\text{BEDT-TTF})_2\text{-ReO}_4$  at  $T_c = 2$  K under 0.4 GPa of pressure [119].  $\beta$ - $(\text{BEDT-TTF})_2\text{X}$  ( $X = \text{AuI}_2, \text{I}_3, \text{IBr}_2$ ) are ambient pressure superconductors, and  $T_c$ 's of these compounds decrease with an increase in applied pressure [120]. Depending on applied pressure,  $\kappa$ -type BEDT-TTF salts exhibit a long-range antiferromagnetic (AF) ordering. The  $P$ - $T$  phase diagram for a series of  $\kappa$ -type BEDT-TTF is shown in Fig. 16a. There exists a Mott-Hubbard antiferromagnetic insulating state in the vicinity of the superconducting state [121]. The bandwidth ( $W$ ) of the electronic bands increases with an increase in pressure (Fig. 16b). Therefore, by applying pressure or changing  $U/W$  ( $U$  is the on-site Coulomb repulsion), the antiferromagnetic state is transformed to a metallic and a superconducting state.

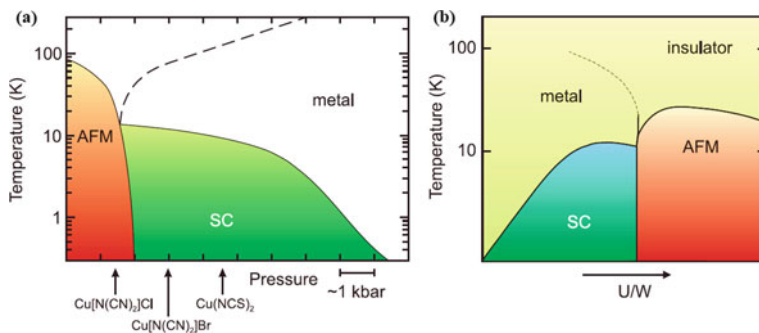


**Fig. 16** Phase diagram of  $\kappa$ -type BEDT-TTF salts: **a** Temperature ( $T$ )—Pressure ( $P$ ), and **b** ( $U/W$ ) versus  $T$ . diagrams

### **BETS salts**

BETS molecules were synthesized by introducing Se atoms to a TTF structure. In the quasi-2D organic salt  $\lambda$ -(BETS)<sub>2</sub>FeCl<sub>4</sub>, superconductivity is originated  $T_c = 0.1$  K by the application of a strong external magnetic field (17 T) [122]. In contrast, BETS salts are antiferromagnetic insulators below 8.5 K at the zero-field condition.

### **DMET, $M(\text{dmit})_2$ [ $M = \text{Ni}, \text{Pd}$ ]**

DMET compounds have been developed to get superior donor compounds. B-(DMET)<sub>2</sub>X (X = AuI<sub>2</sub>, Au(CN)<sub>2</sub>) show SDW transition [123], similar to TMTSF salts. Again,  $\kappa$ -(DMET)<sub>2</sub>AuBr<sub>2</sub> is an ambient pressure superconductor, similar to  $\kappa$ -BEDT-TTF salt [124]. Therefore, the DMET superconductors possess both characteristic features of BEDT-TTF and TMTSF salts.  $\alpha$ -(TTF)[Ni(dmit)<sub>2</sub>]<sub>2</sub> is the first M(dmit)<sub>2</sub> superconductor with  $T_c = 1.62$  K under 0.7 GPa of pressure [125]. This salt is a multi-band system, and for this, despite a CDW is formed at 40 K in Ni(dmit)<sub>2</sub> columns, it is semi(metallic) with the resistivity minimum at  $\sim 3$  K at ambient pressure. Under pressure, the superconducting state competes with the CDW state.

## **7.2 Fullerides**

The fullerenes (C<sub>60</sub>, C<sub>70</sub>, ...) were officially discovered in 1985 by Kroto et al. [126]. It gained much interest when the metallic behavior is observed in solid C<sub>60</sub> by the intercalation of alkali metal atoms in solid C<sub>60</sub> [127]. Very soon after this, superconductivity was observed in a few alkali-metal-doped C<sub>60</sub> with  $T_c$  less than the cuprates [128]. The highest  $T_c$  at ambient pressure is observed in RbCs<sub>2</sub>C<sub>60</sub> at 33 K [129], and for Cs<sub>3</sub>C<sub>60</sub>, the superconducting transition at  $T_c = 40$  K is observed under a pressure of 1.2 GPa [130].

C<sub>60</sub> crystals have face-centered cubic symmetry. When doped with alkali atoms, the alkali atoms can easily fit in the space between the C<sub>60</sub> molecular balls. Figure 17a shows the unit cell of A<sub>3</sub>C<sub>60</sub>. The small spheres represent the alkali ions, and the large spheres represent the C<sub>60</sub> molecules. In the tri-alkali-fullerides, for example, K<sub>3</sub>C<sub>60</sub>, potassium becomes positively ionized K<sup>+</sup>, and each C<sub>60</sub> molecule accepts three electrons to form C<sub>60</sub><sup>3-</sup>. These extra electrons in the C<sub>60</sub> molecules are delocalized electrons and can jump from one molecule to another and contribute to the electrical conductivity [131]. When A<sub>3</sub>C<sub>60</sub> crystal is formed, its lattice constant slightly increases compared to that of C<sub>60</sub> crystal, and as the dopant size increases, the lattice constant and the interfullerene separation also increases. It is found that the  $T_c$  of fcc A<sub>3</sub>C<sub>60</sub> increases monotonically with the increase in the lattice constant [128] (see Fig. 17b).

The dominant pairing mechanism in the fullerides is the electron–phonon interaction [131]. Also, antiferromagnetic spin fluctuations participate in mediating superconductivity in fullerides [134]. These are type-II superconductors. Fullerides burn



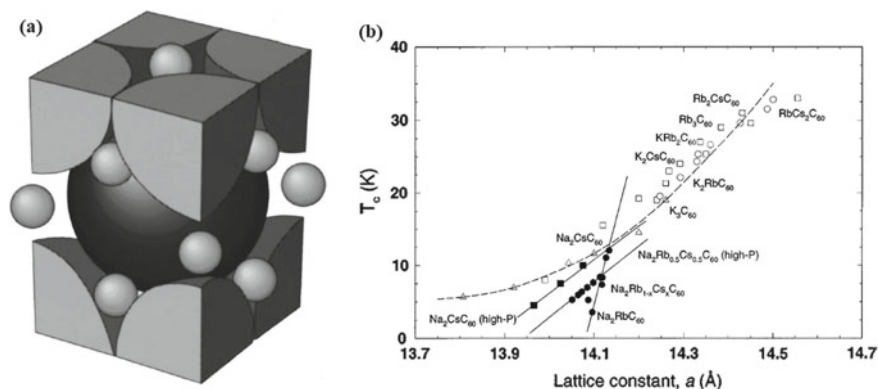


**Fig. 17** **a** Unit cell of  $A_3C_{60}$ . **b**  $T_c$  versus lattice constant  $a$  for various compositions of fcc  $A_3C_{60}$  and primitive cubic  $Na_2A_1C_{60}$  ( $A_1 = Rb, Cs$ ). Reproduced with permission from Refs. [132, 133]

spontaneously and are extremely air-sensitive, and hence, they must be preserved in an inert atmosphere.

## 8 Chevrel Phases

Chevrel and Sergent [135] discovered a new class of materials in 1971 presenting spectacular physical and chemical properties. The general chemical formula of this class of materials is  $M_xMo_6X_8$ , where  $M$  stands for a large number of monovalent, divalent, or trivalent metals with  $x$  varying from 0 up to 4, depending on their ionic size.  $X$  is an anion, mainly chalcogen (S, Se, or Te). This class of materials is known as Chevrel phases. The highest transition temperature of the Chevrel phases is 15 K for  $PbMo_6S_8$  [136]. The Chevrel phases have a remarkably high upper critical magnetic field ( $H_{c2}$ ). Table 5 shows the values of  $T_c$  and  $H_{c2}$  for some Chevrel phases.

Figure 18a shows the crystal structure of  $PbMo_6S_8$ . The Chevrel phases crystallize in a hexagonal-rhombohedral structure, and the building blocks of the crystal structure are the element  $M$  (e.g., Pb) and the  $Mo_6X_8$  ( $X=S$  in the figure) molecular cluster. Each  $Mo_6X_8$  is a moderately distorted cube where the anion  $X$  is at the corners, and the Mo atoms arrange on the faces of the cube. Mo atoms within the cubes form an

**Table 5**  $T_c$  and  $H_{c2}$  values of some Chevrel phases. Data were collected from Refs. [136–139]

Compounds	$T_c$ (K)	$H_{c2}$ (T)
$PbMo_6S_8$	15	60
$SnMo_6S_8$	12	34
$LaMo_6S_8$	7	44.5
$LaMo_6Se_8$	11	5

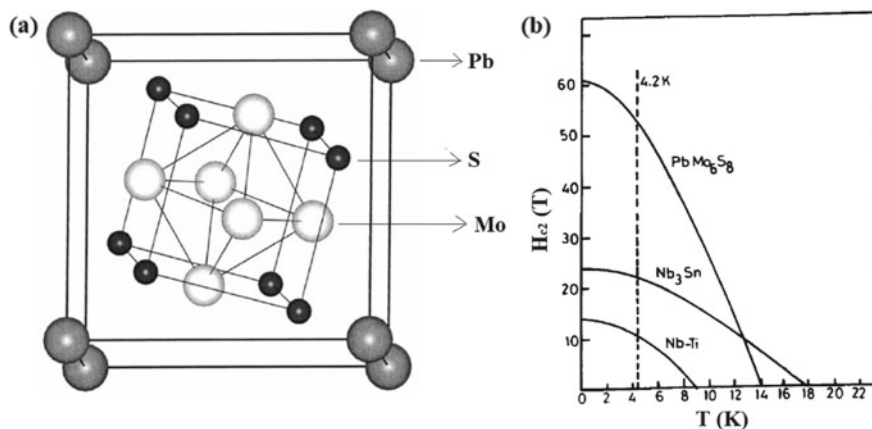


**Fig. 18** a Crystal structure of the Chevrel phase  $\text{PbMo}_6\text{S}_8$ . b Upper critical field  $H_{c2}$  versus temperature (Reproduced with permission from Ref. [140])

octahedron, and this octahedron is a strongly bonded electronic entity. The M atoms (Pb atoms) lie between the cubes. Eight  $\text{Mo}_6\text{S}_8$  cubes surround each Pb atom.

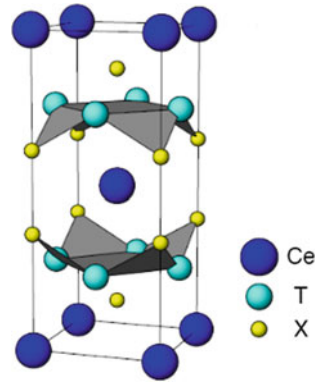
The localized 4f-shell electrons of rare-earth atoms are responsible for magnetic ordering in Chevrel phases, while the 4d-shell electrons of Mo are associated with superconductivity. Most  $(\text{RE})\text{Mo}_6\text{X}_8$  become superconducting (except Ce and Eu) well above their antiferromagnetic ordering temperature  $T_N$ . So, it is evident that superconductivity coexists with antiferromagnetism in the Chevrel phases [140, 141].

High values of upper critical field make Chevrel phases attractive candidates for practical applications. Figure 18b shows the comparison plots for the  $H_{c2}$  for  $\text{PbMo}_6\text{S}_8$ ,  $\text{Nb}_3\text{Sn}$ , and  $\text{NbTi}$  compounds. It is seen from the figure plots that the  $\text{PbMo}_6\text{S}_8$  has a much higher  $H_{c2}$  than that of the  $\text{Nb}_3\text{Sn}$  and  $\text{NbTi}$ . Nevertheless, Chevrel phases are brittle materials, so it is not easy to make wires or ribbons out of these materials. However, a broad range of applications has been opened based on the electrochemical properties [142]. Chevrel phases appear promising candidates for applications to batteries and cathode materials, a new generation of thermoelectrical devices, etc. [143, 144].

## 9 Heavy-Fermion Superconductors

Heavy-fermion systems are intermetallic alloys or compounds which consist of an element or elements being s, p or d-electron metals, and one magnetic ion with localized 4f or 5f electrons. The effective mass of the charge carriers in Heavy-fermion systems is enormous, which is several hundred times greater than that of free electrons. This large effective mass of the charge carriers is the consequence of coupling

**Fig. 19** Body-centered tetragonal crystal structure of  $CeT_2X_2$  ( $T = Cu, Rh, Ni, Pd$ ;  $X = Si, Ge$ ) heavy-fermion compounds



between the conduction electrons of s, p, or d-electron metal and f-electrons of the magnetic ion. The first discovery of superconductivity in a heavy-fermion system was made by Steglich et al. in 1979 [145]. The compound was  $CeCu_2Si_2$  with  $T_c$  at 0.65 K. after that; superconductivity was found in  $UBe_{13}$  at 0.85 K [146] and  $UPt_3$  at 0.54 K [147].

The crystal structure of these compounds varies for different materials in this family. The crystal structure of the first discovered heavy-fermion superconductor  $CeCu_2Si_2$  has a body-centered tetragonal structure (see in Fig. 19, [148]), but  $UPt_3$  and  $UBe_{13}$  have hexagonal and cubic structures, respectively.

The heavy-fermion superconductors are unconventional superconductors that exhibit an interplay between magnetism and superconductivity. Superconductivity and antiferromagnetic order do not compete in heavy-fermion systems since superconductivity is mediated by spin fluctuations [149].

## 10 Journey to the Room-Temperature Superconductivity

The quest for room-temperature superconductors has been going for many years. Over the years, since the first discovery of superconductivity, the field has continuously evolved, and superconductors with higher and higher  $T_c$ 's have been discovered. In 1968, Ashcroft [150] predicted that the atomic metallic phases formed at high pressure (>25 GPa) be stable and could also be a high-temperature superconductor. This conjecture was based on BCS considerations. It is known that hydrogen does not transform directly from an insulating molecular phase to an atomic metallic solid. However, it undergoes a series of transformations to semiconducting and semimetallic molecular phases with increasing pressure to several hundred GPa [151]. The transformation to the atomic metallic phase is currently constrained to be near 500 GPa [152]. Recent calculations predict that this crystalline phase could be a superconductor with a very high  $T_c$  of almost 400 K [152]. However, this prediction is yet to be proved experimentally due to the constraints of the current technology.

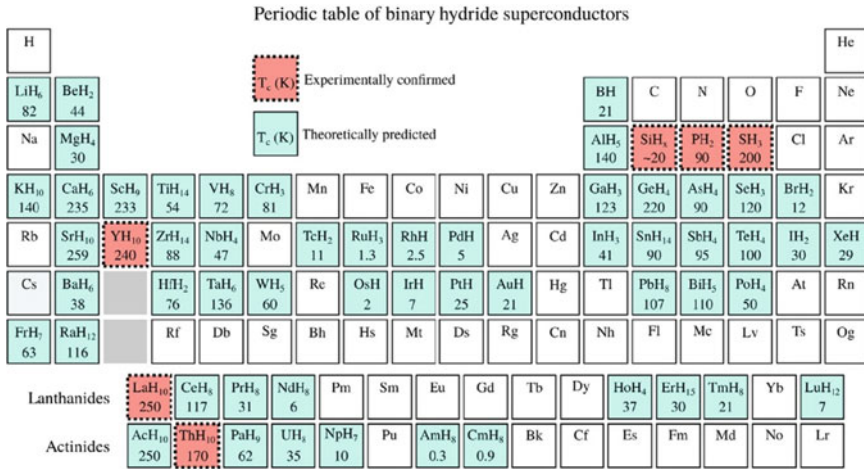


Fig. 20 Periodic table of superconducting binary hydrides (0–300 GPa). Reproduced from Ref. [7]

Ashcroft et al. later suggested a different way to effectively reduce the transition to atomic metallic hydrogen by using the dopants in the structure [153]. In 2004, Ashcroft [154] extended the above considerations and postulated that the hydrogen molecules in dense structure might be expected to dissociate at a pressure well below the pressure required for pure hydrogen, realizing an effective chemical precompression of the hydrogen sublattice. This idea led to rapid progress in both the experimental and the computational structure search for high- $T_c$  high-pressure hydride, which was started with the discovery of  $T_c$  at 235 K in  $CaH_6$  [155]. In 2015, superconductivity was observed in the high- $T_c$  hydride  $H_3S$  at 203 K at 155 GPa of pressure [156]. In 2019, near room-temperature superconductivity was discovered in  $LaH_{10}$  with a  $T_c$  of 250 K at a pressure of 180–200 GPa [157]. Figure 20 shows the periodic table of both experimentally confirmed and theoretically predicted superconducting binary hydrides available till now. This table shows the compositions with the highest  $T_c$  predicted in the pressure range 0 to 300 GPa.

## 11 Conclusion

This chapter has attempted to discuss the structures, properties, and applications of few important classes of non-cuprate superconductors. It provides a review on non-cuprate superconductors is sketchy, considering the vastness of literature available on these materials. Hopefully, this chapter will give a broad overview of the vibrant area of superconductivity research.

## References

1. H.K. Onnes, *Leiden Commun.* **124**, 1226 (1911)
2. W. Meissner, R. Oschenfeld, *Naturwissenschaften* **21**, 787 (1933)
3. F. London, H. London, *Proc. Roy. Soc.* **71**, A149 (1935)
4. V.L. Ginzburg, L.D. Landau, *Sov. Phys. JETP* **20**, 1064 (1950)
5. J. Bardeen, L.N. Cooper, J.R. Shrieffer, *Phys. Rev.* **108**, 1175 (1957)
6. H.K. Onnes, *Commun* (Phys. Lab. Univ, Leiden, 1913)
7. J.A. Flores-Livas et al., *Phys. Rep.* **856**, 4 (2020)
8. G.F. Hardy, J.K. Hulm, *Phys. Rev.* **93**, 1004 (1954)
9. B.T. Matthias et al., *Phys. Rev.* **139**, A1501 (1965)
10. G.R. Stewart, B.L. Brandt, *Phys. Rev. B* **29**, 3908 (1984)
11. D.F. Moore et al., *Phys. Rev. B* **20**, 2721 (1979)
12. B.T. Matthias et al., *Phys. Rev.* **95**, 1435 (1954)
13. S. Foner, *IEEE Trans. Appl. Supercond.* **5**, 121 (1995)
14. J.M. Rowell et al., *IEEE Trans. Magn.* **13**, 644 (1977)
15. R.H. Willens et al., *Solid State Commun.* **7**, 837 (1969)
16. B.T. Matthias et al., *Science* **156**, 645 (1967)
17. A. Godeke, *Supercond. Sci. Technol.* **19**, R68 (2006)
18. L.R. Testardi, *Rev. Mod. Phys.* **47**, 638 (1975)
19. A. Vostner, E. Salpietro, *Supercond. Sci. Technol.* **19**, S90 (2006)
20. P.J. Lee et al., *IEEE Trans. Appl. Supercond.* **13**, 3422 (2003)
21. W.S. Williams, *Prog. Solid. State Ch.* **6**, 57 (1971)
22. G.W. Webb, F. Marsiglio, J.E. Hirsch, *Physica C* **514**, 24 (2015)
23. B.T. Matthias, T.H. Geballe, V.B. Compton, *Rev. Phys.* **85**, 1 (1963)
24. R.H. Willens, E. Buehler, *Appl. Phys. Letters* **1**, 25 (1965)
25. E.V. Pechen et al., *Physica C* **235–240**, 2511 (1994)
26. D. Dew-Hughes, R. Jones, *Appl. Phys. Lett.* **36**, 856 (1980)
27. K. Inoue, K. Tachikawa, *Appl. Phys. Lett.* **18**, 235 (1971)
28. K. Inoue, T. Kuroda, K. Tachikawa, *J. Nucl. Mater.* **133–134**, 815 (1985)
29. J. Nagamatsu et al., *Nature* **410**, 63 (2001)
30. O.F. de Lima et al., *Phys. Rev. Lett.* **86**, 5974 (2001)
31. S.B. Samanta et al., *Phys. Rev. B* **65**, 092510 (2002)
32. P.C. Canfield, G.W. Crabtree, *Phys. Today* **56**, 34 (2003)
33. D.G. Hinks, H. Claus, J.D. Jorgensen, *Nature* **411**, 457 (2001)
34. K. Vinod, N. Varghese, U. Syamaprasad, *Supercond. Sci. Technol.* **20**, R31 (2007)
35. M.E. Jones, R.E. Marsh, *J. Am. Chem. Soc.* **76**, 1434 (1954)
36. P. Ravindran et al., *Phys. Rev. B* **64**, 224509 (2001)
37. H.J. Choi, M.L. Cohen, S.G. Louie, *Physica C* **385**, 66 (2003)
38. H.J. Choi et al., *Nature* **418**, 758 (2002)
39. I.I. Mazin, V.P. Antropov, *Physica C* **385**, 49 (2003)
40. P. Szabó et al., *Phys. Rev. Lett.* **87**, 137005 (2001)
41. S. Tsuda et al., *Phys. Rev. Lett.* **87**, 177006 (2001)
42. H. Suhl, B.T. Matthias, L.R. Walker, *Phys. Rev. Lett.* **3**, 552 (1959)
43. Yu. Eltsev et al., *Phys. Rev. B* **66**, 180504 (2002)
44. P.C. Canfield, *Phys. Rev. Lett.* **86**, 2423 (2001)
45. S.C. Erwin, I.I. Mazin, *Phys. Rev. B* **68**, 132505 (2003)
46. W. Goldacker et al., *Supercond. Sci. Technol.* **17**, S363 (2004)
47. D. Larbalestier et al., *Nature* **414**, 368 (2001)
48. C. Escribe-Filippini et al., *Physica C* **210**, 133 (1993)
49. Y. Kamihara et al., *J. Am. Chem. Soc.* **128**, 10012 (2006)
50. Y. Kamihara et al., *J. Am. Chem. Soc.* **130**, 3296 (2008)
51. Z.A. Ren, W. Lu et al., *Chin Phys Lett* **25**, 2215 (2008)
52. K. Haule, J.H. Shim, G. Kotliar, *Phys. Rev. Lett.* **100**, 226402 (2008)

53. D.J. Singh, *Physica C* **469**, 418 (2009)
54. X. Chen et al., *Nat. Sci. Rev.* **1**, 371 (2014)
55. Y. Zhang et al., *Phys. Rev. B* **83**, 054510 (2011)
56. I.I. Mazin, *Nature* **464**, 183 (2010)
57. J. Dong et al., *EPL* **83**, 27006 (2008)
58. R. Khasanov et al., *Phys. Rev. B* **84**, 100501(R) (2011)
59. Q. Huang et al., *Phys. Rev. B* **78**, 054529 (2008)
60. S. Avci et al., *Phys. Rev. B* **85**, 184507 (2012)
61. S. Nandi et al., *Phys. Rev. Lett.* **104**, 057006 (2010)
62. S. Kasahara et al., *Phys. Rev. B* **81**, 184519 (2010)
63. W. Zhen, C. Yao et al., *Chin. Phys. B* **22**, 087409 (2013)
64. P.M. Aswathy, J.B. Anooja, P.M. Sarun, U. Syamaprasad, *Supercond. Sci. Technol.* **23**, 073001 (2010)
65. J. Zhao et al., *Nat. Mater.* **7**, 953 (2008)
66. P.M. Shirage et al., *Phys. Rev. B* **78**, 172503 (2008)
67. C. Lee, *J. Phys. Soc. Jpn.* **77**, 083704 (2008)
68. H. Takahashi, K. Igawa et al., *Nature* **453**, 376 (2008)
69. X.C. Wang et al., *Solid State Commun.* **148**, 538 (2008)
70. F.-C. Hsu, J.-Y. Luo et al., *Proc. Natl. Acad. Sci. USA* **105**, 14262 (2008)
71. D.S. Inosov, J.T. Park et al., *Nat. Phys.* **6**, 178 (2010)
72. S. Chi et al., *Phys. Rev. Lett.* **102**, 107006 (2009)
73. A.D. Christianson et al., *Nature* **456**, 930 (2008)
74. K. Horigane et al., *J. Phys. Soc. Jpn.* **78**, 063705 (2009)
75. M. Ishikado et al., *Physica C* **471**, 639 (2010)
76. Z. Deng et al., *EPL* **87**, 37004 (2009)
77. Y. Mizuguchi et al., *EPL* **90**, 57002 (2010)
78. S. Margadonna et al., *Phys. Rev. B* **80**, 064506 (2009)
79. C. Huang et al., *J. Phys. Soc. Jpn.* **78**, 084710 (2009)
80. H. Ogino et al., *Appl. Phys. Express* **3**, 063103 (2010)
81. B. Wei, H. Qing-Zhen et al., *Chin. Phys. Lett.* **28**, 086104 (2011)
82. H. Ogino, Y. Matsumura et al., *Supercond. Sci. Technol.* **22**, 075008 (2009)
83. B. Wei et al., *Chin. Phys. Lett.* **28**, 086104 (2011)
84. Z. Gao, L. Wang et al., *Supercond. Sci. Technol.* **21**, 105024 (2008)
85. D. Li, K. Lee et al., *Nature* **572**, 624 (2019)
86. A.S. Botana, M.R. Norman, *Phys. Rev. X* **10**, 011024 (2020)
87. Q. Li, C. He et al., *Commun. Mater.* **1**, 16 (2020)
88. A.S. Botana, F. Bernardini, A. Cano, *J. Exp. Theor. Phys.* **132**, 618–627 (2021)
89. Y. Nomura et al., *Phys. Rev. B* **100**, 205138 (2019)
90. P. Adhikary et al., *Phys. Rev. B* **102**, 100501(R) (2020)
91. D. Li, B.Y. Wang et al., *Phys. Rev. Lett.* **125**, 027001 (2020)
92. G.-M. Zhang, Y.-F. Yang, F.-C. Zhang, *Phys. Rev. B* **101**, 020501 (2020)
93. Y. Cui, C. Li et al., *Chinese Phys. Lett.* **38**, 067401 (2021)
94. A.W. Sleight, J.L. Gillson, P.E. Bierstedt, *Solid State Commun.* **17**, 27 (1975)
95. L.F. Mattheiss, E.M. Gyorgy, D.W. Johnson Jr., *Phys. Rev. B* **37**, 3745 (1988)
96. R.J. Cava et al., *Nature* **332**, 814 (1988)
97. N.L. Jones et al., *J. Solid State Chem.* **78**, 319 (1989)
98. S. Pei et al., *Phys. Rev. B* **41**, 4126 (1990)
99. S. Kondoh et al., *Physica C* **157**, 469–477 (1989)
100. S.Y. Liu et al., *J. Am. Ceram. Soc.*, 1–8 (2016)
101. E.S. Hellman, E.H. Hartford Jr., *Phys. Rev. B* **47**, 11346 (1993)
102. B. Dabrowski et al., *Physica C* **156**, 24–26 (1988)
103. Y.J. Uemura et al., *Nature* **335**, 151–152 (1988)
104. J. Schooley, W. Hosler, M.L. Cohen, *Phys. Rev. Lett.* **12**, 474 (1964)
105. J.K. Hulm, C.K. Jones, *J. Low Temp. Phys.* **7**, 291 (1972)

106. A.W. Sleight, *Phys. Today* **44**(6), 24 (1991)
107. A.W. Sleight, T.A. Bither, P.E. Bierstedt, *Solid State Commun.* **7**, 299–300 (1969)
108. D.C. Johnston, H. Prakash et al., *Mater. Res. Bull.* **8**, 777 (1973)
109. Y. Maeno et al., *Nature* **372**, 532 (1994)
110. J. Ferraris, D.O. Cowan et al., *J. Am. Chem. Soc.* **95**, 948 (1973)
111. D. Jerome, A. Mazaud, M. Ribault, K. Bechgaard, *J. Phys. Lett.* **41**, L95 (1980)
112. H. Mori, *J. Phys. Soc. Jpn.* **75**, 051003 (2006)
113. V. Vescoli et al., *Eur. Phys. J. B* **13**, 503 (2000)
114. M. Dumm et al., *Phys. Rev. B* **61**, 511 (2000)
115. R. Laversanne, C. Coulon et al., *J. Phys. Lett.* **45**, L393 (1984)
116. D.S. Chow et al., *Phys. Rev. Lett.* **85**, 1698 (2000)
117. C. Coulon et al., *J. Physique* **43**, 1721 (1982)
118. T. Adachi et al., *J. Am. Chem. Soc.* **122**, 3238 (2000)
119. S.S.P. Parkin et al., *Phys. Rev. Lett.* **50**, 270 (1983)
120. J.E. Schirber et al., *Phys. Rev. B* **33**, 1987 (1986)
121. J. Wosnitza, *Curr. Comput.-Aided Drug Des.* **2**, 248 (2012)
122. S. Uji et al., *Nature* **410**, 908 (2001)
123. K. Kanoda et al., *Phys. Rev. B* **38**, 39 (1988)
124. K. Kikuchi et al., *Solid State Commun.* **66**, 405 (1988)
125. L. Brossard et al., *C. R. Acad. Sci. Paris, Ser. II* **302**, 205 (1986)
126. H.W. Kroto et al., *Nature* **318**, 162 (1985)
127. R.C. Haddon et al., *Nature* **350**, 320 (1991)
128. R.M. Fleming et al., *Nature* **352**, 787 (1991)
129. K. Tanigaki et al., *Nature* **352**, 222 (1991)
130. T.T.M. Palstra et al., *Solid State Commun.* **93**, 327 (1995)
131. O. Gunnarsson, *Rev. Mod. Phys.* **69**, 575 (1997)
132. C.H. Pennington, V.A. Stenger, *Rev. Mod. Phys.* **68**, 855 (1996)
133. C.M. Brown et al., *Phys. Rev. B* **59**, 4439 (1999)
134. Y. Takabayashi et al., *Science* **323**, 1585 (2009)
135. R. Chevrel, M. Sergent, J. Prigent, *J. Solid State Chem.* **3**, 515 (1971)
136. Ø. Fischer, *Appl. Phys.* **16**, 1 (1978)
137. T. Jarlborg, A.J. Freeman, *Phys. Rev. Lett.* **44**, 178 (1980)
138. O. Peña, M. Sergent, *Prog. Solid St. Chem.* **19**, 165 (1989)
139. R.N. Shelton, R.W. McCallum, H. Adrian, *Phys. Lett.* **56A**, 213 (1976)
140. R. Chevrel et al., *Polyhedron* **5**, 87 (1986)
141. R.J. Cava, *J. Am. Ceram. Soc.* **83**, 5–28 (2000)
142. Z. Kaidi et al., *J. Solid State Chem.* **147**, 199 (1999)
143. T. Uchida et al., *J. Electrochem. Soc.* **137**, 7 (1990)
144. V. Vasudeva Rao et al., *J. Phys. F: Met. Phys.* **14**, 973 (1984)
145. F. Steglich et al., *Phys. Rev. Lett.* **43**, 1892 (1979)
146. H.R. Ott et al., *Phys. Rev. Lett.* **50**, 1595 (1983)
147. G.R. Stewart et al., *Phys. Rev. Lett.* **52**, 679 (1984)
148. O. Stockert et al., *J. Phys. Soc. Jpn.* **81**, 1 (2012)
149. G.R. Stewart, *Rev. Mod. Phys.* **56**, 755 (1984)
150. N.W. Ashcroft, *Phys. Rev. Lett.* **21**, 1748 (1968)
151. H.K. Mao, R.J. Hemley, *Rev. Mod. Phys.* **66**, 671 (1994)
152. J.M. McMahon et al., *Rev. Mod. Phys.* **84**, 1607 (2012)
153. A.E. Carlsson, N.W. Ashcroft, *Phys. Rev. Lett.* **50**, 1305 (1983)
154. N.W. Ashcroft, *Phys. Rev. Lett.* **92**, 187002 (2004)
155. H. Wang et al., *Proc. Natl. Acad. Sci. USA* **109**, 6463 (2012)
156. A.P. Drozdov et al., *Nature* **525**, 73 (2015)
157. A.P. Drozdov et al., *Nature* **569**, 528 (2019)

# Design of Cuprate HTS Superconductors



Devendra K. Namburi and David A. Cardwell

**Abstract** This chapter focuses on two important aspects of advancing and engineering rare-earth, cuprate-based bulk high-temperature superconductors [(RE)BCO] for both established and more innovative applications of these technologically important materials. This chapter presents a brief review of recent advances in processing, including the reliability of single grain growth, enhancement in the superconducting properties of melt-grown and infiltration-grown (RE)BCO bulk materials, achieved via engineering of the sample microstructure. Subsequently, the design of single grain (RE)BCO bulk superconductors for a range of novel applications, including hybrid trapped field magnetic lensing, high-performance magnetic shields, large-gradient magnetic separation and bench-top NMR/MRI ring-shaped stacks will be discussed. The second part of the chapter focuses on the applications where large electromagnetic stresses are characteristically a limiting factor. In this context, the in-situ and ex-situ reinforcement strategies explored in the (RE)BCO bulk framework to transform these ceramic-like materials into more robust, high performance bulk superconductors is reviewed and summarized. In-situ reinforcement strategies such as the addition of Ag, introducing thin-wall artificial holes in bulk samples during processing and the integration of fibres into the bulk (RE)BCO microstructure and ex-situ reinforcement strategies such as composite stacking comprising of laminated (RE)BCO bulk discs sandwiched between layers of stainless-steel plates and pre-stressing the bulk single grains with stainless-steel rings via a shrink-fit approach will be discussed and reviewed. Overall, therefore, this chapter will address the advances made in bringing single grain (RE)BCO bulk superconductors closer to deployment in both established and more innovative and challenging applications.

---

D. K. Namburi (✉) · D. A. Cardwell  
Department of Engineering, University of Cambridge, Cambridge, UK  
e-mail: [ndevendra@gmail.com](mailto:ndevendra@gmail.com)

D. A. Cardwell  
e-mail: [dc135@cam.ac.uk](mailto:dc135@cam.ac.uk)

D. K. Namburi  
Electronic and Nanoscience Engineering, University of Glasgow, Glasgow, UK



**Keywords** High-temperature cuprate superconductors · Processing · Melt growth · Infiltration growth · Superconducting properties · Mechanical properties

## 1 Introduction

Over the last three decades, extensive research has been carried out on cuprate-based high-temperature superconducting (HTS) oxide materials which led to significant advancements in both the processing and properties of these materials [1–4]. (RE)Ba<sub>2</sub>Cu<sub>3</sub>O<sub>7- $\delta$</sub>  (RE-123), where RE stands for rare-earth component such as Gd, Sm, Nd, Yb, Y etc., is the composition which exhibits critical temperature ( $T_c$ , of ~90 K) well above the boiling temperature of liquid nitrogen (77.3 K). Liquid nitrogen being more economical and with abundance availability in comparison to liquid helium (which is required for invoking the superconducting properties in low temperature superconducting ‘LTS’ materials) encouraged more research to be carried out on (RE)BCO-based materials, especially due to the merits associated with this system in terms of enhanced irreversibility fields ( $H_{irr}$ ) and large current carrying ability (often referred to as critical current density  $J_c$  or more practically engineering critical current density  $J_e$ ) possible at practical cryogenic temperatures.

Since the discovery of YBCO by Chu and Wu in 1987 [5], substantial effort has been made to improve both the critical aspects namely the single grain growth and the critical current densities in these materials [1–4, 6]. In the initial efforts, the fabrication procedures as followed in conventional ceramics such as solid state sintering were tried to produce YBCO superconducting material but it was soon realized that obtaining a single grain was the first and foremost task as the grain boundaries could adversely affect the superconducting properties. If the material is not processed properly, it can result in multiple grains as shown in Fig. 1. Two examples of the occurrence of multiple grains, one where no seed crystal was employed during processing of YBCO and the other where seed crystal was used but the heat treatment was not appropriate i.e., when the sample assembly was fast-cooled through its peritectic temperature ( $T_p$ ), are shown in Fig. 1. In this figure, an optical micrograph exhibiting presence of multiple and tilted grains is shown which outlines the fact that the single grain need be achieved. The current carrying ability within each of these little grains is high (of the order of  $10^3$ – $10^4$  A/cm<sup>2</sup> at 77 K), but across the grain-boundaries, the value of  $J_c$  can be smaller by 2–3 orders of magnitude and hence the (RE)BCO bulk as a whole will exhibit poor superconducting properties—i.e. nearly no considerable magnetic field can be trapped and hence the material will be unusable in applications.

Several fabrication processes (involving either hot-seeding or cold-seeding based approaches) have been developed and modified to achieve single grain growth in (RE)BCO. Initially, the hot-seeding based approach [7, 8] was developed and explored but the complexity and the practical challenges associated with this approach did not encourage considerable research in this direction. Subsequently, cold-seeding based approaches which employed higher peritectic temperature (RE)BCO material (such as NdBCO or SmBCO) as the seed crystal for the

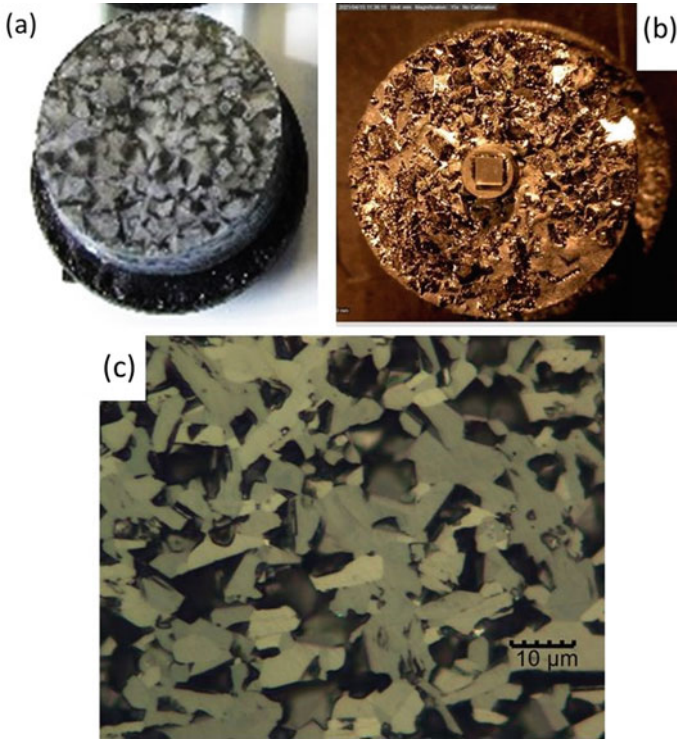


**Fig. 1** Occurrence of multiple grains in (RE)BCO bulks where **a** no seed was employed and **b** seed was used but the sample assembly was cooled rapidly through the peritectic temperature of the compound. **c** Optical micrograph recorded in sintered YBCO material showing presence of different grains with different orientations. The marker in the optical micrograph is 10  $\mu\text{m}$  in length

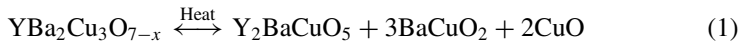
YBCO system. Some of the cold-seeding approaches which were successful in producing reasonable single grains of (RE)BCO are quench melt growth (QMG) [9], melt-powder melt growth (MPMG) [10], melt-textured growth (MTG) [11], oxygen-controlled melt growth (OCMG) [12], top-seeded melt growth (TSMG) [13, 14] and top-seeded infiltration and growth (TSIG) [15, 16]. Every processing technique has its own merits and demerits. In this present chapter, we will confine our discussion to TSMG and TSIG-based approaches, as these are the two fabrication processes that are being followed currently due to the advanced technical readiness level these have got to in terms of enabling batch- and mass-production of (RE)BCO single-grain materials. Since the superconducting and mechanical properties of the (RE)BCO materials are largely governed by their microstructure, special attention is to be given to the microstructural engineering aspect. In this chapter, the designing of the (RE)BCO material for its microstructure, flux pinning ability and novel reinforcement strategies investigated will be reviewed and the details will be discussed. Some of the novel designed geometries in (RE)BCO bulks including long cavities with fused caps for magnetic shielding performance, conical geometries for magnetic

lensing effects, ring-shaped bulks with lens assembly working as hybrid-trapped field magnetic lens (HTFML) will also be discussed and highlighted.

## 2 Processing of (RE)BCO via Melt-Growth Approaches

The melt growth (MG) process, initially developed by Jin et al. [17] had been improved significantly to enable single grain growth of (RE)BCO. The information often derived from the phase diagram is crucial, to tailor the heat-treatments that enables single grain growth in (RE)BCO. A pseudo-binary phase diagram of (RE)BCO with an example of YBCO [18] is shown in Fig. 2.

It can be seen from the Fig. 2 that the YBCO material when heated in air, above 900 °C, the liquid phase gets initiated and when heated its characteristic temperature called the peritectic temperature  $T_p$ , of the compound, the Y-123 phase undergoes incongruent melting and forms solid Y-211 component and the liquid phase comprising of  $BaCuO_2$  and  $CuO$ , as described in Eq. (1). The (RE)BCO system when heated above its melting temperature and slow-cooled through  $T_p$ , the Y-211 and liquid phase reacts and recombines to form Y-123.



### 2.1 Fabrication via Top Seeded Melt Growth

In the top-seeded melt growth (TSMG) approach, choosing an appropriate seed crystal is crucial. A material which possesses characteristics as (i) higher

**Fig. 2** Pseudo-binary phase diagram of Y–Ba–Cu–O system [18]. Here  $L$  stands for the liquid phase (largely comprising of  $BaCuO_2$  and  $CuO$ ) and  $T_p$  for the peritectic temperature

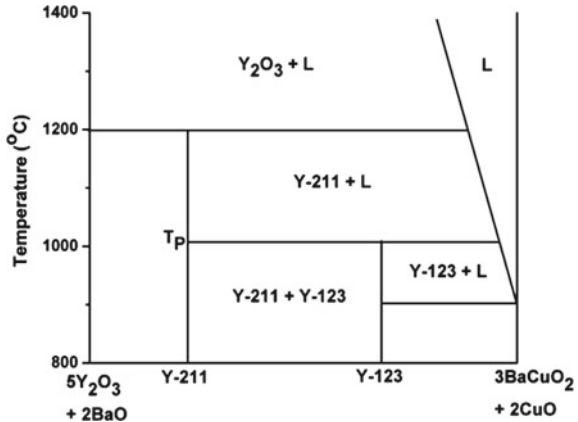


**Table 1** Peritectic temperature ( $T_p$ ) of various (RE)BCO compounds. *Data were taken from Ref. [2]*

RE in (REBa <sub>2</sub> Cu <sub>3</sub> O <sub>7-<math>\delta</math>)</sub>	Peritectic Temperature $T_p$ (°C) ( $\pm 5$ °C)
Yb	960
Er	990
Y	1005
Ho	1005
Dy	1010
Gd	1030
Eu	1046
Sm	1054
Nd	1068

melting/peritectic temperature compared to the material being fabricated, (ii) similar crystal structure as the material being grown, and (iii) exhibiting phase stability with the melt, categorizes it as a seed crystal. To fabricate YBCO single grain, cleaved slab of SmBCO or NdBCO bulk or even the recently developed NdBCO film seed [19, 20] works as a seed crystal. The peritectic temperature of some of the (RE)BCO compounds in air atmosphere can be appreciated from Table 1. It has been found that the growth rate of Y-123 is very small ( $\sim 0.035$  mm/h) and hence often Y-211 phase is added to the precursor powder to increase the growth rate of Y-123 through supply of Y-ions during the growth. Further, the presence of Y-211 inclusions in the final product is known to aid the magnetic flux pinning strength through creation of suitable interfacial defects. The size and amount of RE-211, and its distribution in the matrix of RE-123 is known to control the superconducting properties. Since finer the size of RE-211, larger are the interfacial defects and hence higher the current densities achieved. In order to refine the size of RE-211 inclusions in the final product microstructure, Pt or CeO<sub>2</sub> is added to the precursor powder which changes the viscosity of molten liquid thereby inhibits the grain growth of RE-211 in the matrix of RE-123.

The YBCO sample assembly configuration and the single grain formed employing TSMG are shown in Fig. 3. In the TSMG process, the precursor composition of 75% RE-123 + 25% RE-211 + 0.5% CeO<sub>2</sub> is compacted into a pellet and supported with a seed crystal and heat-treated by exposing the sample to a temperature above the  $T_p$  of the (RE)BCO material being fabricated. At this temperature, as described in Eq. 1, the RE-123 phase undergoes incongruent melting and forms RE-211 and liquid phase. On slow-cooling through the  $T_p$  of the REBCO compound, the liquid phase reacts with RE-211 phase to form RE-123. During this process, the heterogenous nucleation occurs at the seed location and the single grain grows transforming the entire material into a single grain. The growth sectors and growth sector boundaries both in  $a$ -growth and  $c$ -growth regions of the single-grain sample can also be seen in the figure. Though the single grain is achieved, the reliability aspect was of great concern in TSMG as the success rate was limited to 30–40%. Some of the typical

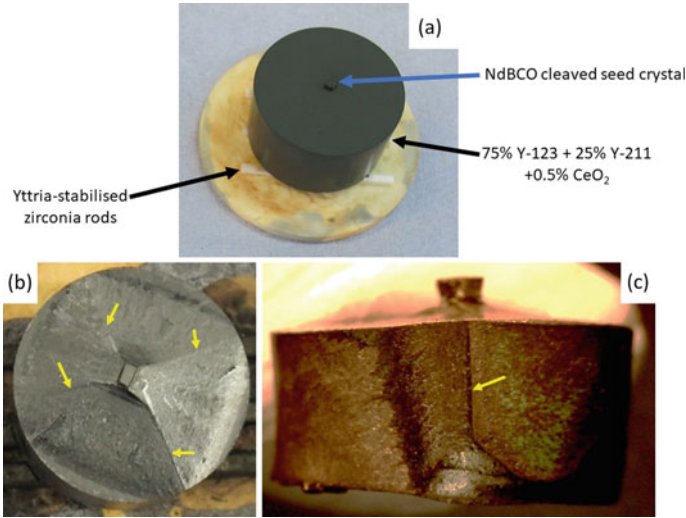


**Fig. 3** **a** Sample assembly configuration for producing YBCO bulk via top-seeded melt growth (TSMG) technique. NdBCO seed crystal positioned on the top of the YBCO precursor pellet, prepared for TSMG processing can be seen. The top and side-views of the TSMG-processed single grain of YBCO are shown in **(b)** and **(c)** respectively. The growth sector boundaries as observed both in *a*-growth and *c*-growth regions are highlighted with arrows (yellow in color)

failures in terms of single grain usually observed via conventional TSMG are shown in Fig. 4. It can be seen that the aggressive liquid phase component that forms during the peritectic reactions can get in contact with the seed crystal resulting in either a partial or complete melting of the seed crystal. These deleterious effects get worse with longer duration of heat treatments. In this context, the buffer technique initially developed and explored by Yao et al. [21, 22] and C-J Kim et al. [23] was further improved and optimized by the Cambridge Bulk Superconductivity Group (BSG) [24–26] is indeed appealing as the success rate of TSMG was enhanced significantly to >90%, via this integrated and modified TSMG referred as buffer-aided TSMG ‘BA-TSMG’ technique. The details of this BA-TSMG are discussed in the next section.

## 2.2 Buffer-Aided TSMG (BA-TSMG) Approach

In this fabrication approach, a buffer pellet comprising of the same composition as the main sample but without added RE-211 grain-refining agent, is compacted into a mini-pellet and is arranged between the seed crystal and the main sample being grown. This aspect of sample arrangement is shown in Fig. 5a. The processed YBCO samples (both via TSMG and BA-TSMG) and the cross-sectional optical micrographs recorded in these samples indicating the growth regions can be seen in

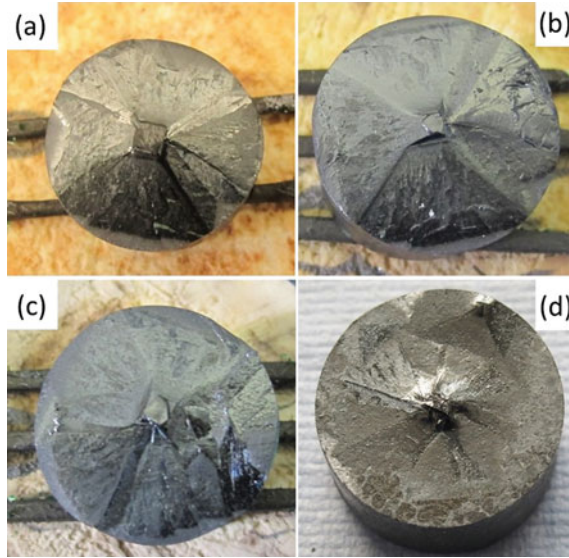


**Fig. 4** Occurrence of partial (a, b) or complete (c, d) melting of the seed crystal as observed in TSMG processed YBCO samples. The failure of the seed crystal is because of its contact with the aggressive liquid phase component

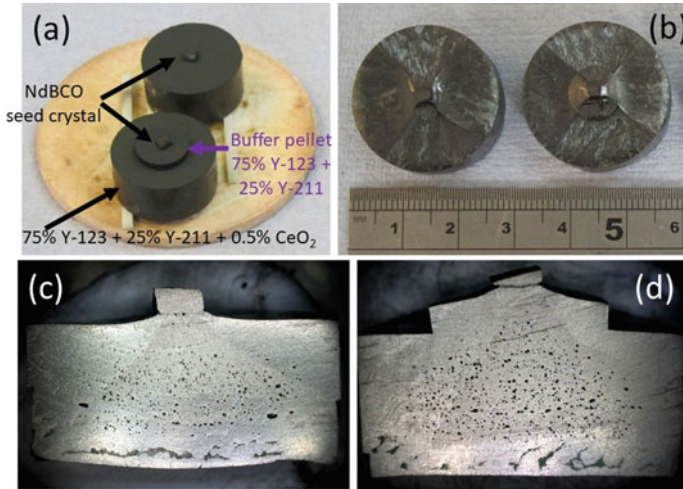


**Fig. 5 a** Arrangement of the YBCO sample assemblies in the TMG and buffer-aided TSMG approaches. In the case of YBCO system, a buffer pellet (of ~5–8 mm in diameter and ~2–3 in height) composed of 75% Y-123 + 25% Y-211 is placed between the seed crystal and the main sample being fabricated. **b** Single grain YBCO samples obtained via TSMG and BA-TSMG are shown. The cross-sectional, optical micrographs obtained in both the TSMG and BA-TSMG processed YBCO samples are shown in (c) and (d) respectively

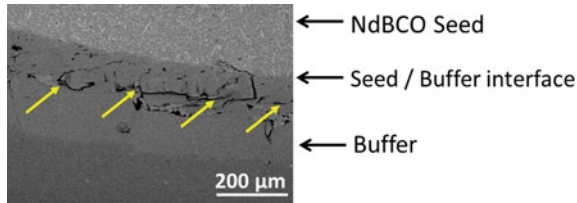


**Fig. 6** A scanning electron micrograph recorded at the interface between seed-buffer location in a BA-TSMG processed YBCO sample. The lattice mismatch effects causing cracks are present at the seed-buffer interface and getting confined within the buffer pellet region can be seen in the micrograph. The cracks and defects occurring at the interface are indicated with arrows (yellow in color)

Fig. 5b–d. Introduction of the buffer pellet has resulted out to be of a great advantage [24–26] as outlined below:

- (i) The reliability of single grain growth has increased appreciably as the liquid phase component that gets into contact with the seed crystal is reduced significantly.
- (ii) The lattice mis-match effects arising due to seed-sample system are all absorbed within the buffer pellet thereby shielding the main sample from these defects.
- (iii) The buffer pellet shields the diffusion of the seed crystal element from getting into main sample thereby enabling better uniformity in the superconducting properties as observed across the volume of the samples.
- (iv) The buffer pellet also shields Ag from diffusing upwards—Ag in (RE)BCO + Ag sample from reaching the seed crystal.

The cracks and defects that occur due to lattice-mismatch effects, at the seed-sample interface are absorbed within the buffer pellet as shown in Fig. 6. Further, the seed crystal element (Nd in this case) diffusion was found to be confined within the buffer pellet thereby overcoming the problem of solid-solution or low  $T_c$  phase formation with the main sample being fabricated. The aspect of buffer pellet deployment shielding the seed crystal element (Nd) diffusion into the (RE)BCO sample, aiding improving uniformity in  $T_c$  and  $J_c(H)$  [24], can be appreciated from Fig. 7.

### 3 Microstructural Engineering of (RE)BCO Bulks

Presence of microstructural defects such as pores and cracks remain one of the weak spots in the rare-earth, cuprate based bulk superconducting materials. In order to improve this aspect, two approaches investigated recently are reviewed and summarized in this section.

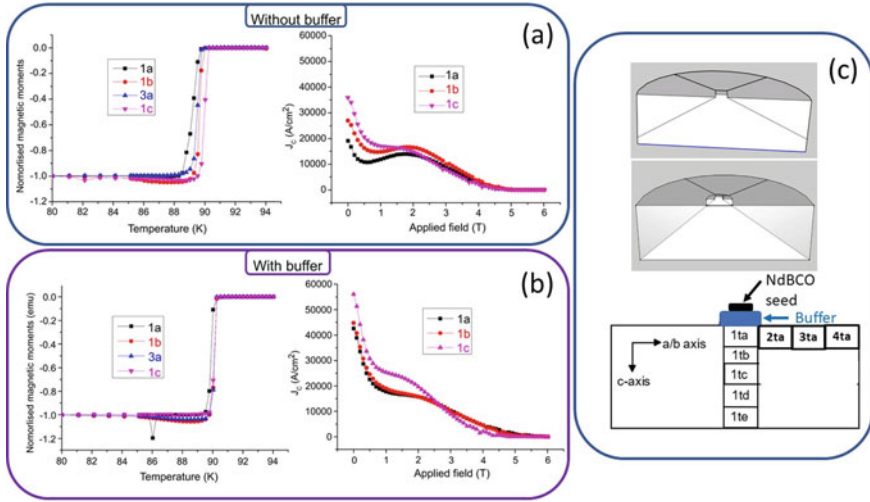
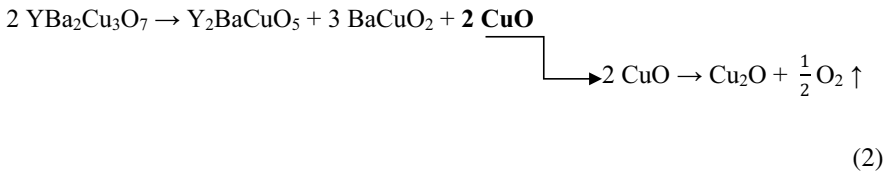


**Fig. 7** Critical temperature ‘ $T_c$ ’ and field dependence of critical current density ‘ $J_c(H)$ ’ (measured at 77 K) in YBCO samples fabricated via TSMG (without buffer) and buffer-aided TSMG (with buffer) are shown in (a) and (b) respectively. *The figures were reproduced from [24].* The positions corresponding to 1ta, 1tb, 1tc, and 3ta are schematically shown in (c)

### 3.1 Thin-Walled YBCO Bulks—Improved Microstructure

(RE)BCO bulk superconductors are limited by their mechanical and thermal properties rather than the superconducting properties and hence have been hindering them from being deployed in some challenging applications where electromagnetic stresses have been of concern. Typical microstructure of YBCO bulk superconductor obtained via TSMG is shown in Fig. 8. It can be seen that significant fraction of pores and cracks are present within the microstructure of the material. The reason for the occurrence of these microstructural defects is associated with the oxygen gas evolution that happens during the peritectic reactions, as explained in Eq. 2.



Very often, presence of cracks and pores within the microstructure of these materials creates further defects (at their interfaces with the matrix) that tend to aggravate and hence break the entire material when excited sufficiently either via mechanical or electromagnetic pressure. The pores occurring in the circumferential/outer regions of the bulk can diffuse out relatively easily but the ones formed within the core of



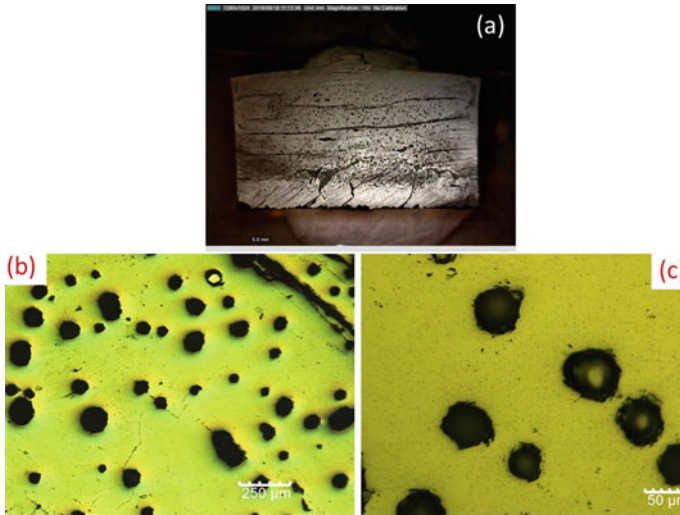


**Fig. 8** a Cross-section of a YBCO bulk superconductor fabricated via TSMG approach. Optical micrographs recorded under a magnification of  $50\times$  and  $1000\times$  are shown in (b) and (c) respectively. Presence of pores and cracks occurring within the microstructure of the bulk sample can be seen

the bulk remains trapped as indicated in Fig. 9. Hence, the weak spot within the bulk sample is present at its central location [27].

To address this aspect of excess porosity within the bulk and also to create permeation channels for oxygen to reach the centre of sample during the oxygenation

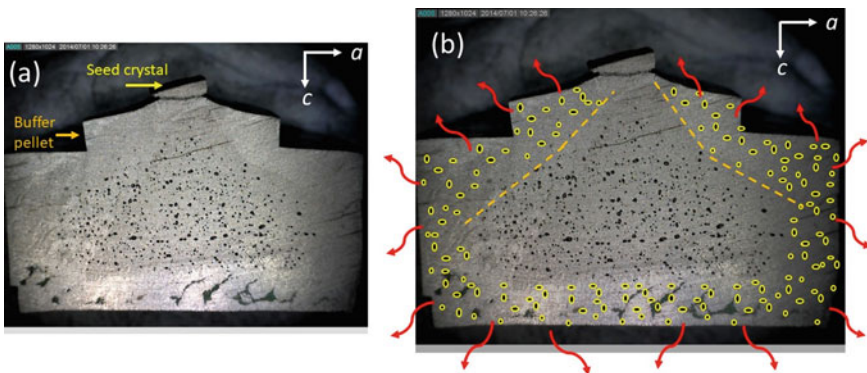


**Fig. 9** a Cross-sectional optical micrograph exhibiting the presence of pores within the TSMG-processed YBCO sample is shown. The same optical micrograph is presented again in (b) but with a schematic version indicating how the pores that would have appeared in the outer/edge regions of the bulk sample would have diffused out into the atmosphere during the processing step. *Reproduced with permission from Ref. [27]*

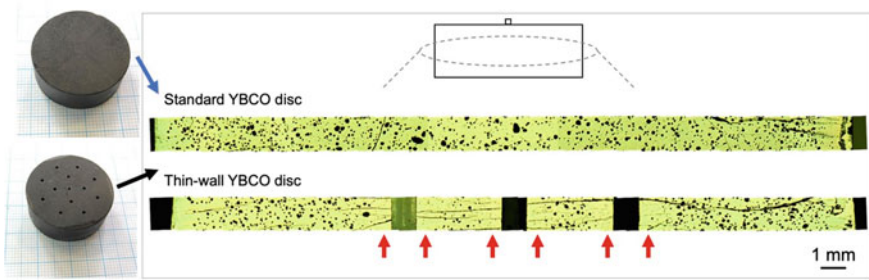


**Fig. 10** Microstructures at the centre of the YBCO bulks—both in standard and thin-walled bulk containing artificial holes. Reduction of pores in the areas close to the artificially drilled hole regions are highlighted with arrows (red in color). *These figures were reproduced from Ref. [31]*

process, few efforts have been made. Initially Chaud et al. [28] and Noudem et al. [29] and recently Hlasek et al. [30] and Huang et al. [31] explored pathways by creating artificial holes in the bulk during the compaction stage. The advantage of introducing artificial holes in (RE)BCO bulks is threefold: (i) to enable  $O_2$  gas formed during peritectic reactions to diffuse out thereby reducing the porosity levels, (ii) to speed up the oxygenation process, and (iii) to enable enhancing the thermal properties of the bulk by subsequently filling these artificial holes with resin/conducting paste/wires. It was found that fraction of pores reduced in the samples containing artificial holes, as can be seen in Fig. 10. Furthermore, the mechanical properties exhibited by these bulks were found to be higher compared to the standard (RE)BCO bulks. Huang et al. [31] recently further filled these open holes with copper wires and solder to minimize the stress-concentration points and further assisting the cooling process. Such a reinforced YBCO sample could overcome Lorentz forces with applied fields of up to 11.5 T and could trap a magnetic field of  $\sim 8$  T at 35 K and  $\sim 9$  T at 30 K. The presence of copper in the matrix has improved the thermal conductivity of bulk and hence assisted in overcoming flux jumps to a moderate extent. Hence, these results are greatly encouraging from large-stress applications perspective.

### 3.2 Processing of (RE)BCO via Infiltration Growth Approach

To address some of the limitations unavoidable with the conventional TSMG, the infiltration and growth (IG) process was developed [15, 32, 33], inspired from the ceramic-based technology. The IG-based fabrication approach enables near-net shape fabrication of the (RE)BCO material and further can improve its microstructure by reducing the fraction of pores and cracks significantly. If the processing parameters are well tuned, this fabrication approach can produce (RE)BCO bulks with improved superconducting and mechanical properties. In the IG process, the sample assembly comprises of an RE-211 preform placed in contact with the liquid phase reservoir pellet. A buffer pellet capped with a seed crystal is then arranged on the top of

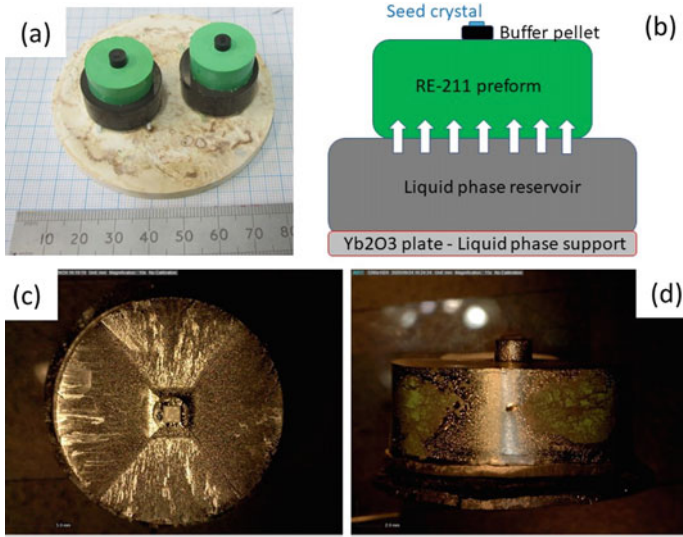
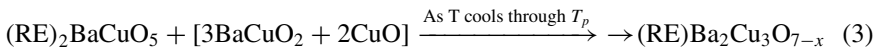


**Fig. 11** a Sample assembly arrangement as followed in buffer-aided TSIG approach is shown. The description of each of the pellets involved (i.e. RE-211 preform pellet, the liquid phase reservoir pellet, the liquid phase support pellet—Yb<sub>2</sub>O<sub>3</sub> plate in this case, the buffer pellet and the seed crystal) is provided in (b). The liquid phase infiltration into RE-211 preform during the heat treatment is schematically indicated with arrows in (b). The top and side-views of a GdBCO + Ag single grain as obtained via BA-TSIG process are shown in (c) and (d) respectively

the RE-211 preform to aid the seeding process. During the heat treatment step, the copper rich liquid phase (comprising of BaCuO<sub>2</sub> and CuO) is made to infiltrate into porous RE-211 preform above the  $T_p$  of the compound, which subsequently below  $T_p$ , reacts with the RE-211 phase to form RE-123, as described in Eq. 3. The sample assembly arrangement and the seed configuration along with the buffer pellet are shown in Fig. 11a, b. The top and side-views of a typical single grain GdBCO + Ag bulk obtained via buffer-aided TSIG approach are shown in Fig. 11c, d.



### 3.2.1 Potential of TSIG Approach

Some of the merits possible due to the employment of TSIG approach are:

- (i) Near-net shaping of (RE)BCO bulks with nearly no shrinkage.
- (ii) Supports dense microstructures with significantly reduced pores and cracks, in comparison to the ones possible via conventional TSMG approach,

- (iii) enables homogeneous distribution of RE-211 particles in the final (RE)BCO product thereby supporting uniform current densities across the volume of the samples,
- (iv) Enables improvement in the mechanical properties, partly due to reduced pores and cracks in the microstructure of the material.

In the conventional TSMG approach, the samples suffer a shrinkage of ~18–20% and this is unavoidable as the RE-123 phase undergoes incongruent melting during which there is an outflow of the liquid phase component. In contrast, in the TSIG approach, no liquid phase forms in the RE-211 preform pellet. During the heat treatment, the liquid phase that forms in the liquid phase reservoir pellet gets infiltrated into the preform pellet and hence results in nearly no shrinkage. This infiltrated liquid phase, under suitable heat treatment condition, reacts with the RE-211 phase to form RE-123. Typical shrinkage observed in TSMG and TSIG processed YBCO samples are shown in Fig. 12a. Optical micrographs recorded under low magnification of 50 $\times$  in the TSMG and TSIG processed YBCO samples, indicating the level of porosity, are provided in Fig. 12b and c respectively. Due to this ability of near-net shaping, the IG approach has been extended and explored to produce shielding cavities [15, 34], superconducting fabrics and foams [35–37].

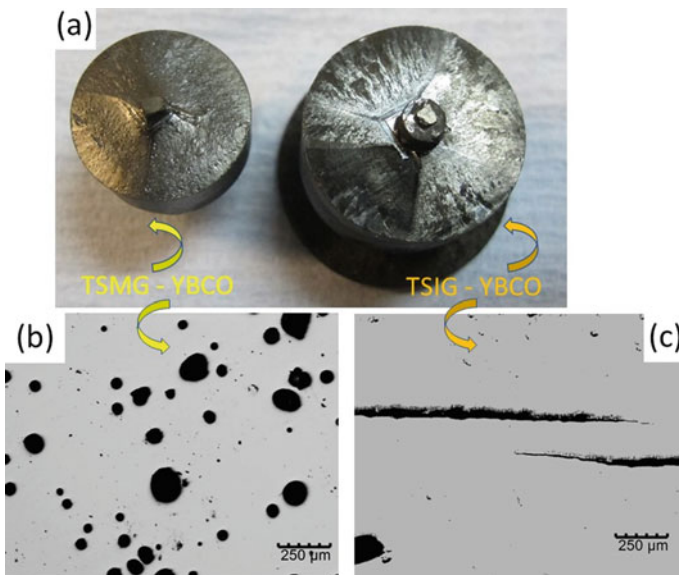


**Fig. 12** a Shrinkage as observed in the YBCO samples fabricated via TSMG and TSIG. Both these sample preforms were of the same size but due to the outflow of the liquid phase, the TSMG one (sample on the left) suffered ~20% shrinkage while the TSIG processed sample (the sample on the right) retained its shape and size. Optical micrographs obtained in each of these samples (produced via TSMG and TSIG) are shown in (b) and (c) respectively

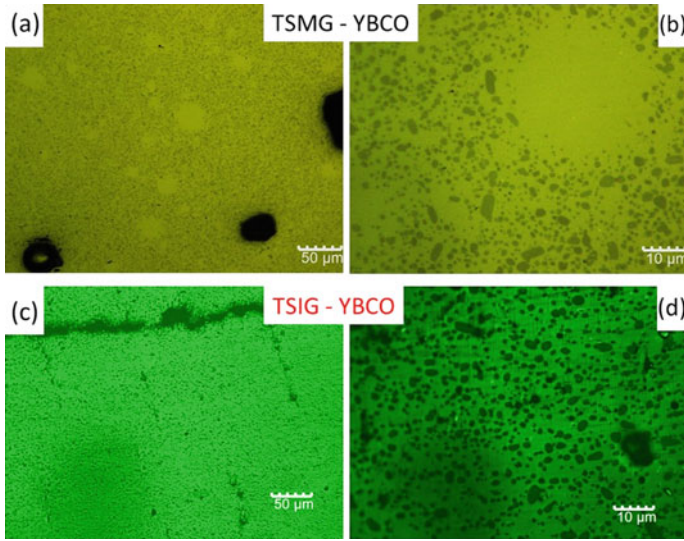


**Fig. 13** Comparison of TSMG and TSIG processed YBCO samples' microstructure from the perspective of the presence of RE-211-free regions. Optical micrographs recorded under magnifications of  $200\times$  and  $1000\times$  in both the samples—one processed via TSMG (a and b) and the other via TSIG (c and d) are shown

In TSMG processing, during the heat treatment step, some of the pores/voids occurring due to the evolution of oxygen gas can get filled with liquid phase pools, which, while cooling via  $T_p$  of the compound react completely with RE-211 phase, forming RE-123. Such regions transform themselves as RE-211-free regions in the final product microstructure as shown in Fig. 13a, b. Such RE-211-free regions affect the homogeneity in the distribution of RE-211 and hence the uniformity of  $J_c$  across the sample volume. This also leads to variation in the mechanical properties across the sample volume. In TSIG, as described above, no gas evolutions occur in the main (RE)BCO sample and hence no RE-211-free regions occur in the microstructure. These aspects are shown in Fig. 13c, d.

Recently, three important advancements, as listed below, have been made to the TSIG processing to increase the reliability of single grain growth and to achieve improved superconducting properties.

1. Integrating the buffer pellet strategy to TSIG to shield or reduce significantly the interaction of the liquid phase with the seed crystal during the processing step.
2. Identifying the suitable liquid phase component that would effectively and efficiently infiltrate into the RE-211 preform under optimized conditions and further will not cause sub-grain from forming.
3. Separating the infiltration and growth, steps and carrying them sequentially—this refined and advanced process is termed as 2-step buffer-aided TSIG (2-step BA-TSIG)

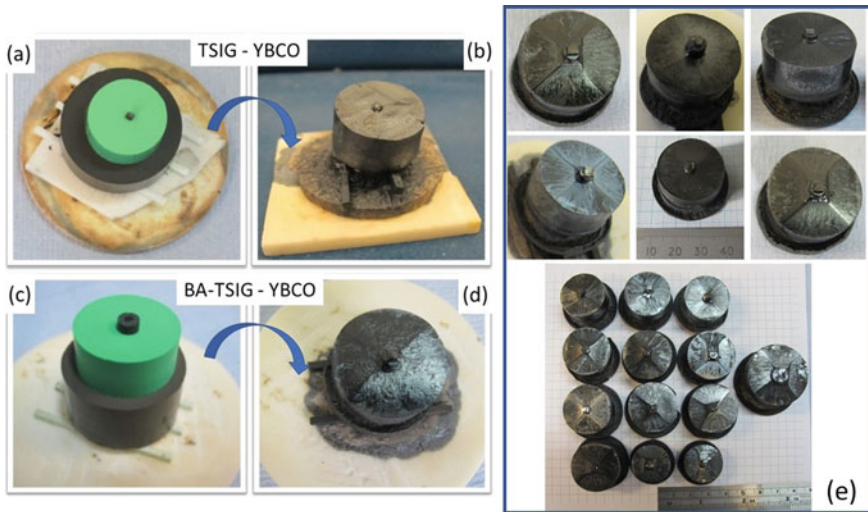


**Fig. 14** Comparison of single grain growth in two different configurations of TSIG—one with no buffer assembly and the other with buffer pellet arranged between the RE-211 preform and the seed crystal. It can be seen that the single grain growth is reliable and successful when buffer strategy is adapted in TSIG. Collection of several single grain (RE)BCO samples produced via BA-TSIG is shown in (e)

The buffer pellet integration in TSIG, as described earlier in the case of BA-TSMG, has been very productive in enhancing the success rate of single grain growth for (RE)BCO materials [24, 25]. In the context of TSIG, the buffer pellet role is furthermore more crucial as the liquid phase component is higher in this approach and hence can get into the vicinity of the seed crystal relatively easily. A comparison of YBCO sample fabrication via TSIG employing no buffer and with buffer pellet assembly is shown in Fig. 14. It can be seen that when buffer pellet strategy is employed, the reliability of single grain growth is higher, as indicated in Fig. 14e. Further, employing a suitable liquid phase component overcomes issues such as stability and sub-grain formation in the material. The success rate of single-grain fabrication via BA-TSIG is now in excess of 90% and hence has emerged as potential fabrication approach enabling mass production of these materials.

### 3.2.2 Controlling the RE-211 Content in the TSIG Approach

The size of RE-211 inclusions and the content of RE-211 phase in the final product microstructure, plays a crucial role in governing the flux pinning strength of the material and hence the superconducting properties (i.e. both the trapped field and the current density performance). In this context, in the TSMG processing the RE-211 content can be conveniently controlled by adjusting the starting composition as RE-123 + x% RE-211. However, in TSIG approach, the control of RE-211 content

is more complex and is indeed very challenging. This is due to the fact that the final RE-211 content depends on a number of parameters including the compaction porosity present in the RE-211 preform pellet, the particle size of the initial RE-211 phase, and amount of the liquid phase that gets infiltrated into the RE-211 preform pellet during the heat-treatment step. These processing parameters are too complex to tune and are further inter-dependent, making the task of controlling the RE-211 content in TSIG processing very challenging. In conventional TSIG processing, the RE-211 content in final product microstructure often results between 40 and 55% by volume fraction which is too large a content for the non-superconducting phase to be present in the matrix and affects the superconducting properties of (RE)BCO material significantly.

D. K. Namburi et al. tuned and optimised the critical parameters in TSIG such as infiltration temperature ( $T_i$ ) and infiltration time ( $t_i$ ) to achieve optimum levels of liquid phase infiltration into the RE-211 preform, which subsequently, below  $T_p$ , reacts with RE-211 and leaves back suitable amount of RE-211 flux pinning inclusions in the final product microstructure thereby supporting higher current densities and hence can trap large magnetic fields. In this context, the 2-step buffer-assisted TSIG (2-step BA-TSIG) approach emerged advantageous as it enables reliable single-grain growth, supports enhanced superconducting and mechanical properties due to the improved microstructures (with reduced pores and cracks and with optimum RE-211 content) possible. These aspects are shown in Fig. 15.

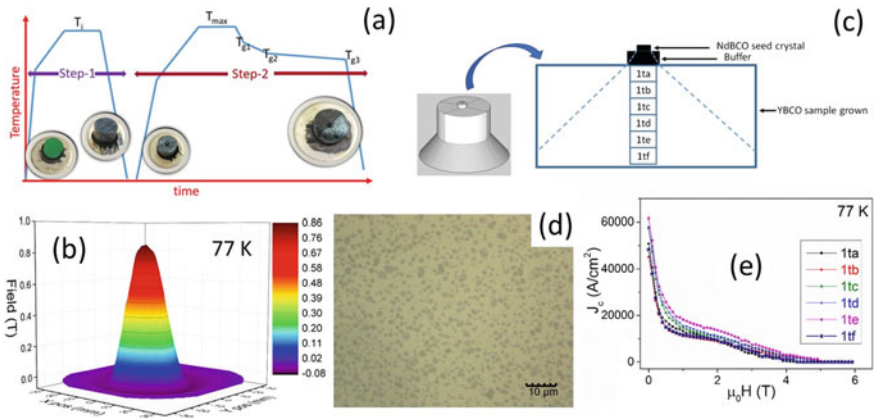


**Fig. 15** **a** Steps involved for obtaining (RE)BCO samples via 2-step buffer-aided TSIG approach are shown schematically. Here,  $T_i$  stands for infiltration temperature,  $T_{max}$  for maximum temperature to which the sample assembly is heated to, and  $T_g$  refers to the growth-temperatures. The step-1 and step-2 referring to the infiltration and growth steps are also indicated in the figure. **b** Trapped field profile (at 77 K) obtained in one of the YBCO samples fabricated via 2-step BA-TSIG approach. **c** Sectioning of the sample and labelling scheme followed are schematically shown. **d** Typical optical micrograph exhibiting presence of Y-211 inclusions and **e**  $J_c(H)$  at 77 K, obtained in 2-step BA-TSIG processed YBCO sample are shown

### 4 Reinforcement Strategies in (RE)BCO Bulks

The reliability in single grain growth of (RE)BCO achieved encouraged various designs and shapes to be explored for applications. But, to reliably deploy these materials in real-scale applications especially in the ones where large electromagnetic stresses get generated, some form of reinforcement is essential. While magnetizing a bulk superconductor an external magnetic field need by applied and this creates a magnetic pressure ( $\propto \frac{B^2}{2\mu_0}$ ) which is indeed experienced by the superconducting bulk as the Lorentz force. A plot between the applied magnetic field and the magnetic pressure it creates is shown in Fig. 16a. It can be seen that in order to take magnetic fields beyond 7–8 T, the (RE)BCO bulk need some form of reinforcement to aid its mechanical strength. An example where a (RE)BCO sample is exposed to a 10 T magnetic field, generated using a superconducting magnet, undergoing cracking/breaking is shown in Fig. 16b, c.

To magnetise the bulk superconductors, a field cooled magnetization (FCM) approach is commonly used. In the FCM method, the bulk superconductor to be magnetized is positioned firmly in the sample holder at room temperature and then exposed to an applied magnetic field ( $B_{appl}$ ) (generated using either an electromagnet or a superconducting solenoidal magnet) with  $B_{appl} \parallel c$ -axis of the sample and subsequently cooled (with cryogen) to the required experimental operating temperature ( $T < T_c$ ). Once the sample reaches thermal equilibrium, the external applied magnetic field is removed, and the superconductor is found to trap magnetic field based on its magnetic flux pinning strength. A (RE)BCO superconductor, depending on its

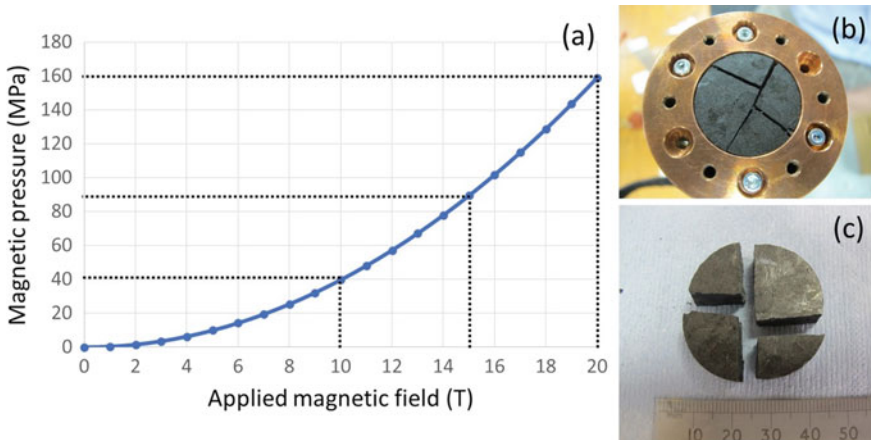


**Fig. 16** a Magnetic pressure as a function of applied external magnetic field. It can be seen that the superconducting sample experiences a magnetic pressure of 40 MPa, 90 MPa, and 160 MPa for applied fields of 5 T, 10 T and 20 T respectively. Typical failure occurring in a (RE)BCO sample when exposed to a magnetic field of 10 T applied field (generated using a superconducting magnet) is shown in (b) and (c)



microstructure and its magnetic flux pinning capability, can trap a magnetic field of  $\sim 6\text{--}8$  T on its surface. If larger fields are applied, the Lorentz force generated is so high that the material can crack/break (as shown in Fig. 16b) due to its poor tensile strength. The mechanical properties and methods to improve them will be discussed in this section.

## 4.1 In-Situ Reinforcement Approaches

Two of the in-situ reinforcement approaches investigated in (RE)BCO bulk superconducting materials namely Ag addition and fibre-integration into the superconducting matrix are discussed in this section.

### 4.1.1 Ag Addition

The addition of Ag into (RE)BCO has been explored to improve the strength and fracture toughness of this ceramic-natured brittle material. It has been observed that addition of Ag reduces the peritectic temperature of the (RE)BCO phase being fabricated. Simultaneously it was observed that Ag particles get accumulated in the pore-regions within the microstructure of the final (RE)BCO product thereby increasing the strength of the composite. Both the factors namely the pores reduction and the pore-regions being occupied by ductile, high conductivity Ag particles in advantageous from the aspects of mechanical and thermal conductivity properties. The microstructures of Ag-free and Ag-added YBCO samples are shown in Fig. 17. It can be seen from this figure that the pore-regions are dominantly filled with the ductile Ag particles which indeed is advantageous from mechanical properties perspective [38, 39].

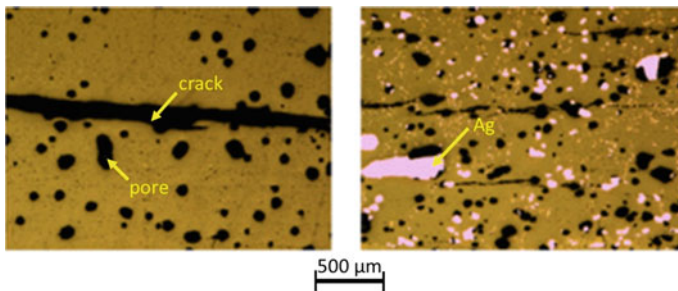


**Fig. 17** Effect of Ag addition on the microstructure in YBCO is shown. Optical micrographs obtained in Ag-free and Ag-added YBCO bulk superconductors are shown in (a) and (b) respectively. It can be seen that Ag is getting segregated in pore and cracks regions of the sample thereby improving the microstructure significantly. *Reproduced with permission from Ref. [39]*

### 4.1.2 Fibre Integration

In conventional ceramics, introduction and integration of suitable fibres have resulted in the enhancement of stiffness and strength of the composite. An example is a glass-fibre-reinforced-polymer (GFRP) where the polymer matrix is significantly strengthened through addition of glass fibres. In the same spirit, attempts have been made to enhance the mechanical strength of (RE)BCO bulks via fibre integration. A variety of fibres including Ti, W, Ta, quartz, SiC etc. have been tested in order to integrate them into (RE)BCO bulks with an aim to increase the strength of these ceramic-like materials. The task here is furthermore challenging as the choice of suitable fibres, their method of introduction and integration into the superconductor matrix is involved but crucial to retain the superconducting properties and simultaneously enhance the mechanical properties of the reinforced (RE)BCO bulk.

Since most of the fibre components have their melting temperature well above the peritectic temperature of (RE)BCO, it is highly likely that the fibres can cause sub-grain formations if not well introduced. Hence, the pre-processing step where the (RE)BCO precursor powders are treated and homogenized with the fibres is indeed vital. A recent work where a careful study was carried out investigating the reinforcement with W–SiC hybrid fibres has been very promising [40, 41]. These fibres of  $\sim 100\ \mu\text{m}$  in diameter with a W-core of  $\sim 20\ \mu\text{m}$  when successfully introduced into the matrix improved the tensile strength of such reinforced bulk superconductors significantly. Two examples where fibres were chopped and homogeneously distributed within the YBCO bulk single grain and the other where fibres were aligned in a preferential direction are shown in Fig. 18. In both these cases, the tensile strength of the fibre-reinforced YBCO bulk was found to be higher by at least 40% compared to the reference/standard fibre-free YBCO bulk samples, as shown in Fig. 18f.

## 4.2 *Ex-Situ Reinforcement Approaches*

Two of the potential ex-situ reinforcement approaches being greatly considered and followed for bulk superconducting materials are discussed and reviewed in this section.

### 4.2.1 Pre-stressing via Shrink-Fit Approach

RE–Ba–Cu–O bulk superconductors are brittle ceramics and need reinforcement for realizing practical applications. Pre-compression is known to be very effective in reinforcing bulk superconductors. YBCO bulks were encapsulated with Fe–Mn–Si-based shape-memory alloy ring to generate large pre-compression as the shape recovery strain achieved using this material was  $\sim 2\%$  [42]. This approach showed an enhancement in the mechanical property of the YBCO bulk. Even more interesting, in 2003, Tomita and Murakami [43] used a combined reinforcement strategy and

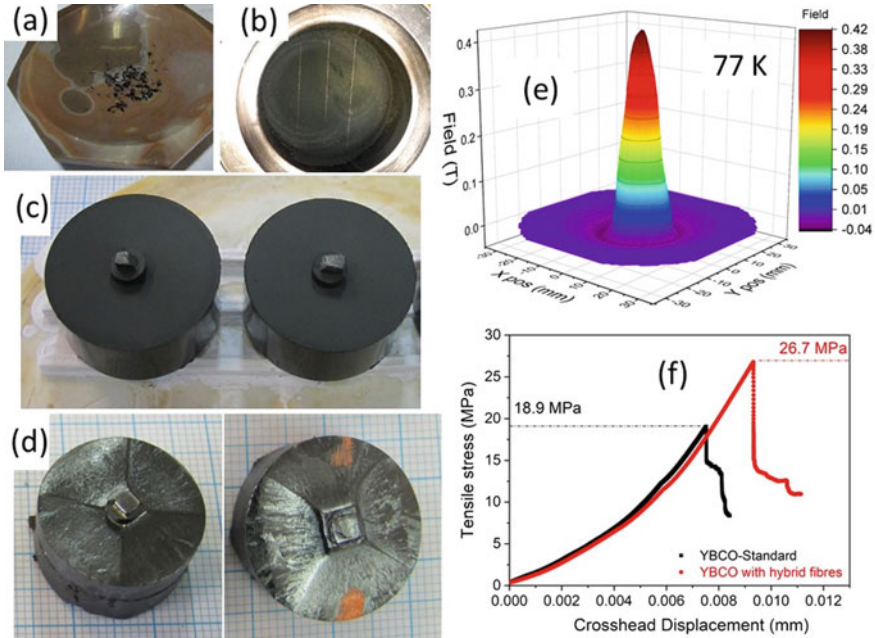


**Fig. 18** Hybrid SiC (containing W at its core) fibres chopped and aligned in the YBCO precursor powders before heat treatment are shown in (a) and (b). Sample assemblies prepared with the added fibres are shown in (c) and as-obtained single grain samples are shown in (d). Trapped field measured at 77 K in one of the fibre-added samples is shown in (e) and tensile strength as measured, via Brazilian technique, in fibre-free standard YBCO (represented with black squares) and in fibre-added YBCO sample (represented in red circles) are shown in (f). Some of these figures were reproduced from Ref. [40]

achieved a trapped field of 17.24 T at 29 K between two YBCO samples (26 mm in diameter) impregnated with resin and Wood's metal and further reinforced with carbon fibre.

Due to higher critical temperature and high  $J_c$  performance, GdBCO + Ag bulk superconductors are attractive from the potential of trapping higher magnetic field. In this context, in 2014, Durrell et al. [44] used the pre-stressing mechanism to shrink-fit the machined GdBCO bulks with stainless steel (SS) rings as shown in Fig. 19b. For this purpose, the SS ring was made with smaller radii compared to the machined GdBCO bulk and the ring was heated to a temperature of 350 °C and then dropped over the bulk sample, to obtain the pre-stressing. Two such shrink-fitted GdBCO + Ag bulks were arranged one above the other with Hall sensors positioned between them to measure the trapped magnetic field during the field-cooled magnetisation experiments. A schematic of the field cooled magnetization approach, followed for trapping the magnetic field in the superconducting bulks is shown in Fig. 19a. Some of the sample fabrication aspects and the obtained trapped field results from the stacked bulks are shown in Fig. 19.

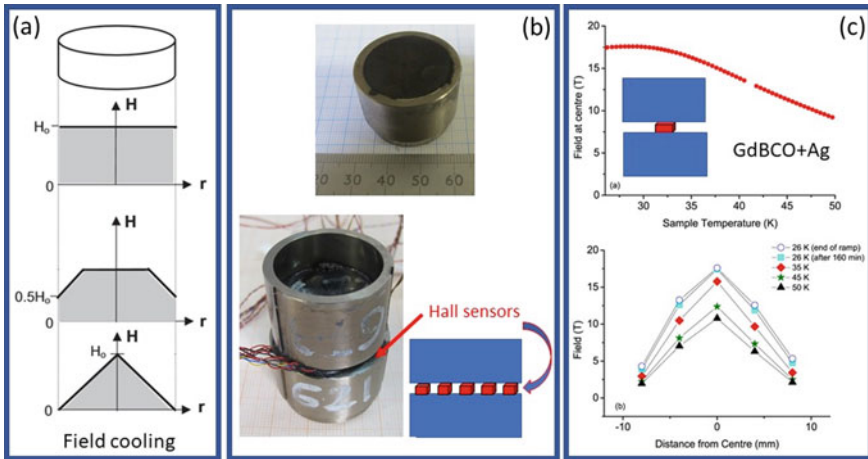


**Fig. 19** a Field cooled magnetization process is shown schematically. b Photograph of the shrink-fitted GdBCO+Ag sample and stacked two-sample configuration with five Hall sensors positioned between the bulks are shown. c Trapped field as measured between two GdBCO + Ag bulks at 26 K and in temperature range 26–50 K. Some of these figures were reproduced from Refs. [4] and [44]

### 4.2.2 Composite Stacking/Laminating Approach

It is very challenging to trap large magnetic fields, in excess of 16 T, even in the two sample stacked configurations of (RE)BCO. This is partially due to the fact that the tensile strength of these materials are poor, due to the presence of pores and cracks within the (RE)BCO material microstructure as discussed earlier. In this context, a reinforcement concept initially suggested by Morito et al. [45] later extended and investigated for (RE)BCO tapes by Patel et al. [46] and laminated GdBCO + Ag bulks by Huang et al. [47]. As an example, we discuss the laminated structure as followed recently in GdBCO + Ag bulk materials. In this approach, thin layers (of 1.5–2 mm thickness) were sliced from single grain GdBCO + Ag bulk superconductors (of ~25 mm in diameter). Stainless steel discs (~22 mm in diameter and ~0.5 mm thickness) were sandwiched between the layers of superconductors as shown in Fig. 20a. The entire composite structure thus obtained was machined and subsequently shrink-fitted in stainless steel ring (as can be seen in Fig. 20b), to provide the pre-stress. This reinforced sample assembly on field-cooled magnetization succeeded trapping magnetic fields in excess of 17 T reliably, as can be seen in Fig. 20c, d and also in repeated cycles, which is promising from real-scale applications perspective.

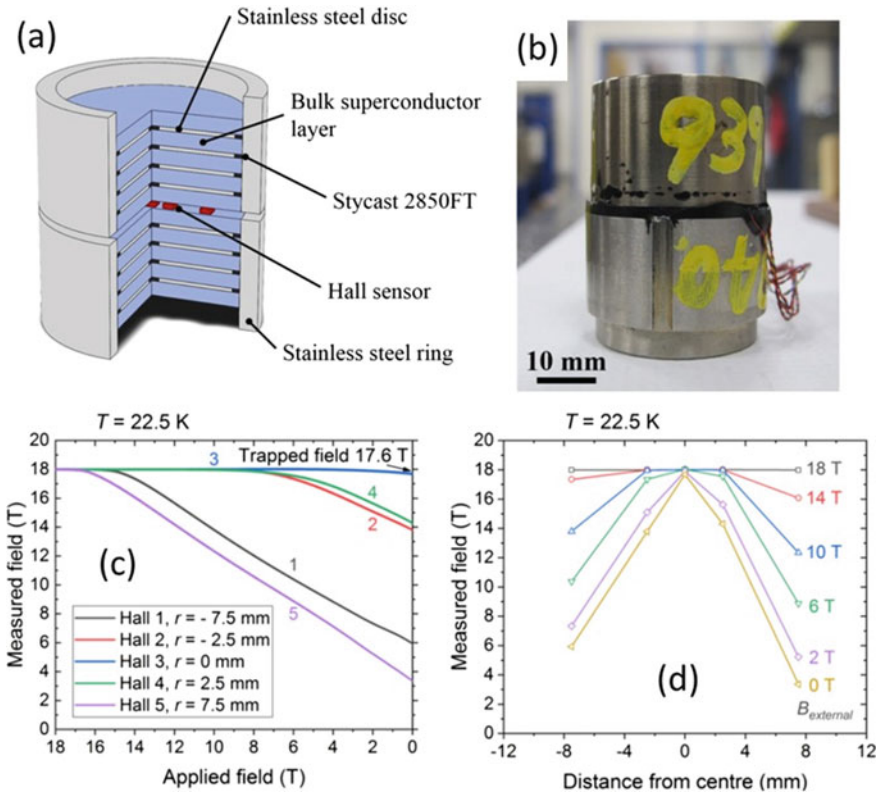


**Fig. 20** a A schematic showing the sample assembly arrangement with the laminated layers of GdBCO+Ag thin slices and stainless-steel discs in between, termed as composite structure is shown. The entire sample assembly is then machined and shrink-fitted in stainless steel rings as shown in (b). Trapped field data, obtained via field cooling, at 22.5 K are shown in (c) and (d). The numbers 1–5 in (c) corresponds to Hall sensors which are positioned symmetrically on the sample surface. *These figures were reproduced from Ref. [47]*

## 5 Novel Applications Employing Bulk Superconducting Materials

Deployment of hybrid-reinforced (RE)BCO bulk superconductors in real-scale, novel applications are discussed in this section.

### 5.1 Hybrid Trapped Field Magnetic Lensing (HTFML)

Here, initially, a description on the superconducting magnetic lens and the method/mechanism by which it can generate higher concentrated field than the

applied magnetic field is presented. Subsequently, the hybrid trapped field magnetic lens (HTFML) is described, where bulk superconductors of two different geometries (one as solenoidal discs, for trapping the magnetic field, and the other as conical hollow lens, for concentrating the magnetic field) are arranged and integrated.

A magnetic lens is conventionally used for focusing and therefore achieving enhancement in the strength of magnetic field (greater than the applied field) at the focus point. These magnetic lenses are used in a range of applications including electron microscopes, cathode-ray tubes and particle accelerators. Superconductors due to their inherent characteristic property of magnetic flux expulsion (Meissner effect) can aid concentrating the magnetic flux. Hence, these materials when shaped in the form of a hollow cone and provided with a slit to suppress the circumferential current loops, guide the current loops for concentrating the magnetic flux and hence works as efficient magnetic lenses. NbTi on Cu-rings fabricated in the form of lens exhibited a concentrated field of 0.618 T for an applied magnetic field of 0.339 T at 4 K, accounting to a concentration ratio of 1.82 [48]. At 20 K, GdBCO bulk conical lens with the slit exhibited a lensing field of 12.42 T for an applied field of 8 T, with a concentration ratio of  $\sim 1.55$  [49]. At 4 K, employing a GdBCO bulk lens assembly, the concentrated field reached 14.76 T with an increase from 12 to 13 T of the external applied field [50]. At 4.2 K, long GdBCO lens samples (60 mm in height) exhibited a concentrated field of 5.65 T with an applied external magnetic field of 2 T [51]. MgB<sub>2</sub> bulk, shaped in the form of a magnetic lens, exhibited a concentration field of 2.1 T with an applied field of 1 T, at 17 K [52]. The side and top-views of (RE)BCO lens supported with a stainless-steel tube are schematically shown in Fig. 21a and b respectively. A YBCO bulk superconductor fabricated in the form of a magnetic lens and also the slit created in the bulk, are shown in Fig. 21c–e. The bulk was zero-field cooled and the lensing effect was studied in different field ranges, measured at 30 K, for this lens are shown in Fig. 21f. At every field step, the sample assembly was given sufficient time to achieve equilibrium in terms of magnetic flux arrangement and hence on the concentrated field achieved.

The HTFML system proposed and developed recently by Keita Takahashi et al. [53], comprises of two major components: (i) conical structure with slit which works as lens, and (ii) ring-shaped, solenoidal stacked cylinders which work as the source for trapping magnetic field during a field-cooling experiment. Both these materials are superconductors but the way of cooling them (i.e. the way the material is brought into superconducting state), governs which property (i.e. magnetic flux pinning or diamagnetic shielding) is being utilised to exhibit the property of interest. The concentric arrangement of the conical lens and cylindrical solenoidal discs are schematically shown in Fig. 22a. The advantage of HTFML is that the external applied magnetic field need not be continuous. Once the superconducting solenoid is magnetised and the field is trapped in it, the external field can be removed and the system yet behaves as a complete, independent and continuous lensing facility (as long as the temperature is maintained), leading to a potential pathway for portable efficient trapped field magnets with higher capabilities. The cooling steps of the arrangement is illustrated in Fig. 22b.

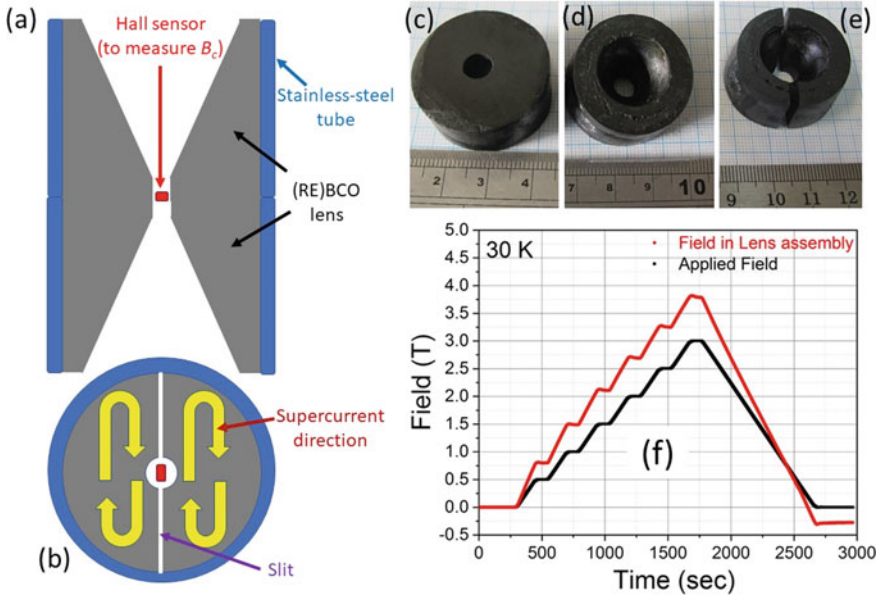


**Fig. 21** a A schematic showing the side and top views of the lens-assembly configuration are shown in (a) and (b) respectively. The slit made is also indicated in the figure. A stainless tube encapsulated over the lens bulk is shown in blue color and the current path in the bulk sample is indicate in yellow arrows. The photographs obtained on the bulk lens-configured sample along with slicing and slit formation, are in shown in (c)–(e). The external magnetic field applied, and the concentrated magnetic field measured in the bore of the YBCO lens, in a zero-field cooled experiment carried out at 30 K, are shown in (f)

As an example two superconductors: i.e. GdBCO lens (with  $T_c$  of  $\sim 92$  K) and  $\text{MgB}_2$  solenoidal cylindrical discs (with  $T_c$  of  $\sim 39$  K) as studied in Ref. [53] The basic science behind the experiment is involved in cooling the sample assembly and in applying the magnetic field. Initially, entire HTFML is cooled to 40 K (where the  $\text{MgB}_2$  is in the normal state but GdBCO lens is in the superconducting state) and then the external magnetic field ( $B_{\text{appl}}$ ) is applied and subsequently the sample assembly is cooled to 20 K. This approach enables  $\text{MgB}_2$  cylindrical discs to get field cooled making them as trapped field magnets while the GdBCO lens to work opposing the applied field due to its diamagnetic approach. This enables concentrated field to obtain at the centre of the system, and is measured with the Hall sensor. At the end of the step, the external field is switched off and the trapped field in the  $\text{MgB}_2$  bulk remains trapped (depending on its pinning ability). The trapped field as measured in plain- $\text{MgB}_2$  cylinder and also the concentrated field in the assembled configuration of HTFML are shown in Fig. 23. It can be seen that a concentrated field of 3.55 T has been achieved in the HTFML, with an applied field of 2 T at 20 K. In yet another study [54], the HTFML consisting of a GdBCO bulk magnetic lens and EuBCO bulk cylinder was investigated at liquid nitrogen temperature where concentrated field of 0.8 T was achieved with an applied field of 0.5 T.

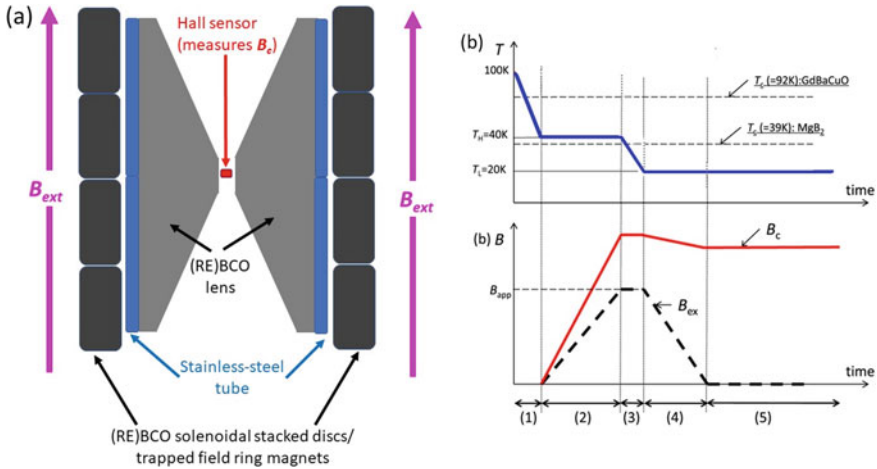
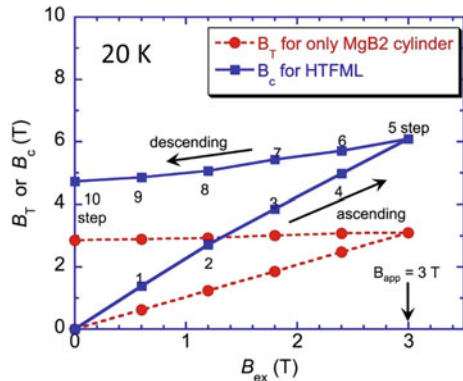


**Fig. 22** **a** A schematic showing the side-view of the hybrid-trapped field magnet lens (HTFML) assembly. The direction in which the external magnetic field is applied can also be seen in the figure. **b** The cooling scheme followed in an example case where the lens was made of GdBCO bulk and solenoidal trapped field discs were made of MgB<sub>2</sub> is shown. The sequential steps followed while cooling and applying/removing the magnetic field is schematically shown in the figure. *The figure in (b) was reproduced from Ref. [53]*

**Fig. 23** Trapped field measured in the MgB<sub>2</sub> cylinder (shown as red circles) and concentrated field ( $B_c$ ) as measured in the hybrid trapped HTML (comprising of MgB<sub>2</sub> cylinder in which the GdBCO lens is arranged at the centre) is shown in blue squares [53]



### 5.2 High-Performance Magnetic Shields

Conventionally the ferromagnetic materials/mu-metals due to their large magnetic permeability, are used for magnetic shielding applications. However, the performance of the shield is limited by the saturation magnetization of the material, and hence the deployment of the shield is confined to the low frequency range (<1 kHz). Superconductors, due to their property of magnetic flux expulsion (referred to Meissner effect) can work as efficient magnetic shields. Superconducting cavities can work



effectively as frequency independent (in a wide range of 80 Hz–100 kHz) passive magnetic shields [55]. The field up to which the magnetic flux entry into the material is completely shielded is defined as the limiting field ( $B_{lim}$ ). In two different configurations, the magnetic shields can be of immense use:

- (i) To safeguard the sensitive devices such as SQUID magnetometers from the external electromagnetic noise.
- (ii) To shield the outside atmosphere from the magnetic field generated by the device e.g. to attenuate the magnetic field strength outside a superconducting high-field magnet.

When external magnetic field is seen by the superconducting material, macroscopic current loops get generated in its outer core to repel the magnetic flux entry thereby shielding the material. However, if the external magnetic field is beyond the threshold limit (referred to as limiting field  $B_{lim}$ ), then the magnetic flux enters the material, as shown in Fig. 24a. Two examples where a BSCCO tube (made by CAN Superconductors) and a YBCO cavity with one-end fused are shown in Fig. 24b, c. The shielding performance as measured in a YBCO cavity in the temperature range 77–20 K are shown in Fig. 24d. Effective shielding has been achieved of ~1.5 T at 20 K in a YBCO tube of 30 mm in height.

The performance of the superconducting shield is often governed by two characteristic parameters: the limiting field  $B_{lim}$ , and the shielding factor ( $SF$ , defined as  $\propto \frac{B_{appl}}{B_{in}}$ ), where  $B_{appl}$  is the applied magnetic field and  $B_{in}$  is the induced field. Several superconducting materials, composed of (RE)BCO/Bi-2223/MgB<sub>2</sub>, shaped in the form of hollow tubes, cavities with bottom- or top-sealed have been explored as effective magnetic shields [34, 56–61]. The values for  $B_{lim}$  or  $SF$  as observed in superconducting magnetic shields made from bulk materials are shown in Table 2.

### 5.3 Bench-Top NMR/MRI with (RE)BCO Bulk Materials

Requirement of large magnetic fields is getting important and essential both in the medical and science and research-based applications. Two prominent high-field applications are Magnetic Resonance Imaging (MRI) and Nuclear Magnetic Resonance (NMR). Achieving large and uniform magnetic field comprises of employing low temperature superconducting materials (e.g. NbTi/Nb<sub>3</sub>Sn wires or tapes, which need liquid helium to exhibit the superconducting properties) or more expensive (RE)BCO tapes (which can work with liquid nitrogen but mostly operated at liquid hydrogen or liquid helium temperatures for better performance) which makes the entire facility expensive and a bit involved. In this context, economical bench-top NMR/MRI facilities employing bulk superconducting materials is a novel and attractive approach which can address some of the mid-range tasks to a satisfactory level, by operating the facility at liquid nitrogen temperature.

(RE)BCO bulk superconductor fabricated in the form of rings when field cooled can provide high magnetic field within its bore. (RE)BCO ring-shaped discs when

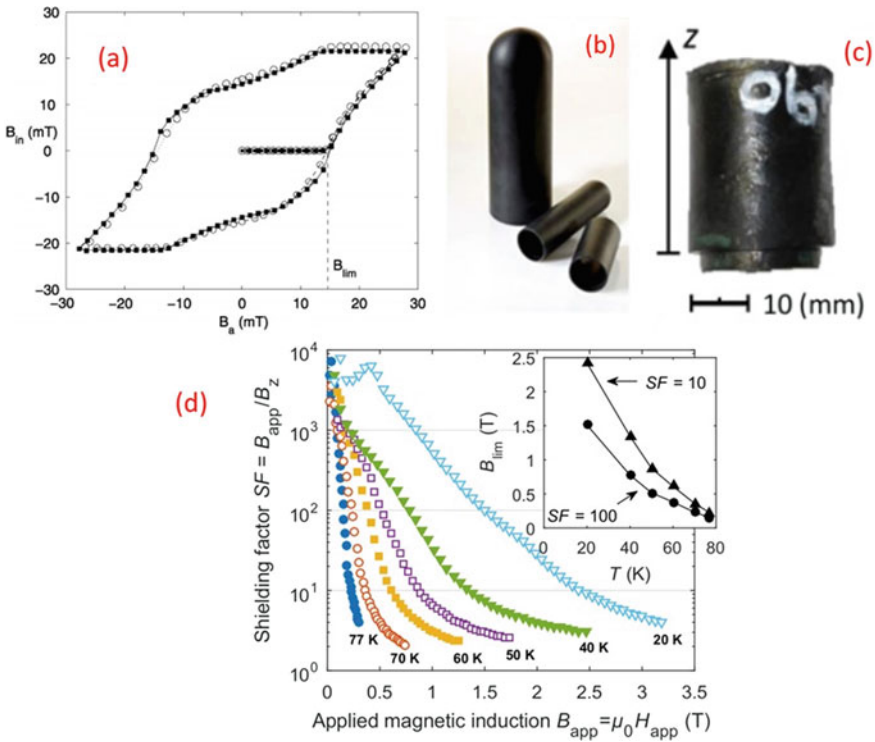


**Fig. 24** a Typical plot between induced magnetic field ( $B_{in}$ ) and applied magnetic field ( $B_a$ ) is shown. The field up to which there is no entry of the magnetic flux occurs is referred to as the limiting field ( $B_{lim}$ ). Typical images obtained on a BSCCO tube and an YBCO cavity which when zero-field cooled can work as magnetic shields are shown in (b) and (c) respectively. Shielding performance obtained in a YBCO cavity, in the temperature range 77–20 K is shown in (d). *Reproduced with permission from Ref. [2]*

**Table 2** Shielding properties of various (RE)BCO cavities, made from bulk superconductors

Sample/configuration	$B_{lim}$	References
Bi-2223	14 mT @ 77 K	[59]
YBCO	51 mT @ 77 K	[60]
YBCO	1.5 T @ 20 K	[60]
GdBCO (32 mm OD; 10 mm ID; 13 mm height)	0.4 T @ 77 K	[34]
GdBCO (20 mm OD; 2 mm ID; 20 mm height)	2 T @ 30 K	[61]

stacked can provide relatively uniform magnetic fields. Two SmBCO ring-shaped bulk superconductors with a bore diameter of 7 mm enabled NMR (123 MHz) signal detection at 2.89 T, with a NMR signal sensitivity of 1850 ppm [62]. In another experiment, six Eu–Ba–Cu–O ring-shaped bulks (each of 60 mm OD and 28 mm ID,

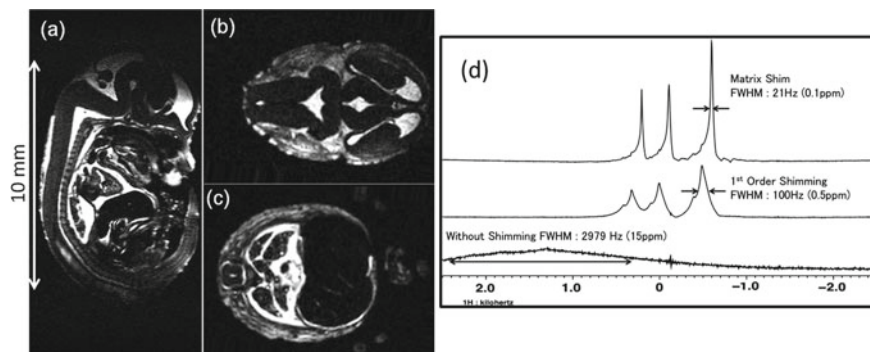


**Fig. 25** Cross-sectional 3-D images obtained, employing a bench-top MRI facility, from a chemically-fixed mouse fetus are shown in (a)–(c). In a similar experiment, the NMR spectrum obtained in ethanol is shown in (d). Spectrum with no shimming, with 1st order shimming and with shimming via multichannel shim coils are shown in the same figure (d). Images were reproduced with permission from Ref. [63]

20 mm height, reinforced with 5 mm-thick aluminum rings to shield them from the electromagnetic hoop stress) were stacked and field-cooled in 4.7 T applied field. The magnetic field trapped in the solenoidal bulk magnet was used for capturing 3-D magnetic resonance images from formalin-fixed mouse fetus [63]. Employing ring-shaped bulk superconductors in the trapped field mode, MRI scanned images in chemically fixed mouse fetus are shown in Fig. 25a–c and a NMR spectra obtained (with and without shimming) in ethanol are shown in Fig. 25d.

Similarly high and large-gradient magnetic fields are being actively considered in clinical environments. An example of this is the magnetically targeted drug-delivery system [64] employing bulk superconductors, for treating cancer cells/tumours. In this approach, the drug is associated with the biocompatible magnetic particle and with the help of the large-gradient magnetic field facility, the drug is made to reach the tumour location with the help of the magnetic force (as governed by  $B \cdot \nabla B$ ). Here, the magnetic particle and hence the drug is released and confined at the tumour location by removing the magnetic field, by simply switching off the applied magnetic field (by increasing the operating temperature to above the  $T_c$  of the superconducting bulk). Two major advantages via this approach are: (i) healthy tissues/cells need not get exposed to cancer-related drugs/radiation, overcoming side-effects related problems to a large extent, and (ii) smaller quantities of medicine will be sufficient as all of the injected drug reaches the tumour location, thereby reducing the cost of the treatment significantly. The pulse-field magnetisation (PFM) [65] approach can be very effective and convenient for charging the bulk superconductors in portable mode, and hence can have a great influence in some of the real-scale applications.

**Acknowledgements** The authors acknowledge the current and past members of the Bulk Superconductivity Group (BSG), and especially John Durrell, Yunhua Shi, Mark D Ainslie and Tony Dennis for their valuable support received while carrying out some of the experiments described in this book chapter. Authors also acknowledge King Abdulaziz City for Science and Technology

(KACST); and the Engineering and Physical Sciences Research Council (EPSRC) with grant code: EP/P00962X/1. The Henry Royce Institute (Equipment grant ref. EP/P024947/1) is acknowledged for the 12 T superconducting magnet.

## References

1. J.H. Durrell, M.D. Ainslie, D. Zhou, P. Vanderbemden, T. Bradshaw, S. Speller, M. Filipenko, D.A. Cardwell, Bulk superconductors: a roadmap to applications. *Supercond. Sci. Technol.* **31**, 103501 (2018). <https://doi.org/10.1088/1361-6668/aad7ce>
2. D.K. Namburi, Y. Shi, D.A. Cardwell, The processing and properties of bulk (RE)BCO high temperature superconductors: current status and future perspectives. *Supercond. Sci. Technol.* **34**, 053002 (2021). <https://doi.org/10.1088/1361-6668/abde88>
3. D.A. Cardwell, D.S. Ginley (eds.), *Handbook of Superconducting Materials Volume I: Superconductivity, Materials and Processes* (IOP Publishing Ltd., Cornwall, 2003). ISBN 0 7503 0432 4
4. G. Krabbes, G. Fuchs, W.-R. Canders, H. May, R. Palka, *High Temperature Superconductor Bulk Materials: Fundamentals—Processing—Properties Control—Application Aspects* (2006). <https://doi.org/10.1002/3527608044>. Print ISBN: 9783527403837, Online ISBN: 9783527608041
5. M.K. Wu, J.R. Ashburn, C.J. Torng, P.H. Hor, R.L. Meng, L. Gao, Z.J. Huang, Y.Q. Wang, C.W. Chu, Superconductivity at 93 K in a new mixed-phase Y-Ba-Cu-O compound system at ambient pressure. *Phys. Rev. Lett.* **58**, 908 (1987). <https://doi.org/10.1103/PhysRevLett.58.908>
6. D.A. Cardwell, Processing and properties of large grain (RE)BCO. *Mat. Sci. Eng. B* **53**, 1–10 (1998). [https://doi.org/10.1016/S0921-5107\(97\)00293-6](https://doi.org/10.1016/S0921-5107(97)00293-6)
7. H.S. Chauhan, M. Murakami, Hot seeding for the growth of *c*-axis-oriented Nd-Ba-Cu-O. *Supercond. Sci. Technol.* **13**, 672 (2000). <https://doi.org/10.1088/0953-2048/13/6/308>
8. S.J. Scruggs, P.T. Putman, Y.X. Zhou, H. Fang, K. Salama, Hot seeding using large Y-123 seeds. *Supercond. Sci. Technol.* **19**, S451 (2006). <https://doi.org/10.1088/0953-2048/19/7/S06>
9. M. Morita, S. Takebayashi, M. Tanaka, K. Kimura, K. Miyamoto, K. Sawano, Quench and melt growth (QMG) process for large bulk superconductor fabrication, in *Advances in superconductivity III*, ed. by K. Kajimura, H. Hayakawa (Springer, Tokyo, 1991). [https://doi.org/10.1007/978-4-431-68141-0\\_162](https://doi.org/10.1007/978-4-431-68141-0_162)
10. K. Yamaguchi, M. Murakami, H. Fujimoto, S. Gotoh, T. Oyama, Y. Shiohara, N. Koshizuka, S. Tanaka, Microstructures of the melt-powder-melt-growth processed YBaCuO. *J. Mater. Res.* **6**, 1404–1407 (1991). <https://doi.org/10.1557/JMR.1991.1404>
11. P. Fox, E.J. Hardman, G.J. Tatlock, D.G. McCartney, The growth of melt-textured YBa<sub>2</sub>Cu<sub>3</sub>O<sub>7- $\delta$</sub>  superconductors, 1998. *Supercond. Sci. Technol.* **11**, 541 (1998). <https://doi.org/10.1088/0953-2048/11/6/001>
12. Y. Adachi, T. Goto, K. Watanabe, Oxygen controlled melt growth process of filamentary Gd123 superconductors. *Physica C* **357–360**, 1077–1080 (2001). [https://doi.org/10.1016/S0921-4534\(01\)00551-2](https://doi.org/10.1016/S0921-4534(01)00551-2)
13. M. Murakami, Melt processing of YBaCuO superconductors and critical currents. *Mod. Phys. Lett. B* **4**, 163–179 (1990). <https://doi.org/10.1142/S0217984990000234>
14. Y. Shi, N. Hari Babu, K. Iida, D.A. Cardwell, Growth rate and superconducting properties of Gd-Ba-Cu-O bulk superconductors melt processed in air. *IEEE Trans. Appl. Supercond.* **17**, 2984–2987 (2007). <https://doi.org/10.1109/TASC.2007.899474>
15. E.S. Reddy, T. Rajasekharan, Fabrication of textured REBa<sub>2</sub>Cu<sub>3</sub>O<sub>7</sub>/RE<sub>2</sub>BaCuO<sub>5</sub> (RE=Y, Gd) composites by infiltration and growth of RE<sub>2</sub>BaCuO<sub>5</sub> pre-forms by liquid phases. *Supercond. Sci. Technol.* **11**, 523–534 (1998). <https://doi.org/10.1088/0953-2048/11/5/014>

16. D.K. Namburi, Y.H. Shi, K.G. Palmer, A.R. Dennis, J.H. Durrell, D.A. Cardwell, An improved top seeded infiltration growth method for the fabrication of Y–Ba–Cu–O bulk superconductors. *J. Eur. Ceram. Soc.* **36**, 615–624 (2016). <https://doi.org/10.1016/j.jeurceramsoc.2015.09.036>
17. S. Jin, T.H. Tiefel, R.C. Sherwood, R.B. van Dover, M.E. Davis, G.W. Kammlott, R.A. Fastnacht, Melt-textured growth of polycrystalline  $\text{YBa}_2\text{Cu}_3\text{O}_{7-\delta}$  with high transport  $J_c$  at 77 K. *Phys. Rev. B* **37**, 7850 (1988). <https://doi.org/10.1103/PhysRevB.37.7850>
18. M. Murakami, Melt processed high-temperature superconductors. *World Sci.* **19** (1992). <https://doi.org/10.1142/1892>. ISBN: 978-981-02-1244-5
19. H.H. Xu, Y.Y. Chen, L. Cheng, S.B. Yan, D.J. Yu, L.S. Guo, X. Yao, YBCO-buffered NdBCO films with higher thermal stability in seeding REBCO growth and recycling failed bulk superconductors. *J. Supercond. Novel Mag.* **26**, 919–922 (2013). <https://doi.org/10.1007/s10948-012-1981-7>
20. Y. Chen, Cui X, Yao X, Peritectic melting of thin films, superheating and applications in growth of REBCO superconductors. *Prog. Mater. Sci.* **68**, 97–159 (2015). <https://doi.org/10.1016/j.pmatsci.2014.09.001>
21. T.Y. Li, L. Cheng, S.B. Yan, L.J. Sun, X. Yao, Y. Yoshida, H. Ikuta, Growth and superconductivity of REBCO bulk processed by a seed/buffer layer/precursor construction. *Supercond. Sci. Technol.* **23**, 125002(2010). <https://doi.org/10.1088/0953-2048/23/12/125002>
22. Y. Zhu, Y. Mu, L. Zeng, M. Wang, X. Yao, Progress in buffer-supported seeding architectures for reliable epitaxial growth of  $\text{REBa}_2\text{Cu}_3\text{O}_{7-\delta}$  bulk cryomagnets with superior properties. *Cryst. Growth Des.* **20**, 7533–7549 (2020). <https://doi.org/10.1021/acs.cgd.0c01131>
23. C.-J. Kim, J.H. Lee, S.-D. Park, B.-H. Jun, S.C. Han, Y.H. Han,  $\text{Y}_2\text{BaCuO}_5$  buffer block as a diffusion barrier for samarium in top seeded melt growth processed  $\text{YBa}_2\text{Cu}_3\text{O}_{7-y}$  superconductors using a  $\text{SmBa}_2\text{Cu}_3\text{O}_{7-d}$  seed. *Supercond. Sci. Technol.* **24**, 015008 (2010). <https://doi.org/10.1088/0953-2048/24/1/015008>
24. Y. Shi, D.K. Namburi, W. Zhao, J.H. Durrell, A.R. Dennis, D.A. Cardwell, The use of buffer pellets to pseudo hot seed (RE)–Ba–Cu–O–(Ag) single grain bulk superconductors. *Supercond. Sci. Technol.* **29**, 015010 (2016). <https://doi.org/10.1088/0953-2048/29/1/015010>
25. D.K. Namburi, Y.H. Shi, W. Zhai, A.R. Dennis, J.H. Durrell, D.A. Cardwell, Buffer pellets for high-yield, top-seeded melt growth of large grain Y–Ba–Cu–O superconductors. *Cryst. Growth Des.* **15**, 1472–1480 (2015). <https://doi.org/10.1021/cg501813y>
26. D.K. Namburi, Y. Shi, A.R. Dennis, J.H. Durrell, D.A. Cardwell, A robust seeding technique for the growth of single grain (RE)BCO and (RE)BCO–Ag bulk superconductors. *Supercond. Sci. Technol.* **31**, 044003 (2018). <https://doi.org/10.1088/1361-6668/aaad89>
27. D.K. Namburi, K. Singh, K.-Y. Huang, S. Neelakantan, J.H. Durrell, D.A. Cardwell, Improved mechanical properties through recycling of Y–Ba–Cu–O bulk superconductors. *J. Eur. Ceram. Soc.* **41**, 3480–3492 (2021). <https://doi.org/10.1016/j.jeurceramsoc.2021.01.009>
28. X. Chaud, S. Meslin, J. Noudem, C. Harnois, L. Porcar, Chateigner D, Tournier R, Isothermal growth of large  $\text{YBaCuO}$  single domains through an artificial array of holes. *J. Cryst. Growth* **275**, e855–e860 (2005). <https://doi.org/10.1016/j.jcrysgro.2004.11.124>
29. J.G. Noudem, S. Meslin, C. Harnois, D. Chateigner, X. Chaud, Melt textured  $\text{YBa}_2\text{Cu}_3\text{O}_y$  bulks with artificially patterned holes: a new way of processing c-axis fault current limiter meanders. *Supercond. Sci. Technol.* **17**, 931 (2004). <https://doi.org/10.1088/0953-2048%2F17%2F7%2F018>
30. T. Hlášek et al., Enhanced mechanical properties of single-domain YBCO bulk superconductors processed with artificial holes. *IEEE Trans. Appl. Supercond.* **29**(5), 1–4 (2019). <https://doi.org/10.1109/TASC.2019.2896538>
31. K.Y. Huang, T. Hlášek, D.K. Namburi, A.R. Dennis, Y. Shi, M.D. Ainslie et al., Improved trapped field performance of single grain Y–Ba–Cu–O bulk superconductors containing artificial holes. *J. Am. Ceram. Soc.* **00**, 1–10 (2021). <https://doi.org/10.1111/jace.18017>
32. Y.L. Chen, H.M. Chan, M.P. Harmer, V.R. Todt, S. Sengupta, D. Shi, A new method for net-shape forming of large, single-domain  $\text{YBa}_2\text{Cu}_3\text{O}_{6+x}$ . *Physica C* **234**, 232 (1994). [https://doi.org/10.1016/0921-4534\(94\)90568-1](https://doi.org/10.1016/0921-4534(94)90568-1)

33. N.V.N. Viswanath, T. Rajasekharan, N. Harish Kumar, L. Menon, S.K. Malik, Infiltration-growth processing of  $\text{SmBa}_2\text{Cu}_3\text{O}_y$  superconductor. *Supercond. Sci. Technol.* **11**, 420 (1998). <https://doi.org/10.1088/0953-2048/11/4/011>
34. P. Yang, J.-F. Fagnard, Ph. Vanderbemden, W. Yang, Magnetic shielding of a short thick GdBCO tube fabricated by the buffer aided top-seeded infiltration and growth method. *Supercond. Sci. Technol.* **32**, 115015 (2019). <https://doi.org/10.1088/1361-6668/ab4309>
35. E.S. Reddy, J.G. Noudem, M. Tarka, G.J. Schmitz, Mono-domain  $\text{YBa}_2\text{Cu}_3\text{O}_y$  superconductor fabrics prepared by an infiltration process. *Supercond. Sci. Technol.* **13**, 716 (2000). <https://doi.org/10.1088/0953-2048/13/6/317>
36. E.S. Reddy, G.J. Schmitz, Superconducting foams. *Supercond. Sci. Technol.* **15**, L21 (2002). <https://doi.org/10.1088/0953-2048/15/8/101>
37. J.G. Noudem, E. Guilmeau, D. Chateigner, S. Lambert, E.S. Reddy, B. Ouladdiaf, G.J. Schmitz, Properties of  $\text{YBa}_2\text{Cu}_3\text{O}_y$ -textured superconductor foams. *Physica C* **408–410**, 655–656 (2004). <https://doi.org/10.1016/j.physc.2004.03.098>
38. K. Konstantopoulou, Y.H. Shi, A.R. Dennis, J.H. Durrell, J.Y. Pastor, D.A. Cardwell, Mechanical characterization of GdBCO/Ag and YBCO single grains fabricated by top-seeded melt growth at 77 and 300 K. *Supercond. Sci. Technol.* **27**, 115011 (2014). <https://doi.org/10.1088/0953-2048/27/11/115011>
39. J.V.J. Congreve, Y. Shi, K.Y. Huang, A.R. Dennis, J.H. Durrell, D.A. Cardwell, Improving mechanical strength of YBCO bulk superconductors by addition of Ag. *IEEE Trans Appl. Supercond.* **29**, 1–5 (2019). <https://doi.org/10.1109/TASC.2019.2907474>
40. D.K. Namburi, K.-Y. Huang, W. Lau, Y.-H. Shi, K.G. Palmer, A.R. Dennis, D.A. Cardwell, J.H. Durrell, A simple, reliable and robust reinforcement method for the fabrication of (RE)–Ba–Cu–O bulk superconductors. *Supercond. Sci. Technol.* **33**, 054005 (2020). <https://doi.org/10.1088/1361-6668/ab7ec4>
41. D.K. Namburi et al., Reinforced bulk high temperature superconductors and method for their manufacture, UK patent United Kingdom (GB) Patent Application No: 1908788.1 and International patent PCT/EP2019/078582
42. H. Seki, Y. Honma, M. Nomura, C. Nakayama, N. Koshizuka, T. Maruyama, M. Murakami, Reinforcement of bulk Y-Ba-Cu-O superconductors by using Fe-Mn-Si-Ni shape memory alloy rings. *Phys. Procedia* **27**(144–147), 1875–3892 (2012). <https://doi.org/10.1016/j.phpro.2012.03.431>
43. M. Tomita, M. Murakami, High-temperature superconductor bulk magnets that can trap magnetic fields of over 17 tesla at 29 K. *Nature* **421**, 517–20 (2003). <https://doi.org/10.1038/nature01350>
44. J.H. Durrell et al., *Supercond. Sci. Technol.* **27**, 082001 (2014). <https://doi.org/10.1088/0953-2048/27/8/082001>
45. M. Morita, H. Teshima, S. Nariki, Development of new reinforcement method and 10T magnetization of QMG magnet. *Nippon Steel & Sumitomo Metal Technical Report* **117**, 36–43 (2017). <https://www.nipponsteel.com/tech/report/nssmc/pdf/407-07.pdf>
46. A. Patel, A. Baskys, T. Mitchell-Williams, A. McCaul, W. Coniglio, J. Hänisch, M. Lao, B.A. Glowacki, A trapped field of 17.7 T in a stack of high temperature superconducting tape. *Supercond. Sci. Technol.* **31**, 09LT01 (2018). <https://doi.org/10.1088/1361-6668/aad34c>
47. K.Y. Huang et al., *Supercond. Sci. Technol.* **33**, 02LT01 (2020). <https://doi.org/10.1088/1361-6668/ab5e12>
48. Z.Y. Zhang, S. Matsumoto, S. Choi, R. Teranishi, T. Kiyoshi, A new structure for a magnetic field concentrator using NbTi sheet superconductors. *Physica C* **471**, 1547–1549 (2011). <https://doi.org/10.1016/j.physc.2011.05.235>
49. Z.Y. Zhang, S. Matsumoto, R. Teranishi, T. Kiyoshi, Magnetic field, temperature and mechanical crack performance of a GdBCO magnetic lens. *Supercond. Sci. Technol.* **25**, 115012(2012). <https://doi.org/10.1088/0953-2048/25/11/115012>
50. S. Choi, T. Kiyoshi, S. Matsumoto, Magnetic field amplifier employing high  $T_c$  bulk superconductor. *J. Appl. Phys.* **105**, 07E705 (2009). <https://doi.org/10.1063/1.3068645>

51. T. Kiyoshi, S. Choi, S. Matsumoto, T. Asano, D. Uglietti, Magnetic flux concentrator using Gd-Ba-Cu-O bulk superconductors. *IEEE Trans. Appl. Supercond.* **19**, 2174–77 (2009). <https://doi.org/10.1109/TASC.2009.201844>
52. Z.Y. Zhang, S. Choi, S. Matsumoto, R. Teranishi, G. Giunchi, A.F. Albisetti, T. Kiyoshi, Magnetic lenses using different MgB<sub>2</sub> bulk superconductors. *Supercond. Sci. Technol.* **31**, 025009 (2012). <https://doi.org/10.1088/0953-2048/25/2/025009>
53. K. Takahashi, H. Fujishiro, M.D. Ainslie, A new concept of a hybrid trapped field magnet lens. *Supercond. Sci. Technol.* **31**, 044005(2018). <https://doi.org/10.1088/1361-6668/aaae94>
54. S. Namba, H. Fujishiro, T. Naito, M.D. Ainslie, D. Zhou, Realisation of hybrid trapped field magnetic lens (HTFML) consisting of REBCO bulk lens and REBCO bulk cylinder at 77 K. *J. Phys.: Conf. Ser.* **1559**, 012079 (2020). <https://doi.org/10.1088/1742-6596/1559/1/012079>
55. H. Niculescu, R. Schmidmeier, B. Topolski, P.J. Gielisse, Shielding effects in ceramic superconductors. *Physica C* **229**, 105–112 (1994). [https://doi.org/10.1016/0921-4534\(94\)90818-4](https://doi.org/10.1016/0921-4534(94)90818-4)
56. J. Claycomb, *Magnetic Shields Applied Superconductivity: Handbook on Devices and Applications*, vol. 1, ed. by P. Seidel (Wiley, New York, 1999), pp. 780–806. ISBN: 3527670653, 9783527670659
57. J.F. Fagnard, S. Elschner, J. Bock, M. Dirickx, B. Vanderheyden, P. Vanderbenden, Shielding efficiency and E(J) characteristics measured on large melt cast Bi-2212 hollow cylinders in axial magnetic fields. *Supercond. Sci. Technol.* **23**, 095012 (2010). <https://doi.org/10.1088/0953-2048/23/9/095012>
58. K. Takahata, S. Nishijima, M. Ohgami, T. Okada, S. Nakagawa, M. Yoshiwa, Magnetic shielding by a tubular superconducting winding in parallel and transverse fields. *IEEE Trans. Magn.* **25**, 1889 (1989). <https://doi.org/10.1109/20.92674>
59. L. Tomkow, M. Cizek, M. Chorowski, Combined magnetic screen made of Bi-2223 bulk cylinder and YBCO tape rings: modeling and experiments. *J. Appl. Phys.* **117**, 043901 (2015). <https://doi.org/10.1063/1.4906399>
60. L. Wéra, J.-F. Fagnard, D.K. Namburi, Y. Shi, B. Vanderheyden, P. Vanderbenden, Magnetic shielding above 1 T at 20 K with bulk, large grain YBCO tubes made by buffer-aided top seeded melt growth. *IEEE Trans. Appl. Supercond.* **27**, 6800305 (2017). <https://doi.org/10.1109/TASC.2016.2633301>
61. Z.Y. Zhang, S. Matsumoto, R. Teranishi, T. Kiyoshi, Magnetic shielding properties of GdBCO bulks with different crystal orientation. *Phys. Procedia* **27**, 180–183 (2012). <https://doi.org/10.1016/j.phpro.2012.03.440>
62. T. Nakamura, Y. Itoh, M. Yoshikawa, T. Oka, J. Uzawa, Development of a superconducting magnet for nuclear magnetic resonance using bulk high-temperature superconducting materials. *Concepts Magn. Reson. B* **31B**, 65–70 (2007). <https://doi.org/10.1002/cmr.b.20083>
63. T. Nakamura, D. Tamada, Y. Yanagi, Y. Itoh, T. Nemoto, H. Utumi, K. Kose, Development of a superconducting bulk magnet for NMR and MRI. *J. Magn. Reson.* **259**, 68–75 (2015). <https://doi.org/10.1016/j.jmr.2015.07.012>
64. S. Nishijima, S. Takeda, F. Mishima, Y. Tabata, M. Yamamoto, J.-I. Joh, H. Iseki, Y. Muragaki, A. Sasaki, K. Jun, N. Saho, A study of magnetic drug delivery system using bulk high temperature superconducting magnet. *IEEE Trans. Appl. Supercond.* **18**, 874–877 (2008). <https://doi.org/10.1109/TASC.2008.921967>
65. M.D. Ainslie, H. Fujishiro, T. Ujiie, J. Zou, A.R. Dennis, Y. Shi, D.A. Cardwell, Modelling and comparison of trapped fields in (RE)BCO bulk superconductors for activation using pulsed field magnetization. *Supercond. Sci. Technol.* **27**, 065008 (2014). <https://doi.org/10.1088/0953-2048/27/6/065008>

# Fabrication Technologies of Superconducting Cables and Wires



Yassine Slimani and Essia Hannachi

**Abstract** Nowadays, MRI and NMR magnets, high magnetic fields measurement devices, high-field magnets for accelerators or for nuclear fusion equipment are some examples that largely utilize superconducting cables and wires, which are largely made of the low-temperature superconducting materials (LTS)  $\text{Nb}_3\text{Sn}$  and  $\text{Nb-Ti}$ . The high-temperature superconductors (HTS), with critical temperature exceeding 77 K, displayed very great values of critical current density ( $J_c$ ), and critical magnetic field ( $B_{c2}$ ). Therefore, the ability to utilize cryo-free cooling or liquid nitrogen-based systems for HTS tapes is leading to significant advancements in technical applications like power transmission lines. Among HTS materials, BSCCO was easily made in the forms of round wires and tapes. However, making REBCO into the form of tapes faced some challenges due to the high production cost. Numerous investigations have been focused on these kinds of materials and further developments are still under progress for better industrialization and commercialization.  $\text{MgB}_2$  superconductor (having  $T_c \sim 39$  K) has also the opportunity to be a low-cost superconductor, which can operate at lower refrigerating costs. Promising  $J_c$  values have also been attained by the new family of iron-based superconductors (called as pnictides). However, very few studies were performed on tapes based on  $\text{MgB}_2$  and pnictide materials. The present chapter summarizes the most important requirements for superconducting cables and wires. Then, based on the kind and family of materials, the main manufacturing processes/technologies and recent developments for superconducting tapes and wires are reported.

**Keywords** Superconductor · Critical transition temperature · Critical magnetic field · Critical current density · Flux pinning · Low-temperature superconductors ·

---

Y. Slimani (✉)

Department of Biophysics, Institute for Research & Medical Consultations (IRMC), Imam Abdulrahman Bin Faisal University, P.O. Box 1982, Dammam 31441, Saudi Arabia  
e-mail: [yaslimani@iau.edu.sa](mailto:yaslimani@iau.edu.sa); [slimaniyassine18@gmail.com](mailto:slimaniyassine18@gmail.com)

E. Hannachi

Department of Nuclear Medicine Research, Institute for Research & Medical Consultations (IRMC), Imam Abdulrahman Bin Faisal University, P.O. Box 1982, Dammam 31441, Saudi Arabia  
e-mail: [hannechi.essia@gmail.com](mailto:hannechi.essia@gmail.com)



High-temperature superconductors · Superconducting cables and tapes ·  
Superconducting wires · Superconducting multifilament · Mechanical properties ·  
High field magnets

## 1 Introduction

Superconductivity was identified for the first time in 1911 by Heike K. Onnes (University of Leiden, Holland). Indeed, some materials lose their resistance to the circulation of electrical current at lower temperatures. The superconductivity phenomenon continues to remain a research interest in laboratory till the year 1954 when G. Yntema (from University of Illinois) [1] successfully created the first magnet based on superconductor material, which produced about 0.7 T at 4.2 K. This success signaled the beginning of the era of engineering superconductivity. During that moment, the performances of the magnet are greatly lower than the anticipated characteristics of a superconductor. The slow growth could be moderately ascribed to: (i) the difficulties in achieving the needed very low temperatures, and (ii) the insufficient knowledge on the way to make thermally and electrically stable superconducting wires. The main issue is that the superconductivity was limited not just to lower temperatures but even to a limited range of electrical current density and magnetic field. The range of these parameters was specifically limited in earlier superconducting materials. The critical values of magnetic field ( $H_c$ ), electrical current ( $I_c$ ) or current density ( $J_c$ ), and transition temperature ( $T_c$ ) are dependent to each other and together constitute the so-called ‘critical surface’. The first superconductors including Hg, Al, and Pb are categorized as type I superconductors.

The magnetic field is expelled from the volume of these superconductors, and the  $J_c$  is limited to a surface layer of about 1/10 of a micron. In most cases, the greatest fields that these superconductors could generate are below 0.1 T. Because of these drawbacks, type-I superconductors are unsuitable for a wide range of practical applications. The different ‘technological superconductors’ (meaning superconducting materials that could be easily manufactured in the form of cables and/or wires for high-currents and high-fields applications) are type-II superconductors. The magnetic field is penetrating the volume of these superconducting materials, forming the so-called vortices [2–4].  $Nb_3Sn$  ( $T_c \sim 18$  K) and Nb-Ti ( $T_c \sim 9.7$  K) are the largely exploited materials as technological superconductors for wires and cables, where  $J_c$  values higher than  $10^9$  A/m<sup>2</sup> could be transported. The upper critical magnetic fields ( $B_{c2}$ ) are about 14.5 and 30 T for Nb-Ti and  $Nb_3Sn$ , respectively.

The engineering  $J_c$  values at 4.2 K for tapes or strands with lengths greater than 100 m are evaluated in Fig. 1. Low temperature superconducting (LTS) materials have a limited range of temperature. However, the costs of insulation and refrigeration are often higher than compensated by the lower energy expenses caused by non-resistive current flow. Since the wasted energy quantity during the circulation of current via a superconductor magnet is very low, it could be run with no supplying power once it is charged. This ‘permanent current’ is greatly suitable for NMR and

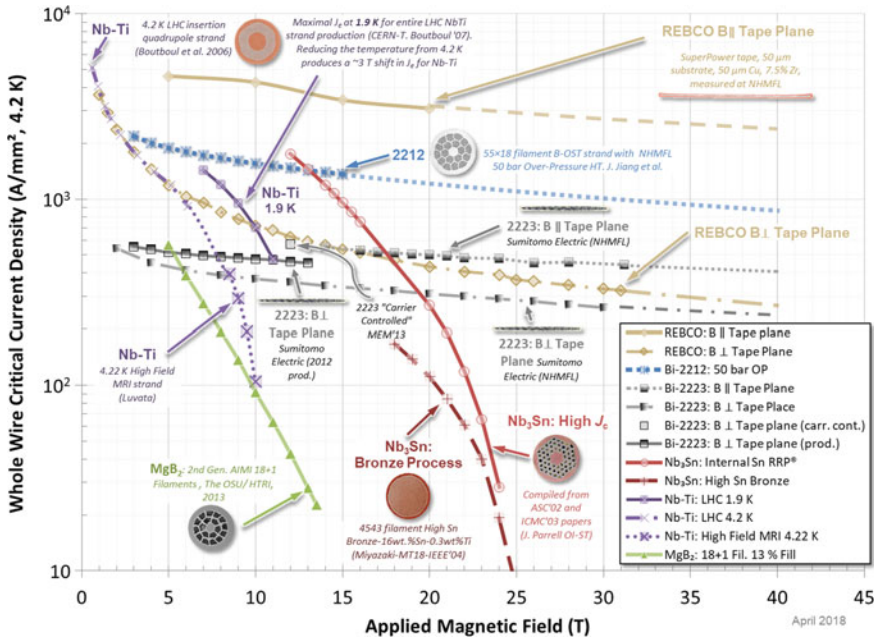


**Fig. 1** Engineering  $J_c$  values for superconducting wires and/or tapes (updated in 2018) (Image was taken from National MagLab, Tallahassee, USA [5].)

MRI applications due to the high stability of current flow (and hence for the field also). Liquid helium (LHe) could be produced, which offers a cooling to around 4.2 K and reach a much lower temperature around 1.8 K at diminished pressure. The use of superconducting materials has become increasingly interesting and widely investigated due to the recent developments in cooling and refrigerating technologies.

The finding of materials that are classified as high-temperature superconductors (HTS) in 1986 (ceramics displaying  $T_c$  greater than 77 K (the boiling point of liquid nitrogen,  $LN_2$ )) driven a surge in interest in superconductivity applications. The detection of superconductivity phenomena in  $MgB_2$  (2001, with  $T_c = 39$  K) and iron-based superconductors (in 2008, called also as pnictides, highest  $T_c$  is around 57.5 K) expanded the range of magnetic field and temperature for intermetallic superconducting materials.

Despite the fact that HTS conductors are still struggling to find a viable commercial market, the ability to operate at  $LN_2$  temperatures or at medium temperatures (20–50 K) has broadened the range of prospective applications.

Aiming to be employed in high-currents and high-fields applications, superconducting materials should be manufactured and designed in the form of wires, which could also be cabled. Since superconducting materials have a broad range of mechanical characteristics (such as fragile ceramics like HTS materials and strong ductile alloys like Nb-Ti), the techniques for manufacturing wires and cables will vary substantially. Among HTS materials, only Bi-2212 compound is made as round

wires, while the others are made in the form of tapes, either by performing an epitaxial growth of the material on suitable substrate (coated conductors) like for REBCO (RE means rare earth) or by employing roll and heat-treatments on powdered precursors like in the BSCCO 2223 phase. Since brittle superconducting materials (like those in the A-15 family, like  $\text{Nb}_3\text{Sn}$ ) could not be wire-drawn, they are mechanically treated as fine powders or ductile precursors, which are then reacted to generate the final composite. Although Nb-Ti could be cold worked to a large degree, heating processes are involved during manufacturing steps to create a secondary phase within the microstructure, which will eventually trap the vortices in the final wire and give improved superconducting performances (much higher  $J_c$  and  $B_{c2}$ ).

Due to these discrepancies, different manufacturing techniques will be presented individually and based on the superconducting materials. Nevertheless, there exist some critical components that all superconducting wires and cables have in common. All these points will be reported and discussed in the next sections of this chapter.

## 2 Usual Requirements for Cables and Wires

### 2.1 *Filaments and Matrix*

Superconductor wires have a multifilamentary architecture where single filaments (each with a diameter ranging from a few to tens of  $\mu\text{m}$ ) are implanted in a highly conductive matrix. When the critical surface conditions in a localized region of a superconductor are exceeded, this region starts to conduct resistively and produces localized heating. The generated heat and current transport present a falling tendency, causing the entire superconductor to quickly transit to its normal state. The capacity to transport heat and currents away from localized areas by separating the filaments into a highly conductive matrix is the main step for making practical superconducting materials. The basic parts of cryogenic stabilization were not created until the middle of 1960s and the initial multifilament NbTi wires were not accessible till 1967 [6]. Al and/or Cu were found to be the most preferred matrices. Silver is essential to process HTS superconducting materials that require oxygen diffusion across the matrix during heat treatments. Following heat treatments, external stabilizers are frequently included. Besides the needs for stability, fine filaments are also required to reduce hysteretic losses, which is important in both ac and dc applications wherein pinned magnetization and jumps of flux must be prevented. The diameter criteria of filaments for ac applications are extremely stringent where a diameter lesser than 1  $\mu\text{m}$  is being preferred. For this case, a Cu-Mn and/or Cu-Ni or matrices are frequently utilized to minimize filaments' proximity coupling.

Multifilamentary designs are not possible to be fabricated by using the manufacturing methods of coated conductors. Superconducting layers are generally of one  $\mu\text{m}$  in thickness in commercial tapes of 2–12 mm in wideness. When an additional

subdivision is needed (such as in the case of ac applications), one should reduce the width of tapes by the striation of the wire into individual strands.

## 2.2 Uniformity of Filaments

The current that could be transported by each filament is lowered when the diameter of the filament is locally reduced. Although currents might be transported to neighboring filaments, the critical current transition is widened, and the time the wire can be worked in continuous mode is reduced (important for NMR and MRI applications). Because diameters lesser than 20  $\mu\text{m}$  are frequently needed, the preparation of wires necessitates a high degree of controlling the quality. As much as the superconducting transition is sharp with rising currents, it will reflect the uniformity degree of filaments. The following power law may be used to describe the curve of voltage versus current (V-I) in the early steps of the resistive transition:

$$V \propto I^n \quad (1)$$

A superconducting material that carries a current density ( $J$ ) will generate an electric field ( $E$ ):

$$E = E_c(J/J_c)^n \quad (2)$$

where  $n$  is transition index and  $J_c$  is the critical current density.

With increasing the field, the transition index reduces. The initial low field value is larger and the decline in  $n$  value is more pronounced when the filament cross-sectional areas are more uniform. In the case of  $\text{Nb}_3\text{Sn}$  for NMR applications, the  $n$  values (at 12 T) are in the 40–80 interval. The  $n$  values (at 5 T) are in the range of 50–100 in composites based on Nb-Ti wires. The large values of  $n$  in the former Nb-Ti wires correspond to less than 2% variations in filaments' cross-sectional area [7]. The values of  $n$  are usually low for HTS materials.

## 2.3 $J_c$ and Flux Pinning

Because a Lorentz force is created on the vortices when current runs throughout a pure annealed superconductor, it cannot transport very high amount of current. The flux lines lead to energy dissipation during their motion, and the superconducting material gradually returns to normal state [8, 9]. Nevertheless, defects in the superconducting matrix could block the vortices in their places (called flux pinning [3, 10, 11]). Flux pinning capability could be enhanced using various ways depending on the material. For example, the vortices are principally trapped by grain boundaries in A15-based superconducting materials (like  $\text{Nb}_3\text{Sn}$ ), hence improving the

density of grain boundaries will lead to improve the critical currents. Furthermore, the incorporation of elements like Ta and Ti in the superconducting matrix rises the resistivity and thus the upper critical field ( $H_{c2}$ ). The increment in  $H_{c2}$  value will lead to increase the critical current in the presence of large magnetic fields. Also, the inclusion or generation of defects that act as artificial pinning centers (APC) showed widely positive effect on pinning efficacy for LTS materials. Trapping is highly anisotropic in HTS materials due to their layered crystal structure. Vortices are efficiently trapped by the lattice planes once the magnetic field is parallel to the (ab)-planes. However, the trapping along the c-axis is depending on the APC and generated defects (such as columnar defects, dislocations, precipitates, etc.). In conclusion, the grains size refinement and the inclusion of efficient pinning defects are the main factors to develop technological superconductors.

## ***2.4 Twisting***

It is commonly necessary to twist the wire about its drawing axis to decrease the non-stability of flux-jump induced by the variations of applied magnetic fields, as well as to diminish eddy-current losses. Twisting is preferably done shortly before the multifilament wire reaches its final size, allowing the twist to be held in position by a subsequent die-pass. As the twist pitch is tighter, as the rate of field changes is higher. In the Large Hadron Collider (LHC), about 80 rotations along the drawing axis per meter were needed for continuous-state dipole magnets. For AC applications of comparably sized wire, the twisting number per meter may reach 300. Twisting pitches of about 10–20 times the diameter are commonly utilized.

## ***2.5 Final Shaping and Cladding***

The size and shape of the die or the use of independently regulated rollers working along the wire surface could control the final cross-section of a strand. Filaments having rectangular or square cross-sections could be made accordingly. Otherwise, a larger duct, such as a rectangular Al or Cu external stabilizer, could be used to introduce and strand the wire into it.

## ***2.6 Mechanical Characteristics***

Mechanical strength is a necessity for different superconducting cables and wires working with high currents and magnetic fields. This is required to withstand the deformations caused by the differential thermal contractions during cooling and by the electromagnetic forces that develop during function. Cooling creates some

tenths of a percent longitudinal compressive strain in the superconducting materials in today's accelerator magnets, but Lorentz loadings in forthcoming systems might yield transverse stresses of up to 200 MPa [12]. The deformations in cables and wires can generate a reversible deterioration of superconducting characteristics via a typical curve of  $I_c$  versus strain ( $\epsilon$ ), the rupture of the active filaments above particular  $\epsilon_{irr}$  values, and hence an irreversible degradation of performances. The ductile Nb-47 wt% Ti alloys are strain-insensitive in operationally relevant ranges. However, the fragile Nb<sub>3</sub>Sn has a bell-shaped curve with a strain-free maximum and a comparative decline in critical current density. Nb<sub>3</sub>Al, as an alternate A-15 superconducting material, displays substantially lower sensitivity to strain, however, it is not easy to be fabricated.

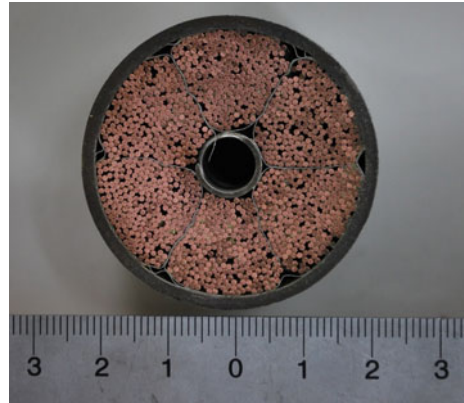
The electromechanical effects on the performance of Nb<sub>3</sub>Sn superconductors have been extensively investigated, both experimentally and theoretically. The incorporation of additives, A15 constitution and development throughout the heat treatments, and the cable design are the main factors that alter the irreversibility limits and strain sensitivity of technological wires.

RE-Ba<sub>2</sub>Cu<sub>3</sub>O<sub>y</sub> (noted RE-BCO, where RE is a rare earth element) tapes are mechanically stronger than LTS wires because of the existence of a steel substrate. With modest strain sensitivity of superconducting characteristics in the reversible area, axial stresses of up to 700 MPa could be achieved, favoring HTS to be used with metallic materials. In contrast, because of differential thermal contraction of insulators, certain concerns have been noticed once applying transverse tensile stresses [13]. In bismuth-based HTS materials, the dependency of  $J_c$  on strain is dissimilar. A linear tendency in  $J_c$  versus  $\epsilon_{axial}$  was observed within the reversibility zone [14]. This indicates that the  $T_c$  is pressure-dependent. Adequately packed tapes based on Bi-2223 have exhibited modest dependency on the axial strain with reversibility reaching 0.35% axial tensile strain [15]. Different from other compounds, the irreversibility happens even for extremely tiny compressive strains. The phenomena could be linked to porosity in filaments for the example of Bi-2212 wires, where the compression provokes collapsing of unsupported grains. The densification seems to be the main factor for achieving high strain resistance and  $J_c$  values in this product. The efforts made to utilize HTS products, that are capable to produce very intense magnetic fields, are inspired from the continuous advances in their mechanical performances.

## 2.7 Performing Cables

One could cable or braid single filaments together to make a superconductor wire/cable of very high capacity to carry very large currents. Amongst the greatest prevalent architectures for round wires based on LTS, the design of Rutherford cables (consisting of a completely flattened, compacted, and transposed cable) is usually utilized in accelerator magnets, wherein great engineering current densities, magnet shape, and field quality constitute the major design operating criteria. Cables with a high-aspect ratio of up to 46 wires could be made by employing this process [12].

**Fig. 2** Cross-sectional view of a cable-in-conduit conductor ( $\sim 4.4$  cm) wound to form toroidal field coil. It comprises 900 Nb<sub>3</sub>Sn strands mixed with 522 Cu strands. The outer part is an austenitic stainless steel conduit tube. The central channel is used for helium flow (*Image was extracted from [17].*)



As well, wires could be joined together in a multi-stage and twisted form and then placed within a conduit. This duct acts as a structural template as well as a containment structure for the circulation of the coolant, with a void portion for coolant circulation (by keeping a certain hole/empty part). Figure 2 shows a cross-section of the CICC (cable-in-conduit-conductor) cable as an example of the mentioned model. CICC cables are necessary for nuclear fusion magnets, which need conductors with very great capacities to transport higher currents and remove heat [16]. The technology of cabling for superconducting tapes is in advanced stages, where several cable architectures are studied for the integration of many wires. Certain cables are formed in a way that the tapes are stacked within aluminum or copper structures that act as stabilizers. Some are created in a way that the tapes are wound in consecutive layers on a circular core. Using another process, tapes can be initially chopped to a meander form and subsequently assembled in Roebel architecture to achieve a completely transposed structure.

The designs of cables must be improved for different kinds of materials to reduce strain on the superconductors, with a focus on keeping it in the interval of  $\varepsilon < \varepsilon_{irr}$ . The control of transverse pressure effects (that impact for instance the transportation characteristics of Nb<sub>3</sub>Sn wires) is a major concern in the uses of accelerator magnets [18]. The empty/hole part in CICC cables, which is required for cooling fluid circulation, could enable changes in cables under electromagnetic forces. As a result of the combined influence of contact, transverse, and axial stress parts, the filament in Nb<sub>3</sub>Sn strands could be fractured during repetitive loading cycles. The resistance to transverse stress could be enhanced by modifying the conductor design or improving the cable twist pitch sequence, which leads to disperse the stress across the wires that make up the cable.

## 2.8 Length

Commercial Nb<sub>3</sub>Sn and Nb-Ti cables come in some tens of Km lengths. Due to changes in mechanical characteristics of the constituents and connection of the filaments that happened through mechanical reduction, the modifications could happen on the length of the cable. As established by Kanithi et al. [19], the changes in  $I_c$  values over the length of Nb-Ti cables are closely ascribed to the changes in Cu/Nb-Ti ratio alongside the length. The researchers generated cables for the project “Superconducting Supercollider”. They demonstrated that the variations in  $I_c$  values (because of changes in the extrinsic characteristics, cable diameters, and ratio between Cu and Nb-Ti) were more than the double changes observed in  $J_c$  values (intrinsic property). The industry recently supplied huge amounts of Nb-Ti wires of around 1300 tons to be used for magnets in the CERN LHC accelerator. This is a huge amount, which corresponds approximately to the world production each year (around 1700 tons per year). In another project, the ITER nuclear fusion needed around 250 tons of fine Nb-Ti multi-filaments and massive amounts of Nb<sub>3</sub>Sn. Actually, an amount of around 500 tons Nb<sub>3</sub>Sn wires are used to develop the ITER toroidal magnet system. Cables based on HTS materials are still in the early stages of development, where the length of single wire is of certain hundred meters. In this case, a distinct phenomenon is seen. Since it is exceedingly hard to preserve the perfect environments (such as lower porosity and grains alignment) required for an excellent HTS cable across long lengths, the global value of  $I_c$  will decrease with increasing the length.

## 3 Materials for Manufacturing Superconducting Wires and Cables

### 3.1 Low-Temperature Superconductor (LTS) Materials

#### 3.1.1 Niobium-Titanium (Nb-Ti) Alloys

Due to that it could be made in a robust and ductile structure with great  $J_c$  values, Nb-Ti material is being the most popular superconductor in commerce. Manufacturing Nb-Ti cable requires an alloy containing 46–50 wt% of titanium, which is commonly denoted as Nb-47 wt% Ti. Reducing the amount of titanium below this interval will lead to diminish the values of  $T_c$  and  $H_{c2}$ .  $H_{c2}$  value can reach a value of about 12 T at LHe temperature with a Ti amount of 44 wt%. The rise in  $H_{c2}$  and  $T_c$  values is largely attributed to the  $\alpha$ -Ti precipitates that are beneficial for strengthening the flux-pinning and hence improving  $J_c$  value. The hardness of the final Nb-Ti product is greatly altered by the composition of the Nb-Ti, which affects the morphology of precipitates. Therefore, it is crucial to start with homogeneous alloys. For a filament having a diameter lesser than 0.05 mm, the alloy should be devoid of non-melted niobium or inductile additives that might cause breaking in filaments and hence in



the cable. Nb and Ti show a wide difference in their melting temperatures, which hardens the manufacturing of the alloys. The levels of homogeneity in currently commercially available alloys of Nb-47Ti are often substantially better than 1.5 wt% titanium. Previously, it is recognized that the amount of impurities should be as much as low, nevertheless, it has been demonstrated nowadays that raising the tolerable amount of Fe could lead to significant precipitates size refinement with no affection on the volume of the precipitate.

The Nb-Ti slab is hot-shaped to the needed diameter and subsequently subjected to annealing process. Next, the Nb-Ti bar is wrapped within a Cu extrusion container of high purity, which is then hot-extruded to generate well-connected monofilament. To prevent the introduction of particles that could not be deformed to below the size of a filament of 0.05 mm, the assembly of the billet should be done in a clean environment. Nb-Ti rods are wrapped by a Nb diffusion barrier to prevent the creation of fragile Ti-Cu intermetallics throughout the heating process, which is desirable for achieving higher  $J_c$  values and producing fine wires. Wire drawing is used to reduce the diameters of filaments, which are then finished using a hexagonal die to generate filaments that could be easily restacked. For Cu/Nb-Ti monofilaments, the thickness of copper surrounding the Nb-Ti at this phase dictates the space among Nb-Ti filaments. A ratio between spacing and diameter filament ( $s/d$ ) of 0.15–0.20 is very good for greatest mechanical stability in Cu/Nb-Ti multi-filaments [20]. The addition of stabilizers is typically needed, which could be provided by the addition of a central core of stabilizers or by enlarging the wall thickness of the swelling container. Ghosh and co-workers [21] determined that a least 0.4–0.5  $\mu\text{m}$  copper thickness is needed for dc magnet applications. If a pure Cu matrix is utilized, the least need for the copper thickness restricts the least diameter of filaments to about 3  $\mu\text{m}$  for  $s/d$  ratios of 0.15–0.20. One could add Mn or Ni to the Cu among filaments when finer filaments are needed.

To produce the multi-filamentary composite, the filament is layered within another copper extrusion container. The diameter of the extrusion container could reach 330 mm with 400 kg in weight. In a single extrusion, up to 4000 filaments could be combined. A formerly produced multifilamentary ingot could be restacked to yield enormous quantities of finer filaments. Cables of up to 40,000 wires were produced by employing this route. Nb-Ti bars could be directly incorporated within the drilled holes in a hard copper extrusion billet when a limited number of wide filaments is required (usually for low-field MRI applications). It should be noted that warm extrusion largely aids in the bonding of the multifilamentary composites.

Precipitation heat treatment is conducted when adequate cold working has been done after multifilament extrusion. If very limited cold working is done prior to the heat treatment, precipitates of Widmanstätten-type will form, which cause an increase in the hardness (lowering the drawability) and produce a non-optimal precipitates distribution and size. The amount of needed pre-strain rises in a linear way with the weight % of titanium. As a consequence, a greater pre-strain is needed to prevent precipitation of Widmanstätten structures in chemically inhomogeneous alloys than in homogeneous alloys. The pre-strain needed for Nb-47Ti alloys is about 5, which increases significantly to about 9 for a 55 wt% of titanium.

Heat treatment steps generally take 20–80 h and are carried out at intervals of 370–420 °C. To achieve great  $J_c$  values, several sets of drawing and heat treatment are necessary. Although the first heat treatment will just generate about 10 vol% precipitation, the influence of the sluggish diffusion rate at these temperatures is surmounted and more precipitates are generated by exerting further cold working strain. The second and third treatment processes usually give 15 and 20 vol% of alpha-Ti precipitates, respectively. Between heat treatment steps, there is a strain of 0.8–1.5, and at minimum three heat treatment stages are commonly used.

Lee et al. [22] demonstrated that the  $J_c$  values and the vol% of precipitates in Nb-47Ti are linearly correlated. At 4.2 K and 5 T, a 20 vol% of alpha-Ti precipitates are enough to achieve  $J_c$  values greater than  $3 \times 10^3$  A/mm<sup>2</sup>. Raising the amount of titanium will raise the rate and concentration of precipitates, however larger pre-strains are necessary to retain excellent ductility and long piece lengths. Alternately, the artificial pinning centers could be physically inserted by hand-assembling the desirable microstructures at a large scale, similar to how multifilament billets are constructed, and afterward lowering the dimensions to meet the fluxoid spacing by numerous restacking and drawing stages. There is no need for extra heat treatments for APCs' strands, and the microstructural constituents would be more flexible. The APCs methodology is not yet commercialized due to the higher expenses linked to the repeated restacking procedure, even though the low field (<5 T) performances are great.

The alpha-Ti precipitations are almost equiaxed in transversal cross-section following the last heating process, where a diameter of 100–200 nm having an extension along the axis of the wire gives a 5–20 aspect ratio. The substantial last wire drawing results in a slight strain in the b.c.c. beta-Nb-Ti that is sustained by Nb-Ti grains inter-curling. Throughout the last wire drawing, the alpha-Ti precipitates will be distorted to tightly folded plates. The folding technique quickly reduces the spacing and thickness of precipitates while rising the lengths of precipitates per area [23]. When the microstructure is optimized, the  $J_c$  value rises until it achieves a peak and then starts to fall gradually. The maximum in  $J_c$  value for multifilamentary strands having homogeneous filaments for a monofilament happens at a strain of about 5. When the cross-section of the filaments is non-uniform, the maximum appeared early and at a lower  $J_c$ . Strands that have an early and reduced peak in  $J_c$  during the last drawing process is considered as 'extrinsically limited' since it did not reach the intrinsic  $J_c$  of the microstructure. Sausaging of the strands because of a lack of coupling among the constituents of the composite or the intermetallic development is by far the most frequent cause of extrinsic limitations. Hence, a tight quality control is required.

To present, the major technical issue has been for the applications, in which a reduced filament diameter is desired while ensuring lower vicinity coupling conditions, reducing ac losses, and improving  $J_c$ , quench protection, and stability.

### 3.1.2 Niobium-Tin ( $\text{Nb}_3\text{Sn}$ ) Alloys

The second largely utilized superconducting material is  $\text{Nb}_3\text{Sn}$ , which displays a  $T_c$  (around 18 K) higher than that of Nb-Ti.  $\text{Nb}_3\text{Sn}$  is largely produced and has demonstrated significant strain tolerance in application, allowing it to be utilized in huge solenoids like the ITER CS model coils that store 640 MJ of energy and in high-field (above 20 T) magnets for NMR applications [24, 25]. Since A15 products are fragile, the different manufacturing processes employ ductile precursors that are heated to generate the A15 at desired dimensions via solid-state diffusion. Earlier, it was established that the existence of copper considerably helps the creation of  $\text{Nb}_3\text{Sn}$  at temperatures lower than 800 °C. Under intense magnetic fields (above 12 T), the addition of 7.5 wt% of Ta or 0.7–1.0 wt% of Ti enhances the  $J_c$  values.

Commercially available  $\text{Nb}_3\text{Sn}$  is produced using mainly one of the following three approaches: powder-in-tube (PIT) technique, internal Sn process, and bronze process. Figure 3 illustrates these three techniques.

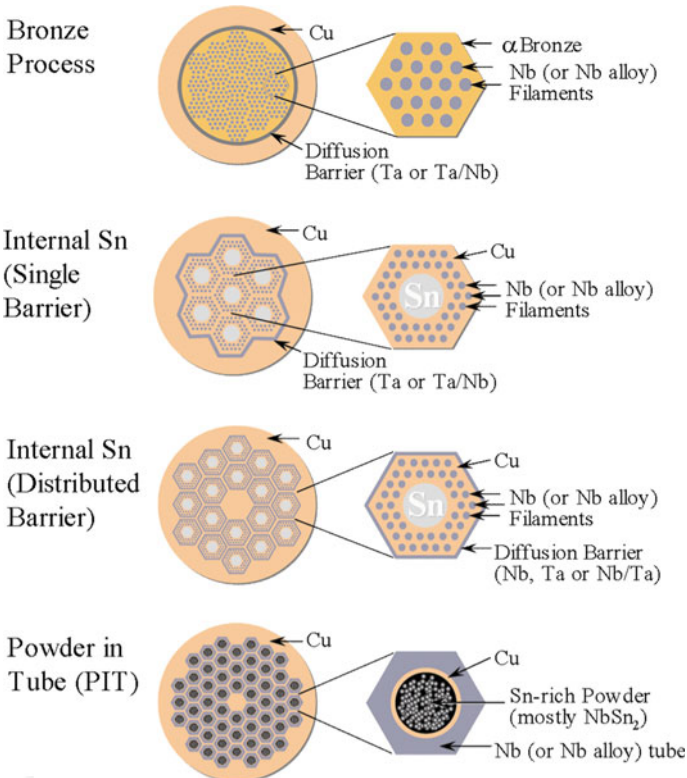


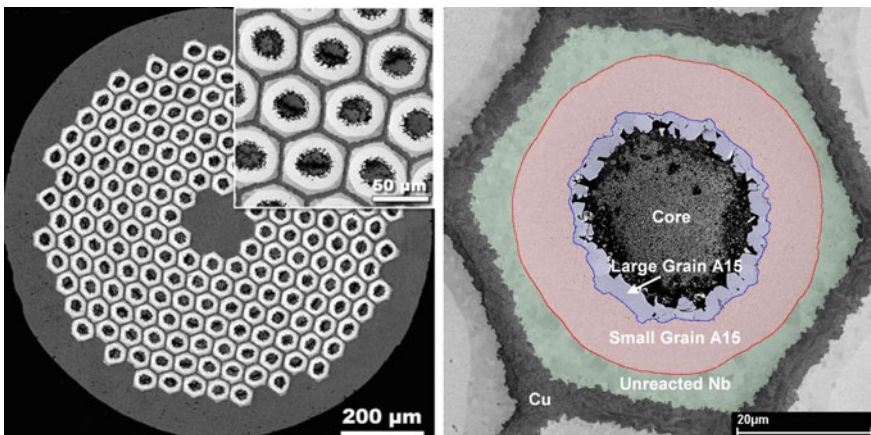
**Fig. 3** Schematic illustration of the three main designs of commercial  $\text{Nb}_3\text{Sn}$ -based superconducting strands: PIT, internal Sn, and bronze process techniques

- **PIT technique:**

$Nb_3Sn$  can be made using greater Sn concentration in Nb-Sn compositions ( $NbSn_2$  and  $Nb_6Sn_5$ ) by placing the powdered intermetallics inside Niobium tubes and heating at 650–700 °C. Copper too is needed for the creation of the A-15 phases at temperatures ranging between 650 and 700 °C while maintaining fine grains size. To increase the Sn/Nb ratio, Sn element is also added. These cables do not require low-temperature heating process, and the heating process for forming the A-15 phases requires merely a short duration (from 50 to 75 h). The optimum combination of great  $J_c$  values (up to  $2.5 \times 10^3$  A/mm<sup>2</sup> at 4.2 K and 12 T) and smaller filament diameter (lower than 35 mm for cables with higher  $J_c$  values, or lesser than 25 mm for cables with relatively low  $J_c$  values) is used in this approach [26]. This enables them to overcome the lower instabilities of magnetic fields related to large filaments in distributed barriers, large- $J_c$  internal Sn wires. Limited amounts for demanding applications were manufactured using this method. Although the viability of the approach has been shown in a variety of areas, like nuclear fusion and high-energy physics, the costs to commercialize the products are still very high. For PIT wires, the amount of A-15 phases inside the non-copper region, the concentration of tin within the A-15 layer, and the high-field pinning capabilities should be greatly optimized [26]. Figure 4 shows images obtained by field-emission scanning electron microscope (FE-SEM) for a PIT composite wire manufactured by ShapeMetal Innovation (SMI).

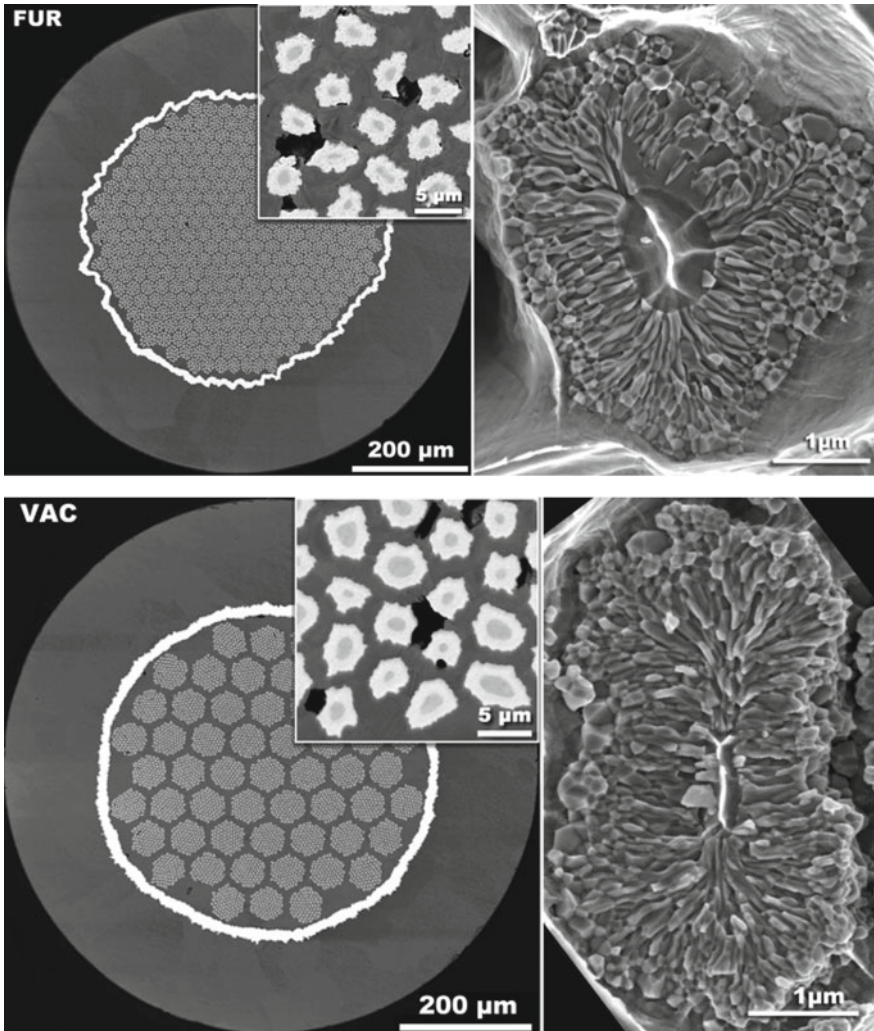
- **Bronze process:**

The ‘bronze process’ is by far the popular method for MRI applications. Here, rods of niobium alloy are wrapped in ductile Cu/Sn bronze and afterward joined within another tube of Cu/Sn, like in the preparation of Nb-Ti multifilament inside



**Fig. 4** Micrographs obtained by FE-SEM technique for a PIT composite wire produced by SMI (Holland). Images were taken from Refs. [27] (Left image) and [28] (Right image)

copper for niobium-tin strands. Several restacking cycles could be utilized to enhance the number of filaments, like in the case of Nb-Ti alloys. The tin from the bronze will react with the niobium during the heating step (usually between 600 and 700 °C) to generate the superconducting A-15 material. Since the Cu-Sn alloys do not operate as stabilizers, extra highly pure copper should be placed inside and/or outside the bronze-Nb filament composite, along with a diffusion barrier of Nb and/or Ta, to prevent the stabilizer from being contaminated with tin. Figure 5 shows two examples

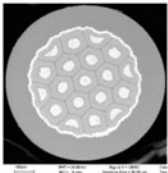
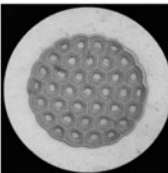
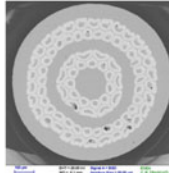
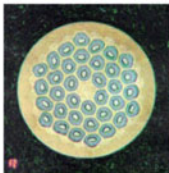


**Fig. 5** Cross-section images obtained by FE-SEM for bronze process ITER wires produced by: Furukawa (reacted at 650 °C for 240 h), and Vacuumschmelze (reacted by a diffusion step at 570 °C for 220 h followed by a A-15 creation stage at 650 °C for 175 h). *Images were taken from Ref. [27]*

of wires prepared via the ‘bronze process’. Although vanadium was being utilized as a barrier, it resulted in lowering  $J_c$  value. This approach could produce strands with highly uniform sized and distributed filament, making them appropriate products for high-fields NMR and other applications that need lower hysteresis loss. The bronze, on the other hand, rapidly became hard during the draw of wires and should be subjected to annealing regularly to preserve the ductility of strands, which influences the production costs. The amount of tin, that could be added (generally less than 16 wt%) to the bronze whilst preserving the ductility, also limits the tin concentration in the composite. At 12 T and 4.2 K,  $J_c$  values cannot exceed roughly  $10^3$  A/mm<sup>2</sup> (low  $J_c$  values) for inadequate Sn amount.

• **Internal tin process:**

By maintaining the tin isolated from the copper during strands manufacturing, one could achieve very high amount of tin and  $J_c$  values. The internal tin process, where a tin core is placed within a niobium-filament/copper matrix, is based on this. The tin core could be alloyed to serve as a carrier for Nb<sub>3</sub>Sn alloys or to enhance the mechanical performances of the soft tin. Figure 3 shows how the Cu/Nb-Sn composites could be utilized in subelements inside single and/or distributed diffusion barriers. Figure 6 shows real cross-sectional images of the well-known Nb<sub>3</sub>Sn wires manufactured using the internal-Sn process, as well as their main characteristics. In this Figure, the products labeled with OKSC and OST-I correspond to the first typology of wires, and those designated with EM-LMI and OCSI abbreviations belong to the second typology. These different products were investigated at the ENEA-Italy laboratory [29]. Strands generated by this technique by employing the dispersed barrier architecture attained the greatest  $J_c$  values for Nb<sub>3</sub>Sn (more than  $3 \times 10^3$  A/mm<sup>2</sup> at 12 T and 4.2 K). High  $J_c$  values are accomplished by lowering the quantity of copper within the copper/filament/tin composite: increasing Sn/Cu

Sample	OST-I	OKSC	OCSI	EM-LMI
				
Manufacturer	Oxford Superconducting Technology	Outokumpu Superconductors	Outokumpu Copper Superconductors Italy	Europa Metall, Italy
Technology	Internal tin	Internal tin	Internal tin	Internal tin
OD (mm)	0.81	0.81	0.81	0.81
No. filaments	151 × 19 bundles	37 bundles	82 bundles	150 × 36 bundles
Twist pitch (mm)	15	24	15	10
Barrier type	Ta	Ta	Nb	Nb and Ta

**Fig. 6** Cross-section images of the well-known Nb<sub>3</sub>Sn wires manufactured through the internal-Sn process along with their main characteristics. *Image was reproduced with permission from [29]*

ratio leads to higher tin concentration inside the A-15 layers. Moreover, the heating process can bridge the filament, provoking undesired enlargement in the diameters of filaments. Filaments with smaller sizes (5–10  $\mu\text{m}$ ) could be obtained for certain wire designs, but for wires with greatest  $J_c$  values, individual filaments have coalesced into macrostructures specified by the subelements, as shown in Fig. 3, with practical diameters exceeding 50  $\mu\text{m}$ .

To avoid contamination of the copper stabilizer, diffusing barriers (Nb and/or Ta or NbTa alloys) are needed, like in the case of the ‘bronze process’. At the temperatures (can reach 700 °C) utilized for the formation of A-15 compounds, tin is diffusing quickly via copper, posing a serious threat to barrier integrity. Several lower-temperature stages precede the heating process of strands to generate the A-15 phases, which are intended to join the tin and the copper in a certain manner that the niobium filaments are not dissolved by the liquid tin or  $\text{Cu}_6\text{Sn}_5$ .

As a part of the US Department of Energy’s Conductor Development Program (CDP) for applications in high-energy physics, Oxford Instruments—Superconducting Technology (OI-ST) pioneered the production method enabling them to achieve the maximum  $J_c$  value of  $3 \times 10^3 \text{ A/mm}^2$  (at 12 T and 4.2 K) [30]. In the designated ‘Rod Restack Process (RRP)’, hot extrusion is employed to generate subelements of filamentary niobium alloys within a Cu matrix where the core consists of tin alloys, which are subjected subsequently to restacking and hot extruding process in highly conductive copper for the stabilization of wires. In the sub-elements, rods of pure niobium or Ta-Nb alloys could be utilized. Instead that tin cores being alloyed, some of the niobium rods might be changed by Nb-47Ti rods as a supplier of titanium. Optimizing the  $\text{Nb}_3\text{Sn}$  layers is the main advance to reach great  $J_c$  values in these wires [31]. This could be accomplished by reducing microstructural and chemical inhomogeneities and getting a large proportion of the layer near to stoichiometric Sn concentration. Each sub-element surrounded by Ta-Nb or Nb alloying barrier is intended to partly interact and improve to the global  $J_c$  value.

### 3.1.3 $\text{Nb}_3\text{Al}$ Superconductor

Strands based on  $\text{Nb}_3\text{Al}$  compound did not yet reach commercialization. However, it could be designated as a practical superconductor since it is produced with uniform kilometer lengths and good performances, which have been used to build full-scale devices.  $J_c$  values close to those of  $\text{Nb}_3\text{Sn}$  strands could be achieved under magnetic fields greater than 20 T. Over 24 T, effective  $J_c$  values up to  $4.1 \times 10^3 \text{ A/mm}^2$  could be attained. The great strain tolerance of  $\text{Nb}_3\text{Al}$  strands in comparison to  $\text{Nb}_3\text{Sn}$  ones is by far the most significant property of  $\text{Nb}_3\text{Al}$  superconductor. A total length of 210 km (approximately 1 ton in mass) of ‘jelly-roll’ processed  $\text{Nb}_3\text{Al}$ -based strands was produced for use in the ITER Central Solenoid coils [32].

Co-winding sheets of niobium and aluminum together on a pure Cu core (free of oxygen) leads to create the Cu/Nb-Al jellyrolls (Fig. 7). This will constitute a single filament in the multifilamentary strand. To produce an extruded tape, the assembled core and jellyroll are placed inside a pure Cu tube. The ingot is pulled down to

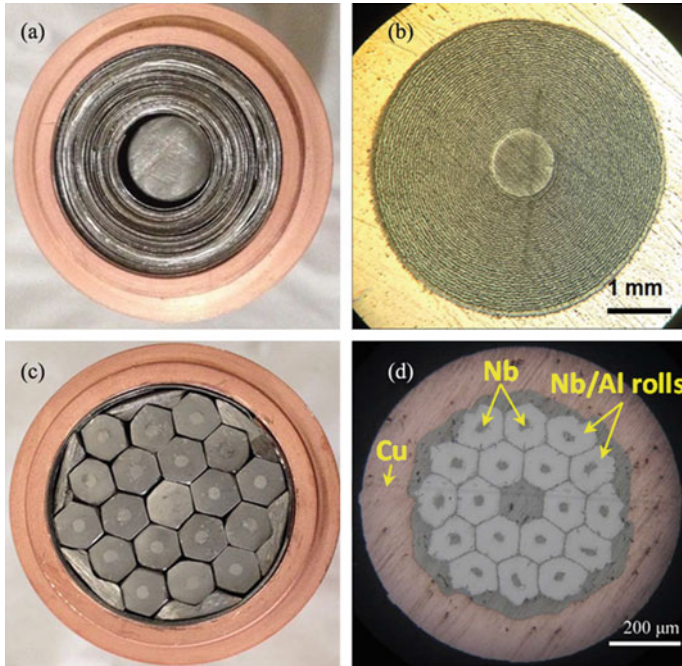


**Fig. 7** Fabrication procedures of the jellyroll Cu/Nb<sub>3</sub>Al precursors [34]: **a** 1st stacking of Nb-Al composite, **b** individual filament having 0.6 cm in diameter, **c** restacking of Cu/Nb-Al billets, and **d** Cross-section image for final Cu/Nb-Al precursor (having 18 cores and size of 0.9 mm in diameter)

a tiny sufficient diameter upon hydrostatic extrusion, which could be subjected to a restacking cycle to form a multifilamentary ingot. The strand is again subjected to hydrostatic extrusion and drawing to reach the appropriate diameter size. In the filaments, the Nb-Al layers' thickness is reduced to less than 1 μm upon extruding and restacking steps. The ITER insert strand's manufacturing yields are about 70% for cables with a distance exceeding 1.5 km and that can reach up to 11 km in length. To make Nb<sub>3</sub>Al, the final strands are subjected to heat treatment (often at 800 °C for 10 h). At 4.2 K-12 T, this approach could yield J<sub>c</sub> values up to 600 A/mm<sup>2</sup> [33].

The largest T<sub>c</sub> and H<sub>c2</sub> values for Nb<sub>3</sub>Al alloys are obtained upon heating at high temperatures followed by quick cooling. In the quick heating-quenching-transformation approach, Nb-Al products are heat-treated at temperatures ranging between 1900 and 2000 °C and afterward quickly quench treated in a molten Ga bath at about 40 °C, which yields the metastable b.c.c. super-saturated solid solution, Nb(Al)<sub>ss</sub>, within a niobium matrix [35]. The heat treatment duration is about 0.1 s. Since the Nb(Al)<sub>ss</sub> is highly ductile, the strands could be mechanically cabled with copper at this phase, and the stabilized strands can also be wrapped in devices. At 800 °C, Nb(Al)<sub>ss</sub> will be converted into Nb<sub>3</sub>Al. Nb<sub>3</sub>Al products manufactured through the quick heating-quenching-transformation approach revealed B<sub>c2</sub> of about 26 T and T<sub>c</sub> around 17.8 K, which are 4 T and 0.7 K smaller than those observed



in products achieved via electron or laser beam irradiation [36]. The stacking faults generated within the A-15 product are thought to be responsible for this discrepancy [37]. The basic the quick heating-quenching-transformation approach follows the double quickly heating-quenching process, however in the place of a low heat-treating temperature (lesser than 1000 °C), the second the quick heating-quenching procedure forms the A-15 composition, which is then followed by a long-range ordering heating process at 800 °C for 12 h [38]. Strands that do not display these stacking faults showed  $T_c$  of about 18.4 K, indicating excellent stoichiometry. At 25 T, a  $J_c$  value of about 135 A/mm<sup>2</sup> was also achieved [25]. The brittle A-15 composition is generated throughout high-temperature treatment, which is a drawback of this approach. Similarly, the transformation-heating-based up-quenching approach uses a rapid heat treatment phase at 1000 °C after the first quick heating-quenching of the quick heating-quenching-transformation procedure. At this temperature, the heat generated by localized transition from the Nb(Al)<sub>ss</sub> toward the A-15 composition induces quick localized heating and reaction diffusion over the lengths of the strands. Since the self-heating is confined to the A-15 region, the heat will promptly dissipate after the reaction through the niobium and stabilizer regions, preventing the outer copper stabilizer from melting [36].

The optimization margins of the performance could be predicted as:  $J_c$  could be enhanced by refining the grains, the diameter of filaments should be minimized, and irreversible stress limit could be raised, which all can be achieved by the application of an extra stacking well after the quick heating-quenching process.

### 3.2 High-Temperature Superconductors (HTS)

HTS products technology has reached a point that allows them to be utilized for actual applications in a wide range of sectors. Superconducting Magnetic Energy Storage (SMES) systems, Superconducting Fault Current Limiters (SFCLs), power transmission cables, and high-field magnets (like for MRI, NMR, fusion, and high-energy physics, etc.) are just a few examples.

The increased attention on HTS materials is mainly attributed to their interesting performances and elevated temperatures in comparison to LTS ones. For instance, HTS materials can show superconductivity phenomena by using low-cost liquid nitrogen as coolant and they display outstanding superconducting performances. Nevertheless, owing to the greater difficulty of creating low-cost lengthy conductors, HTS tapes and wires did not yet achieve great commercial interest like the case of LTS wires/cables. The current flow barrier posed by grain boundaries with high angle, as well as the anisotropy of their superconducting properties, are the major factors of this issue. As a result, the strands should be made with the excellent alignment of grains.

Until today, there exist two main kinds of HTS products on the market that are suitable for technical applications; (Bi,Pb)<sub>2</sub>Sr<sub>2</sub>Ca<sub>n-1</sub>Cu<sub>n</sub>O<sub>y</sub> (noted as abbreviations BSCCO, or Bi-2212 if n = 2 and Bi-2223 if n = 3) and REBa<sub>2</sub>Cu<sub>3</sub>O<sub>y</sub> (noted REBCO,

where RE is a rare earth element like Y, Pr, Sm, Pr, Gd, etc.). Despite not fully adhering to the HTS class, the magnesium-diboride ( $MgB_2$ ) material with medium temperature will be addressed (see Sect. 3.2.3). As well, the new family of iron-based superconducting materials (or called as pnictides) will be covered in Sect. 3.2.4.

### 3.2.1 Tapes and Wires Based on Bi-2212 and Bi-2223 Materials

Just Bi-2212 material, out of different HTS materials, could be easily formed in the form of round wires and multifilamentary strands. Cross-sectional views of Bi-2212 round wire are depicted in Fig. 8, as an example [39]. The design of round wires enables researchers and engineers to use the techniques and processes that are already developed for LTS cables and wires. In general, the PIT manufacturing approach involves a conventional heating step in pure  $O_2$  at 1 bar. During

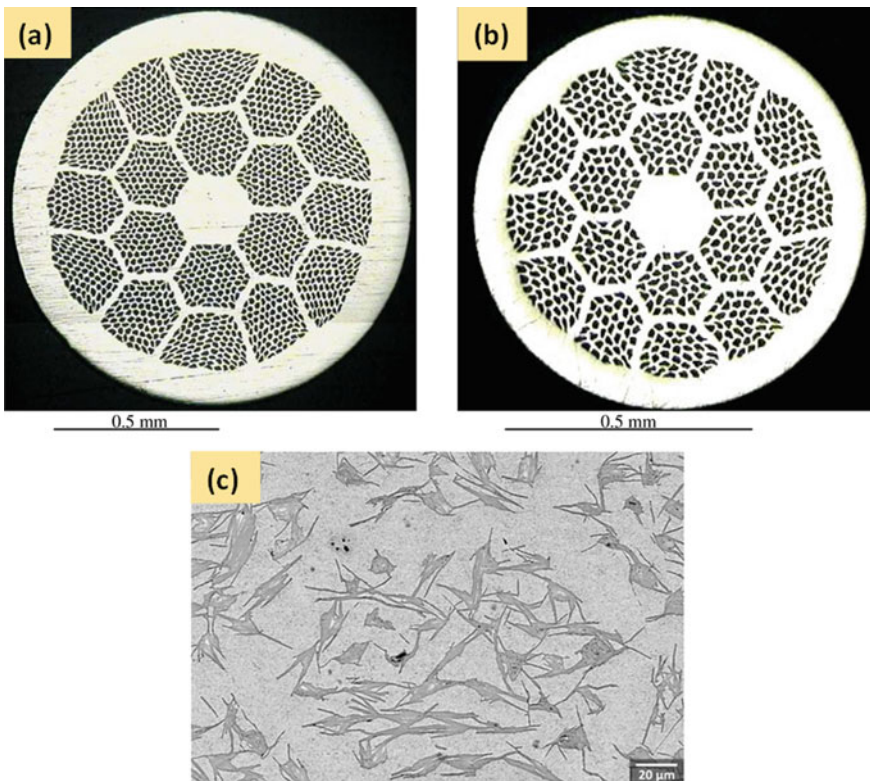


**Fig. 8** **a, b** Cross-sectional SEM images of as drawn Bi-2212 wire with  $18 \times 85$  configuration (left) and  $18 \times 37$  configuration (right). **c** An enlarged view of a fully-heat-treated Bi-2212 wire after overpressure heat treatment. Images were taken from Refs. [41, 42]

the melting of the powder upon the conventional heating step, an enormous agglomeration of bubbles appears in the filaments, which is one of the biggest downsides of this method. During the conventional heating step in a  $O_2$ -Ar environment, an over-pressure must be applied to avoid the creation of bubbles and detrimental creep densification [40]. Due to the necessity for high-pressure, high-temperature furnaces limit the size of coils that could be manufactured. One should react Bi-2212 phase after the fabrication of coils since it is brittle. Another challenge in fabricating the BSCCO 2212 material is the great sensitivity to heating temperatures. For example, at  $890^\circ C$  and round 100 bar, lesser than one-degree Celsius control should be applied over the whole length of the strand. Furthermore, this technique necessitates oxygen diffusion within the HTS material during production. This basically implies that an argon sheath (that is more costly and soft than the traditional stabilizers Al and Cu) should be utilized as a stabilizer for the superconducting strands.

Bi-2212 round wires with great  $J_c$  values (near to those found with REBCO tapes) are now widely available today and have been seen in coils. Bi-2212 has achieved  $J_c$  values (at 4.2 K) of  $3.2 \times 10^3 A/mm^2$  and  $2.5 \times 10^3 A/mm^2$  under 12 and 20 T applied fields, respectively [40, 43]. This material also reached irreversibility larger than 100 T (at 4.2 K). As a result, this material gained great interest to be used in the forthcoming upgraded-LHC and for high-fields MRI and NMR applications.

On the other hand, the Bi-2223 HTS material ( $T_c$  around 110 K) showed also great capabilities to be employed in diverse applications including motors, fault current limiters, transformers, magnetic energy storage devices, superconducting power cables, and so on. However, these applications necessitate a substantial decrease in manufacturing costs. PIT approaches are widely utilized for the fabrication of Bi-2223 by packing Bi-2212 powders with different precursor oxides ( $(Sr,Ca)_{14}Cu_{24}O_x$ ,  $CuO$ ,  $Ca_2PbO_4$ ) inside a silver tube (very similar to  $Nb_3Sn$  production). It is crucial to utilize highly pure powders in the PIT approach to prevent unwanted organic contaminations. In most cases, Pb is used for stabilizing the Bi-2223 phase. To restacking the size of monofilaments, groove rolling is used in addition to typical wire drawing processes. The composite multifilament could be then bonded by hot extrusion, which increases the density of powder and reduces the diameter of the billet. Following the extrusion step, there is further drawing and groove rolling before rolling into a tape. By profiting from the lamellated structure of the BSCCO 2212 composition and its capability to be oriented towards the c-axis once compressed, the last step (known as texturing step) is required to optimally align the c-axes of grains normal to the plane of tape. A first partial heat treatment step is employed to create the HTS phase when it has been rolled into tapes. Since it produces a significant loss in density, the first thermal process is terminated prior to the entire creation of the Bi-2223 phase. After this partial heat treatment, the ceramic core is densified by a deformation process. Lastly, under high  $O_2$  pressure, an additional heating step will complete the transformation to the HTS phase. This material is easily exploited to produce high amounts of largely sized products since the material is subjected to conventional mechanical processes. Nowadays, the available commercial tapes could exhibit a  $15^\circ$  full-width at half maximum (FWHM) uniaxial texturing with no in-plane texturing, as well

as a  $J_c$  value of near to  $500 \text{ A/mm}^2$  at 77 K and in the absence of applied magnetic field [44].

Researchers and engineers succeeded in employing tapes based on Bi-2223 in accelerator magnets, especially in the HTS current leads [45]. From 2010, over 1300 Bi-based HTS current leads are running at the CERN LHC: About 65 current leads having  $I_{\text{rated}} \sim 13 \times 10^3 \text{ A}$  are used in the main dipoles and quadrupoles, the insertion magnets use around 300 current leads having  $I_{\text{rated}} \sim 0.6 \text{ kA}$ , and the corrector magnets use more than 800 current leads of  $I_{\text{rated}} \sim 0.6 \text{ kA}$ . The overall energetic power was thus decreased from 1290 kW using traditional leads to 450 kW by adopting the BSCCO HTS leads.

Superconducting power lines are another interesting application for BSCCO materials. Despite their small diameter, these cables have the capability of transporting huge amounts of currents with low losses. Particularly, superconducting power cables look to be highly exciting in populous regions, where high-voltage traditional cables can be changed by superconducting cables, which will lead to eliminate the need for substations attached to cables. Numerous DC or AC superconducting power cables were constructed and evaluated in Korea, China, European Union, the United States, and Japan. Table 1 lists some projects on typical examples of superconducting power cables. Figure 9 depicts a Bi-2223 superconducting cable of three phases manufac-

**Table 1** List of some projects on typical examples of superconducting power cable

Region	Project	Place	Length (m)	Voltage (kV)	Current (kA)
Korea	DAPAS2	Lab	30	154	3.75
	DAPAS1	Lab	100	22.9	1.25
	KEPCO	Lab	100	22.9	1.25
China	IEE/CAS (DC)	Factory	380	1.3	10
	Lanzhou	Factory	75	10.5	1.5
	Yunnan	Grid	33.5	35	2
Europe	St. Petersburg (DC)	Grid	2500	20	2.5
	Essen	Grid	1000	10	2.3
	VNIIEP	Grid	200	20	1.4
	Denmark	Grid	30	30	0.2
USA	LIPA	Grid	600	138	2.4
	Ohio	Grid	200	13.8	3
	Albany	Grid	350	34.5	0.8
Japan	METI (DC)	Grid	2000	10	5
	RTRI (DC)	Lab	30	1.5	5
	Sumitomo	Factory	70	3.3	0.4
	Yokohama	Grid	240	66	2
	Chubu University (DC)	Lab	200	20	2
	EPCO/CRIEPI/Sumitomo	Lab	100	66	1

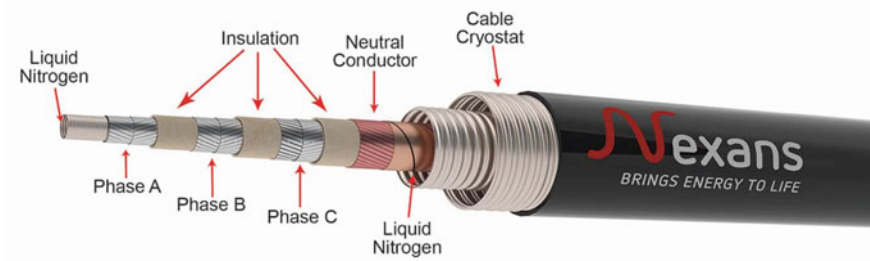


**Fig. 9** Constituents of Bi-2223 superconducting cable of three phases designed by Nexans. *Image was taken from [46]*

tured by Nexans. A neutral shielding conductor, three BSCCO 2223 conductors separated by a dielectric, electrical insulation, and cable cryostat make up this cable. The cooling fluid could effectively circulate via both the outer and inner channels of the cable. A vacuum layer separates the structure from its outside shell, preventing the transfer of the thermal energy to the surrounding medium.

### 3.2.2 REBCO Coated Conductors

REBCO superconductors have also attracted the interest as be potential candidates for high-fields magnet technologies due to their outstanding  $B_{irr}$  and  $J_c$  values. For instance,  $B_{irr}$  value along the c-axis of bulk YBCO ( $T_c = 92$  K) could reach 100 T at 0 K [47, 48]. Although REBCO tapes showed outstanding superconducting performances, round wires based on this material are still unavailable by utilizing the present approaches. The PIT technique could not be employed here. Actually, REBCO conductors could only be made as epitaxial films deposited on flat and flexible metallic tapes that have been coated with stabilizing layers and buffering metal oxides. 2nd generation (2G) technology of HTS coated conductors is the name given to this technology. Figure 10 shows the design of a lengthy coated conductor that SuperPower Co. is presently commercializing. Some of the characteristics of this product can be found in the website of SuperPower Inc. [49].

The main factor that limits the preparation of REBCO materials in the form of round wires is the more pronounced deterioration of  $J_c$  (owing to the misalignment of crystal grains) in these products compared to that seen in BSCCO materials. Indeed,  $J_c$  decreases rapidly in an exponential way when the misorientation angles of neighboring crystallites increase (surpassing  $5^\circ$ – $10^\circ$ ). Therefore, texturing the substrate could help to reduce grain boundaries misorientation. To make coated conducting tapes, many producers have implemented a range of advanced approaches. The sophisticated techniques are the ion beam assisted deposition (IBAD) and rolled assisted biaxially-textured substrates (RABiTS) technologies. Due to the fact that the IBAD technique does not need a textured substrate, polycrystalline Hastelloy or stainless-steel tapes could be employed. In basic pulsed laser

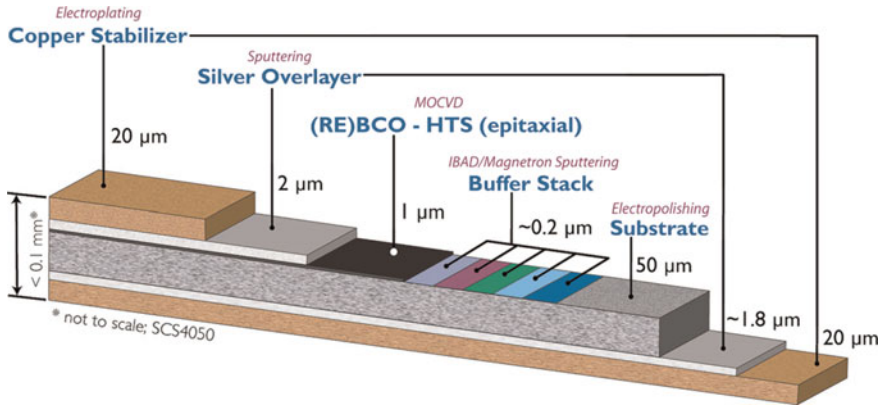


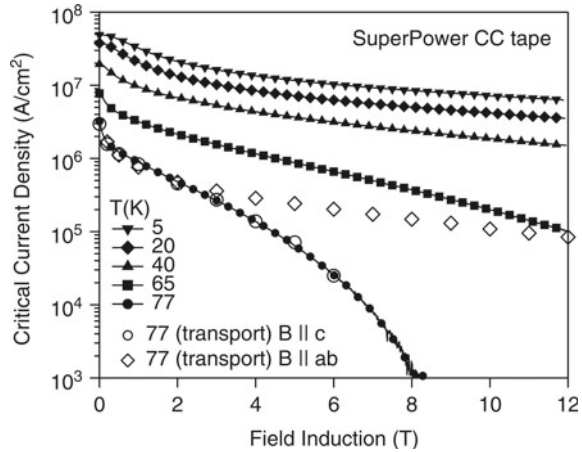
**Fig. 10** Design of REBCO 2G HTS coated conductors commercialized by SuperPower Inc. *Image was taken from [49]*

deposition (PLD) configuration, one will deposit a seed layer ( $Y_2O_3$ ) and a diffusion-barrier layer ( $Al_2O_3$ ) on the metallic substrate’s surface, proceeded by depositing a biaxially textured layer (MgO) by an assisted ion beam of 1 keV  $Ar^+$ . For coated conductors made using RABiTS method, the texture is readily incorporated in a NiW substrate (biaxial texture) by rolling procedures and recrystallizing heat treatments [50]. After that, epitaxial buffer layers are coated on the NiW textured substrate to offer a lattice matching for growing the superconducting layer. The superconductor’s cross-section is around 1% of the cross-section of the entire tape owing to the existence of many buffer layers and stabilizers (see Fig. 10). Because the dimensions of these layers cannot be reduced, the thickness of the superconducting layer must be increased to boost the  $J_c$  value. Nevertheless, maintaining an ideal texture in thicknesses over 1  $\mu m$  is extremely difficult challenging.

The active REBCO layers may be deposited using a variety of procedures, including physical (such as PLD and reactive co-evaporation (RCE)) and chemical (metal–organic chemical vapor deposition (MOCVD) and metal–organic deposition (MOD)) techniques. Nowadays, several coated conductors’ manufactures use some of these methods such as MOCVD by SuperPower Inc.; RCE by STI and SuNAM Co.; PLD by SuperOx, Sumitomo, Fujikura, and Bruker Co.; MOD by American Superconductors.

Coated conducting tapes are often intended to operate under specified circumstances. The tapes with APCs reveal improved performances under applied magnetic fields (potential for high-field magnets). Other tapes have been developed to function under low fields at liquid nitrogen temperature (promising for transmission cables). Figure 11 depicts the  $J_c$  values versus magnetic fields of a coated conducting tape designed by SuperPower Co., as an example [51]. It is clear that the  $J_c$  values are extremely high and illustrate a weak dependency on the field, indicating that coated conductor tapes have a lot of potentials.  $J_c$  is about  $2 \times 10^6 \text{ A/cm}^2$  at 77 K and 0 T and increased with reducing the temperature. When the thickness of the film

**Fig. 11** Variations of  $J_c$  versus magnetic field for a coated conductor tape manufactured by SuperPower Co. Image was reproduced with permission from Ref. [51]



is raised further, a dead layer composed of secondary phases and pores could be formed. Numerous approaches are currently being proposed to address this issue.

### 3.2.3 Magnesium Diboride

$MgB_2$  superconductor has attracted the attention (discovered in 2001) since it possesses the greatest  $T_c$  ( $\sim 39$  K) in comparison to other intermetallic superconductors.  $MgB_2$  crystallized in hexagonal structure and displays anisotropic superconducting characteristics. Nevertheless, this anisotropy is less pronounced in comparison to HTS materials, and the material behaves more like LTS materials. PIT is a scalable method that has previously been used to fabricate strands using both ex-situ [52] and in-situ [53] processing for future manufacture of kilometer-lengthy  $MgB_2$ . The combined  $MgB_2$  powder mixtures are subjected to an annealing step at high temperature during the ending deformation step for the case of ex-situ wires. However, the in-situ process begins by mixing  $MgB_2$  precursors (B and Mg powders) and a heating treatment at  $650^\circ C$  is applied at the ending deformation step. Giunchi and co-workers [54] established another interesting mechanism designated as the Internal Magnesium Diffusion (IMD) process. Here, magnesium rods are inserted within a tube constructed of pressed B powders, and the reaction takes place after the deformation step. Among these three techniques, products generated by means of this approach showed the greatest density of mass.

Since the perpendicular Birr value of  $MgB_2$  is smaller than that of  $Nb_3Sn$  (the extensively utilized intermetallic superconductor), it might limit its applications at lower fields. However, the greater  $T_c$  makes it particularly interesting for applications in the temperature interval of 10–30 K, which may be obtained using gas helium, liquid hydrogen, or cryogen-free cooling systems. The ability to operate with no LHe is extremely interesting since it is either excessively costly or not available in several places of the world. In terms of transport performances, Li et al. [55] achieved

the highest  $J_c$  value in 2012 ( $J_{eng} \sim 1.7 \times 10^4$  A/cm<sup>2</sup> at 4.2 K and 10 T) using the IMD technique. Ex-situ wires showed superior performances at lower fields, while in-situ and IMD wires showed greater  $J_c$  at high fields. Furthermore, carbon-based additives are easy to be introduced to enhance pinning capabilities.

MgB<sub>2</sub> material is currently being exploited for numerous technological applications, such as for 10 MW direct drive offshore wind turbine generators [56], current busbars at CERN [57], MRI magnets [58].

### 3.2.4 Iron-Based Superconductors (Pnictides)

The first iron-based superconductor was discovered in 2008 in LaFeAsO<sub>1-x</sub>F<sub>x</sub> material with  $T_c$  of about 26 K [59]. This discovery was followed by the observation of superconductivity phenomena in numerous similar compositions that belong to the same family where  $T_c$  can reach up to 60 K. Like in HTS materials, iron-based superconductors display high anisotropy (but lower than those of YBCO and BSCCO materials), as well as extremely great  $B_{c2}$  (can reach up to 100–200 T at 0 K) and  $J_c(B,T)$  values.

For practical applications, the physical and crystalline features of iron-based superconductors enable the utilization of PIT technologies to fabricate superconducting wires [60]. For example, the measured  $J_c$  values, reaching up to  $10^5$  A/cm<sup>2</sup> (at 4.2 K and 10 T) in the ‘122’ pnictide family [61, 62], surpass the practical applications criterion for high-field magnets. The fabrication of pnictide wires via PIT technique, exhibiting comparable  $J_c$  values, received also great interest. Nevertheless, when employing the PIT approach to make wires, the chemical reaction between the iron-based superconducting phase with the metallic sheath poses a problem [63, 64] has established the efficacy of FeSe<sub>0.5</sub>Te<sub>0.5</sub> coated conducting tapes, transporting  $J_c$  greater than  $10^5$  A/cm<sup>2</sup> at 30 T, as an alternate route.

## 4 Conclusion

Nb<sub>3</sub>Sn and Nb-Ti superconducting materials have been well commercialized. They have a solid market for MRI and NMR instruments, and high magnetic field measurement devices. New developments will be driven by the future markets in energy storage, accelerator magnets, and fusion reactors. Nb<sub>3</sub>Al’s strain tolerance must keep it in the spotlight for high-fields applications wherein the cost of conductors will not be a problem. Using LN<sub>2</sub> as a cooling fluid for HTS conductors, like REBCO or Bi-2223 tapes, is absolutely interesting for using these tapes in diverse applications like power transmission lines. Bi-2212 round wires have outstanding features that make them promise for extremely high-fields applications at lower temperatures, but they still need to be further industrially developed. REBCO tapes will need to be less expensive prior to being economically feasible for broad applications. Because of its moderate  $T_c$ , MgB<sub>2</sub> has the ability to be a low-cost superconductor and thus several



investigations on making it into the form of cables or tapes are still under development. The new family of iron-based superconductors has revealed outstanding  $J_c$  values, which, alongside their lower magnetic field anisotropy and lesser dependency on the field, make them interesting for low-temperatures and high-fields applications.

## References

1. G.B. Yntema, Niobium superconducting magnets. *IEEE Trans. Magn.* **23**, 390–395 (1987). <https://doi.org/10.1109/TMAG.1987.1065154>
2. M.K. Ben Salem, E. Hannachi, Y. Slimani, A. Hamrita, M. Zouaoui, L. Bessais, M. Ben Salem, F. Ben Azzouz, SiO<sub>2</sub> nanoparticles addition effect on microstructure and pinning properties in YBa<sub>2</sub>Cu<sub>3</sub>O<sub>y</sub>. *Ceram. Int.* **40**, 4953–4962 (2014). <https://doi.org/10.1016/j.ceramint.2013.10.103>
3. Y. Slimani, M.A. Almessiere, E. Hannachi, M. Mumtaz, A. Manikandan, A. Baykal, F. Ben Azzouz, Improvement of flux pinning ability by tungsten oxide nanoparticles added in YBa<sub>2</sub>Cu<sub>3</sub>O<sub>y</sub> superconductor, *Ceram. Int.* **45**, 6828–6835 (2019). <https://doi.org/10.1016/j.ceramint.2018.12.176>
4. A. Hamrita, Y. Slimani, M.K. Ben Salem, E. Hannachi, L. Bessais, F. Ben Azzouz, M. Ben Salem, Superconducting properties of polycrystalline YBa<sub>2</sub>Cu<sub>3</sub>O<sub>7</sub>—D prepared by sintering of ball-milled precursor powder. *Ceram. Int.* **40**, 1461–1470 (2014). <https://doi.org/10.1016/j.ceramint.2013.07.030>
5. Plots—Comparisons of superconductor critical current densities—MagLab (2018), <https://nationalmaglab.org/magnet-development/applied-superconductivity-center/plots>
6. P.F. Chester, Superconducting magnets. *Rep. Prog. Phys.* **30**, 561–614 (1967). <https://doi.org/10.1088/0034-4885/30/2/305>
7. P.J. Lee, D.C. Larbalestier, An examination of the properties of SSC phase II R&D strands. *IEEE Trans. Appl. Supercond.* **3**, 833–841 (1993). <https://doi.org/10.1109/77.233833>
8. E. Hannachi, M.K. Ben Salem, Y. Slimani, A. Hamrita, M. Zouaoui, F. Ben Azzouz, M. Ben Salem, Dissipation mechanisms in polycrystalline YBCO prepared by sintering of ball-milled precursor powder. *Phys. B Condens. Matter.* **430**, 52–57 (2013). <https://doi.org/10.1016/J.PHYSB.2013.08.028>
9. R. Algarni, M.A. Almessiere, Y. Slimani, E. Hannachi, F. Ben Azzouz, Enhanced critical current density and flux pinning traits with Dy<sub>2</sub>O<sub>3</sub> nanoparticles added to YBa<sub>2</sub>Cu<sub>3</sub>O<sub>7-d</sub> superconductor. *J. Alloys Compd.* **852**, 157019 (2021). <https://doi.org/10.1016/J.JALLCOM.2020.157019>
10. Y. Slimani, M.A. Almessiere, E. Hannachi, A. Manikandan, R. Algarni, A. Baykal, F. Ben Azzouz, Flux pinning properties of YBCO added by WO<sub>3</sub> nanoparticles. *J. Alloys Compd.* **810**, 151884 (2019). <https://doi.org/10.1016/j.jallcom.2019.151884>
11. Y. Slimani, E. Hannachi, A. Ekicibil, M.A. Almessiere, F. Ben Azzouz, Investigation of the impact of nano-sized wires and particles TiO<sub>2</sub> on Y-123 superconductor performance. *J. Alloys Compd.* **781**, 664–673 (2019). <https://doi.org/10.1016/j.jallcom.2018.12.062>
12. L. Bottura, A. Godeke, Superconducting materials and conductors: fabrication and limiting parameters. *Rev. Accel. Sci. Technol.* **05**, 25–50 (2012). <https://doi.org/10.1142/s1793626812300022>
13. C. Senatore, M. Alessandrini, A. Lucarelli, R. Tediosi, D. Uglietti, Y. Iwasa, Progresses and challenges in the development of high-field solenoidal magnets based on RE123 coated conductors. *Supercond. Sci. Technol.* **27**, 103001 (2014). <https://doi.org/10.1088/0953-2048/27/10/103001>
14. N. Cheggour, X.F. Lu, T.G. Holesinger, T.C. Stauffer, J. Jiang, L.F. Goodrich, Reversible effect of strain on transport critical current in Bi<sub>2</sub>Sr<sub>2</sub>CaCu<sub>2</sub>O<sub>8+x</sub> superconducting wires: a modified

- descriptive strain model. *Supercond. Sci. Technol.* **25**, 015001 (2012). <https://doi.org/10.1088/0953-2048/25/1/015001>
15. K.I. Sato, S.I. Kobayashi, T. Nakashima, Present status and future perspective of bismuth-based high-temperature superconducting wires realizing application systems. *Jpn. J. Appl. Phys.* **51**, 010006 (2012). <https://doi.org/10.1143/JJAP.51.010006/XML>
  16. L. Muzzi, G. De Marzi, A. Di Zenobio, A. Della Corte, Cable-in-conduit conductors: lessons from the recent past for future developments with low and high temperature superconductors. *Supercond. Sci. Technol.* **28**, 053001 (2015). <https://doi.org/10.1088/0953-2048/28/5/053001>
  17. Completion of first Tokamak hardware acknowledged (n.d.), <https://www.iter.org/newsline/141/354>
  18. E. Barzi, N. Andreev, G. Apollinari, F. Bucciarelli, V. Lombardo, F. Nobrega, D. Turrioni, R. Yamada, A.V. Zlobin, Superconducting strand and cable development for the LHC upgrades and beyond. *IEEE Trans. Appl. Supercond.* **23**, 6001112–6001112 (2013). <https://doi.org/10.1109/TASC.2013.2240038>
  19. H. Kanithi, M. Erdmann, P. Valaris, F. Krahula, R. Lusk, E. Gregory, B. Zeitlin, A status report on the development of inner and outer conductors for the SSC dipole and quadrupole magnets. *Supercollider* **2**, 601–609 (1990). [https://doi.org/10.1007/978-1-4615-3728-1\\_55](https://doi.org/10.1007/978-1-4615-3728-1_55)
  20. E. Gregory, T.S. Kreilick, J. Wong, A.K. Ghosh, W.B. Sampson, Importance of spacing in the development of high current densities in multifilamentary superconductors. *Cryogenics (Guildf.)* **27**, 178–182 (1987). [https://doi.org/10.1016/0011-2275\(87\)90016-6](https://doi.org/10.1016/0011-2275(87)90016-6)
  21. A.K. Ghosh, W.B. Sampson, E. Gregory, T.S. Kreilick, Anomalous low field magnetization in fine filament NbTi conductors. *IEEE Trans. Magn.* **23**, 1724–1727 (1987). <https://doi.org/10.1109/TMAG.1987.1064987>
  22. P.J. Lee, J.C. McKinnell, D.C. Larbalestier, *Restricted, Novel Heat Treatments for Obtaining High J<sub>c</sub> in Nb 46.5 wt% Ti* (Springer, Boston, MA, 1990). [https://doi.org/10.1007/978-1-4613-9880-6\\_37](https://doi.org/10.1007/978-1-4613-9880-6_37)
  23. C. Meingast, P.J. Lee, D.C. Larbalestier, Quantitative description of a high J<sub>c</sub> Nb-Ti superconductor during its final optimization strain. I. Microstructure, T<sub>c</sub>, H<sub>c2</sub>, and resistivity, *J. Appl. Phys.* **66**, 5962 (1998). <https://doi.org/10.1063/1.343624>
  24. T. Kato, H. Tsuji, T. Ando, Y. Takahashi, H. Nakajima, M. Sugimoto et al., First test results for the ITER central solenoid model coil. *Fusion Eng. Des.* **56–57**, 59–70 (2001). [https://doi.org/10.1016/S0920-3796\(01\)00235-6](https://doi.org/10.1016/S0920-3796(01)00235-6)
  25. A. Kikuchi, Y. Iijima, K. Inoue, M. Kosuge, New Nb<sub>3</sub>Al conductor made by DRHQ process. *AIP Conf. Proc.* **614**, 1025 (2002). <https://doi.org/10.1063/1.1472645>
  26. A. Godeke, A. den Ouden, A. Nijhuis, H.H.J. ten Kate, State of the art powder-in-tube niobium-tin superconductors. *Cryogenics (Guildf.)* **48**, 308–316 (2008). <https://doi.org/10.1016/J.CRYOGENICS.2008.04.003>
  27. A. Godek, Performance boundaries in Nb<sub>3</sub>Sn superconductors. *Ph.D. thesis* (University of Twente, Enschede, The Netherlands, 2005)
  28. C.M. Fischer, Investigation of the relationships between superconducting properties and Nb<sub>3</sub>Sn reaction conditions in powder-in-tube Nb<sub>3</sub>Sn conductors. *Master thesis* (University of Wisconsin-Madison, US, 2002)
  29. P. Fabbriatore, S. Farinon, V. Corato, G. De Marzi, T. Spina, U. Gambardella, A. Saggese, Experimental investigation of the transverse resistivity in Nb<sub>3</sub>Sn wires through ac susceptibility. *Supercond. Sci. Technol.* **26**, 085001 (2013). <https://doi.org/10.1088/0953-2048/26/8/085001>
  30. D.R. Dieterich, A. Godeke, Nb<sub>3</sub>Sn research and development in the USA—wires and cables. *Cryogenics (Guildf.)* **48**, 331–340 (2008). <https://doi.org/10.1016/J.CRYOGENICS.2008.05.004>
  31. P.J. Lee, D.C. Larbalestier, Microstructural factors important for the development of high critical current density Nb<sub>3</sub>Sn strand. *Cryogenics (Guildf.)* **48**, 283–292 (2008). <https://doi.org/10.1016/J.CRYOGENICS.2008.04.005>
  32. Y. Yamada, N. Ayai, K. Takahashi, K. Sato, M. Sugimoto, T. Ando, Y. Takahashi, M. Nishi, Development of Nb<sub>3</sub>Al/Cu multifilamentary superconductors. *Adv. Cryog. Eng. Mater.* **40**, 907–914 (1994). [https://doi.org/10.1007/978-1-4757-9053-5\\_116](https://doi.org/10.1007/978-1-4757-9053-5_116)

33. F. Hosono, G. Iwaki, K. Kikuchi, S. Ishida, T. Ando, K. Kizu, Y. Miura, A. Sakasai, Production of a 11 km long jelly roll processed Nb<sub>3</sub>Al strand with high copper ratio of 4 for fusion magnets. *IEEE Trans. Appl. Supercond.* **12**, 1037–1040 (2002). <https://doi.org/10.1109/TASC.2002.1018578>
34. C. Chen, Z.M. Bai, X.F. Pan, L.J. Cui, G. Yan, P.X. Zhang, Superconducting properties of jelly-roll Nb<sub>3</sub>Al short wire prepared by rapid heating, quenching, and transformation method. *IEEE Trans. Appl. Supercond.* **26**, 1–5 (2016). <https://doi.org/10.1109/TASC.2016.2594264>
35. Y. Iijima, M. Kosuge, T. Takeuchi, K. Inoue, Nb<sub>3</sub>Al multifilamentary wires continuously fabricated by rapid-quenching, in *Advances in Cryogenic Engineering Materials* (Springer US, Boston, MA, 1994), pp. 899–905. [https://doi.org/10.1007/978-1-4757-9053-5\\_115](https://doi.org/10.1007/978-1-4757-9053-5_115)
36. T. Takeuchi, N. Banno, T. Fukuzaki, H. Wada, Large improvement in high-field critical current densities of Nb<sub>3</sub>Al conductors by the transformation-heat-based up-quenching method. *Supercond. Sci. Technol.* **13**, L11 (2000). <https://doi.org/10.1088/0953-2048/13/10/101>
37. A. Kikuchi, Y. Iijima, K. Inoue, Microstructures of rapidly-heated/quenched and transformed Nb<sub>3</sub>Al multifilamentary superconducting wires. *IEEE Trans. Appl. Supercond.* **11**, 3615–3618 (2001). <https://doi.org/10.1109/77.919847>
38. A. Kikuchi, Y. Iijima, K. Inoue, Nb<sub>3</sub>Al conductor fabricated by DRHQ (double rapidly-heating/quenching) process. *IEEE Trans. Appl. Supercond.* 3968–3971 (2001). <https://doi.org/10.1109/77.919950>
39. J. Jiang, A. Francis, R. Alicea, M. Matras, F. Kametani, U.P. Trociewitz, E.E. Hellstrom, D.C. Larbalestier, Effects of filament size on critical current density in overpressure processed Bi-2212 round wire. *IEEE Trans. Appl. Supercond.* **27**, 1–4 (2017). <https://doi.org/10.1109/TASC.2016.2627817>
40. D.C. Larbalestier, J. Jiang, U.P. Trociewitz, F. Kametani, C. Scheuerlein, M. Dalban-Canassy, M. Matras, P. Chen, N.C. Craig, P.J. Lee, E.E. Hellstrom, Isotropic round-wire multifilament cuprate superconductor for generation of magnetic fields above 30 T. *Nat. Mater.* **13**, 375–381 (2014). <https://doi.org/10.1038/nmat3887>
41. H. Miao, Y. Huang, M. Meinesz, S. Hong, J. Parrell, Development of Bi-2212 round wires for high field magnet applications. *AIP Conf. Proc.* **1435**, 315 (2012). <https://doi.org/10.1063/1.4712111>
42. D.C. Larbalestier, J. Jiang, U.P. Trociewitz, F. Kametani, C. Scheuerlein, M. Dalban-Canassy, M. Matras, P. Chen, N.C. Craig, P.J. Lee, E.E. Hellstrom, A transformative superconducting magnet technology for fields well above 30 T using isotropic round wire multifilament Bi<sub>2</sub>Sr<sub>2</sub>CaCu<sub>2</sub>O<sub>8-x</sub> conductor (2013), ArXiv1305.1269
43. Jianyi Jiang, Hanping Miao, Yibing Huang, Seung Hong, J.A. Parrell, C. Scheuerlein, M. Di Michiel, A.K. Ghosh, U.P. Trociewitz, E.E. Hellstrom, D.C. Larbalestier, Reduction of gas bubbles and improved critical current density in Bi-2212 round wire by swaging. *IEEE Trans. Appl. Supercond.* **23**, 6400206–6400206 (2013). <https://doi.org/10.1109/TASC.2013.2237873>
44. F. Kametani, J. Jiang, M. Matras, D. Abraimov, E.E. Hellstrom, D.C. Larbalestier, Comparison of growth texture in round Bi2212 and flat Bi2223 wires and its relation to high critical current density development. *Sci. Rep.* **5**, 8285 (2015). <https://doi.org/10.1038/srep08285>
45. A. Ballarino, Large-capacity current leads. *Phys. C Supercond.* **468**, 2143–2148 (2008). <https://doi.org/10.1016/J.PHYSC.2008.05.217>
46. Nexans—Superconductors—Nexans interconnects central Chicago (n.d.), <https://www.nexans.com/newsroom/news/details/2020/06/nexans-wins-amsc-contract-chicago-resilient-electric-grid-project.html>
47. E. Hannachi, Y. Slimani, A. Ekicibil, A. Manikandan, F. Ben Azzouz, Magneto-resistivity and magnetization investigations of YBCO superconductor added by nano-wires and nanoparticles of titanium oxide. *J. Mater. Sci. Mater. Electron.* **30**, 8805–8813 (2019). <https://doi.org/10.1007/s10854-019-01205-3>
48. Y. Slimani, E. Hannachi, M.K. Ben Salem, A. Hamrita, M. Ben Salem, F. Ben Azzouz, Fluctuation induced magneto-conductivity of Y<sub>3</sub>Ba<sub>5</sub>Cu<sub>8</sub>O<sub>18±x</sub> and YBa<sub>2</sub>Cu<sub>3</sub>O<sub>7-d</sub>. *Mod. Phys. Lett. B.* **29**, 1550227 (2015). <https://doi.org/10.1142/S0217984915502279>

49. S.I.-F. Group, 2G HTS Wire Specification (n.d.), <https://www.superpower-inc.com/specification.aspx>
50. A. Goyal, D.P. Norton, D.M. Kroeger, D.K. Christen, M. Paranthaman, E.D. Specht, J.D. Budai, Q. He, B. Saffian, F.A. List, D.F. Lee, E. Hatfield, P.M. Martin, C.E. Klabunde, J. Mathis, C. Park, Conductors with controlled grain boundaries: an approach to the next generation, high temperature superconducting wire. *J. Mater. Res.* **12**, 2924–2940 (1997). <https://doi.org/10.1557/JMR.1997.0387>
51. G. De Marzi, L. Muzzi, P.J. Lee, Superconducting wires and cables: materials and processing, in *Reference Module in Materials Science and Materials Engineering* (Elsevier, 2016). <https://doi.org/10.1016/B978-0-12-803581-8.01917-2>
52. G. Grasso, A. Malagoli, C. Ferdeghini, S. Roncallo, V. Braccini, A.S. Siri, M.R. Cimberle, Large transport critical currents in unsintered MgB<sub>2</sub> superconducting tapes. *Appl. Phys. Lett.* **79**, 230 (2001). <https://doi.org/10.1063/1.1384905>
53. M.A. Susner, Y. Yang, M.D. Sumption, E.W. Collings, M.A. Rindfleisch, M.J. Tomsic, J.V. Marzik, Enhanced critical fields and superconducting properties of pre-doped B powder-type MgB<sub>2</sub> strands. *Supercond. Sci. Technol.* **24**, 012001 (2010). <https://doi.org/10.1088/0953-2048/24/1/012001>
54. G. Giunchi, S. Ceresara, G. Ripamonti, A. Di Zenobio, S. Rossi, S. Chiarelli, M. Spadoni, R. Wesche, P.L. Bruzzone, High performance new MgB<sub>2</sub> superconducting hollow wires. *Supercond. Sci. Technol.* **16**, 285 (2003). <https://doi.org/10.1088/0953-2048/16/2/328>
55. G.Z. Li, M.D. Sumption, M.A. Susner, Y. Yang, K.M. Reddy, M.A. Rindfleisch, M.J. Tomsic, C.J. Thong, E.W. Collings, The critical current density of advanced internal-Mg-diffusion-processed MgB<sub>2</sub> wires. *Supercond. Sci. Technol.* **25**, 115023 (2012). <https://doi.org/10.1088/0953-2048/25/11/115023>
56. A.B. Abrahamsen, N. Magnusson, B.B. Jensen, D. Liu, H. Polinder, Design of an MgB<sub>2</sub> race track coil for a wind generator pole demonstration. *J. Phys. Conf. Ser.* **507**, 032001 (2014). <https://doi.org/10.1088/1742-6596/507/3/032001>
57. A. Ballarino, Development of superconducting links for the large hadron collider machine. *Supercond. Sci. Technol.* **27**, 044024 (2014). <https://doi.org/10.1088/0953-2048/27/4/044024>
58. Y. Lvovsky, E.W. Stautner, T. Zhang, Novel technologies and configurations of superconducting magnets for MRI. *Supercond. Sci. Technol.* **26**, 093001 (2013). <https://doi.org/10.1088/0953-2048/26/9/093001>
59. Y. Kamihara, T. Watanabe, M. Hirano, H. Hosono, Iron-based layered superconductor La[O<sub>1-x</sub>F<sub>x</sub>]FeAs (x = 0.05–0.12) with T<sub>c</sub> = 26 K. *J. Am. Chem. Soc.* **130**, 3296–3297 (2008). <https://doi.org/10.1021/ja800073m>
60. Y. Ma, Progress in wire fabrication of iron-based superconductors. *Supercond. Sci. Technol.* **25**, 113001 (2012). <https://doi.org/10.1088/0953-2048/25/11/113001>
61. X. Zhang, C. Yao, H. Lin, Y. Cai, Z. Chen, J. Li, C. Dong, Q. Zhang, D. Wang, Y. Ma, H. Oguro, S. Awaji, K. Watanabe, Realization of practical level current densities in Sr<sub>0.6</sub>K<sub>0.4</sub>Fe<sub>2</sub>As<sub>2</sub> tape conductors for high-field applications. *Appl. Phys. Lett.* **104**, 202601 (2014). <https://doi.org/10.1063/1.4879557>
62. J.D. Weiss, C. Tarantini, J. Jiang, F. Kametani, A.A. Polyanskii, D.C. Larbalestier, E.E. Hellstrom, High intergrain critical current density in fine-grain (Ba<sub>0.6</sub>K<sub>0.4</sub>)Fe<sub>2</sub>As<sub>2</sub> wires and bulks. *Nat. Mater.* **11**, 682–685 (2012). <https://doi.org/10.1038/nmat3333>
63. M. Palombo, A. Malagoli, M. Pani, C. Bernini, P. Manfrinetti, A. Palenzona, M. Putti, Exploring the feasibility of Fe(Se, Te) conductors by ex-situ powder-in-tube method. *J. Appl. Phys.* **117**, 213903 (2015). <https://doi.org/10.1063/1.4921902>
64. W. Si, S.J. Han, X. Shi, S.N. Ehrlich, J. Jaroszynski, A. Goyal, Q. Li, High current superconductivity in FeSe<sub>0.5</sub>Te<sub>0.5</sub>-coated conductors at 30 tesla. *Nat. Commun.* **4**, 1347 (2013). <https://doi.org/10.1038/ncomms2337>

# Progress in Superconducting Materials for Powerful Energy Storage Systems



Essia Hannachi, Zayneb Trabelsi, and Yassine Slimani

**Abstract** With the increasing demand for energy worldwide, many scientists have devoted their research work to developing new materials that can serve as powerful energy storage systems. Thus, the number of publications focusing on this topic keeps increasing with the rise of projects and funding. Superconductor materials are being envisaged for Superconducting Magnetic Energy Storage (SMES). It is among the most important energy storage systems particularly used in applications allowing to give stability to the electrical grids. SMES is an electrical energy storage technology which can provide a concrete answer to serious problems related to the electrical cut causing a lot of damage. It features high power, strong power conversion efficiency and instant response times. It is capable to deliver a great amount of electricity in milliseconds when the electrical system fails and improve the quality of the electrical network. All these characteristics render them strong competitors in marketing, particularly with the arising and quickly upward energy storage market pushed by renewables, carbon emissions focus, smart grids, and transportation electrification. This chapter of the book reviews the progression in superconducting magnetic storage energy and covers all core concepts of SMES, including its working concept, design limitations, evolution, different types, advantages over other storage methods as well as its drawbacks, applications, potential solutions, and the future perspectives.

**Keywords** SMES system · Stored energy · Power efficiency · Superconducting coil · Mechanical limits · Quench protection

---

E. Hannachi (✉)

Department of Nuclear Medicine Research, Institute for Research and Medical Consultations (IRMC), Imam Abdulrahman Bin Faisal University, P.O. Box 1982, Dammam 31441, Saudi Arabia

e-mail: [hannechi.essia@gmail.com](mailto:hannechi.essia@gmail.com)

Z. Trabelsi

Department of Physics, Faculty of Sciences Bizerte, University of Carthage, Zarzouna, 7021 Bizerte, Tunisia

Y. Slimani

Department of Biophysics, Institute for Research and Medical Consultations (IRMC), Imam Abdulrahman Bin Faisal University, P.O. Box 1982, Dammam 31441, Saudi Arabia

e-mail: [yaslimani@iau.edu.sa](mailto:yaslimani@iau.edu.sa); [slimaniyassine18@gmail.com](mailto:slimaniyassine18@gmail.com)

## 1 Introduction

Global electricity consumption has known an abundantly increase, propelled by technological progress and stable global economic growth, pushed by technological progress and steady global economic evolution. As stated by to the latest evaluation of global energy demand by the International Energy Agency (IEA), the demand of global energy is set to rise by 4.6% in 2021 [1]. Nearly 70% of the expected increase in global energy demand is in the markets. Emerging and developing economies, where demand is expected to rise to 3.4% above 2019 levels. A device that can store electrical energy and able to use it later when required is called an “energy storage system”. There are various energy storage technologies based on their composition materials and formation like thermal energy storage, electrostatic energy storage, and magnetic energy storage [2]. According to the above-mentioned statistics and the proliferation of applications requiring electricity alongside the growing need for grid stability, SMES has a role to play. This system is among the most important technology that can store energy through the flowing a current in a superconducting coil without resistive losses. The energy is then stored in act direct current (DC) electricity form which is a source of a DC magnetic field. The conductor operates to carry current at extremely cold temperatures where it features a superconducting state and therefore has virtually no loss in resistance since it generates the magnetic field. Niobium–titanium (NbTi) alloys, that operate at liquid helium temperatures (2–4 K), are the most exploited for storage. The use of superconductors with higher critical temperatures (e.g., 60–70 K) needs more investigation and advancement. Today’s total cooling and superconducting technology defines and builds the components of an SMES device. The integrated module seems to be feasible for certain utility applications at a cost competitive with other technologies. SMES is the sole technology based on superconductivity appropriate to electrical utilities that is commercially available today [3]. Compared to others energy storage energy, SMES have different advantages: (i) high cyclic productivity, (ii) quick response time (few milliseconds) i.e. SMES possesses direct electrical power conversion (over 95%), whereas the other different energy storage systems include electrical–mechanical conversion or electrical-chemical conversion, which is very slow. (iii) Inherent recharge and discharge capacity-contrasting to batteries, SMES could recharge and discharge absolutely for an unrestricted number of times [4]. Nevertheless, the SMES system is not free from ingrained drawbacks such as weak volumetric and gravitational energy density, physical fatigue, and high cost. Due to its great efficiency and extremely low response time, the SMES systems has strong potential in diverse applications. This makes them very attractive and are of primary interest to a large number of researchers seeking to develop these systems and overcome the problems they encounter.

This chapter book provides the basic operation of SMES emphasizing their exceptional characteristics, related to its energy production, that are valuable to powerful energy storage. Advances so far in several SMES have also been described. The challenge of these systems and future perspectives have also reviewed.

## 2 Operation Concept of Superconducting Magnetic Energy Storage System (SMES)

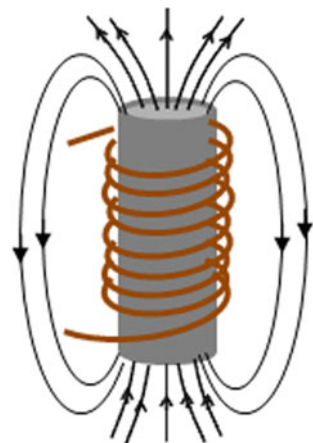
### 2.1 General Description

SMES systems store electrical energy directly within a magnetic field without the need to mechanical or chemical conversion [5]. In such device, a flow of direct DC is produced in superconducting coils, that show no resistance to the flow of current [6] and will create a magnetic field where electrical energy will be stored. Therefore, the core of SMES consists of the superconducting magnet, which should meet certain exigencies like a poor stray field and a suitable mechanical conception to sustain the large Lorentz forces. A schematic drawing of a typical superconducting magnet is given in Fig. 1 in which a current flow through a closed-circuit coil. The working principle of SMES is that when a DC voltage is exerted through the terminals of the coil, the energy will be stored. The current in the coil will peruse to circulate even after the voltage source is eliminated. This is in fact due to the prior cooling of the superconducting coil to a temperature under its critical superconductivity temperature allowing the coil to have no resistance [7]. Thus, when the electrical energy will pass through the cable surrounding the coil. The latter will not undergo any resistance and therefore will not heat up, which will allow energy not to be lost and will be stored by the magnetic field generated by its inherent current. The total energy coupled to the magnetic field is then written as follows [8]:

$$E = \int_{\tau_{\infty}} \frac{B^2}{2\mu_0} d\tau \tag{1}$$

where  $B$  represents the magnetic flux density and  $\tau_{\infty}$  denotes the infinite space.

**Fig. 1** Storing energy in magnetic form in a short-circuited superconducting winding



Over a medium of huge magnetic fields, the integral can be limited without causing a significant error. When the coil is in its superconducting state, no resistance is observed which allow to create a short circuit at its terminals. Thus, the indefinitely storage of the magnetic energy is possible as no decay of the current takes place. As another option, if the terminals are linked through a weak resistance contact, a quite dissipation will be occurred, and the energy can be stored for long periods of time.

To avoid energy losses, superconducting materials, such as the cheapest Niobium-Titanium alloy, are used for the cables surrounding the coil [9]. The energy stored in DC can be subsequently transformed into alternating current (AC) and delivered to the electrical network by discharging the coil. Such transformation will be done through the use of a power converter module [9]. SMES can go from full charged state to full discharge state very quickly and back, because the efficiency of SMES is ultrahigh compared to normal coils. In general, SMES has a very fast self-discharge due to self-cooling by the coolant liquid. Among the most important characteristics of this system, we cite [7, 9, 10]: a power density of 4000 W/L, a discharge in less than 1 min, the cycle efficiency of its charges/discharges is between 95 and 98%, a lifetime of more than 30 years, an energy storage efficiency over 97% and a high discharge rate around 10–15%.

Figure 2 illustrates the general components of SMES. It mainly involves three main components: (1) a low-temperature/high-temperature superconducting coil magnet which will be cooled by a cryostat to a temperature under its critical superconducting temperature. (2) a cryogenic refrigerator; here liquid helium at 4.2 K ( $-268.95\text{ }^{\circ}\text{C}$ ) or super fluid Helium at 1.8 K ( $-271.35\text{ }^{\circ}\text{C}$ ) will generally be used to cool the system

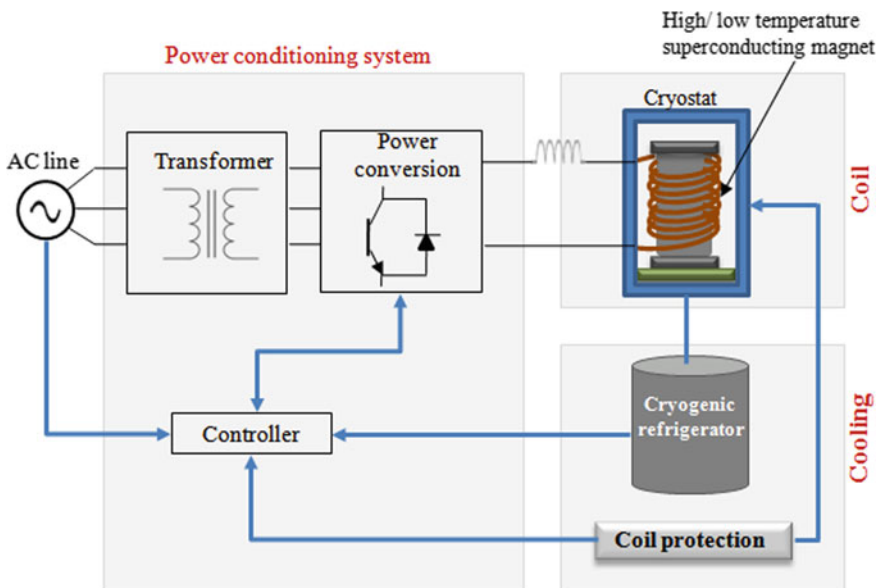


Fig. 2 Basic components of an SMES system



and (3) a driving circuit that will ensure the DC–AC conversion and vice versa. A control system is also introduced in order to regulate the energy exchanges between the electricity network and the SMES and therefore ensures the stability and fluidity of exchanges. Superconducting coil magnet and coolant are serving for storing the energy. While the driving circuit is employed for removing the power from SMES.

## 2.2 Superconducting Coils

Superconducting coil is the core of any SMES. It is composed of several superconducting wire/tape windings. This is done by employing diverse superconducting materials arranged in thin wires. To provide better strength and protection against quenches, a matrix of Cu, Al or Ag alloys is used. Instead of normal coils, it significantly lessens the energy desirable for the production of a magnetic field. Rarely is additional power from externally sources needed to preserve current in such coils for an extended period of time. All one has to do is compensate for the negligible power losses in the resistive busbars and transferring devices connected in series with the coils and in the contacts links. Power build-up continues before the trial campaign and power extraction from the coils after the campaign is completed for an extended period of time which essentially makes it possible to reduce the power of the power supply, i.e., AC/DC converter. This one provides the current increment and decrement of files according to a specific program and its stability at a specific level. Protecting the coil in the local transition from the superconducting state to the normal state (quench) is actually the major challenge in designing a superconducting coil power supply system. This will be shown in detail below in the following subsections. Generally, in the superconducting coils, there exists a ferromagnetic core that promotes the energy storage capacity of SMES due to its ability to store, at low current density, a massive amount of energy. For elevated gain the core configuration is “closed core (CC)”. The configuration of (CC) lodges the volume both outside and inside the coil. This layout avoids the leakage of the flux. For rendering the leakage trivial, the novel modified configuration of CC is “pot core (PC)”. In PC configuration, the cross-sectional area lengthways the flux line or a flux path is maintained invariable, so that the flux leakage from the core is minimal.

Since the superconducting coil is the main component of a SMES system, the maximum stored energy is affected by three main factors: (i) the size and the shape of the coil; the stored energy amount increases while increasing the size of the coil, (ii) the characteristics of the conductor, that define the maximum current and (iii) the mechanical structure.

### 2.2.1 Superconducting Coil Design for SMES

Overall, the design of the superconducting coil is directed towards specific goals. This element must minimize the amount of superconducting material, provide a

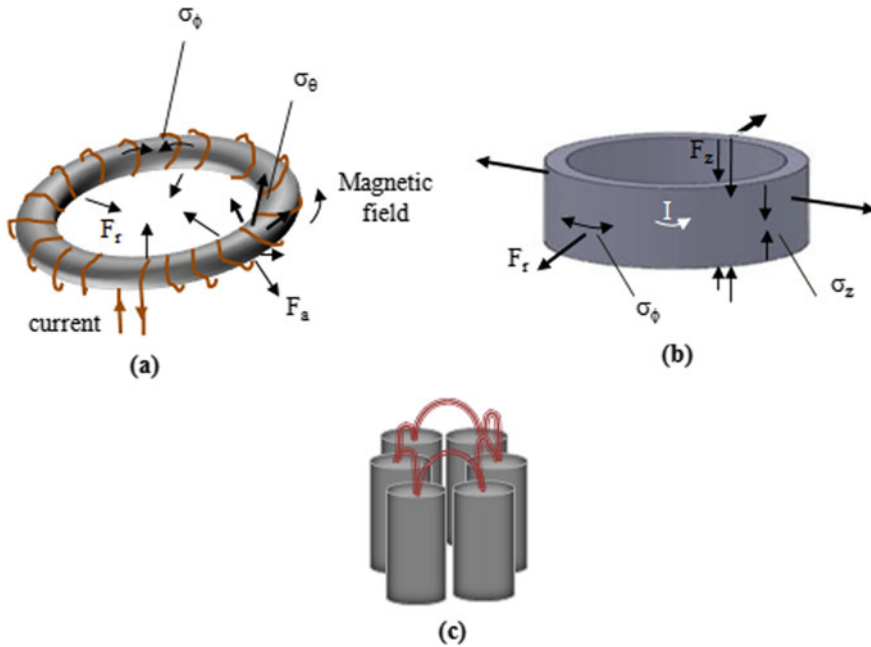


**Fig. 3** Toroidal (a) and solenoidal (b) topologies with generated stresses. c schematic illustration of hexagonal arrangement

rigid platform for electromagnetic forces, and ensure good cooling. In this design, the magnet must be well protected against quenches which should be avoided as much as possible. There are two recognized topologies of the superconducting coil: the solenoid and the toroid. Superconducting windings generally consist of assembled modular elements. If these modules are flat, they are called pancakes. As shown in Fig. 3a, b, two different configurations are possible: solenoid if these pancakes are stacked or toroid if they are spaced at a regular angle. The solenoid shape consists of linearly stacked pancake coils in which electromagnetic forces are easier to manipulate compared to in a toroid that is subjected to additional radial forces. Solenoid design can store higher energy, but a stray field can be induced outside the cryostat yielding to adverse effects on the environment. Such an unwanted field is very limited in case of toroid shape since the perpendicular component of the magnetic field is reduced hence the AC current is lowered. However, it stores only approximately 1/2 of the energy that can be stored by the solenoid. In general, the presence of a such field requires a very large active shielding and therefore greater amounts of superconductor.

It has been shown that a hexagonal arrangement of solenoids, as illustrated in Fig. 3c, helps in minimizing the induced stray fields appreciably [11]. This topology is advantageous by its modular conception with elemental solenoid which optimize the energy per unit conductor volume with a diameter to height ratio of 5. For small

dimensions and if the shielding is not taken into consideration, the solenoid is more adopted due to its cost effectiveness since it is simpler to manufacture, uses a smaller amount of superconducting material and allows easier processing of the electromagnetic stress [12, 13]. It has been proven that; a thin solenoid coil is found to be a relevant shape for energy storage [14].

However, in the case of large dimensions, the toroidal shape is more desired for two reasons: (i) they have the possibility of being built in parts in the form of small modules which will subsequently be easily and directly assembled in the land, (ii) this design can reduce the external magnetic forces and hence the dimensions of the mechanical structure. In fact, a great size of SMES leads to an increase in mechanical forces. The toroidal form is also given preference whenever second generation HTS or anisotropic superconductor such as YBCO are considered [14, 15]. Indeed, if a solenoidal coil is used in such a case, a significant radial component is generated on the conductor thus causing a remarkable degradation of the quality of the wire. Thus, the choice of the coil shape is strongly related to the used superconducting material, the size and power of the device to be manufactured, the generated electromagnetic constraints and the cost. We note that there are other coil designs that are envisioned for SMES such as dipoles, tilted toroidal coil, bunch of solenoids, etc. Although these topologies are complex and difficult to achieve, they are interesting and offer relevant solutions for certain problems. For instance, Tilted Toroidal Coils, Force Balanced Coils and Stress Balanced Coils have been applied for large scale applications and they showed satisfactory results.

### 2.2.2 Conductor Characteristics

The magnetic conductor used in SMES systems has to meet certain requirements [16]. It must mainly withstand stresses and strains without losing their superconducting properties, be cheap, operate at a temperature as high as possible and exhibit elevated engineering critical current density in high magnetic field. Beside the appropriate superconducting section that the conductor must have, it must include a sufficient quantity of stabilizing material in order to protect itself well from quenches and to provide adequate mechanical resistance. In addition, a very low AC loss is also required. This can be achieved using low AC loss conductors in which the conductor filaments must be surrounded by resistive barrier. Since the magnetic field shows a linear trend with the total current per unit length, a reduced mass of conductor that operates with substantially high current density or vice versa (i.e., large mass and reduced current density) can generate the desired high magnetic field. From a practical point of view, this field must be of the order of several Tesla to provide volume energy densities suitable for SMES. Due to these strong magnetic fields, the conductor must withstand the stress distribution caused by the presence of large Lorentz forces in the coil.

Until now, the NbTi conductors are the most used for the SMES since they meet all the requirements except for the operating temperature which is very low requiring cryogenics with liquid helium. This process remains costly in terms of investment

and operating cost. The progressive advances in large cryocoolers aim to reduce the electrical refrigeration load and extend the maintenance cycle. Another improvement is to introduce HTS conductors. The cooling process of these materials can be done using liquid nitrogen near to its boiling temperature of 77 K which can significantly reduce losses as well as the quantity of energy input needed for refrigeration hence the cryogenic operating cost. If such high operating temperature are considered, high voltage protection can be provided by using thicker electric insulation. This must be optimized while keeping the temperature difference between the conductor and the coolant low.

### 2.2.3 Mechanical Structure

Good mechanical design is a major key to have better performance of SMES systems. It is admitted that the maximum energy stored by a superconducting magnet is restricted by the strength of the mechanical structure (see Sect. 3.3). In order to contain the Lorentz forces causing significant stresses, it is essential to consider a vigorous structure. For this purpose, two techniques are envisioned. The first is to bury the magnet system in the ground. Thus, the rocks and the reinforcements will withstand all the efforts. In this case a rigid infrastructure is required. In the second technique, the magnet will support the forces via its cold structure. The support material may be a glass fiber reinforced epoxy that fits with cryogenic. The second method is widely used for SMES systems reaching an energy of the order of GJ. It appears to be a more economical technique.

## 2.3 Cryogenic Refrigerator

The temperature of the superconducting SMES coil should be kept low enough to maintain a superconducting state without any loss. A Cryogenic refrigerator is therefore indispensable. It contains compressor, cryostat, coolant, vacuum, enclosures, etc. Energy cannot be stored in a normal conductor because of the small resistance nature of the conductor. This resistance can be eliminated from the conductor by lowering its temperature. For this reason, coolant is used in the SMES system. On the basis of the coolant, SMES are subdivided into two sets. High Temperature (HTS) and Low Temperature (LTS) Superconductors. HTS are cooled at liquid nitrogen (LN<sub>2</sub>) temperature of 77 K while LTS is generally cooled using liquid helium (LHe) at 4.2 K. As LN<sub>2</sub> is lower priced than LHe, so now all commercial SMES used currently LN<sub>2</sub> as a coolant. Also, LN<sub>2</sub> is higher operational temperature with supreme cooling effectiveness [17]. The current flowing in the coil is directly dependent on the coolant, and the power of cooling is proportionate to the operating temperature  $T$  and the room temperature  $T_{room}$  as  $T/(T_{room} - T)$ . The productivity of SMES directly depends on the accuracy and performance of the used coolant [18].

The maximum energy stored in the SMES is [19]:

$$E_{max} = \frac{1}{2}LI^2 = \frac{1}{2}NB_{sat}IS \tag{2}$$

in which  $L$  represents the inductance,  $I$  is the current flowing in the coil,  $N$  denotes the number of turns,  $S$  is the coil section and  $B$  the magnetic field. Based to (Eq. 2) the stored energy caused by ferromagnetic core is directly proportional to the induction of the coil and core.

### 2.4 Driving Circuit

The SMES also contains a protection system, which serves to shield the superconductor from damage, that may occur because of abrupt quench [20]. Figure 4 illustrates the equivalent electrical circuit of the SMES system. The main components of the SMES are transformer (converter), inverter, two DC connection capacitor, four switches and one varistor.

The transformer delivers DC power to charge the SMES, and the switches define the charging and discharging situations. SMES is being charged once switching Sw1 and Sw4 are shut and Sw2, Sw3 are unlocked. While during the discharging, Sw2 and Sw3 are locked whereas Sw1 and Sw4 are unlocked. The double DC link capacitors are intended for redressing at the output and input side. The varistor is used for overvoltage protection in SMES. The inverter is employed to supply power to the AC load [21, 22]. In this entire assembly the losses of power are within the transformer and switches, as all the settings are operating at extremely low temperature, so the resistance characteristic of the switches and transformer is lower than the normal value and the power loss is much less compared to normal operation.

As mentioned above by (Eq. 2), the maximum energy  $E_{max}$  is proportionate to the saturated magnetic field  $B_{sat}$ . The magnetic field strength and the proficiency of the superconducting coil depend on the quality factor  $Q$  that is expressed as follows:

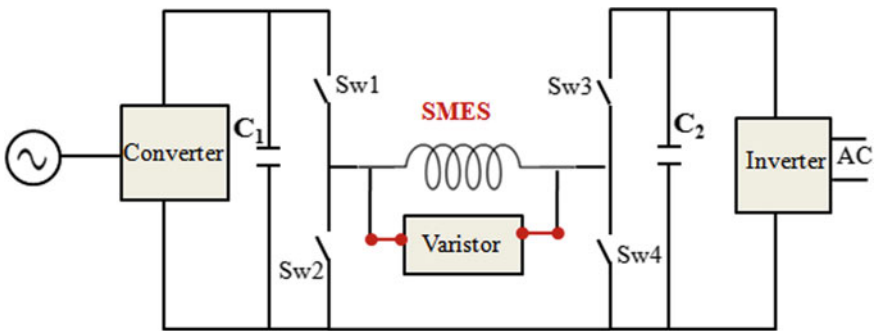


Fig. 4 Electric circuit of SMES

$$Q = 5 \times 10^3 \left( \frac{E_{max}}{B_{max}} \right)^{0.33} \times \frac{1}{\left\{ \left( \frac{r}{a} - 1 \right) \left[ \frac{r}{a} - \left( \frac{r^2}{a^2} - 1 \right)^{0.5} \right]^2 \right\}^{1/3}} \quad (3)$$

$a$  and  $r$  denoted the minor and the major radius of the coil, respectively, and  $B_{max}$  is the maximum magnetic field. To avoid normal phase spread, which can drive an arc accident, the stored energy must be rapidly eliminated from the coils.

The power discharge time is specified in order to protect the error coil partition. Nevertheless, voltage reinforcement is necessary when the discharge time is very short. The current flowing throughout the coil can be rapidly minimized by introducing a discharge resistor in the circuit. It is firstly connected with the coil in series mode, whereas in normal functioning mode it is bypassed by a circuit breaker (CB). The protection signal renders the contacts of CB open, inserting a resistor into the circuit. The constant time is dependent on the inductance of the coil and the active resistance of the discharge resistor. More details on superconducting coil power supply system were given in Ref. [23].

## 2.5 Thermal Design and Protection

When designing a coil for SMES, the temperature should be assumed to be uniform and fixed. In practice, heat loss can be caused in several ways, reason for which the coil cannot be ideally protected. These losses can come from the radiation of the external surface of the cryostat, from the conduction across the mechanical support of the coil and from the current wires which are used for the electrical connection. On the other hand, losses by Joule effect can be created by the superconducting connection wires. The superconducting coil in turn generates operating heat when the conductor gets very close to its critical current. Thus, the design of the thermal system must meet two important criteria: a sufficiently low coil temperature, and a uniform and stable operating temperature.

On the other hand, a sudden extinction due to unexpected events must be taken into account. Passive or active protection of the coil against quenches is then necessary. The device must be equipped with a quench detection system.

### 2.5.1 LTS Magnet

Heat dissipation in LTS magnets is almost zero until transition. However, the specific heat of these materials at a very low temperature of around 4.2 K is highly inferior to at room temperature. Thus, the thermal inertia (the resistance of the material to the change of temperature when a disturbance of its thermal equilibrium occurs) is low and a quench can occur even following a small event (cosmic ray, vibration, etc.). To

increase thermal inertia, a significant amount of conductive material such as copper alloys must be incorporated into LTS wires. This can ensure reliable operation with stable temperature.

LTS coils can provide intrinsic protection against quenches [24]. Indeed, because the thermal conductivity is excellent, the coil limits the temperature gradient in the conductor. In addition, the low thermal inertia favors a massive extinction of the coil, and the dissipation of the stored energy will take place throughout the volume of the coil. Thus, just a small rise in the average temperature is reported. However, the design constraints alongside to the giant size of the system make this intrinsic protection more difficult [25].

### 2.5.2 HTS Magnet

Unlike LTS magnets, dissipation in HTS magnets is not negligible and must be taken into consideration during design. If the cooling system cannot absorb these heat flows, the temperature will gradually increase, and the heat dissipation will slowly develop. This has the effect of causing a slow thermal runaway. Since the operating temperature is higher than for LTS, the temperature stability problem is more manageable. Indeed, in these materials the low thermal inertia does not cause a problem because the transition is not rigid and small events can be sustained.

In HTS magnets, the specific heat is high, and its propagation is very slow on the order of a few centimeters per second [26]. Heat dissipation will then take place in very limited volumes called hot spots. High mechanical stresses and strains can be generated in hot spots due to thermal expansion and the superconducting signature can be lost at very high temperature. Thus, protection against quenches for these HTS magnets is a major issue [27, 28] and active protection is required to reduce the maximum temperature of hot spots.

Two classic routes of active protection are considered [16]. The first is to avoid the creation of hot spots. To do this, the conductor must be heated at the start of a quench in order to promote dissipation of the energy stored over the entire volume of the coil. This method requires reinforcement by heating elements which must be in good thermal contact with the winding and having sufficient heating power which ensures rapid and uniform temperature growth. The second method consists of dissipation of the stored energy in an external load. In this case, the magnet must be discharged as soon as a quench occurs which requires a rapid discharge as well as a high discharge voltage.

## 2.6 *Summary of the Main SMES Design Criteria*

When designing an SMES system, the superconducting coil structure must have the best performance depending on the application for which the SMES will be used. The general objective, apart from the minimization of the production cost

and the maximization of the discharge speed etc., is to abase the losses over the charges/discharges of the system.

The first step is to design a system so that the volume density of stored energy is maximum. A configuration for which the magnetic field inside the system is at all points as close as possible to its maximum value is then required. This value will be determined by the currents circulating in the superconducting materials.

Afterwards, the amount of superconductor to be used should be minimized as much as possible. This is imposed by the problem of the relatively high cost of superconducting materials compared to conventional copper conductors. It is advisable to carefully choose the superconductor to be used, ensuring the correct functioning of the system and minimizing the manufacturing costs. Looking for a favorable material by taking into account its cost, performance, manufacturing complication and accuracy remains a key challenge in the conception of SMES systems and it strongly related to the application features.

The last condition is to minimize as much as possible the electromagnetic pollution of the surrounding space caused by the system. Indeed, during the charges and discharges of the system, the variation of the induction will induce losses by eddy currents in the surrounding metal parts as well as losses in the cryostat. In addition, with the increasing requirements in terms of electromagnetic compatibility between the various devices, the minimization of magnetic leakage fields is today a key point in the design of SMES.

### 3 Fundamentals of SMES

#### 3.1 Stored Energy

Biot-Savart's law postulates that an electric current flowing through a wire induces a magnetic field. The magnetic energy  $E_{mag}$  of a circuit is given by the following relation:

$$E_{mag} = \frac{1}{2} \iiint_{space} BH dx dy dz \quad (4)$$

where  $B$  is the magnetic flux density and  $H$  represents the magnetic field. A simplification of Eq. (4) is given by:

$$E_{mag} = \frac{1}{2} \iiint_{space} \frac{B^2}{\mu_0 \mu_r} dx dy dz \quad (5)$$



with  $\mu_0$  is the vacuum permeability,  $\mu_r$  is the relative permeability. Equation (5) can be interpreted as follow:

- The confinement of the magnetic field in a restricted volume (with the aim of limiting electromagnetic pollution for example) causes a decrease in the energy storage capacity since the integration is done over the entire volume.
- Generally, the energy is stored in the media for which  $\mu_r$  is minimal. The use of magnetic materials does not bring improvement in the energy storage capacity, especially with their heavy mass.

It then turns out to be more adequate to analyze the energy storage in terms of inductance  $L$  which defines a coil. The stored energy can be written in terms of the current  $I$  and the inductance  $L$  as follows:

$$E_{mag} = \frac{1}{2}LI^2 \quad (6)$$

Noting that relation of Eq. (6) highlights the similarities with energy storage in capacitors defined by

$$E_{cap} = \frac{1}{2}CV^2 \quad (7)$$

where  $C$  and  $V$  denote the capacity the voltage, respectively. SMES and capacitors are the only energy storage technologies that can power an electrical circuit without resorting to energy conversion.

By relying on the first approximation of a superconducting winding which considers the material as purely inductive, the relation between the voltage of the circuit  $U$  and the inductance  $L$  will be given by the relation which follows:

$$U = L \frac{dI}{dt} \quad (8)$$

### 3.2 Relation Between Nominal Current and Inductance

For a winding with homogeneous current density  $J$ , the distribution of the magnetic field and consequently the stored energy are independent of the turns number and of the conductor section chosen for the winding. On the other hand, they depend on the value of  $J$  and on the geometry of the windings. For further explanation, let's take two windings having a 10 by 1 cm cross section, the first consists of 1 by 1 cm square conductor with 10 turns and the second is made of 1000 turns of 1 by 1 mm square conductor. These two windings have the same total magnetic energy and the same value of  $J$ , but they have different inductances and nominal

currents. According to Eq. (6) and for a given energy, the inductance undergoes an evolution inversely proportional to the square of the nominal current. To protect a superconducting magnet during sudden extinction, rapid discharge is required. Thus, an adequate choice of the rated current must be taken into consideration to provide such a discharge. The voltage across a superconducting magnet, considered as a perfect inductance, is given by Eq. (8). From Eqs. (5) and (8), it is apparent that a faster discharge of the magnet can be obtained if its rated current is higher, or in other words its inductance is lower. However, achieving a high current source remains difficult.

### 3.3 Mechanical Constraints

Any portion of a conductor of length  $dl$ , which transports a current  $I$  and subjected to a magnetic field  $B$ , is then subjected to a Laplace force  $\vec{F}_L$  (see Eq. (9)); whose volume density in a winding is defined by the vector product of the current density  $J$  and the local field  $B$  as expressed by Eq. (10).

$$d\vec{F}_L = I d\vec{l} \wedge \vec{B} \quad (9)$$

$$\frac{d\vec{F}_L}{dV} = \vec{J} \wedge \vec{B} \quad (10)$$

The conductor must then be able to withstand these forces induced by the magnetic flux. By relying on the fact that the Laplace force is zero if the magnetic flux density and the circulating current are oriented in the same direction, it is convenient to create coils without force, thus avoiding the problem of mechanical structure. To achieve this, a well-suited geometry of the coil must be taken into consideration.

#### 3.3.1 The Virial Theorem

A system that induces a magnetic field is necessarily subjected to mechanical stresses. The virial law can govern the maximum energy density in an SMES system from a mechanical point of view. From this theorem, a theoretical determination of the minimum amount of material needed for storing a given energy is possible. The Lorentz force, created in a magnet following the interaction between the operating current and the magnetic field, will produce a tensile stress on the conductor. The stress present in the body of a non-ferromagnetic system and the energy stored within it are related by the following relation [19, 29]:

$$\int_{Body} Tr(T_\sigma) dV = \int_{space} \frac{B^2}{2\mu_0} dV = E_{mag} \quad (11)$$

with  $Tr(T_\sigma)$  is the trace of the stress tensor. It is clear that the magnetic energy stored by the system and the integral of the stress on its body are proportional. This equation needs to have a more simplified form to understand its physical meaning. Therefore, the new equation can be established by considering that the absolute value of the stress is equal to  $\sigma$  and by neglecting the components of compression and tension of the stress tensor. Equation (11) is then rewritten as:

$$\sigma(V_T - V_C) = E_{mag} \quad (12)$$

where  $V_T$  represents the volume of the body in tension while  $V_C$  is its volume when it is in compression. Equation (12) means that the majority of the body of an energy storing system is in traction. In addition, it shows that the stress of a body with a given volume is proportional to the system energy.

Considering a hypothetical geometry in which only one tensile stress is present, the optimal energy per volume ratio is given by

$$\sigma = \frac{E}{V_{optim}} \quad (13)$$

This relation allows to estimate the absolute limit of the energy stored by an inductive storage system [19].

Let us denote by  $\rho$  the density of the system body, Eq. (12) can be written in the following form:

$$\frac{\sigma}{\rho} = \frac{E_{mag}}{M_T - M_C} \quad (14)$$

where  $M_T$  is the mass of the body in tension and  $M_C$  is its mass when it is in compression. Note that the stress distribution is affected by the topology of the system. This dependence allows to write this relation:

$$k \frac{\sigma}{\rho} = \frac{E_{mag}}{M_{total}} \quad (15)$$

where  $k$  is a positive coefficient such that  $k < 1$  and  $M_{total}$  denotes the total mass of the body. In the ideal case, where the entire body is uniformly subjected to a tensile stress equal to  $\sigma$ ,  $k$  reaches its limit called virial limit, i.e.,  $k = 1$ . According to Eq. (15) the maximum specific energy depends on three parameters: (i) the system

geometry, (ii) the maximum admissible stress and (iii) the average density of the body.

The analytical calculation of the value of  $k$  for some topologies was then possible. For example, it has been shown that  $k$  ranged from  $1/3$  for longer thin solenoids to  $1/1.62$  for very shorter thin solenoids [19, 30]. Another study on a thin-walled toroid shows that  $k$  is less than or equal to  $1/3$  [31]. From these results, a solenoid is then more suitable compared to a toroid to achieve a highly specific energy. Furthermore, a study carried out on a comparison between thick-walled and thin-walled solenoids shows that  $k$  is lower if the walls are thicker because the stress is no longer uniform in this case [30].

### 3.3.2 Mechanical Limits

According to the virial law, an important factor must be taken into account in the SMES conception which is the mechanical stability. The conductive material, the insulating materials and the mechanical support must be sufficiently resistant to the tensile stress which takes place within the magnet. Thus, the mechanical support material should be chosen with care during the winding process. As a consequence of the virial law given by (Eq. 13), optimum coil design should meet to two characteristics:

- The coil should be designed to keep the volume subjected to compressive stress to a minimum as much as possible. This comes down to the fact that energy is only actually stored by the winding sections subjected to tensile stress.
- The conductor should work as close to its mechanical limits as possible and its resistance should be extremely high. In the case of a uniform conductor, the tensile stress to which it is subjected must also be uniform. Otherwise, a reinforcement can be added.

### 3.3.3 Nature of the Stored Energy in SMES Systems

According to the virial theorem, the generated magnetic field induces a stress inside the system body. A question on the nature of the energy stored by the system (magnetic or elastic) is then asked. Since the body of a coil under tension is stiff and relying on the fact that the elastic energy stored by a system under elastic stress is inversely proportional to the stiffness of the material, the elastic energy stored by the coil is very low. Therefore, the elastic energy in the coil is insignificant in comparison with the magnetic energy.

### 3.4 Parameters Affecting SMES Technology

Power exchange between the storage system and the grid is controlled by a set of solid-state power converters (PCS). Additional processes as cooling and control are required for proper functioning of the system. It is to note that, such system is affected by some parameters ensuring its better functioning. The main ones are (i) the maximum power  $P$  or the charge–discharge rate; (ii) the number of cycles  $N$  performed during the lifetime; (iii) the system response time  $t_r$ , and (iv) the duration of the power delivery,  $\Delta t$ .

Rapid discharges cause AC losses which can cause quenches if they exceed the available cooling power. Necessarily, a minimum amount of energy  $E_m$  always have to exist in the storage device. Thus, the rated energy  $E$  is expressed by:

$$E = E_m + P \Delta t \quad (16)$$

and the storage system efficiency in one cycle is given by:

$$\eta = \frac{P \Delta t}{\frac{P \Delta t}{\eta_s \eta_c} + P_{loss} \Delta t_{loss} + P_{sup} \Delta t_{cycle}} \quad (17)$$

where  $\eta_c$  is the converters efficiency while  $\eta_s$  is the storage device round trip efficiency.  $P_{sup}$  denotes the power needed for supplied services and  $P_{loss}$  is the power loss over the idling phase.

According to this equation, supplied and idling losses must be low to provide long-term storage efficiency. On another side, this efficiency can reduce if the SMES operates with minimized input/output power during long cycles. Some solutions were then proposed to reduce these losses such as the use of cables composed by transposed conductors, optimization of the cooling system and cryostat for the reduction of eddy losses, etc.

Alongside losses, the maximum power of SMES have other limitations related to current and voltage. It is well known that the product of the maximum current of an SMES by the maximum voltage that it can withstand defines its maximum power. In an SMES, the maximum operating current is related to the design of the coil which in turn is limited by mechanical stress. On another side, the voltage imposed by the load impedance must not exceed the breakdown voltage of the insulating layers which protect the conductive parts. However, high voltage isolation complicates the coil cooling process, and, in this case, a more powerful cooling system is required. To have a high power SMES, the energy density must be low especially when operating temperatures below 50 K are considered.

Likewise, the leakage magnetic field must necessarily be reduced, especially in the case of a solenoid-shaped magnet. In the case of a toroid, the leakage field is self-constrained by the magnet. Such a field causes serious dangers both for engineers

handling and for electronic devices. SMES systems must meet safety and health regulations. An accurate calculation of the leakage field must then be provided.

## **4 Development of Superconducting Magnetic Energy Storage System (SMES)**

### **4.1 LTS Based SMES**

The first SEMS, designed in 1963, was based on a low-temperature superconducting material (LTS). At that time, this design has faced some structural complications. Indeed, this type of system is designed for an energy storage of more than 5000 MWh [32]. The coils are then so large. Thus, to provide a strong mechanical structure which can withstand giant electromagnetic forces, the use of underground rocks has been proposed. Since then, research has focused mainly on the study of design and cost analysis. The charging and discharging of LTS-SMES was first demonstrated in 1971. This gain allowed the design and development of SEMS for useful applications achieved in 1979. The SEMS system design was intended to suppress the low-frequency oscillations of the American Western Power System by Los Alamos National Laboratory (LANL) in the USA, and was first installed commercially in 1981. Subsequently, American Super Conductor (ASC) began developing and marketing various SMES for various commercial uses which led to global research to enhance SMES quality at reasonable cost. To effectively compete with the other energy storage systems (EES), SMES must be cost-effective (initial costs and lower lifetime costs). Compared to the other ESS, SMES displays high cyclic productivity exceeding 90%, high power density, rapid response time and indefinite discharging and charging cycles. SMES has been developed worldwide at three levels: small scale (kJ), medium scale (MJ) and large scale (GJ). Japan has developed numerous MJ and KJ class LTS-SMES only for voltage flabbiness and immediate voltage stability respectively [33, 34]. China also developed MJ and KJ class SMES to enhance the stability of the voltage [35–37] and energy fluctuation compensation [38, 39]. Korea developed SMES to improve the quality and the stability of the power system [40, 41] and to regulate the synchronization of smart micro power grid [5, 42]. India developed LTS-SMES. For example, the Indian Institute of Technology Kharagpur has fabricated an SMES/UPS with a capacity of 0.5 MJ, that is able to deliver few kilowatts of power for breaks of few seconds. The Variable Cyclotron Centre (VECC) in India designed 0.6 MJ SMES for the purpose of voltage compensation [43]. Other countries such as Australia, Germany and France have manufactured SMES principally for voltage stabilization and pulse energy source for sensitive load [43].

## 4.2 HTS Based SMES

The discovery, in 1986, of high-temperature superconductors (HTS) led to a main advance in SMES devices, letting the construction of magnets able to support high critical currents densities and fields, at higher operating temperatures. Thus, making these materials into practical conductors was the major goal. Since the critical transition temperatures in HTS surpass 90 K, it became possible to work SMES components at temperature range of 20–30 K, with a much wider temperature margin compared with LTS cases. To reduce the refrigeration load during operation, SMES technology has introduced HTS, mainly BSCCO and REBCO tapes. Thanks to the exceptional high field properties possessed by HTS, the capacities of SMES has greatly improved giving rise to GJ class SMES using second generation YBCO.

### 4.2.1 First-Generation (1G) HTS for SMES

The primary HTS based SMES based on projects utilized first-generation (1G) materials, consist essentially of bismuth-based superconductors, with two structures: Bi-2212 and Bi-2223. Bi-2212 is a very versatile material and have the advantage to be fabricated into wires, bulks, and rods. Round wires devoid of anisotropic features like LTS materials are also possible with Bi-2212. The first practical use of this material dates back to 1990. At that time, its current-carrying capacity was very low in an external field, reason for that it not widely exploited in HTS magnet. However, the advancement on this material in the last years make it more desired for high field magnet applications, especially SMES devices, than NbTi and Nb<sub>3</sub>Sn [44]. Bi-2223 was another kind of HTS which has been made into practically used wires. Relying on the powder-in-tube process, it has been successfully made into tapes with high aspect ratio. The disadvantage of this material over LTS and Bi-2212 is its anisotropic character which makes the design of the magnet some difficult because of the propagation of the fields in different directions. These two HTS magnets have experienced different uses for SMES. One of the first SMES (5 kJ) using BSCCO-2223 conductors was built in 1997 by American Superconductor. The solenoid shape was adopted for this magnet and the system was capable to operate at 25 K [45]. A 150 kJ SMES based on Bi-2223 bands was developed by ACCEL Instruments and supported by the German Ministry of Education and Research. This system can operate at 20 K relying on a cryostat free of cryogen. It may be used as an uninterruptible power supply and furnish a power of 20 kVA [46]. In France, the National Center for Scientific Research has developed an SMES unit using Bi-2212 wires which operates at 20 K and have the potential to store 814 kJ of energy [47]. This system has been designed to offer wide pulsed power for rail gun applications. Other SMES has been also developed like a 600 kJ SMES based on Bi-2223 conceived by the Electrical Research Institute in Korea [5] and the 1 MJ SMES Bi-2212 proposed by Chubu Electric Power Corporation [48].

### 4.2.2 Second-Generation (2G) HTS for SMES

Recently, researchers introduced the second generation (2G) HTS to improve the skills of SMES systems. These materials are rare earth element copper ReBaCuO (Re = Y, Sm, Gd). They have a multilayered structure completely different from all other superconductors. Compared with 1G HTS, the 2G materials can maintain higher critical currents in analogous external magnetic fields, thus enhancing the SMES systems quality. As the 2G HTS tape manufacturing technologies are not yet mature, a few small size units have been made including a 4 kJ YBCO magnet [49] and a 93 J GdBCO unit [50]. Concept designs for larger 2G HTS SMES modules have been suggested in many publications, ranging from a 90 kJ YBCO module to improve photoelectric transient performance [51], a 5 MJ YBCO module to compensate for voltage drop [52] and up to a 2.4 GJ toroidal YBCO module to compensate for fluctuation load [53]. Recently Japan and China have designed kJ SMES for the stabilization of the power fluctuation of micro grid and wind generator. China developed, through the National Natural Science Foundation, 100 kJ SMES with a conduction cooling system to function at 20 k to dampen the power fluctuation of a small 25 MW grid [54]. A conduction-cooled HTS hybrid magnet is developed for a 150 kJ SMES system. This system is composed by twin pancake coils using 1G BSCCO at the top and the bottom and 2G YBCO tapes at the middle part to enhance the technical functioning and cost efficiency [55]. Contrariwise, a collaboration between China Electric Power Research Institute, University of Cambridge and University of Bath allowed the design of 6 kJ SMES with BSCCO 1G coils sited in middle, and YBCO 2G coils sited in the top and the bottom sections of solenoid coil. Such arrangement allowed the passage of high operating current and dealing with high vertically magnetic field at the top and bottom parts of the solenoid [56]. The operating temperature of this system ranges between 65 and 77 K relying on subcooled liquid nitrogen and it has been proven to deliver better quality energy and dampen power oscillations in a very short period. On other side, a hybrid energy storage system has been developed with YBCO tapes based SMES combined with batteries [57]. In this structure, the batteries have the role of regulating the low frequency components and increasing their lifetime. While the SMES is used in order to compensate the high frequency fluctuations thanks to their ultra-fast response. This kind of system finds potential applications in electric vehicles and renewable energies. The design of a 60 kJ SMES using YBCO bands and its simulation for a 10 kW wave energy converter provided a remarkable increase in battery life [58, 59]. A prototype of a 2 kJ SMES-battery hybrid system is also proposed for a micro-grid use and subsequently for renewable energy integration [57].

### 4.3 $MgB_2$ Compound for SMES

$MgB_2$  compound has experienced a continuous increase in the critical current density which explains the success of devices based on  $MgB_2$  magnets of small size. It has



been used several times thanks to its critical temperature which is around 39 K. For that reason,  $MgB_2$  have also been contemplated for SMES systems which can operate at 20 K reached by the liquid hydrogen. For instance, an SMES system was developed by The High Energy Accelerator Research Organization in Japan by adopting liquid hydrogen for cryogenics [60]. It is designed to fill the electricity deficit in hospitals. Another 48GJ SMES with similar design based on  $MgB_2$  materials was also suggested by Karlsruhe Institute of Technology [61]. On the other hand, Atomura et al. [62] proposed a design of a 100 MJ  $MgB_2$  SMES in order to stabilize the fluctuations of renewable energies, namely wind turbines and photovoltaics. A hybrid energy storage system is considered in this design. It is a combination of a fuel cell electrolyzer (FC-H<sub>2</sub>-EL) and an  $MgB_2$  PME with a storage capacity of 100 MJ. This SMES is part of an advanced superconducting energy conditioning system.

## 5 Advantages and Drawbacks of SMES

Several advantages have been attributed to SMES but the most interesting one is related to the speed of operation. SMES features a high efficiency of charging and discharging (>95%) since no conversion of the electric energy from or to different forms is associated. As a consequence, a rapid response within seconds is achieved for SMES [7] making them suitable for power quality applications [63, 64]. Power is almost instantly available and extremely high output power can be provided for an extremely short delay. Compared to other energy storage systems equivalent in terms of the amount of storage like Compressed Air Energy Storage (CAES) or Pumped Storage hydropower (PHS), this short time response constitutes an excellent advantage in the event of an accidental failure of the power grid where the SMES can react more quickly. Therefore, SMES present promising alternative in case of immediate demand. This type of system can also be used to enhance the stability of the power grid. In addition, SMES results in less power loss compared to other storing systems since electric currents experience negligible resistance. Unlike batteries, this storage system based on superconducting materials is preferred for the environment because no chemical reaction is necessary and thus have little environmental impact [65]. SMES are also able to improve the capacity and performance of the transmission line thanks to their extremely high energy recovery rate and significant dynamic range. An SMES is then a real key for non-interruptible power supplies or certain FACTS (Flexible AC Transmission System) in order to improve the operation of electrical grids. It provides clear benefits in terms of productivity, lightness and congestion; it is the smallest system that has seen commercial success, especially for energy conditioning. In this context, several SMES, especially those based on conventional superconductors, have proven their efficiency and operational capabilities for powers in the megawatt range with very short duration. They are exploited as non-interruptible source for sensitive loads or to stabilize certain electrical grids. The obtained results are generally satisfactory, but the high cost of SMES as well as

the competition with other more mature technologies face the development of this system.

Economically seen, the use of low temperature (LTS) or high temperature (HTS) superconductors explains the difference in cost since the cryogenic system represents 15% of the total cost of SMES. Indeed, when the SMES was invented, the price of HTS was higher than that of LTS because technical advances in the field were not yet sufficient. But with the technical developments, research was focused on HTS technology accessible by cooling with liquid nitrogen as an alternative to the expensive liquid hydrogen. Thus, the use of HTS will reduce the refrigeration required and, consequently, the operating cost of this energy storage system [9]. However, since the costs of HTS material remain high, they cannot yet bring satisfactory reductions in the total cost of SMES and they are still far from being economically viable. For instance, when compared to the 1G HTS wire (PIT, Powder-In-Tube, using BSCCO superconductor), the cost of NbTi is more lower by approximately two orders of magnitude. Thus, HTS conductors require additional research and development. Despite of all, this does not prevent that such materials make SMES more attractive because they show a remarkable improvement in energy density with much less restrictive cryogenic conditions reaching temperatures in the order of  $-253\text{ }^{\circ}\text{C}$  [66]. Therefore, the need of cooling is the main drawback of SMES that implies permanent power consumption and high cost when LTS are used. Another limit is that high power necessarily requires relevant electrical insulation and high currents. However, the production of very high current remains difficult. Because of this disadvantage, SMES technology is currently exploited for short duration energy storage.

## 6 Comparison with Other Energy Storage Systems

Currently, there are different types of energy storage technologies (electrochemical, mechanical, thermal, magnetic) that are in serious competition. The SMES is an inductive device. We have chosen to compare this system with two other energy storage technologies: the flywheels that share it the same nature and the supercapacitors of a capacitive nature which appear to be the most competitive technology for SMES.

### 6.1 Comparison with Flywheels

The specific mass energy of the two systems, SMES and flywheel, is fundamentally limited by the virial theorem. They then have comparable specific energies. However, for the energy conversion process (from mechanical energy into electrical energy), the flywheel must be equipped with a generator whose size depends on the nominal power required. This operation is never necessary in the case of SMES because the

electric energy is directly stored in a magnetic field. In addition, the flywheel must also be fitted with a reinforced housing in order to protect the system against breakage. The large sizing of these two elements, generator, and reinforced housing, are added to the mass and to the overall system volume resulting in degraded energy and power densities. The SMES, in turn, needs a cooling system as well as a conditioning system whose dimensions are also important. Nevertheless, the SMES seems safer than a flywheel.

## 6.2 Comparison with Supercapacitors

SMES are characterized by higher specific mass and volume energy than supercapacitor banks. In the case where the thickness of the coil is neglected and the magnetic field  $B$  is assumed to be homogeneous, the volume energy  $E_v$  of an SMES system can be estimated by the following relation:

$$E_v = \frac{B^2}{2\mu_0} \quad (18)$$

From this equation, a volume specific energy of 40 MJ/m<sup>3</sup> can be achieved with a magnetic field  $B$  of 10 T. In addition, HTS conductors provide the opportunity to have magnetic fields that can reach 20 T at low temperatures which corresponds to a volume specific energy of MJ/m<sup>3</sup>. The volume specific energy of supercapacitor banks, however, is around 1 MJ/m<sup>3</sup>. It should be noted that the SMES is an inductive system whereas the high-power capacitor banks are capacitive. Thus, SMES are designated for more specific applications such as electromagnetic launchers [67]. If not, they must be equipped with a suited power conditioning system to transmit the stored energy [68].

## 6.3 Further Comparison

A detailed comparison of the three energy storage technologies through relevant metrics like response time, power density, round-trip efficiency and cost in terms of both power and energy is given in the following paragraph and recapitulated in Table 1 [57].

**Response time:** The fastest response times are attributed to SMES and supercapacitors. This is due to the fact that in these systems the stored electrical energy can be supplied directly without energy conversion. Flywheels, however, have a longer response time due to the time lost in the mechanical conversion of energy.

**Table 1** Comparison between SMES, supercapacitors and flywheels

	SMES	Supercapacitors	Flywheels
Relative response time (%)	0.1–1	0.1–1	1–10
Life time (years)	20	20	20
Self discharge (% day)	10–15	2–40	20–100
Power cost (€/kW)	100–400	100–400	100–300
Energy cost (€/kW)	700–7000	300–4000	100–3500

*Data were collected from Ref. [57]*

**Power density:** Compared to flywheels and supercapacitors, SMES have a considerably high-power density which is limited by the current flowing in the magnet as well as the voltage of the winding insulation.

**Lifetime:** The three technologies considered have practically the same lifetime. For the SMES system, there is a slight degradation of materials for each operational cycle which makes their lifetime very long.

**Round-trip efficiency:** Since the losses related to the charge/discharge process of the SMES are very low, their cyclic efficiency is the highest in comparison with the other energy storage technologies. This is because most of the losses come from semiconductor switches.

It is clear that SMES systems are endowed by rapid response time, long lifetime, large power density and high cyclic efficiency allowing them to be prime candidates for power dense applications. However, this technology appears more expensive with respect to energy when compared to flywheel and supercapacitor systems.

## 7 Challenges and Future Developments

Since the built of the 10 MVA/30 MJ Nb–Ti SMES system in 1983 whose effectiveness was confirmed by successful laboratory tests [69], a lot of other prototypes designed for power quality applications have been constructed worldwide. These systems exhibit a rated power ranging between 0.1 and 10 MW and supplied energy around 0.2–10 MJ, [70, 71]. For instance, a typical micro-SMES unit providing a storage capacity of 3 MJ (0.83 kWh) and able to deliver 3 MW of power for 1 s is commercially available today. As an advancement, these small units can be placed in a container to facilitate its deployment. They are then used in industrial operations requiring high-quality power. Another prospect in this sector is to integrate larger superconducting coils that can maintain the stability of the generation system. These new systems are expected to have outputs 10 times greater than the power supplied

by the micro-SMES [72]. Thus, the development of these large systems will compete with batteries in energy storage. The future advancement of SMES system strongly depends on the maturity of superconducting materials technology in terms of their critical temperature, prices and properties. The ultimate goal is then to discover superconductors at room temperature. Although that SMES has been found to be a promising energy storage technology offering fast response time and high efficiency, it has some disadvantages mainly related to the cryogenic technology and high cost and posing challenges to research.

### ***7.1 HTS Conductors, Cost, and Refrigeration Issue***

Despite that the development of HTS materials helped to reduce the operating cost of the cryogenic refrigerator, the cost of the SMES system does not reduce significantly since the refrigeration process is only a part of the whole arrangement. Therefore, this slight reduction is not sufficient to compete with alternative technologies. However, compared to LTS which operate at about 4 K, Carnot efficiency rises by a factor of 5.3 and 14.8 when it comes to 20 and 50 K operations respectively. Over the last decade, the research on SMES based on HTS has seen an interesting progression. SMES prototypes based on Bi-2212 and Bi-2223 conductors have been developed. They showed a rated energy of about 0.6–1.0 MJ. In this study a 4.2 K operating temperature has been chosen [71, 73]. In case of special demand, such system can be carried out with operating temperature of 20 K [74]. However, as mentioned previously, the cost of the superconductor materials constitutes a real barrier to the development of SMES based 1G HTS conductors that operate at about 20 K like Powder-In-Tube (PIT), using BISSCO superconductor. It remains also two orders of magnitude higher than the classical NbTi conductor cost. Additional efforts were devoted in order to reduce the cost in the near future by using 2G HTS wires, such as the Coated Conductor (CC) [75–77], that is expected to provide savings for SMES. These generation is estimated to operate at 50–60 K for SMES magnetic flux densities of a few Teslas. Currently, CC technology is showing rapid advancement and a CC with several hundred meters in length is available now and more of kilometers in length are in production. Research studying SMES based on YBCO-coated conductors with high field and high energy density are in progress [71, 73, 78]. Recently, a design of an SMES device with 100 MW/2GJ characteristics exploiting high-performance YBCO tape that operate at 20 K to 11 T have been established [78]. The challenge now is to achieve a SMES of 20 kW/3.2 MJ based on YBCO which operate at 4.2 K to 25 T. Other projects are focused on carrying out SMES with the  $MgB_2$  compound which is less expensive than YBCO. This system is expected to operate at 20 K relying on liquid hydrogen technology [61, 79]. Nevertheless,  $MgB_2$  have lower critical field resulting in a limited volume energy density which need larger windings and more cryogenic requirements.

In the future, additional advantages, other to those associated with cryogenics, can be reached. The high operating temperatures may bring more stability to the

HTS magnet, making it more resistant to external disturbances. Indeed, the increase in temperature causes a significant increase in specific heat. On the other hand, the high temperature causes the electrical insulation to be thicker, thus promoting an improvement in power by adopting a higher operating voltage. In addition, the allowable temperature difference between the conductor and the cold source  $\Delta T$ , mainly caused by AC losses during charges and discharges, can also be increased. This difference is related to the AC loss and the thickness of the insulation  $d_i$ , by the following relation:

$$d_i = \lambda \frac{\Delta T}{AC_{loss}} \quad (19)$$

in which  $\lambda$  is the thermal conductivity of the insulation. The problem lies in providing good protection of the magnet at high temperature. Indeed, the high temperature favors too long quench causing remarkable damage.

If the cost of the refrigeration process is eliminated by using a room temperature (or near room temperature) superconductor material, other technical challenges toward SMES must be taken into consideration.

## 7.2 Protection

A superconducting magnet enable to store a great amount of energy which can be liberated in a short duration. In addition, the power is hugely high that can reach 100 MW/kg and massive magnetic field are involved. Therefore, special precaution and an excellent isolation should be available mainly in case of a coil failure or an accidental loss of coolant. In such event, the fast release of the energy will damage the coil and the surrounding system. Assumptions have been put forward to overcome this problem which mainly consist in equipping the SMES system with a superconducting cable allowing to absorb the energy after coil failure [80].

## 7.3 Precooling Time

Because of the extremely low operating temperature of a SMES (4.2 K), superconducting magnet takes four months, until now, to be cooled from room temperature to operating temperature. Thus, after maintenance or in case of outage and even an emergency energy release, the system needs the same period of time to be recovered. This outcome is strongly linked to the improvement of the critical temperature of superconducting materials. In other words, this time problem can be solved if the design of HTS based SMES that work at temperature is successfully completed.

## 7.4 *Size and Infrastructure*

To ensure sufficient and commercially useful energy storage of about 5 GWh (3.6 TJ) (600 m), an SMES center necessarily requires a loop of about 0.5 mile to be properly installed while respecting all the requirements. This large area of land must necessarily be confined in a vacuum flask of liquid nitrogen essential for the cooling process. Thus, a very stable support must be founded by burying the installation and kept underground [63], adding to the expense of the system. This infrastructure problem will no longer be posed if superconducting materials at room temperature are involved.

## 7.5 *Challenge Related to Integration with Renewables and Hybrid EES*

It is well known that SMES systems are characterized by a strong potential allowing the support of the renewable systems integrated in distributed production grids. However, further study of the behavior of such systems in the long term is still lacking. The study of the commercial, technical, and regulatory aspects of the application of SMES is essential because it allows to better understand and develop this technology. The use of liquid hydrogen (LH<sub>2</sub>) fuel in renewable technologies would unleash the potential of SMES. Indeed, LH<sub>2</sub> storage tanks can be considered in order to maintain the SMES coils under very precise transition temperatures, which leads to a significant reduction in the operating cost and a prospect towards hybrid systems [61].

Creating hybrid EES is a key point to improve their performance and analyze the optimal operational scenario. A complete hybrid system can be created by combining an SMES with high energy density technologies as a complement (because SMES has a low energy density). The applications of this system span a wider range including shaving and voltage stability, power management and quality control [81]. This new approach has the advantage of reducing the cost of EES. For example, a hybrid ESS with an SMES and a pumped hydro energy storage brings a reduction of more than 90% in cost compared to a single SMES having the same energy storage capacity [82]. The design of these systems has already been developed and they are used in transportation to provide impulses by storing braking energy [83].

## 8 Applications of SMES

Load imbalance in electrical systems is inherent because of the random fluctuations in loads induced either by customers or by unstable production from renewable sources. This causes oscillations of frequencies which can cause serious damage in

the event of a delay in compensation. To overcome this problem, persistent and rapid control of the generated power loads is therefore essential. SMES systems represent a potential route to minimize load imbalance and ensure the efficiency of the electrical system. The customer, in turn, can benefit from appropriated power quality and power absorption smoothing of impulse loads by using SMES. Thanks to their power deliverable, energy density and efficiency, very rapid response time, and practically high/unlimited number of cycles, SMES have found a wide range of applications. These characteristics make it well appropriated for frequency regulation, power quality control, and pulsed power supply. Noting that, until now, only SMES exhibiting small storage capacities are commercially available and they found a great success. They have been in use for several years in order to enhance industrial power performance and to give a satisfactory service for individual customers exposed to voltage fluctuations. However, large-scale applications remain in the experimental phase and require large monetary investments [84].

### ***8.1 Frequency Regulation***

The net load of a power system is defined as the difference between the power absorbed by all customers and the produced power from renewable sources. This has the effect of continuously fluctuating the net load over a time scale of tens of seconds or minutes [85]. Such fluctuations, usually in order of several tens of megawatt, will disturb the frequency and therefore cause an instability of the system. SMES system can compensate the load mismatch owing its rapid response time and its great number of cycles. It provides a reliable frequency regulation as it is capable to deliver tens of megawatts with a response time in the order of seconds. Moreover, SMES is also used as spinning reserve in order to balance the frequency. Indeed, it can reserve an additional capacity which will be used in case of need, i.e., in case of electrical network failures or if a significant grid of transmission lines is out of service.

### ***8.2 Uninterruptible Power Supply (UPS)***

Unexpected voltage disturbances can take place either as prolonged and repetitive phenomena or occasionally. Certain applications such as data centers, industrial plants, etc. are unable to support voltage disturbance for more than few milliseconds, hence they need continuously available power supplies with fast response to avoid a lot of problems that can affect customers in terms of malfunctions, lack of production, or security concerns. SMES-based UPSs can provide this compensation due to their dynamic capabilities and long-term lifecycle. They have received a much interest since they can instantly provide the necessary power requested and ensure a continuous operation of systems [86]. Military and research laboratory applications as well as other applications requiring extremely clean power for sensitive



treatments have benefited greatly from these SMES-based UPS devices which are mainly provided by American Superconductor company. It reported an accumulation of more than 35 unit-years of operation.

### ***8.3 Flexible AC Transmission System (FACTS)***

FACTS is a stationary device which can be installed in the power grid in order to improve the controllability and the power transfer capability. SMES systems are widely used as FACTS devices. The first superconducting application has been implemented in 1980 by the Bonneville Power Authority in U.S.A to attenuate the low frequency [80, 87]. This device has successfully operated over a year with 1200 h of energy transfer which corresponds to  $10^6$  cycles for the magnet. In this device, the refrigerator and the power converter constitute the major problems in the operation of SMES and no other problems have been encountered at the level of the cryostat or the magnet. Thereafter, SMES systems using FACTS devices will act as a system stabilizer. For instance, six SMES-based FACTS units have been installed at different key locations in the northern Winston in 2000 to improve the stability of the electrical grid. They increased the voltage by providing reactive power in the grid. Electricity transmission capacities have also been improved by 15%. Each SME has the capacity to continuously supply 2.8 Mvar and 2 MW for a short period. Furthermore, such devices are also exploited in renewable energy technologies such as wind generator [80].

### ***8.4 Electromagnetic Launchers***

Electromagnetic launchers for military or civilian purposes, requiring pulsed energy sources, also offer other opportunities for SMES. This device is an electric weapon capable of accelerating projectiles to extremely high speeds. To benefit from a better functioning of these rockets, high power pulse sources are essential. SMES as fast releasers of stored energy with high power density provide a potential energy storage device for creating high performance electromagnetic launchers [80].

### ***8.5 Load Leveling***

The quantity of electrical energy required, whether commercially or residentially, fluctuates significantly during the day and throughout the seasons. Energy stability is determined by the difference between the amount of energy consumed and that generated. The role of the SMES system is to store energy when the power generated exceeds the demands [86, 88]. This energy will be released to compensate

for power fluctuations during high demands. In this way, conventional production units can operate more conveniently and efficiently at constant output. In the event of a persistent imbalance between supply and demand, the SMES may be totally discharged.

## ***8.6 Circuit Breaker Reclosing***

Electrical networks are generally equipped with conventional circuit breakers which are used to close and put the transmission line back into service after an accidental failure. This operation is performed whenever the power angle difference across the circuit breaker reaches a certain limit. Otherwise, i.e., the power angle difference is too great exceeding the imposed limit, the protection relays prevent the circuit breakers from reclosing. In this situation, SMES systems can intervene to diminish the power angle difference across a circuit breaker. They will provide a portion of the power normally transmitted by the transmission line allowing the circuit breaker to be reset. Rapid restoration of system power is then provided during severe transmission line failures [86, 88].

## ***8.7 Microgrid and Electrical Vehicle***

The main purpose of microgrid sources is to serve energy to rural areas. The best-known sources are fuel cell (FC), solar photovoltaic (PV) systems, wind power systems and diesel generators. However, these technologies encounter certain problems related to intermittent power outputs which generate system instability. SMES appears to be an appropriate solution to confront stability problems. The results obtained depend on the reliability of the SMES used [89]. The energy stored in the superconducting coil will be exchanged through the DC-DC converter and the DC-AC inverter. To ensure a better self-switching capacity, the SMES is connected to a voltage source converter. This technique will make it possible to reduce the disturbances affecting the micro-grid. Consequently, a microgrid benefits from an improvement in the quality of the power supply and the voltage if an SMES is associated with it [46].

Electric vehicles will be the future of the transportation area. These require significant load requirements. Indeed, load fluctuations are possible in electric vehicles caused by their sudden power load. These fluctuations, in turn, will cause harmonics in the system. Intermittent powering of photovoltaic and wind power systems makes the situation more serious if the sudden power load is connected to a microgrid. Minimizing harmonics and compensating for the difference between intermittent electricity from renewable sources and electric vehicles are therefore essential. The microgrid system with SMES works much better and allows harmonics to be reduced.

In addition, the introduction of SMES can keep the charging voltage constant and dampen the circulating currents [14].

Noting that new SMES designs such as 10 kJ class SMES, high-field HTS SMES coil or 200 kJ 2G HTS solenoidal SMES coil were recently studied [13, 90]. These new designs provide further opportunities for SMES that can be used in mitigating wind energy system fluctuations, voltage harmonics and other perspectives are offered [82, 91–93]. In China, superconducting plants have already been installed and are in operation [94]. It is expected that, in the near future, SMES will be found in space shuttles, satellite systems and also in medicine area.

## 9 Different SMES Scales: Some Examples

### 9.1 Large Scale SMES

The power scale required for an ESS to be able to balance the load in the electricity distribution grid is in the range of GW. For this reason, the SMES were not entrusted to fulfill this role. Indeed, this application requires a gigantic dimension (about 1 km in diameter) of superconducting magnets. The construction of such a magnet encounters certain problems related to the cryogenics, the mechanical structure and the quantity of the conductor to be used. The mechanical structure must be sufficiently robust so that it can withstand the weight of the magnet and the components of the large Lorentz forces: the radial component which tends to extend the coil and the axial component which is symmetric with respect to the vertical line central.

The design of a large SMES system with a capacity of 1000 MW was developed in 1987 in the United States but its construction has not been carried out until now. This SMES must meet certain specific parameters such as its size which corresponds to a diameter of 1 km and a height of 19 m. It should operate at a temperature of 1.8 K with an operating current of 200 K and a magnetic field of 5.18 T. The energy storage capacity of this system is 18.9 TJ. Further characteristics are found in [12, 95].

### 9.2 Medium Scale SMES

In 1987, a 400MWSMES program was initiated from the United States Defense Nuclear Agency (DNA). This SMES is designed for later use as a pulsed energy source for electron laser directed energy weapons. It is also intended for load leveling and stabilizing the electrical network. For this type of system, two different designs were proposed by two teams, Bechtel and Ebasco. In Bechtel's design, the magnet has a diameter of 129 m and a height of 7.5 m. It was planned to use an Nb–Ti Cable-in-Conduit Conductor (CICC) having very low losses in alternating current. This system should operate at 1.8 K at a current of 303 kA generating a magnetic

field of 5 T. The CICC conductor is designed with a Liquid Helium flow channel, so the Liquid Helium vessel is not present in this design making cryostat construction less complicated. Such high current as the proposed one can reduce the required amount of conductor and keep the working voltage stable and not exceeding the safe limit (10–12 kV).

In Ebasco's design, a 60 kA Nb–Ti conductor was considered with Al stabilization. The coil is 134 m in diameter and 4.2 m in height with a solenoidal magnet configuration. In this design, extra effort is dedicated for mechanical support, electrical insulation and quench protection by introducing fiberglass reinforced epoxy G-10CR finger plates. More information is provided in [12, 96].

### 9.3 *Micro Scale SMES*

Small-sized micro SMES have the opportunity to be constructed and even successfully used in industries having remarkable sensitivity to semiconductors and liquid crystals. Their role is to provide protection against unexpected voltage drops for high power. Since 2011, 5 and 10 MVA [34, 71] commercial SMES manufactured by Toshiba Corporation Power System Co and Chubu Electric Power Co. are operational. A four-pole solenoidal configuration is adopted for the 5 MVA SMES to reduce the leakage magnetic field. The SMES was designed with a current of 2.66 kA at a temperature of 4.2 K and a magnetic field of 5.3 T. The compensation time is 1 s. YBCO class 1 kA wires have been proposed to join the current wires in parallel. They are able to support a voltage of 6 kV. The same company also distributed SMSE 10 MVA units. Currently, a number of these units are operational in Japan.

## 10 Conclusion

Through SMES, superconductivity provides an alternative to store magnetic energy and power an electrical circuit without energy conversion. These SMES have become a realizable device thanks to approved advancements in superconducting materials and cryogenics. They are therefore considered a suitable solution for several applications as they are attractive pulse/transient power sources allowing perfect frequency control and promoting transient stability in power grids. The main advantages of SMES system consist of the rapid power response and the high power and energy density with outstanding conversion efficiency. Although their specific energy is reasonable, beyond that of the batteries, the stored energy in an SMES system can be released in an extremely short time and with negligible losses. This property is not recognized for batteries. A certain number of projects dealing with the conception of SMES used as a power source for short-term duration have demonstrated the versatile and potential applications of this device which can be found in electrical

energy and power systems as pulse power source, frequency regulator, power fluctuations stabilizer, etc. SMES can be revisited in smart grid projects, in particular for intermittency management. This is related to the advancement in HTS materials and conductor technologies which allow for more compact and robust SMES at lower costs. Further creativity and persistence would be required in the future to meet the SMES challenges.

## References

1. A. Rode, T. Carleton, M. Delgado, M. Greenstone, T. Houser, S. Hsiang, J. Yuan, Estimating a social cost of carbon for global energy consumption. *Nature* **598**(7880), 308–314 (2021). <https://doi.org/10.1038/s41586-021-03883-8>
2. Y. Balali, S. Stegen, Review of energy storage systems for vehicles based on technology, environmental impacts, and costs. *Renew. Sustain. Energy Rev.* **135**, 110185 (2021). <https://doi.org/10.1016/j.rser.2020.110185>
3. B.G. Marchionini, L. Martini, H. Ohsaki, High temperature superconductor-based technologies as enabler for efficient and resilient energy systems. *IEEE Trans. Appl. Supercond.* **29**(5), 1–5 (2019). <https://doi.org/10.1109/TASC.2019.2909735>
4. E.A. Gouda, A. Abd-Alaziz, M. El-Saadawi, Design modeling, and control of multi-stage SMES integrated with PV system. *J. Energy Storage* **29**, 101399 (2020). <https://doi.org/10.1016/j.est.2020.101399>
5. H.K. Yeom, S.J. Park, Y.J. Hong, D.Y. Koh, K.C. Seong, H.J. Kim, T.B. Seo, An experimental study of the conduction cooling system for the 600 kJ HTS SMES. *IEEE Trans. Appl. Supercond.* **18**(2), 741–744 (2008). <https://doi.org/10.1109/TASC.2008.921217>
6. X.Y. Chen, M.S. Zhang, S. Jiang, H.Y. Gou, Q. Xie, Y. Chen, R.H. Yang, An SMES-based current-fed transformerless series voltage restorer for DC-load protection. *IEEE Trans. Power Electron.* **36**(9), 9698–9703 (2021). <https://doi.org/10.1109/TPEL.2021.3058696>
7. N. Amaro, J. Murta Pina, J. Martins, J. Maria Ceballos, Superconducting magnetic energy storage: A technological contribute to smart grid concept implementation, in *Proceedings of the 1st International Conference on Smart Grids and Green IT Systems* (2012), pp. 113–120
8. P. Seidel (ed.), *Applied Superconductivity: Handbook on Devices and Applications*, vol. 12, 1st edn. (Wiley-VCH Verlag GmbH & Co. KGaA, Boschstr, Weinheim, Germany 2015), p. 69469
9. X. Luo, J. Wang, M. Dooner, J. Clarke, Overview of current development in electrical energy storage technologies and the application potential in power system operation. *Appl. Energy* **137**, 511–536 (2015). <https://doi.org/10.1016/j.apenergy.2014.09.081>
10. H. Chen, T. Ngoc Cong, W. Yang, C. Tan, Y. Li, Y. Ding, Progress in electrical energy storage system: a critical review. *Prog. Nat. Sci.* **19**, 291–312 (2009). <https://doi.org/10.1016/j.pnsc.2008.07.014>
11. W. Weck, P. Ehrhart, A. Müller, G. Reiner, Superconducting inductive pulsed power supply for electromagnetic launchers: design aspects and experimental investigation of laboratory set-up. *IEEE Trans. Magn.* **33**, 524–527 (1997). <https://doi.org/10.1109/20.560067>
12. P. Tixador, *Superconducting Magnetic Energy Storage: Status and Perspective*, *ESAS European Superconductivity NEWS FORUM*, vol. 3 (2008).
13. J.H. Kim, S. Hahn, C.H. Im, J.K. Kim, H.K. Jung, S.Y. Hahn, Design of a 200-kJ HTS SMES System. *IEEE Trans. Appl. Supercond.* **12**(1), 774–777 (2002). <https://doi.org/10.1109/TASC.2002.1018516>
14. G.V.S. Vulusala, S. Madichetty, Application of superconducting magnetic energy storage in electrical power and energy systems: a review. *Int. J. Energy Res.* (2017). <https://doi.org/10.1002/er.3773>

15. Y. Oga, S. Noguchi, M. Tsuda, Comparison of optimal configuration of SMES magnet wound with MgB2 and YBCO conductors. *IEEE Trans. Appl. Supercond.* **23**(3), 5700204 (2013). <https://doi.org/10.1109/TASC.2012.2231452>
16. A. Badel, Superconducting magnetic energy storage haute temperature critique comme source impulsionnelle. *Supraconductivité [cond-mat.supr-con]*. Institut National Polytechnique de Grenoble-INPG, (2010). Français. fftet-00654844ff
17. Y. Kanamaru, Y. Amemiya, Numerical analysis of magnetic field in superconducting magnetic energy storage. *IEEE Trans. Magn.* **27**(5), 3935–3938 (1991). <https://doi.org/10.1109/20.104964>
18. B.K. Kang, S.T. Kim, B.C. Sung, J.W. Park, A study on optimal sizing of superconducting magnetic energy storage in distribution power system. *IEEE Trans. Appl. Supercond.* **22**(3), 5701004 (2012). <https://doi.org/10.1109/TASC.2011.2174571>
19. F.C. Moon, The virial theorem and scaling laws for superconducting magnet systems. *J. Appl. Phys.* **53**(12), 9112–9121 (1982). <https://doi.org/10.1063/1.330423>
20. B.G. Marchionini, Y. Yamada, L. Martini, H. Ohsaki, High-temperature superconductivity: a roadmap for electric power sector applications, 2015–2030. *IEEE Trans. Appl. Supercond.* **27**, 0500907 (2017). <https://doi.org/10.1109/TASC.2017.2671680>
21. IEEE Task Force on Benchmark Models for Digital Simulation of FACTS and Custom-Power Controllers, T&D Committee. Detailed Modeling of Superconducting Magnetic Energy Storage (SMES) System. *IEEE Trans. Power Deliv.* **21**(2), 699–710 (2006). <https://doi.org/10.1109/TPWRD.2005.864075>
22. M.V. Aware, D. Sutanto, Improved controller for power conditioner using high-temperature superconducting magnetic energy storage (HTS-SMES). *IEEE Trans. Appl. Supercond.* **13**(1), 38–47 (2003). <https://doi.org/10.1109/tasc.2003.811352>
23. A.G. Roshal, Power supply systems, in *Fundamentals of Magnetic Thermonuclear Reactor Design* (Woodhead Publishing Series in Energy, 2018), pp. 323–349. <https://doi.org/10.1016/B978-0-08-102470-6.00011-1>
24. M.N. Wilson, *Superconducting magnets* (Clarendon Press, United Kingdom, 1983)
25. Y. Iwasa, M.W. Sinclair, Protection of large superconducting magnets: maximum permissible undetected quench voltage. *Cryogenics* **20**(12), 711–714 (1980). [https://doi.org/10.1016/0011-2275\(80\)90025-9](https://doi.org/10.1016/0011-2275(80)90025-9)
26. F. Trillaud, H. Palanki, U.P. Trociewitz, S.H. Thompson, H.W. Weijers, J. Schwartz, Normal zone propagation experiments on HTS composite conductors. *Cryogenics* **43**(3–5), 271–279 (2003). [https://doi.org/10.1016/S0011-2275\(03\)00044-4](https://doi.org/10.1016/S0011-2275(03)00044-4)
27. Y. Iwasa, HTS magnets: stability; protection; cryogenics; economics; current stability/protection activities at FBML. *Cryogenics* **43**(3–5), 303–316 (2003). [https://doi.org/10.1016/S0011-2275\(03\)00046-8](https://doi.org/10.1016/S0011-2275(03)00046-8)
28. J. Schwartz, T. Effio, X.T. Liu, Q.V. Le, A.L. Mbaruku, H.J. Schneider-Muntau, T.M. Shen, H.H. Song, U.P. Trociewitz, X.R. Wang, H.W. Weijers, High field superconducting solenoids via high temperature superconductors. *IEEE Trans. Appl. Supercond.* **18**(2), 70–81 (2008). <https://doi.org/10.1109/TASC.2008.921363>
29. J.X. Bouillard, Preliminary investigation of force-reduced superconducting magnet configurations for advanced technology applications (1992). <https://doi.org/10.2172/10130232>
30. I.N. Sviatoslavsky, W.C. Young, Structural design features for commercial fusion power reactor magnet systems. *Nuclear Eng. Des.* **58**(2), 207–218 (1980). [https://doi.org/10.1016/0029-5493\(80\)90124-7](https://doi.org/10.1016/0029-5493(80)90124-7)
31. Y. Eyssa, R. Boom, Considerations of a large force balanced magnetic energy storage system. *IEEE Trans. Magn.* **17**(1), 460–462 (1981). <https://doi.org/10.1109/tmag.1981.1061108>
32. R.J. Loyd, G.F. Moyer, J.R. Purcell, J. Alcom, Conceptual design and cost of superconducting magnetic energy storage plant. EPRI Report, EM-3457 (1984)
33. A. Kawagoe, S. Tsukuda, F. Sumiyoshi, T. Mito, H. Chikaraishi, T. Baba, M. Iwakuma, AC losses in a conduction-cooled LTS pulse coil with stored energy of 1 MJ for UPS-SMES as protection from momentary voltage drops. *IEEE Trans. Appl. Supercond.* **18**(2), 783–786 (2008). <https://doi.org/10.1109/TASC.2008.921301>

34. S. Nagaya, N. Hirano, M. Kondo, T. Tanaka, H. Nakabayashi, K. Shikimachi, S. Kawashima, Development and performance results of 5 MVA SMES for bridging instantaneous voltage dips. *IEEE Trans. Appl. Supercond.* **14**(2), 699–704 (2004). <https://doi.org/10.1109/TASC.2004.830076>
35. X.G. Zhu, X.H. Jiang, 150 kVA/0.3 MJ current source type dynamic voltage compensation device. *Power Electron. Technol.* **41**(1), 1–3 (2007)
36. J. Shi, Y. Tang, Y. Zhou, J. Chen, D. Xu, H. Wang, S. Cheng, Development of a conduction-cooled HTS SMES. *IEEE Trans. Appl. Supercond.* **17**(3), 3846–3852 (2007). <https://doi.org/10.1109/TASC.2007.902120>
37. Q. Wang, Y. Dai, S. Song, H. Wen, Y. Bai, L. Yan, K. Kim, A 30 kJ Bi2223 high temperature superconducting magnet for SMES with solid-nitrogen protection. *IEEE Trans. Appl. Supercond.* **18**(2), 754–757 (2008). <https://doi.org/10.1109/TASC.2008.922273>
38. S. Dai, L. Xiao, Z. Wang, J. Zhang, D. Zhang, D. Hui, L. Lin, Design of a 1 MJ/0.5 MVA HTS magnet for SMES. *IEEE Trans. Appl. Supercond.* **17**(2), 1977–1980 (2007). <https://doi.org/10.1109/TASC.2007.899194>
39. L. Xiao, Z. Wang, S. Dai, J. Zhang, D. Zhang, Z. Gao, L. Lin, Fabrication and tests of a 1 MJ HTS magnet for SMES. *IEEE Trans. Appl. Supercond.* **18**(2), 770–773 (2008). <https://doi.org/10.1109/TASC.2008.922234>
40. S. Kwak, S. Lee, S. Lee, W.S. Kim, J.K. Lee, C. Park, S.Y. Hahn, Design of HTS magnets for a 2.5 MJ SMES. *IEEE Trans. Appl. Supercond.* **19**(3), 1985–1988 (2009)
41. J.H. Choi, H.G. Cheon, J.W. Choi, H.J. Kim, K.C. Seong, S.H. Kim, A study on basic insulation characteristics of 2.5 MJ class conduction-cooled HTS SMES. *IEEE Trans. Appl. Supercond.* **20**(3), 1344–1347 (2010). <https://doi.org/10.1109/TASC.2010.2042158>
42. W.S. Kim, S.Y. Kwak, J.K. Lee, K.D. Choi, H.K. Jung, K.C. Seong, S.Y. Hahn, Design of HTS magnets for a 600 kJ SMES. *IEEE Trans. Appl. Supercond.* **16**(2), 620–623 (2006). <https://doi.org/10.1109/TASC.2005.864244>
43. P. Mukherjee, V.V. Rao, Design and development of high temperature superconducting magnetic energy storage for power applications—a review. *Physica C Supercond. Appl.* **563**, 67–73 (2019). <https://doi.org/10.1016/j.physc.2019.05.001>
44. D.C. Larbalestier, J. Jiang, U.P. Trociewitz, F. Kametani, C. Scheuerlein, M. Dalban-Canassy, M. Matras, P. Chen, N.C. Craig, P.J. Lee, E.E. Hellstrom, Isotropic round-wire multiilament cuprate superconductor for generation of magnetic fields above 30 T. *Nat. Mater.* **13**, 375–381 (2013). <https://doi.org/10.1038/nmat3887>
45. S.S. Kalsi, D. Aized, B. Conner, G. Snitchier, J. Campbell, R.E. Schwall, J. Kellers, T. Stephanblome, A. Tromm, P. Win, HTS-SMES magnet design and test results. *IEEE Trans. Appl. Supercond.* **7**(2), 971–976 (1997). <https://doi.org/10.1109/77.614667>
46. R. Kreutz, H. Salbert, D. Krischel, A. Hobl, C. Radermacher, N. Blacha, P. Behrens, K. Dutsch, Design of a 150 kJ high-Tc SMES (HSMES) for a 20 kVA uninterruptible power supply system. *IEEE Trans. Appl. Supercond.* **13**(2), 1860–1862 (2003). <https://doi.org/10.1109/TASC.2003.812929>
47. P. Tixador, M. Deleglise, A. Badel, K. Berger, B. Bellin, J.C. Vallier, A. Allais, C.E. Bruzek, First tests of a 800 kJ HTS-SMES. *IEEE Trans. Appl. Supercond.* **18**(2), 774–778 (2008). <https://doi.org/10.1109/TASC.2008.921319>
48. K. Shikimachi, H. Moriguchi, N. Hirano, S. Nagaya, T. Ito, J. Inagaki, S. Hanai, M. Takahashi, T. Kurusu, Development of MVA class HTS SMES system for bridging instantaneous voltage dips. *IEEE Trans. Appl. Supercond.* **15**(2), 1931–1934 (2005). <https://doi.org/10.1109/TASC.2005.849338>
49. Y. Li, P. Song, Y. Kang, F. Feng, T. Qu, Design of a 30-K/4-kJ HTS magnet cryocooled with solid nitrogen. *IEEE Trans. Appl. Supercond.* **28**(4), 4603606 (2018). <https://doi.org/10.1109/TASC.2018.2814960>
50. Z.X. Zheng, X.Y. Chen, X.Y. Xiao, C.-J. Huang, Design and evaluation of a mini-size SMES magnet for hybrid energy storage application in a kW-class dynamic voltage restorer. *IEEE Trans. Appl. Supercond.* **27**(7), 5700911 (2017). <https://doi.org/10.1109/TASC.2017.2748954>

51. L. Chen, H. Chen, J. Yang, H. He, Y. Yu, G. Li, Y. Xu, Z. Wang, L. Ren, Conceptual design and evaluation of an HTS magnet for an SMES used in improving transient performance of a grid-connected PV system. *IEEE Trans. Appl. Supercond.* **28**(3), 4600708 (2018). <https://doi.org/10.1109/TASC.2017.2783349>
52. A. Morandi, B. Gholizad, M. Fabbri, Design and performance of a 1MW-5s high temperature superconductor magnetic energy storage system. *Supercond. Sci. Technol.* **29**(1), 015014 (2016). <https://doi.org/10.1088/09532048/29/1/015014>
53. K. Shikimaki, N. Hirano, S. Nagaya, H. Kawashima, K. Higashikawa, T. Nakamura, System coordination of 2GJ class YBCO SMES for power system control. *IEEE Trans. Appl. Supercond.* **19**(3), 2012–2018, (2009). <https://doi.org/10.1109/TASC.2009.2018491>
54. M. Song, J. Shi, Y. Liu, Y. Xu, N. Hu, Y. Tang, J. Li, 100 kJ/50 kW HTS SMES for micro-grid. *IEEE Trans. Appl. Supercond.* **25**(3), 1–6 (2014). <https://doi.org/10.1109/TASC.2014.2386345>
55. L. Ren, Y. Xu, H. Liu, Y. Liu, P. Han, J. Deng, Y. Tang, The experimental research and analysis of a HTS SMES hybrid magnet. *IEEE Trans. Appl. Supercond.* **25**(3), 1–5 (2014). <https://doi.org/10.1109/TASC.2014.2368271>
56. J. Zhu, W. Yuan, M. Qiu, B. Wei, H. Zhang, P. Chen, Y. Yang, M. Zhang, X. Huang, Z. Li, Experimental demonstration and application planning of high temperature superconducting energy storage system for renewable power gridIII. *Appl. Energy* **137**(1), 692–698 (2015). <https://doi.org/10.1016/j.apenergy.2014.07.022>
57. J. Yan, *Handbook of Clean Energy Systems Superconducting Magnetic Energy Storage (SMES) Systems* (2015), pp. 1–16. <https://doi.org/10.1002/9781118991978.hces210>
58. H. Zhang, Z. Nie, X. Xiao, R. Aggarwal, Q. Kang, M. Ainslie, J. Zhu, T. Coombs, W. Yuan, Design and simulation of SMES system using YBCO tapes for direct drive wave energy converters. *IEEE Trans. Appl. Supercond.* **23**(3), 5700704 (2013). <https://doi.org/10.1109/TASC.2012.2232954>
59. Z. Nie, X. Xi, Q. Kang, R. Aggarwal, H. Zhang, W. Yuan, SMES-battery energy storage system for conditioning outputs from direct drive linear wave energy converters. *IEEE Trans. Appl. Supercond.* **23**(3), 5000705 (2013). <https://doi.org/10.1109/TASC.2013.2246852>
60. Y. Makida, H. Hirabayashi, T. Shintomi, S. Nomura, Design of SMES system with liquid hydrogen for emergency purpose. *IEEE Trans. Appl. Supercond.* **17**(2), 2006–2009 (2007). <https://doi.org/10.1109/TASC.2007.898177>
61. M. Sander, R. Gehring, H. Neumann, LIQHYSMES—a48 GJ toroidal MgB2-SMES for buffering minute and second fluctuations. *IEEE Trans. Appl. Supercond.* **23**(3), 5700505 (2013). <https://doi.org/10.1109/TASC.2012.2234201>
62. N. Atomura, T. Takahashi, H. Amata, T. Iwasaki, K. Son, D. Miyagi, M. Tsuda, T. Hamajima, T. Shintomi, Y. Makida, T. Takao, K. Munakata, M. Kajiwar, Conceptual design of MgB2 coil for the 100 MJ SMES of advanced superconducting power conditioning system (ASPCS). *Phys. Proc.* **27**, 400–403 (2012). <https://doi.org/10.1016/j.phpro.2012.03.495>
63. H. Ibrahim, A. Ilinca, J. Perron, Energy storage systems: characteristics and comparisons. *Renew. Sustain. Energy Rev.* **12**, 1221–1250 (2008)
64. A. Kumar, J.V.M. Jeyan, A. Lal, Electromagnetic analysis on 2.5MJ high temperature superconducting magnetic energy storage (SMES) coil to be used in uninterrupted power applications. *Mater. Today Proc.* **2**, 1755–1762 (2020). <https://doi.org/10.1016/j.matpr.2020.01.228>
65. K. Bradbury, *Energy Storage Technology Review* (Duke University, 2010). [https://people.duke.edu/~kjb17/tutorials/Energy\\_Storage\\_Technologies\\_2010.pdf](https://people.duke.edu/~kjb17/tutorials/Energy_Storage_Technologies_2010.pdf)
66. B. Vincent, P. Tixador, T. Lecrevisse, J.M. Rey, X. Chaud, Y. Miyoshi, HTS magnets: opportunities and issues for SMES. *IEEE Trans. Appl. Supercond.* **23**, 5700805 (2013). <https://doi.org/10.1109/TASC.2012.2236141>
67. A. Badel, P. Tixador, M. Amiet, V. Brommer, SMES to supply an electromagnetic launcher. *IEEE Trans. Appl. Supercond.* **22**(3), 5700204–5700204 (2012). <https://doi.org/10.1109/TASC.2011.2174549>
68. W.V. Hassenzähl, Superconducting magnetic energy storage. *Proc. IEEE* **71**(9), 1089–1098 (1983). <https://doi.org/10.1109/proc.1983.12727>



69. H.J. Boenig, J.F. Hauer, Commissioning tests of the Bonneville power administration 30 MJ superconducting magnetic energy storage unit. *IEEE Trans. Power Appar. Syst.* **104**(2), 302–312 (1985). <https://doi.org/10.1109/tpas.1985.319044>
70. W. Buckles, W.V. Hassenzahl, Superconducting magnetic energy storage. **20**(5), 0–20 (2000). <https://doi.org/10.1109/39.841345>
71. S. Nagaya, N. Hirano, T. Katagiri, T. Tamada, K. Shikimachi, Y. Iwatani, F. Saito, Y. Ishii, The state of the art of the development of SMES for bridging instantaneous voltage dips in Japan. *Cryogenics* **52**(12), 708–712 (2012). <https://doi.org/10.1016/j.cryogenics.2012.04.014>
72. P. Breeze, Power system energy storage technologies. *Supercond. Magn. Energy Storage* 47–52 (2018). <https://doi.org/10.1016/B978-0-12-812902-9.00005-5>
73. M. Park, S. Kwak, W. Kim, J. Lee, J. Han, K. Choi, H. Jung, J. Bae, S. Kim, K. Sim, H. Kim, K. Seong, S. Hanh, Conceptual design of HTS magnet for a 5 MJ class SMES. *IEEE Trans. Appl. Supercond.* **18**(2), 750–753 (2008). <https://doi.org/10.1109/tasc.2008.922533>
74. P. Tixador, B. Bellin, M. Deleglise, J.C. Vallier, C.E. Bruzek, A. Allais, J.M. Saugrain, Design and first tests of a 800 kJ HTS SMES. *IEEE Trans. Appl. Supercond.* **17**(2), 1967–1972 (2007). <https://doi.org/10.1109/tasc.2007.898520>
75. M.W. Rupich, U. Schoop, D.T. Verebelyi, C.L.H. Thieme, D. Buczek, X. Li, W. Zhang, T. Kodenkandath, Y. Huang, E. Siegal, W. Carter, N. Nguyen, J. Schreiber, M. Prasova, J. Lynch, D. Tucker, R. Harnois, C. King, D. Aized, The development of second generation HTS wire at American Superconductor. *IEEE Trans. Appl. Supercond.* **17**, 3379–3382 (2007). <https://doi.org/10.1109/TASC.2007.899076>
76. A. Usoskin, L. Kirshhoff, J. Knoke, B. Prause, A. Rutt, V. Selsjij, D.E. Farrell, Processing of long length YBCO coated conductors based on stainless steel tapes. *IEEE Trans. Appl. Supercond.* **17**, 3235–3238 (2007). <https://doi.org/10.1109/TASC.2007.900041>
77. V. Selvamannickam, Y. Chen, X. Xiong, Y.Y. Xie, J.L. Reeves, X. Zhang, Y. Quiao, K.P. Lenseh, R.M. Schmidt, A. Rar, D.W. Hazelton, K. Tekletsadik, Recent progress in second generation HTS conductor scale-up at Superpower. *IEEE Trans. Appl. Supercond.* **17**, 3231–3234 (2007). <https://doi.org/10.1109/TASC.2007.899360>
78. K. Shikimachi, N. Hirano, S. Nagaya, H. Kawashima, K. Higashikawa, T. Nakamura, System coordination of 2 GJ Class YBCO SMES for power system control. *IEEE Trans. Appl. Supercond.* **19**(3), 2012–2018 (2009). <https://doi.org/10.1109/TASC.2009.2018491>
79. T. Shintomi, T. Asami, G. Suzuki, N. Ota, T. Takao, Y. Makida, T. Hamajima, M. Tsuda, D. Miyagi, M. Kajiwara, J. Hirose, Design study of MgB<sub>2</sub> SMES coil for effective use of renewable energy. *IEEE Trans. Appl. Supercond.* **23**(3), 5700304 (2013). <https://doi.org/10.1109/TASC.2012.2234181>
80. P. Tixador, Superconducting magnetic energy storage (SMES) systems. In *High temperature superconductors (HTS) for energy applications* (2012), pp. 294–319
81. Z. Zhang, R. Miyajima, Y. Sato, D. Miyagi, M. Tsuda, Y. Makida, T. Shintomi, T. Yagai, T. Takao, T. Komagome, T. Hamajima, H. Tsujigami, S. Fujikawa, K. Iwaki, K. Hanada, N. Hirano, Characteristics of compensation for fluctuating output power of a solar power generator in a hybrid energy storage system using a Bi2223 SMES coil cooled by thermosiphon with liquid hydrogen. *IEEE Trans. Appl. Supercond.* **26**(4) (2016). <https://doi.org/10.1109/TASC.2016.2529565>
82. X.Y. Chen, J.X. Jin, Y. Xin, B. Shu, C.L. Tang, Y.P. Zhu, R.M. Sun, Integrated SMES technology for modern power system and future smart grid. *IEEE Trans. Appl. Supercond.* **24**(5) (2014). <https://doi.org/10.1109/TASC.2014.2346502>
83. J. Li, M. Zhang, Q. Yang, Z. Zhang, W. Yuan, SMES/battery hybrid energy storage system for electric buses. *IEEE Trans. Appl. Supercond.* **26**(4) (2016). <https://doi.org/10.1109/TASC.2016.2527730>
84. V.M. Fthenakis, *Comprehensive Renewable Energy Storage Options for Photovoltaics* (2012), pp. 199–212. <https://doi.org/10.1016/b978-0-08-087872-0.00106-2>
85. P. Denholm, E. Ela, B. Kirby, M. Milligan, *Role of Energy Storage with Renewable Electricity Generation* (National Renewable Energy Lab. (NREL), Golden, CO, United States, 2010). <https://doi.org/10.2172/972169>

86. M.R. Islam, Study of SMES technology for electric power supply and investigation of its utility and possible implementation in Bangladesh. A project report (University of Chittagong, 2014)
87. W. Yuan, M. Zhang, *Handbook of Clean Energy Systems, Superconducting Magnetic Energy Storage (SMES) Systems* (2015) pp. 1–16. <https://doi.org/10.1002/9781118991978.hces210>.
88. M.H. Ali, B. Wu, R.A. Dougal, An overview of SMES applications in power and energy systems. *IEEE Trans. Sustain. Energy* **1**(1), 38–47 (2010). <https://doi.org/10.1109/TSTE.2010.2044901>
89. K. Gong, J. Shi, Y. Liu, Z. Wang, L. Ren, Y. Zhang, Application of SMES in the microgrid based on fuzzy control. *IEEE Trans. Appl. Supercond.* **26**(3), 1–5 (2016). <https://doi.org/10.1109/TASC.2016.2524446>
90. R. Gupta, M. Anerella, P. Joshi, J. Higgins, S. Lalitha, W. Sampson, J. Schmalzle, P. Wanderer, Design, construction, and testing of a large-aperture high-field HTS SMES coil. *IEEE Trans. Appl. Supercond.* **26**(4), 1–8 (2016). <https://doi.org/10.1109/TASC.2016.2517404>
91. J. Lee, J.H. Kim, S.K. Joo, Stochastic method for the operation of a power system with wind generators and superconducting magnetic energy storages (SMESs). *IEEE Trans. Appl. Supercond.* **21**(3), 2144–2148 (2011). <https://doi.org/10.1109/TASC.2010.2096491>
92. A. Abu-Siada, S. Islam, Application of SMES unit in improving the performance of an AC/DC power system. *IEEE Trans. Sustain. Energy* **2**(2), 109–121 (2011). <https://doi.org/10.1109/TSTE.2010.2089995>
93. Y. Wan, J. Zhao,  $H_\alpha$  control of single-machine infinite bus power systems with superconducting magnetic energy storage based on energy-shaping and backstepping. *IET Control Theory Appl.* **7**(5), 757–764 (2013). <https://doi.org/10.1049/iet-cta.2012.0897>
94. G. Zhang, S. Dai, N. Song, Z. Zhu, J. Zhang, W. Guo, D. Zhang, Z. Zhang, L. Xiao, L. Lin, The construction progress of a high-Tc superconducting power substation in China. *IEEE Trans. Appl. Supercond.* **21**(3), 2824–2827 (2011). <https://doi.org/10.1109/TASC.2010.2098471>
95. W. Hassenzhal, Superconducting magnetic energy storage. *IEEE Trans. Magn.* **25**, 750 (1989). <https://doi.org/10.1109/20.92399>
96. J.L. Wu, J.F. Roach, D.C. Johnson, J.T. Dederer, S.K. Singh, D.T. Hackworth, Design and analysis of SMES-ETM electrical insulation. *Adv. Cryog. Eng.* **39**, 813 (1994). [https://doi.org/10.1007/978-1-4615-2522-6\\_98](https://doi.org/10.1007/978-1-4615-2522-6_98)

# Rotating Machines Based on Superconducting Materials



Abdurrahman Erciyas, Şükürü Yildiz, and Fedai Inanir

**Abstract** Novel FEM calculation method based on A-V Formulation of Maxwell Equations have been proposed to compute the transient AC current losses of superconducting rotating machineries, like generators. The calculations are carried out in 2-Dimensions. The model generator under consideration is a three-phase synchronous generator with a 12-pole and 12-slot rotor made of permanent magnets and high-temperature superconducting coils carrying DC and the stator windings made of high-temperature superconducting coils. Superconducting coils are wound with 2G HTS coated conductors and the critical current intensity is around 300 A at  $T = 77$  K. Rotor magnets generate magnetic fields in the  $xy$ -plane and only current is induced in the  $z$ -direction inside the HTS coils. The Loss calculation of the superconducting generator were then repeated with the **H**-formulation and the **A-H** Hybrid model. AC loss is calculated for different rotor speeds using all three calculation approaches. 2D electromagnetic, thermal and mechanical analyzes of MW order superconducting generator designs are performed using the AV method including nonlinear *EJ*. Current, magnetic field, AC losses, temperature and distributions and mechanical stresses in coils wound from Coated Conductors are presented in 2D.

**Keywords** Superconductors · Coated conductor tape · Superconducting generator · Finite element method · AC loss

## 1 Introduction

There is a general tendency for superconducting rotating machines of small sizes and large powers to be more viable commercially. The main reason is that the cryogenic subsystem required to be added to the system is a much smaller portion of the total

---

A. Erciyas · F. Inanir (✉)

Department of Physics, Science and Faculty, Yildiz Technical University, Istanbul, Turkey

e-mail: [inanir@yildiz.edu.tr](mailto:inanir@yildiz.edu.tr)

Ş. Yildiz

Department of Metallurgical and Materials Engineering, Faculty of Engineering and Architecture, Ahi Evran University, Kırşehir, Turkey

machine weight and cost. The commercial availability of stranded *NbTi* superconductors from the late 1960s made it possible to begin applications for superconducting rotary machines [1]. Since these superconductors were only convenient for carrying direct current (DC), they were designed to replace the DC field windings on existing rotary machines in early applications. The most ideal applications for these designs were large synchronous motors, generators and unipolar DC machines.

The magnetic field strength in the air gap of conventional rotary machines is generally limited by the saturation of the iron core teeth on the rotor and stator. However, the high current carrying capacity of superconductors has made it possible to generate much higher air-gap field strength with a small volume field winding and the lower energy loss. First, the resistance losses are equal to the field and the armature windings. From this point of view, the promised efficiency increase can be realized by replacing the superconducting windings with the copper field windings (representing about half of the total copper losses). In this sense, major synchronous generator designs are General Electric [2], Westinghouse, Super-GM, etc. implemented by companies [3, 4]. Although Super-GM implemented the project in the 1990s in which it tested 70 MVA generators with three different rotors using three different *NbTi* field windings, none of them were found economically attractive due to technical problems such as the inadequacy and cost of low-temperature cooling systems, instability in the superconducting wire.

The discovery of HTS in 1986 provided an acceleration for the development of various electrical machines based on these new superconductors. In particular, the ability of these superconductors to operate at the higher temperatures (between 25 and 77 K) with the lower cost cooling systems has enabled applications around the world where HTS technologies such as full-scale high or low speed motors and generators are employed.

The American Superconductor Corporation (AmSC) built a 36.5 MW 120 rpm ship propulsion engine for the United States navy between 2003 and 2007. The motor is a synchronous air-core machine with an HTS field windings on the rotor. The stator was constructed without iron teeth and cooled by a dielectric liquid [5]. An average torque of 2750 kNm was obtained from the engine. This work has been inspiring for all superconductor applications.

Siemens reached a torque of 320 kNm with its 4 MW ship propulsion engine, which it completed in 2009, provided a 1/3 weight and volume advantage over similar diesel engines, and the efficiency of the engine was announced as approximately 97–98% [6]. This work has also been inspiring for all superconductor applications. However, some improvements are still needed. In particular, the development of 2G HTS tapes with cheaper, better mechanical properties and higher current density, overcoming structural difficulties, developing efficient cooling systems, performing robust fabrication and acceptance testing, and proposing new methods for verification in computational tools still remain as formidable challenges.

There are many studies on direct-drive high-power synchronous wind turbine generators [7–11]. For a full-size machine, there is no reported production or testing. However, some turbine components have been successfully built and tested [8–11]. In this type of generator and other superconducting rotating devices, knowing the AC

losses beforehand is essential for optimal machinery design. As a result, both very high costs and very long laboratory studies are required in experimental studies. It is important to advance on to the design of the complete system, especially starting from the components. In this sense, as mentioned before, the use of models containing the Finite Element Method (FEM) is used for the analysis of both the components and full devices. However, a coil or coil stack that is one of these basic components can have hundreds or even thousands of turns. It is very difficult to enter such a system separately into the program and to make loss calculations, and the calculation times take quite a long time due to the meshing done. Even these calculation times vary with a quadratic exponential relation with the number of the meshing elements [12]. In order to shorten this period, it was necessary to make some smart assumptions and approximations that would not reduce the quality of the model. For this, the first questions that come to mind are: (i) Is it necessary to simulate a whole system? (Can symmetry or periodicity be used, or can the size of the problem be reduced?), (ii) What level of physical representation is required? Is a simple guess enough? How accurate is it to use experimental results to validate the model? (iii) Is it necessary to look in detail at results such as the local area and current distribution, or do we only need general quantities such as AC losses? What are the needs of industrialists and manufacturers according to academics? It has developed models containing 2G HTS that answer all these questions within itself. Infinite thin-film approach that reduces the size of the system [13–16], or in some applications where many superconductors are placed or stacked on top of each other, getting rid of the geometry of the individual tapes and stacking them. Special current constrains that make the cross section homogeneous and approximations that preserve the physical behavior of the system [17–20] can be suggested.

References [21–24] investigated the AC losses in HTS tape stacks where the distances between tapes are very small compared to the tape width, with the numerical model they developed using the variational method using the Finite Difference Method based on Critical State Model (CSM). Under the infinitely thin strip approach, a critical current flowed at the edges of the strip perpendicular to the flow, while subcritical currents were observed in the inner regions. Contrary to the previous models, they showed that the AC losses depend on the distance between the strips for the 10 and 20 strip stack, without making any approximations about the shape of the subcritical region, and for small values of this distance, the lowest AC loss takes place in the middle strip [21]. They also revealed that the results of their model converge to the results obtained under the anionic stacked wire approach as the number of tapes approaches 100, and that a scaled stack containing 10 or 20 tapes can be considered in order to reduce the AC loss calculation time to reasonable levels for stacks consisting of hundreds of tapes [21].

A numerical model for the equivalent anisotropic bulk structure approximation in the AC loss calculations of the coil stack is presented by Zermeno et al. [25]. While neglecting the geometry of the insulator, metal, superconductor and substrate layers that make up the coil, the model, which aims to accurately obtain the magnetic behaviors of the real coil stack, also does not make any assumptions about the subcritical current regions in the strip and nonlinear  $EJ$ , as in Prigozhin and Sokolovsky's

approach. It also provides the supercritical flow regions by using the power law relationship [21]. The results obtained by using the H formulation on 16, 32 and 64 strip coated YBCO HTS coils with the model and using Kim CSM were compared with those obtained with the two-dimensional FEM method based on the H formulation in the literature [25]. 2.5% error was determined and the error decreases as the number of strips increases [19]. Using the H formulation and assuming an E-J force law relationship, Xia et al. also provided validation of the approach [26]. Ainslie et al. investigated the total AC transport losses for structures consisting of stacks of HTS tapes on magnetic substrates with symmetrical FEM simulations based on the H formulation [27]. The H formulation, which uses a power law relationship between E-J, was developed for the direct acquisition of magnetic field components in 2 dimensions and produces results that are in good agreement with the experimental results. In their calculations for the total number of strips from 1 to 150, Ainslie et al. showed that the magnetic substrate raised the total AC loss of the stack due to the increase in the local magnetic flux density [23]. They also revealed that as the magnetization of the substrate increases, the flux penetrates deeper, thus increasing the AC losses. They observed that the losses for the magnetic substrate were the highest in the tapes in the middle of the stack. On the other hand, they showed that the results obtained for non-magnetic substrate are compatible with existing approaches such as single-lane and infinite stack confinement cases [28].

## 2 Simulation Methods Used in Design of Superconducting Machinery

In this chapter, we have proposed to evolve a new simulation methods that have been developed by us in frame of FEM in order to solve Maxwell equations for complex generator architectures including both nonlinear current–voltage relation for superconducting coils and also nonlinear magnetic permeability for ferromagnetic body. New simulation methods have been developed for the electromagnetic analysis of the superconducting synchronous generators. Calculations were performed in two dimensions and the model generator was designed (Fig. 1). The model design considered is a three-phase synchronous generator the rotor of which has 12 poles and 12 slots and is made of permanent magnets and the stator windings of which are made of superconducting coils. Superconducting coils were wrapped on 2G (RE)BCO coated conductor tapes, The superpower SCS12050-AP REBCO tape, in which the critical current density is approximately 300 A at self-field ( $B \perp$  Tape surface) in  $T = 77$  K ambient temperature. The rotor magnets generate magnetic field in the  $xy$ -plane and current is induced in the HTS coils only in the  $z$ -direction. The parameters used for model generators are given in Table 1. Initially, we aimed to develop a simulation method for SC generators based on  $A$ - $V$  formulation of Maxwell Equations. Therefore,  $A$ - $V$  formulation was primarily highlighted used for the calculations. According to the  $A$ - $V$  formulation based on the Ampère Equation,

**Fig. 1** The model generator adopted in calculations. The rotor of the generator was schemed from permanent magnets, and the magnets were placed in a radial direction to produce an inward and outward magnetic field. The stator is composed of HTS coated conductor coils

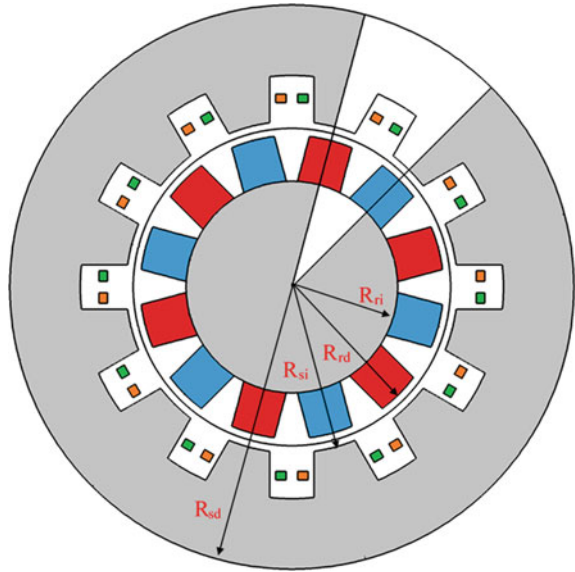


**Table 1** Parameters for the superconducting generator chosen as a model

Parameter (Unit)	Definition	Value
$R_{sd}$ (mm)	Outer radius of stator	320
$R_{si}$ (mm)	Inner radius of stator	188
$R_{rd}$ (mm)	Outer radius of rotor	172
$R_{ri}$	Inner radius of rotor	12
$D_{ag}$ (mm)	Air gap distance	16
$L$ (mm)	Length of generator	600
$p$	The number of poles of the generator	12
$s$	The number of slots of the generator	12
$B_{rem}$ (T)	The magnetic field of permanent magnet	1.2
$\omega$ (rpm)	The angular velocity of generator	10, 30 ... 180
$I_c$ (A)	The critical current density of the tape	300
$w_{sc}$ (mm)	The width of the tape	12
$h_{sc}$ ( $\mu m$ )	The thickness of the tape	100
$E_c$ (V/m)	Electric field criteria	$1 \times 10^{-4}$
$n$	Power-law exponent	25
$N_s$	The number of turn of stator coils	100

the current induced in the generator windings can be calculated as follows:

$$\sigma \frac{\partial \mathbf{A}}{\partial t} + \frac{1}{\mu_0 \mu_r} \nabla \times \nabla \times \mathbf{A} = 0 \quad (1)$$

where  $\sigma$ , represents the conductivity of the materials such as the HTS or the back-iron, etc.  $\mathbf{A}$  the vector potential;  $\mu_0$ , the magnetic permeability of free space, and  $\mu_r$ , the relative magnetic permeability. A new simulation method has been developed within COMSOL Multiphysics environment to be resolved Eq. (1) for defined boundary condition.

For the convenience in the calculations, only the part (sector) of  $2\pi/p$  was taken into account since the generator is a periodic structure. The other approximation was to take the coils consisting of HTS tapes which formed the stator as a whole, that is, the homogenization approach was exploited [29]. As a result of this approach, the critical current density of the superconducting tapes were accepted to decrease at a rate of  $0.78 \times J_c$  [30]. The following geometric transformations were used to model the rotation in a superconducting generator rotating with the angular velocity,  $\omega$ .

$$\begin{pmatrix} X(x, y, t) \\ Y(x, y, t) \end{pmatrix} = \begin{bmatrix} \cos(\omega t) & \sin(\omega t) \\ -\sin(\omega t) & \cos(\omega t) \end{bmatrix} \begin{bmatrix} x \\ y \end{bmatrix} \quad (2)$$

In this formula,  $x, y$  represents the spatial coordinate system and  $X, Y$  the material type coordinate system. Similarly, the transformation as follow was used for the magnetic field.

$$\begin{pmatrix} B_X \\ B_Y \end{pmatrix} = \begin{bmatrix} \cos(\omega t) & \sin(\omega t) \\ -\sin(\omega t) & \cos(\omega t) \end{bmatrix} \begin{bmatrix} B_x \\ B_y \end{bmatrix} \quad (3)$$

Lorentz transformations are performed for the electric field.

$$E(x, y) = E(X, Y) - v(x, y) \times B(X, Y) \quad (4)$$

In here,  $v(x, y)$  indicates the non-relativistic dimensional velocity distribution of rotational material.

The boundary condition is assessed that  $\mathbf{A}$  the vector potential and  $V_m$ , the scalar potential are anti-periodic on the right and left of the generator sector in given in Fig. 1:

$$\begin{aligned} A_{left} &= -A_{right}, \\ V_{m,left} &= -V_{m,right} \end{aligned} \quad (5)$$

In addition, the sector symmetry boundary condition for the boundary pairs separating the rotor and stator was defined as:



$$\mathbf{B} \cdot \hat{n} = 0 \quad (6)$$

Magnetic isolation boundary condition is exploited for the outer envelope of generator sector.

In order to reflect the nonlinear current–voltage relation of superconducting coils in  $\mathbf{A}$ - $\mathbf{V}$  formulation, the conductivity of the HTS material can be defined,

$$\sigma = \frac{J_c}{E_c} \left( \frac{|E|}{E_c} + \delta \right)^{1/n-1} \quad (7)$$

where  $J_c$  is the critical current density,  $E_c = 1 \times 10^{-4} \text{ V/m}$ , the electric field criterion,  $\delta \approx 1 \times 10^{-5} E_c$  the parameter that prevents divergence of the defined expression. This parameter actually sets a lower limit for conductivity of superconductors. The electric field given in Eq. 7 is defined as follow,

$$\mathbf{E} = -\frac{\partial \mathbf{A}}{\partial t} \quad (8)$$

We ignore the gradient of scalar potential that is only provided by the varying magnetic field. Magnetic flux density can be calculated the curl of the vector potential,

$$\mathbf{B} = \nabla \times \mathbf{A} \quad (9)$$

The second simulation method that has been aimed to simulate electromagnetic response of the superconducting generators is actually based on the constraint on the current, which was developed by Gömöry for superconducting tapes and coils under dynamical transport current and magnetic field [31]. To our best knowledge, the electromagnetic computation of the superconducting rotating machinery has not been practiced yet. In this calculation method, supercurrents circulating through superconducting coils are constrained,

$$\mathbf{J}_s = J_c \tanh \left( \frac{-\frac{\partial \mathbf{A}}{\partial t}}{E_c} \right) \quad (10)$$

Likewise, this method enables the solutions of Ampere's equation given in Eq. 1. However, Ampere's equation is figured out in the critical state framework. Therefore, it provides quite reasonable solutions for the amplitudes that are induced less than  $I_c$ . The method is quite simple and stable in practice; however, it gives convergence problems at high frequencies and high current amplitudes. Nevertheless, it is still a reliable method as the generators operate at low rpm and the current is not wanted to rise above a certain level.

The third method that was evolved comprises the approach in which  $\mathbf{A}$ - $\mathbf{V}$ - and  $\mathbf{H}$ -formulation are combined. In frame of available method, HTS coils in the stator of the

model generator is solved by **H**-formulation. Electromagnetic analysis for the ferromagnetic or other solid parts, magnets are solved and also the boundary conditions are implemented by means of the **A** formulation. The purpose of the development of this method is that the periodic (Eq. 5) and continuity boundary (Eq. 6) conditions of the **H**-formulation, especially used in generator design, could not be implemented. **H**-formulation also gives fine results in electromagnetic analysis of superconducting materials and is widely preferred for many research group all round world and we can say that it is almost a defacto-method for modelling superconducting tapes and coils. For this purpose, in order to be able to ascertain solutions with frame of the H-formulation, it is necessary to ensure the time dependent solutions of the Faraday equation given below. The Faraday equation is,

$$\mu_0\mu_r \frac{\partial \mathbf{B}}{\partial t} + \nabla \times \mathbf{E} = 0 \quad (11)$$

The relationship that connects the electric and magnetic fields is as follows;

$$\begin{aligned} \mathbf{J} &= \nabla \times \mathbf{B}, \\ \mathbf{E} &= \rho \mathbf{J} \end{aligned} \quad (12)$$

where  $\rho$  is resistivity of particular material and the resistivity peculiar to superconductors and the nonlinear voltage relation:

$$\rho = \frac{E_c}{J_c} \left( \frac{J}{J_c} \right)^{n-1} + \rho_0 \quad (13)$$

It is the point to be considered that the numerical solution defines a lower limit on the resistivity ( $\rho_0$ ) of the superconducting material for the convergence. This value should be approximately  $\sim 10^{-17} \Omega \text{ m}$ . Another important point is to define the external current density (External Current Density) for regions other than the superconductor in order to use the **A**-**V** formulation into the H-formulation, and to enter the expressions of the induced current densities calculated using the **A**-**V** formulation into the formulation. This constitutes the main idea of the method and can be entered as  $J_x = mf \cdot J_{ix}$ ,  $J_y = mf \cdot J_{iy}$ ,  $J_z = mf \cdot J_{iz}$  in Comsol Software. The formula  $J_x$ ,  $J_y$ ,  $J_z$  on the right side of the equations represents the H-formulation's external current densities to which are assigned value, and  $mf \cdot J_{ix}$ ,  $mf \cdot J_{iy}$ ,  $mf \cdot J_{iz}$  expressions represent the induced current densities calculated by the A-V-formulation. The (Magnetic Field "mf") in the **A**-**V** formulation in COMSOL Multiphysics software denotes here default prefixes for evaluating magnetic field. This method is a bit complicated and it is very difficult to apply directly in the 'Magnetic Field Formulation (mfh)' which produces solutions based on the H-formulation that comes as standard in COMSOL software. Therefore, the H-formulation in this study was solved using the partial differential equation form. In this method, the expression defining the **H**-formulation is given,

$$G_a \frac{dH}{dt} + \nabla \cdot \Theta = T \begin{bmatrix} \mu_0 & 0 \\ 0 & \mu_0 \end{bmatrix} \begin{bmatrix} \frac{dH_x}{dt} \\ \frac{dH_y}{dt} \end{bmatrix} + \nabla \cdot \begin{bmatrix} 0 & E(J) \\ -E(J) & 0 \end{bmatrix} = \begin{bmatrix} 0 \\ 0 \end{bmatrix} \quad (14)$$

The ‘‘General Form’’ in the partial differential equations module in COMSOL software can be used to be entered this Eq. (14) into Comsol. Another point to be emphasized is that  $\rho_0$  resistance in the superconductor part given by Eq. (13) and the resistance of the space outside the superconducting coils are adjusted in harmony with each other. It was found that the ratio between them should be around approximately  $\sim 10^{11}$ . In order for this method to work properly, both parameters must be set very carefully.

In generator modelling, it is necessary to carefully consider the area and angle dependence of the critical current density. Otherwise, as the superconducting coils will be exposed to a high magnetic field, the current density will decrease due to the field dependence of  $J_c$ . Similarly, since they are exposed to a rotating magnetic field, it is necessary to take into account the angle dependence. The expression for the field dependence of the critical current is employed [32],

$$J_c(B) = \frac{J_{c0}}{\left(1 + \frac{\sqrt{k^2 B_{\parallel}^2 + B_{\perp}^2}}{B_0}\right)^{\beta}} \quad (15)$$

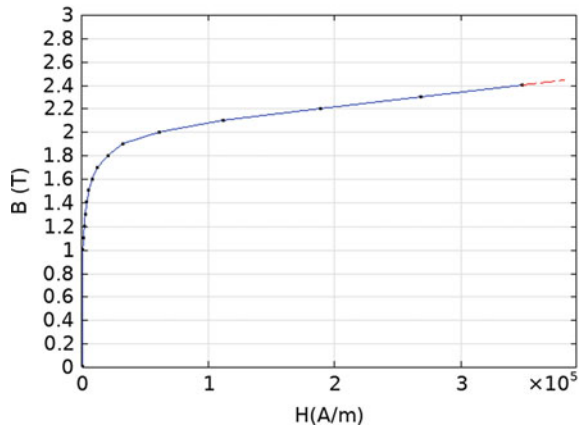
where  $J_{c0}$ ,  $B_0$  and  $\beta$ , are the adjustable parameters of YBCO coated conductor tapes. For the angular dependence of the critical current of the YBCO coated conductor [33], the equation is exploited,

$$J_c(B, \theta) = J_c(B) \frac{0.05}{\sqrt{\sin(\theta - 1.8)^2 + \frac{\cos(\theta - 1.8)^2}{400}}} + 0.3 \sin(\theta) \quad (16)$$

$\theta$ , in here, is the angle between the superconducting turn and the perpendicular component of the magnetic field.

Considering the magnetic field and angle dependence of the critical current, its value decreases by average 9% in per rotation. Above two expression must be taken into account in real machinery design. The nonlinear B-H curve was taken into account for the ferromagnetic iron in the stator and rotor of the generator (Fig. 2). However, its conductivity was taken as zero to disregard the Eddy current losses in the ferromagnetic part in order to avoid confusion in the calculations.

**Fig. 2** Magnetic Field strength  $H$  (A/m) versus magnetic flux density  $B$  (T) corresponding to non-linear magnetic permeability for the ferromagnetic part



### 2.1 Electromagnetic Analysis of Superconducting Model Generators

We present the electromagnetic analysis of superconducting generators for model generator given in Fig. 3. The considered design is a three-phase synchronous generator, the rotor of which has 12 poles and 12 slots and is made of permanent magnets and the stator windings of which are made of HTS superconducting coils. The superconducting coils are wrapped with 2G coated conductors and the critical current density is approximately 300 A at  $T = 77$  K. The rotor magnets generate magnetic

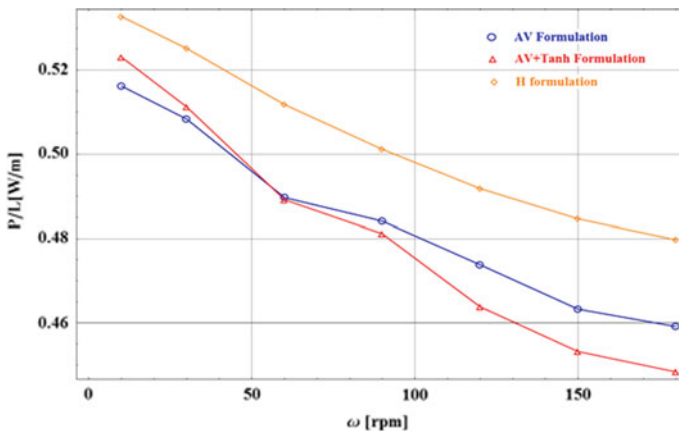


**Fig. 3** The AC losses in a single stator coil during the entire cycle of the rotor that computed using the three methods presented previous section as a function of generator rotational speed

**Table 2** Parameters of the fully superconducting generator

Parameter (Unit)	Definition	Value
$R_{sd}$ (mm)	Outer radius of stator	71.1
$R_{si}$ (mm)	Inner radius of stator	61.3
$R_{rd}$ (mm)	Outer radius of rotor	60.9
$R_{ri}$ (mm)	Inner radius of rotor	56.4
$D_{gap}$ (mm)	Air gap distance	0.6
$N_r$	The number of the winding of rotor coils	200
$N_s$	The number of the winding of of stator coils	100
$\omega$ (rpm)	The angular velocity of the rotor	90
$n_p$	The number of poles	12
$n_s$	The number of slots	16
$I_c$ (A)	Critical current density SC tape	100
$w_{SC}$ (mm)	Width of tapes	4
$h_{SC}$ ( $\mu$ m)	Thickness of tapes	1
$n$	Electric field exponent	25
$E_c$ (V/m)	Electric field criterion	$1 \times 10^{-4}$

field in the  $x$ - $y$ -plane and current is induced in the HTS coils only in the  $z$ -direction. The parameters for the generators are shown in Table 2.

In Fig. 3, AC losses that were computed by all three methods for varied generator velocity were shown. As it can be seen in the figure, AC losses decreased almost linearly as amplitude of the angular velocity increased. The reason can be easily understood by looking at Fig. 4 because the flux penetration depth of the induced current decreases as the rotational speed increases. Therefore, the losses decrease proportionally. In Fig. 3 indicate instantaneous losses. For actual loss values, these values should be multiplied by the frequency corresponding to the speed.

The remarkable point is that the difference between the losses calculated by the pure A-V formulation (Eq. 7) and the A-V + tanh(J) (Eq. 10) formulation is around 1%. This is an expected result, since both the rotation velocity and the amplitude of the induced field are  $f = 3$  Hz for 180 rpm and the amplitude of the current is quite low at 60 A per tapes. Both does not exceed the critical state. The difference between H and AV formulations is about 3% and we think that it is quite a reasonable level. This difference may be due to numerical errors. A striking point in A-V methods is the fluctuations in the loss curves. This can cause because same meshing parameters was employed for each angular velocity value. For a better calculation, it is apparent that the meshing parameters should be adjusted at each angular velocity value. However, the most important point to be considered here is the calculation time. The comparison of calculation times using Intel Xenon CPU E5-2596 @2.3 GHz 7 core and 16 GB RAM is given in Fig. 4.

The calculation time for H formulation is considerably longer than the A-V formulation (Fig. 5). Computational time of pure A-V and A-V + tanh (J) formulations

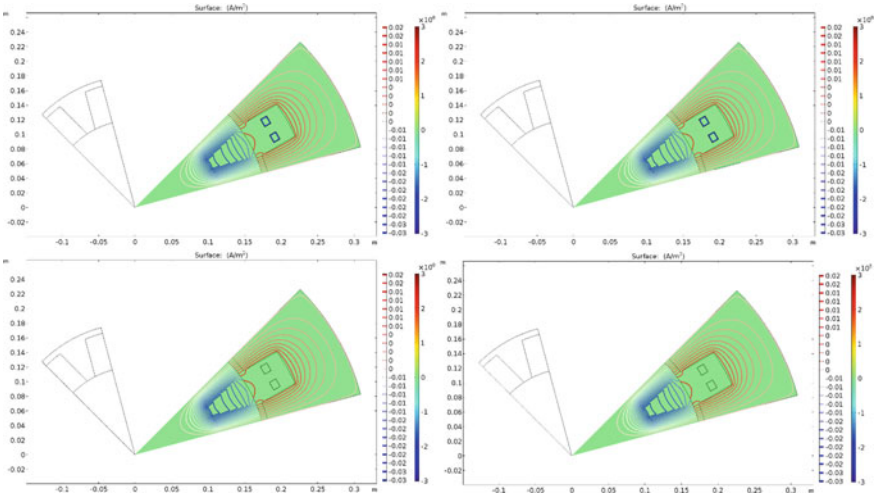


**Fig. 4** The induced current distribution of HTS stator coils when the rotor rotates a quarter round for  $\omega = 10, 30, 150$  and  $180$  rpm velocities and the magnetic field distribution (contours) around whole generator body

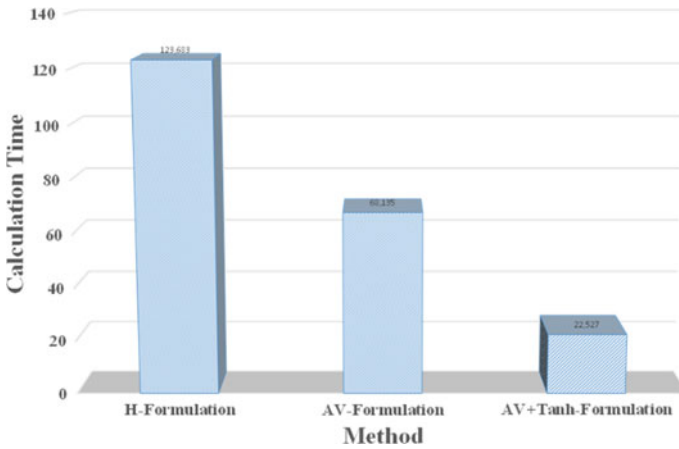


**Fig. 5** Comparison of the calculation times of AC losses using all three methods

are more reasonable. Both methods stand out in any machine optimization problem. However, one of the disadvantages of these methods is that with each physical parameter change, the meshing parameters must be fine-adjusted to be denser or sparser. The meshing type such as triangular or rectangular distribution, can modify as well as the solver parameters need to be fine-tuned, too. In particular, it is necessary to adjust the relative and absolute tolerance values of solver, respectively, in the order of  $10^{-10}$ ,  $10^{-12}$ . The solver type can choose Direct Solver, PRTISO or MUMPS.

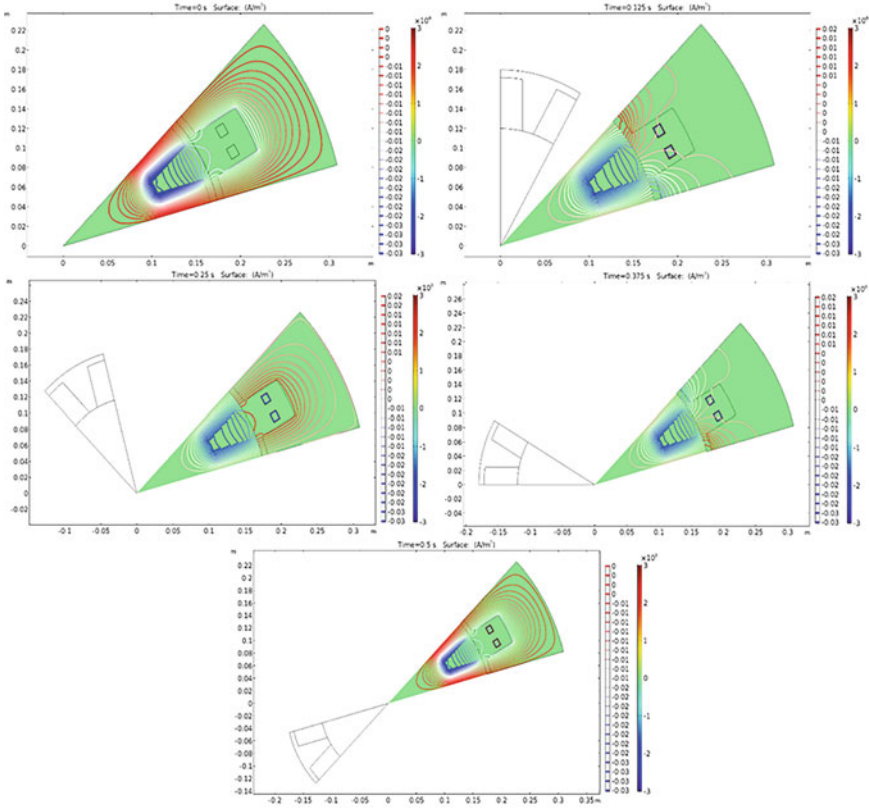


**Fig. 6** The magnetic field distributions of the stator and rotor of the model generator during  $t = 0, 0.125, 0.25, 0.375, 0.5$  s for  $\omega = 60$  rpm

Figure 6 displays the magnetic field distributions for different rotor positions like the varied times. It can be seen in the figure that a large magnetic coupling appears in the stator and rotor. The magnetic field is rather accumulated in the part of the stator iron facing the coils. This is a desirable situation because it increases the leakage, thus increasing the induced electromotor force (emf).

### 3 Stator AC Loss of Whole Superconducting Generators

In this section, electromagnetic analyses of generators both of whose stator and rotor turns are formed with HTS (Re)BCO tapes are accomplished. Fully superconducting generators are preferred for the advantages they provide in weight, size and cooling. In the conceptual design of these generators, it is taken into account that the rotor coils are made of coils wrapped with superconducting coated conductors circulating

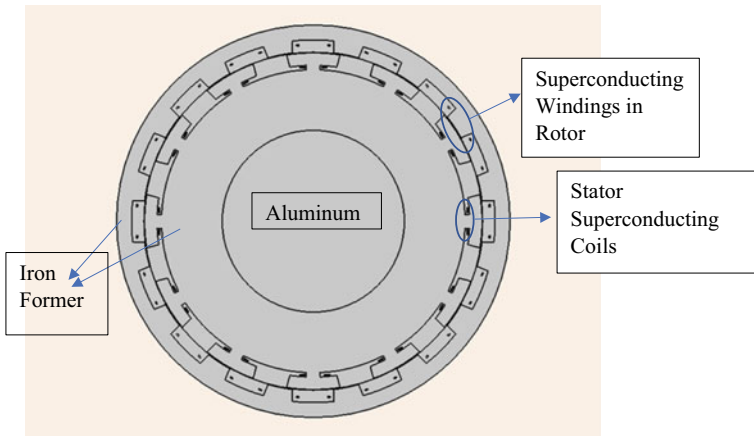
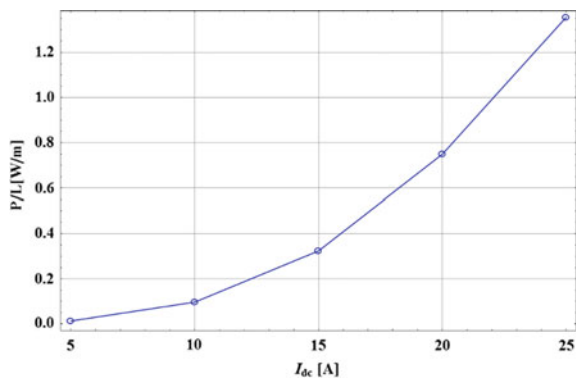


**Fig. 7** Model generator both of whose stator and rotor designed from superconducting coils. The model generator consists of 16 slots with 12 poles. Rotating rotor coils carry DC current and the stator coils are subject to the time varying AC current

DC current. This provides both the adjustment of the applied magnetic field and supplying the stronger magnetic field. In Fig. 7, a two-dimensional cross-sectional view of the fully superconducting generator is given. The rotor coils lie in the  $xy$ -plane and a constant DC current is passed in the  $z$ -direction. Likewise, an AC current is induced in the  $z$ -direction when the stator coils are in the  $xy$ -plane.

In order to create a magnetic circuit in both the stator and rotor of the generator, ferromagnetic iron with  $B(H)$  curve shown in Fig. 8 is used and the conductivity of the material is taken as zero. The part forming the core of the generator is thought to be made of aluminium. The geometric and physical parameters of the generator is given in Table 2. In order to facilitate the calculations, as in the previous section, the discrete structure of the coils are disregarded due to the wrapped tapes. However, for convenience, 1/4 part of the generator is taken into account to reflect the periodic

**Fig. 8** Calculated loss as a function of DA applied in the generator





structure. The nonlinear effect in the ferromagnetic part and the supercurrent is taken into account. The expressions given in Eqs. 15 and 16 are used for the area and angle dependence of the induced current. The width of the HTS coils is taken as approximately 4 mm and the critical current density was 100 A. The substrate magnetism of such commercial superconducting tapes is not considered. The number of the turns of rotor coils is considered as twice that of the stator coils in order to produce a stronger magnetic field. The rotor iron gears are adjusted to be compatible with the width of the area where the stator coils were placed so that they could complete the magnetic circuit. In this way, a better cooling system would be designed for the rotor coils. The expressions given in Eqs. 5 and 6 were used as boundary conditions. With a different meshing technique, free quad latticing was used for both rotor and stator, and calculations were made for 72,548 elements in the calculation sector.

The alternative current (AC) losses in the stator coils against DC current amplitude transported to the rotor coils are demonstrated in Fig. 8. In the calculations, Ampere's equation given by Eq. 1 was solved by using the non-linear conductivity relation given by Eq. 7. Alternative current losses out of the whole coil cross section are evaluated by,

$$P = \frac{1}{T} \int_T^{2T} dt \iint J E dS \quad (17)$$

here,  $T$  is the period of evolution and  $dS$  surface element for one cycle.

In Fig. 8, the AC loss increases with a quadratic dependence as a function of DC current magnitude. This can be expected. Because the increase in current causes the superconducting coils to be exposed to more magnetic fields and more current goes to the stator coils. Briefly, the induced current is a result of  $\propto B_r^2$  the magnetic field created in the air gap. The losses arising from the first application of DC in the rotor were ignored.

For better analysis, it is necessary to examine the magnetic field distributions on the generator. Figure 9 shows the magnetic field distributions in the superconducting generator body in two dimensions. In the figure, the magnetic fields in the rotor and stator form a perfect magnetic coupling. For example, the maximum magnetic field value at a point on the coils is 0.38 T for  $I_{dc} = 25$  A, and the maximum magnetic field value at a point where the rotor and stator gear intersect is around 1.1 T. It is seen that significant eddy currents may be induced in the rotor and stator materials of the generator and lead to additional losses. Such a high field can also give rise to magnetically saturate the stator and rotor irons. In this case, it may not be necessary to use iron in the rotor and stator for the high DC of the fully superconducting generator. However, as it gets closer to the outer envelope, the magnetic field value decreases up to 0.11 T. The magnetic field on the outer stator iron shows a homogeneous distribution. When  $I_{dc} = 5$  A is examined, the magnetic field value at either edge of the superconducting coil is around 0.17 T, and the value in the area between the

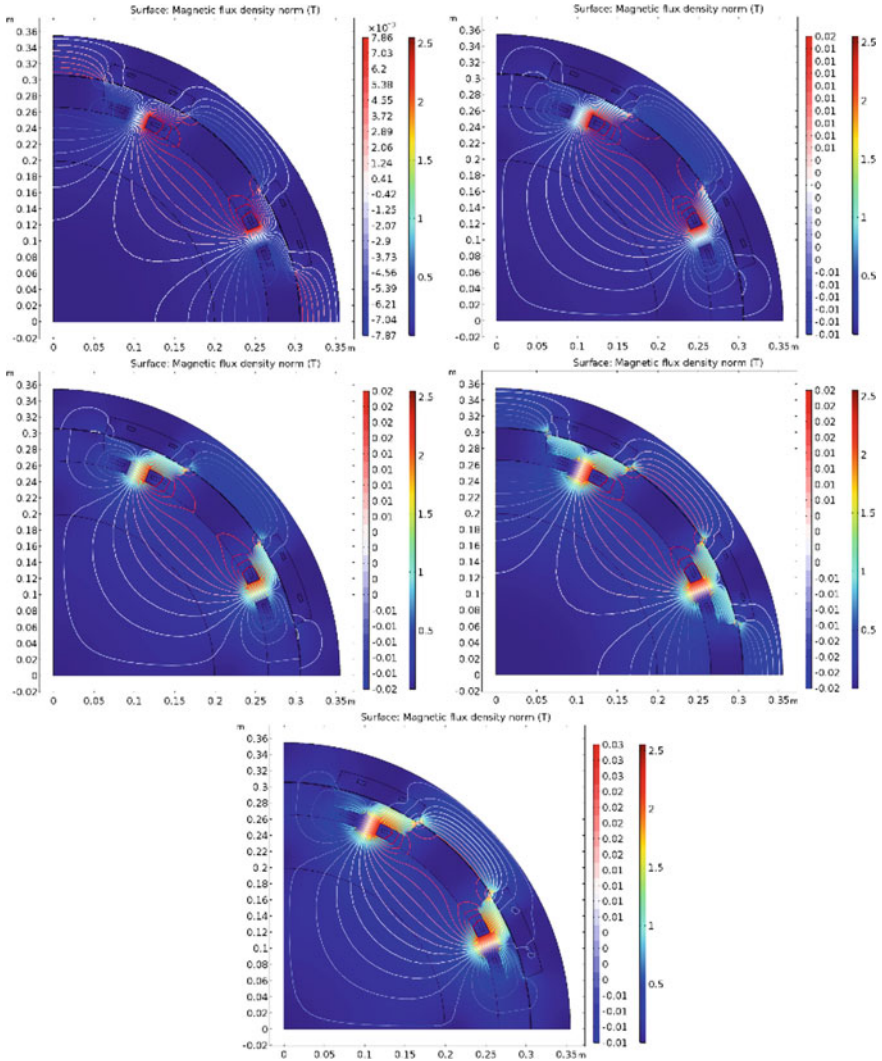


**Fig. 9** The distribution of Magnetic field on the instantaneous generator  $t = T/4$  applied to the stator coils with  $\omega = 90$  rpm velocity for  $I_{DC} = 5, 10, 15, 20, 25$  A

rotor and stator is around 0.54 T. This explains why losses increase with a quadratic correlation.

Figure 10 shows the current distributions in the stator coils for the selected DC current values. Current distributions are consistent with Ref. [34]. The current in the stator coils penetrates more on the right and left sides than in the rotor electromagnets. For  $I_{DC} = 25$  A, the current penetration at the right and left outer edges is approximately three times greater than at the facing edges of the coils. This means

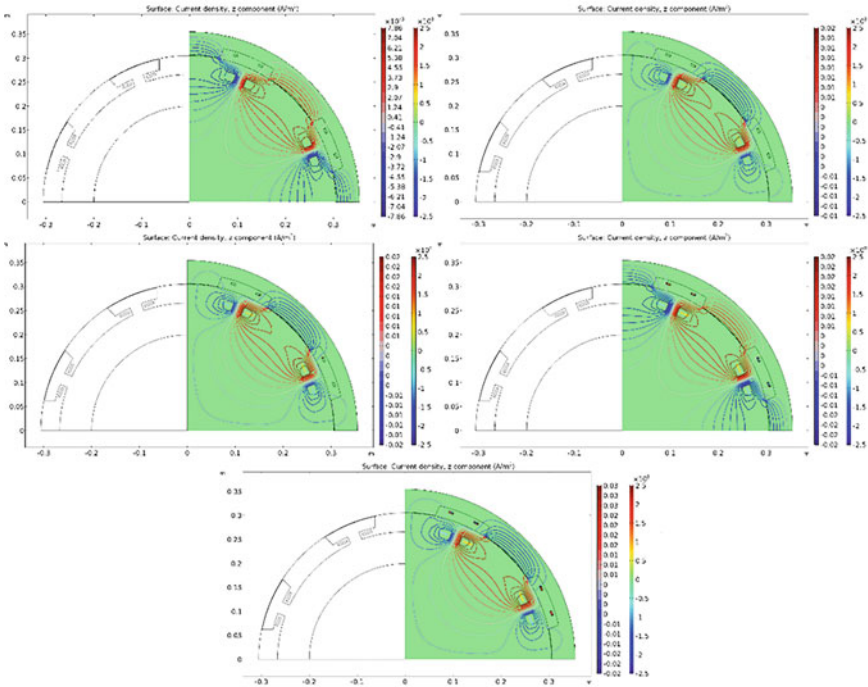


**Fig. 10** The Magnetic field and current distributions on the instantaneous generator  $t = T/4$  applied to the stator coils with  $\omega = 90\text{ rpm}$  velocity for  $I_{DC} = 5, 10, 15, 20, 25\text{ A}$

that the loss will be higher in these areas than others. Therefore, the coolant to be flowed in these areas must have a higher velocity. In addition, as the density of the current flowing in the rotor coils is increased, the penetration of the induced current in the stator also increases. Therefore, this is an important factor that increases the AC losses of stator coils.

### 3.1 Electromagnetic Analysis of Synchronous Generators in the Order of MW, Whose Rotor Consists of Permanent Magnets and Stator Windings of Superconducting Coils

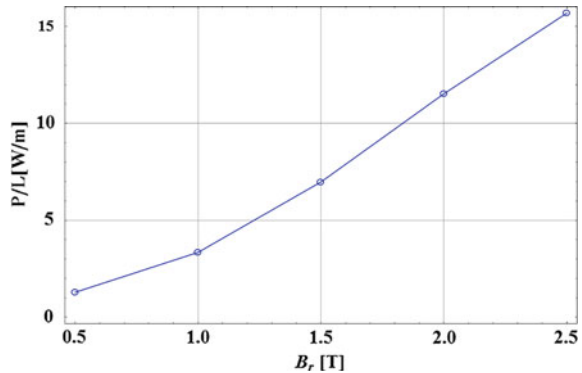
Electromagnetic analyses of the MW order superconducting generator are carried out by means of simulation method based on A-V formulation. The rotor of the generator consists of permanent magnets placed in such a way as to produce a total magnetic field in and out directions. The stator, on the other hand, consists of 36 pancake-shaped coils with 72 slots and wrapped with HTS coated conductors. The generator is considered to produce approximately 3 MW of outcome power. There is

**Table 3** Parameters of the generator model used in the calculations

Parameters (Unit)	Definition	Value
$R_{sd}$ (mm)	Outer radius of stator	1080
$R_{st}$ (mm)	Inner radius of stator	920
$R_{rd}$ (mm)	Outer radius of rotor	872
$R_{ri}$ (mm)	Inner radius of rotor	792
$D_{ag}$ (mm)	Air gap distance	48
$L$ (mm)	Length of generator	500
$p$	The number of poles of the generator	78
$s$	The number of slots of the generator	72
$B_{rem}$ (T)	The magnetic field strength of permanent magnet	0.5, 1, ..., 3
$\omega$ (rpm)	The angular velocity of generator	16
$I_c$ (A)	The critical current density of the tape	300
$w_{sc}$ (mm)	The width of the tape	12
$h_{sc}$ ( $\mu\text{m}$ )	The thickness of the tape	100
$E_c$ (V/m)	Electric field criteria	$1 \times 10^{-4}$
$n$	Power-law exponent	21
$N_s$	The number of turn of stator coils	100

a large air gap between the rotor and the stator. The stator and rotor are supported by ferromagnetic iron. The physical and geometric parameters of the generator are given in Table 3. Ferromagnetic and eddy current losses in the rotor and stator parts are neglected. Calculations are carried out in 2D, the cross-sectional area of the generator is placed in the  $xy$ -plane and current is induced in  $z$ -plane, the HSS pancake coils in the  $xy$ -direction. For the electromagnetic analysis of the superconducting coils, Eq. (1) considering nonlinear EJ such as Eq. (1) are solved. Likewise, in order to shorten the calculation time, the discrete structure of the coils is ignored and symmetrical structure of the machine is exploited. The expressions given by Eqs. 5 and 6 are employed as boundary conditions. For the meshing, the edge method was used at the right and left ends of the sector, and the source and the destination are determined according to the generator rotation direction, such as in here anti-clockwise. Free triangular meshing is adopted for the superconducting turns. The rotor and stator are particularly densely meshed. In total, 53,752 mesh elements are resulted in. A direct MUMPS solver is selected, with relative and absolute tolerance can be taken as  $10^{-10}$  and  $10^{-12}$  respectively. It should be noted that for the method based on the A-V formulation, the tolerances below this value do not reflect the characteristics in the superconducting region quite well. In addition, the magnetic field and angle dependence of the superconducting strips are included in the calculations combining Eqs. 15 and 16. The tape properties used in the simulations are provided by the SuperOX company and are determined as (SuperOx) [35]. The angle dependence of the magnetic field orientation for particularly these kind of tapes is relatively low. In the ferromagnetic part, nonlinear BH curve given in Fig. 1 for lossless steel

**Fig. 11** The evaluated losses in the only one stator coils for different values of the magnetic field strength or rotor magnet,  $\omega = 16$  rpm

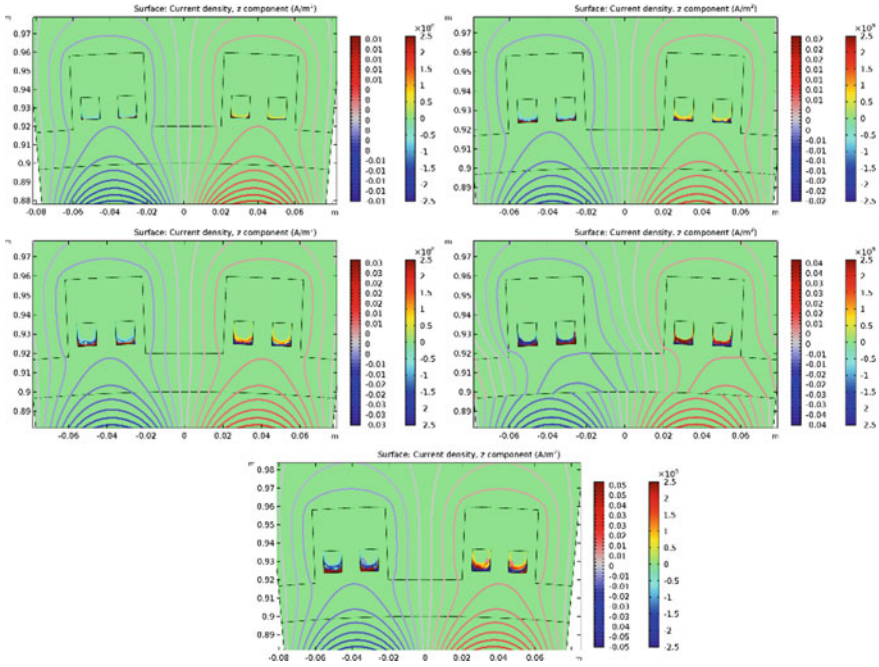


is taken into account. The ferromagnetic part and the Cu stabilizer in the structure of the tapes are neglected.

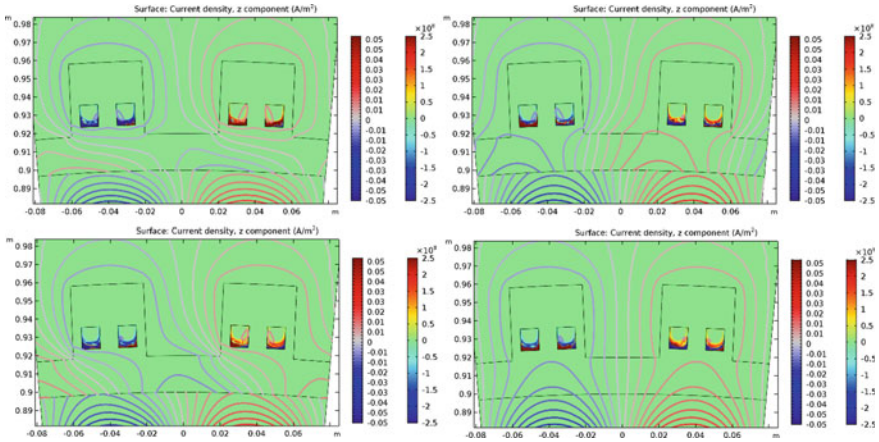
In Fig. 11, the computed losses as a function of the magnetic field strength of rotor magnets are displayed for constant rotor speed. AC losses are calculated over the cross-sectional area of the coils using Eq. 17. As is expected, the losses increase linearly with the magnetic field strength of the magnet. The increase in the magnetic field in the rotor magnet increases the strength of the magnetic field in the gap region between the rotor and the stator, which causes the induced current to penetrate deeper into the lower and upper parts of the strips, thus increasing the loss.

Figure 12 shows the induced superconducting current in the coils for different magnetic field intensities and the magnetic field distribution over the generator cross-sectional area. Here, as the magnetic field generated by magnet increases, the amount of induced current and the depth of penetration increase, so the losses also increase. In addition, the current is not distributed homogeneously over the cross-sectional area of the coils, but rather accumulates at the close edges to the magnets. This may be due to the fact that the radial component  $B_r$  of the magnetic field on the surface of the coils is higher than the tangential component,  $B_t$ . This is an important result because the ferromagnetic part in the stator serves as magnetic circuit, but does not cause current induction at the top of the coils by reducing the radial component of the magnetic field.

In Fig. 13, the magnetic field intensities of the magnet is chosen constant and the induced current and magnetic field distributions in the stator coils for different times are indicated. As can be seen from the figure, the current distributions in the coils are extremely complex. This is due to both the rotational motion and the complexity of the current distribution in the ferromagnetic part. Another result that can be deduced from the figure; Coils 1 to 3, 2 to 4 are coupled. In other words, the current is induced in coil 4 and completes its circuit over coil 2. Another important point here is that the supercurrents induced in the coils try to suppress the magnetic field produced by the rotor magnets. The reason can be clarified that the current prefers to flow in the parts of the coil radially closer to the magnet.



**Fig. 12** Induced current in superconducting coils for selected magnetic field intensities of rotor magnet at a quarter-cycle rotation of generator section. The contours represent magnetic vector potential plots that represent the magnetic field. This figure imply **a**  $B_{rem} = 0.5 T$ , **b**  $B_{rem} = 1 T$ , **c**  $B_{rem} = 1.5 T$ , **d**  $B_{rem} = 2 T$ , **e**  $B_{rem} = 2.5 T$ ,  $\omega = 16 \text{ rpm}$



**Fig. 13** The induced current distribution in the stator coils as the surface plot and the magnetic vector potential distributions around it (contours). Here is the time instantaneous taken for one full revolution of its rotor for **a**  $t = T/4$ , **b**  $t = T/2$ , **c**  $t = 3T/4$  ve **d**  $T = 4 \omega = 16 \text{ rpm}$  and  $B_r = 2.5 T$

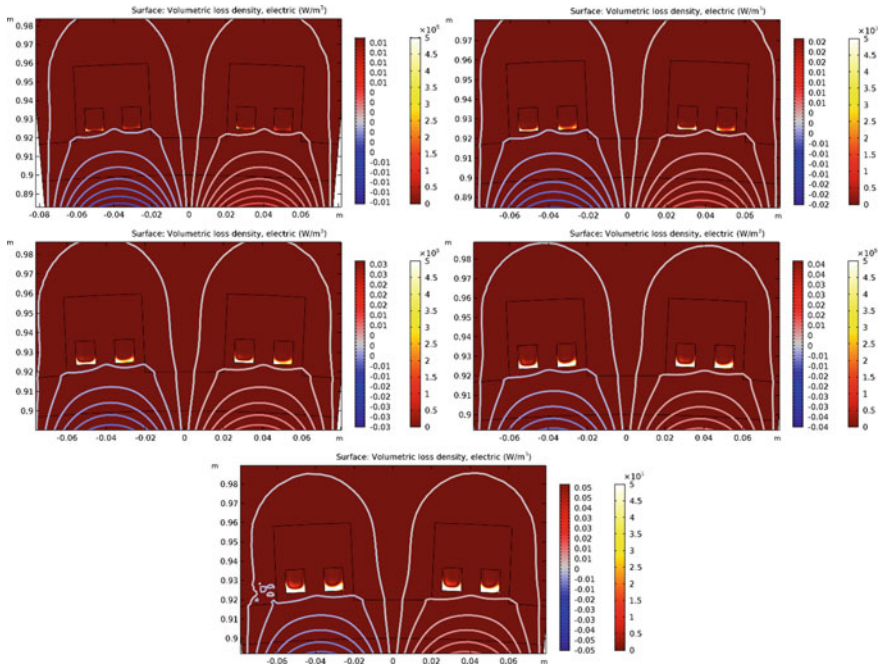


**Fig. 14** Instantaneous losses of superconducting coils in generator cross section for different magnetic field intensities of magnets: **a**  $B_{rem} = 0.5\text{ T}$ , **b**  $B_{rem} = 1\text{ T}$ , **c**  $B_{rem} = 1.5\text{ T}$ , **d**  $B_{rem} = 2\text{ T}$ , **e**  $B_{rem} = 2.5\text{ T}$  for  $\omega = 16\text{ rpm}$  and the instantaneous loss calculated by surface integral  $Q = \iint J E ds [W/m^3]$

In Fig. 14 demonstrates 2D view of the instant loss occurring in the stator coils for different magnetic field amplitudes, when the generator takes half a turn. We intend to show which region of the coils the losses occur the most. In the figure, as the magnetic field strength generated by the magnet raised, the amount of induced current and the size of the region where the current will penetrate, thus the loss enhanced as expected. Another important finding is that the losses occur mostly in the parts of the stator coils facing the rotor directly. The instantaneous loss in the radially inward side is on average 1500 times greater than the loss in the outward facing portion. This is because the current is rather induced and flows in this region. It is also seen in Fig. 14 that the normal component of the magnetic field is much larger than the tangential component in the radial inner region where the loss is very large. This comes into play as a factor that increases the losses. There are two technically worthy results here. First, in the cooling part of the generator, whose stator is made of superconducting coils, especially the part without ferromagnetic substrate should be cooled better, that is, in the cooling design, especially the part of the stator facing the rotor should be made it flow with liquid nitrogen. Another result is that the preferred ferromagnetic material for the magnetic circuit should be chosen very carefully. Because, while these materials do not directly contribute to

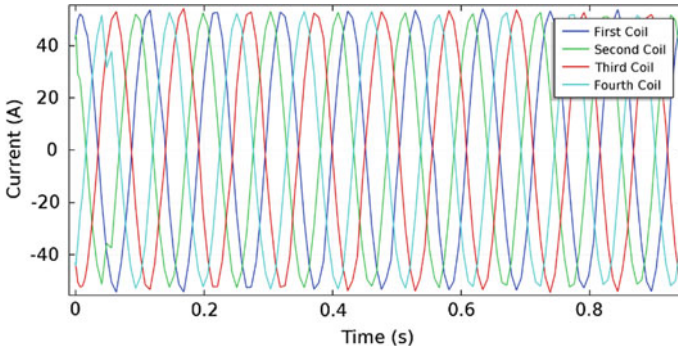


**Fig. 15** The currents in each coil forming the stator coils,  $B_{rem} = 1$  T and  $\omega = 16$  rpm

current induction, they may have additional contributions to the loss as a result of the eddy current losses they will create.

Figure 15 shows the induced currents in each of the turn constituting the stator coils. The currents vary in a sinusoidally without breaking into their harmonics, and in each of them a current of amplitude is induced. It is necessary to multiply the total current induced in the coils by the number of turns. The designed generator shown in the figure is three-phase.

### 3.2 Thermal Analysis of MW Order Superconducting Synchronous Generators

Thermal analyses of the designed generator were carried out. For this purpose, the results in the previous section were used. However, unlike in this section, it is assumed that there is liquid nitrogen around the stator coils and that it does not flow and the velocity field is zero. For the thermal analysis of the superconductor generator, the heat conduction equation and Ampere's equation are self-consistently solved containing the nonlinear conductivity term of the superconducting part. Likewise, for ease of calculation, the continuity of the coils is assumed and only the part of the generator is considered. We solve that the thermal conduction time dependent partial differential equation is,

$$\nabla \cdot (\kappa \nabla T) + Q = \rho C_p \frac{\partial T}{\partial t} \quad (18)$$

where  $\kappa$  is the thermal conductivity coefficient of the material,  $\rho$  is the density of the material,  $C_p$  is its specific heat under constant pressure and the loss is calculated using  $Q = \iint J E ds [W/m^3]$ . The values of materials such as ferromagnetic, magnet and liquid nitrogen used in the generator are given in Table 4.



**Table 4** Parameters adopted in thermal analysis

Parameters (Unit)	Liquid nitrogen	Iron	Magnet
$\kappa(W/m \cdot K)$	0.02583	50.2	50.2
$\rho(kg/m^3)$	1.25	7840	7840
$C_p(J/kg \cdot K)$	1040	502.414	502.414

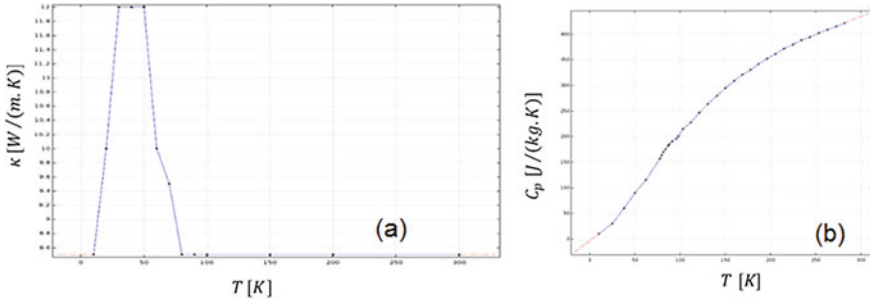


**Fig. 16** Variation of **a** thermal conductivity,  $\kappa$  and **b** specific heat under constant pressure  $C_p$  values of YBCO tapes adopted in calculations with temperature

The values for thermal conductivity and specific heat for coated conductor constituting the superconducting coils instead of constant value is indicted by Fig. 16. The density of YBO coated conductor is taken as  $\rho = 6.3 \times 10^3 \text{ kg/m}^3$ . In Fig. 17, 2D temperature distributions of magnets calculated according to different magnetic field strength of rotor magnet are demonstrated. Here, as the magnetic field produced by

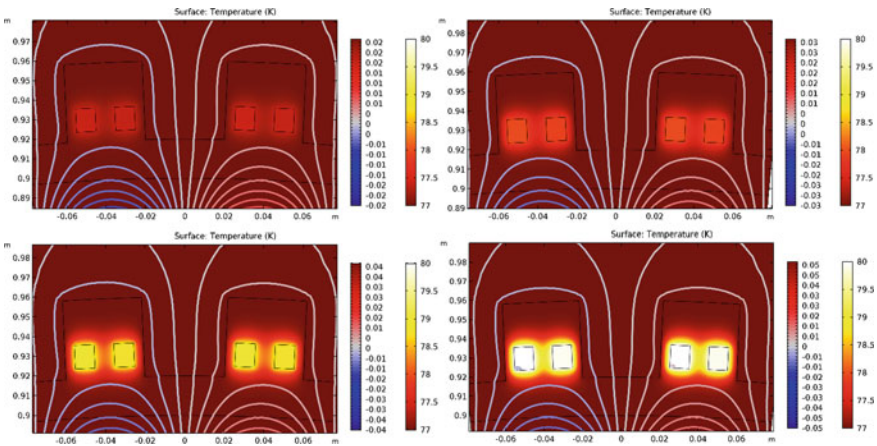


**Fig. 17** Temperature distribution of superconducting coils in generator cross section for different magnetic field intensities of magnets: **a**  $B_{rem} = 0.5 \text{ T}$ , **b**  $B_{rem} = 1 \text{ T}$ , **c**  $B_{rem} = 1.5 \text{ T}$ , **d**  $B_{rem} = 2 \text{ T}$ , **e**  $B_{rem} = 2.5 \text{ T}$ , for  $\omega = 16 \text{ rpm}$ ,  $t = T/2s$

the magnet increases, the temperatures arising in the coils also increase. The temperature of both the coils and the liquid nitrogen around them is highly dependent on the strength of the magnetic field produced in the magnet. Here, the temperature is also distributed homogeneously on the coils. This is important for the stability of the system. It is assumed that the area where the liquid nitrogen circulates and the other parts are perfectly insulated, and there is no heat transfer between the regions. In Fig. 17, it is seen that the temperature changes bring about mostly around the coils. Therefore, it may be technically important to adjust the velocity field of the liquid nitrogen circulating around the coils. In terms of selected parameters, the temperature shows an average increase of 0.5 K.

The temperature variation taking place at any point on the stator coils of the selected generator topology in Fig. 18 are given as a function of time for different magnetic field strength fields. Here, the temperature on the coils increases exponentially and becomes stable towards a certain value. When the generator first starts to rotate, the temperature increases very rapidly. We conclude that this situation may cause due to magnetic instabilities in the generator at the initial rotation.

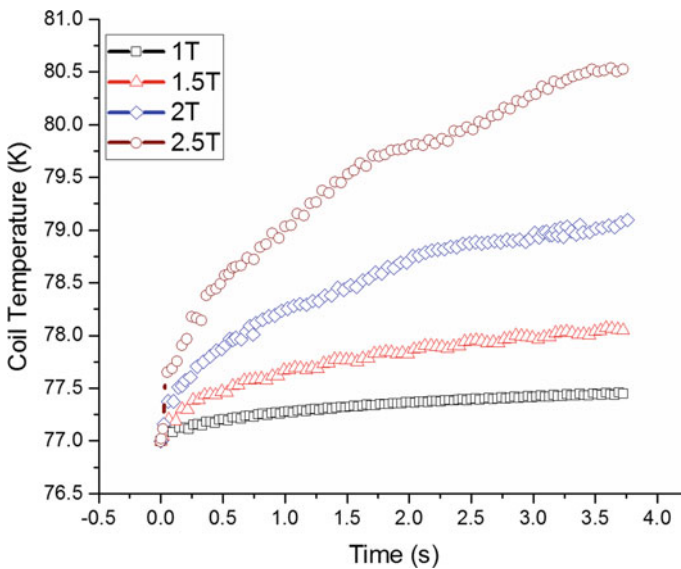


**Fig. 18** The variation of the temperature in the stator coils with time for different rotor magnet field remnant magnetic field of the MW order synchronous generator

### 3.3 *Magneto-mechanical Analysis of Superconducting Model Generators*

Since the superconducting generators are exposed to a high magnetic field and can carry high currents in the stator coils, enormous amounts of structural forces are created in the coils and transfers it to the body of the generator. These forces can cause deformation, especially in the coils of the generator. Therefore, careful calculation of structural forces is required. In this part of the chapter, the structural stress in generators is studied. For this purpose, the method developed in the previous parts of the chapter to examine the stress in the stack structures was applied to semi-superconductor generators.

First of all, the model generator topology given in the previous section was used in the infrastructure of the modelling. In this topology, instead of calculating the entire generator, only a certain section is calculated as two dimensions. Likewise, superconducting pancake coils are placed in the stator part of the generator and super current is induced in the stator by the rotating rotor. For the magneto-mechanical analysis, first of all, it is necessary to obtain the correct solutions of the Ampere equation. Therefore, Eqs. 1–7 is solved self-consistently with the mechanical equilibrium equation. The outline of the developed method can be found in the first section of this chapter. However, here, some clues should be given in order for the calculation to work stable and to give accurate results. Firstly, when dissolving the electromagnetic part, the boundary conditions, the meshing and the solver settings are almost preserved. However, it is very important to enter the correct boundary conditions first when resolving the mechanical part. In the second stage, very densely meshing is required for both the superconducting coils and the back iron of the meshing parameters. Also, a number of tactics have been developed for meshing the slip axis between the rotating rotor and the stationary stator. The first tactic is to choose the minimum element length (minimum element size) at the boundary point where the rotor and stator are located, at a value such as rotor outer radius/2000 for rotor and stator, and stator radius/20000 for stator, respectively. Otherwise, structural forces cannot be transferred from one point to another. It has also been observed that the stator coils must be in the order of the minimum element length  $\sim 10^{-5}$ , i.e. very dense meshing is required. These values may vary according to the selected geometry. It has been concluded that direct solver do not give good results in the solver settings, so iterative solver can be selected. All this significantly increases computation times.

For the electro-mechanical analysis of generators, Ampere and mechanical equilibrium equations must be solved together. For this purpose, the time dependent partial differential equation for mechanical equilibrium can be written as,

$$\rho \frac{\partial^2 u}{\partial t^2} - \nabla \cdot \xi = F_L \quad (19)$$

where  $\rho$  is the density of the material,  $u$  is the displacement area,  $\xi$  is the induced stress and  $F_L$  is the Lorentz force created by the flux pinning. The Lorentz force is

simply calculated by  $F_L = \mathbf{J} \times \mathbf{B}$  in which the Ampere equation is employed to evaluate the current density  $\mathbf{J}$  and magnetic field  $\mathbf{B}$  inside HTS coils. In the cross-sectional area of the generator, the current flows in the  $z$ -direction and hence the Lorentz force disperses in the  $xy$ -direction. In order to compute the forces generated in the stator coils we employ,

$$\begin{aligned} F_x &= J_z B_y \\ F_y &= -J_z B_x \end{aligned} \quad (20)$$

The Lorentz force equation for the ferromagnetic back iron can be calculated with  $F_L = \mathbf{M} \nabla H$ . This give,

$$\begin{aligned} F_x &= \frac{\chi}{\mu_0 \mu_r^2} \left( \frac{\partial A_z}{\partial x} \frac{\partial^2 A_z}{\partial x^2} + \frac{\partial A_z}{\partial y} \frac{\partial^2 A_z}{\partial x \partial y} \right), \\ F_y &= \frac{\chi}{\mu_0 \mu_r^2} \left( \frac{\partial A_z}{\partial x} \frac{\partial^2 A_z}{\partial x \partial y} + \frac{\partial A_z}{\partial y} \frac{\partial^2 A_z}{\partial y^2} \right) \end{aligned} \quad (21)$$

Here,  $\chi$  is the magnetic susceptibility of the material,  $\mu_0$  is the magnetic permeability of vacuum. boşluğun geçirgenliği and  $\mu_r$  is the relative magnetic permeability of the material.

Figures 19 and 20 show the  $x$ -component of magnetic internal stress in the stator coils and back iron of the generator for different magnetic field amplitudes,  $\xi_x$  and its  $y$ -component  $\xi_y$ , respectively. The figures are drawn instantly corresponding to

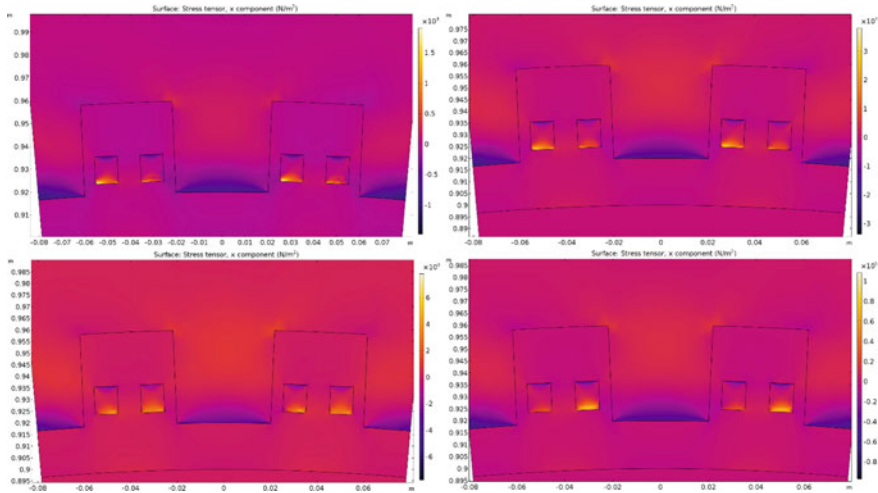


**Fig. 19**  $x$ -component of magnetic stress  $\xi_x$  calculated for different remnant fields of the rotor magnet Rotor mıknatısı tarafından üretilen manyetik alan, **a**  $B_{rem} = 0.5$  T, **b**  $B_{rem} = 1$  T, **c**  $B_{rem} = 1.5$  T, **d**  $B_{rem} = 2$  T, **e**  $B_{rem} = 2.5$  T for  $\omega = 16$  rpm,  $t = T/2$  s

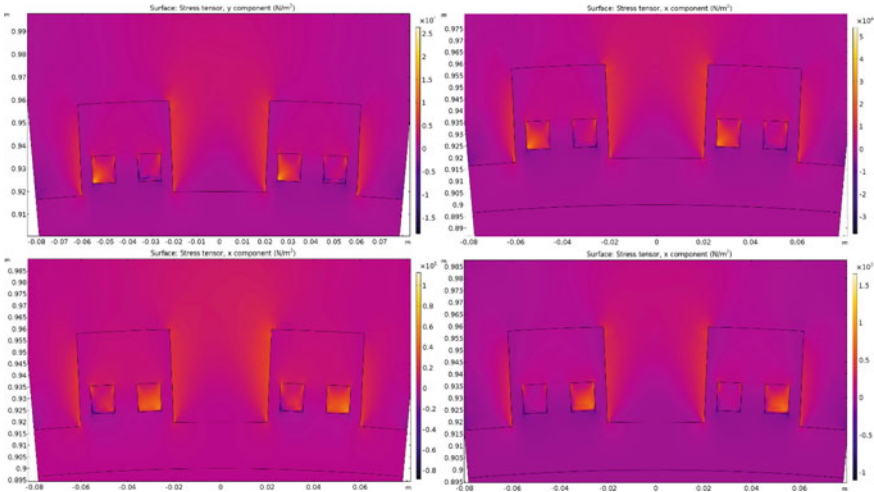


**Fig. 20**  $y$ -component of magnetic stress  $\xi_y$  computed for different remnant fields of the rotor magnet Rotor mknatısı tarafından üretilen manyetik alan **a**  $B_{rem} = 0.5$  T, **b**  $B_{rem} = 1$  T, **c**  $B_{rem} = 1.5$  T, **d**  $B_{rem} = 2$  T, **e**  $B_{rem} = 2.5$  T, for  $\omega = 16$  rpm,  $t = T/2$  s

the situation where the generator is rotated a quarter  $t = T/4$ , in here the period  $T$  indicates the time covered the full rotation. The striking conclusion at first glance is that as the magnetic field strength increases, the stress and its components increase in proportion to its square. This is an expected result, because it is  $\xi_x \propto B_x^2$  and  $\xi_y \propto B_y^2$  [36]. The rotating magnetic field exposed by the rotor induces the large current in the stator coils and this current causes internal stress by interacting its self field. As can be seen in the figure, the  $x$ -component of the stress is higher especially in the region where the current is penetrate deeper (Fig. 19). Another important point is the formation of an expansive stress on the radially inner surfaces of the pancakes and a compressive stress on the radially inner surfaces of the pancakes (Fig. 19). These stresses can primarily cause the coils to move inwards and outwards. Therefore, these regions must be supported with a support that can resist the stresses. In Fig. 20, it is seen that these stresses take place in the lateral directions.

In Figs. 21 and 22, the angular velocity and the remnant magnetic field of the rotating part of generator are kept constant at  $\omega = 16$  rpm and  $B_r = 1.0$  T, respectively, and the  $x$ - and  $y$ -components of the stress appearing at different times are given in 2D. As it is clear from the figures, since the currents flow in the same amount and in opposite directions from coils 1 and 3, the stresses in this coil pair are the same. The same is true for coil pairs 2–4. However, due to the phase difference between the induced currents between 1–3 and 2–4, the tension in these two coil pairs is different from each other. As the rotor rotates, the tension in the coils increases and decreases. However, it does not change direction in any way. This calculation is due to the large number of poles of the model generator. Since the number of poles is high, the generator is exposed is around 20 Hz with respect to the synchronous frequency

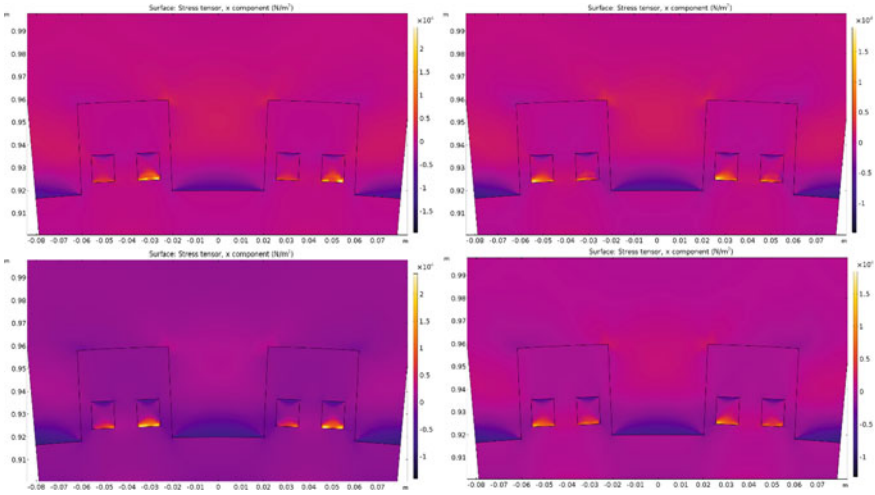


**Fig. 21** The  $x$  component of the magneto stress  $\xi_x$  for the different rotor positions at **a**  $t = T/4$ , **b**  $t = T/2$ , **c**  $t = 3T/4$ , **d**  $t = T$ , the period of rotor  $T$  means time elapsed one full round of the rotor.  $B_{rem} = 1.0$  T and  $\omega = 16$  rpm

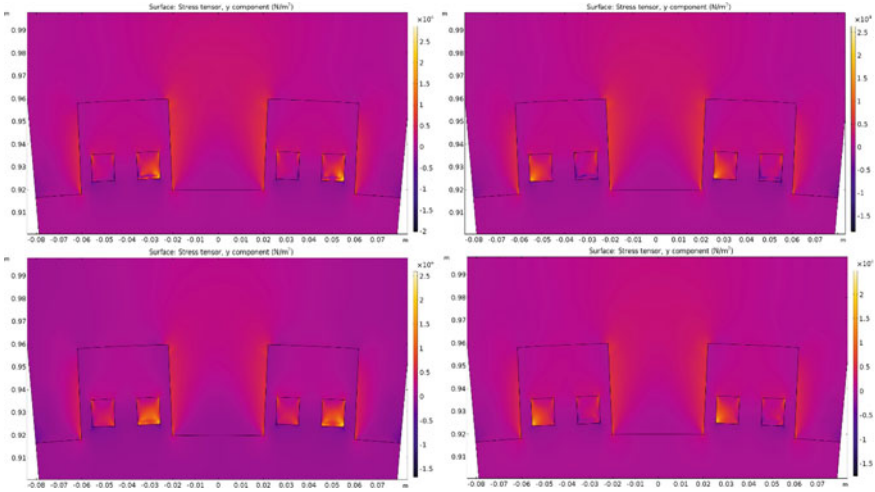


**Fig. 22** The  $y$  component of the magneto stress  $\xi_y$  for the different rotor positions at **a**  $t = T/4$ , **b**  $t = T/2$ , **c**  $t = 3T/4$ , **d**  $t = T$ , the period of the rotor  $T$  means time elapsed one full round of the rotor.  $B_{rem} = 1.0$  T and  $\omega = 16$  rpm

of the magnetic field,  $f = \omega p/60$ . In this case, the magnetic field penetrating the coils changes very rapidly. As a result of this change, there is a significant change in  $x$ -component of the stress,  $\xi_x$ . However, the situation is quite different for the strain component.

In order to study the stress in the back iron, the structural forces are calculated from Eq. 21. The stress is computed by solving the Ampere-the Mechanical Equilibrium equation in the same way. As can be seen from the Fig. 22, especially the electro-mechanical stress in the back iron affected by the eddy current owing to the changing magnetic field and the rotating magnetic field and the eddy current causes an expanding stress in the radially inner parts as expected. What is interesting here is the source of the compressive stress, especially at the sharp edges of the slots where the coils are placed. This situation suggests that there may be a tension arising from the interaction of eddy currents, especially in the back iron, with the magnetic field. However, the value of this stress is quite low and not appreciable. Stress in the ferromagnetic region is generally Hoop stress due to its circular structure and is easier to eliminate. To cope with these stresses, it will be sufficient to use a thicker iron block. However, since these stresses are well below the permissible limits for iron, no additional precautions may be necessary.

As the rotor rotates, the magnetic field both its direction and its intensity of magnetic stresses changes depending of rotor positions (Fig. 22). This may be due to the fact that the radial component of the magnetic field produced in the rotor of the designed generator is higher than the tangential component. Since the radial component of the magnetic field in the air gap  $B_{gap}$  is considerably higher than its tangential component, consequently  $y$ -component of the stress  $\xi_y$  is approximately 20% higher than  $\xi_x$ . This is a remarkable result. Another important point that obtained as a result of the simulations is that both  $\xi_x$  and  $\xi_y$  is not distributed homogeneously over the entire coil surfaces. This situation, above all, complicates the stress analysis. However, it is particularly important that if the stress is not distributed homogeneously, it can cause very serious irreversible deformation within the coils. For the analysis of this, the maximum allowable stress values of the superconducting tapes are below the values of the calculated stress [37, 38].

However, it should be noted that, since the two-dimensional analysis is performed here, the mechanical stress caused by the winding of the coils and the thermal stress arising from the cooling of the coils are not taken into account. When this stress is added, the stress on the coils can lead to permanent deformation. However, it should not be forgotten that the electro-mechanical stress for coils exposed to the magnetic field is considerably higher than the thermal and mechanical stress. However, this electro-mechanical strain can lead to a decrease in the critical current density.

Figure 23 shows the components the stress generated on the superconducting generator for different rotor speeds. The angular speed of the rotor is doubled starting from 16 rpm and simulated. The important point in the figure is that as you go from low angular velocities to high velocities, there is an increase  $x$ -component of the stress  $\xi_y$  initially, but there is no significant change in its  $y$ -component  $\xi_y$ . This may be because, in the same way, the tangential component of the magnetic field is more

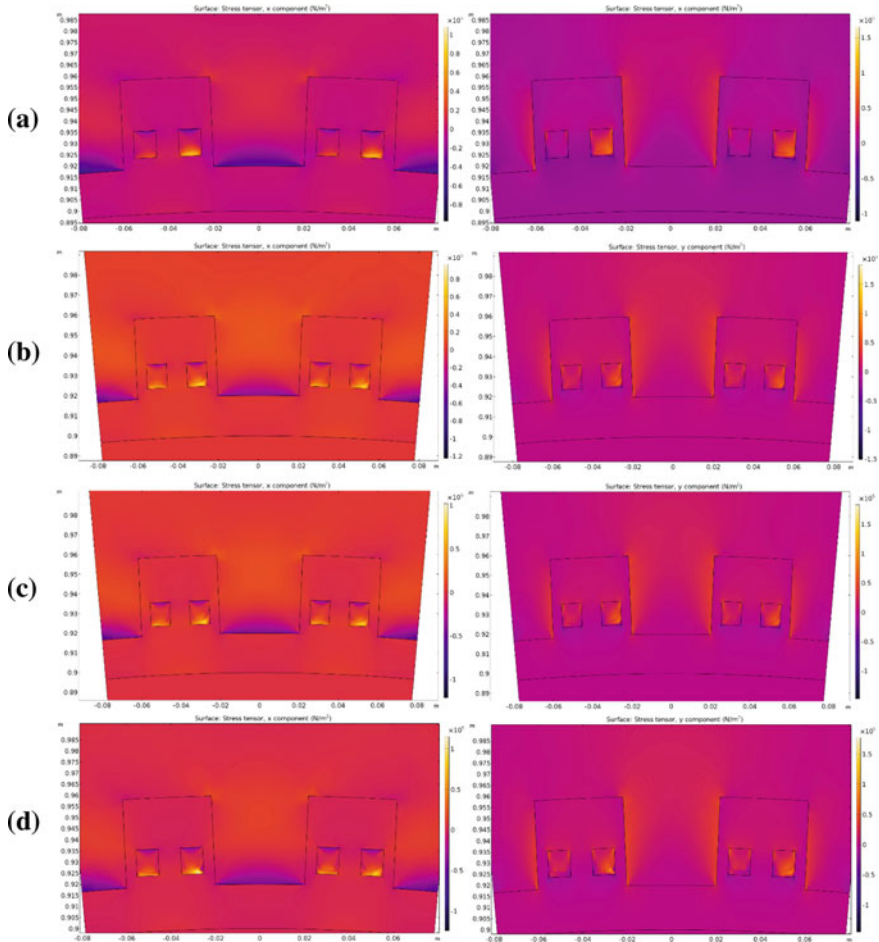


**Fig. 23** The x-component  $\xi_x$  (the left) and y-component  $\xi_y$  (the right) of the induced stress for various rotor speed **a**  $\omega = 16$  rpm, **b**  $\omega = 32$  rpm, **c**  $\omega = 48$  rpm, **d**  $\omega = 64$  rpm by selecting  $B_{rem} = 1.0$  T and  $t = T/4$  s

dominant at low speeds. The development of stresses for each state and the points at which the maximum stress occurs are almost identical.

### 4 Conclusion

The conceptual design of the model superconducting synchronous generators and the calculation of AC losses were performed with three new simulation methods in 2D: the method based on the  $A - V$  formulation based on the solving Ampere Equation



of Maxwell equations, the hybrid method in which the  $A - V + H$  formulations, in which the H formulation solves. The Farady Equation of the Maxwell Equations, are used together, and the method in which the critical current density restricted the  $\tanh(J)$  form is applied on the  $A - V$  formulation. It has been shown that induced currents, magnetic field distributions and losses for different rotational speeds can be calculated separately by these three methods. It was seen that the result of the hybrid method in which A-V and H-formulation are used together is more reliable, but the results of the  $A - V + \tanh(J)$  method are both very fast and (in a three times shorter compared to the hybrid method) the results are within reliable limits. AC losses are analyzed for different magnetic field values of the rotor magnets under a constant rotation speed for different generator designs. The AC loss distributions on each superconducting coil in the generator structure were evaluated for different magnetic field densities of the magnets. It has been concluded that the losses occurring in the radially inward section are on average 1500 times higher than the losses in the outward facing section, and the reason for this is that the current is rather induced and flows in this region. By using the simulation method based on the  $AV$  formulation, it is clearly demonstrated that it can also be used in the design of full superconducting generators and generators producing high power.

The thermal analysis of the permanent magnet model superconductor synchronous generator, designed in 2 dimensions, by solving the A-V formulation and the thermal conductivity equation self-consistently, was also carried out. The instantaneous loss distributions in each superconducting coil in the generator structure for different magnetic field intensities under constant rotation speed were calculated and the temperature distributions in the environment were evaluated. It has been observed that the temperature on the superconducting coils in the generator structure increases exponentially and tends to form a plateau after a certain value.

Structural stress in 2D model superconductor generators is also investigated. The distributions of the radial and the circumferential stress, or hoop stress, components of the magnetic stress are displayed for the different magnetic field values produced by the rotor magnet. It has been evaluated that the stresses in the back iron is expanding radially in the inner parts as contracted, and this may result from the attraction of the iron by the magnet. It is thought that the compressive stress, especially on the sharp edges of the slots where the coils are placed, may be a stress arising from the interaction of the eddy currents in the tread iron with the magnetic field.

**Acknowledgements** The authors acknowledge the financial support of the Scientific and Technological Research Council of Turkey (TUBITAK) under the contract number 114F424.

## References

1. H.H. Woodson, Z.J.J. Stekly, E. Halas, A study of alternators with superconducting field windings: I. Analysis. *IEEE Trans. Power Appar. Syst.* **85**, 264–274 (1966)

2. T.A. Keim, Design and manufacture of 20 MVA superconducting generator. *IEEE Trans. Power Appar. Sys. PAS* **104**, 1475–1483 (1985)
3. T. Nitta, Progress of technology for superconducting generator. *Cryogenics* **42**, 151–155 (2002)
4. H. Rogalla, P.K. Kes (eds.), *100 years of Superconductivity*, 1st edn. (CRC Press, Boca Raton, FL, 2011)
5. B. Gamble, G. Snitcher, T. MacDonald, Full power test of a 36.5 MW HTS propulsion motor. *IEEE Trans. Appl. Supercond.* **21**(3), 1083–1088 (2011)
6. W. Nick, J. Grundmann, J. Frauenhofer, Test results from Siemens low speed, high-torque HTS machine and description of further steps towards commercialisation of HTS machines. *Physica C* **482**, 105–115 (2012)
7. C. Lewis, J. Muller, A direct drive wind turbine HTS generator. In: *IEEE Power Engineering Society General Meeting*, pp. 1–8 (2007). <https://doi.org/10.1109/PES.2007.386069>
8. G. Snitchler, B. Gamble, C. King, P. Winn, 10 MW class superconductor wind turbine generators. *IEEE Trans. Appl. Supercond.* **21**, 1089–1092 (2011). <https://doi.org/10.1109/TASC.2010.2100341>
9. H. Karmaker, E. Chen, W. Chen, G. Gao, Stator design concepts for an 8 MW direct drive superconducting wind generator. In: *XXth International Conference on Electrical Machines*, pp. 769–774 (2012). <https://doi.org/10.1109/ICEIMach.2012.6349962>
10. H. Karmaker, M. Ho, D. Kulkarni, Comparison between different design topologies for multi-megawatt direct drive wind generators using improved second generation high temperature superconductors. *IEEE Trans. Appl. Supercond.* **25**, 1–5 (2015). <https://doi.org/10.1109/TASC.2014.2375872>
11. H. Karmaker, E. Chen, Design concepts for a direct drive wind generator using new superconductors. In: *IEEE Electrical Power and Energy Conference (EPEC)*, London 2015, pp. 22–25 (2015). <https://doi.org/10.1109/EPEC.2015.7379921>
12. K.P. Thakur, M.P. Staines, L.S. Lakshmi, N.J. Long, Numerical computation of AC losses and flux profiles in high-aspect-ratio superconducting strips in perpendicular AC magnetic field. *IEEE Trans. Appl. Supercond.* **19**(6), 3770–3778 (2009). <https://doi.org/10.1109/TASC.2009.2025887>
13. R. Brambilla, F. Grilli, D. Nguyen, L. Martini, F. Sirois, AC losses in thin superconductors: the integral equation method applied to stacks and windings. *Supercond. Sci. Technol.* **22**, 075018 (2009)
14. W.K. Chan, P.J. Masson, C. Luongo, J. Schwartz, Three-dimensional micrometer-scale modeling of quenching in high-aspect-ratio coated conductor tapes—part I: model development and validation. *IEEE Trans. Appl. Supercond.* **20**(6), 2370–2380 (2010)
15. K. Takeuchi, N. Amemiya, T. Nakamura, O. Maruyama, T. Ohkuma, Model for electromagnetic field analysis of superconducting power transmission cable comprising spiraled coated conductors. *Supercond. Sci. Technol.* **24**(8), 085014 (2011)
16. N. Amemiya, T. Tsukamoto, M. Nii, T. Komeda, T. Nakamura, Z. Jiang, *Supercond. Sci. Technol.* **27**, 035007 (2014)
17. J.R. Clem, J.H. Claassen, Y. Mawatari, *Supercond. Sci. Technol.* **20**, 1130–1139 (2007)
18. W.K. Chan, J. Schwartz, *IEEE Trans. Appl. Supercond.* **22**, 4706010 (2012)
19. V.M.R. Zermeno, A.B. Abrahamsen, N. Mijatovic, B.B. Jensen, M.P. Sørensen, Calculation of alternating current losses in stacks and coils made of second generation high temperature superconducting tapes for large scale applications. *J. Appl. Phys.* **114**(17), 173901 (2013)
20. E. Pardo, Calculation of AC loss in coated conductor coils with a large number of turns. *Supercond. Sci. Technol.* **26**, 105017 (2013)
21. L. Prigozhin, V. Sokolovsky, Computing AC losses in stacks of high-temperature superconducting tapes. *Supercond. Sci. Technol.* **24**, 075012 (2011)
22. C.P. Bean, Magnetization of high-field superconductors. *Rev. Mod. Phys.* **36**(1), 31–39 (1964)
23. Y.B. Kim, C.F. Hempstead, A. Srnrad, Magnetization and critical supercurrents. *Phys. Rev.* **129**(2), 528–535 (1963)
24. Y.B. Kim, C.F. Hempstead, A. Srnrad, Critical persistent currents in hard superconductors. *Phys. Rev. Lett.* **9**(7), 306–309 (1962)

25. V.M.R. Zermeno, N. Mijatovic, C. Træholt, T. Zirngibl, E. Seiler, A.B. Abrahamsen, N.F. Pedersen, M. Sorensen, Towards faster FEM simulation of thin film superconductors: a multiscale approach. *IEEE Trans. Appl. Supercond.* **21**, 3273–3276 (2011)
26. J. Xia, H. Bai, J. Lu, A.V. Gavrilin, Y. Zhou, H.W. Weijers, Electromagnetic modeling of REBCO high field coils by the H-formulation. *Supercond. Sci. Technol.* **28**, 125004 (2015)
27. M.D. Ainslie, T.J. Flack, A.M. Campbell, Calculating transport AC losses in stacks of high temperature superconductor coated conductors with magnetic substrates using FEM. *Physica C Supercond.* **472**(1), 50–56 (2012)
28. M.D. Ainslie, W. Yuan, T.J. Flack, Numerical analysis of AC loss reduction in HTS superconducting coils using magnetic materials to divert flux. *IEEE Trans. Appl. Supercond.* **23**, 4700104 (2013)
29. L. Queval, V.M.R. Zermeno, F. Grilli, Numerical models for ac loss calculation in large-scale applications of HTS coated conductors. *Supercond. Sci. Technol.* **29**(2), 0244007 (2016)
30. F. Grilli, R. Brambilla, L. Martini, Modeling high-temperature superconducting tapes by means of edge finite elements. *IEEE Trans. Appl. Supercond.* **17**(2), 3155–3158 (2007)
31. F. Gömöry, M. Vojenèiak, E. Pardo, J. Šouc, Magnetic flux penetration and AC loss in a composite superconducting wire with ferromagnetic parts. *Supercond. Sci. Technol.* **22**(3), 034017 (2009)
32. F. Gömöry, J. Šouc, M. Vojenèiak, B. Klinèok, Phenomenological description of flux pinning in non-uniform high-temperature superconductors in magnetic fields lower than the self-field. *Supercond. Sci. Technol.* **20**(9), S271–S277 (2007)
33. D. Uglietti, H. Kitaguchi, S. Choi, T. Kiyosi, Angular dependence of critical current density in coated conductors at 4.2 K and magnet design. *IEEE Trans. Appl. Supercond.* **19**(3), 2909–2912 (2009)
34. Y. Li, F. Feng, Y. Li, P. Song, S. Zou, M. Wu, C. Gu, P. Zeng, T. Qu, Numerical study on AC loss characteristics of REBCO armature windings in a 15-kW class fully HTS generator. *IEEE Trans. Appl. Supercond.* **27**(4), 5200206 (2017)
35. <https://superoxjapan.com/about-en/>
36. M. Erdogan, S. Yildiz, A. Cicek, F. Inanir, Two-dimensional finite-element analysis of pinning-induced stress in HTS power transmission cables made of 2G superconducting tapes with and without magnetic substrate. *IEEE Trans. Appl. Supercond.* **26**(6), 8402407 (2016)
37. Y. Zhang, Mechanical and electromechanical properties of IBAD-MOCVD-based REBCO coated conductors. In: *International Workshop on Coated Conductors for Applications (CCA2014)*, December 1, 2014, Jeju, South Korea
38. Y. Zhang, D.W. Hazelton, H. Sakamoto, Irreversible tensile stress of 2G HTS wires made by IBAD-MOCVD on Hastelloy substrates. In: *Cryogenic Engineering Conference and International Cryogenic Materials Conference (CEC-ICMC2015)*, June 28–July 2, 2015, Tucson, AZ, USA

# RF and Microwave Applications of High Temperature Superconductors



Essia Hannachi and Yassine Slimani

**Abstract** Since the invention of superconducting oxide materials, tremendous advances have taken place in designing and controlling these materials to meet the requirements of specific applications. For example, the reasonably reproducible preparation of high-quality thin-film superconducting materials has spawned a wide range of prototype microwaves, some of which are already available on the market. This chapter introduces the up-to-date microwave properties of high-temperature superconductive materials. Certain examples of prototype apparatuses derived from superconducting technology will be reviewed. These devices involve filters, mixers, amplifiers transmission lines for microwave signals, and data processing circuits for high-speed digital and analog waveforms, antenna, detectors and mixers. Reflections are given on the long-term applications of superconducting microwave electronic devices. At the end of this chapter, an emphasis will be placed on the superconducting technology that should be advanced to introduce more practical radio frequency and microwave applications.

**Keywords** HTSC materials · Microwave · Radio frequency · Cryogeny · Microwave devices

## 1 Introduction

Microwave (MW) and radio frequencies (RF) are two engineering technologies that operate relatively the same trend. MW radiations are a subgroup of RF radiation and denotes electromagnetic signals with frequencies ranging between 300 MHz

---

E. Hannachi (✉)

Department of Nuclear Medicine Research, Institute for Research & Medical Consultations (IRMC), Imam Abdulrahman Bin Faisal University, P.O. Box 1982, Dammam 31441, Saudi Arabia  
e-mail: [hannechi.essia@gmail.com](mailto:hannechi.essia@gmail.com)

Y. Slimani

Department of Biophysics, Institute for Research & Medical Consultations (IRMC), Imam Abdulrahman Bin Faisal University, P.O. Box 1982, Dammam 31441, Saudi Arabia  
e-mail: [yaslimani@iau.edu.sa](mailto:yaslimani@iau.edu.sa); [slimaniyassine18@gmail.com](mailto:slimaniyassine18@gmail.com)

and 300 GHz. MW and RF bands have been broadly exploited for numerous military and industrial applications like communication and medical imaging systems, radar systems, and heating systems. The fast evolution of communication systems and the developing performance of spectrum sales have progressively imposed an effective practice of the restricted frequency spectrum, and through growing the number of subscribers the interfering between various systems might rise. Examples of communication systems involve direct TV satellite, cell phone and video systems, private communications systems, local wireless networks area, universal positioning systems and multi-point provincial distribution system.

Since Onnes's discovery of superconductivity (SC) in 1911, many attempts have been made to synthesize superconducting materials that have good performance allowing them to be exploited for many practical applications. Inventions and devices with superconductive materials have evolved more rapidly upon the discovery of superconductivity at high temperatures (HTSC). Since that time, the applications of these materials have arisen in diverse fields of communications, high-energy particle physics, engineering, microwave tools, medical and technical equipment [1–3]. HTSC materials are enviable for practice in microwave circuits owing to their ultra-low surface resistance ( $R_s$ ) compared to the good normal conducting metals. For example, at  $T = 77$  K, HTSC displays an SR value three times lesser than that of a copper surface at 1 GHz. This property led to microwave components with minimal input loss and pressurized resonant structures with unusually high-quality factors. Furthermore, significant advancement has been reached in the interim in the design, manufacture, and purposeful display of mono-microwave apparatuses and more complex subsystems, which greatly profit from the use of HTSC. The technology of microwave HTSC is one of the upward technologies for mobile communications like international mobile telecommunications and personal communication systems [4]. In microwave applications, HTSC provide revolutions in the functioning of their components. Also, the main aspects of superconducting technology including lightweight, tiny size, and better functioning are the key handlers in the manufacture of microwave devices. The viability of utilizing this technology to fabricate microwave apparatuses such as filters, antennas, couplers, delay lines, and resonators, etc. with higher functioning has been already established. Initially, scientific research has focused on problems of miniaturization and enhancement of communication system performance concerning choosiness, noise figures, and losses as the main benefits of HTSC apparatuses. Later on, researchers have directed their activities on preparing HTSC with satisfactory and reproductive quality on the one side, in addition to the problems of cryogenic cooling on the other side, as they are considered among the chief obstacles in the way of commercial applications of the HTSC systems. Extended researches were dedicated to the applications of HTSC in microwave and radio frequency systems [5–7] Prospective regulars have become conscious of talented market prospects, and remarkable attempts are presently targeting to commercialize HTSC systems in remote sensing and communication systems. Just to name a few, in 2000, a German team interested in designing promising microwave superconductors subsystems as part of the “Superconductor and Ceramics for Future

Communication Technology” project supported by the German Ministry of Education and Research. Through this subprogram, the research team aims to develop reproducible HTSC with high quality and performance and then tests the systems under real conditions [1]. Although research continues for superconducting materials at room temperature, the quality of existing materials is sufficient to develop superconducting systems with higher RF performance for space and wireless requests, particularly, in wireless base station applications, where the technology is presently being marketed by many companionships in the European continent, Japan and the United States.

This chapter book provides the basic characteristics of the material, emphasizing the exceptional features that are pertinent to MW and RF applications. Advances so far in several superconductivity for MW and RF applications have also been described.

## 2 MW Screening Features

Most normal metals display a conductivity  $\sigma$  that is frequency and real independent in the micro-wave to mm-wave frequency extend. For a plane wave colliding with an ordinary metal fulfilling constitutive Ohm’s law local equivalence, the resolution of Maxwell’s equations led to a complex surface impedance ( $Z_s$ ) expressed as:

$$Z_s = (1 + i)/\sigma\delta \quad (1)$$

$\delta$  is the skin depth, and it is dependent on frequency:

$$\delta(w) = \sqrt{2/\mu_0 w \sigma} \quad (2)$$

The tangential electric field E obeys the following equation:

$$E_s = \exp(-ikz) \quad (3)$$

$k$  is the wavenumber expressed as:

$$k = \sqrt{i\mu_0 w / Z_s} \quad (4)$$

According to the above-mentioned expressions, it can be revealed that MW currents move in quadrature and in-phase to the executed E, and these currents will both vibrate and break down versus the depth into the material as:

$$I(z) = \exp^{iz(\delta(w))} \exp^{-z(\delta(w))} \quad (5)$$

The normal metals have limitations because of the “skin effect” (decay features with the frequency, and their strong dispersion in the oscillation. This prevents the capacity of transmission lines of ordinary metal to transmit large band info [8].

On the other side, SC materials display a complex conductivity  $\sigma = \sigma_1 - i\sigma_2$  ( $\sigma_1 \ll \sigma_2$ ). This gives rise to a dominantly reactive  $Z_s$ :

$$Z_s = R_s + iX_s \quad (6)$$

At low temperatures,  $R_s \ll X_s$ . Hence, the resultant screening currents in the SC (entailed by the Meissner effect) demonstrates an uncomplicated penetration depth that is independent on frequency as:

$$I(z) = \exp^{-z/\lambda} \quad (7)$$

These currents do not oscillate. Therefore, the screening properties of SC are frequency unrelated up to frequencies of the order of the superconducting energy gap (in the THz range). More details on the qualitative comprehension of the MW characteristics of SC are given in Ref. [8].

### 3 Benefits of SC for Radio Frequency (RF) and Microwave (MW) Applications

SC materials show unique properties which are basically dissimilar from those of conventional normal conducting metals. The most outstanding property is the achievement of zero resistivity for temperature lower than to so-called critical temperature  $T_c$ .  $T_c$  is a characteristic temperature for the material. For example, HTSC materials usually exploited in RF-applications exhibit  $T_c$  in the range of 90–110 K. With the expanding progress of multi-service good performance wireless communication systems, MW components and subsystems that strengthen numerous recent communication measures become a prevalent trend. The design of microwave and radio frequency should always pay for better performance—both dimensions and cost. For MW applications, the utmost interesting parameters of superconducting materials are  $R_s$  and the critical current density  $J_c$ , which denotes the supreme current that able to be conducted by the SC before swapping to the non-SC state (normal state). To measure these two parameters, numerous techniques are available [9]. For example, the values of  $R_s$  and  $J_c$  are around 100–200  $\mu\Omega$  and  $10^6 \text{ A/cm}^2$ , respectively for HTSC thin films. In the following, we are going to list some exceptional properties of SC enabled for MW applications.

### 3.1 Low-Loss Characteristics at MW Frequencies

SC materials show only nil loss at just zero frequency. Heinz London was the first to confirm empirically that SC materials display microwave loss different to zero for temperatures lower than  $T_c$ . Later, Pippard showed that SC materials display significant microwave reactance [10]. Plentiful MW applications of SC materials based on the low microwave dissipations existing in the superconducting phase. As demonstrated microscopically, in the beginning, by Mattis and Bardeen [11], the direct absorption of microwave photons un-coupled electrons caused loss. For a full-hole SC material, the losses are drastically negligible in the zero-temperature range since the formation of un-coupled electrons necessitates their thermal activation across a finite energy gap [12]. The  $R_s$  value of a SC material is proportionate to the wasted energy  $E$  [13]. This low dissipation limit permits high productivity of MW particle accelerator cavities with quality factors  $Q$  exceeding  $10^{11}$  [14]. Cavities are considered to exchange MW energy into the kinetic energy of a charged particle beam. The aim is to keep high  $Q$  (minimal loss) characteristics up to high accelerated gradients (big RF electric field on the accelerator axis in a MW cavity) to produce efficient and compact acceleration structures. In order to obtain high-quality factor  $Q$  or minimal loss, they ought to consume coaxial or large and expensive components. Only when specifications are reduced can a microwave designer take advantage of the compact size and ease of manufacture of all-in-one thin-film hybrid microwaves. The problem is moderately resolved by progress in HTSC in 1986. This leads to possibly construct planar microwave apparatuses with similar performance to the waveguide and coaxial analogs. The microwave  $R_s$  mainly determines the performance of the passive microwave HTSC circuit. Although the superconductor provides zero resistance to DC, the resistance is not nil at microwave frequencies. For a well-advanced superconductor, the value of  $R_s$  is lesser tens to a thousand times compared to that for copper normal metal under identical situations. The  $R_s$ 's huge optimization magnitude greatly improves passive component performance. A low  $R_s$  value renders directly into a high  $Q$  value or a low input loss. Therefore, HTSC technology offers a solution of achieving tiny-size, high-order microwave components with minimal input loss.

Despite this, the low loss properties of SC materials can be restricted by elevated power MW signals that provoke currents coming close to the critical current of the SC material [15]. Prior to this, SC harbored few nonlinearities, both indoor and outdoor, it can restrict the performance of SC microwaves [16]. Additionally, if a SC shows nodes in its gap energy, like d-wave superconductors (most HTSC cuprates), a few new qualitative phenomena will emerge [17]. The first is the existence of enhancement of low-temperature nonlinearity correlated to quasiparticle excitation closer to superconducting gap nodes. This leads to increased intermodulation distortion, [18] and Meissner nonlinear and anisotropic effects of both the paramagnetic [19] and diamagnetic [20] behavior. Moreover, the linear dependency of the  $R_s$  as a function of the temperature in the clean limit and at depleted temperatures do not allow nodal superconductors to be efficient for extremely low loss applications.



### **3.2 Superconducting Kinetic Inductance**

The kinetic induction is caused by the inertia of the current-carrying charge carriers and works in series with the conductor's magnetic induction. SC kinetic induction is directly linked to the densities of superfluid  $n_s$  for a DC-carrying superconducting wire of cross-section area ( $A$ ) and a length ( $L$ ). Therefore, any perturbation that decreases the density of the superfluid will lead to improved kinetic agitation. Examples involve high transport currents close to critical current density  $J_c$ , temperature close to  $T_c$ , and great magnetic fields when coming close to  $H_c$ . Nevertheless, a decrease in the density of superfluid is associated with the formation of quasiparticles, and an equivalent rise in  $R_s$  and loosed energy. Therefore, achieving great kinetic inductance in this way is best suited for low frequencies applications like highly accurate thermometry, [21]. A novel set of radiation detectors has been manufactured founded on the sensitivity of superconducting kinetic induction temperature changes. In this situation the inductor is piece of a microwave resonant circuit, such that variations in kinetic induction are translated into shifts of frequency of the resonant element [22].

### **3.3 Dispersion of Close to Zero for SC Transmission Lines**

Transmissions lines are structures considered to supply microwave power from one point to another. Most of microwave circuits are manufactured using planar transmission lines. The scarcity of dispersion of transmission lines in SC materials makes them desirable for highly-speed electronic devices [23] and develops the basis for manifold generations of digital computing and electronics superconductivity. SC transmission lines with low loss also provide the aptitude to reinforce reduce speed waves and produce compressed slowness lines, and other kinds of equivalent microwave designs [16, 24]. Great kinetic induction of SC is intensely reliant on on temperature and DC transmission currents permitting broadly amplifiers and varying MW delay lines [25, 26].

### **3.4 Compact SC Structures**

A mysterious benefit of SC materials as compared to normal metal components is their capacity to carry a great amount of current densities with no losses. This allows construction of quasi-two-dimensional (with high-factor quality planar) structures that are so compact and will subsist high current densities without significant degradation of SC properties. It also enables intense sub-wavelength metaatom to produce efficient mass media metamaterials with specific and low-loss properties. Instances of metaatoms involve split-ring resonators [27] and compressed helical resonators

[28], which are tiny comparing to the wavelength of microwaves resonant such as the atomic hydrogen for visible illumination.

### 3.5 *Macroscopic and Microscopic Quantum Phenomena*

The SC state cannot be comprehended by classical concepts. It can be comprehended only by its quantum mechanical traits. There exist two kinds of SC; class I and class II. The distinction between the two types depends on their response on magnetic field. In Type I SC, there exist only two states, Meissner (below the thermodynamic critical field  $H_c$ ), and normal states (when the magnetic field surpasses the  $H_c$ ). While, type II SC will concede with the magnetic field and form an intermediate state “mixed state” in which magnetic flux can penetrate the SC but only in isolated flux-quantized packs, named vortices. Among the first experiments that evidently prove the presence of vortices in type-II SC is microwave measurements. In reply to microwave currents, the vortex will test the vacillating Lorentz force and create a reactive and dispersive response [29]. Swirls are frequently considered unwanted for numerous MW applications. For instance, they can create residual loss in the cavities, and they can disturb Josephson-based highly-speed digital computing systems. Ideally, eddies are either removed from the materials, or lowered into “trenches” [30] that efficiently disable and isolate them from MW currents. In reply to microwave currents, the magnetic vortex will assess the oscillating Lorentz force and yield to dissipative and reactive response [29].

The theory of Bardeen-Cooper-Schrieffer (BCS) established a microscopic consideration of the SC state and presented that the quantum multiparticle wavefunction describing all electrons in a metal has a microscopic phase coherence and stiffness that describe many exceptional properties [31]. The fundamental quantum behavior of the SC state has allowed numerous applications and powered the upsurge of quantum technology in the last decades. Matisse Bardeen [11] theory of SC electro-dynamics established the significance of the SC energy gap and the effects of quantum coherence in the complex conduction and surface resistance of SC materials. This theory expected that dissipations in full-gap SC become randomly miniature with decreasing temperature, allowing good quality SC resonators for highly efficient accelerators particle. The development of materials and setup upon many years has fabricated solid cavities from niobium. This method was preferred for highly efficient compact and charged accelerators particle, leading to the replacement of ordinary metal accelerator by their superconducting counterparts [32].

Many auxiliary processes with superconducting qubits take benefit. For instance, it is vital to regulate the electromagnetic impedance to which qubits are exposed at MW frequencies [33]. Quantum states are very sensitive and susceptible easily to getting lost due to electromagnetic interactions with the surroundings. The problem is that there are parasitic dual-level systems in dielectrics that stimulate the features of qubits and can pair to them and damage their quantum data [34, 35]. Additional detached disturbances can be controlled by disposing the qubit in a highly impedance

setting. This can be achieved by pairing it to great inductances, such as that offered by high kinetic inductors or dispositions of nearby Josephson junctions [36].

In summary, HTSC devices are predictable to be revolutionary apparatuses in the imminent infrastructure of mobile communications with desired good quality services. HTSC technology is chiefly beneficial in communication apparatus, which can enhance the quality network communications characteristics, deliver the modern cohort of signal filtration solution. In addition, miniaturization of microwave devices may reduce distribution outlays for novel base stations.

## 4 Superconducting Microwave Technologies

### 4.1 Superconducting Microwave Resonators

Microwave resonators are one of the vital building blocks of many microwave circuits. The functioning of SC circuit for quantum computing is restricted by the dissipations of the materials. Particularly, coherence times are usually constrained by double-levels systems (DLS) loss at singular photon powers and milli Kelvin temperature. Defining minimal loss production techniques and thin-films and dielectrics materials is important to attaining accessible designs for SC quantum computing. SC quantum computing contains two main constituents which are the qubit that is employed to process quantum data, and a superconducting microwave resonator, a multi-function component exploited to protect and read qubits [37, 38]. In addition, SC microwave resonators offer a suitable qubit medium for evaluation of performance and study of DLS loss and further mechanisms pertinent to superconducting circuits like vortices and non-equilibrium quasiparticles. The essential resonant circuit is composed by an inductive constituent with an inductance  $L$  attached with a capacitive constituent with capacitance  $C$ . The power stocked in the resonator alternates between the capacitor and the inductor at a resonant frequency  $f^*$  defined by:

$$f^* = \frac{1}{2\pi\sqrt{LC}} \quad (8)$$

To have the merit of trade microwave measurement testing and equipment and commercialized radio frequency components, superconducting microwave resonators are usually fabricated to obtain resonant frequencies in the range of 4–8 GHz for quantum computing. Resonator circuits frequently composed of superconducting thin metals and thin-film electrical insulators, usually on the order of hundreds of nanometers, spotted on an insulating crystal substrate with thick of hundreds of micrometers [39]. Practically, the resonator is attached to power dissipation networks, producing its dissipation and minimizing its energy storage capacity. For SC microwave resonators, the loss is not high when compared to ordinary metallic

resonators owing to the minimal loss behavior of the SC material. All the dissipations of the resonator can be integrated in an effective resistance  $R$  with the input impedance  $Z_{in}$ , expressed as:

$$Z_{in} = \frac{1}{(R^{-1} + (iwL)^{-1} + icw)} \quad (9)$$

The performance of resonator can be evaluating by determining the quality factor  $Q$  that is related to power loss caused by the resistor  $P$ , and the full time-averaged energy  $W$ :

$$Q = (2\pi f^* / P) \quad (10)$$

Generally, the quality factor  $Q$  defines the ratio of the global energy stocked close the resonance and the global energy loss in the system. In qualitative term, the line shape of resonance becomes more acute as  $Q$  increases. To examine the performance of the resonator, a vector network analyzer (VNA) is frequently used. The principle of this set up is as follow: first, the microwave signals are forwarded to the first port” input port of the circuit” via a feedline attached to the resonator, and the answer is considered by the second port “the output port”. The phase and amplitude of signals are experimented, attaining an  $S_{21}$  measurement. The complex  $S_{21}$  can be envisaged by dividing it into magnitude and phase components, or into a real and imaginary parts. Different geometries of the resonators are existing. The most known are lumped element resonators, distributed element resonators and microstrip resonators. Superconducting resonators constructed from strip line, microstrip, coplanar lines or other planar transmission line engineering have the widest possible range of applications. Such resonators are likely to be made of both thick-film and thin-film superconductors. Thin film has the distinct benefit that it has a much lower  $R_s$  than thick film, thus generating higher  $Q$  resonators of identical geometry. Nevertheless, the thick film has the benefit that it could be exploited over huge areas. For low frequency and intermediate  $Q$  devices, an integrated microwave system can be constructed on a single substrate with all, or some connections and components made of a thick layer of superconductor. Presently, coplanar waveguide (CPW) resonators are more frequently applied in the superconducting quantum computing field, because of their simple of design, monolayer lithography manufacture, and the capacity to avoid lost dielectrics. The CPW consists of a central conductor of some micrometers wide detached from the ground planes on both sides by a gap of some micrometers. The ground planes and conductor are made of superconducting metal and are placed on a dielectric substrate. Although the minimal loss of SC resonators, these devices suffer from varieties of intrinsic loss. Describing the sources of these losses is the concern of numerous researches. The dependency of resonator loss on experimental surroundings including temperature and applied power can be employed to assign the losses to numerous mechanisms. More details about the loss mechanisms were reviewed in Ref. [40]. Pappas et al. [41] studied the resonant frequency and loss in superconducting CPW resonators versus temperature and power. The authors showed

an increase of loss at both low temperature and power. This increment is ascribed to the presence of DLS at interfaces, the surfaces, and insulators bulk deposited on the structures. Both the temperature dependency of the resonant frequency and the loss power dependency can be utilized to understand the DLS input to the loss. The intrinsic loss tangent DLS resultant from the shift of frequency data at high power is revealed to coincide with the directly loss measurements at low power. The former permits for quite quick measurement of the TLS loss. J. Gao and J. Zmuidzinas have determined noise in SC thin-film CPW resonators. This noise looks exactly like phase noise, which is correspondent to the resonant frequency jitter. However, the amplitude of fluctuations is not detected at the measurement sensitivity. The fraction between the noise power in amplitude and phase directions is great, exceeding 30 dB. These findings showed significant consequences for the resonance readings of various apparatuses like qubits, amplifiers, and detectors. According to this study, the authors concluded that the phase noise is induced by DLS in the dielectric compounds [42]. Bothner et al. [43] performed experiments on Nb resonators with various spatial scattering of micro pinning centers (antidots) and studied the energy loss induced by vortices. Their study showed that the introduction of antidots into the resonator minimize the loss caused by vortices. Consequently, the value of Q at exerted fields in the milli-T extend can be significantly amplified. The Strategy for relocating these findings to higher magnetic fields may comprise appropriate flux reduction focused on ground level regions as well as application of trapping arrays at well-modeled length scales in the submicron range.

## 4.2 Superconducting Detectors and Mixers

All microwave and RF systems detect signals in some way. This can be performed by means of a simple detector circuit, or via a mixing circuit which also converts the signal from one frequency to another. This frequency conversion allows the capacity to transmit different signals at the same time at various frequencies. SC detectors are tremendously sensitive and have large applications assortment including astrophysics, mostly at millimeter via far-IR wavelengths, where the scientific prospects face major difficulties in cosmology and astronomy. Amongst cryogenic detectors, superconducting detectors are exclusively desirable due to lithographic manufacture, possible thin-film deposition, exceptional sensitivity, and great array sizes, particularly via the latest advance of multiplexing techniques. Numerous kinds have been established, involving tunnel junction detectors [44, 45]. These types have proven their efficiency in power-solved detection of discrete X-ray photons, ultraviolet, optical, and sensitive detection of power at millimeter and submillimeter wavelengths. For instance, Day et al. [22] proposed a broadband SC detector. The detection principle of this device is illustrated in Fig. 1. Photons of enough energy ( $h\nu > 2\Delta$ ) may smash one or many Cooper pairs (Fig. 1a). High-energy photon absorption leads to the formation of quasiparticles. Afterwards, excess quasiparticles reassembled into Cooper pairs at time scales  $\tau \approx 10^{-3}-10^{-6}$  s. Throughout this

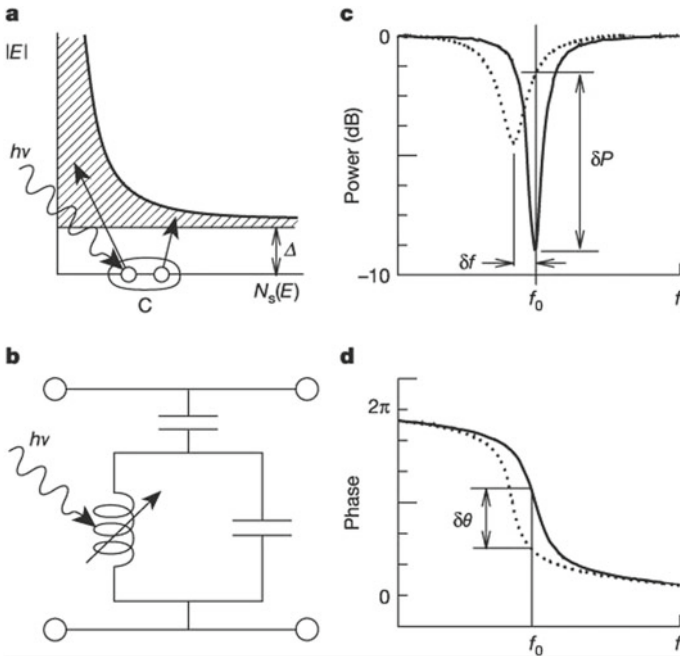


**Fig. 1** Detection principle of a broadband SC detector proposed by Day et al. [22]

period, quasiparticles can propagate at a certain distance. Correspondingly, absorption of a continuous stream of minimal energy (millimeter/submillimeter) photons will increase the density of the stable state quasiparticles over their thermal equilibrium level. The proposed detector takes advantage of the dependency of surface resistance  $Z_s$  on the density of quasiparticles. Despite the small variations in  $Z$ , highly sensitive measurements can be performed by means of a resonant circuit (Fig. 1b). The variations in the surface inductance  $L_s$  and in the surface resistance  $R_s$  influences the resonant frequency and its width, respectively, leading to a modification in the amplitude and phase of the microwave signal spread over the circuit (Fig. 1c, d).

This designed detector showed good performance for some applications like sub-millimeter terrestrial imaging. Despite this, the authors suggested developing a detector with ultra-low noise and ultra-sensitivity that can be easily applicable in most applications. The ultra-sensitive superconducting detectors and mixers play a significant role in THz astronomy. Indeed, terahertz (THz) range includes a part of far infrared and the shortest wavelengths. THz regime occupies nearly half the photon energy in the cosmos. Superconducting films based on Hot electronic barometer frequency lower mixers (HEBM) provide standard sensitivity for THz receivers for use in radio astronomy. The HEBM device has a simple structure; it mainly involves an extremely short bridge made of a superconducting thin film. Such device structure is moderately uncomplex compared to Schottky-diode system. This make it easily integrated into a planar antenna structure. For frequencies higher than the bandgap

frequency of the SC, the arriving radiation is absorbed by both quasiparticles and Cooper pairs. The correctly aligned resistance varies very fast with the variation in the energy absorbed. Thermal time constant is on the order of tens of ps and permits for a supreme middle frequency (MF) of some gigahertz. Two sorts of HEBM were settled: phonon-cooled HEBM, in which radiation-heated electrons are cooled by phonons in the SC network [46]. The second type of HEBM uses hot electrons diffusion cooling, in which cooling is achieved when heated electrons diffuse to the device contact pads. For instance, Denis Büchel et al. [47] proposed SC waveguide mixer hot electron bolometer (HEB) functioning at 4.7 THz. The assessment of the performance of the proposed mixer showed an advanced dual sideband noise temperature of 1100 K, with a mean MF bandwidth of 0.2–3.5 gigahertz. The noise rotation rate is 3 dB at 3.5 GHz. This mixer has been successfully exploited in GREAT (the German receiver for Astronomy Terahertz) instrument at the SOFIA (Stratospheric Observatory for Far Infrared Astronomy).

### **4.3 Microwave Filter**

In recent years, microwave filters have been attracted important commercial interest. Microwave filters are consisting of many mutually and externally attached discrete resonators. Hence, the exceptional features of superconducting resonators, i.e. being very small or exhibiting unsurpassed high-quality factors, determine the specific properties of the superconducting filters. For radio receivers, the superconductor filter (SCF) acts as a frontal side attached to the antenna between it and the receiver. The filter can be connected to a standing radio receiver as an application without re-engineering the initial unit. HTSC filtration technologies are one of the most important technologies of HTSC applications all over the world which can compete with traditional microwave filters.

#### **4.3.1 LTSC Filter Against HTSC Microwave Filters**

In last years, microwave filters have attracted excessive attention due to their significant role in a diversity of digital and analog superconducting systems. LTSC microwave circuits have been expansively explored for superconducting quantum computing systems (SQCS) [48–50]. The design of microwave filter was started by using niobium LTSC thin films on rectangular sapphire substrates, which are anisotropic dielectric materials [51]. The objective of this attempts was to launch the main technological challenging in manufacturing microwave devices with extremely low loss, which were operating at cryogenic temperature. Overall, the majority of the mechanical and thermal difficulties linked to cooling a device are similar at 77 K as they are inferior to this temperature (i.e. 4.2 K in the case of the LTSC filters). Moreover, the usage of sprayed thin niobium films is considered to be risk-free from a material point of view, so it is easily to get good quality films on relatively large

monocrystalline sapphire substrates. One benefit of sputtered niobium films is that they can be deposited on both sides of the substrate. However, the quality of one of the films can deteriorate during the process. After depositing the film, the substrate had to be removed from the spray chamber in order to invert it to coat the back side. When the substrate was heated again to grow the second film, decomposition of the layer of the niobium oxide ( $\approx 5$  nm) that grows on the surface of the first film takes place. A diffusion of oxygen inside this film can be occurred resulting in its contamination. To avoid the degradation of the film, the mechanism should be divided to flip the substrate inside the chamber, without stopping the vacuum. LTSC thin films lead to make two six-pole strip line filters with contiguous passbands and 1.2% bandwidth and around 3 dB crossovers [51]. In 2009, Raihan Rafique and co-workers [52] proposed a Nb-based SC tunable filter. The tunable filter resonators use sequential arrays of superconducting quantum interference design (SQUID) as tunable inductance. The attainable interval of induction tuning for a chain of 50 series SQUID is 65–200 pH. This filter showed frequency tunability of 40% with an input loss ranging from 0.5 to 3.0 dB and an unloaded Q of 40. The filter's power range is restricted by the critical current of the Josephson junctions, and for this proposal it is lower than 52 dBm. Yuxing He et al. [53] developed a novel type of LTSC filter for grouped elements to reach acute selectivity and irregular group delay performance. the proposed LTSC filter displays impressive advantages: (i) extremely simple built-in topology (deprived of any cross-coupling), (ii) highly dense size based on combined capacitor inductor elements, and (iii) manifold zeros transmission are separately produced and regulated (across each resonant coupling). A set of bundled element circuit models has been detailed, in which serial inductor capacitor units are implemented for both resonant connections and resonators to enable physical operations. The whole filter is then constructed by sequencing the assembled forms one by one. A class 5 band filter stationed at 5 GHz, with a bandwidth of 500 MHz and 3 TZs was conceived, simulated, and experienced at a cooling temperature of 4.2 K. The obtained results are encouraging making the proposed filter effective for SQCS applications. The first era of the research and progress of HTSC led to major improvements in material properties and especially in standardizing those properties. Over recent years, research has focused on designing thin films HTS filters, and improving as well as standardizing their performances. Compared with traditional filters, HTSC filters is able to decrease the unwarranted interference, enhance the rate of data transmission, enhance the battery lifetime and reduce the requirement for extra mobile phones base stations. The phenomenon of interference is also anticipated to be resolved.

### 4.3.2 HTSC Filter Design

The largely employed HTSC filter structures are microstrip line and stripline configurations. Jumped element filters, dual mode resonator filters can also be utilized [54]. The most frequent filter structure is the microstrip line, due to its relatively simple structure in addition to the facility of making external connections to the circuit.



Theoretically, stripline configurations are more effective than microstrip lines for two reasons: (i) The group and the phase velocities of the stripline are invariant with the frequency. (ii) the phase velocities of the even and odd models are equivalent for attached lines. These two features are of great interest for conceiving narrow-phase filters. However, stripline circuits have practical drawbacks due to the air disparity between the two substrates. Since the substrates used in HTSC circuits display extremely high dielectric constant. Even a minor air disparity between the substrates results in a large impact on the resonant frequency.

### 4.3.3 Properties of HTSC Filter

In the recent decades, numerous types of HTSC filters have been erected and fruitful applications in various area have been accomplished. HTSC filters display outstanding performance like low input loss, deep drop out of range, and a sharp slope of the skirt, which can enhance the sensitivity and selection of the microwave system.

- ***Input loss (IL)***

In addition to  $R_s$ , the IL of the filter is associated with the center frequency (CF), the fractional band width (FBW), and the sum of poles of the filter. For filters with elevated FBW, the IL is lower than 0.05 dB [55, 56], which is unimportant for MW receivers' systems but appropriate for receptors in radio astronomy observatory. For filters with very tiny FBW, with the correct selection of the resonator structure, extremely small input loss can be also attained. Hong and his co-workers [57] manufactured a ten-pole HTSC bandpass filter for mobile communication systems with a 0.5% FBW at 2 GH that showed a least input loss of 0.2 dB. A10-pole HTSC filter with CF of 2.185 GH and an FBW of 0.45% was developed by Cui et al. [58]. This HTSC filter shows an IL lower than 0.15 dB. Overall, irrespective the CF and FBW, the IL is lower than 1 dB for the most HTSC developed in the recent years.

- ***Fractional band width (FBW)***

In recent years, the station records and the complication of communication systems have progressively increased. A set of narrowband HTSC filters possibly will be a major constituent of microwave channel receivers. Therefore, there is an increasing demand for narrow bandpass filters for radar connections, satellite receivers, and mobile communications. For a traditional MW filter, the IL will be unsatisfactorily intense if the FBW is extremely tiny. Owing to the minimal  $R_s$ , HTSC filters can display a minor FBW. In the past decades, numerous filters have been fabricated with FBW less than 1%. By choosing suitable resonators with elevated quality factor and using well-made coupling structures with feeble coupling constants, some HTSC filters can exhibit FBW less than 0.1%. In 2003, Dustakar et al. [59] developed an extremely narrow bandpass HTSC filter with 0.014% FBW and CF of 700 MHz. In 2009, Kawaguchi and his co-workers [60] introduced an HTSC filter with a 0.056%

FBW at 5370 GHz. The filter was fabricated with microstrip hairpin resonators with a wavelength of 1.5 times and displays an IL of 2.04 dB. Lately, a very narrow bandpass HTSC filter with 0.02% FBW in the C band has been developed by Li et al. [61]. New methods have been adopted to resolve the drawbacks of weak conjugation and parasitic conjugation.

- ***Skirt slope and out-of-band rejection***

The design of filter with a great quantity of poles, extremely high out-of-band rejection and skirt slope is easy to manufacture when using HTSC materials exhibiting low  $R_s$ . For instance, in 2001, Hattori et al. [62] fabricated a 21-pole HTSC microstrip thin-film filter having sharp degradation. This filter showed its applicability in IMT-2000 (the International Mobile Telecommunications-2000) base stations receiving systems, where elevated selectivity is required to preclude interference from signals in the personal phone system band undermost the band of IMT-2000 directly. This filter has the out-of-band rejection of 1 MHz under the passband edge is over 40 dB. Due to design and manufacturing process improvements, the authors were able to eliminate the necessity for alteration method in manufacturing procedures to minimize the expenses of production and delivery time. In 2003, a Chinese group designed 20-pole HTSC thin-film microstrip filter with sharp band edges to solve the problems of low call rate, poor sound quality that mobile phone calls have been confronting in China [63]. The filter was designed by means of YBCO thin films with dual sides deposited on  $\text{LaAlO}_3$  substrate. The IL of this filter is lower than 0.35 dB in the bandpass, the sharpness of the band-edge is over 18 dB/MHz. In 2006, Zhang and his co-workers [64] proposed an extremely discerning twenty-four-pole Chebyshev HTSC bandpass filter. The filter was considered at 1748 MHz CF with bandwidth of 75 MHz, which was appropriate for the mobile base station. The filter was developed by means of YBCO dual-sided films deposited on sapphire substrate. The filter presented an outstanding discernment. At the band edge of the design, the slope of skirt was around  $17 \text{ dB MHz}^{-1}$ . Out-of-band rejection is superior than  $-90 \text{ dB}$ .

- ***In-band group delay (In-BGD)***

The selectivity as well as In-BGD are two challenging goals in the design of filter. Many scientific publications are assigned to HTSC filters with effective In-BGD and good selectivity. Conventionally, there are two routes to enhance the filter group delay. The first route is to sequence the filter using an equalizer of externally set delay via a circular or 3 dB turning coupler. Lately, Zhang et al. [65] established an eight-pole semi-elliptic HTSC filter, and a unipolar set delay equalizer was integrated to compress the In-BGD. The ultimate change of the In-BGD was  $<50 \text{ ns}$  above bandwidth around 79%. The second route for settling the In-BGD is to use dummy frequency transmission zeros in the filter system. Hong et al. [66] fabricated an 18-pole HTSC bandpass filter with self-balancing set delay. The fabricated filter exhibited a 15 MHz passband at a CF of 1967.5 MHz. Two convergent quadrupole perceptron were established to realize either reduction poles at a finite frequency or linear phases for set delay self-balancing. Both elevated selectivity and horizontal

set delay were attained in the measured responses. HTSC filter with group delay swells greater than 80% of the pass range of lower than 20 ns and an out-of-band rejection superior than 80 dB have been developed by Zuo et al. [67]. In 2009, Gao and co-workers [68] reported a narrowband 14-pole HTSC filter with bandwidth of 3 dB of 42 MHz and a CF of 8.625 GHz. By inserting single pair of transmission zeros for better selectivity and double pairs of transmission zeros for horizontal set delay, both elevated band edge slope and outstanding group delay smoothness were accomplished. Band edge regression was measured above  $11.7 \text{ dB MHz}^{-1}$  at low and high frequencies edges, consisting with a rectangle ratio of 60 dB; lower than 1.25. The out-of-band rejection was more than 70 dB at 5.98 MHz from the edge of the 3 dB range. The set delay variance was below 23 ns above 33 MHz (78.5% of the 3 dB bandwidth), and less than 30 ns above 34.5 MHz.

#### 4.3.4 Types of HTSC Filter

Generally, there are three chief kinds of HTSC filters: (i) HTSC planar thin-film filters; (ii) hybrid dielectric/HTSC filters; (iii) thick-film HTSC coated filters. In HTSC thick-films coated and thin-films planar filters, the enhancement of quality factor  $Q$  is principally ascribed to the decrease of  $R_s$  by swapping ordinary metals with HTSC systems. While, the enhancement in  $Q$  in hybrid dielectric/HTSC filters is accredited to the minimization of  $R_s$ , and the minimization of the tangent loss of the substrates during to cooling.

- (i) HTSC planar thin-film filters: The appearance of the HTSC technology has launched the prospect for considerable advance in planar filter designs. During the last years, numerous innovative filters have been suggested letting the fulfilment of relatively innovative filter roles [69–71]. Since the 1990s, the need for HTS planar filters has become evident with the advent of many commercialized computer software packages for the design and simulation of planar circuits. Although these commercialized packages did not consider the properties of superconductors, they have been exploited with success in the fabrication of planar HTSC filters, especially for applications required lower energy.
- (ii) Hybrid dielectric/HTSC filters: Numerous hybrid dielectric/HTSC filters have been designed and tested by many researchers [72, 73]. This filter configuration presents many benefits as comparing to HTSC planar thin-film filters. Indeed, this filter design eradicates the necessity of gold contacts deposition that are mandatory for thin-films filters. Besides, there is no necessity to produce contact masks and circuit. In addition, in this filter the chip is cut into tiny parts of “short plates”. The chip is utilized effectively. In contrast to thin-films filters where a great fraction of the HTSC compound is lost owing to etching process. Finally, the filter has excellent counterfeit performance. The image panel not only aids to diminish the size of filter, but also assists to remove spurious modes, allowing it probable to fabricate filters of this kind

with a false-free window of width above 2 GHz positioned in the center at a frequency of 4 GHz. This type of filter presents a drawback regarding to the mechanical design complexity.

- (iii) Thick films HTSC coated filters: For microwave applications, thick films YBCO prepared by melt-processing method were used [40]. Thick films YBCO commonly exhibits a  $J_c$  of  $10^3 \text{ A/cm}^2$  and have a minor value of  $R_s$  of around  $0.5 \text{ m}\Omega$  (5 GHz at 77 K). Recently, Woo Il Yang et al. [74] have designed large YBCO superconductor films coated with gold. The objective of this investigation is to study the effect of homogeneity in the microwave  $R_s$  of Au/YBCO films. This design allows the fabrication of multiple HTSC filter for mobile communication and others microwave devices. The homogeneity in the properties of the film is imperative for manufacture multipole filters with steep skirt properties. S. Y. Lee and B. Oh have used pulsed laser deposition to prepare YBCO films on MgO substrates. For microwave applications, it is preferable that the thickness of YBCO film be three to four times the depth of penetration at the operating temperature of interest to attain an effective  $R_s^{\text{eff}}$  nearly the intrinsic  $R_s$  of YBCO. The authors have tested the homogeneity of  $R_s^{\text{eff}}$  at different temperatures of 45, 60 and 77 K of a typical thick YBCO film on MgO. Their results showed more homogenous distributions of  $R_s^{\text{eff}}$  at 45 and 60 K than that of 77 K. That is means that the homogeneity degree of  $R_s^{\text{eff}}$  examined at 77 K is not inevitably similar at the temperature of interest, for example, the operating temperature ( $\sim 70 \text{ K}$ ) of the HTSC microwave devices. The main causes for the dissimilarity of  $R_s^{\text{eff}}$  on the surface of film are not yet clearly comprehended. More details on the homogeneity in the  $R_s$  of large HTSC films can be found in Ref. [19].

#### 4.4 Superconducting Amplifier

An amplifier is an electronic device that can upsurge signal strength (time-varying current or voltage). It is a double-port electronic circuit that utilizes electrical energy from a power source to rise the amplitude of the signal applied to its input terminals, resulting in a relatively larger amplitude signal at its output. The quantity of amplification offered by an amplifier is decided by its gain: the ratio of the current voltage output, or power to the input. An amplifier is a circuit that displays a power gain higher than 1. A perfect amplifier displays extremely negligible noise, works above a wide range of frequency, and exhibits huge dynamic range. Recently SC amplifier was established, which displays an auspicious commercial application. Cryogenic amplifier plays a leading role in the receiver's design. SC front-end is categorized by the bandwidth frequency out of band rejection, sharpness of filter, and the low noise amplifiers (LNA). Such kind will upsurge the sensitivity and conserve voice or data signal in better quality. For instance, Wang et al. [75] designed a cryogenic amplifier which has a better performance in band frequency range of 780–880 MHz at 77 K. Scattering parameters (S parameters) measure moving waves instead of

total voltages and currents. S-parameters let for calculations performance of system by means of the design's room-temperature single-component sequence. These S parameters are altered at cryogenic temperatures to result in high-electron-mobility transistor (HEMT) working point bias. The gate voltage was regulated to correct the change of the S- and phase parameters. At cryogenic temperature, the noise figure can be minimized to be lower than 0.3 dB compared to the 0.55 dB at 25 °C. In the meantime, the gain augmented about 1 dB in the working frequency band. Over the last era, the amalgamation of good performance SC microprocessors and negligible noise microwave frequency-cooled transistor amplifier data has demonstrated to be effective for a large applications range, involving photon detecting tests and quantum data. These progresses have renovated attention in SC amplifiers that attain minimal reading noise. Extremely low-noise MW amplification has an essential role in measuring microwave domains to speedily and correctly infer the state of qubits. For this purpose, parametric amplification, which was a familiar notion for low-noise amplifiers in the sixties and seventies of the last century, became the principal technology to enable highly effective MW measurements of these quantum circuits. These superconducting parametric amplifiers take advantage of the nonlinear Josephson junction inductance that is nearly perfectly reactive with negligible loss lower than the critical current  $I_c$ . Consequently, Josephson parametric amplifiers (JPA) can be ultra-sensitive, approximating the typical half-photon quantum limit ( $\hbar\omega/2$ ) for the noise power added per unit bandwidth in the normal situation when the signal quadrants are equally amplified at frequency  $\omega$  [76]. Noise can be reduced in cases of amplification of only one quadrature. By comparison, the supplementary noise of cooled transistor amplifiers is usually 10–20 times quantum limits [77]. Nevertheless, the dynamic range of Josephson parametric amplifiers is controlled by the Josephson power  $E_J = I_c/2e$  ( $e$  is the electron charge) to much lower values than for transistor amplifiers. As alternative to resonator, the electrical or optical track can be opened into waveguide or a long non-linear transmission line. This leads to a travel wave parametric amplifier which has a very wide internal frequency range [26]. Nevertheless, a sufficiently low non-linear loss medium along an achievable length ought to be acquired. At infrared and visible wavelengths, these necessities are satisfied in silicon waveguides and optical fibers by the non-linear four-wave mixing (FWM) process that induced by the refractive index intensity dependence, that is, the Kerr effect. Fiber parametric amplifier reach high gain (exceeding 60 dB) and the mono-square versions displayed noise levels under the normal quantum limits [79]. Castellanos-Beltran et al. [78] fabricated JPA from a transmission line resonator whose internal conductor consists of series of a SQUID device. This tunable JPA exhibited gain higher than 28 dB and showed more sensitivity to a feeble microwave signal than a small noise HEMT amplifier. In 2012, Byeong Ho Eom and his co-workers proposed a parametric superconducting amplifier by using the geometry of travel-wave and the non-linear kinetic inductance of a superconducting transmission line. The gain extended above 2 GHz on either side of the 11.56 GHz pump tone and set a superior limit for the supplementary noise of 3.4 photons at 9.4 GHz. The dynamic range is quite great, and the notion of the authors can be implemented from frequencies of GHz to  $\sim 1$  THz [26].

## 4.5 Superconducting Antenna

Antennas is the important component of all receiving and transmitting systems in wireless communications, radar spreading, surveillance, and other applications. Antennas is identified as connecting apparatuses between free space and electronic circuits. The size of the antenna is a direct function of the signal wavelength. To ensure supreme transmission of input power to free spaces and to avert reflections towards the generators, the antenna should be paired. To link the dipole antenna to the transmission line, the entry point has to be selected where the antenna impedance is approximately equivalent to the typical impedance of the line. Small electric superconducting antennas and superconducting antennas were first verified several years ago [80]. The emergence of HTSC materials has renewed these thoughts [81]. The minimal loss of the SC significantly decreases the electrical dissipation in the antenna, especially in the antenna feed and match network. They are also exploited in communications arrangements to enhance the gain and to provide a solution for physical tiny antennas particularly in the RF range [82, 83]. HTSC materials enhance the performance of electrically tiny antennas (ETA) mainly by preventing the decay in the efficiency of radiation related to reducing the size of the radiator. Small HTSC loop antennas display radiation productivities approximating 95% compared to 5% for counterparts' copper elements having the same size. The influences of using a SC in antenna construction can be explained by meticulous study of the effects of the internal and external fields. For example, in a cylindrical dipole antenna, the radiating field and its related radiation resistance, the energy stored in the proximate field and the associated interaction, are produced by currents on the dipole surface; these are external fields. Whereas, the internal fields of a bipolar cylinder are only significant with respect to the conduction loss, which is regularly tiny. Using a SC will cause little change in the external fields, and thus in the pattern, impedance, and direction, as the diameter of the dipole cylinder is miniature in wavelengths. Only the internal fields undergo significant change, which of course leads to zero or low conduction loss. All antenna characteristics excepting for efficiency are reliant on external fields, which are unaffected by SC. Recently, Kawakami et al. [84] have fabricated nano-antennas to enhance the superconducting infrared detectors superconductors. The nano-antenna comprises of a dual pole antenna made of aluminum strips and strips thin film NbN superconducting antenna that is placed in the center. It was shown that the transition temperature of the SC strips is preserved after the manufacture of nano-antenna. By evaluating the spectral transmission properties of the nano-antenna of NbN strip-load impedance nano-antennas, notable absorption properties with elevated polarization dependence at about  $1400\text{ cm}^{-1}$  were detected. The calculated impedance of the designed antenna was identical as the valued load impedance. These findings confirmed that the designed nano-antennas can act as infrared antennas. Active broadband antennas are essential for wireless information technologies applications, particularly for broadband receivers with directly digitization of the inserted signals [85, 86]. Broadband receivers are allowed by high-performance analog to digital superconductor converters (ADSCs). Current ADSCs

show both elevated dynamic and linearity extend of 90 dB and even above [87, 88]. Nevertheless, small noise amplifier and the minimal performance features of the receiving antenna in comparison to those of ADSCs limit the global performance of the receiving systems. The development of a highly efficient active ETA able of offering high linear reception and synchronous amplification with a large dynamic interval will enhance the entire system. In recent years, many types of superconducting antenna have been developed. For example, Victor K. Kornev et al. [89] reported a guide for the correct usage of an ETA founded on superconducting quantum array (SQA). Active ETA based on SQAs is a double ways active network with bias and output in one port. Hence, unlike conventional passive antennas, the active ETA must be highly incompatible with the associated load to maintain the intense linearity of the output voltage. When the output signal is connected to a low-impedance device such as an ADSC, a broadband superconducting impedance converter could be employed to link all other networks in the interface used and avoid permanent wave constitution. Although it is necessary to use a strongly mismatched load for the active ETA, a satisfactorily high output power can be offered with the support of the active antenna bias source. The realized ETA using SQAs is able of simultaneously the broadband reception and amplification of electromagnetic signals. Very recently, scientists have directed their researches on Low-terahertz antenna. This innovative technology is predicted to deliver extraordinary data rates in forthcoming generations of wireless communication system (like the 6th generation mobile). Rising the carrier's frequencies from millimeter wave to THz is a probable solution to assure the broadcast rate and channel capacity. Owing to the high transmission dissipation of Low-THz wave in free space, it is predominantly imperative to design antennas with highly gain to recompense the extra path dissipation, and to overawe the energy restraint of Low-THz source. Mei Yu and his co-workers [90] proposed a new kind of bowtie antenna. This proposed design is joined with stubs pair and zigzags to match HTSC YBCO Josephson junction impedance. Stubs pair were used to match small impedance, whereas the zigzags were employed to regulate the impedance reactance as a paired impedance association with the stub. This proposed antenna retained the symmetric radiation designs even as a couple of zigzags were hosted asymmetrically into the bowtie structure due to the cancellation of radiation from the two winding arms, required by wide THz detection. In 2019, Holdengreber et al. [91] executed developed electromagnetic simulations to get the ideal pattern of an antenna system for the radiation of THz range. These simulations are based on the Josephson junctions, which act as a detector component. This junction is consisting of bi-crystal substrate technology and is executed by HTSC YBCO thin films. The junction is positioned in the center of antenna to minimize the losses. Based on their theoretical electromagnetic simulations, the authors fabricated experimental design. Their results showed high sensitivity YBCO HTSC Josephson junction antenna for 200 GHz detection.

## 5 Limitations of Superconducting Technology and Future Directions

A major limitation for a long time on the implementation of superconducting microwave and RF technology has been the matter of cryogeny. A lot of past research on superconductivity has been done with liquid cryogens, i.e., nitrogen and helium, which are liquids for consumption with an unpredictable source, at fully in helium case. The cryogenic cooler technique could be categorized into two key categories: closed and open cycle. Open coolers session is huge and dispersive materials and require frequent mobilization of compressed gas or chillers. Hence, they are perfect for workroom settings or in applications in which repairs of the equipment is regularly. Yet, the initiation of closed-cycle mechanical cryogenic coolers, several derivatives with increased productivity and scarcer dynamic parts, has renovated cryogenic technology [92, 93]. Closed-cycle coolers are own-contained freezers that use only electrical energy, needing no repairs under the considered lifespan. Closed-cycle cryogenic chillers are mostly established for military applications and infrared devices. The principal design for a closed-cycle refrigeration chiller is size, reliability, and energy consumption. Cryogenic coolant reliability still the main obstacle to the large spread commercial approval of superconducting devices. Nowadays, there are numerous opportunities for cost effective and extremely reliable cryogenic equipment, particularly those that have been exploited for cryogenic MW and RF applications [94]. For instance, in the past years, the reliability of the pulse-tube refrigerator, which eradicates all dynamic portions at low temperatures, has significantly increased.

The capacity to have signals with superior frequency back and forth to the cryogenic environs without yielding signal integrity or the efficacy of the cooling cryogeny system present also big problem with microwave superconductivity. This has guided to the progress of low-loss microwave transmission lines, which are at the same time have a minor heat load on the cooled environs [95]. Superconductors are poor thermal conductors at temperatures lower than  $T_c$ , in most situations, no worse than insulators. The quantum computing innovation open the way to commercially fabricated microwaves eligible for cryogeny [96]. MW devices have recently shown huge progress in terms of low-noise, low-dispersion broadband amplifiers that are well suitable to a cooled environment. This vast MW engineering defies are in stock for the progress of broad scale coherent quantum computing apparatuses, producing numerous prospects for innovative applications of SC materials. It is probable that novel superconductors with exciting characteristics will persist to be invented. The utmost pertinent superconductors are s-wave superconductors. These SC materials usually display a complete energy gap excitation on the Fermi surface, leading to a considerably few number of quasiparticles in the zero-temperature limit. A growing number of SC discovered since the last decades have revealed clear evidence of the quantum angular momentum states of coupling of electrons. These systems usually exhibit nodes in their energy gap, which means that the quasiparticles could be provoked even at the lowermost temperature, producing various minimal energy



characteristic of these materials. To date, rare of these interesting materials can be implemented in practical applications based precisely on these coupling properties. Additionally, it is prospective that novel SC materials with  $T_c$  beyond 100 K will persist to be invented. Until now, many of these HTSC have been hard to be exploited due to their poisonous chemical components, fragile mechanical traits, or they can only be manufactured under extremely elevated pressure. Nevertheless, the desire of scientific committee to expect the characteristics of novel materials, and their steadiness, is being increasingly complex with time [97, 98]. These theoretical attempts conduce to the discovery of innovative superconductors with  $T_c$  coming close to ambient temperature [99, 100]. Transforming these innovative materials into real-world apparatuses and fabrics will need period, but it looks most probably that superconducting microwaves and RF will be widely used in the future.

## 6 Conclusion

Since the discovery of HTSC, it has been evident that one of the most common ranges of application and marketing of these systems is microwave and radio frequency electronics devices. First prototypes are ingoing service in industries of the mobile communications, and a broad array of other apparatuses are at a somewhat advanced step. This chapter of the book provided an overview of the microwave as well as the radio frequency properties of superconducting materials. It also provided a review of the most important microwave and radio frequency HTSC devices. This has made great promise to young engineers and technologists in this exciting field. Researchers in this field are intensely encouraged to pursuit reading on the topic and to understand more about the possible, defies, and restrictions of this innovative technology. In the near future, an integrated cryogenic technology based on HTSC materials should be developed to put into practice.

## References

1. M. Klauda, T. Kasser, B. Mayer, C. Neumann, F. Schnell, B. Aminov, A. Baumfalk, H. Chaloupka, S. Kolesov, H. Piel, N. Klein, Superconductors and cryogenics for future communication systems. *IEEE Trans. Microw. Theory Tech.* **48**, 1227–1239 (2000)
2. G. Ciovati, G. Cheng, U. Pudasaini, R.A. Rimmer, Multi-metallic conduction cooled superconducting radio-frequency cavity with high thermal stability. *Supercond. Sci. Technol.* **33**, 07LT01 (2020)
3. S. Max, J. Fox, M. Wind (eds.), *Handbook of Microwave Measurements*, vol. 1 (Polytechnic Press of the Polytechnic Institute of Brooklyn, 1963)
4. S.Y. Lee, B. Oh, Recent progress in microwave HTS technologies in Korea and Japan. *J. Supercond.* **16**, 823–831 (2003)
5. W. Harold, M. Nisenoff (eds.), *Microwave Superconductivity*, vol. 375 (Springer Science & Business Media, 2012)

6. M.J. Lancaster, *Passive Microwave Device Applications of High Temperature Superconductors* (Cambridge Univ. Press, Cambridge, MA, 1997)
7. Z.Y. Shen, *High Temperature Superconducting Microwave Circuits* (Artech House, Norwood, MA, 1994)
8. S.M. Anlage, Microwave superconductivity. *IEEE Microw. Mag.* **1**, 389–402 (2021)
9. H. Weinstock, M. Nisenoff (eds.), *Microwave Superconductivity*, vol. 375 (Springer Science & Business Media, 2012)
10. A.B. Pippard, W.L. Bragg, An experimental and theoretical study of the relation between magnetic field and current in a superconductor. *Proc. R. Soc. A* **216**, 547–568 (1953)
11. D.C. Mattis, J. Bardeen, Theory of the anomalous skin effect in normal and superconducting metals. *Phys. Rev.* **111**, 412 (1958)
12. J.P. Turneaure, J. Halbritter, H.A. Schwettman, The surface impedance of superconductors and normal conductors: the Mattis-Bardeen theory. *J. Supercond.* **4**, 341–355 (1991)
13. S.M. Anlage, Microwave superconductivity. *IEEE J. Microw.* **1**, 389–402 (2021)
14. H. Padamsee, J. Knobloch, T. Hays, *RF Superconductivity for Accelerators* (Wiley, New York, 1998)
15. T.C. Yaw, High Tc superconductor, ferroelectric thin films and microwave devices (2006)
16. R. Gerbaldo, G. Ghigo, L. Gozzelino, E. Mezzetti, *Handbook of Advanced Electronic and Photonic Materials and Devices, High-Tc Superconductors Toward Small Scale Applications* (Academic Press, 2001), pp. 1–70
17. J. Mao, S.M. Anlage, J.L. Peng, R.L. Greene, Consequences of d-wave superconductivity for high frequency applications of cuprate superconductors. *IEEE Trans. Appl. Supercond.* **5**, 1997–2000 (1995)
18. D.E. Oates, S.H. Park, G. Koren, Observation of the nonlinear Meissner effect in YBCO thin films: evidence for a d-wave order parameter in the bulk of the cuprate superconductors. *Phys. Rev. Lett.* **93**, 197001 (2004)
19. A.P. Zhuravel, B.G. Ghamsari, C. Kurter, P. Jung, S. Remillard, J. Abrahams, J., A.V. Lukashenko, A.V. Ustinov, S.M. Anlage, Imaging the anisotropic nonlinear Meissner effect in nodal  $\text{YBa}_2\text{Cu}_3\text{O}_{7-\delta}$  thin-film superconductors. *Phys. Rev. Lett.* **110**, 087002 (2013)
20. A.P. Zhuravel, S. Bae, S.N. Shevchenko, A.N. Omelyanchouk, A.V. Lukashenko, A.V. Ustinov, S.M. Anlage, Imaging the paramagnetic nonlinear Meissner effect in nodal gap superconductors. *Phys. Rev. B* **97**, 054504 (2018)
21. D.G. McDonald, Novel superconducting thermometer for bolometric applications. *Appl. Phys. Lett.* **50**, 775–777 (1987)
22. P.K. Day, H.G. LeDuc, B.A. Mazin, A. Vayonakis, J. Zmuidzinas, A broadband superconducting detector suitable for use in large arrays. *Nature* **425**, 817–821 (2003)
23. K.S. Kale, High temperature superconducting microwave devices. *Doctoral dissertation* (University of Oxford, 1996)
24. R.S. Withers, R.W. Ralston, Superconductive analog signal processing devices. *Proc. IEEE* **77**, 1247–1263 (1989)
25. Q.Y. Zhao, D. Zhu, N. Calandri, A.E. Dane, A.N. McCaughan, F. Belle, H.Z. Wang, D.F. Santavicca, K.K. Berggren, Single-photon imager based on a superconducting nanowire delay line. *Nat. Photonics* **11**, 247–251 (2017)
26. B.H. Eom, P.K. Day, H.G. LeDuc, J. Zmuidzinas, A wideband, low-noise superconducting amplifier with high dynamic range. *Nat. Phys.* **8**, 623–627 (2012)
27. M. Ricci, N. Orloff, S.M. Anlage, Superconducting metamaterials. *Appl. Phys. Lett.* **87**, 034102 (2005)
28. C. Kurter, J. Abrahams, S.M. Anlage, Miniaturized superconducting metamaterials for radio frequencies. *Appl. Phys. Lett.* **96**, 253504 (2010)
29. M.W. Coffey, J.R. Clem, Unified theory of effects of vortex pinning and flux creep upon the RF surface impedance of type-II superconductors. *Phys. Rev. Lett.* **67**, 386 (1991)
30. V.K. Semenov, M.M. Khapaev, How moats protect superconductor films from flux trapping. *IEEE Trans. Appl. Supercond.* **26**, 1–10 (2016)

31. J. Bardeen, L.N. Cooper, J.R. Schrieffer, Theory of superconductivity, in *Selected Papers of J. Robert Schrieffer: In Celebration of His 70th Birthday* (2002), pp. 15–44
32. D. Gonnella, R. Eichhorn, F. Furuta, M. Ge, D. Hall, V. Ho, G., Hoffstaetter, M. Liepe, T. O'Connell, S. Posen, P. Quigley, Nitrogen-doped 9-cell cavity performance in a test cryomodule for LCLS-II. *J. Appl. Phys* **117**, 023908 (2015)
33. D. Rosenberg, S.J. Weber, D. Conway, D.R.W. Yost, J. Mallek, G. Calusine, R. Das, D. Kim, M.E. Schwartz, W. Woods, J.L., Yoder, Solid-state qubits: 3D integration and packaging. *IEEE Microw. Mag.* **21**, 72–85 (2020)
34. W.D. Oliver, P.B. Welander, Materials in superconducting quantum bits. *MRS Bull.* **38**, 816–825 (2013)
35. C. Müller, J.H. Cole, J. Lisenfeld, Towards understanding two-level-systems in amorphous solids: insights from quantum circuits. *Rep. Prog. Phys.* **82**, 124501 (2019)
36. P. Krantz, M. Kjaergaard, F. Yan, T.P. Orlando, S. Gustavsson, W.D. Oliver, A quantum engineer's guide to superconducting qubits. *Appl. Phys. Rev.* **6**, 021318 (2019)
37. A. Blais, R.S. Huang, A. Wallraff, S.M. Girvin, R.J. Schoelkopf, Cavity quantum electrodynamics for superconducting electrical circuits: an architecture for quantum computation. *Phys. Rev. A* **69**, 062320 (2004)
38. A. Wallraff, D.I. Schuster, A. Blais, L. Frunzio, R.S. Huang, J. Majer S. Kumar, S.M. Girvin, R.J. Schoelkopf, Strong coupling of a single photon to a superconducting qubit using circuit quantum electrodynamics. *Nature* **431**, 162–167 (2004)
39. J. Zmuidzinas, Superconducting microresonators: physics and applications. *Annu. Rev. Condens. Matter Phys.* **3**, 169–214 (2012)
40. C.R.H. McRae, H. Wang, J. Gao, M.R. Vissers, T. Brecht, A. Dunsworth, D.P. Pappas, J. Mutus, Materials loss measurements using superconducting microwave resonators. *Rev. Sci. Instrum.* **91**, 091101 (2020)
41. D.P. Pappas, M.R. Vissers, D.S. Wisbey, J.S. Kline, J. Gao, Two level system loss in superconducting microwave resonators. *IEEE Trans. Appl. Supercond.* **21**, 871–874 (2011)
42. J. Gao, J. Zmuidzinas, B.A. Mazin, H.G. LeDuc, P.K. Day, Noise properties of superconducting coplanar waveguide microwave resonators. *Appl. Phys. Lett.* **90**, 102507 (2007)
43. D. Bothner, T. Gaber, M. Kemmler, D. Koelle, R. Kleiner, Improving the performance of superconducting microwave resonators in magnetic fields. *Appl. Phys. Lett.* **98**, 102504 (2011)
44. A. Peacock, P. Verhoeve, N. Rando, A. Van Dordrecht, B.G. Taylor, C. Erd, M.A.C. Perryman, R. Venn, J. Howlett, D.J. Goldie, J., Lumley, Single optical photon detection with a superconducting tunnel junction. *Nature* **381**, 135–137 (1996)
45. D. Twerenbold, Giaever-type superconducting tunnelling junctions as high-resolution X-ray detectors. *EPL-Europhys. Lett.* **1**, 209 (1986)
46. E.M. Gershenzon, G.N. Goltsman, I.G. Gogidze, Yu.P. Gousev, A.I. Elantev, B.S. Karasik, A.D. Semenov, *Sov. J. Supercond.* **3**, 1582 (1990)
47. D. Büchel, P. Pütz, K. Jacobs, M. Schultz, U.U. Graf, C. Risacher, H. Richter, O. Ricken, H.W. Hübers, R. Güstenand, C.E. Honingh, 4.7-THz superconducting hot electron bolometer waveguide mixer. *IEEE Trans. Terahertz Sci. Technol.* **5**, 207–214 (2015)
48. Z.R. Lin, K. Inomata, K. Koshino, W.D. Oliver, Y. Nakamura, J.S. Tsai, T. Yamamoto, Josephson parametric phase-locked oscillator and its application to dispersive readout of superconducting qubits. *Nat. Commun.* **5**, 1–6 (2014)
49. K.M. Sliwa, M. Hatridge, A. Narla, S. Shankar, L. Frunzio, R.J. Schoelkopf, M.H. Devoret, Reconfigurable Josephson circulator/directional amplifier. *Phys. Rev. X* **5**, 041020 (2015)
50. M. Pechal, J.C. Besse, M. Mondal, M. Oppliger, S. Gasparinetti, A. Wallraff, Superconducting switch for fast on-chip routing of quantum microwave fields. *Phys. Rev. Appl.* **6**, 024009 (2016)
51. S.H. Talisa, M.A. Janocko, C. Moskowitz, J. Talvacchio, J.F. Billing, R. Brown, D.C. Buck, C.K. Jones, B.R. McAvoy, G.R. Wagner, D.H. Watt, Low-and high-temperature superconducting microwave filters. *IEEE Trans. Microw. Theory Techn.* **39**, 1448–1454 (1991)

52. R. Rafique, T. Ohki, P. Linner, A.Y. Herr, Niobium tunable microwave filter. *IEEE Trans. Microw. Theory Techn.* **57**, 1173–1179 (2009)
53. Y. He, S. Michibayashi, N. Takeuchi, N. Yoshikawa, Sharp-selectivity in-line topology low temperature superconducting bandpass filter for superconducting quantum applications. *Supercond. Sci. Technol.* **33**, 035012 (2020)
54. B.K. Sarkar, P. Usha, High temperature superconducting microwave filters. *IETE Tech. Rev.* **16**, 169–175 (1999)
55. G. Zhang, M.J. Lancaster, F. Huang, N. Roddis, An HTS wideband microstrip bandpass filter for L band receivers in radio astronomy observatory, in *European Microwave Conference (IEEE, 2007)*, pp. 450–453
56. T. Yu, C. Li, F. Li, Q. Zhang, L. Sun, L. Gao, Y. Wang, X. Zhang, H. Li, C. Jin, J. Li, Y. He, A wideband superconducting filter using strong coupling resonators for radio astronomy observatory. *IEEE Trans. Microw. Theory Tech.* **57**, 1783–1789 (2009)
57. J.S. Hong, E.P. McErlean, B. Karyamapudi, Narrowband high temperature superconducting filter for mobile communication systems. *IEE Proc.-Microw. Antennas Propag.* **151**, 491–496 (2004)
58. B. Cui, X. Zhang, L. Sun, Y. Bian, J. Guo, J. Wang, C. Li, H. Li, Q. Zhang, Y. He, A high-performance narrowband high temperature superconducting filter. *Chin. Sci. Bull.* **55**, 1367–1371 (2010)
59. K. Dustakar, S. Berkowitz, An ultra-narrowband HTS bandpass filter. In *IEEE MTT-S International Microwave Symposium Digest*, vol. 3 (2003), pp. 1881–1884
60. T. Kawaguchi, N. Shiokawa, K. Nakayama, T. Watanabe, T. Hashimoto, H. Kayano, Superconducting narrowband filter for receiver of weather radar. *IEICE Trans. Electron.* **92**, 296–301 (2009)
61. C. Li, T. Yu, Y. Bian, Y. Wu, J. Wang, X. Zhang, L. Sun, H. Li, Y. He, An ultranarrowband high-temperature superconducting bandpass filter with a fractional bandwidth of 0.02%. *IEEE Trans. Appl. Supercond.* **26**, 1–4 (2016)
62. W. Hattori, T. Yoshitake, K. Takahashi, An HTS 21-pole microstrip filter for IMT-2000 base stations with steep attenuation. *IEEE Trans. Appl. Supercond.* **11**, 4091–4094 (2001)
63. B.C. Liu, B.S. Cao, M.H. Zhu, G.Y. Zhang, W.J. He, X.B. Guo, S. He, Y.M. Wang, X.P. Zhang, Y.G. Zhao, H.S. Huang, An HTS 20-pole microstrip filter for GSM-1800 base stations. *J. Supercond.* **16**, 819–822 (2003)
64. X. Zhang, Q. Meng, F. Li, C. Li, S. Li, A. He, H. Li, Y. He, A 24-pole high T<sub>c</sub> superconducting filter for mobile communication applications. *Supercond. Sci. Technol.* **19**, S394 (2006)
65. T. Zhang, K. Yang, Z. Luo, Development of integration HTSC linear phase filter with external equalization. *IEEE Trans. Appl. Supercond.* **23**, 1501805–1501805 (2013)
66. J.S. Hong, E.P. McErlean, B. Karyamapudi, High-order superconducting filter with group delay equalization, in *IEEE MTT-S International Microwave Symposium Digest (IEEE, 2005)*, 4 pp
67. Z. Tao, Z. Xin-Jie, W. Xiao-Kun, Y. Hong-Wei, F. Lan, Y. Shao-Lin, High temperature superconducting filter with linear phase on LaAlO<sub>3</sub> substrates. *Acta. Phys. Sin.* **58**, 4194–4198 (2009)
68. L. Gao, L. Sun, F. Li, Q. Zhang, Y. Wang, T. Yu, J. Guo, Y. Bian, C. Li, X. Zhang, H. Li, 8-GHz narrowband high-temperature superconducting filter with high selectivity and flat group delay. *IEEE Trans. Microw. Theory Tech.* **57**, 1767–1773 (2009)
69. K.F. Raihan, R. Alvarez, J. Costa, G.L. Hey-Shipton, Highly selective HTS band pass filter with multiple resonator cross-couplings. *Presented at MTT-S International Microwave Symposium Digest (Cat. No. 00CH37017)*, vol. 2 (IEEE, 2000), pp. 661–664
70. G. Tsuzuki, M. Suzuki, N. Sakakibara, Superconducting filter for IMT-2000 band. *IEEE Trans. Microw. Theory Tech.* **48**, 2519–2525 (2000)
71. R.R. Mansour, S. Ye, S.F. Peik, V. Dokas, B. Fitzpatrick, Quasi-dual-mode resonators. *IEEE Trans. Microw. Theory Tech.* **48**, 2476–2481 (2000)
72. R.R. Mansour, Microwave superconductivity. *IEEE Trans. Microw. Theory Tech.* **50**, 750–759 (2002)

73. R.R. Mansour, V. Dokas, U.S. Patent 5,585,331 (1996)
74. W.I. Yang, S. Lee, H.S. Jung, H.R. Kim, S.Y. Lee, Homogeneity in the microwave surface resistance of large  $\text{YBa}_2\text{Cu}_3\text{O}_{7-8}$  superconductor films coated with Au. *Electron. Mater. Lett.* **16**, 216–223 (2020)
75. F. Wang, X.P. Zhang, L.M. Gao, B. Wei, B.S. Cao, B.X. Gao, Characteristics of low noise 800 MHz amplifier at cryogenic temperature. *Paper Presented at ICMMT 4th International Conference on, Proceedings Microwave and Millimeter Wave Technology* (IEEE, 2004), pp. 991–994
76. W.H. Louisell, A.Yariv, A.E. Siegman, Quantum fluctuations and noise in parametric processes. I. *Phys. Rev.* **124**, 1646 (1961)
77. M.W. Pospieszalski, Extremely low-noise amplification with cryogenic FETs and HFETs: 1970–2004. *IEEE Microw. Mag.* **6**, 62–75 (2005)
78. Z. Tong, C. Lundström, P.A. Andrekson, C.J. McKinstrie, M. Karlsson, D.J. Blessing, E. Tipsuwannakul, B.J. Puttnam, H. Toda, L. Grüner-Nielsen, Towards ultrasensitive optical links enabled by low-noise phase-sensitive amplifiers. *Nat. Photonics* **5**, 430 (2011)
79. M.A. Castellanos-Beltran, K.W. Lehnert, Widely tunable parametric amplifier based on a superconducting quantum interference device array resonator. *Appl. Phys. Lett.* **91**, 083509 (2007)
80. N. Newman, W.G. Lyons, High-temperature superconducting microwave devices: fundamental issues in materials, physics, and engineering. *J. Supercond.* **6**, 119–160 (1993)
81. R.C. Hansen, Superconducting antennas. *Paper presented at Seventh International Conference on Antennas and Propagation, ICAP 91 (IEE)* (IET, 1991), pp. 555–558
82. W.M. Faisal, High  $T_c$  superconducting fabrication of loop antenna. *Alex. Eng. J.* **51**, 171–183 (2012)
83. X. Gao, J. Du, A.R., Weily, T. Zhang, C.P. Foley, Y.J. Guo, Broadband antenna-coupled high-temperature superconducting Josephson-junction mixer for terahertz communication applications. *Paper presented at 41st International Conference on Infrared, Millimeter, and Terahertz waves (IRMMW-THz)* (IEEE, 2016), pp. 1–2
84. A. Kawakami, S. Saito, M. Hyodo, Fabrication of nano-antennas for superconducting infrared detectors. *IEEE Trans. Appl. Supercond.* **21**, 632–635 (2011)
85. T. Ulversoy, Software defined radio: challenges and opportunities. *IEEE Commun. Surv. Tutor.* **12**, 531–550 (2010)
86. I.V. Vernik, D.E. Kirichenko, V.V. Dotsenko, R. Miller, R.J. Webber, P. Shevchenko, A. Talalaevskii, D. Gupta, O.A. Mukhanov, Cryocooled wideband digital channelizing radio-frequency receiver based on low-pass ADC. *Supercond. Sci. Technol.* **20**, S323 (2007)
87. A. Inamdar, S. Rylov, A. Talalaevskii, A. Sahu, S. Sarwana, D.E. Kirichenko, I.V. Vernik, T.V. Filippov, D. Gupta, Progress in design of improved high dynamic range analog-to-digital converters. *IEEE Trans. Appl. Supercond.* **19**, 670–675 (2009)
88. D. Gupta, A.A. Inamdar, D.E. Kirichenko, A.M. Kadin, O.A. Mukhanov, Superconductor analog-to-digital converters and their applications. *Paper presented at IEEE MTT-S International Microwave Symposium* (IEEE, 2011), pp. 1–4
89. V.K. Kornev, A.V. Sharafiev, I.I. Soloviev, N.V. Kolotinskiy, O.A. Mukhanov, A guide to active antennas based on superconducting quantum arrays. *IEEE Trans. Appl. Supercond.* **26**, 1–4 (2016)
90. M. Yu, H. Geng, T. Hua, W. Xu, Z.N. Chen, Reactance matching for superconducting YBCO Josephson junction detector using bowtie antenna. *Paper presented at IEEE Asia-Pacific Conference on Antennas and Propagation (APCAP)* (IEEE, 2018), pp. 1–2
91. E. Holdengreber, A.G. Moshe, M. Mizrahi, V. Khavkin, S.E. Schacham, E. Farber, High sensitivity high  $T_c$  superconducting Josephson junction antenna for 200 GHz detection. *J. Electromagn. Waves Appl.* **33**, 193–203 (2019)
92. H.J.M. Ter Brake, Cooling and packaging of RF components, in *Microwave Superconductivity* (Springer, Dordrecht, 2001), pp. 271–304
93. H.J. ter Brake, G.F.M. Wiegerinck, Low-power cryocooler survey. *Cryogenics* **42**, 705–718 (2002)

94. H.J. ter Brake, F.I. Buchholz, G. Burnell, T. Claeson, D. Cr  t  , P. Febvre, G.J. Gerritsma, H. Hilgenkamp, R. Humphreys, Z. Ivanov Jutzi, SCENET roadmap for superconductor digital electronics. *Phys. C Supercond.* **439**, 1–41 (2006)
95. D.B. Tuckerman, M.C. Hamilton, D.J. Reilly, R. Bai, G.A. Hernandez, J.M. Hornibrook, J.A. Sellers, C.D. Ellis, Flexible superconducting Nb transmission lines on thin film polyimide for quantum computing applications. *Supercond. Sci. Technol.* **29**, 084007 (2016)
96. S. Steinhauer, S. Gyger, V. Zwiller, Progress on large-scale superconducting nanowire single-photon detectors. *App. Phys. Lett.* **118**, 100501 (2021)
97. V. Struzhkin, B. Li, C. Ji, X.J. Chen, V. Prakapenka, E. Greenberg, I. Troyan, A. Gavriluk, H.K., Mao, Superconductivity in La and Y hydrides: remaining questions to experiment and theory. *Matter Radiat. Extrem.* **5**, 028201 (2020)
98. F. Peng, Y. Sun, C.J. Pickard, R.J. Needs, Q. Wu, Y. Ma, Hydrogen clathrate structures in rare earth hydrides at high pressures: possible route to room-temperature superconductivity. *Phys. Rev. Lett.* **119**, 107001 (2017)
99. A.P. Drozdov, P.P. Kong, V.S. Minkov, S.P. Bes  din, M.A. Kuzovnikov, S. Mozaffari, L. Balicas, F.F. Balakirev, D.E. Graf, V.B. Prakapenka, E. Greenberg, Superconductivity at 250 K in lanthanum hydride under high pressures. *Nature* **569**, 528–531 (2019)
100. M. Somayazulu, M. Ahart, A.K. Mishra, Z.M. Geballe, M. Baldini, Y. Meng, V.V. Struzhkin, R.J. Hemley, Evidence for superconductivity above 260 K in lanthanum superhydride at megabar pressures. *Phy. Rev. Letts* **122**, 027001 (2019)